UNIVERSITY OF SOUTHAMPTON

Faculty of Engineering and Physical Sciences
School of Physics and Astronomy

Probing the Inner Regions of Active Galactic Nuclei through Variability Analysis

by

Ella Guise

MPhys

ORCiD: 0000-0002-5957-6202

A thesis for the degree of
Doctor of Philosophy

November 2022

University of Southampton

Abstract

Faculty of Engineering and Physical Sciences
School of Physics and Astronomy

Doctor of Philosophy

Probing the Inner Regions of Active Galactic Nuclei through Variability Analysis

by Ella Guise

Active Galactic Nuclei (AGN) are the some of the most luminous objects in the Universe, however their large distances and compact sizes limits our ability to directly study the physical processes that are occurring within their inner regions. Indirect methods are therefore necessary to probe the central regions, including analysing the strong variability that is a ubiquitous property of AGN emission. The motivation of this thesis is therefore to expand upon our knowledge of the inner regions of different types on AGN through in depth analysis of individual objects, as well as to prepare for the large influx of AGN that will be observed in future large scale surveys.

Firstly, I present spectral and temporal variability analysis of the blazar PKS 0027-426 using optical and infrared (IR) observations. The results show that the emission from different wavelength ranges occurs either simultaneously, or on timescales smaller than the cadences of observations, and I further demonstrate that the emission could contain different contributions from multiple different coloured variable components within the different wavelength ranges. I then measure delays between the IR response to the optical light curves of the Seyfert 1 galaxy Zw229-015, and proceed to model the IR response using simulations of the dust distribution. The results show that the different IR wavelength ranges are likely dominated by the same hot dust emission, and that the observed IR emission is not well modelled by a single dust component, but the majority of dust is distributed in an inclined extended flat disk. Finally, I simulate mock AGN light curves in an attempt to understand the capabilities and limitations of recovering properties of the underlying power spectral density functions (PSDs) for AGN that will be observed with the upcoming Vera C. Rubin Observatory Legacy Survey of Space and Time (LSST). I find that the ability to recover properties such as characteristic timescales or power law slopes is reasonably similar for the main proposed observing strategy and for the more frequent, deeper observations, however I also show that very few potential quasi-periodicities within the AGN light curves can be recovered with the current proposed LSST cadencing using this PSD analysis.

"Long story short, I survived."

- Taylor Swift: Long Story Short

Contents

List of Figures

List of Tables

Declaration of Authorship

I declare that this thesis and the work presented in it is my own and has been generated by me as the result of my own original research.

I confirm that:

1. This work was done wholly or mainly while in candidature for a research degree at this University;
2. Where any part of this thesis has previously been submitted for a degree or any other qualification at this University or any other institution, this has been clearly stated;
3. Where I have consulted the published work of others, this is always clearly attributed;
4. Where I have quoted from the work of others, the source is always given. With the exception of such quotations, this thesis is entirely my own work;
5. I have acknowledged all main sources of help;
6. Where the thesis is based on work done by myself jointly with others, I have made clear exactly what was done by others and what I have contributed myself;
7. Parts of this work have been published as: E. Guise et al. Multiwavelength optical and NIR variability analysis of the Blazar PKS 0027-426. *Monthly Notices of the RAS*, 510(3):3145–3177, March 2022a. , E. Guise et al. Dust reverberation mapping and light-curve modelling of Zw229-015. *Monthly Notices of the RAS*, 516(4):4898–4915, November 2022b.

Signed:..... Date:.....

Acknowledgements

I would like to firstly thank my supervisor, Sebastian Hönig, for his guidance and support throughout this entire PhD. Without his enthusiasm and faith in my work, I would not have been able to accomplish everything that I have.

I would also like to thank Triana Almeyda, who might not have officially been my secondary supervisor but always acted as one. I truly appreciate her advice and encouragement throughout, and am especially thankful for the support that she gave along with Bella Boulderstone at the start of my PhD.

My time at Southampton would not have been the same without the past and present members of the Astronomy group. I would like to thank those that I shared office 4053 with, for their dedication to procrastination and for eagerly participating in office drinks whenever the opportunity arose. I also extend my thanks to those who I embarked on numerous trips to the pub with, and those whose friendship continued throughout the pandemic virtually.

I would also like to thank my family and my friends outside of Southampton. I'd especially like to thank my mother for constantly critiquing my vegetable intake while simultaneously sending me chocolate throughout my thesis writing, and my father for sharing my enthusiasm for space (and the moon in particular) - without that trip to the Kennedy space center I might not have even considered this as a career path.

Finally, I extend my eternal thanks to Michael Johnson. Though his jokes are nearly always terrible, and his advice at times can be questionable (yet usually well-meaning), I would not have been able to complete this PhD without his support. His role as a rubber duck was truly invaluable, and I am endlessly grateful to him for all of the proofreading (of this thesis, my papers, and far too many emails), and for always being around to answer my questions. I am also indebted to him, as well as his parents Viv and Andy, for keeping me housed and for supporting me even after he ran away to Germany.

This work was made possible by financial support from the Science and Technology Facility Council (STFC).

Nomenclature

Definitions

ACF Auto Correlation Function

AD Accretion Disk

AGN Active Galactic Nuclei

BEL Broad Emission Line

BL Lac BL Lacertae Objects

BLR Broad Line Region

BPL Broken Power Law

BWB Bluer When Brighter

CCF Cross Correlation Function

DDF Deep Drilling Field

DES Dark Energy Survey

DRM Dust Reverberation Mapping

DRW Damped Random Walk

DTF Dust Transfer Function

FOV Field of View

FSRQ Flat Spectrum Radio Quasar

HJD Heliocentric Julian Date

ICCF Interpolated Cross Correlation Function

IR Infrared

JD Julian Date

LSP Lomb-Scargle Periodogram

LSST Vera C. Rubin Observatory Legacy Survey of Space and Time

M-ICCF Modified Interpolated Cross Correlation Function

MCMC Monte Carlo Markov Chain

MIR Mid Infrared

MJD Modified Julian Date

NEL Narrow Emission Line

NIR Near Infrared

NLR Narrow Line Region

PSD Power Spectral Density

QPO Quasi-Periodic Oscillation

QSO Quasi-Stellar Object (Quasar)

RL Radio Loud

RM Reverberation Mapping

RQ Radio Quiet

RWB Redder When Brighter

S-ICCF Standard Interpolated Cross Correlation Function

SED Spectral Energy Distribution

SF Structure Function

SMBH Super-Massive Black Hole

SMBHB SMBH Binary

SPL Single Power Law

SWB Stable When Brighter

VEILS VISTA Extragalactic Infrared Legacy Survey

VOILETTE VEILS OptIcal Infrared Light curves of Extragalactic TransienT Events

WFD Wide Fast Deep

Symbols

c	Speed of light in a vacuum
G	Gravitational constant
h	Planck constant
k	Boltzmann constant
$M_\odot$	Solar mass

Chapter 1

Introduction

Some galaxies in our universe contain a compact, highly luminous ($L \sim 10^{42} - 10^{48}$ erg s^{-1}, Woo and Urry 2002) central region that emits such high amounts of radiation that it can outshine the emission from the rest of the galaxy. Such galaxies are known as active galaxies. The excessive radiation occurs when the supermassive black hole (SMBH), which has been established to exist in the centre of most, if not all, galaxies (Ferrarese and Ford, 2005), is actively accreting material from its surroundings, during which time it presents as an active galactic nuclei (AGN).

AGN are some of the most powerful, persistent sources of luminosity in the universe, and are known to emit widely across the entire electromagnetic spectrum. One key observational feature of AGN emission is their variability, which occurs on timescales of minutes to years (e.g., Ulrich et al., 1997). This variability has been frequently used to both identify AGN from other extragalactic objects (e.g., Kozłowski et al., 2010; Peters et al., 2015) and to classify them into the various sub-types (e.g., Choi et al., 2014; Cartier et al., 2015).

Whilst some regions of AGN can be spatially resolved, this is only possible for the larger components (down to the order of parsecs; e.g., Prieto et al. 2004; Kishimoto et al. 2009; Gravity Collaboration et al. 2020) and is limited to nearby, relatively bright sources. As such, the inner regions of a larger sample of AGN require indirect analysis in order to further constrain the dynamics and geometries of the central regions. The variable nature of AGN emission is one such probe that allows us to explore the central regions and physical processes that occur within the AGN that are not directly resolvable due to their small angular sizes.

1.1 Accretion onto SMBHs

The majority of the thermal radiation produced in AGN is believed to be a result of accretion onto the SMBH, where a huge amount of energy is released as the binding gravitational energy of the in-falling material is converted into heat and radiation.

For matter of mass m that is falling onto a compact object of mass M from a large distance (assumed to be infinity for simplicity) to a distance of r from the central compact object, the kinetic energy is at equilibrium with the gravitational potential energy when,

$$\frac{1}{2}mv^2 = \frac{GMm}{r} \tag{1.1}$$

where v is the velocity of the particle in free-fall.

When the matter reaches the surface of the compact object at radius $r = R$, some of the kinetic energy is radiated away as thermal energy at a rate of $\frac{1}{2}\dot{m}v^2$, where $\dot{m}$ is the accretion rate of material onto the SMBH. The luminosity, L, is therefore given in Equation 1.2.

$$L = \frac{1}{2}\dot{m}v^2 = \frac{GM}{R}\dot{m} \tag{1.2}$$

Considering the Schwarzchild radius, R_S, of the black hole that is expressed as $R_S = \frac{2GM}{c^2}$, the luminosity from the accretion onto the SMBH can be expressed as given in Equation 1.3.

$$L = \eta\dot{m}c^2 \tag{1.3}$$

where $\eta = \frac{R_S}{2R}$ is the efficiency factor that converts the potential energy to radiation.

Assuming a steady spherical accretion flow of fully ionized gas, an upper limit for the radiative luminosity was defined where the gravitational force is equal to the radiation pressure. The luminosity that satisfies this condition is referred to as the Eddington luminosity, L_{Edd}, and is shown in Equation 1.4 to depend solely on the mass of the accreting object.

$$L_{\text{Edd}} = \frac{4\pi GMm_p c}{\sigma_T} \simeq 1.26 \times 10^{38}\frac{M}{M_\odot} \tag{1.4}$$

where m_p is the mass of a proton and σ_T is the Thomson scattering cross section of an electron.

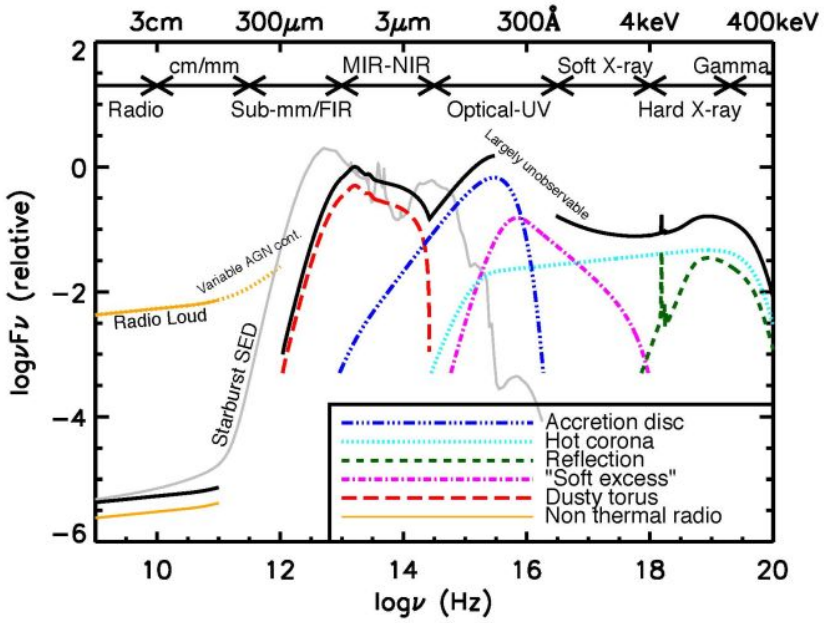

FIGURE 1.1: An example multiwavelength SED of an unobscured type 1 AGN, with contributions from different components, where the black solid line represents the total SED and the various coloured lines represent the individual components. The arrows depict the different wavelength regions. Image Credit: Harrison (2014).

If the object is only powered by accretion, then this also puts a limit on the accretion rate, $\dot{M}_{\rm Edd}$ (i.e., the Edddington rate), which is related to the Eddington Lumnoisty as,

$$\dot{M}_{\rm Edd} = L_{\rm Edd}\frac{r}{GM} \tag{1.5}$$

Theoretically, if the luminosity were to surpass $L_{\rm Edd}$, or the accretion exceeded $\dot{M}_{\rm Edd}$, the then radiation pressure would overtake the gravitational attraction and accretion would halt. However in reality, this limit can be exceeded due to non-spherical geometry or instabilities. Objects with luminosities greater than $L_{\rm Edd}$ with super-Eddington accretion rates are therefore believed to exist, for example, short periods of super-Eddington accretion have been suggested to explain the fast growth of SMBHs (e.g., Volonteri et al., 2015).

1.2 Structure of an AGN

The standard model of AGN suggests that they are composed of several main components, including; the SMBH, accretion disk (AD), corona, broad line region (BLR), torus, and a narrow line region (NLR). Additionally, in radio loud galaxies, relativistic jets are also present. These components are outlined in more detail here, in order of distance from the centre of the AGN. Figure 1.1 displays an example of a

typical spectral energy distribution (SED) of an unobscured AGN, showing the components that contribute to the overall SED in each wavelength range.

SMBH Located at the centre of the AGN is a SMBH, whose mass ranges from 10^6-10^{10} $M_\odot$ (e.g., Kormendy and Richstone, 1995), that is actively accreting matter from its surroundings due to its high gravitational field. The first image of a SMBH in the centre of the elliptical galaxy M87 was taken recently using the Event Horizon Telescope (Event Horizon Telescope Collaboration et al., 2019).

Accretion Disk Due to the conservation of angular momentum, the material that is drawn in to the SMBH is forced to spin in the object's plane of rotation, forming a geometrically thin, optically thick AD (e.g., Shakura and Sunyaev, 1973b; Sun and Malkan, 1989), which spans $\sim 10^{-2}$ pc (e.g., Peterson, 1993). The AD is believed to be responsible for the majority of thermal emission detected from AGN, as the gravitational potential energy of the infalling matter is converted into thermal energy. This heats the AD to temperatures of $10^4 - 10^5$ K (Bonning et al., 2007), and results in a large amount of energy being re-radiated away in a black body spectrum, as given in Equation 1.6 (Rybicki and Lightman, 1986).

$$B_v(T(R)) = \frac{2h\nu^3}{c^2} \frac{1}{e^{(h\nu/kT(R))} - 1} \tag{1.6}$$

where $T(R)$ is the temperature of the disk at a given radius from the centre, R, which for an optically thick AD is approximately given Equation 1.7 (Peterson, 1997), and ν is the frequency.

$$T(R) \propto \left(\frac{R}{R_S}\right)^{-3/4} \tag{1.7}$$

where R_S is approximately the inner radius of the AD.

The total spectrum of emission from the AD is therefore a composite black body spectrum, containing emission corresponding to different locations (and therefore temperatures) within the AD, as depicted in Figure 1.2. For the expected AD temperatures, the emission is primarily observed in the optical/UV spectrum (Peterson, 1997), creating the "Big Blue Bump" seen in the overall spectra at these wavelengths.

AD physics is often described by dynamical, thermal, and viscous processes that correspond to different timescales. The fastest is the dynamical (or orbital) timescale, $\tau_{\rm dyn}$, which describes the time necessary for the system to reach hydrostatic equilibrium. If the AD is Keplerian and non self-gravitating, this can be related to the mass, M, of the central object as shown in Equation 1.8.

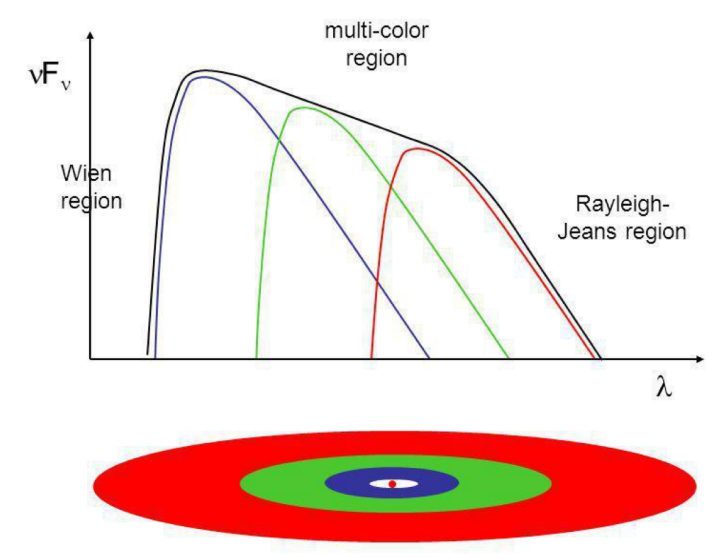

FIGURE 1.2: Composite SED emitted by an accretion disk. Image Credit: Disk Thermal Structure Lecture by C.P. Dullemond.

$$\tau_{\rm dyn} = \sqrt{\frac{r^3}{GM}} \tag{1.8}$$

The thermal timescale, $\tau_{\rm th}$, describes the time necessary for the disk to recover thermal equilibrium, and is shown to be related to the dynamical timescale in Equation 1.9.

$$\tau_{\rm th} = \alpha^{-1}\tau_{\rm dyn} \tag{1.9}$$

where $\alpha \lesssim 1$ is the viscosity parameter of the thin disk model as introduced by Shakura and Sunyaev (1973a).

Lastly, the viscous timescale, $\tau_{\rm visc}$, describes the time in which matter diffuses through the disk over a distance, r, as given in Equation 1.10.

$$\tau_{\rm visc} = \tau_{\rm th}\left(\frac{r}{H_d}\right)^2 \tag{1.10}$$

where H_d is the thickness of the AD.

Assuming $\alpha = 0.1$ (e.g., King et al., 2007), these timescales are expected on the order of $\tau_{\rm dyn} \sim$ days, $\tau_{\rm th} \sim$ months - years, $\tau_{\rm visc} \gtrsim$ years for AGN (e.g., Noda and Done, 2018).

Corona An optically thin, hot (T $\sim 10^9$ K) cloud of relativistic electrons is thought to reside around the AD, forming the corona (Haardt and Maraschi, 1993), however the exact location, geometry, and origin are not well understood. One theory suggests that electrons scatter from the disk to form the corona, and photons emitted from the AD

are then inverse Compton scattered by these electrons to hard X-ray energies (Liang and Thompson, 1979).

Broad Line Region A region of high velocity ($\sim 10^3$-10^4 km/s), dense ($\sim 10^{10}$ cm^{-3}) gas clouds is located at a distance of 0.1-1 pc from the SMBH (e.g., Peterson, 1993). As the name suggests, these clouds produce broad emission lines in the optical spectra due to photo-ionisation of the gas by radiation from the AD (Davidson and Netzer, 1979). The widths of these lines are broad owing to the high velocities of the gas (i.e., due to Doppler broadening, Clavel et al. 1991), and as a result, assuming virial equilibrium the widths of the emission lines, ΔV, can be used to estimate the mass of the black hole, $M_{\rm BH}$, as shown in Equation 1.11. Furthermore, the size of the BLR has been shown to correlate with the luminosity of the AGN (e.g., Kaspi et al., 2000; Bentz et al., 2013) and as such, a method of estimating the mass of the black hole using data from a single epoch has been developed (e.g., Vestergaard, 2002; Shen et al., 2011).

$$M_{\rm BH} = \frac{R_{\rm BLR} V_{\rm BLR}^2}{G} = \frac{R_{\rm BLR} f \Delta V^2}{G} \tag{1.11}$$

where $R_{\rm BLR}$ is the radius of the BLR, and f is the virial factor that accounts for differences between the observed widths of the lines and the virial velocity, $V_{\rm BLR}$ which arises due to the geometry of the gas distribution being unknown.

The virial factor is typically determined by comparing these measurements of $M_{\rm BH}$ with masses estimated using a relation with the stellar velocity dispersion in local galaxies (e.g., Onken et al., 2004; Woo et al., 2015; Graham, 2016). Assuming that this virial factor remains constant could lead to uncertainties in the estimation of the mass of the SMBH however, as it could have a dependence on additional physical properties of the AGN, including the relative thickness of the BLR orbital plane (e.g., Gaskell, 2009), and the inclination angle of this plane with respect to our line of sight (e.g., Wills and Browne, 1986; Shen and Ho, 2014).

Dusty "Torus" A geometrically and optically thick dust emitting region surrounds the central engine at a distance of $\sim$ 1-10 pc (e.g., Krolik and Begelman, 1988b). The inner radius of the dust emitting region corresponds to the dust sublimation radius, which correlates with the AGN luminosity (e.g., Barvainis, 1987; Suganuma et al., 2006), and the outer radius bound by the gravitational sphere of influence from the SMBH (e.g., Alexander and Hickox, 2012). It has long been believed that this dust emission region can obscure direct observations of the optical and UV emissions depending on orientation of the AGN with respect to the observer (e.g., Krolik and Begelman, 1988a).

The dust absorbs the emission from the central engine, re-emitting it as a blackbody at infrared (IR) wavelengths. The radial temperature profile of the dust emission is given by Equation 1.12.

$$T(R) = T_{\text{sub}} \left(\frac{R}{R_{\text{sub}}} \right)^{\frac{-2}{4+\gamma}} \tag{1.12}$$

where T_{sub} is the sublimation temperature, R_{sub} is the sublimation radius, and γ is the dust IR opacity power law index, which is approximately 1.6 for standard interstellar dust material dust grains (Barvainis, 1987).

Initially, models of the dust followed a smooth, homogeneous distribution, however it is actually believed to be distributed in clumps, both theoretically (e.g., Krolik and Begelman, 1988b; Tacconi et al., 1994) and with evidence from observations (e.g., Shi et al., 2006; Tristram et al., 2007).

Furthermore, there has been evidence provided that suggests the classical circumnuclear torus model is not solely able to explain the observed behaviour of all AGN. For example, a torus-like structure might be missing from AGN that are observed with little to no obscuration detected but are still missing the broad optical emission lines (dubbed "true" type 2 AGN), though these are believed to be uncommon in AGN (Shi et al., 2010). Furthermore, a second component which takes the form of an extended polar structure can also exist (e.g., Raban et al., 2009; Hönig et al., 2012, 2013; Leftley et al., 2018) as the result of a radiatively driven dust wind from the inner region (Hönig et al., 2012).

The distribution of dust within the AGN can be spatially resolved using IR interferometry for relatively bright, nearby AGN. For example, near-IR (NIR) interferometry has been performed to constrain the inner radius of the dust emitting region for several objects (e.g., Swain et al., 2003; Kishimoto et al., 2009; Weigelt et al., 2012). Additionally, mid-IR (MIR) interferometry has been used to estimate the overall size of the dust distribution in multiple AGN, and furthermore has shown that polar dust can be the dominant source of MIR emission in AGN (e.g., Raban et al., 2009; Hönig et al., 2012, 2013; Leftley et al., 2018).

Narrow Line Region The NLR is a bi-conical structure of less dense ($\sim 10^3 \text{cm}^{-3}$), slower moving ($\sim$ 500 km/s) gas clouds than in the BLR, which extends beyond the torus to distances of a few kpcs (e.g., Peterson, 1997). The gas in the NLR is also ionized by radiation from the central engine, producing emission lines in the optical spectra that are narrower than the BLR due to the slower velocities. As the gas is less dense in the NLR than the BLR, collisional timescales can be longer than forbidden radioactive decay timescales, therefore both permitted and forbidden narrow emission lines are commonly observed (e.g., Peterson, 1997).

As the NLR spans distances of up to a few kpcs, it has been resolved in some optical and IR images (e.g., Tadhunter and Tsvetanov, 1989; Bennert et al., 2006; Scharwächter et al., 2011).

Jets Collimated relativistic jets of plasma have been detected in 10-15 % of AGN (e.g., Kellermann et al., 1989; Wilson and Colbert, 1995). They are aligned in the polar direction and have been observed to extend up to distances of kpc - Mpc from the central engine.

An electromagnetic origin, initially introduced by Blandford and McKee (1982), is typically used to explain the formation of these jets. This theory suggests that the jets are powered by a strongly magnetised AD that surrounds a rotating SMBH, which can create an electric field that is capable of accelerating charged particles to velocities approaching the speed of light.

Two basic components are thought to contribute to the emission produced in the jets. The first of which is synchrotron radiation, which dominates the frequency ranges of radio to X-rays and peaks in the UV to IR. The synchrotron radiation is produced as the collimated jets of plasma are threaded with magnetic fields, and the charged relativistic particles spin around these field lines (e.g., Urry and Mushotzky, 1982). The high frequency emission, which spans the X-rays to gamma-rays, is said to be dominated by inverse Compton scattering in leptonic models, either from synchrotron photons scattered to higher energies by the relativistic charged particles (synchrotron self-Compton, e.g. Urry and Mushotzky 1982) or from external photons (external Compton, e.g. Dermer and Schlickeiser 1993). Alternatively, hadronic models explain the high frequency radiation as emission from relativistic protons (e.g., Mücke and Protheroe, 2001).

1.3 AGN Taxonomy and Unification Theories

AGN are often divided into a large number of different classes depending on different criteria including properties such as their luminosities and observable wavelengths. The most relevant subclasses of AGN to this thesis are outlined here.

Seyfert Galaxies Seyfert galaxies are lower luminosity AGN, typically described by $M_B > -23$ (Schmidt and Green, 1983). They are found as point-like nuclei that are clearly visible in their host galaxies, which are predominantly early type spiral galaxies (e.g., Adams, 1977). The emission from the AGN is of the order of the entire host galaxy, which was the original definition of these objects from Seyfert (1943).

Initially they were divided into type 1 or 2 (Sy1 or Sy2) depending on the Balmer lines in their spectra (Osterbrock, 1977), though now they are typically related to the orientation of the object, as described in Section 1.3.1.1. Intermediate types were later defined by Osterbrock (1981) with values between 1 and 2 that are classified by the widths of the Balmer lines.

Quasars Quasars are often considered to be the more luminous versions of Seyfert galaxies, with $M_B < -23$ (Schmidt and Green, 1983). They are found at greater distances and are so luminous that they completely outshine their host galaxies. As a result, they resemble stellar-like objects in the optical bands, and as such were named quasi-stellar objects (QSOs) which was eventually contracted to the term 'quasar' (Page, 1964). Similar to Seyfert galaxies, quasars can be further divided into type 1 and type 2 depending on the presence of broad emission lines in their spectra as described in Section 1.3.1.1.

Blazars Blazars are the most extreme subclass of AGN, whose radiation is considered to be dominated by the bright, relativistic jet less than 10° from the line of sight (e.g., Urry and Padovani, 1995b).

Blazars can be further divided into two main categories based on their optical spectra; Flat Spectrum Radio Quasars (FSRQs) and BL Lacertae objects (BL Lacs), as the spectra of FSRQs contain strong, broad emission lines similar to quasars, whilst BL Lacs are characterized by a relatively featureless optical continuum.

1.3.1 Unification

Despite the observational differences between the different subclasses of AGN, unification theories have been presented in an attempt to explain the many shared characteristics that are also observed. As a result, AGN are typically classified based on two main properties; the first of which is their optical/UV spectra and the second is by their radio emission, as shown in Table 1.1.

1.3.1.1 Classification by Optical Spectra

AGN can be divided into three main subtypes based on their optical/UV spectra; type 1, which are AGN that have broad emission lines (BELs) and narrow emission lines (NELs) present in their spectra, type 2, which are AGN that only have NELs in their spectra, and type 0, which are AGN with weak or unusual optical/UV line emission. Examples of the optical/UV spectra of different subclasses of AGN are displayed in Figure 1.3.

Properties of Optical Spectra

Radio Loudness	Type 0 (unusual)	Type I (bright continua and BELs[a] and NELs[b])	Type II (weak continua and only NELs[b])
Radio Quiet		Seyfert I QSO[c] LINER[d] I	Seyfert II QSO[c] 2 LINER[d] II
Radio Loud	BL Lacs[e]	BLRG[f] { SSRQ[g] / FSRQ[h] }	NLRG[i] { FR[j] I / FR[j] II }

[a] = Broad Emission Lines.
[b] = Narrow Emission Lines.
[c] = Quasi-Stellar Objects.
[d] = Low-Ionization Nuclear Emission line Region.
[e] = BL Lacertae Objects.
[f] = Broad Line Radio Galaxies.
[g] = Steep Spectrum Radio Quasars.
[h] = Flat Spectrum Radio Quasars.
[i] = Narrow Line Radio Galaxies.
[j] = Fanaroff Riley.

TABLE 1.1: Classification of AGN based on properties of their optical spectra and radio loudness. Adapted from Lawrence (1987).

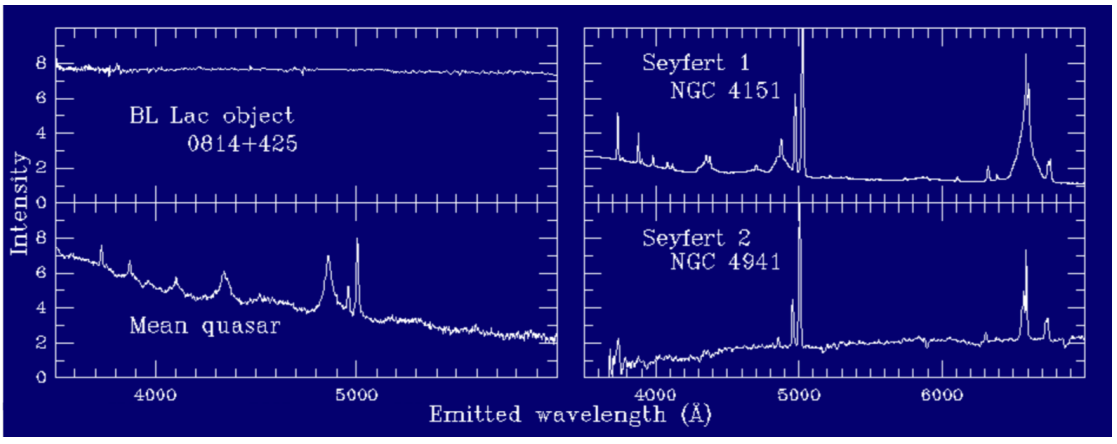

FIGURE 1.3: Example optical spectra for different subclasses of AGN. Adapted from: https://pages.astronomy.ua.edu/keel/agn/spectra.html

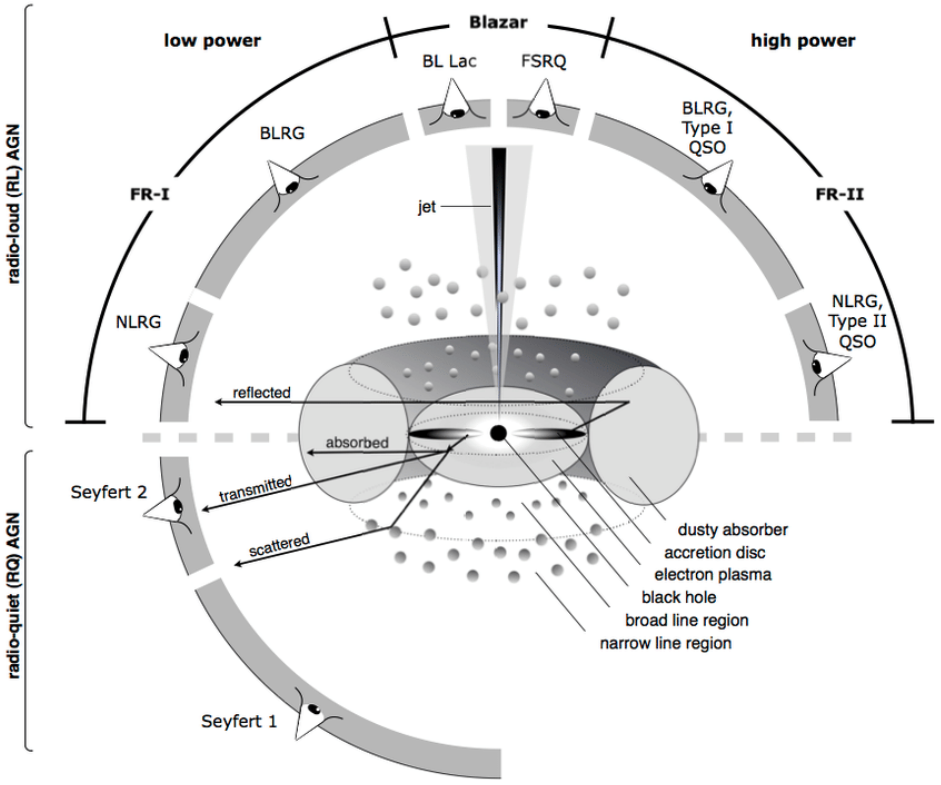

FIGURE 1.4: A schematic representation of the structure of an AGN and the unified models. Image Credit: Beckmann and Shrader (2012).

Unification schemes attempt to unite these subclasses of AGN through their observed orientation with respect to our line of sight, where the presence of a dusty torus can obscure the broad line emission (e.g., Antonucci, 1993; Krolik and Begelman, 1988b; Urry and Padovani, 1995a), as demonstrated by Figure 1.4. In this model, AGN that are viewed with angles close to the disk (i.e., that are viewed edge-on) correspond to type 2, where direct emission from the BLR is blocked by the dust emitting region. Alternatively, AGN viewed with angles closer to the pole (i.e., that are viewed face-on) have a clear line of sight to the BLR and correspond to type 1. NELs are visible in both type 1 and 2 as the NLR is shown to be more extended than the BLR and lies above the dust emission region which means it is therefore not obscured by it. Unusual spectral behaviour seen in type 0 AGN is thought to occur when the AGN are viewed with very small angles to the pole, as their spectra can be influenced by the non-thermal relativistic jet or by outflowing gas along the line of sight.

Unifying type 1 and 2 AGN through an obscuring dusty torus could explain some observed phenomena, such as the presence of a high polarization in the broad Hα line of 3C 234 (Antonucci, 1984), as if the emission from the BLR is obscured and scattered by the torus, it could produce the observed polarized spectra.

There are still some discrepancies within this unification theory however, as changing-look AGN have been observed to vary from type 1 to type 2 via the

appearance or disappearance of their Balmer emission lines on timescales of $\sim$ a few years (e.g., LaMassa et al., 2015). Additionally, some AGN have been observed without broad emission lines and with little to no obscuration detected, though these objects are believed to be rare (e.g., Shi et al., 2010).

1.3.1.2 Classification by Radio Loudness

An estimated $10-15\%$ of AGN are observed to be radio loud (RL) (e.g., Kellermann et al., 1989; Wilson and Colbert, 1995). These sources produce powerful radio jets that originate near to the SMBH and eject material at close to the speed of light (Kauffmann et al., 2008). They are typically classified according to the ratio of their 5 GHz radio flux to optical B-band flux, where ratios of $R = F_{5GHz}/F_B \gtrsim 10$ are considered to be RL, while $R \lesssim 10$ are radio quiet (RQ) AGN (Kellermann et al., 1989). However, several authors have found continuous distributions of R, with no distinct separation between the population of RL and RQ AGN (e.g., Becker et al., 1995; White et al., 2000; Mahony et al., 2012), which could imply that they may not be 2 distinct populations. Furthermore, the IR-X-ray spectra of RL and RQ galaxies are observed to be very similar (e.g., Sanders et al., 1989), which has lead to unification schemes attempting to unite the two classes, though this is more contentious than unification by orientation.

For example, it has been suggested that the difference between RL and RQ AGN is caused by black hole spin, where high black hole spin resulting from galaxy mergers can lead to the formation of radio jets (e.g., Wilson and Colbert, 1995), however this still remains uncertain (e.g., Heckman and Best, 2014). Alternatively, the host galaxies of RL and RQ AGN have been found to differ, for example, RL AGN are typically found in ellipticals, while RQ AGN are predominantly found in spiral galaxies (e.g., Smith et al., 1986), and furthermore, the host galaxies of RQ AGN have been found to be less luminous (e.g., Smith et al., 1986; Dunlop et al., 1993). Additionally, the mass accretion rate has also been used to attempt to explain the differences in RL and RQ AGN (Rees et al., 1982).

1.4 Variability of AGN Emission

One key observational feature of AGN emission is their variability that covers a range of timescales and amplitudes over the entire observable electromagnetic spectrum. In fact, variability was one of the first recognisable properties of quasars (Matthews and Sandage, 1963; Smith and Hoffleit, 1963). This variability has been used to both classify AGN into the various sub-types as described above (e.g., Choi et al., 2014; Cartier et al., 2015), and also to identify AGN from other extragalactic objects (e.g., Kozłowski et al., 2010; Peters et al., 2015). Furthermore, studying the variability of

AGN is important in inferring information about the dynamics and processes occurring within the unresolvable inner regions of the AGN.

The amplitudes and timescales of the variability differs both depending on subclass of AGN, and within the different wavelength ranges observed as different mechanisms are believed to be responsible for the different fluctuations. The typical variability observed for RQ type 1 AGN (specifically Seyfert 1s and Quasars) is outlined in Section 1.4.1, and for blazars in Section 1.4.2. Additionally, periodic variability of both type 1 AGN and blazars is described in Section 1.4.3.

1.4.1 Variability of Radio Quiet Type 1 AGN Emission

Light curves of AGN are typically characterized by aperiodic variability, which is well-described by stochastic processes and implies that the mechanism responsible for this variability is random in nature. Though the physical processes that cause these variations are not clear, it has been suggested to be the result of AD instabilities (e.g., Rees, 1984). Other models also predict external origins such as supernova or starburst explosions (Aretxaga and Terlevich, 1994) or gravitational microlensing (Hawkins, 1993).

For example, variations in the accretion rates within the AD have been employed to explain fluctuations seen in the light curves (Lyubarskii, 1997), as the change in accretion rate results in a change of temperature and therefore varying amounts of emission is released. These fluctuations are thought to originate at different locations within the disk and propagate inwards towards the X-ray emitting region. This would result in variations that occur over viscosity timescales, which is of the order of months to years at the optical emission region of AGN (e.g., Breedt et al., 2010). This has therefore be used to explain the longer variations seen in the light curves, both in the optical (e.g., Arévalo and Uttley, 2006; Arévalo et al., 2008) and the X-ray (e.g., Wilkins et al., 2016), however it is not sufficient to explain the observed shorter variability.

Models of an inhomogenous AD that experiences local temperature fluctuations that are expected on shorter timescales corresponding to the thermal timescales have also been suggested (e.g., Dexter and Agol, 2011). These thermal timescales have been shown to be consistent with characteristic timescales of variability in the optical (Kelly et al., 2009) and the X-ray (Ishibashi and Courvoisier, 2009).

Furthermore, much of the variability observed at different wavelength ranges are assumed to be the response to reprocessing emission from different components within the AGN. For example, both the light curves of broad emission lines and IR emission are shown to vary similarly to the optical continuum following a delay corresponding to the light travel time (e.g., Blandford and McKee, 1982), which is

further described in Section 1.4.1.3. Additionally, illumination of the AD by the corona has often been used to explain short term optical variability that correlates with the X-ray variability following a short delay (e.g., Krolik et al., 1991). While this behaviour has been observed in some AGN (e.g., Breedt et al., 2009), there are other objects that show no correlation between the lightcurves (e.g., Maoz et al., 2000, 2002), and furthermore there are some sources in which the variations in the optical are greater than the X-ray (e.g., Breedt et al., 2009) which means X-ray reprocessing isn't enough to explain the observed optical variability.

As mentioned above, studies of this variability in AGN light curves are often used to probe the inner regions that are not directly resolvable. In the following sections, I outline some of the different methods that are invoked in studying variable emission of type 1 AGN.

1.4.1.1 Power Spectral Density Functions

One common tool used to study the variable emission of AGN is the power spectral density (PSD) function that describes the amount of variability power over a range of temporal frequencies, f. For continuous data, this is given by the modulus squared of the Fourier transform of the light curve.

For AGN, these PSDs are found to be well-modelled by a power law, $P(f) \propto f^{-\alpha}$, and are shown to contain more power in longer timescales which corresponds to red-noise processes. Constraining the underlying PSDs of AGN emission can provide insights into the variability processes that are responsible for observations, such as relating observed behaviours to the different timescales described in Section 1.2.

Extensive studies have been performed on the flux variability of the hard X-ray emission using space telescopes that provide continuous monitoring. The PSDs of the AGN emission in the X-ray frequencies have been shown to be well-modelled by a slope of $\alpha = 2$ at higher frequencies, which changes to a slope of $\alpha = 1$ at a characteristic break frequency, ν_B (e.g., Green et al., 1993; Lawrence and Papadakis, 1993; Uttley et al., 2002) as shown for example in Figure 1.5a. This characteristic break frequency correlates with the mass of the SMBH, as AGN with higher masses have been found to have longer characteristic timescales (e.g., McHardy, 1988; Edelson and Nandra, 1999; Uttley et al., 2002). Additionally, a second break frequency is expected to occur at lower frequencies corresponding to timescales much longer than the observational baselines, at which point the power law will flatten to $\alpha = 0$.

The PSDs of the optical emission of AGN are less well studied than the X-rays due to the limitations of optical AGN monitoring programmes which are predominantly performed using ground based optical telescopes that are incapable of the continuous monitoring that is observed by X-ray space telescopes. There is not a consistently

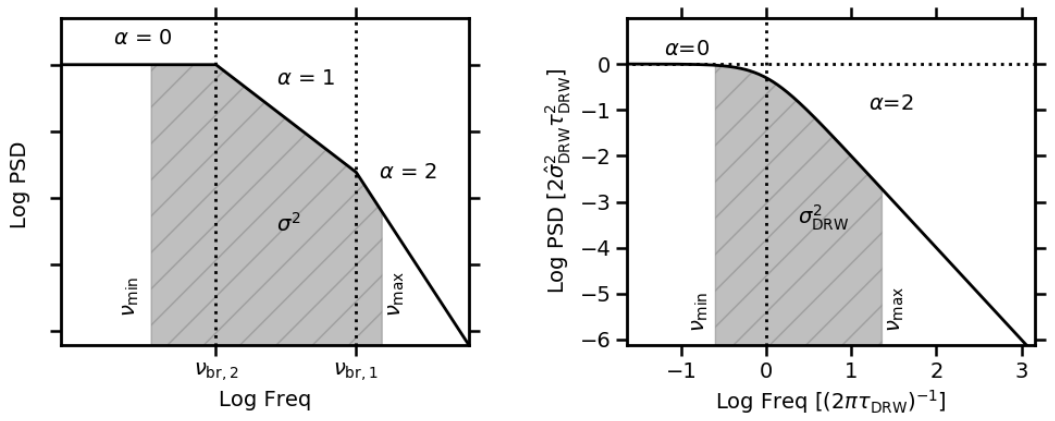

(A) Example of an X-ray AGN PSD with different power law slopes and break frequencies labelled.

(B) Example of the DRW model of an optical AGN PSD with different power law slopes labelled.

FIGURE 1.5: Examples of AGN PSDs. The grey shaded region corresponds to the variance of an observed light curve with minimum and maximum observation separations corresponding to the frequency ranges of $\nu_{\rm max}$ and $\nu_{\rm min}$.

agreed upon model of the optical PSD shape like in the X-rays, though Kelly et al. (2009) proposed that the optical flux variations could be modelled by a damped random walk (DRW), as shown in Figure 1.5b. This resembles a random walk process which corresponds to a PSD slope of $\alpha = 2$ and has short-timescale variability, $\hat{\sigma}_{\rm DRW}$, that flattens at frequencies corresponding to timescales longer than the characteristic timescale, $\tau_{\rm DRW}$. Many studies found agreements between this DRW model and observed AGN light curves, (e.g., Kozłowski et al., 2010; MacLeod et al., 2010; Zu et al., 2013), and furthermore the model parameters $\hat{\sigma}_{\rm DRW}$ and $\tau_{\rm DRW}$ have been shown to correlate with physical properties of the AGN (Kelly et al., 2009; Kozłowski et al., 2010; MacLeod et al., 2010). However, deviations of many AGN from the power law slope of $\alpha = 2$ have also been reported, often finding steeper slopes (e.g., Mushotzky et al., 2011; Kasliwal et al., 2015; Caplar et al., 2017; Smith et al., 2018a), and some have even been shown to be best fit by PSDs that correspond to broken power laws (e.g., Edelson et al., 2014; Simm et al., 2016; Smith et al., 2018a).

1.4.1.2 Structure Functions

In addition to the PSD, AGN variability is often explored using the structure function (SF; Simonetti et al. 1985), especially when analysing unevenly sampled data. For any given separation between observations, Δt, the SF gives the mean difference in flux as shown by the first-order SF given in Equation 1.13 (Suganuma et al., 2006).

$$SF(\Delta t) = \frac{1}{N(\Delta t)} \sum_{i<j} [f(t_i) - f(t_j)]^2 \tag{1.13}$$

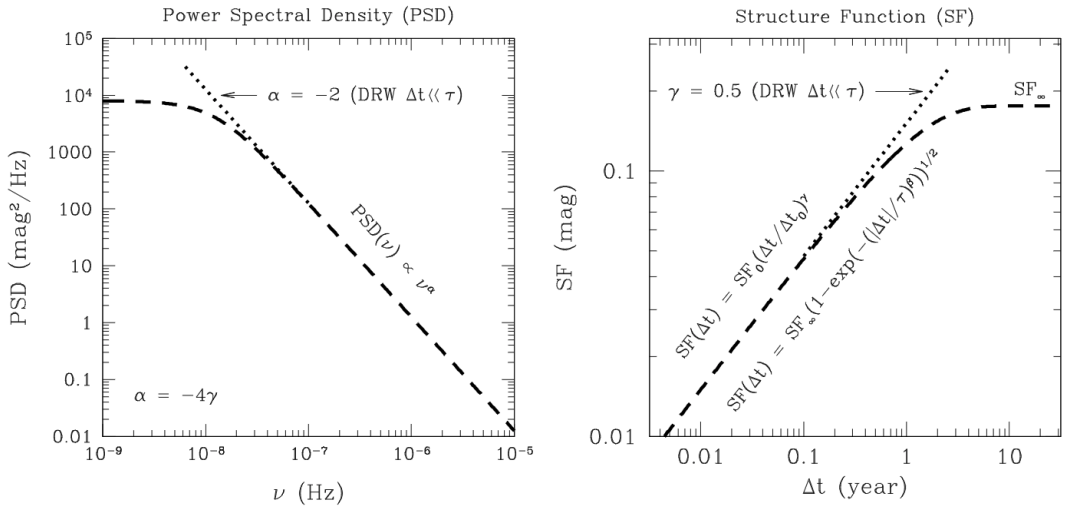

FIGURE 1.6: Comparison between the DRW model of optical AGN PSD and the SF. Image Credit: Kozłowski (2016).

where $f(t)$ is the flux at time t, the separation between data points is $\Delta t = t_j - t_i$, and $N(\Delta t)$ is the number of pairs of data points that correspond to the given separation.

The SF of AGN can be fit by a power law of the form $SF(\Delta t) \propto \Delta t^{\gamma}$, where γ is related to the slope of the PSD by the relation $\alpha = -4\gamma$. A comparison between the DRW model PSD and the corresponding SF are given in Figure 1.6.

1.4.1.3 Reverberation Mapping

As mentioned in Section 1.4.1, some amount of the emission produced in the inner regions of AGN is intercepted and reprocessed by the surrounding components. As a result, the reprocessed emission is shown to vary similarly to the driving continuum emission, but is observed after a delay that corresponds to the light travel time between the source of the emission and the location corresponding to the reprocessing site (assuming that the reprocessing time is negligible in comparison). Measuring this delay as a means of estimating the distance between different objects in the unresolvable central regions of AGN is a technique known as reverberation mapping (RM; Blandford and McKee 1982).

Observations of the reprocessed emission also depend on the location and geometry of the re-emitting region, and the angle it makes to the observer. Therefore for most geometries, the reprocessed emission is actually observed over a range of delays that correspond to different distances of the reprocessing region to the observer. Isodelay surfaces, as depicted in Figure 1.7, form surfaces that correspond to locations that result in equal delays being observed. As the driving continuum is constantly varying, the reprocessed emission that is detected at any given time is a superposition of variations from different locations in response to the continuum fluctuations.

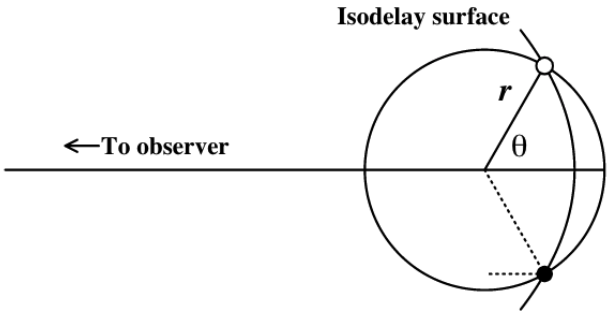

FIGURE 1.7: An example of the isodelay surface of a thin shell. Image Credit: Peterson and Horne (2004)

Therefore the overall observed reprocessed emission can be expressed as shown in Equation 1.14 (Blandford and McKee, 1982).

$$L_r(t) = \int_{-\infty}^{\infty} \Psi(\tau') L_c(t - \tau') d\tau' \tag{1.14}$$

where $L_r(t)$ is the reprocessed light curve observed at time, t, $L_c(t - \tau')$ is the continuum light curve observed at an earlier time $(t - \tau')$, where τ' is an arbitrary delay, and $\Psi(\tau')$ is the transfer function.

The transfer function therefore contains information about the geometry and structure of the reprocessing region, and so can be used to probe the inner regions of the AGN, however it is not directly measurable. Provided that the observed continuum and reprocessed light curves contain high quality data, this transfer function can be obtained using Fourier transforms (Maoz et al., 1991), or using maximum entropy methods (Krolik et al., 1991; Peterson, 1993). However, most observations of AGN do not meet the quality requirements for obtaining the transfer function this way, so cross correlational analysis comparing the observed continuum and reprocessed light curves can measure the mean lag, which gives a reasonable estimate for the characteristic separations of the emission regions (Peterson, 1993). The majority of reverberation mapping analysis therefore employs this technique, and examples of its use for BLR and dust reverberation mapping are described in more detail below. Additionally, some studies model the transfer function using simulations convolved with the observed continuum light curve to find the best fit to the reprocessed light curve (e.g., Hönig and Kishimoto, 2011; Pancoast et al., 2011; Brewer et al., 2011; Pancoast et al., 2012, 2014; Almeyda et al., 2017, 2020).

BLR Reverberation Mapping Extensive analysis has been performed using the cross correlation techniques to provide estimates for the size of the BLR in > 100 AGN (e.g., Bentz and Katz, 2015; Grier et al., 2017). Furthermore, it has been shown this estimate of the radius of the BLR, $R_{\rm BLR}$, can be used to infer the mass of the SMBH using

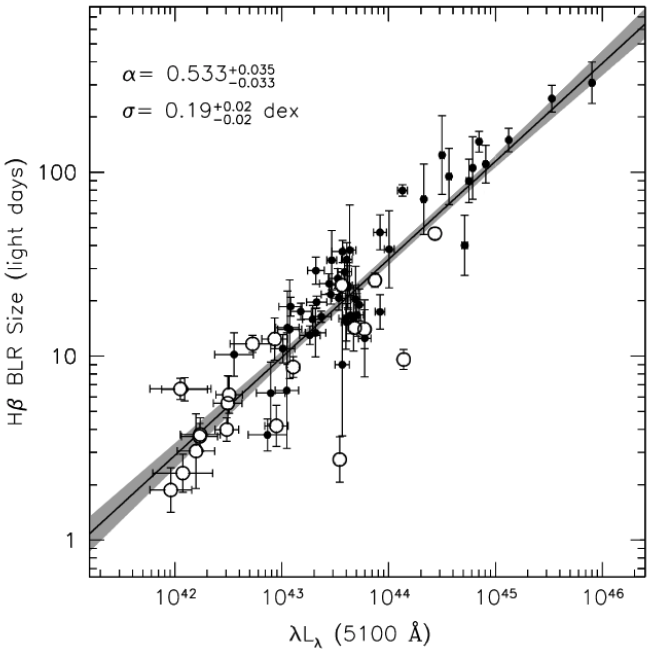

FIGURE 1.8: BLR radius-luminosity relationship for type 1 AGN. Image Credit: Bentz et al. (2013).

Equation 1.11 (e.g., Ho, 1999; Wandel et al., 1999), as the BLR clouds are assumed to be in virialised motion around the black hole. However, as described in Section 1.2, uncertainties arise in this estimation as a result of ignorance of the geometrical distribution of gas in the BLR. To overcome this, some studies have used modelling of the transfer function and observed light curves to attempt to constrain the geometry and dynamics of the BLR (e.g., Pancoast et al., 2011; Brewer et al., 2011; Pancoast et al., 2012, 2014).

A correlation between the luminosity of the AGN and the size of the BLR was also discovered in the form of $R_{\rm BLR} \propto L^{\sim 0.5}$ (e.g., Kaspi et al., 2000; Peterson and Horne, 2004), as shown in Figure 1.8. Such a relation is particularly relevant in the context of using AGN as cosmological probes, as reverberation lags are relatively easy to measure and would therefore be ideal for using AGN as standardisable candles.

Dust Reverberation Mapping The same reverberation methods have also been used to estimate sizes of the dust emitting region. Most of these compare light curves in the NIR to the optical continuum to probe the size of the inner radius of the dust emission region, as for AGN with redshifts of $z < 1$ the NIR K band ($\sim 2.2\mu$m) traces the hottest dust with sublimation temperatures of $T_{\rm sub} \approx 1500$ K (Barvainis, 1987). Similar to the BLR RM, the NIR lag has also been found to correlate with luminosity of the AGN (e.g., Oknyanskij and Horne, 2001; Minezaki et al., 2004; Suganuma et al., 2006) as shown in Figure 1.9, thus providing the possibility for NIR RM lags to be used to make AGN standardisable candles for cosmology. It can actually be considered more

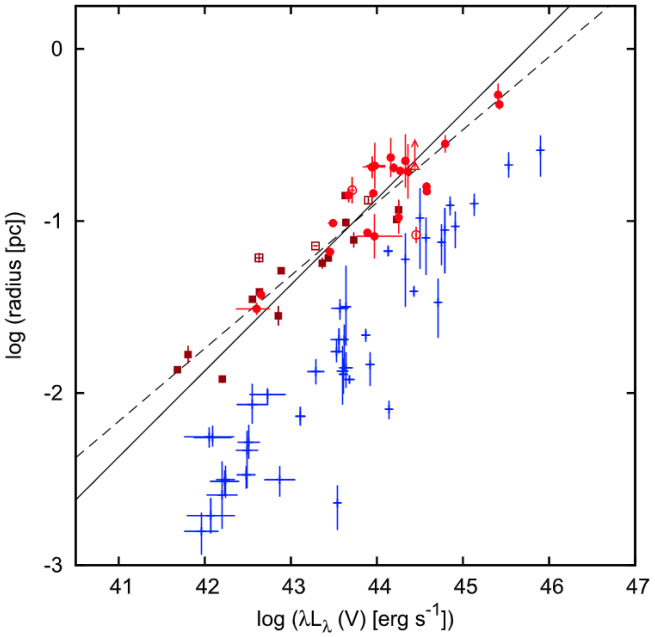

FIGURE 1.9: Dust Radius-luminosity relationship (red) compared to the BLR radius-luminosity relationship (blue), where the solid and dashed line corresponds to a fixed slope of 0.5 and the best fit slope to the data respectively. Image Credit: Minezaki et al. (2019).

advantageous to use the NIR lag-luminosity relation for this use as Koshida et al. (2014) showed that the relation between lag and luminosity was tighter for the NIR lags than the BLR lags for the same set of AGN, and additionally, repeated photometric observations are easier to obtain than spectroscopy. Though conversely, higher redshift detections are possible using broad emission lines which therefore suggests both methods could be used in conjunction with one another.

Furthermore, several studies of dust reverberation mapping have also been performed using longer wavelength IR light curves in an attempt to better constrain the spatial information in the dust emitting region. These results often find that the longer wavelength light curves are tracing cooler dust at larger distances than the shorter IR wavelength light curves (e.g., Vazquez et al., 2015; Lyu et al., 2019). However, Hönig and Kishimoto (2011) explain that the MIR emission observed from AGN can originate in the peak of the black body emission of cooler dust, but can also be tracing the Rayleigh-Jeans tail of the hot dust that is emitted at the inner radius of the dust emission region. Therefore in objects where the dust emitting region is compact, the MIR emission can be dominated by the hot dust.

Though IR interferometric observations of AGN have been able to resolve some spatial information about the torus, this is only possible for nearby, relatively bright AGN, which therefore makes estimates using dust reverberation mapping a relevant probe.

1.4.1.4 Spectral Variability

Numerous studies have shown that the variable nature of the AGN emission has a dependence on wavelength. In the optical, quasars and Seyfert 1 galaxies frequently demonstrate a bluer when brighter (BWB) behaviour (e.g., Giveon et al., 1999; Webb and Malkan, 2000; Vanden Berk et al., 2004; Sakata et al., 2010; Schmidt et al., 2012). This BWB trend reflects the underlying nature of the central engine within the AGN, though the interpretation of the commonly observed phenomena is not necessarily agreed upon. Some authors claim this to be the result of spectral hardening, in which the variable component of the emission becomes bluer as it gets brighter (e.g., Giveon et al., 1999; Webb and Malkan, 2000; Vanden Berk et al., 2004), however this argument has been disputed as linear flux-to-flux relationships have been detected in AGN observed in different filters on the same night (e.g., Winkler, 1997; Suganuma et al., 2006). Other authors instead claim that there is a blue variable component that becomes brighter and therefore dominates over a non-variable red component which is often considered to be host-galaxy emission that is usually redder than the AGN continuum emission (e.g., Sakata et al., 2010). Furthermore, the observed colour behaviour has also been considered as the result of hot spots in the AD (e.g, Schmidt et al., 2012).

1.4.2 Variability in Blazar Emission

Blazars are the most violently variable subclass of AGN, and they demonstrate strong variability at all observable wavelengths, which includes significant variability at radio and gamma-ray wavelengths unlike most of the RQ type 1 AGN discussed previously. This variability is predominantly linked to the non-thermal emission which is amplified by relativistic beaming by the relativistic jet that is orientated < 10 degrees to our line of sight.

The flux variations of blazars has been observed over a range of timescales, from $\sim$ minutes to hours (intra-day variations), over $\sim$ days to weeks (short-term variations), and over $\sim$ months to years (long-term variations). These variations in the flux at different wavelength ranges have been found to correlate with each other, implying that the source of the emission for the different wavelength ranges are connected (e.g., Hufnagel and Bregman, 1992; Wagner et al., 1995; Ulrich et al., 1997), as discussed in more detail in Section 1.4.2.1. Furthermore, flux variations are often accompanied by changes in the spectral shape (e.g., Marscher and Gear, 1985), which will also be further explained in Section 1.4.2.2.

The exact physical mechanisms responsible for the variations in blazars are not known, though several theories have been presented that correspond to either intrinsic processes within the jet or extrinsic geometrical effects. For example,

variability has been modelled by a relativistic shock propagating outwards along the inhomogeneous jets (e.g., Marscher and Gear, 1985; Spada et al., 2001). These shocks are believed to be triggered by variations in properties relating to the jet such as the electron density or the magnetic field that moves through the it (e.g., Nishikawa et al., 2005). Emission from different frequency ranges is expected to be produced at different distances behind the shocks, with high frequency photons from the synchrotron component being emitted sooner towards the front of the shock. Alternatively, a change in the viewing angle of the jet has also been proposed as an explanation for the flux variations (e.g., Villata and Raiteri, 1999; Marscher et al., 2008), as it can cause a change to the relative Doppler factors, meaning that outbursts can occur when the jet is at the smaller viewing angles.

1.4.2.1 Temporal Variability

As described in Section 1.4.1.3, measuring delays between correlating variability in different wavelength light curves can be used to estimate the distances between their emission regions. In blazars, the dominant source of emission is expected to be in the relativistic jet for all wavelength ranges, and as such, short delays between light curves of different wavelength ranges are often detected. For example, gamma-ray flares have been shown to lead flares in the optical light curves in several sources by a few days (e.g., D'Ammando et al., 2011; Agudo et al., 2011; Hayashida et al., 2012). Furthermore, several studies show that the IR light curves lag the optical on timescales of < 1 day, or strongly correlate with no significant lag detected between them (e.g., D'Ammando et al., 2013; Zhang et al., 2013; Kaur and Baliyan, 2018), which implies that the emission regions are co-temporal, or possibly co-spatial. However, some blazars have also been observed with longer delays between the optical and IR (e.g., Li et al., 2018; Safna et al., 2020), which Li et al. (2018) attributed to be due to higher energy emission emerging closer to the front of the shocks within the jet than the lower energy emission.

1.4.2.2 Spectral Variability

Flux variations in blazars are often accompanied by changes in the spectral shape (e.g., Marscher and Gear, 1985), characterised by the steepening or flattening of the spectral slope as the object brightens. Studying this change in spectral shape therefore allows us to probe the physical processes responsible for the observed emission.

Figure 1.10 contains examples of the SED of blazars. The emission is shown to be dominated by two broad peaks in the SED in Figure 1.10a which correspond to the synchrotron radiation dominating in the lower frequencies and the inverse Compton scattering in the higher frequencies, as described in Section 1.2. In the SED of the

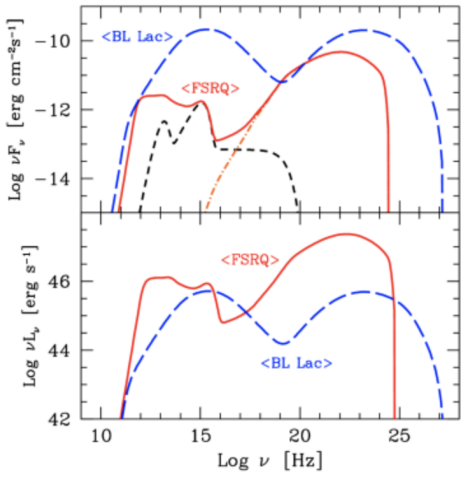

(A) Comparison between example SEDs of the different subclass of blazar, with BL Lac in blue and FSRQ in red, with example of disk emission in the black dashed line. Image Credit: Ghisellini et al. (2010).

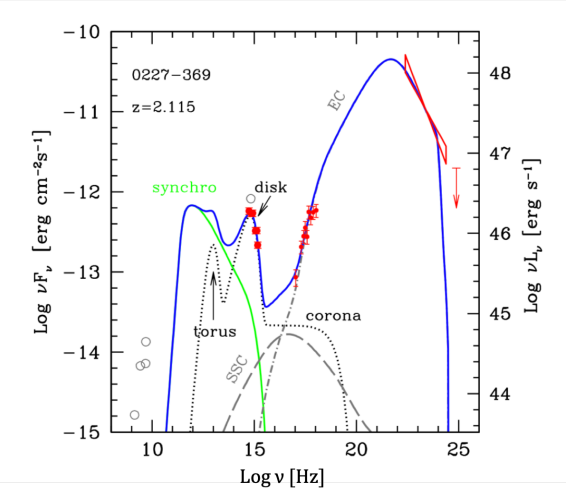

(B) Example of the SED of a FSRQ with contributions from different components labelled. Image Credit: Ghisellini (2011).

FIGURE 1.10: Examples of the SEDs of Blazars.

FSRQ in Figure 1.10b, thermal emission from the AD and torus are shown to also significantly contribute to the observed optical and IR emission.

Most studies of the spectral variability use simultaneous (or quasi-simultaneous) multi-wavelength observations of the object, particularly in the optical and IR wavelength ranges, and characterise the spectral variability through colour-magnitude diagrams (e.g., Ciprini et al., 2003). Three main colour behaviours are observed; bluer when bright (BWB), redder when brighter (RWB), or achromatic/stable when brighter (SWB).

Multiple theories have been presented to explain the different colour trends observed. The first invokes the idea that the overall emission is a sum of contributions from the thermal and non-thermal emission, which can vary on different timescales to each other (e.g., Fiorucci et al., 2004; Bonning et al., 2012; Agarwal et al., 2019). When the object is observed as BWB, this could therefore indicate that the the thermal emission (the bluer component) is varying faster than the synchrotron emission (the redder component). The reverse can therefore also be used to explain RWB trends. Additionally, single component synchrotron models have been used for explaining the BWB trends, particularly in agreement with the shock-in-jet model of variability introduced previously. Emission at different frequency ranges is expected to be produced at different distances behind the shock front, with the higher frequency emission being released closer to the shock front and therefore sooner than the lower frequency emission. Due to synchrotron cooling, the higher frequency electrons lose

energy faster, which makes the higher frequency emission more variable (e.g., Kirk et al., 1998; Agarwal et al., 2019).

Some believe that these colour trends correspond to the different subclass of blazar, as the RWB trends are most commonly observed in FSRQs, while the BWB trends are detected in BL Lacs (e.g., Gu et al., 2006; Rani et al., 2010; Bonning et al., 2012; Meng et al., 2018). However, multiple studies find that the reverse is also true, and additionally, SWB trends have been observed in both types of blazar (e.g., Gu and Ai, 2011; Zhang et al., 2015; Mao and Zhang, 2016).

Finally, while most studies find the spectral variability to be explained by simple single colour trends, some observations have been found to be more complex. For example, several sources have been shown to display colour trends that change over different timescales (e.g., Bonning et al., 2012; Isler et al., 2017), that has been attributed to flares behaving differently from the overall emission, which implies that different contributions to the emission can become important over different timescales. Furthermore, it has also been shown that for several blazars, colour behaviours change from RWB when the object is in the low flux state to a SWB or a BWB trend in the high flux states (e.g., Zhang et al., 2015; Acosta-Pulido et al., 2017). This has been explained by contributions from the non-thermal emission varying faster than the thermal emission when the object is in the low flux state, resulting in RWB colour behaviour being observed. Then when the object becomes brighter than some saturation magnitude, the emission is predominantly due to the synchrotron emission and the observed colour behaviour can be influenced by the single synchrotron component models as described above, resulting in a BWB behaviour being observed. Additionally, in individual blazars, varying colour trends have been detected depending on the combination of wavelength ranges being used to study it (Wu et al., 2011), which also implies that the emission processes within the blazar are more significant at different emission regions.

1.4.3 Periodic Variability in AGN Emission

The previous sections consider the case when the AGN emission corresponds only to aperiodic, stochastic variability. However various recent claims of periodicity have been presented with respect to AGN light curves, both in RQ type 1 AGN and blazars. Theses periodicities are usually linked to quasi-periodic oscillations (QPOs) or SMBH binary systems (SMBHBs), which are both discussed in more detail below.

Periodic behaviour can be detected in the light curves of AGN through auto-correlation analysis, or through variability probes such as the SF which will contain dips corresponding to periodic timescales, and the PSD which will contain peaks at timescales corresponding to the period of oscillations. Detecting potential

periodic oscillations in AGN light curves has proven to be difficult as red-noise processes can mimic periodic behaviour (Vaughan et al., 2016). Furthermore, the baselines of AGN observations often do not cover many periodic cycles which does not allow for tests the persistence of the periodicity (Vaughan and Uttley, 2005). This therefore means that studies of potential periodicity within AGN are still of great interest.

Quasi-Periodic Oscillations The initial search for QPOs in AGN emission was motivated by the idea that AGN could be mass-scaled analogies of stellar mass black holes in X-ray binaries (BH-XRBs), which are objects that are strongly associated with QPOs. Recent evidence of similarities between properties of these objects supports the idea that the accretion physics of AGN and BH-XRBs are similar, such as their X-ray variability and spectra (McHardy et al., 2006; McHardy, 2010).

As the majority of QPOs are detected in the X-ray emission of BH-XRBs, the physics will be explained for these objects first to give context of the possible detections in AGN that will be explained after. BH-XRB QPOs are usually divided into two classes based on their frequencies; low frequency (LF) QPOs which are the most commonly detected, and high frequency (HF) QPOs. The origin of these oscillations are still unclear, however several theories have been suggested that are either related to waves in the accretion flow, such as unstable spiral density waves (Tagger and Pellat, 1999), or relativistic effects associated with the black hole spin. An example of the latter describes LF QPOs in terms of the Lense-Thirring precession (Stella and Vietri, 1998; Stella et al., 1999), which is a relativistic effect where an inertial frame of reference is dragged around a spinning compact object, causing gyroscopes to precess with a Lense-Thirring precession frequency (Lense and Thirring, 1918; Bardeen and Petterson, 1975). For LF QPOs, the fundamental frequency of the QPO therefore corresponds to this Lense-Thirring frequency at a certain radius that is usually taken to be the truncation radius of the disk. The HF QPOs are then expected to be related to periastron precession and orbital motions.

Whilst the majority of QPOs of BH-XRBs are detected in the X-ray emission, several objects also detect QPOs in the optical light curves. The fundamental frequencies of these QPOs are often found to be coincident with the fundamental frequency of the QPO in the X-ray emission (e.g., Durant et al., 2009; Gandhi et al., 2010), though others have been shown to occur at half of the X-ray QPO frequency (e.g., Kalamkar et al., 2016). The presence of the QPO in the optical could suggest that either the optical emission region is reprocessing some of the X-ray emission, as described in Section 1.4.1, or that the oscillations are also occurring within the optical emission region of the disk (e.g., Smith et al., 2018b).

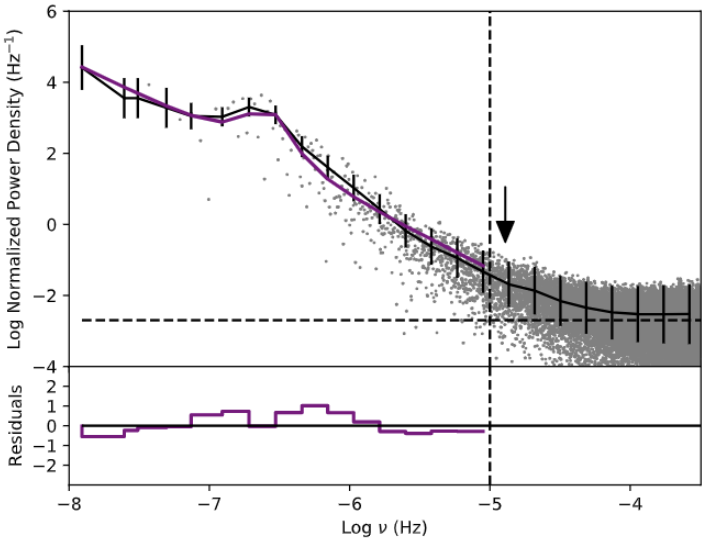

FIGURE 1.11: Raw (grey dots) and binned (black line) PSD of KIC 9650712 which demonstrates a potential QPO that is fit with a single power law with a Lorentzian component superimposed (purple). Image Credit: Smith et al. (2018b).

Another important discovery of QPOs in BH-XRBs is the inverse correlation between the fundamental frequency of the QPOs and the mass of the black hole, which has been found for both LF and HF QPOs (e.g., Abramowicz et al., 2004; Zhou et al., 2015). This could provide an additional method of estimating the mass of black holes using their observed periodicities.

The first QPO detected in an AGN was discovered by Gierliński et al. (2008) in the X-ray light curve of REJ1034+396 with a period of $\sim$ 1 hour (and was later confirmed by Alston et al. 2014), and is considered to be analogous to a HF QPO from a BH-XRB (Middleton and Done, 2010). Since this first discovery, many more claims of QPOs have been reported in the X-ray light curves of other AGN (e.g., Alston et al., 2015; Zhang et al., 2017, 2018), and Smith et al. (2018b) report evidence of the first potential QPO detected in optical AGN light curve as shown in Figure 1.11. The mass-frequency relations found for the BH-XRBs have shown to extend up to the masses of SMBHs for these objects (e.g., Abramowicz et al., 2004; Zhou et al., 2015), which provides further evidence that AGN and BH-XRBs are analogous.

Super Massive Black Hole Binaries Galaxies have long been known to merge with each other (e.g., Lacey and Cole, 1993; Lotz et al., 2011; Rodriguez-Gomez et al., 2015), and as every galaxy is believed to host a SMBH, this leads to the idea that there should exist galaxies in which multiple AGN reside (e.g., Kelley et al., 2017). Indeed, many multi-SMBH systems have been observed in recent years with kpcs separations (Dual AGN, Comerford et al. e.g., 2012).

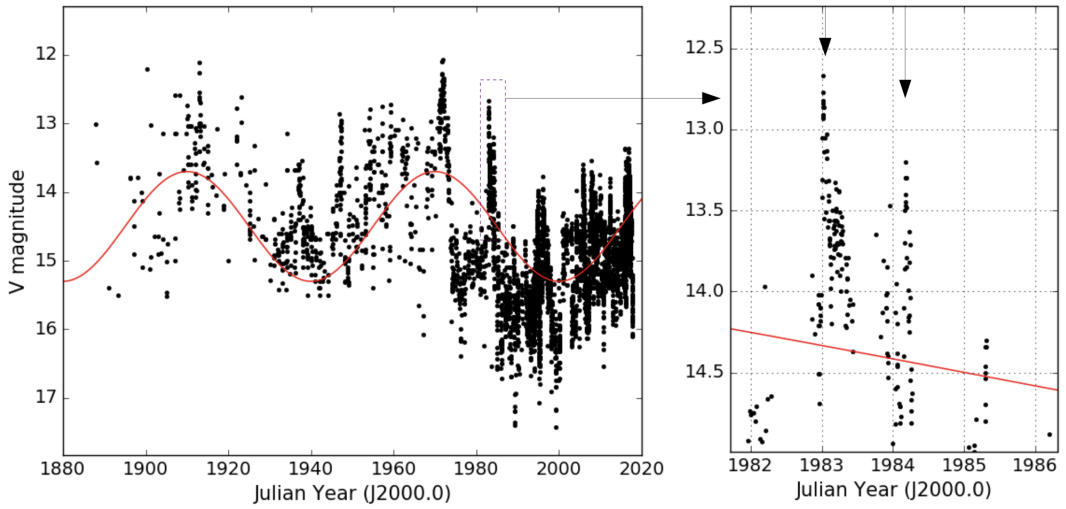

FIGURE 1.12: *Left Panel*: Optical light curve of OJ 287 between 1888 and 2018, with a 60 year sinusoidal curve overplotted. *Right Panel:* Optical light curve between 1982 and 1986 to demonstrate the double peaked nature of the outbursts. Image Credit: Dey et al. (2019)

Over time, it is expected that these systems will evolve and that the SMBHs will be brought together by dynamical friction (e.g., Kelley et al., 2017). Once the SMBHs reach sub-pc separations they become gravitationally bound, forming a Keplerian binary system. Furthermore, if these binaries are able to reach separations of the order of $\lesssim 10^{-3} - 10^{-2}$ pc, gravitational wave emission will dominate and could cause them to coalesce. This would make SMBHBs the strongest sources of gravitational waves in the Universe (e.g., Bowen et al., 2018), and thus make them particularly interesting sources to study.

SMBHBs cannot be spatially resolved due to their compact sizes, therefore identifying these objects relies on the presence of quasi-periodicity within their emission, or observing the effects that the SMBHB has on the components such as the precessing relativisitc jet (e.g., Britzen et al., 2018; Charisi et al., 2018). The emission is observed as quasi-periodic as the mass accretion rate onto the SMBHBs is perturbed by the Keplerian binary orbital motion (e.g., Hayasaki et al., 2007; MacFadyen and Milosavljević, 2008; D'Orazio et al., 2013; Farris et al., 2014).

Though many potential SMBHB candidates have been proposed (e.g., Graham et al., 2015; Liu et al., 2015; Charisi et al., 2016), so far none have been confirmed. OJ 287 is a blazar that is commonly considered to be the current best candidate for a SMBHB (e.g., Sillanpaa et al., 1988; Valtonen et al., 1988) due to the quasi-periodic pattern observed in its $\sim$ 130 year light curve as shown in Figure 1.12. Two quasi-periodicities are detected at $\sim$ 12 and $\sim$ 60 years, which could be explained as a secondary SMBH orbiting the primary SMBH in an eccentric orbit, where the $\sim$ 12 and 60 year quasi-periodicites correspond to the orbital period timescale and periastron timescales

respectively (e.g., Dey et al., 2019). Furthermore, double peaked outbursts are seen in the light curve which could be described as the secondary black hole impacting the AD of the primary black hole twice.

1.5 Motivation and Structure

The motivation for this thesis is to expand on the understanding that we currently have of the unresolvable inner regions of AGN by invoking detailed optical and IR variability analysis on individual AGN, and to prepare for the large number of AGN that will be observed with future optical observational surveys by exploring the limitations of variability analysis using simulations of these surveys.

The thesis is structured as follows. Chapter 2 introduces the relevant observational surveys that will be discussed within the later chapters, and describes the data reduction performed to convert the raw telescope observations into usable science images. In Chapter 3, I outline some of the common methods of variability analysis that will be used throughout the thesis. In Chapter 4, I perform in depth analysis of the spectral and temporal variability of the FSRQ PKS 0027-426. In Chapter 5 I explore dust reverberation mapping of the Seyfert 1 galaxy Zw229-015 which has one of the most complete, high quality optical light curves of AGN to date, and further study modelling of the light curves to constrain properties of the inner regions of the AGN. In Chapter 6 I study the extent to which variability analysis of optical AGN using their PSDs can be explored for the large number of AGN expected to be observed with the upcoming Vera C. Rubin Observatory Legacy Survey of Space and Time (LSST) survey, through simulations of light curves created with different underlying PSDs. Finally, in Chapter 7 I summarise the work in this thesis and discuss the implications and possible extensions that can be undertaken in the future to further expand our understanding of the unresolvable inner regions of AGN.

Chapter 2

Observational Surveys and Data Reduction Methods

In this chapter I will describe the different observational surveys and relevant data reduction methods for the analysis used in Chapters 4, 5, and 6. I will start by outlining common techniques for extracting AGN light curves from the raw data in Section 2.1. In Section 2.2 I will then describe the specific observational surveys from which data is used in the later analysis.

I was actively involved in extracting AGN light curves from data in various stages of calibration from the DES (Section 2.2.4), OzDES (Section 2.2.7) and VOILETTE (Section 2.2.6) surveys, which I will describe in detail. In some of the remaining observational surveys the light curves were extracted by collaborators so I will only provide brief descriptions of these for context.

2.1 Obtaining AGN Light Curves from Photometric Observations

2.1.1 Photometric Data Corrections

Optical and IR astronomical telescopes typically use mirrors or lenses to focus photons from the observed objects onto a charged coupled device (CCD) to collect data for scientific analysis. These CCDs are arrays of pixels that release electrons in response to the photons, creating a current which can be measured as a signal.

Before these raw signals can be used for science however, they need to be corrected for systematic uncertainties that are introduced, such as readout noise, accumulation of charge, and uneven illumination of the CCD.

Bias When an image is read out from a CCD, values are added to each of the pixels to prevent negative signals caused by readout noise. These added values are known as a bias, and this is removed from the data by subtracting exposures that are taken with negligible exposure times, known as bias frames.

Dark Currents Accumulation of charge can occur in the pixels as the temperature of the CCD causes thermal excitation of the electrons and therefore adds thermal noise to the observations. To account for this additional thermal noise, dark current frames, which are observed with no illumination for exposure times equal to the science image, are subtracted from the data. These dark current frames include the bias noise as described above.

Flat Fielding Uneven illumination of the CCD can be the result of bad pixels, the presence of dust on the lens, or differences in the sensitivity of each pixel. These effects are counteracted by dividing the science images by flat fields, which are created by evenly illuminating the CCD to create what should give an equal signal, usually by observing the sky at twilight or by illuminating the telescope dome.

Sky Subtraction The sky background of the science images taken with ground-based telescopes often needs to be subtracted as regions of the image without visible sources can still be illuminated by photons that are scattered by the atmosphere. Furthermore, internal reflections in the CCD (especially towards longer wavelengths) can give rise to fringes in the sky background, which are caused by emission lines in the sky and can be highly variable. Both of these can be subtracted from the science images using sky frames which are often made from the science images themselves, using a combination of dithered observations to prevent stars from being subtracted. An alternative to subtracting an entire sky frame is to measure the sky background local to the target source and subtract it during aperture photometry.

Bad Pixel Masking Some CCDs have small defects that need to be accounted for, such as hot or cold pixels which need to be masked out before the science images can be analysed.

2.1.2 Photometry

Though most AGN are classified as point sources in the sky, the light observed by the telescope typically spans numerous pixels. This occurs as the path of the photons can be spread, for example as a result of diffraction by the instruments, or because of atmospheric turbulence in ground based telescopes. This therefore results in a peak in

the central pixel and a count rate that falls further out that can be approximated as a Gaussian function.

Therefore to measure the total flux from the target object in the calibrated observations, aperture photometry is often used to sum the total counts within a given aperture (usually a circle) centred on the object. The choice of aperture is often considered by attempting to contain as much of the light from the object while limiting the contribution from the background.

These fluxes can be influenced by nightly effects such as changes in seeing or changes in the atmospheric conditions, therefore they still need to be corrected before being used for science. Assuming these nightly differences are consistent across the detector, differential or relative photometry uses non-varying reference stars to correct the inconsistencies. For differential photometry, the differential magnitude (Δm) is calculated each night to demonstrate the variability of the target objects emission against itself as $\Delta m = |C - T|$ where T is the target object and C is the non-varying reference star. For relative photometry, the apparent magnitudes (m_{app}) are calculated from the observed magnitude (m_{obs}) using a zero-point (ZP), which is estimated using reference stars of known magnitude, with the equation $m_{\text{app}} = m_{\text{obs}} + ZP$.

2.2 Observational Surveys

2.2.1 Kepler Space Telescope

The *Kepler Space Telescope* (Borucki et al., 2010) launched in March 2009 and observed until May 2013 as part of the original *Kepler* mission. The sole science instrument, the *Kepler* photometer, consisted of an array of 42 CCDs, and had a 115 square degree field of view (FOV). The photometer utilised one broad bandpass over the range of 420 to 900 nm to encompass the optical spectrum.

The primary science goal of *Kepler* was the detection of exoplanets, and as such was designed with fast sampling ($\sim$ 30 minutes) and excellent precision. To provide near-continuous observations of possible exoplanets, it observed the same pointing in the Milky Way for the entire mission.

Kepler was placed in an Earth-trailing heliocentric orbit, but as it was designed to perform near-continuous monitoring of a single pointing, quarterly space-craft rolls were introduced to ensure the solar panels remained oriented towards the sun (rolling every 93 days). The camera would therefore rotate by 90 degrees and as a result, the observed objects would fall on different parts of the CCD.

Due to the high cadenced observations and numerous CCDs, only a small portion of the data taken could be stored onboard the spacecraft. As a result the images were

mostly stored as targeted pixels in which smaller images were centred on the target objects with size dependent on brightness of the object. Most of these target objects chosen were candidates for exoplanet detection, however Guest Observer proposed targets also included a few AGN. Initially only one AGN was known within the *Kepler* FOV; Zw229-015, though more were discovered since *Kepler* started operating. As a result, Zw229-015 has one of the highest quality optical light curves of AGN to date, with the longest baseline from any of the *Kepler* AGN.

The *Kepler* light curve of Zw229-015 used in this thesis was produced by Edelson et al. (2014). The raw *Kepler* data was processed by the *Kepler Mission* Science Operations Center, and included bias and dark current subtraction, flat fielding and correcting for gain and non-linearity corrections (Jenkins et al., 2010). The light curve extraction from the data in the standard *Kepler* processing pipeline was designed for exoplanet detection and as such, it optimised small flux changes and removes long term trends making it inappropriate to use for AGN. Therefore Edelson et al. (2014) separately extracted the AGN light curve from the calibrated target pixel data using different extraction masks than the pipeline.

As the *Kepler* space-craft rolled every 93 days, the target objects were observed on different CCDs every quarter, each of which could differ slightly and therefore, interquarter scaling was necessary to create the entire light curve of Zw229-015. This was done by averaging the five observations before and after the change in CCD to correct for the mean difference.

2.2.2 Spitzer Space Telescope

The *Spitzer Space Telescope* (Werner et al., 2004) was an infrared space telescope that launched in 2003. It was composed of a telescope with an 85cm mirror and three science instruments; the infrared spectrograph (IRS; Houck et al. 2004), the multiband imaging photometer for Spitzer (MIPS; Rieke et al. 2004), and the infrared array camera (IRAC; Fazio et al. 2004).

Spitzer's primary mission required cooling of the instruments using a supply of liquid helium, however the supply of coolant ran out in 2009, after which *Spitzer* began its "warm mission". After the loss of coolant, only the 3.6 and 4.5 μm channels on the IRAC were still operational, and observations with these detectors continued until January 2020.

Spitzer was designed to follow an Earth-trailing, heliocentric orbit in order to passively cool the telescope for the primary mission and therefore reduce the amount of coolant needed (and thus reduce the payload).

Each observing cycle, investigators were invited to submit proposals for observations with *Spitzer*, with all of the observing time in the warm mission being divided among peer-reviewd general observer (GO) proposals, excluding the Director's Discretionary Time (DDT). Among the approved warm mission GO proposals included IR monitoring of Zw229-015 between August 6, 2010 and January 26, 2015 (Gorjian et al., 2010, 2014), which provided concurrent IR observations to the optical *Kepler* observations.

Zw229-015 was proposed to be observed with an average cadence of 3 days with limits of $\pm$ 0.5 days. In the first two cycles, only data from the 3.6μm band was requested, however in cycles 8 and 9 the 4.5 μm observations were included. Due to the orbit of *Spitzer* and therefore the visibility of Zw229-015 to the telescope, observations were not possible year round, and instead observation seasons consisted of $\sim$ 5 months. Uneven gaps between observations seasons were observed as a result of a mismatch between the visibility of Zw229-015 and the proposal cycles for *Spitzer*.

Gorjian et al. (2014) reduced these light curves following the procedures in the IRAC Instrument Handbook [1], including subtraction of dark current and bias and flat-fielding.

Aperture photometry was performed using a 4 pixel radius aperture (correrssponding to 2″4), which was chosen as to contain most of the light from the AGN, without containing too much background. An additional background annulus of 12-20 (7″2 - 12″) pixels was used to subtract a significant portion of the host-galaxy. Due to the high quality of the data, the AGN light curves did not need to be corrected using relative measurements from non-varying nearby stars.

2.2.3 Combined Ground-based Optical Monitoring of Zw229-015

Additional optical V-band monitoring of Zw229-015 was performed using a combination of ground-based facilities which are briefly described here. The 2010 portion of the data used in this thesis was published in Barth et al. (2011), though additional years of observations are used in the analysis in this thesis.

KAIT The 0.76 m Katzman Automatic Imaging Telescope (KAIT) at Lick Observatory (Filippenko et al., 2001) observed Zw229-015, with data requested nightly though observations were limited by weather and instrument faults. The data from KAIT was reduced with the automatic KAIT data-processing pipeline which included bias subtraction and flat fielding.

[1] https://irsa.ipac.caltech.edu/data/SPITZER/docs/irac/

WMO The 0.9 m telescope of West Mountain Observatory (WMO) in Utah observed Zw229-015 with two exposures each night that telescope operations were permitted. The WMO standard processing pipeline also included bias subtraction and flat fielding.

LCO Telescope Network Observations of Zw229-015 were also taken using telescopes that make up part of the Las Cumbres Observatory (LCO) global telescope network, including the 1m telescopes located at McDonald Observatory (Brown et al., 2013) and the 2m Faulkes Telescope North located at Haleakala Observatory. These images were also processed by the standard reduction pipelines for the respective facilities, including bias subtraction and flat fielding.

Aperture photometry was performed on all calibrated images from each telescope using a circular aperture of radius 4″, with a sky annulus between 10 and 20″ to subtract the sky background as described by Barth et al. (2011). Discrepancies between the images from different telescopes were removed by scaling the light curves to match observations taken on the same night by WMO. Relative photometry used non-varying nearby reference stars (listed in Barth et al. 2011) to convert the light curves into V band magnitudes.

2.2.4 DES

The Dark Energy Survey (DES) was a 5-year survey that observed using DECam on the 4m Blanco telescope at the Cerro Tololo Inter-American Observatory (CTIO) between 2013-2018 (Flaugher et al., 2015). DECam was composed of 62 CCDs arranged into the hexagonal pattern giving a FOV of 3 square degrees.

DES consisted of two programmes; a wide-area survey that covered 5000 square degrees, in which each region was observed 10 times in each of the DES *grizY* filters over the course of the survey, and a time-domain survey (DES-SN; Kessler et al. 2015) that covered a smaller region of 27 square degrees, but was observed repeatedly and regularly in the DES *griz* bands. The observed 27 square degrees of the DES-SN programme was divided between 4 fields; the Chandra Deep Field South (CDFS), Elias South (ES), Sloan Digital Sky Survey (SDSS) Stripe 82 field and the XMM deep field, each of which were observed with $\sim$ 6 month observation seasons per year, with $\sim$ 6 day cadences. To provide multi-wavelength monitoring, most observation sequences involved consecutive observations in all filters. The per-epoch 10σ limiting magnitudes of DES are given as $g < 23.6$, $r < 23.3$, $i < 22.8$ and $z < 22.1$ (Abbott et al., 2018).

DES was primarily designed with the goal of probing cosmic acceleration and the nature of dark energy in the universe, though the high quantity of data would

inevitably contain many AGN (with predictions of $\sim$ 670,000 with z $<$ 4 in the wide-area survey given the 10σ depth; Dark Energy Survey Collaboration et al. 2016).

The raw data from DES was processed by the National Center for Supercomputing Applications (NCSA) in conjunction with data scientists at Fermilab, using the image processing pipeline described by Morganson et al. (2018). This specifically involved standard data reduction methods including subtraction of the bias and sky frames, bad pixel masking and flat fielding. The images were then rescaled such that the zero points were fixed at 31 mags for each filter.

My Contributions I extracted AGN light curves from the reduced DES images by adapting the VEILS/VOILETTE extraction code (Hönig, 2018) for reduced DES observations. This involved first identifying sources using the DES photometric catalogue (Abbott et al., 2018) and using aperture photometry to extract light curves for these objects for a range of fixed aperture sizes. Quasars were then selected from these using the coordinates given by the OzDES Quasar catalogue (Tie et al., 2017) using adapted versions of the codes by Almeyda (2019). As I was only interested in combining the optical DES observations with the NIR observations from VEILS (as explained in the following section), I only extracted light curves from the overlapping observation regions depicted in Figure 2.1. The overall number of quasar light curves extracted from the DES observations in the regions that overlapped with VEILS was 518. These light curves were converted from counts into AB magnitudes using the fixed zero point of 31 mags.

2.2.5 VEILS

The VISTA Extragalactic Infrared Legacy Survey (VEILS) is an ESO Public Survey which repeatedly targeted 9 square degrees of sky in the *JKs* bands starting in 2017 using VISTA InfraRed CAMera (VIRCAM) on the Visible and Infrared Survey Telescope for Astronomy (VISTA) telescope at the Paranal Observatory (Emerson et al., 2006). VIRCAM has 16 CCDs with a 1.5 x 1 square degree FOV.

The primary science goals of VEILS included understanding the era of the epoch of reionization, supernova cosmology, AGN dust reverberation lags, and providing photometric redshifts for galaxies. Most of these rely on complimentary optical observations, and as such VEILS was designed to observe regions that were covered by DES (3 square degrees in each of the CDFS, ES and XMM fields) as shown in Figure 2.1. The observation strategy therefore also contained $\sim$ 6 month observation seasons and had planned cadences of 10-14 days (with actual mean observed cadences of $\sim$ 12 days). The single epoch SNR=5 depths are J $<$ 23.5 and Ks $<$ 22.5 magnitudes.

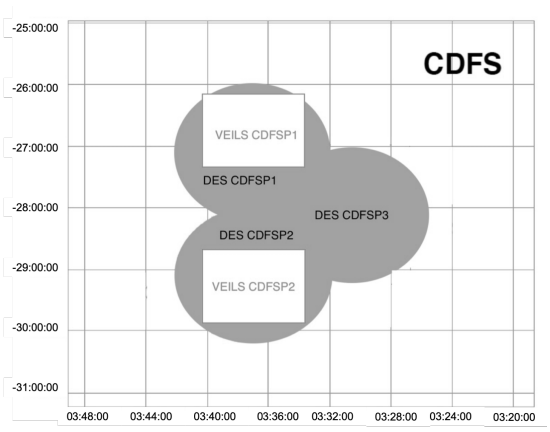

(A) Chandra Deep Field South

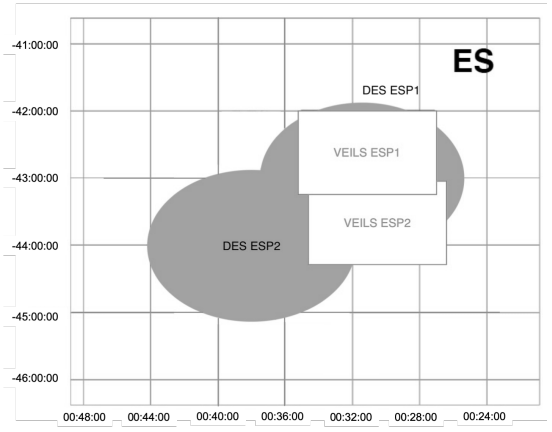

(B) Elias South

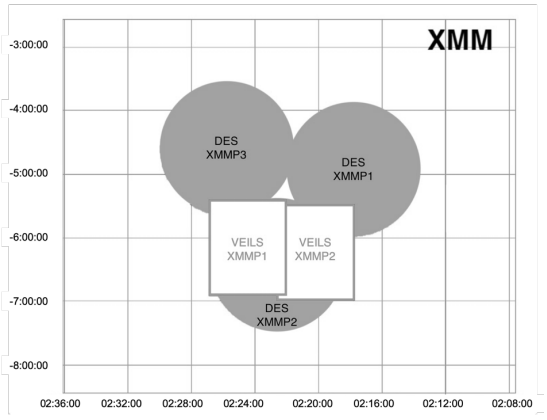

(C) XMM Deep Field

FIGURE 2.1: The overlap between the VEILS and DES surveys in the different observation regions. Adapted from https://www.ast.cam.ac.uk/~mbanerji/VEILS/survey.html

The raw VEILS observations were reduced by a collaborator using the standard data reduction techniques introduced in Section 2.1, by subtracting dark and sky frames and flat fielding. AGN light curves were extracted from the reduced VEILS images using the 2MASS catalogue (Skrutskie et al., 2006) for identifying sources which were extracted using aperture photometry and known quasars were identified from these using the OzDES Quasar Catalogue. Differential photometry was performed for a range of fixed apertures to correct the light curves, but due to inconsistencies across the detectors with this data, the reference stars (defined here as sources that varied less than 0.5 dex over the entire observational period) were restricted to those within a certain distance from the object.

2.2.6 VOILETTE

The VEILS OptIcal Light curves of Extragalactic TransienT Events (VOILETTE) survey was designed to provide complementary optical SDSS *griz* band observations to VEILS after DES finished observing in 2018, using OmegaCAM on the VST (VLT

Survey Telescope) also at the Paranal Observatory (Kuijken et al., 2002). OmegaCAM contains 32 CCDs providing a 1x1 square degree FOV.

The primary science goals of VOILETTE included discovering and classifying type Ia supernovae, monitoring optical variability of AGN for dust reverberation lag analysis and to provide complementary observations of infrared transients that might not have an optical counterpart.

VOILETTE was specifically designed to compliment VEILS, and as such, images were taken to overlap with the VEILS by using a dithering/offset pattern that would account for the differences between the VLT and VST FOV. The observation seasons of VOILETTE were also $\sim$ 6 months long, with planned cadences of $\sim$ 6 days in the *r* band and cadences of $\sim$ 10 days in the *giz* filters. However, the actual observation cadences did not meet the requirements in the 2018 season which had mean cadences of $\sim$ 9 and 13 days in the *r* and *i* bands and only $\sim$ 2-3 observations in each of the *gz* bands, and furthermore in 2020 the observation seasons were restricted to $\sim$ 1 month as the observatories were shut down due to COVID-19[2]. The 5σ per-epoch limiting magnitude were expected to be r $<$ 23.8 mag, $g < 23.2$, $i < 23.8$ and $z < 23.6$.

My Contributions I reduced the raw data from VOILETTE using the VOILETTE data reduction pipeline depicted in Figure 2.2 and described below. This utilised the VOILETTE Soton Reduction Pipeline codes (Hönig, 2018) created for OMEGACam observations.

- A master bias frame was made for each detector by mean combining bias frames observed with zero second, closed shutter exposures.
- A master dark frame was made from mean combining the dark frames in each detector that consisted of one hour exposures taken with the camera shutter closed. These dark frames were scaled to match the exposure times of the science images in each filter using the master bias. The noise created by the read-out bias is included in the master dark frame, so dark subtraction from here-on includes the subtraction of bias as well.
- The master flat frame was created using a combination of dome and sky flat frames in each detector and in each filter. The dome and sky flats were bias and dark subtracted before being median combined to create the master flat frames.
- The master sky frames were created for each detector using the set of 10 dithered science observations. Each raw science image was dark subtracted and flat fielded, and the bad pixels were masked before the sky background was

[2] https://www.eso.org/public/announcements/ann20010/

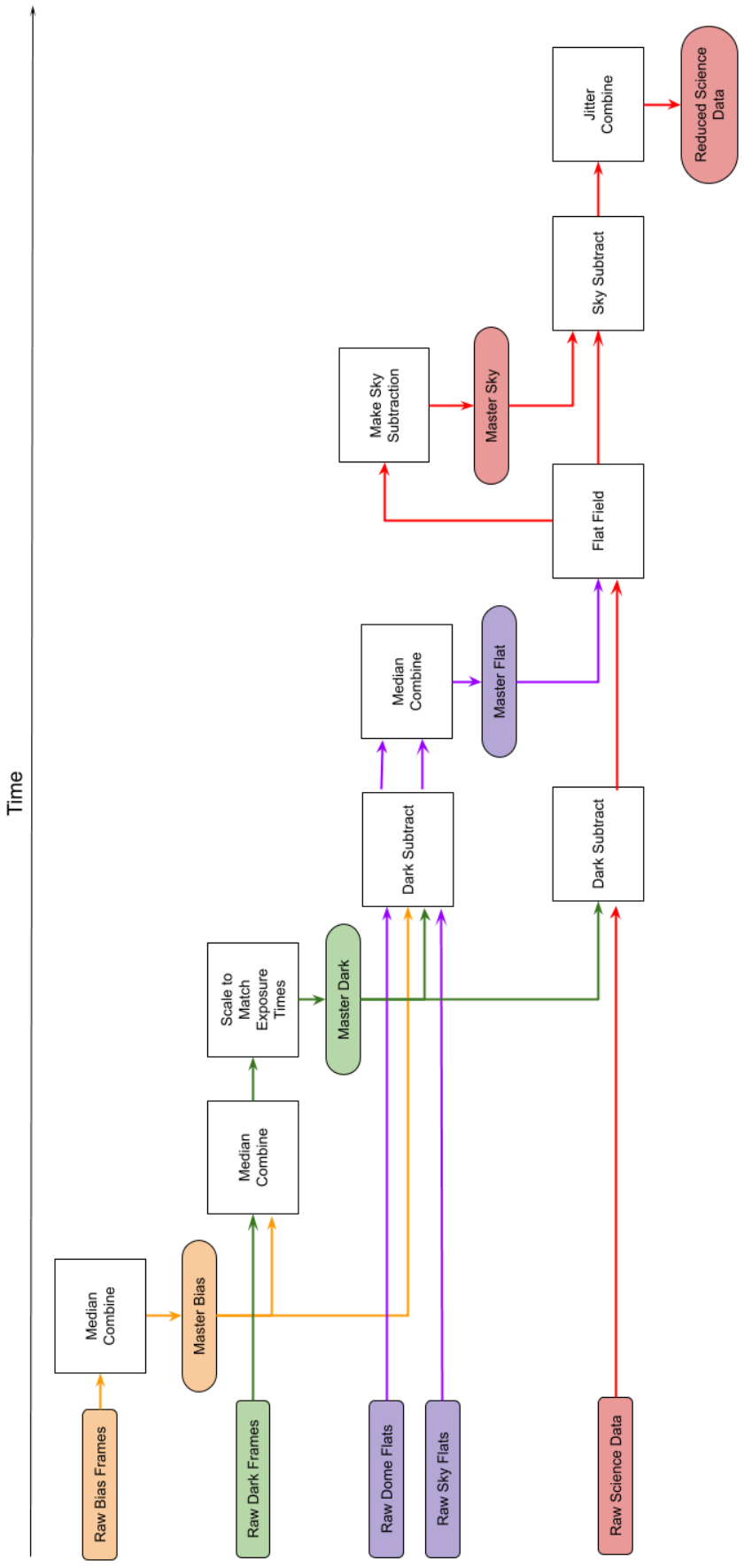

FIGURE 2.2: Flow chart demonstrating the steps followed during the VOILETTE data reduction pipeline

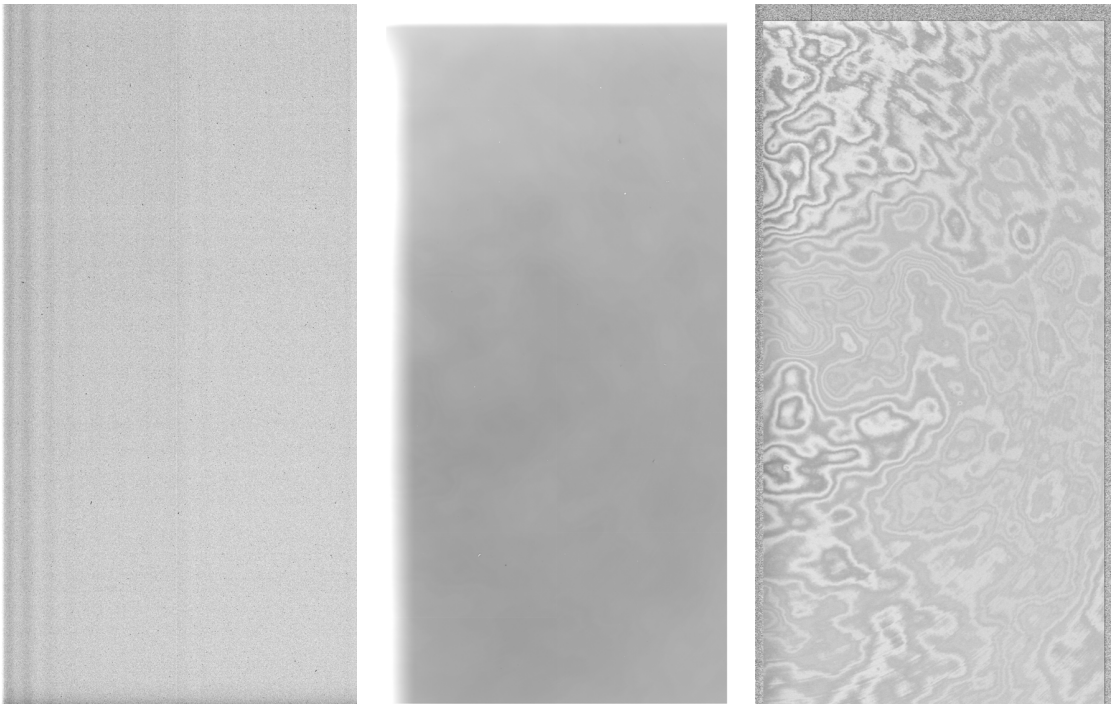

(A) Master dark frame from September 2019.

(B) Master flat field frame from September 2019.

(C) The sky frame for the science observations in CDFS on 2019-09-17.

FIGURE 2.3: Examples of the different calibration images used to reduce the raw data from VOILETTE, made for *z* band data in September 2019.

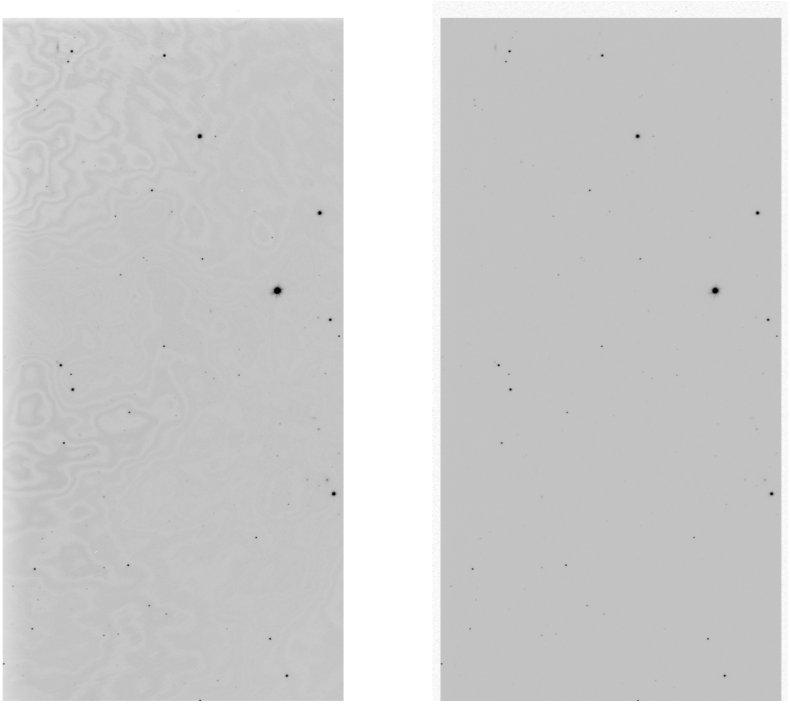

(A) An example of a raw image from VOILETTE.

(B) An example of the raw image in Figure 2.4a reduced using the calibration images in Figure 2.3.

FIGURE 2.4: An example of the comparison between the raw and reduced images from VOILETTE, for observations in the CDFS pointing using *z* band on 2019-09-17.

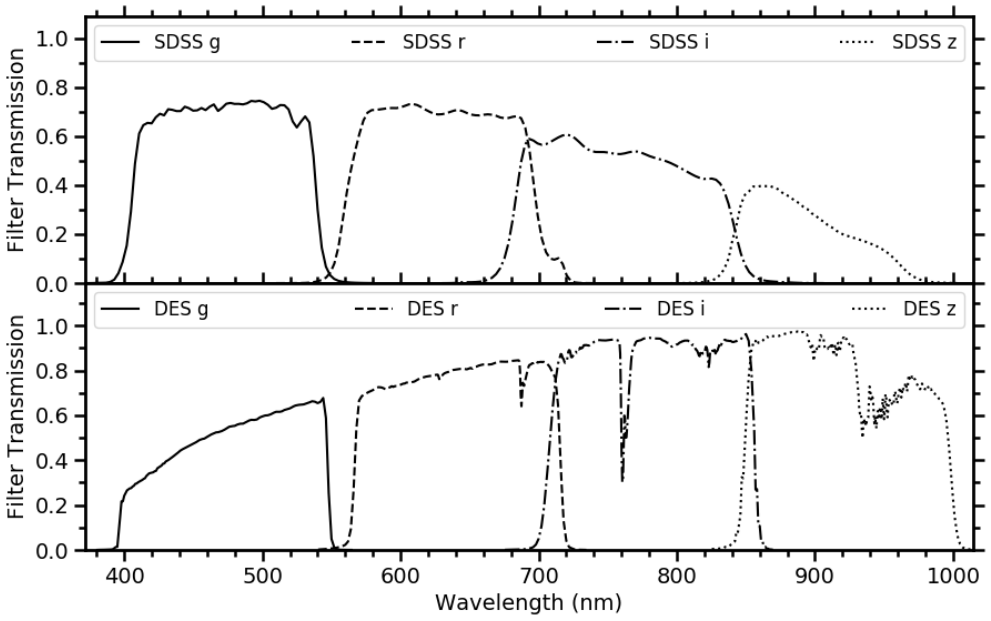

FIGURE 2.5: Comparison between the optical filter transmissions used in the DES and VOILETTE surveys.

estimated using the IDL procedure MMM[3] which was adapted from the DAOPHOT routine (Stetson, 1987). These estimated sky backgrounds were then median combined to create the master sky frame for that set of observations.

- The raw science images were therefore dark subtracted, flat fielded, bad pixel masked and sky subtracted before being jitter combined (to account for the difference in FOV of VEILS and VOILETTE) to create the reduced science images.

An example of the master data calibration images are given in Figure 2.3 to show the different types of systematic noise that need to be removed before the science images can be analysed. Additionally, Figure 2.4 shows an example of the comparison between the raw and reduced science image made using the master calibration images from Figure 2.3.

I then performed aperture photometry on the reduced science images using the VOILETTE source extraction code (Hönig, 2018). This worked by first identifying astronomical objects within each image using the IDL procedure FIND[4]. The IDL procedure APER[5] is then used to compute concentric aperture photometry on this list of objects for numerous aperture sizes, ranging from 2. to 24. pixels. In this procedure, the fluxes of each object are measured by integrating over the specified apertures and

[3] https://www.l3harrisgeospatial.com/docs/mmm.html
[4] https://www.l3harrisgeospatial.com/docs/find.html
[5] https://www.l3harrisgeospatial.com/docs/aper.html

subtracting the estimation of the sky background. Furthermore, the uncertainties in the flux measurement are given as a combination of random noise inside the aperture which is estimated from the scatter in the sky background, Poisson statistics of the observed objects brightness, and the uncertainty in the estimation of the mean sky brightness, all added in quadrature. The RA and DEC were then used to compare these objects to the sources listed in the DES photometric catalogue, and quasars were identified from these sources using the OzDES Quasar Catalogue.

Nightly observational effects were corrected from the AGN light curves using relative photometry to estimate the apparent magnitudes of the objects via non-varying (again defined here as sources that varied less than 0.5 dex over the entire observational period) reference stars of known magnitude found in the same detector with similar count rates using adapted versions of the codes by Almeyda (2019). DES and VOILETTE use slightly different filter systems, as depicted in Figure 2.5, however it can be assumed that the differences have negligible effect on the light curves.

Overall, I detected 676 quasars from the OzDES quasar catalogue in the VOILETTE observations, and of these, 368 were also detected in the DES observations.

2.2.7 OzDES

The Australian spectroscopic Dark Energy Survey (OzDES) is the spectroscopic follow up survey to DES-SN fields. OzDES uses the 3.9m Anglo-Australian Telescope (AAT; Smith et al. 2004) at Siding Spring Observatory in Australia, along with the AAOmega spectragraph with the Two Degree Field (2dF) 400 multi-object fibre positioning system (Lewis et al., 2002), which covers the wavelength range of 3700-8800 $\dot{A}$ with spectral resolution of 1400-1700 (Lidman et al., 2020).

OzDES was expected to target each field approximately 25 times over the entire 5 year observation period, with cadences of $\sim$ 1 month. The primary goal of OzDES was to obtain redshifts for supernova host galaxies, though some of the fibres ($\sim$ 50-100) in each field were also dedicated to quasars as part of the OzDES BLR reverberation mapping (OzDES RM) programme (Childress et al., 2017). The OzDES RM programme chose the quasar sample to observe based on the presence of Hβ, Mg II or C IV lines in the spectra from the first 2 years of observations with a SNR of greater than 10 for quasars with redshifts of $z < 3$ or a SNR greater than 5 for redshifts of $z > 3$ (King et al., 2015).

My contributions Spectroscopic observations also need to be calibrated to remove any differences from each epoch due to factors including image quality, airmass, transparency, and fibre placement. I flux-calibrated the raw spectra of one blazar, PKS 0027-426, that was provided to me using the photometry from DES and the code

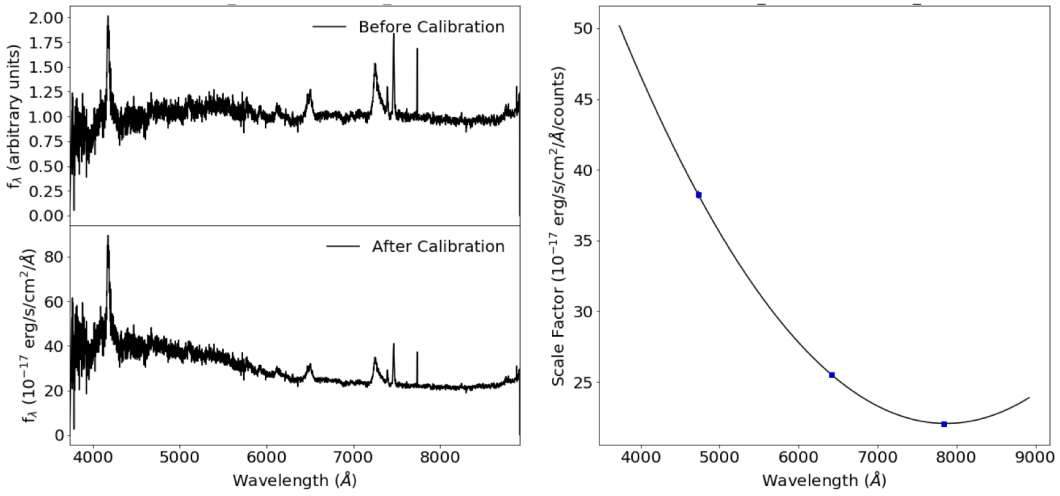

FIGURE 2.6: Example of the calibration of the OzDES spectra of PKS 0027-426 using the code by Hoormann et al. (2019).

by Hoormann et al. (2019). This involved linearly interpolating the DES photometric light curves to estimate the flux in the *gri* bands for each spectroscopic epoch, and comparing these to *gri* band fluxes estimated using the OzDES spectra and DES filter transmission curves to find the scaling polynomial that needs to be applied to the spectra. This is shown for example in Figure 2.6.

2.2.8 LSST

The Vera C. Rubin Observatory Legacy Survey of Space and Time (LSST) is a 10 year synoptic survey that will repeatedly image the sky in the *ugrizY* filters(Ivezić et al., 2019), expected to start observing in 2022/2023. LSST has a FOV of 9.6 square degrees, and will have single epoch depths of up to $r \sim 24.5$ mags (LSST Science Collaboration et al., 2009), and final co-added depths of up to ~ 27.5 mags.

LSST is designed to meet the following four main science objectives; probing dark energy and dark matter in the universe, cataloguing the solar system, exploring the transient optical sky, and mapping the Milky Way.

Though the exact observation strategy for LSST is not yet finalised, it is currently planned that more than 2/3 of the observing time will be dedicated to the main baseline survey, often referred to as the Wide Fast Deep (WFD) survey, which will repeatedly observe a region of $\sim$ 20,000 square degrees (with $\sim$ 200 visits per filter). The remaining time will be dedicated to smaller observing programmes, including the Deep Drilling Field (DDF) survey which will obtain deeper and more frequent observations of 5-10 specific fields to allow for additional science objectives to be

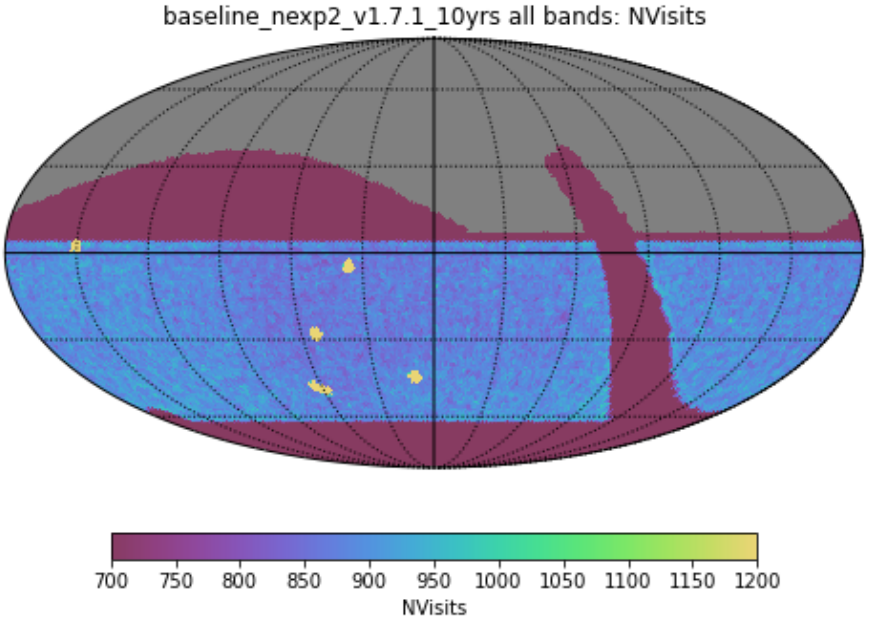

FIGURE 2.7: The total number of observations in each region of the sky for all filters combined over the proposed 10 years, made using the baseline v1.7.1 observation strategy. Image Credit: http://astro-lsst-01.astro.washington.edu:8081.

fulfilled. 4 DDFs have already been selected, which include the Elias South, Chandra Deep Field South, and XMM. An example of the number of observations expected in each region of sky is given in Figure 2.7 for all filters combined over the 10 years. It has also been proposed that a rolling cadence could be used for the WFD region instead, in which regions of the sky are alternatively observed with more intensity one year and less the next, however this is not confirmed.

With the current observation strategy, it is predicted that LSST will provide hundreds of observations for up to 10 million quasars with redshifts up to 7 (LSST Science Collaboration et al., 2009), therefore providing an opportunity to greatly advance our knowledge of AGN.

Chapter 3

Variability Analysis Methods

In this chapter, I will describe some of the common methodology that will be used for the analysis in Chapters 4, 5, and 6.

3.1 Interpolation

For much of the upcoming analysis, continuous, evenly sampled observations of AGN are needed, however most of the observations described in Chapter 2 do not meet these requirements. This is common in optical and IR astronomy, especially when using ground based telescopes, so interpolation methods are often employed to estimate the flux between observations.

Linear Interpolation The simplest method of interpolating the data fits the missing data points onto a straight line between the nearest two observations. This method is generally considered adequate when resampling the light curve to finer resolutions than necessary for the analysis. However, as discussed in Section 1.4.1, AGN are typically characterized by their stochastic variability, so if the light curves that are being interpolated contain large gaps, this method can create biases in the results as it underestimates the expected variability.

Interpolating using the Structure Function An alternate method of replicating the expected variability in AGN when interpolating the missing data points is to use the SF described in Section 1.4.1.2 (Suganuma et al., 2006). The SF is obtained from the observed light curves using Equation 1.13 for each combination of observations, where the data is resampled into evenly sampled bins whose size is given by the mean difference between observations. This resampled SF is then fit to give a continuous structure function over the range required. An example of this is demonstrated in

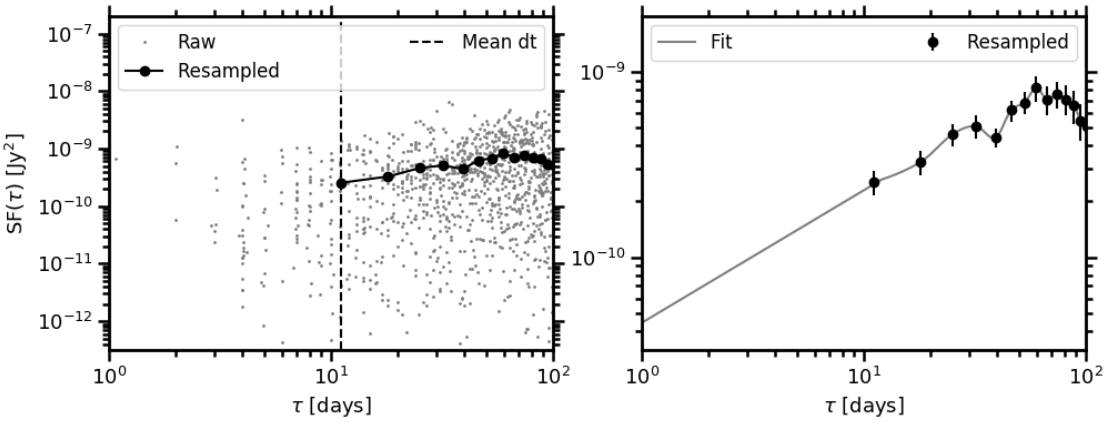

FIGURE 3.1: Example of the structure functions made from observed AGN light curves. In the left plot, the grey points represent the individual observations, while the black line and points represents the resampled structure function (also shown in the right plot) and the dashed line represents the mean sampling rate of the observations.

Figure 3.1. This SF is then used to simulate the variability of the emission between observations, using the value of the SF corresponding to the time separation between a missing data point and the nearest data point on the new light curve, where the observed fluxes are varied between their 1σ uncertainties.

This method is data driven and non-parametric, however it relies on temporal sampling of the light curve used to create the SF that is representative of the overall underlying SF, which could lead to inaccurate estimations of the variability if this is not the case.

JAVELIN Many authors choose to replicate the expected variability of AGN in interpolated light curves by modelling the PSD of the light curve as a DRW (Kelly et al., 2009) using JAVELIN (Zu et al., 2011, 2013). In contrast to using the SF as outlined in the previous section, this method is model driven and parametric. Discrepancies have frequently been found between the DRW model and observed PSDs as described in Section 1.4.1, which means the underlying assumptions of this method could be incorrect.

3.2 Cross Correlation Function

To measure the similarity between the variability of two AGN light curves as a function of time, cross correlation functions (CCFs) are often utilised, which are defined in Equation 3.1 (Suganuma et al., 2006).

$$CCF(\tau) = \int I(t)\, C(t-\tau)\, dt \tag{3.1}$$

where $I(t)$ and $C(t)$ are the light curves at time t and $t-\tau$ respectively, and τ is the time lag being tested.

For observed light curves, the CCF can be expressed using Equation 3.2 (Suganuma et al., 2006).

$$CCF(\tau) = \frac{1}{N} \sum_{i=1}^{N} \frac{[C(t_i-\tau) - \langle C \rangle][I(t_i) - \langle I \rangle]}{\sigma_C \sigma_I} \tag{3.2}$$

where N is the number of pairs of observations, $\langle C \rangle$ and $\langle I \rangle$ are the mean fluxes for each light curve, and σ_C and σ_I are their respective standard deviations.

For each time τ, the CCF returns a value between $\pm$ 1 where a CCF of 1 and -1 corresponds to a perfect correlation and anti-correlation respectively.

Cross correlating a light curve with itself gives the auto-correlation function (ACF) which allows for a search of similar variability within the same object's emission at different times, and can indicate potential periodicity within the emission. As mentioned above, much of the data that will be used in this thesis is not continuous or evenly sampled, which is a requirement of the CCF to generate the light curve pairs. The following methods are commonly utilised to overcome this, by interpolating the light curves as described above (interpolated CCF; ICCF) or by resampling the light curves into evenly spaced bins (Discrete CCF; DCF).

Standard ICCF The standard method of ICCF (S-ICCF) interpolates both light curves to evenly sampled cadences, either using the SF or by linearly interpolating. The CCF is then calculated using the IDL package, c_correlate.pro[1]. Interpolating introduces uncertainties however, which can largely impact the results especially when considering observations with large gaps between observing seasons (often as a result of the visibility of the object being observed from Earth).

Modified ICCF To reduce the effect of large portions of interpolated data in the light curves being cross-correlated, I also use a modified version of the S-ICCF method which is outlined below.

1. The first light curve, $f_1(t_1)$, is interpolated using the SF to get a light curve, $f_1^*(t)$, with the desired sampling period, δt.

$$f_1(t_1) \rightarrow f_1^*(t)$$

[1] https://www.l3harrisgeospatial.com/docs/c_correlate.html

where $t_1 = \{t_{1,0}, ..., t_{N_1}\}$ contains the epochs of observations of the first light curve, $t = \{\delta t, 2\delta t, ..., t_{N_1}\}$.

2. The epochs of the second light curve's observations plus each delay in the range that is being explored are then extracted:

$$f_1^*(t) \rightarrow f_1^*(t_2 + \tau)$$

where $t_2 = \{t_{2,0}, ..., t_{N_2}\}$ contains the epochs of observations of the first light curve, and τ is the range of lags being explored.

3. The second light curve is then varied between its 1σ uncertainties, $\sigma_2(t_2)$, for each epoch, t_2:

$$f_2(t_2) \rightarrow f_2(t_2) + (a \times \sigma_2(t_2))$$

where -1 < a < 1.

4. These light curves are then cross correlated with 0 delay using Equation 3.2

5. This method is then repeated, interpolating the second light curve and matching observations to the first.

DCF To prevent interpolations from impacting the results, the DCF was introduced by Edelson and Krolik (1988), in which the light curves were binned into evenly sampled bins to provide an estimate of the CCF. This method assumes no underlying physics, though it does limit the precision to which a delay can be recovered, especially for inconsistently sampled data. Furthermore, the DCF method cannot be used on light curves that contain large gaps between observation seasons which are commonly found in ground based telescopes that are limited by when objects are visible to that location.

3.3 Simulating Mock AGN Light Curves

For simulating mock AGN light curves in this thesis, I will be using the method of Timmer and Koenig (1995). This is a commonly used method of producing Gaussian light curves in astronomy from power spectrum as power spectrum are the Fourier transforms of the light curves. This method specifically works by randomising the phase and amplitude of the Fourier components of the Fourier transform used to construct the time-series from the power spectrum. In this thesis, the Timmer-Konig algorithm is performed using the IDL function, timmerlc.pro[2]. It is worth noting that the light curves created using the Timmer-Konig algorithm are Gaussian distributed,

[2] http://astro.uni-tuebingen.de/software/idl/aitlib/timing/timmerlc.pro

however observed AGN light curves are known to deviate from this behaviour, often exhibiting burst-like behaviour (e.g., Emmanoulopoulos et al., 2013), which can be a limitation of using this method.

3.4 Periodograms

AGN PSDs are estimated using periodograms (Bloomfield, 2000), which are given by the modulus squared of the discrete Fourier transforms (DFT) of the observed light curves. For an evenly sampled light curve with fluxes, x_i, measured at times t_i (for i = 1, 2, ..., N), this is shown by Equation 3.3.

$$|DFT(f_j)|^2 = \left| \sum_{i=1}^{N} x_i \, e^{(2\pi i f_j t_i)} \right|^2 = \left\{ \sum_i x_i \cos(2\pi f_j t_i) \right\}^2 + \left\{ \sum_i x_i \sin(2\pi f_j t_i) \right\}^2 \quad (3.3)$$

where f_j are the N/2 evenly spaced frequencies, given by $f_j = \frac{j}{N\Delta T}$ (for j = 1, 2, ..., N/2) and ΔT is the sampling period of the light curve.

In AGN variability analysis, the DFT is usually normalized by the factor, A, given in Equation 3.4 (van der Klis, 1997) so that the integrated periodogram gives the fractional variance of the data (Vaughan et al., 2003).

$$A = \frac{2\Delta T_{\rm samp}}{\bar{x}^2 N} \quad (3.4)$$

where $\Delta T_{\rm samp}$ is the sampling interval and $\bar{x}$ is the mean flux.

3.4.1 PSRESP Method of Estimating Power Spectrum Shapes

Observed AGN periodograms are often distorted from the underlying PSD due to effects including red-noise leakage, which is the transfer of variability power from low to high frequencies, windowing effects due to the sampling of the light curves, and as a result of rebinning the periodgrams. To account for this when searching for the fits to the periodogram, I follow the Monte Carlo technique for Power Spectral RESPonse (PSRESP) introduced by Uttley et al. (2002), in which the periodogram of the observed light curve is compared to the mean periodogram from a large sample of simulated light curves whose underlying PSD is known.

This technique is performed as follows. First, I use the Timmer and Koenig (1995) algorithm to simulate N light curves with the same mean and standard deviation flux as the observed light curve, using a fixed PSD shape. These light curves are made with

initial length longer than entire length of observations to account for the red-noise leakage. I then extract the same cadencing as the observed light curve on each of the simulated light curves and estimate their periodogram. The mean and RMS spread of these simulated periodograms are used as the model periodogram.

To determine the goodness of fit of the observed periodogram to this model, a statistic, $\chi^2_{\rm dist}$, is defined in Equation 3.5 (Uttley et al., 2002).

$$\chi^2_{\rm dist} = \sum_{f=f_{min}}^{f_{max}} \frac{(\overline{P_{sim}}(f) - P_{obs}(f))^2}{\Delta\overline{P_{sim}}(f)^2} \tag{3.5}$$

where $\overline{P_{sim}}(f)$ is the mean of the simulated power spectra at frequency f, $P_{obs}(f)$ is the observed power spectra at that same frequency, and $\Delta\overline{P_{sim}}(f)$ is the RMS spread of the simulated model powers about the mean.

This χ^2_{dist} value cannot be compared to the standard χ^2 distribution as the number of simulated periodograms used to make the model is relatively small. Instead, a value of χ^2_{dist} is calculated for each of the simulated periodograms, and this is compared to the value of χ^2_{dist} from the observed periodogram. The goodness of fit is measured by calculating the percentage of simulated periodograms whose χ^2_{dist} is exceeded by the χ^2_{dist} from the observed periodogram. This gives the percentage confidence with which the model periodogram can be rejected.

3.4.2 Lomb-Scargle Periodogram

For the majority of PSD analysis in this thesis, the interpolation methods discussed above are used to create the evenly sampled light curves required for the DFT in Equation 3.3. Some cases are particularly sensitive to the effects of interpolation however, such as periodicity detection, so for these I will use the Lomb-Scargle periodogram described here instead.

The Lomb-Scargle periodogram (LSP; Lomb 1976; Scargle 1982) is a modified version of the classical periodogram that is commonly used in Astronomy for detection of periodicity in unevenly sampled light curves. The LSP is given in Equation 3.6 (Scargle, 1982) for a range of frequencies, f.

$$P_{LS}(f) = \frac{1}{2}\left\{ \frac{\left(\sum_i x_i \cos(2\pi f[t_i - \tau])\right)^2}{\sum_i \cos^2(2\pi f[t_i - \tau])} + \frac{\left(\sum_i x_i \sin(2\pi f[t_i - \tau])\right)^2}{\sum_i \sin^2(2\pi f[t_i - \tau])} \right\} \tag{3.6}$$

where τ is given in Equation 3.7, t_i are the observations and x_i the associated fluxes.

$$\tau = \frac{1}{4\pi f} \tan^{-1}\left(\frac{\sum_i \sin(4\pi f t_i)}{\sum_i \cos(4\pi f t_i)}\right) \tag{3.7}$$

In this thesis, the LSP is calculated from observations using the astropy python package[3].

Peaks in the LSP correspond to potential periodicities, however they can also occur as the result of the sampling of the data, and furthermore, as the underlying power spectrum of an AGN is described by a red noise process, peaks corresponding to the lower frequencies can also be confused with peaks from periodic behaviour. The significance of the peak therefore needs to be estimated, which is done using Monte Carlo simulations of a large number of red-noise light curves to determine how likely a peak is to occur from just the red-noise process and sampling rate of the object.

The underlying red-noise process is estimated following the PSRESP technique of Uttley et al. (2002) as described above. The best fitting power law is then used to simulate light curves with the same flux and variability as the observed source, and these are resampled to the same sampling pattern. The LSP of each of these simulated light curves is then measured, and the distribution of power is used to quantify the significance contours to establish how likely a stochastic light curve is to create any of the detected peaks.

[3] https://docs.astropy.org/en/stable/timeseries/lombscargle.html

Chapter 4

Multi-wavelength Variability Studies of the Blazar, PKS 0027-426

In Chapter 1 I introduced blazars as the most variable subclass of AGN due to the bright relativistic jet that is orientated along our line of sight. This variability is observed over the entire EM spectrum, both in terms of temporal variability (flux variations over time) and spectral variability (flux variations over different observed wavelength ranges). Multi-wavelength variability studies of blazars can provide further information on the emission processes responsible for the observed variability. Specifically, temporal variability analysis can be used to infer the location of the different emitting regions within the AGN, and spectral variability studies can give insight into how the contributions from the thermal and non-thermal emission vary with respect to each other. In this chapter, I analyse the temporal and spectral variability of the blazar PKS 0027-426 using optical *griz* observations from DES and VOILETTE between 2013-2020 and NIR *JKs* observations from VEILS between 2017-2020.

The structure is as follows; in Section 4.1 I summarise variability analysis of blazars in the optical and IR and in Section 4.2 I describe the observations and quantify the flux variability of PKS 0027-426. In Sections 4.3 and 4.4 I present the results of temporal variability analysis and discuss the implications. In Sections 4.5 I present the results of the spectral variability analysis which are further discussed in Section 4.6, and I provide additional analysis of the spectra to explain the colour behaviour observed. Finally, in Section 4.7 I give a summary of the conclusions of this chapter.

A journal article based on the work described in this chapter using the data between 2013-2019 was published in the Monthly Notices of the Royal Astronomy Society as Guise et al. (2022a).

4.1 Introduction

The emission from blazars is composed of both thermal and non-thermal contributions which originate in different components of the AGN. Their SEDs contain two characteristic bumps; one at low energies which covers the range from radio to UV and a higher energy bump which is located in the X-rays to gamma-rays (e.g., Fossati et al. 1998). The dominating emission processes corresponding to these bumps are considered to be synchrotron radiation from the relativistic electrons in the jet at lower energies (e.g., Urry and Mushotzky 1982) and at higher energies can be described by either leptonic models where the bump is due to inverse Compton scattering of the low-energy emission (e.g., Böttcher 2007), or hadronic models in which the bump is due to emission from relativistic protons (e.g., Mücke and Protheroe 2001). In the optical and NIR, additional contributions are expected from thermal emission from the AD and torus. Multi-wavelength variability studies of blazars have been used to provide further information on these emission processes.

Studies of the correlations between the flux variations from different wavelength ranges of blazars commonly show that they are strongly correlated with short lags between the light curves on timescales < 1 day or with no significant lag determined on the order of days (e.g., D'Ammando et al., 2013; Zhang et al., 2013; Kaur and Baliyan, 2018). This implies that the dominant source of the emission in the different wavelength ranges is co-temporal in the blazar, and possibly co-spatial. However, some studies have also reported lags on the order of 10-100 days between optical and NIR light curves in blazars (e.g., Li et al. 2018, Safna et al. 2020). These longer lags could imply that the sources of the emission are located with a distance between them, or Li et al. (2018) suggest that if the emission is produced by shocks in the jet, the higher energy emission could emerge closer to the front of the shock than the lower energy emission, resulting in a delay.

Studies of the spectral variation of blazars have shown three main colour behaviours; bluer when brighter (BWB), redder when brighter (RWB) or achromatic/stable when brighter (SWB). These colour trends are often explained as a result of variations between the different emission processes that contribute to the overall emission, for example a RWB trend could indicate that a red component, such as synchrotron emission from the relativistic jet, is more quickly varying than the bluer component, such as the thermal emission from the AD, and vice versa for a BWB trend (e.g., Fiorucci et al. 2004, Bonning et al. 2012, Agarwal et al. 2019). Alternatively, BWB trends have also been explained by processes associated with the relativistic jet only; for example Fiorucci et al. (2004) describe a one component synchrotron model in which the more intense the energy release, the higher the particle's energy. A shock-in-jet model has also be used to describe the BWB trend as accelerated electrons at the front of the shock lose energy while propagating away, and because of

synchrotron cooling the higher frequency electrons lose energy faster, thus making the high frequency bands more variable (e.g., Kirk et al. 1998, Agarwal et al. 2019). The RWB trend is most frequently observed with FSRQs, and similarly the BWB trend is most commonly observed in BL Lacs (e.g., Gu et al. 2006, Bonning et al. 2012, Meng et al. 2018). This could be related to the luminosity dependent blazar sequence, where more luminous blazars (e.g., FSRQs) are found to have redder SEDs, which has been interpreted by Ghisellini et al. (2017) to be the result of more severe radiative cooling being experienced by the emitting electrons of more luminous blazars. However FSRQs and BL Lacs do not always follow these trends, as some studies find the reverse or find SWB trends (e.g., Gu and Ai 2011, Zhang et al. 2015, Mao and Zhang 2016). Furthermore, while many studies find these simple colour behaviours, some find that the colour trends can be complex; for example, Isler et al. (2017) showed that the *B-J* colour behaviour of the FSRQ 3C 279 varied on different timescales, and over different periods during the 7 years of observation. Specifically, the average colour trend of the entire 7 years is BWB, however the colour variability is shown to deviate for individual observation seasons, such as from achromatic or a SWB trend between May and August 2008, RWB between September 2009 and April 2010 and BWB between February and August 2011. Furthermore, the colour trend of some blazars has been shown to change at a certain magnitude; for example, Zhang et al. (2015) found that several sources showed RWB trends in the low flux state and then kept a SWB trend or a BWB trend in the high flux states.

4.2 PKS 0027-426

PKS 0027-426 was first identified as a possible QSO by Savage (1976) and later classified as a FSRQ by Healey et al. (2007). It has a redshift of z = 0.495 (Hook et al. 2003), and is located at RA = 00h 30m 17.584s, DEC = -42d 24m 46.02s (J2000) which is in the FOV of the Elias South pointing in DES, VEILS and VOILETTE. As a result, it has been observed in the optical *griz* bands with DES from 2013-2018 and VOILETTE from 2018-2021, with concurrent observations in the NIR *J* and *Ks* bands with VEILS from 2017-2021. PKS 0027-426 was found to be the most variable AGN detected in the VEILS fields thus far, which is why I initially chose to study it in detail.

4.2.1 Light Curves

I extracted light curves of PKS 0027-426 in the *griz* bands between 2013-2020 from the DES and VOILETTE images using aperture photometry as described in Chapter 2, with fixed aperture sizes of 1.3″. The light curves were corrected for nightly effects using nearby reference stars of known magnitude, which are listed in Appendix A. A stacked *r* band image from 2019 of PKS 0027-426 with some of the reference stars is

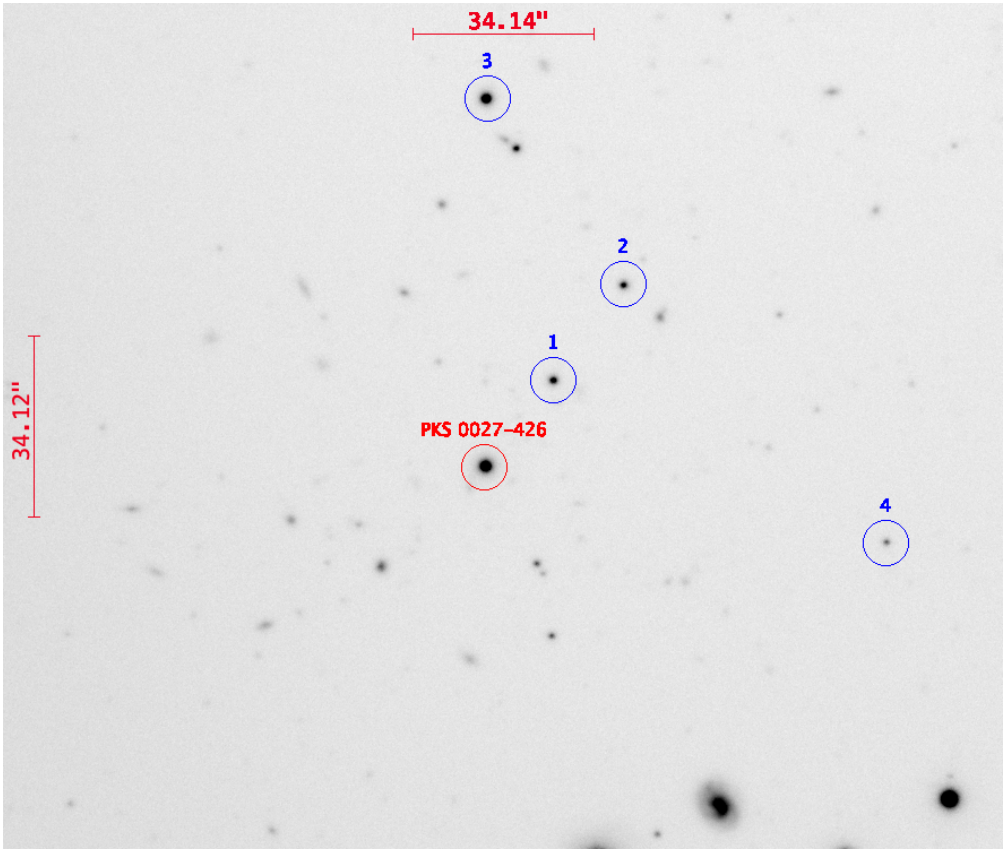

FIGURE 4.1: Stacked *r* band image of PKS 0027-426 and some of the nearby reference stars made from 31 observations from VOILETTE in June-December 2019. Note that the apertures here are used solely to highlight the position and do not correspond to the aperture sizes used for the aperture photometry.

displayed in Figure 4.1, and a comparison of the variability of PKS 0027-426 compared to a reference star in 2017-2019 is displayed in Figure 4.2. The VEILS light curves were similarly extracted by a collaborator.

The top 4 panels of Figure 4.3 show the optical light curves of PKS 0027-426 over 7 years in the *griz* bands, with each season separated by the dotted lines. The cadences of the observations in the *griz* bands are 6.3 $\pm$ 4.9 nights, 6.5 $\pm$ 5.3 nights, 6.6 $\pm$ 4.7 nights and 6.2 $\pm$ 4.8 nights respectively over the entire observational period. The variability in the optical bands is relatively low in the seasons starting 2013-2015, but increases in the seasons starting in 2016-2018. The 2017 season displays the largest variability in each optical filter, and contains its peak magnitude in the first of 2 flares that are separated by approximately 75 days. The 2018 season contains only 3 observations in the *g* and *z* filters, however displays a decreasing brightness in all optical filters, while the 2019 season shows an increase in brightness in all optical filters.

The lower 2 panels of Figure 4.3 show the NIR light curves with 3 years of observations in the *J* and *Ks* bands respectively, with cadences of 11.3 $\pm$ 5.9 nights and

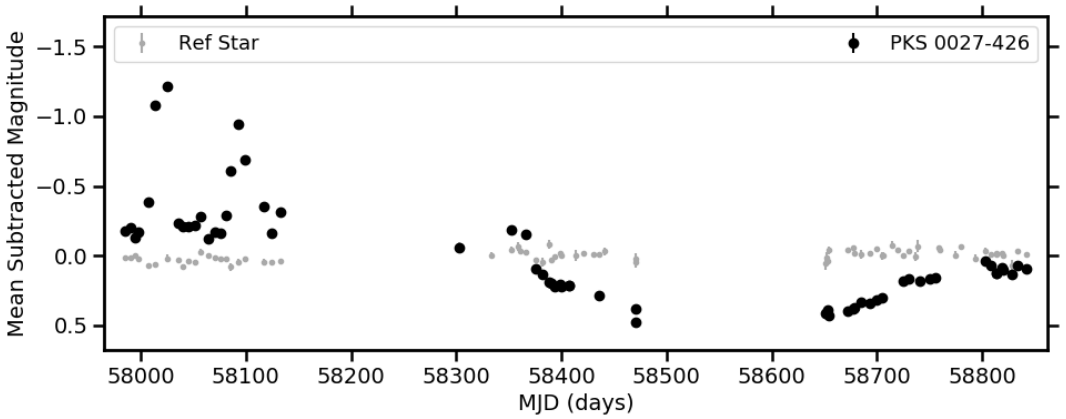

FIGURE 4.2: Light curves of PKS 0027-426 and the reference star labelled 2 in Figure 4.1 in the DES and VOILETTE *r* band for the observation seasons starting 2017-2019 to demonstrate the difference in variability.

11.2 ± 8.1 nights. Similarly to the optical, the 2017 season displays the largest variability in both NIR filters, however, it also contains a gap in the observations between $\sim$ 58000 and 58050 MJD, which corresponds to the epochs containing the first and brightest peak in the optical.

4.2.1.1 Flux Variability Analysis

Amplitude Variability Parameter To further characterise the variability of PKS 0027-426 in each filter and in each season, I calculated the amplitude variability parameter, A, using Equation 4.1 (Heidt and Wagner, 1996).

$$A = \sqrt{(A_{\max} - A_{\min})^2 - 2\sigma^2} \tag{4.1}$$

where $A_{\max}$ and $A_{\min}$ are the maximum and minimum apparent magnitudes, and σ is the average measurement error.

Table 4.1 shows the amplitude variation of the emission observed in each filter in each year. The variation in the *griz* light curves is relatively small in the seasons starting in 2013-2015 with amplitude variability parameters of $\sim$ 0.25 - 0.5, but in the 2016 and 2017 seasons they increase to $\sim$ 0.6 - 0.9 and > 1 respectively, in the 2018 season decreases back to $\sim$ 0.6 - 0.7 and finally in the 2019 season they decrease further back to $\sim$ 0.25 - 0.5. The *J* and *Ks* bands in the 2017-2019 seasons are shown to vary similarly to the optical.

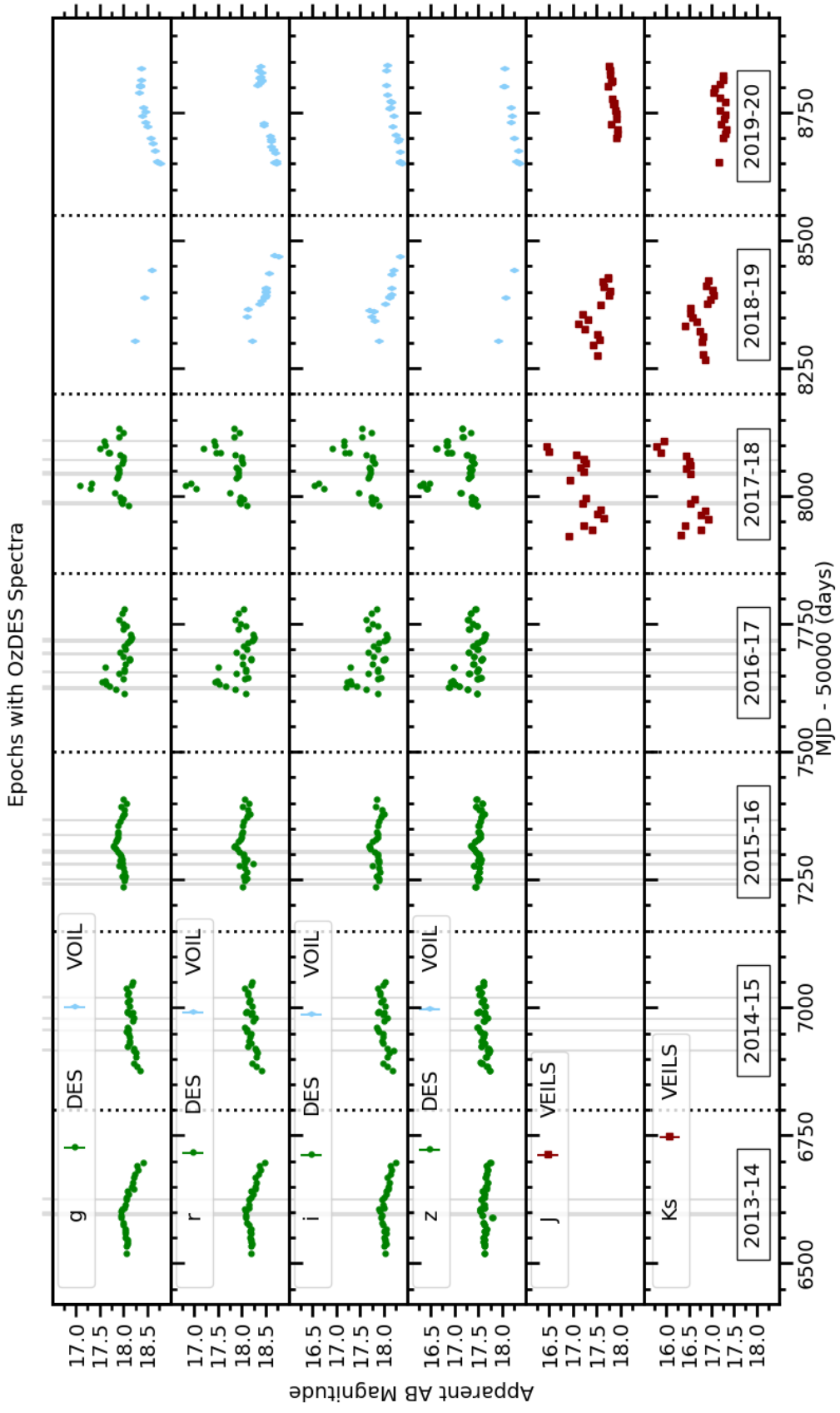

FIGURE 4.3: Light curves of PKS 0027-426 in the optical *griz* bands and NIR *JKs* bands. The optical light curves contain a combination of DES (green circles) in the seasons starting in 2013-2017 and VOILETTE (blue diamonds) in the seasons starting in 2018-2019 and the NIR observations are from VEILS (red squares) in seasons starting in 2017-2019. Each observation season is separated by the dotted lines and the epochs corresponding to OzDES observations are shown with the grey lines.

TABLE 4.1: The amplitude variation of the light curves in different filters in each observation season, calculated using Equation 4.1. The 2013-2016 seasons contain only data from the *griz* bands from DES, the 2017-2019 seasons also contains the *JKs* bands from VEILS, and the 2018 season only has the *r* and *i* bands from VOILETTE due to limited *g* and *z* data.

Year Starting	*g* (mag)	*r* (mag)	*i* (mag)	*z* (mag)	*J* (mag)	*Ks* (mag)
2013	0.46	0.41	0.35	0.26	-	-
2014	0.28	0.36	0.36	0.27	-	-
2015	0.26	0.39	0.32	0.27	-	-
2016	0.63	0.81	0.85	0.76	-	-
2017	1.03	1.29	1.33	1.20	1.13	1.19
2018	-	0.66	0.61	-	0.62	0.66
2019	0.44	0.39	0.36	0.34	0.27	0.47

Flux-Flux Plots As PKS 0027-426 was mostly observed on the same night with each DES filter, I analysed the flux variations in each optical filter relative to another using flux-flux plots for the seasons starting 2013-2017. The light curves in Figure 4.3 are in AB magnitudes, m_{AB}, however these are converted to fluxes, f_ν, using Equation 4.2.

$$m_{\mathrm{AB}} = -2.5\,\mathrm{Log}\left(\frac{f_\nu}{3631\mathrm{Jy}}\right) \tag{4.2}$$

Figure 4.4 displays the *r*, *i* and *z* band fluxes compared to the *g* band fluxes. The flux in each filter is shown to increase as the *g* band flux increases, and though the relationships aren't necessarily linear overall, Figure 4.5 shows that the relationship in the individual seasons of the *g*-*z* flux-flux plots are approximately linear.

Furthermore, Figure 4.6 displays the flux-flux plots for the seasons that also used observations from VEILS and VOILETTE, however as the observations with each VEILS and VOILETTE filter were not taken on the same night, I interpolated the *rizJKs* light curves using the SF so that the flux on the same epoch as the *g* band observations could be compared. All seasons show approximately linear relations between the flux in each band vs the *g* band flux, though the 2018 season only had 3 *g* band observations.

4.2.2 Optical Spectra

Optical spectra of PKS 0027-426 were obtained on 37 epochs between 2013 to 2018 by OzDES. I flux calibrated the spectra using the photometry from DES using the code by Hoormann et al. (2019) as described in Chapter 2 to remove any differences from each epoch. Figure 4.7 displays the mean and smoothed RMS spectra of PKS 0027-426, for the entire observational period and the individual observations seasons, with most relevant emission lines labelled. An excess in the red wing can be seen in some of the broad emission lines (BELs) in Figure 4.7, which is a phenomenon observed in many radio loud quasars (Punsly et al., 2020).

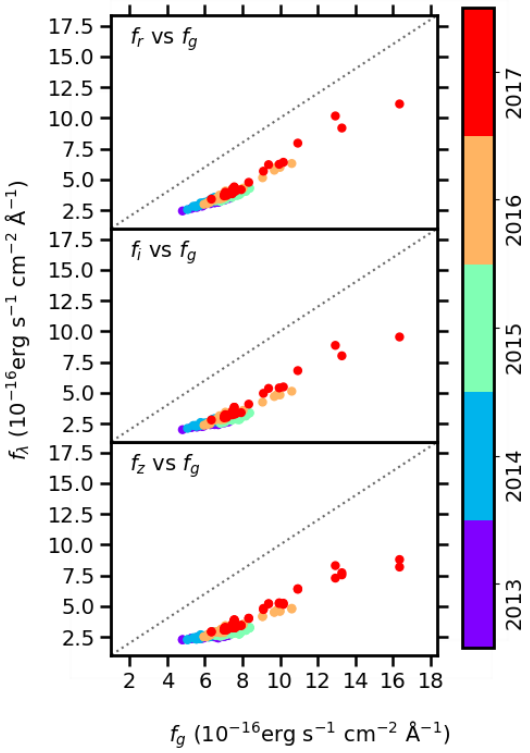

FIGURE 4.4: Flux variations in each DES r, i, z filter compared to the DES g band, where the data points are coloured according to observation season.

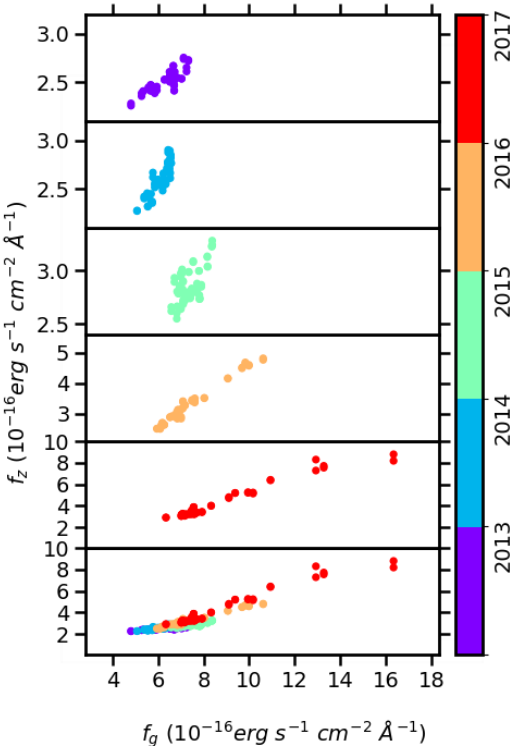

FIGURE 4.5: Flux variations in each season of DES z filter compared to the DES g band, where the data points are coloured according to observation season.

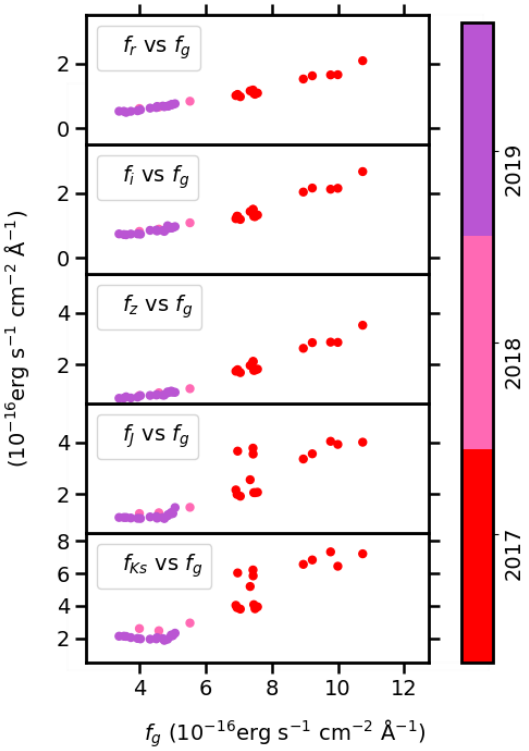

FIGURE 4.6: Flux variations in each filter compared to the g band for the seasons starting 2017-2019. The light curves in these seasons had to be interpolated to extract simultaneous data to the g band observations.

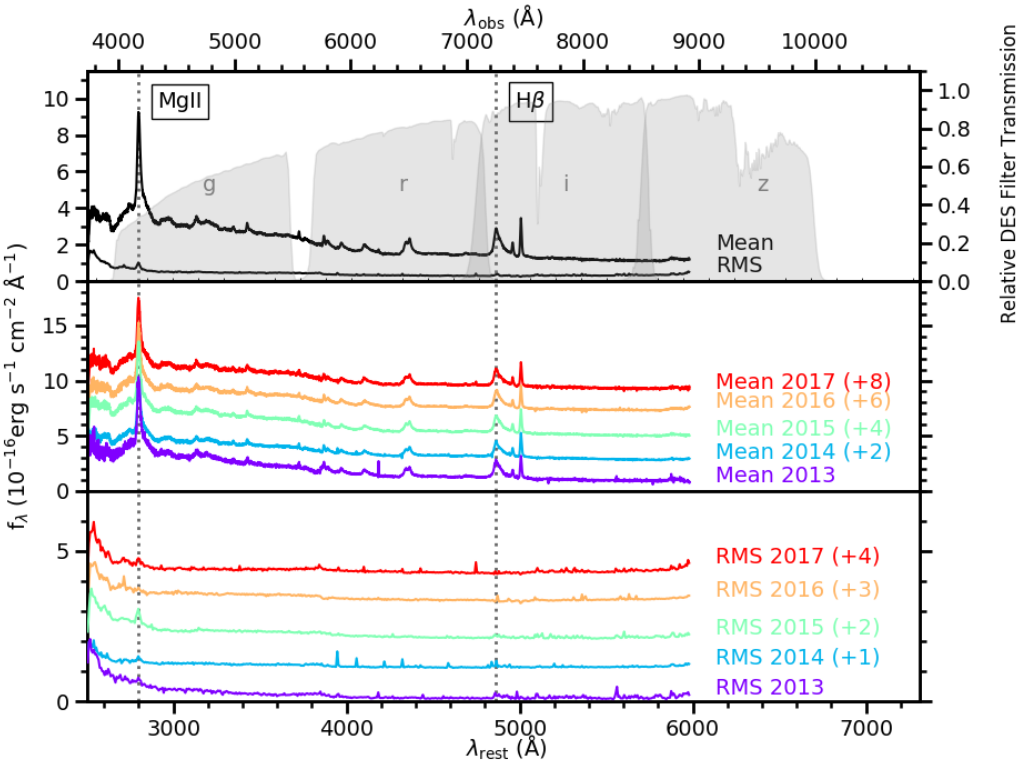

FIGURE 4.7: *Top Panel*: Overall mean spectra of PKS 0027-426 using 92 observations from OzDES over 37 epochs between 2013-2018, with some of the relevant emission lines labelled. The filter transmission curves for DES are overlaid to demonstrate which filter each emission line lies in. *Middle panel*: the mean spectra for each individual observation season, labelled with the starting year of observations. *Lower panel*: The Smoothed RMS spectra for each individual observation season, labelled with the starting year of observations.

4.2.2.1 Single Epoch Black Hole Mass Estimates

As mentioned in Chapter 1, due to the correlation between BLR radius and luminosity of the AGN, methods of estimating the mass of the black hole using single epoch observations of broad emission lines have been developed (e.g., Vestergaard, 2002). I therefore used the Mg II and Hβ lines in the spectra to obtain an estimate for the virial mass of the SMBH of PKS 0027-426, $M_{\rm BH}$, using Equation 4.3.

$$\mathrm{Log}\left(\frac{M_{\rm BH}}{M_\odot}\right) = a + b\,\mathrm{Log}\left(\frac{\lambda L_\lambda}{10^{44}\mathrm{erg\ s^{-1}}}\right) + 2\mathrm{Log}\left(\frac{\mathrm{FWHM}}{\mathrm{kms^{-1}}}\right) \tag{4.3}$$

where the coefficients a and b for the Mg II line are 0.74 and 0.62 respectively (Shen et al., 2011), and for the Hβ line are 0.91 and 0.50 respectively (Vestergaard and Peterson, 2006), the FWHM is the full width half maximum of the emission line, and λL_λ is the monochromatic luminosity at 3000 $\dot{A}$ and 5100 $\dot{A}$ for the Mg II and Hβ lines respectively, which are calculated from the *gri* magnitudes using Equation 4.4 (Kozłowski, 2015).

$$\mathrm{Log}(\lambda L_\lambda) = \mathrm{Log}(L_F) - \mathrm{Log}(R) \tag{4.4}$$

where $\mathrm{Log}(R)$ is linearly dependent on the redshift as $\mathrm{Log}(R) = a_R + b_R z$ where a_R and b_R are given in Kozłowski (2015), and L_F is the luminosity in each filter which is calculated using Equation 4.5.

$$L_F = \nu L_\nu = 4\pi D_L^2 \alpha_F \nu_F 10^{-0.4 * m_F} \tag{4.5}$$

where L_F is the luminosity of each filter in units of 10^{23} erg/s, α_F is the zero-point flux for each filter, m_F is the observed magnitude in a specific filter, ν_F is the central frequency of the filter, and D_L is the luminosity distance which is given as 2687 Mpc for PKS 0027-426 in NASA/IPAC Extragalactic Database (NED)[1].

I estimated the black hole mass for each OzDES spectra, and found the mean to be $\mathrm{Log}(M_{\mathrm{BH}}) = 8.16 \pm 0.08\ M_\odot$ for the Mg II line and $8.06 \pm 0.28\ M_\odot$ for the Hβ line, which are consistent within their 1σ uncertainties.

4.2.3 Spectral Energy Distribution

I plotted the SED of PKS 0027-426 using archival data from NED in Figure 4.8, with a comparison to the average SED generated for FSRQs from Ghisellini et al. (2010). The lower energy peak commonly thought to be due to the synchrotron emission from the relativistic jet can be seen in the frequency range corresponding to Log $\nu \sim$ 10-18 Hz, and a dip is present at $\sim$ 14 Hz which corresponds to the optical-NIR frequency range.

4.3 Temporal Variability Analysis

Temporal variability studies of blazars typically report lags between the optical and NIR emission on timescales $<$ 1 day (e.g., D'Ammando et al., 2013; Zhang et al., 2013; Kaur and Baliyan, 2018), which implies that the dominant emission regions are co-spatial and could be expected to be due to the synchrotron emission from the relativistic jet. This expected lag is smaller than can be detected with the cadences of observations from DES, VOILETTE and VEILS, as these surveys were designed to detect dust reverberation lags in AGN. However, I perform temporal variability analysis on PKS 0027-426 here to explore whether any larger lags, possibly one corresponding to a delay between the thermal emission in the optical and NIR, could be detected as well, as other studies have reported significant lags between the optical and NIR in blazars on the order of 10-100 days (e.g., Li et al., 2018; Safna et al., 2020).

[1]The NASA/IPAC Extragalactic Database (NED) is operated by the Jet Propulsion Laboratory, California Institute of Technology, under contract with the National Aeronautics and Space Administration.

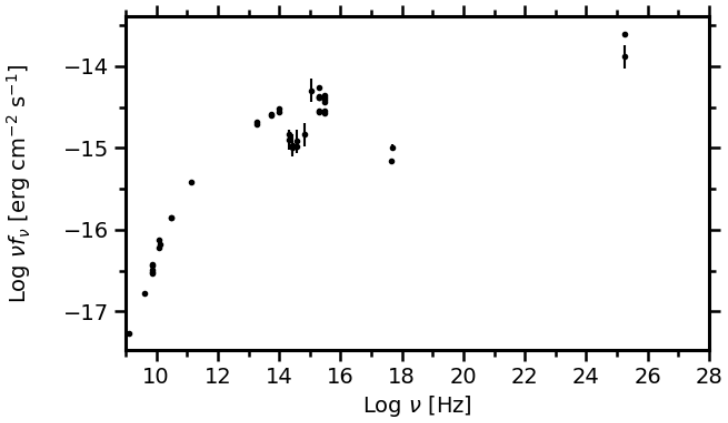

FIGURE 4.8: The spectral energy distribution of PKS 0027-426 made using archival data from NED.

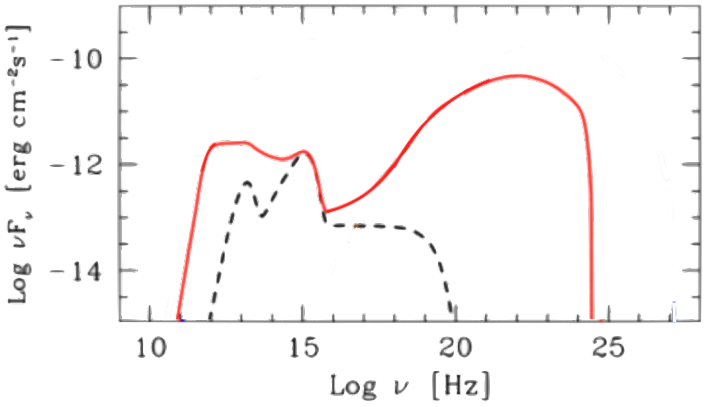

FIGURE 4.9: An example of the shape of the SED of a FSRQ in red, with the SED of a typical AD and torus in the black dashed line. Image adapted from Ghisellini et al. (2010).

In order to quantitatively study the temporal variability between the light curves from DES, VOILETTE and VEILS, I computed both the S-ICCF and M-ICCFs here, as described in Chapter 3. I did this for the entire light curves of each combination of filters in both the optical and NIR, as well as for the light curves from individual observation seasons to test whether the results remain consistent throughout. As each light curve was interpolated using the SF, filling in the missing data in a random order to estimate the variability from different time separations, the S-ICCF and M-ICCF methods were therefore repeated 10,000 times for each combination of light curves to decrease the impact of the interpolated data in each instance on the cross correlation results.

Each combination of light curves was cross-correlated over possible observed lags between $\pm$100 days due to the length of the individual season light curves. The CCFs were also compared with the ACFs of each light curve to determine whether the peaks in the CCFs were a result of a lag between the light curves, or an effect of similar

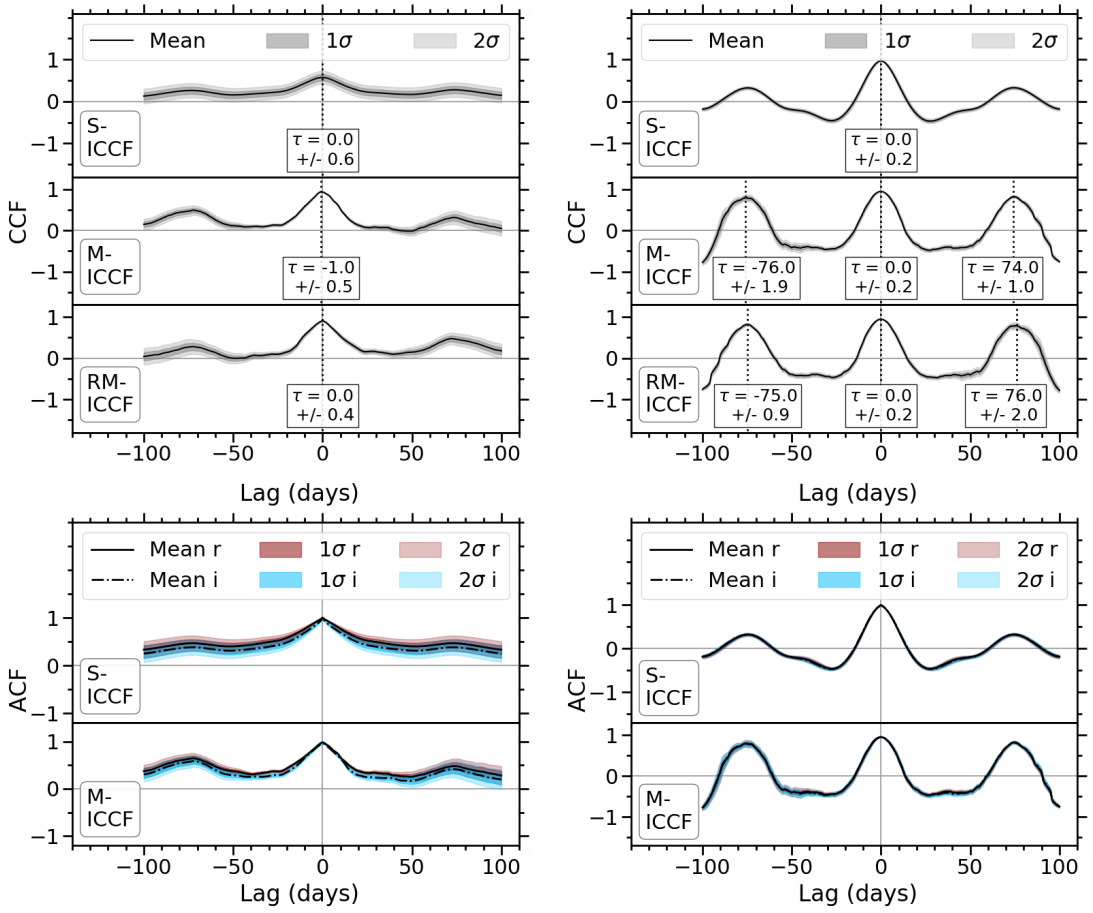

(A) CCFs and ACFs of the entire *r* and *i* light curves.

(B) CCFs and ACFs of the 2017 *r* and *i* light curves.

FIGURE 4.10: *Top Panels*: Mean CCFs of the *r* and *i* light curves in the season starting 2017 and in the entire observation period between 2013 and 2019. *Lower panels*: The corresponding ACFs. Here, the M-ICCF method refers to the interpolated *r* band, and the RM-ICCF method refers to the interpolated *i* band.

variability within the individual light curves (i.e., aliasing). Potential lags that were measured from peaks on the mean CCFs were considered positive detections if the CCF values were greater than 0.5. This was chosen as the limit as most non-zero peaks in the ACFs had values smaller than this. The possible lags that were classified as positive detections are labelled on the plots, with the uncertainties calculated as the standard deviations of the peak of the CCF for each interpolation around the peak of the mean CCF.

4.3.1 Cross Correlations of the Optical Light Curves

As the *r* and *i* band had the highest number of observations, I will discuss them in detail here. The cross-correlation between the *r* and *i* band light curves and their ACFs are displayed in Figure 4.10, for the entire observational period and the individual

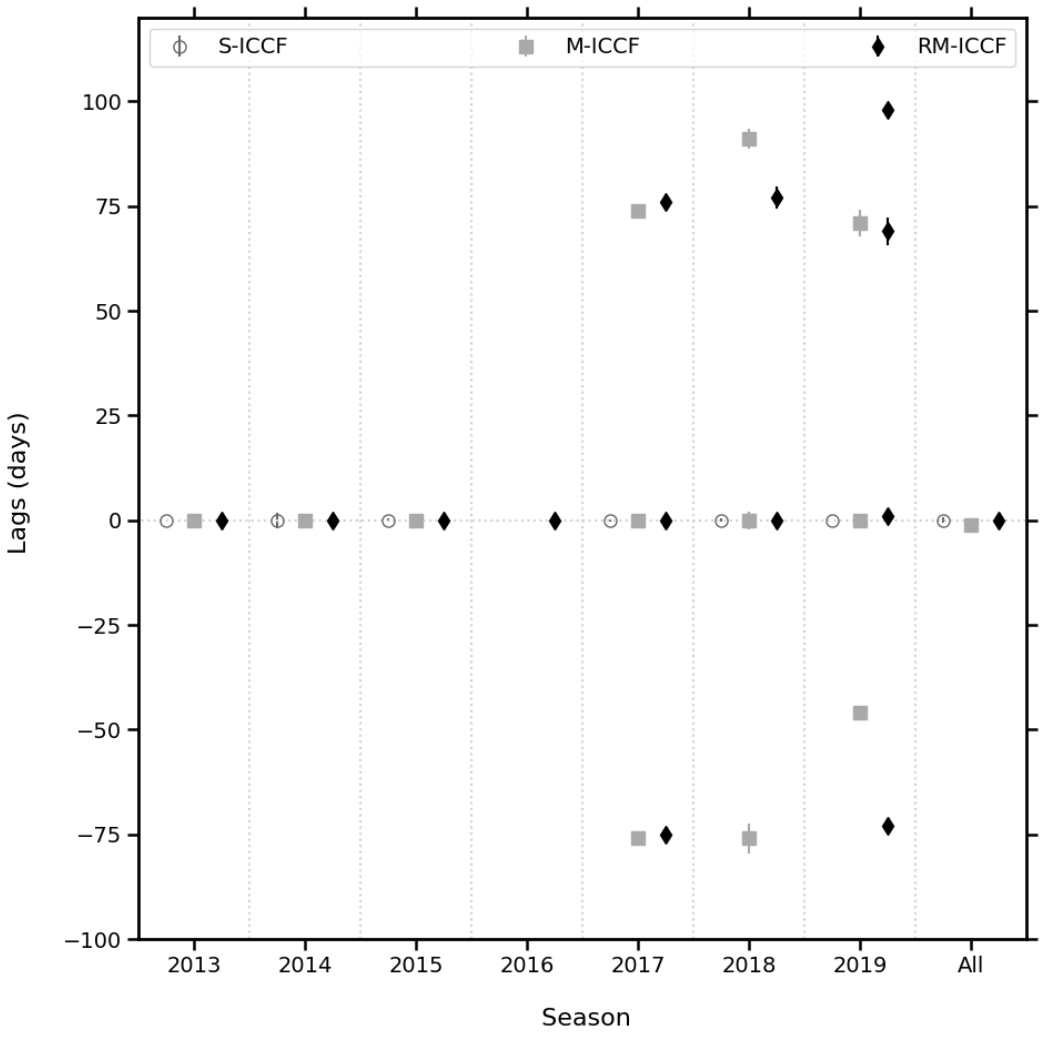

FIGURE 4.11: A comparison of all the potential lags detected in each method of cross correlation for the entire *r* and *i* band light curves and for the individual observation seasons.

season starting 2017. The CCFs of the other individual observation seasons are displayed in Appendix A, and a comparison for all lags detected in the different season *r* and *i* CCFs is plotted in Figure 4.11.

Figure 4.11 shows that there is a correlation between *r* and *i* band light curves at ~ 0 days, which is consistently present in the CCFs of each year, except the season starting in 2016 whose CCF is relatively level, which could be due to the shape of the light curves in that season that contain multiple peaks that likely correlate with each other. The overall mean lag is therefore found with a value of -0.1$\pm$0.2 days, which implies that the emission in both filters is co-temporal, or any delay between the emission regions is on timescales smaller than the cadences of observations.

An additional lag at $\sim \pm$ 75 days is also observed in the both M-ICCF and RM-ICCF

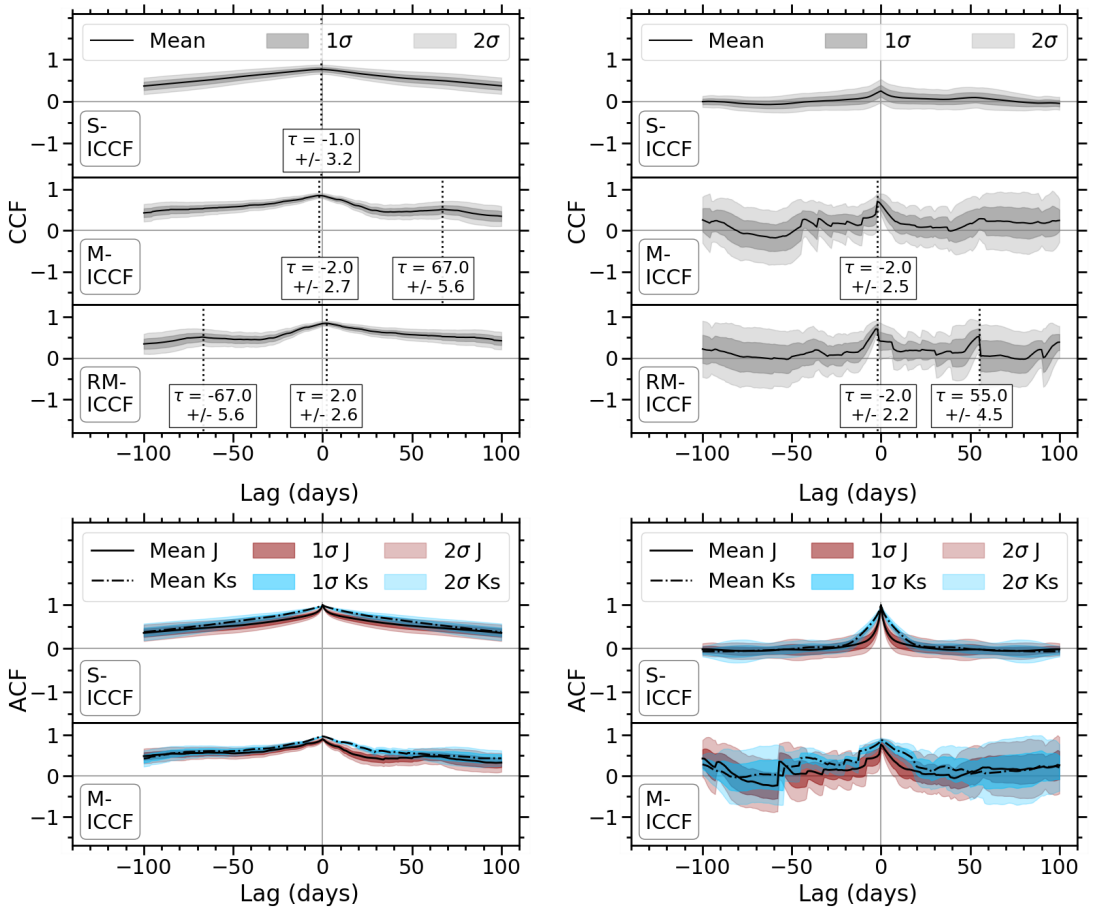

(A) CCFs and ACFs of the entire *J* and *Ks* light curves.

(B) CCFs and ACFs of the 2017 *J* and *Ks* light curves.

FIGURE 4.12: *Top Panels*: Mean CCFs of *J* and *Ks* light curves in the season starting 2017 and in the entire observation period between 2017 and 2019. *Lower Panels*: The corresponding ACFs. Here, the M-ICCF method refers to the interpolated *J* band and the RM-ICCF method refers to the interpolated *Ks* band.

methods of the 2017 CCFs which are displayed in Figure 4.10b, and in some of the 2018 and 2019 M-ICCF and RM-ICCF methods, however a corresponding peak is found in at least one of the ACFs in these observation seasons which implies that it is not a delay between emission regions but a consequence of aliasing in the light curves. This is explored further in Section 4.3.4.

4.3.2 Cross Correlations of the NIR Light Curves

To explore possible delays between the NIR light curves, I also cross correlated the *J* and *Ks* band light curves in each individual observation season and the entire light curves. The cross-correlation between the light curves for the individual season starting in 2017 and the entire light curves are displayed in Figure 4.12, along with

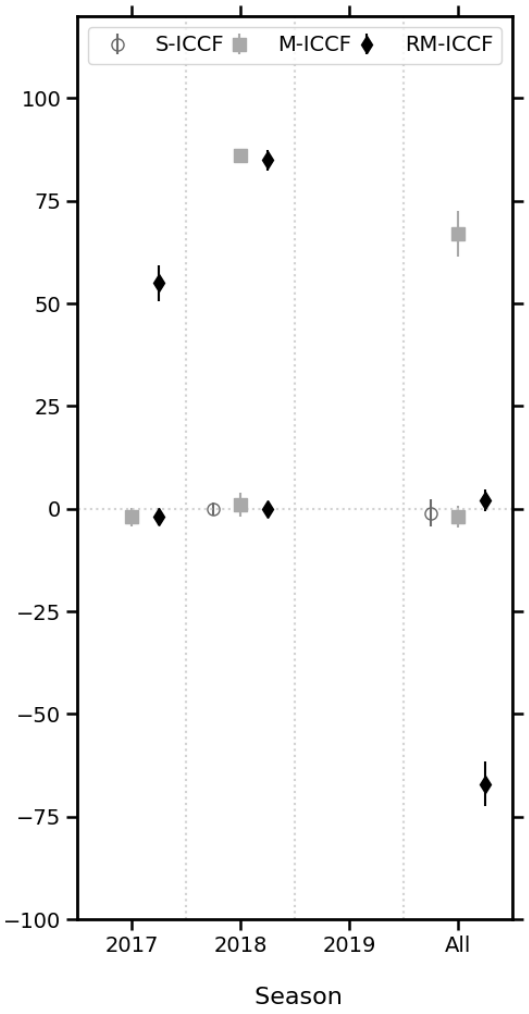

FIGURE 4.13: A comparison of all the potential lags detected in each method of cross correlation for the entire *J* and *Ks* band light curves and for the individual observation seasons.

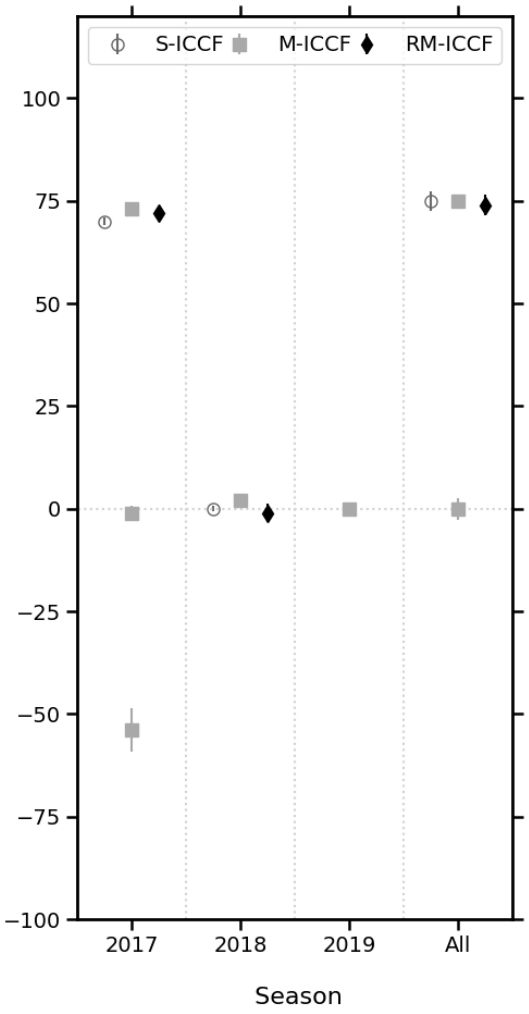

FIGURE 4.14: A comparison of all the potential lags detected in each method of cross correlation for the entire *r* and *Ks* band light curves and for the individual observation seasons.

their ACFs. The individual 2018 and 2019 season CCFs are displayed in Appendix A, and a comparison plot of the lags detected is shown in Figure 4.13.

These CCFs show the presence of a strong correlation at ~ 0 days in at least one method in all seasons except 2019 with a mean value of -0.8 ± 1.0 days. However, the $\sim$ 0 day is not observed in the 2017 S-ICCF method, which is assumed to be due to large gaps in the light curves and the interpolations between these observations diluting the overall correlation, and additionally, no lag is detected in the the 2019 season as each CCF is mostly shown to be level.

Additional possible lags are detected with values between $\pm$55-90 days in these CCFs

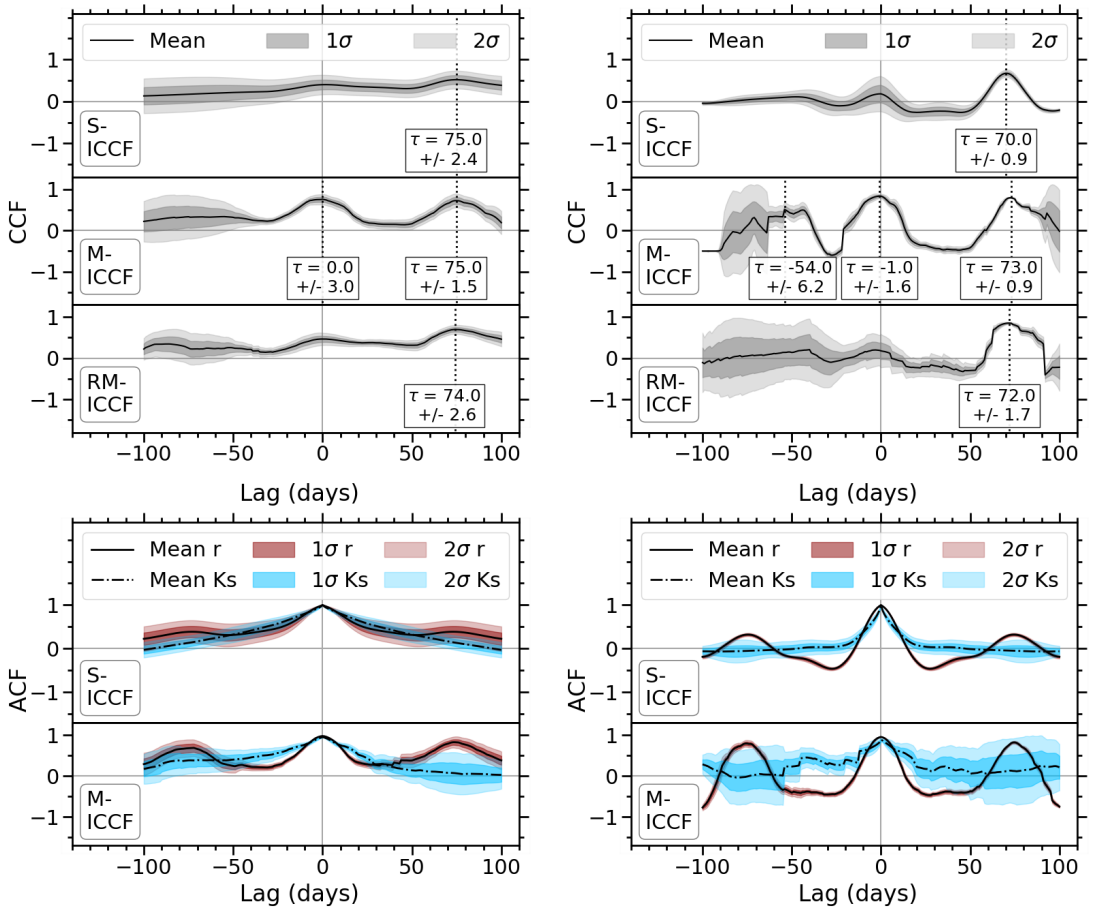

(A) CCFs and ACFs of the entire *r* and *Ks* light curves.

(B) CCFs and ACFs of the 2017 *r* and *Ks* light curves.

FIGURE 4.15: *Top Panels*: Mean CCFs of *r* and *Ks* light curves in the season starting 2017 and in the entire observation period between 2017 and 2019. *Lower Panels*: The corresponding ACFs. Here, the M-ICCF method refers to the interpolated *r* band and the RM-ICCF method refers to the interpolated *Ks* band.

(excluding 2019), all of which have corresponding peaks in one of the ACFs which implies that this not a delay between light curves but again is the result of similarity in the emission in the individual light curve.

4.3.3 Cross Correlations of the Optical-NIR Light Curves

I also explored the cross correlation between optical and NIR light curves, focusing here on the *r* and *Ks* bands as they had the highest number of observations. The results of each CCF method for the *r* and *Ks* band light curves are therefore displayed in Figure 4.15 along with their ACFs for the 2017 season and the entire overlapping observational period. The CCFs and ACFs of the 2018 and 2019 seasons are displayed in Appendix A, and an overall comparison between lags detected in each season is given in Figure 4.14.

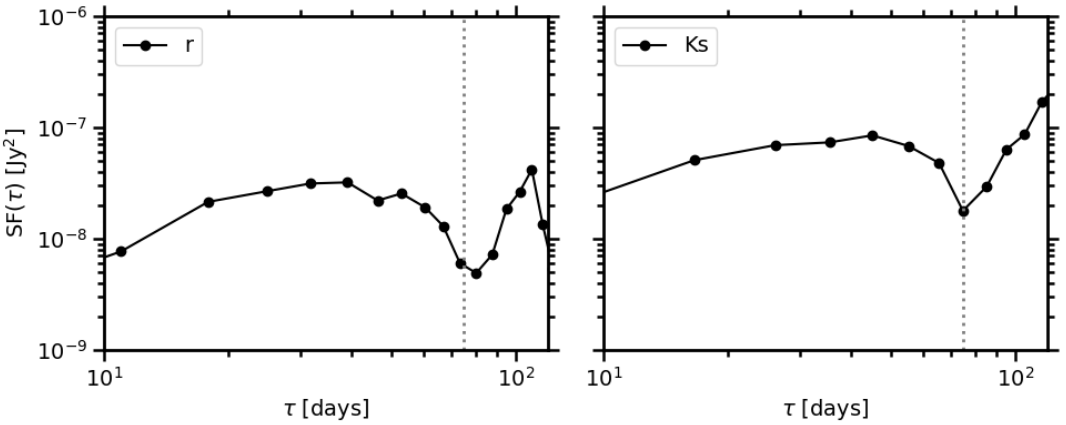

FIGURE 4.16: Structure functions of PKS 0027-426 from the *r* and *Ks* band combined 2017-2019 light curves.

The *r* and *Ks* band CCFs show the presence of strong correlations at ~ 0 days in at least one method in all seasons, with a mean of 0.0 ± 1.2 days, however this is not consistently detected across all methods. Specifically, in the S-ICCF methods, the light curves are not as well correlated at 0 days, which could be due to the interpolated epochs equally impacting the CCFs, and therefore reducing the overall correlation. Furthermore, there is a lower correlation at 0 days for RM-ICCF method particularly when the 2017 season is used, but this is suspected to be due to the lack of observations in the NIR when the optical light curve displays the first of 2 peaks. As the NIR light curve is interpolated and epochs extracted matching the observed optical epochs, the interpolations during the unobserved month will reduce the overall correlation.

An additional lag is detected at $\sim \pm 75$ days in the 2017 season and in the entire overlapping light curve which similarly to the *r-i* cross correlations has a corresponding peak in the ACF and therefore is expected to be due to aliasing in the light curves.

4.3.4 Potential Periodicity in the Light Curves

In multiple CCFs a possible lag is detected at $\sim \pm 75$ days which appears to be due to aliasing of the light curves as a corresponding peak appears in the ACFs of each filter, and furthermore the structure functions display a dip around this time as shown in Figure 4.16 for the *r* and *Ks* band light curves between 2017-2019. This could imply a potential periodicity within the light curves, so therefore I investigated the significance of the 75 day timescale here.

I explored whether or not this dip in the structure function was intrinsic to properties of PKS 0027-426 by simulating AGN light curves of varying properties using the codes

introduced in Hönig et al. (2014), which followed the algorithm presented by Timmer and Koenig (1995), where the PSD of the AGN were modelled as a DRW (Kelly et al., 2009). Specifically, I varied properties of the AGN including the luminosity and Eddington ratio, which in turn varied the characteristic timescales and white noise amplitudes of the PSD. I then extracted the epochs of observation of PKS 0027-426 from the simulated light curves and calculated the SF in the same way, before measuring the number of SFs that similarly displayed dips at $\sim$ 75 days.

To choose the range of luminosities and Eddington ratios to explore, I first calculated the mean bolometric luminosity of PKS 0027-426 over the observational period to be $\mathrm{Log}L_{\mathrm{Bol}} = 45.8$ erg s^{-1} from the monochromatic luminosity, and estimated the Eddington luminosity to be $\mathrm{Log}L_{\mathrm{Edd}} = 46.1$ erg s^{-1} using Equation 1.4, where the mass was the mass calculated from the emission lines previously. I varied the luminosity between $\mathrm{Log}L_{\mathrm{Bol}} \pm 1$ and the Eddington ratio, $\lambda_{\mathrm{Edd}} = L_{\mathrm{Bol}}/L_{\mathrm{Edd}}$, between $\mathrm{Log}\lambda_{\mathrm{Edd}} \pm 0.7$. A dip in the SF at $\sim$ 75 days was identified if the value of the SF corresponded to the minimum of the 3 data points either side.

The percentage of the SFs from 10,000 simulated light curves that also displayed a dip at $\sim$ 75 days were found to be $\sim$ 9% and $\sim$ 10% in *r* and *Ks* bands respectively. Furthermore, the distributions of the SFs with varied inputs that returned the dip at $\sim$ 75 days are plotted in Figure 4.17 and compared to the distribution of SFs from all simulated light curves. The shape was shown to be similar for each value of luminosity in Figures 4.17a and 4.17c, and Eddington ratio in Figures 4.17b and 4.17d, which therefore implies that the $\sim$ 75 day dip does not depend on specific properties of the light curve of PKS 0027-426, but occurs for a random $\sim$ 10% .

In addition, Appendix A contains further analysis of the Lomb-Scargle periodograms of the *r* band light curves as described in Chapter 3, and again shows that the 75 day lag is not significant considering the 2 and 3σ significance contours made from purely simulated red-noise light curves.

4.4 Temporal Variability Discussion

I studied the temporal variability of PKS 0027-426 using cross correlation functions of the optical and NIR light curves amongst themselves and with each other to determine possible lags between the light curves emission. In this chapter the *r* and *i*, *r* and *Ks*, and *J* and *Ks* CCFs were discussed as representations of optical-optical, optical-NIR and NIR-NIR correlations as they had the most observations.

Over each combination of filters, the most consistent correlation present was at $\sim$ 0 days, which implies that the emission is simultaneous or any time delay between the light curves is on timescales less than the cadence of the surveys used (which have

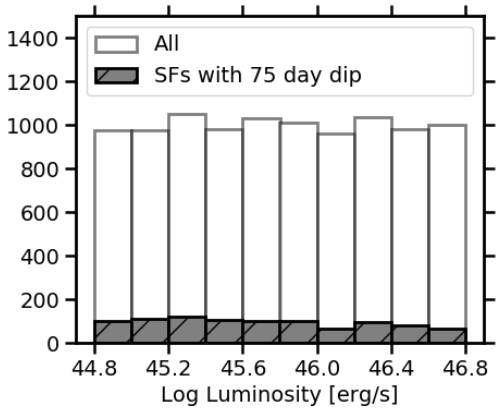

(A) Comparisons between the distributions of the luminosity for *r* band.

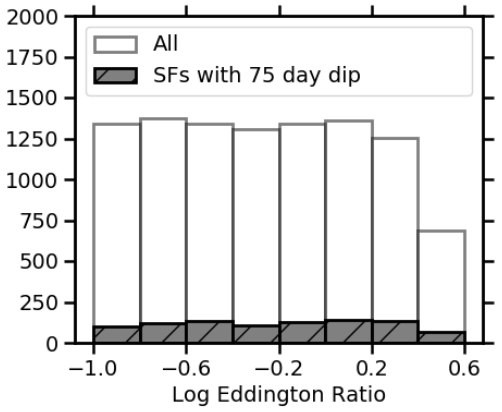

(B) Comparisons between the distributions of the Eddington ratio for *r* band.

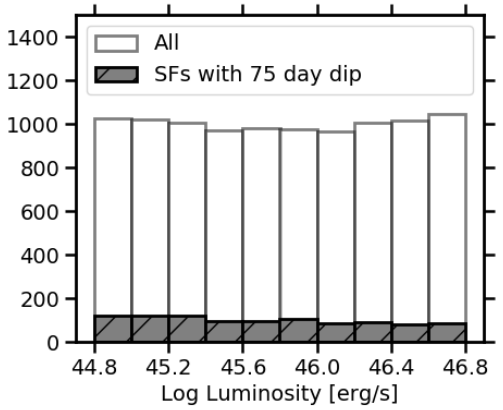

(C) Comparisons between the distributions of the luminosity for *Ks* band.

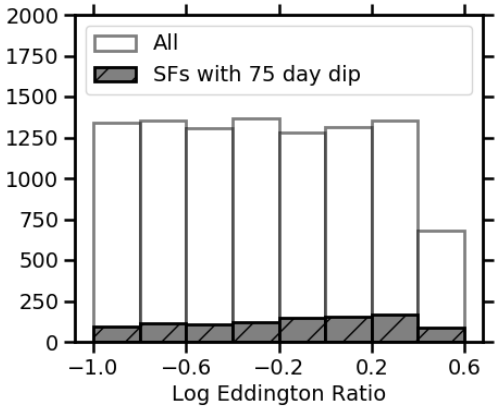

(D) Comparisons between the distributions of the Eddington ratio for *Ks* band.

FIGURE 4.17: Comparisons between the distributions of the parameters of the light curves corresponding to the structure functions that demonstrate a dip at $\sim$ 75 days with all simulated light curves in *r* and *Ks* bands.

mean values of $\sim$ 6 days in the optical and $\sim$ 11 days in the NIR). Many studies of other blazars have also shown strong correlations between the optical and NIR light curves with time lags shorter than 1 day which implies that the source of the emission processes are co-spatial (e.g., Bonning et al., 2012; D'Ammando et al., 2013; Gupta et al., 2017; Kushwaha et al., 2017). This could be due to the synchrotron radiation in the inner jet originating in similar regions for the optical and NIR. As this possible detected lag is smaller than the cadences of observations, multiple intra-day observations would be necessary to further constrain it.

Longer lags have also been found between the optical and NIR light curves in other blazars, for example, Safna et al. (2020) found significant time delays for three FSRQs on the order of 10-100 days. Similarly, Li et al. (2018) found that the NIR light curves variations lagged the optical by a few weeks in PKS 0537-441. Additional non-zero lags were also measured for PKS 0027-426 inconsistently across the light curves, for

example, in the 2017 season, when optical light curves were included in the cross-correlation, an observed lag of $\sim \pm 75$ days (which corresponds to a rest frame lag of $\sim \pm 50$ days) was often recorded. Further analysis of these lags shows that they are unlikely to be a delay between the emission regions and instead are caused by aliasing in the light curves. This lag was further explored as a potential periodicity within the light curves of PKS 0027-426, however the analysis shows that it is not significant compared to simulated red-noise light curves.

4.5 Spectral Variability Analysis

Spectral variability studies of blazars commonly use the slopes of colour indices vs magnitude plots in order to quantify the spectral variability with brightness. As blazars are such highly varying objects, these colour indices are usually calculated for quasi-simultaneous observations in different filters, however the observations of PKS 0027-426 only meet this requirement when taken with DES optical filters. I therefore first measure the spectral variability of PKS 0027-426 in DES observations only in Section 4.5.1, before considering interpolated light curves in Section 4.5.2.

4.5.1 Spectral Variability from Quasi-Simultaneous Observations

I first studied the optical colour behaviour of PKS 0027-426 by measuring the colour indices of each combination of the observed *griz* bands with DES. Each colour index from DES was calculated using quasi-simultaneous observations from the same instrument that were first corrected for galactic extinction using the measurements from Schlafly and Finkbeiner (2011), and had an average time difference of ~ 12 minutes between observations in the different bands, and a maximum time difference of ~ 18.5 minutes.

The optical colour indices (*g*-*r*, *g*-*i*, *g*-*z*, *r*-*i*, *r*-*z* and *i*-*z*) were plotted against the *r* magnitude in Figure 4.18, and the colour behaviour was quantified using the slope of the plot, the Spearman rank correlation coefficient (ρ-values) and the probability of no correlation (p-values). The slope here is calculated as described by Kelly (2007) using a Bayesian method of linear regression, excluding outliers as explained in Appendix A. The Spearman rank correlation coefficient is a non-parametric measure of the strength and direction of the relationship between variables, which returns a value between ± 1, where values of 0 corresponds to no correlation, and correlations of ± 1 is an exact monotonic relationship. A large p value indicates a high probability of no correlation and a small p value indicates a low probability that the correlation is due to random noise. Positive slopes and Spearman rank correlation coefficients imply the colour increases with decreasing brightness (increasing magnitude), which corresponds to a

TABLE 4.2: The slopes, Spearman rank coefficients, probability of no correlation, and colour trend of the DES filters in the colour vs *r* magnitudes plots in Figure 4.18.

Colour	Slope of Colour vs *r* mag	ρ-value	p-value	Colour Trend
g-r	-0.30 $\pm$ 0.02	-0.60	2.45 $\times 10^{-15}$	RWB
g-i	-0.36 $\pm$ 0.02	-0.52	5.50 $\times 10^{-11}$	RWB
g-z	-0.25 $\pm$ 0.02	-0.33	1.67 $\times 10^{-8}$	RWB
r-i	-0.06 $\pm$ 0.01	-0.26	1.73 $\times 10^{-3}$	RWB
r-z	0.06 $\pm$ 0.01	0.31	1.25 $\times 10^{-7}$	BWB
i-z	0.12 $\pm$ 0.01	0.73	5.06 $\times 10^{-48}$	BWB

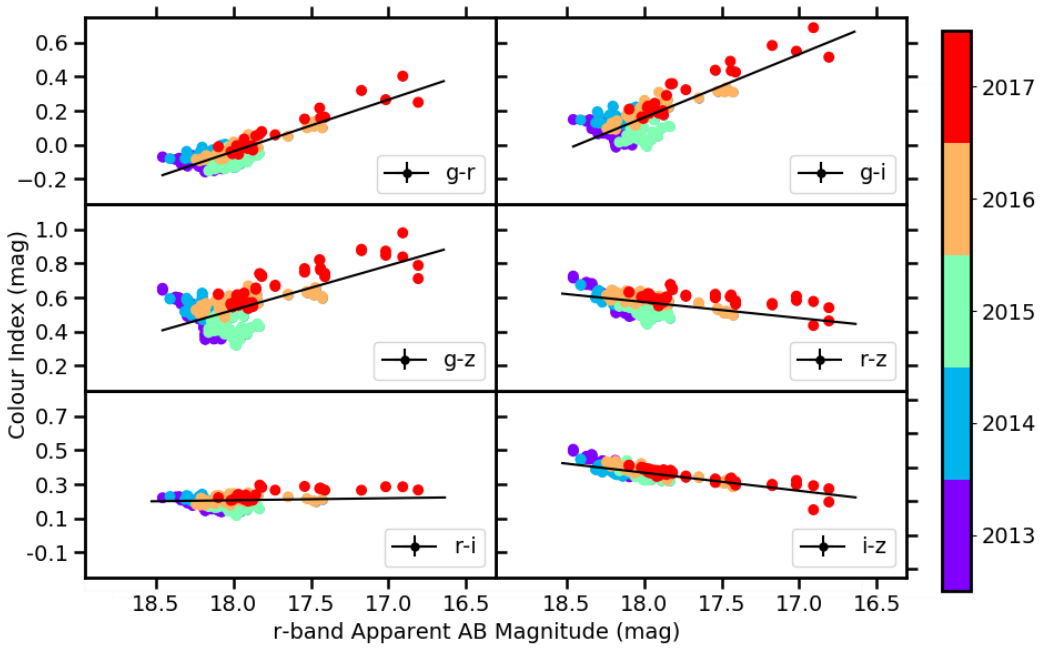

FIGURE 4.18: Optical colour variability plots of each colour combination of DES light curves for their entire observational periods.

BWB trend, while negative slopes and Spearman rank correlation coefficients imply RWB trends. These possible colour trends were deemed significant if the linear slopes were consistent within 3σ. The plots with colour trends that were not significantly BWB or RWB within 3σ have corresponding p-values that were relatively large ($p > 0.01$) and ρ-values that were relatively small ($|\rho| < 0.4$) compared to those with significant colour trends, which therefore imply a SWB trend. The data points in Figure 4.18 were coloured according to observation season. Table 4.2 contains the slope of each colour-magnitude plot, the Spearman rank correlation coefficient, the probability that no correlation is present between the colour and *r* magnitude, and the colour trend.

The overall *g-r*, *g-i* and *g-z* colours are shown to be RWB by the strong anti-correlations present, with slopes of -0.30 $\pm$ 0.02, -0.36 $\pm$ 0.02 and -0.25 $\pm$ 0.02 respectively, and ρ values of -0.60, -0.52 and -0.33 respectively. The *r-i* colour has a

TABLE 4.3: The slopes, Spearman rank coefficients, probability of no correlation, and colour trend for each season of DES in the *g*-*z* colour vs *r* magnitude plots in Figure 4.19.

Season	Slope of *g*-*z* vs *r* mag	ρ-value	*p*-value	Colour Trend
2013	0.74 $\pm$ 0.06	0.8	5.77 $\times 10^{-13}$	BWB
2014	0.06 $\pm$ 0.06	0.09	0.52	SWB
2015	0.12 $\pm$ 0.09	0.17	0.18	SWB
2016	-0.14 $\pm$ 0.02	-0.77	3.58 $\times 10^{-12}$	RWB
2017	-0.26 $\pm$ 0.02	-0.78	3.68 $\times 10^{-11}$	RWB

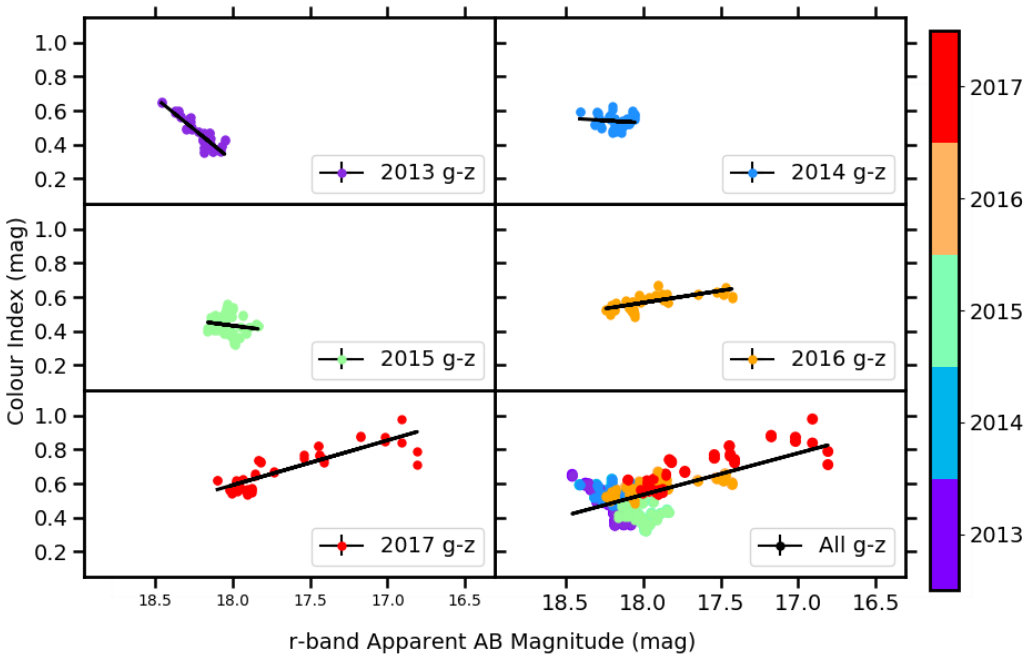

FIGURE 4.19: Optical *g*-*z* colour variability for each observation season of DES.

slope of -0.06 $\pm$ 0.01 and ρ = -0.26 which indicates a slight RWB trend, but also has a relatively high probability of no correlation with a *p* value of 1.73 $\times 10^{-3}$, which implies this RWB trend is not as significant as in the *g*-*r*, *g*-*i* and *g*-*z*. Finally, the *r*-*z* and *i*-*z* colours show positive correlations which implies the source becomes BWB with slopes of 0.06 $\pm$ 0.01 and 0.12 $\pm$ 0.01 and ρ values of 0.31 and 0.73 respectively.

The colour behaviours of each season are also shown to vary; for example, Figure 4.19 displays plots of the colour behaviour of *g*-*z* in the different observations seasons of DES. Table 4.3 contains the slope, the Spearman rank correlation coefficient, the probability of no correlation for each season of *g*-*z*, and the colour trend. The 2013 season shows a strong BWB trend, with slope and ρ values of 0.74 $\pm$ 0.06 and 0.8 respectively. The 2014 and 2015 seasons both display a small positive correlation with slopes of 0.06 $\pm$ 0.06 and 0.12 $\pm$ 0.09 respectively, and ρ-values of 0.09 and 0.17

TABLE 4.4: Colour behaviour of each combination of optical *griz* filters in each season.

Colour	2013	2014	2015	2016	2017
g-*r*	BWB	RWB	SWB	RWB	RWB
g-*i*	BWB	SWB	SWB	RWB	RWB
g-*z*	BWB	SWB	SWB	RWB	RWB
r-*i*	BWB	SWB	SWB	SWB	RWB
r-*z*	BWB	BWB	BWB	BWB	BWB
i-*z*	BWB	BWB	BWB	BWB	BWB

respectively, however the positive slopes are not significant within 3σ uncertainties, and they also have a large probability of no correlation with p values of 0.52 and 0.18 respectively, which indicates the colour behaviour follows a SWB trend. The seasons starting in 2016 and 2017 demonstrate RWB trends, with slopes of -0.14 $\pm$ 0.02 and -0.26 $\pm$ 0.02, and ρ values given as -0.77 and -0.78 respectively. The *g*-*z* colour behaviour over the entire observational period is shown to follow a RWB trend due to the 2016 and 2017 seasons which are the brightest, most variable seasons and therefore dominate the correlation.

The colour-magnitude plots and tables containing slopes of each season of the remaining combination of optical DES *griz* filters are given in Appendix A, and a summary of the colour trends of each combination of filters in each observation season is given in Table 4.4.

4.5.2 Spectral Variability from Interpolations

The optical and NIR light curves in each filter were not observed even quasi-simultaneously with VOILETTE and VEILS as is necessary for studying the colour behaviour of highly variable objects such as blazars. Therefore in order to investigate the spectral variability in the later observation seasons I explored using interpolated light curves to obtain the quasi-simultaneous light curves.

4.5.2.1 Spectral Variability of DES Light Curves from Interpolations

To test the reliability of obtaining the colour behaviour from interpolated light curves, I first used the optical colour variability from interpolated DES light curves after removing half of the observations (randomly selected) from one light curve, and interpolating the remaining light curve using the structure function method to produce a light curve with a cadence of 1 day. The dates matching the observations from the second filter were then used to recreate the colour-magnitude plots.

TABLE 4.5: Comparison between the slopes of the colour-magnitude plots and those made from 10,000 interpolated light curves. The uncertainties of the interpolated slopes are the 1σ uncertainties.

Colour Index	Actual Slope	Mean Slope from Filter 1	Mean Slope from Filter 2
g-r	-0.30 ± 0.02	-0.39 ± 0.09	-0.18 ± 0.13
g-i	-0.36 ± 0.02	-0.45 ± 0.09	-0.24 ± 0.14
g-z	-0.25 ± 0.02	-0.32 ± 0.09	-0.21 ± 0.05
r-i	-0.06 ± 0.01	-0.18 ± 0.13	0.06 ± 0.13
r-z	0.06 ± 0.01	-0.05 ± 0.13	0.09 ± 0.05
i-z	0.12 ± 0.01	0.01 ± 0.14	0.15 ± 0.05

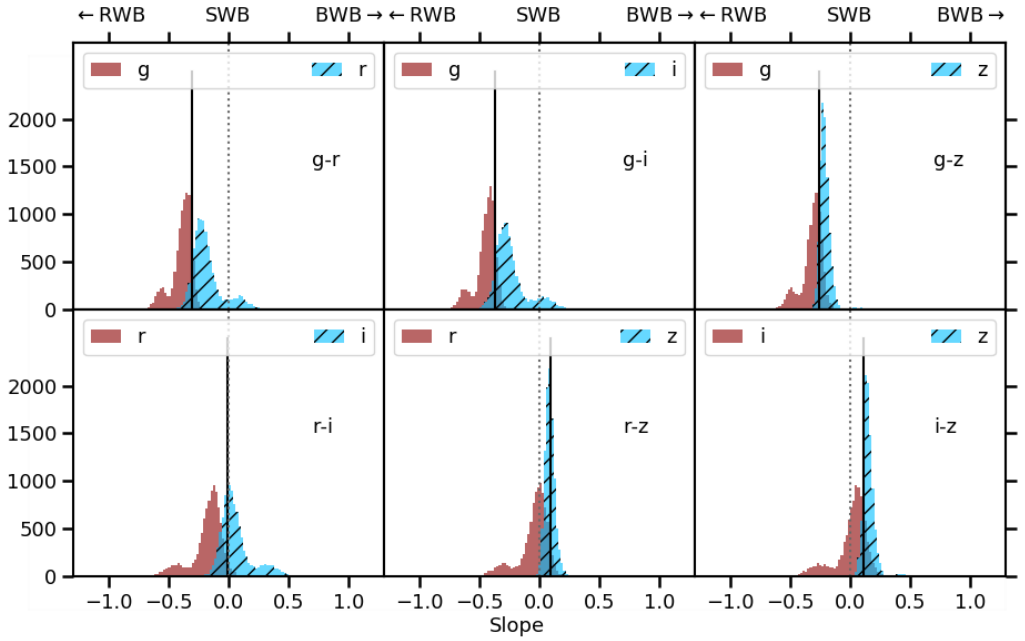

FIGURE 4.20: The distributions from 10,000 interpolations of each combination of DES light curves for their entire observational periods. The black solid line represents the value of the slope obtained from the quasi-simultaneous colour-magnitude diagrams and each colour corresponds to the results from the interpolation of the light curves in each filter.

This method was repeated 10,000 times for each light curve. The distribution of slopes given from the colour-magnitude plots from interpolated DES light curves are shown in Figure 4.20 and the results of these were then compared to the values obtained from Figure 4.18 in Table 4.5. The results from each of the interpolated light curves are shown to be consistent with each other and within 1σ uncertainties of the results from Figure 4.18. It is shown in Figure 4.20 that distributions from interpolating filter 1 return a smaller slope of the filter 1 - filter 2 colour index vs *r* band magnitude than the distributions from interpolating filter 2, and often the result from interpolating filter 1 and filter 2 return a smaller and larger slope than the actual measured slope from Figure 4.18 respectively. This could be due to the interpolations underestimating some of the larger variability in the light curves, which therefore means that when filter 1 is interpolated it could be less variable than filter 2 during these regions of large

TABLE 4.6: Comparison between the slopes of the DES *g*-*z* colour-magnitude plots in each season and those made from 10,000 interpolated light curves. The uncertainties of the interpolated slopes are the 1σ uncertainties.

Season	Actual Slope	Mean Slope from *g*	Mean Slope from *z*
2013	0.74 ± 0.06	0.67 ± 0.11	0.76 ± 0.06
2014	0.06 ± 0.06	-0.18 ± 0.17	0.14 ± 0.14
2015	0.12 ± 0.09	0.01 ± 0.10	0.19 ± 0.08
2016	-0.14 ± 0.02	-0.32 ± 0.16	-0.06 ± 0.14
2017	-0.26 ± 0.02	-0.51 ± 0.15	-0.30 ± 0.12
All	-0.25 ± 0.02	-0.32 ± 0.09	-0.21 ± 0.05

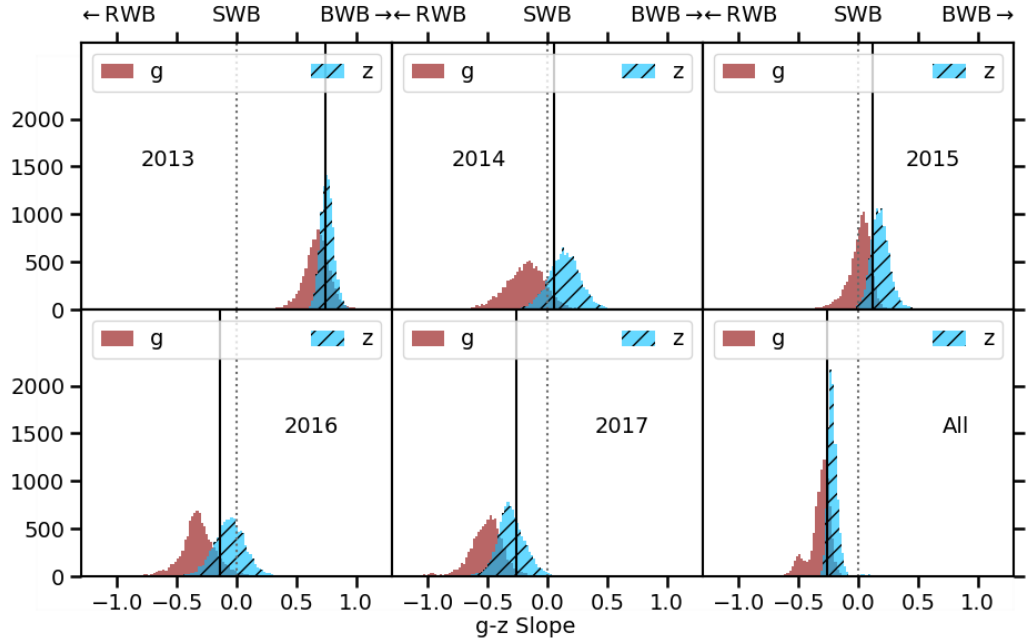

FIGURE 4.21: The distributions from 10,000 interpolations of each season of light curve of g-z. The black solid line represents the value of the slope obtained from the quasi-simultaneous colour-magnitude diagrams and each colour corresponds to the results from the interpolation of the light curves in each filter.

variability and therefore the filter 1 - filter 2 colour is smaller, and vice versa for filter 2. Furthermore, some of the histograms in Figure 4.20 also display a secondary, smaller peak, which corresponds to a slope less than the slope of the main peak when filter 1 is interpolated and a slope greater than the slope of the main peak when filter 2 is interpolated. Analysis of this peak has shown that it occurs when the brightest points in the light curve are removed before interpolation, specifically the dates between MJD 58014 and 58025. This results in a smaller peak to the left when filter 1 is interpolated as the interpolated light curve is then shown to vary less than filter 2, hence the slope becomes steeper, and the smaller peak to the right when filter 2 is interpolated as in this case the slope becomes shallower as the subtracted filter varies less.

To further investigate this method, it was then replicated for each colour combination in each individual season of DES, for example, Figure 4.21 shows the distribution of

the slope of *g*-*z* in each season of DES, with the mean slopes from interpolating each filter given in Table 4.6. It was found that 82% of the mean slopes from interpolations of individual years for all combination of filters were consistent with the slopes from individual years within 1σ and all were consistent within 1.5σ.

4.5.2.2 Spectral Variability of VEILS and VOILETTE Light Curves from Interpolations

The interpolation method was shown to be consistent for the DES colour indices, so I therefore used it to explore the spectral variability of each combination of optical and NIR in the 2017-2019 seasons. Constraining the exact colour behaviour with this method is difficult, so I am using this only to get an indication of the significant colour behaviours that are consistent within at least 3σ.

Optical and NIR Spectral Variability in 2017 The colour behaviour of the NIR light curves compared to the DES optical light curves and to each other in the 2017 season against the *r* band are displayed in Figure 4.22. VEILS did not observe in the 2017 season between MJD 57993 and 58044, during which time a peak was present in the optical, so therefore the light curves were restricted to MJD greater than 58044 to prevent large portions of interpolations impacting the results as explained in Appendix A. Figure 4.22 was plotted against the *r* band to show comparable colour trends with the optical colours in Figure 4.18, however, this required additional interpolation of the *r* band when the dates matching the NIR light curves were extracted. The other interpolated light curve and the *r* band light curve in this situation therefore did not necessarily follow the same variations during the interpolations which could have an effect on the slope of the interpolated optical and NIR colour vs *r* band magnitude plot.

The results in Figure 4.22 show that 55% of the interpolated slopes of the colour vs *r* magnitude plot are consistent within 1σ of each other, and all are consistent within 1.8σ. Furthermore, it was found that the plots of *g*-*J* and *g*-*Ks* vs *r* have negative slopes within 5σ and 4σ uncertainties respectively, which implies RWB trends. The plots of *r*-*J*, *r*-*Ks*, *i*-*J*, *i*-*Ks*, *z*-*J*, *z*-*Ks* and *J*-*Ks* do not show a conclusive trend within their 3σ uncertainties.

Optical and NIR Spectral Variability in 2018 In the 2018 season, only the optical *r* and *i* bands could be used in the colour-magnitude plots as there were very few epochs observed in the *g* and *z* bands with VOILETTE during this time. Figure 4.23 displays the histograms of the slope from each colour combination of optical, *r* and *i*, and NIR, *J* and *Ks* bands, plotted against the *r* band. It was found that 75% of the

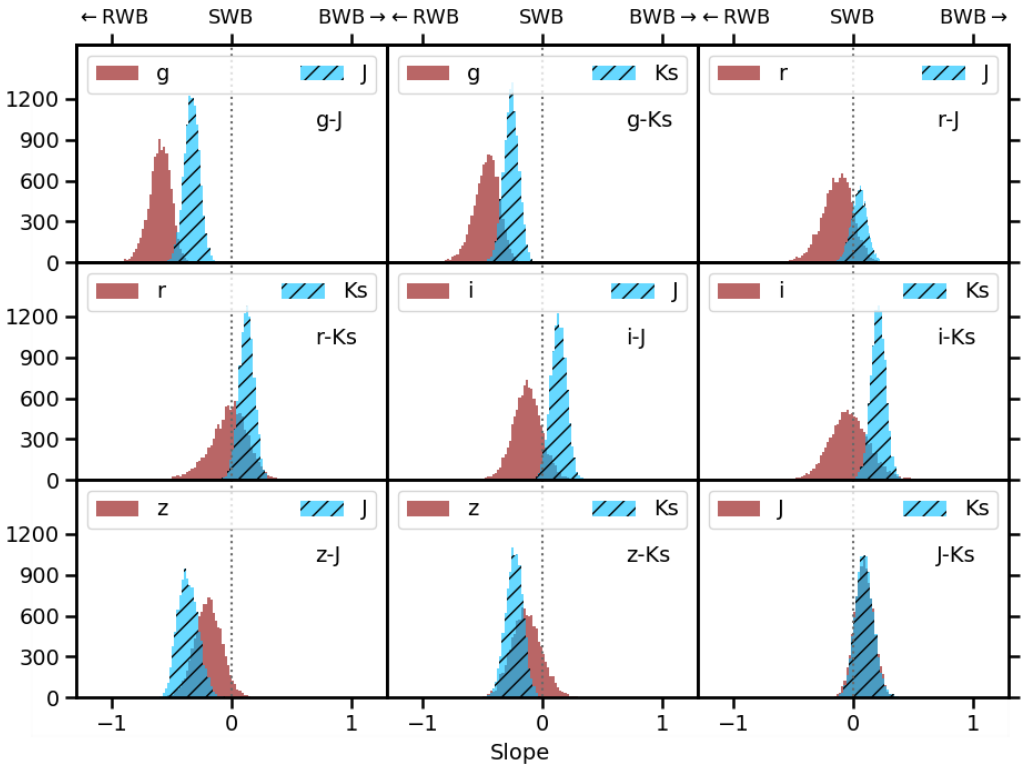

FIGURE 4.22: The distributions of the slope of the 2017 optical and NIR colour vs *r* magnitude plots returned from 10,000 interpolations of each light curve.

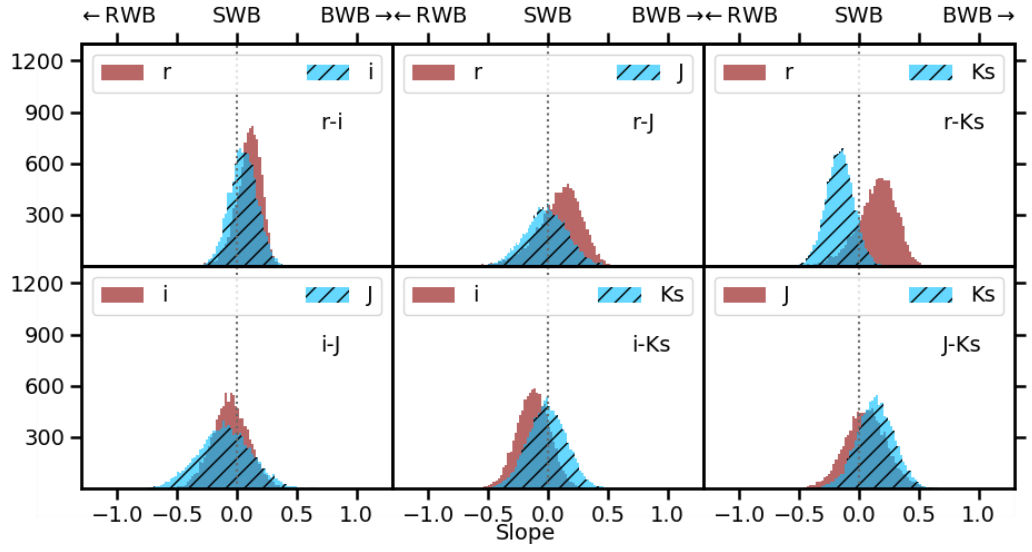

FIGURE 4.23: The distributions of the slope of the 2018 optical and NIR colour vs *r* magnitude plots returned from 10,000 interpolations of each light curve.

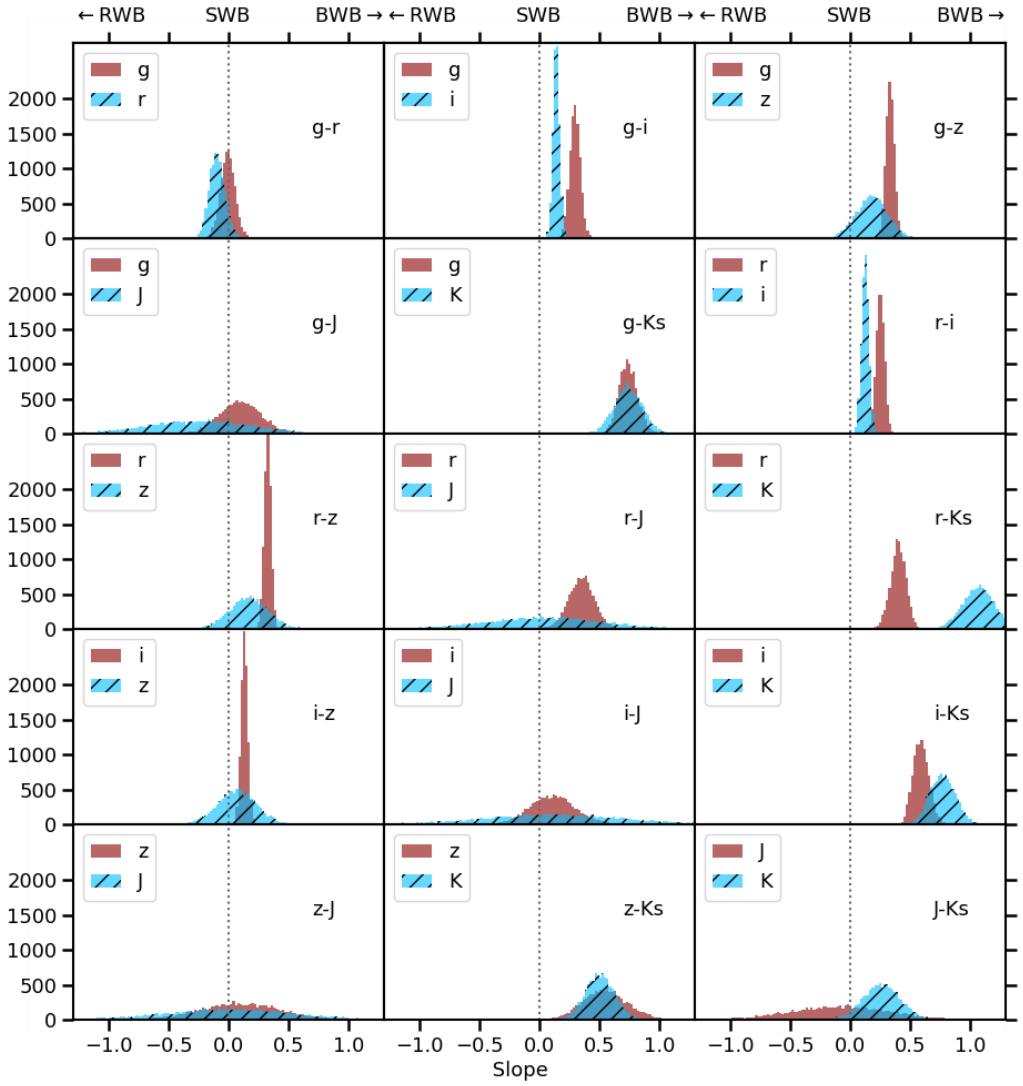

FIGURE 4.24: The distributions of the slope of the 2019 optical and NIR colour vs *r* magnitude plots returned from 10,000 interpolations of each light curve.

colour vs *r* band slopes for each interpolated filter are consistent with each other within 1σ and all are consistent within 1.1σ. The slopes for the 2018 season show inconclusive colour behaviours within 3σ.

Optical and NIR Spectral Variability in 2019 The histograms of the slope from each colour combination of optical, *griz*, and NIR, *JKs* bands, are plotted against the *r* band in Figure 4.24. 80% of the slopes for each interpolated filter are found to be consistent within 1σ and all are consistent within 3.5σ. Many of the histograms, especially those including the *z* or *J* band interpolations, have a large spread making it difficult to

TABLE 4.7: Colour behaviour of each combination of optical *griz* and NIR *JKs* filters in the 2017-2019 seasons with DES, VOILETTE and VEILS observations.

Colour	2017	2018	2019
g-r	RWB	-	BWB
g-i	RWB	-	-
g-z	RWB	-	BWB
r-i	RWB	-	BWB
r-z	BWB	-	-
i-z	BWB	-	-
g-J	RWB	-	-
g-Ks	RWB	-	BWB
r-J	-	-	-
r-Ks	-	-	BWB
i-J	-	-	-
i-Ks	-	-	BWB
z-J	-	-	-
z-Ks	-	-	BWB
J-Ks	-	-	-

constrain the colour behaviour, however BWB colour trends are consistently found within at least 3σ for the *g-i*, *g-Ks*, *r-i*, *r-Ks*, *i-Ks* and *z-Ks* plots.

A summary of the colour behaviours detected for each combination of optical and NIR light curves in the 2017-2019 observation seasons using this interpolated colour-magnitude plot method is given in Table 4.7, where only the colour behaviours that are consistently detected over more than 3σ are counted as detections.

4.6 Spectral Variability Discussion

I studied the spectral variability of PKS 0027-426 for each combination of optical and NIR light curves by calculating the slopes of the colour vs magnitude plots, and found that PKS 0027-426 demonstrates a complex colour behaviour.

The colour trend for each combination of the DES *griz* filters, which could be studied directly due to the quasi-simultaneous observations, were shown to change both over time and depending on the colours used. For example, in the plot of *g-z* vs *r* band magnitude in Figure 4.19, it changes from BWB in the 2013 season to SWB in the 2014 and 2015 seasons and RWB in the 2016 and 2017 seasons. Furthermore, RWB, SWB and BWB trends were observed simultaneously depending on the combination of filters used to calculate the colour, as shown in Figure 4.18, for example, the overall colour behaviour of the *g-r*, *g-i*, *g-z* and *r-i* demonstrates RWB trends, while the *r-z* and *i-z* follow a BWB trend.

The spectral behaviour of the observations from VEILS and VOILETTE could not be directly measured from their light curves as they were not observed even quasi-simultaneously. Instead, one of the light curves was interpolated so that epochs matching the other light curve could be extracted. This method was first tested by comparing the mean colour vs r magnitude slopes measured by removing 50% of the data and interpolating one of the DES light curves with the original slope measured for that colour, and was shown to be consistent for all DES colours across all seasons within 1.5σ uncertainties. It was found that the *g-J* and *g-Ks* slopes for the 2017 season were negative withing 5σ and 4σ respectively which indicates RWB behaviour, while the *g-i*, *g-Ks*, *r-i*, *r-Ks*, *i-Ks* and *z-Ks* plots in the 2019 seasons all indicate BWB behaviour with positive slopes within 3 σ. The remaining colours showed inconclusive trends within their 3 σ uncertainties.

The possible colour trends observed in blazars have previously been explained independently. For example, a RWB colour behaviour could be explained in terms of the contribution of thermal emission from the AD, which is more slowly varying than the variable jet emission (e.g., Bonning et al., 2012). Similarly, the BWB trend can be explained in terms of a faster varying blue component with a slower varying red component (e.g., Fiorucci et al., 2004). Alternatively, the BWB colour behaviour has been explained by a one component synchrotron model by Fiorucci et al. (2004), who suggest that the more intense the energy release, the higher the particle's energy. Additionally, the BWB trend has been explained in terms of the shock-in-jet model, which suggests that accelerated electrons at the front of the shock lose energy while propagating away, and the higher frequency electrons lose energy faster due to synchrotron cooling, therefore making the higher frequency bands more variable (e.g., Kirk et al., 1998; Agarwal et al., 2019).

The change in colour behaviour over different periods of time shown in Figure 4.19 has similarly been seen by Bonning et al. (2012), who found that individual flares in other blazars can behave differently to the overall colour behaviours, which suggests that different jet components become important at different times. Furthermore, Raiteri et al. (2008) find that 3C 454.3 shows a RWB trend until the blazar reaches a saturation magnitude and turns into a BWB trend in bright states. In the *g-z* colour-magnitude plots of PKS 0027-426, the 2016 and 2017 seasons are brighter than the earlier seasons and do demonstrate a different colour trend, but the 2013 season also follows a different colour behaviour while covering a similar magnitude range to the 2014 and 2015 seasons, which means a saturation magnitude is not likely to be the entire explanation in this scenario. Furthermore, while the 2016 and 2017 seasons demonstrate flares, the 2014 and 2015 seasons do not show any dramatic change in magnitude and yet still follow a SWB trend instead of the BWB trend in the 2013 seasons, thus implying individual flares are not solely responsible for the change in colour behaviour over time.

The varying colour behaviour in different combination of filters has also been observed in 3C 345 by Wu et al. (2011), who explained this phenomenon in terms of the emission features from the AD or BLR, such as the Mg II line, which vary less than the non-thermal continuum and dominate the flux at the shorter wavelength (i.e. g band). This theory was investigated for PKS 0027-426 using the spectra from OzDES that were observed over the same periods as DES.

4.6.1 Possible Contamination of Spectral Variability from Emission Lines

Concurrent spectra of PKS 0027-426 were observed on 37 epochs with OzDES along side the photometric DES observations, so therefore the theory presented by Wu et al. (2011) could be examined. If emission features from the AD varied less and dominated the flux, then it would be expected that synthesised light curves created from the emission lines in the g band would be shown to be less variable than both synthesised light curves from different sections of the continuum and the photometric light curves from DES.

To create synthesised light curves from emission lines within the spectra, I first subtracted an estimation of the continuum emission by fitting a line between points on either side of the emission line in the spectra. For example, the Mg II line is displayed in the upper panels of Figure 4.25a, and exists within a region of the spectra known as the small blue bump, in which the Fe II emission lines contribute substantially to the underlying continuum. A line is fit between points on either side of the emission line, depicted by the blue and red shaded regions, and this is subtracted as this approximate continuum, depicted by the green line, from the spectra. The flux that would be observed from the emission line with DES, $\langle f_\lambda \rangle$, is then estimated using Equation 4.6.

$$\langle f_\lambda \rangle = \frac{\int d\lambda \lambda R f_\lambda}{\int d\lambda \lambda R} \tag{4.6}$$

where f_λ is the flux in the spectrum for each wavelength, λ, in the emission line region and R is the filter transmission curve of the appropriate DES filter. This flux is then converted into AB magnitude using Equation 4.2.

In order to quantify whether or not the emission lines were less variable than the continuum emission, I calculate the amplitude variability parameter described in Equation 4.1 for emission lines in different filters and for synthesised light curves created from portions of the continuum. I also estimated the fraction of the total flux in each synthesised DES band light curve that comes from the individual emission lines to test whether the emission lines dominated in the filters.

TABLE 4.8: The amplitude variations of the synthesised light curves created from OzDES spectra.

Emission Line or Region of the Spectra	Rest Frame Wavelength Range (Å)	Amplitude Variation (mag)	Percentage of Total flux (%)
Synthesised *g* band	2500 - 3780	0.54	100
Synthesised *r* band	3620 - 4930	0.79	100
Synthesised *i* band	4530 - 5830	0.93	100
Mg II	2760 - 2860	0.67	5
Blue Continuum	3020 - 3120	0.59	9
Hβ	4830 - 4930	0.51	5

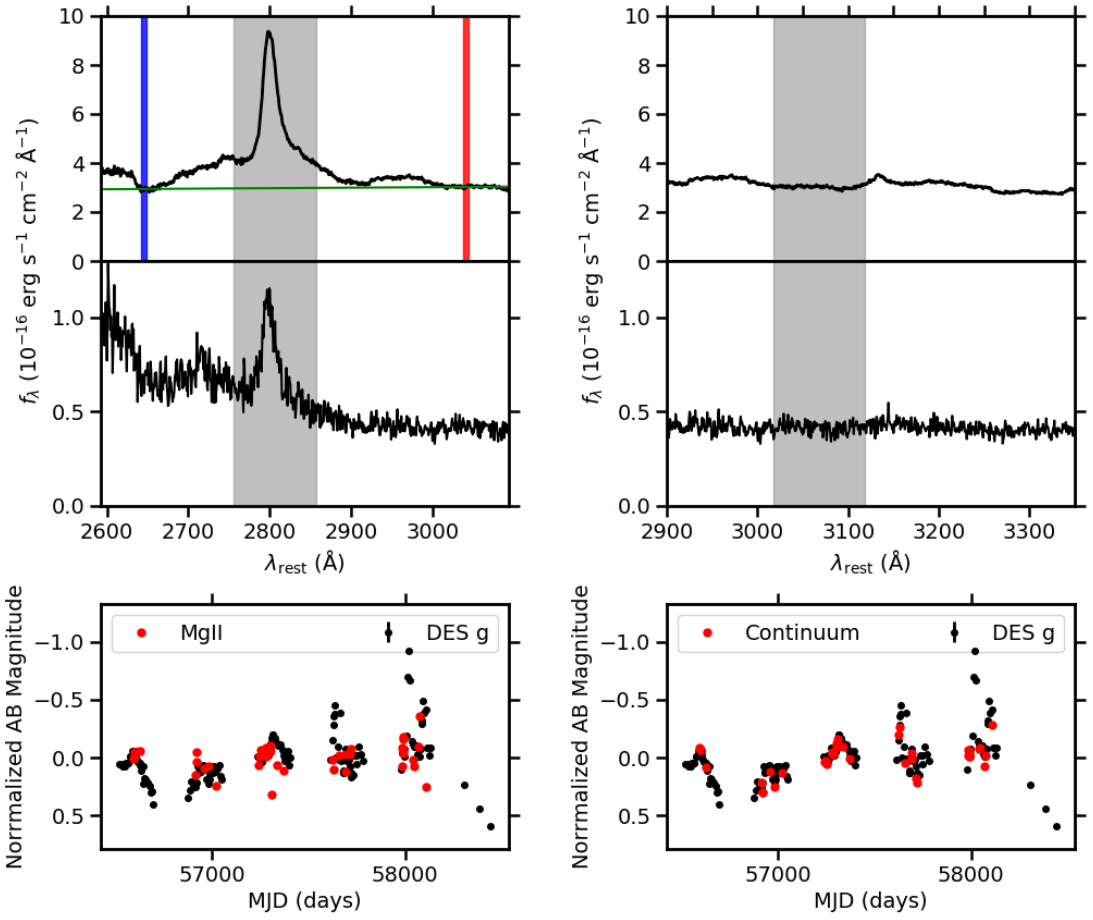

(A) Mean and RMS Mg II spectra and synthesised light curve compared to the DES *g* band.

(B) Mean and RMS continuum spectra and synthesised light curve compared to the DES *g* band.

FIGURE 4.25: *Top Panel*: The regions of OzDES spectra used to create the synthesised light curves (grey shaded regions). The Mg II line is continuum subtracted by fitting a line for the approximate continuum (green line) between points on either side of the emission line region (the blue and red shaded regions). *Middle panel*: RMS Spectra. *Lower Panel*: Synthesised light curves created from spectra compared to the DES photometric light curves.

The lower panels of Figure 4.25a and 4.25b display the normalised light curves created for the Mg II line and a section of the continuum in the g band respectively. It can be seen that the synthesised light curve from a section of the continuum follows similar variability to the photometric DES g band light curve, which is to be expected, however, the synthesised light curve from the continuum subtracted Mg II line varies differently to the photometric g band light curve. Furthermore, Table 4.8 contains the amplitude variations for the Mg II and blue continuum synthesised light curves, as well as from synthesised Hβ light curves. The light curves from the emission lines are shown to vary similarly to the continuum region and to the synthesised DES light curves. Furthermore, the Mg II line is more variable than the Hβ line, and the synthesised light curve from the blue continuum region, which disagrees with the theory presented by Wu et al. (2011) as they suggest that the Mg II line should be the least variable and should dominate in the g band. Table 4.8 also contains the percentage of the flux in each synthesised light curve that contributes to the overall flux of the synthesised DES light curves, and shows that the Mg II and Hβ emission lines contribute to 5% of the overall flux.

4.6.2 Multiple Contributing Components to the Overall Emission

As the previous section disproves the theory presented by Wu et al. (2011) for the differences in colour behaviour that occur simultaneously with different combination of optical *griz* filters, I instead explore whether the observed behaviour can be explained by multiple components that contribute to the overall optical emission.

4.6.2.1 Decomposing the Spectra into Red and Blue Components

The change in spectral behaviour between different filter light curves could be explained by the presence of multiple different coloured components that contribute to the overall optical emission. The different wavelength ranges could be dominated by a different coloured component which would mean when one component varies differently to the other, the colour behaviour will not follow the same trend for each combination of filters.

I investigated this using the optical broadband spectra which were made using the fluxes from the optical DES light curves and the central wavelengths of the corresponding filters for each observed epoch. The overall emission is assumed to follow a power law of $f_\lambda \propto \lambda^{\alpha_\lambda}$, where f_λ is the flux density at wavelength λ and α_λ is the spectral index. The total flux here is assumed to be a combination of the flux from a red component and a blue component, which each follow their own power laws and have spectral indices of α_{red} and α_{blue} respectively.

TABLE 4.9: The slopes (spectral indices, α) and intercepts (int) of the red and blue components that are modelled in Figure 4.26 to match the mean observed brightest and dimmest broadband spectra in each season.

Season	α_{red}	int_{red}	$\alpha_{\text{blue,dim}}$	$\text{int}_{\text{blue,dim}}$	$\alpha_{\text{blue,bright}}$	$\text{int}_{\text{blue,bright}}$
2013	1.5	-21.35	-4.1	-0.99	-3.5	-2.94
2014	1.5	-21.35	-3.8	-2.04	-3.0	-4.75
2015	1.5	-21.35	-3.6	-2.62	-2.9	-4.98
2016	1.5	-21.35	-3.5	-3.03	-2.0	-8.04
2017	1.5	-21.35	-2.9	-5.07	-1.3	-10.33
All	1.5	-21.35	-3.9	-1.70	-1.3	-10.33

For each season I model the broadband spectra of the red and blue emission such that the sum matches the shape of the average spectra of the 3 dimmest epochs that were observed within their 1σ uncertainties. I then varied the spectral index of one of the components so that the new total spectra matched the shape of the average spectra of the brightest 3 epochs that were observed within their 1σ uncertainties.

Figure 4.26 displays the mean brightest and mean dimmest spectra of the *griz* bands in the seasons starting 2013, 2014, 2016 and 2017, along with examples of the modelled red and blue emission that are combined to fit the observed spectral shape. The 2015 season and the model over the entire DES observational period are displayed in Appendix A. In these figures, the red emission was kept constant with the equation $\text{Log}(f_\lambda) = 1.5\ \text{Log}(\lambda_{\text{rest}}) - 21.35$, where $\alpha_{\text{red}} = 1.5$, and the blue emission was varied to match the mean brightest spectra. The value of α_{red} was chosen somewhat arbitrarily here to demonstrate how the change in the blue slope can effect the shape of the overall spectra, however the value is not unique to the broadband spectra as shown in Appendix A, which explores alternative values including plots in which the blue slope is fixed and the red component is varied to match the change in spectra with brightness. The mean and RMS OzDES spectra of each season are plotted below for comparison. Table 4.9 gives the equations of the lines that are modelled for the blue and red components in each season to match the mean brightest and dimmest spectra. The change in the blue slope is shown to increase towards the later seasons where the object has previously been shown to be more variable in Table 4.1.

These simple models in Figure 4.26 demonstrate that if one component is varying when the source gets brighter, the overall variability observed between filters can be different as a result of the dominating emission process in each filter. For example, when the blue emission varies, the overall variation observed in the filters that are more strongly impacted by the red emission is diluted due to the strong constant red emission, whereas in the filters where the blue component dominates, the overall variability will better reflect the blue emission's variability, which could therefore explain why the colour behaviour has been shown to change between different combinations of optical filters.

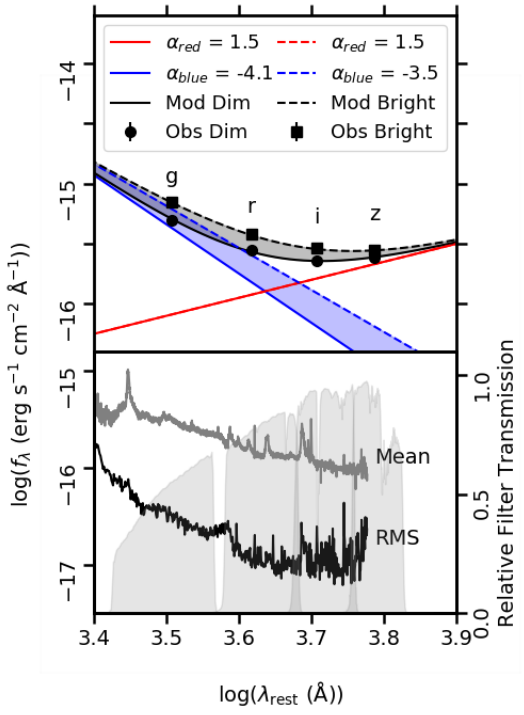

(A) Modelled Spectra of the 2013 Season.

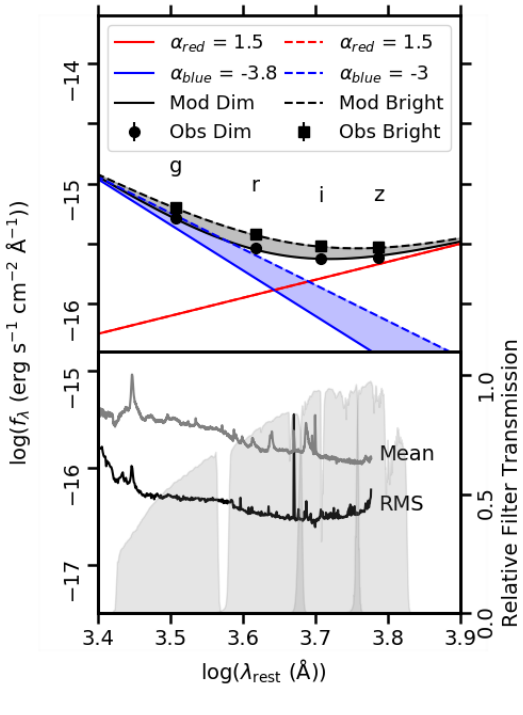

(B) Modelled Spectra of the 2014 Season.

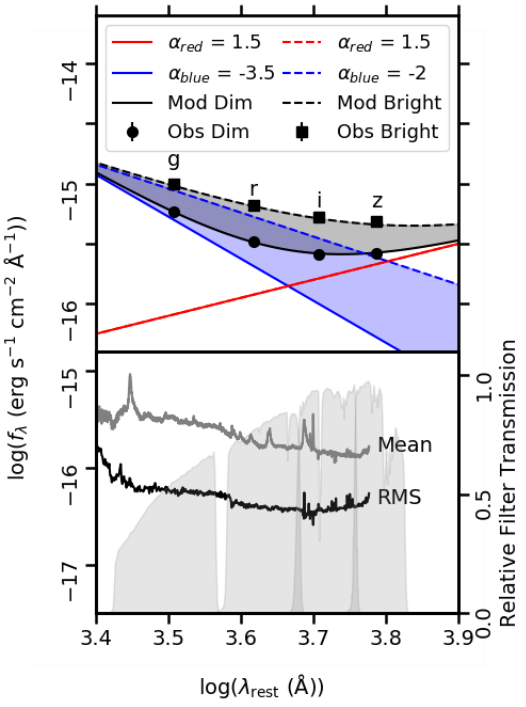

(C) Modelled Spectra of the 2016 Season.

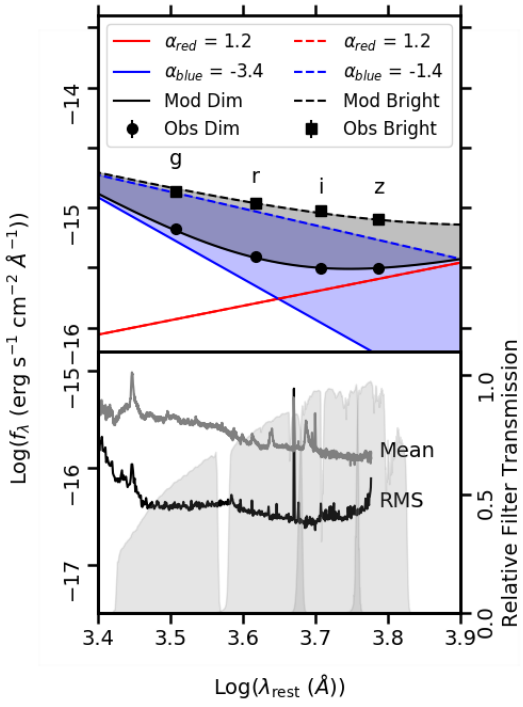

(D) Modelled Spectra of the 2017 Season.

FIGURE 4.26: *Upper panel*: Modelled broadband spectra of the red and blue emission that combine to match the average brightest and dimmest epochs in each observation season compared to the observed broadband spectra. The solid lines correspond to the modelled spectra of the dimmest epochs, and the dashed lines correspond to the modelled spectra of the brightest epochs. *Lower panel*: Mean and smoothed RMS OzDES spectra for each season plotted over the DES filter Transmissions.

The blue and red components used here could correspond to physical processes such as the thermal emission from the AD and the synchrotron emission from the jet respectively. Wills et al. (1992) suggest that the thermal emission generally dominates in the optical-UV region, however, in FSRQs, when bright, the spectrum could be dominated by the synchrotron component towards the longer optical wavelengths and the IR. The spectral indices of the AD and synchrotron emission from the jet have previously been predicted to be $\alpha_{\lambda,\mathrm{AD}} \approx$ -7/3 (Kishimoto et al., 2008) and $\alpha_{\lambda,\mathrm{Sync}} \approx$ -0.5 (Wills et al., 1992), which are not consistent with the steep slopes used in this analysis, however Appendix A demonstrates that the values used for the red and blue slopes here are not unique. This analysis assumes the presence of only one variable component which may be an oversimplification, so therefore, an alternative approach is applied in the following section.

4.6.2.2 Decomposing the Spectra into the Variable and Non-Variable Components

In the previous section I assumed the presence of two different coloured components that contribute to the overall optical emission, however that analysis only implies that one component varies while the other remains constant. To explore this further, the light curves in each wavelength range, $f_\lambda(t)$, are instead decomposed into the variable and non-variable components using the separable model given in Equation 4.7.

$$f_\lambda(t) = A_\lambda + S_\lambda X(t) \tag{4.7}$$

where A_λ is the spectra of the mean light (i.e. the non-variable component), S_λ is the spectra of the variable component and X(t) is the light curve that has been normalized such that $\langle X(t) \rangle = 0$ and $\langle X^2(t) \rangle = 1$.

Figure 4.27 displays the A_λ and S_λ spectra covering the DES *griz* filters in each observation season in DES and for the overall observation period, and Table 4.10 gives the slopes between each filter for the A_λ and S_λ spectra, where the slopes and uncertainties correspond to the mean slope and the standard deviation obtained from bootstrapping the light curves. Appendix A contains similar analysis for the OzDES spectra in each season.

The constant component, A_λ, is shown to follow roughly the same shape for each observations season, where the slope of Log(A_λ) vs Log(λ) is steepest between the *g* and *r* bands and flattest between the *i* and *z* bands. This implies that there are multiple different coloured components that contribute to the non-variable emission, as there is a strong blue component effecting the *g* and *r* region of the spectra and a redder component that is flattening the spectra between the *r* and *i* and the *i* and *z* bands.

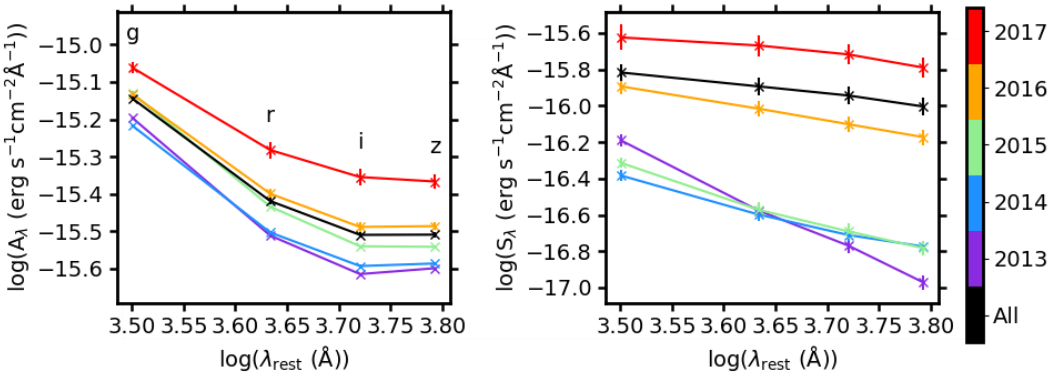

FIGURE 4.27: Decomposition of the spectra into the variable (S_λ) and non-variable (A_λ) components for each season of DES and for the entire observational period.

TABLE 4.10: Slope of Log(A_λ) and Log(S_λ) vs Log(λ) from Figure 4.27 between the *g-r*, *r-i* and *i-z* filters for each season of DES and for the entire observational period.

(A) Slope of Log(A_λ) vs Log(λ) from Figure 4.27.

Season	*g-r*	*r-i*	*i-z*
2013	-2.37 ± 0.01	-1.19 ± 0.01	0.22 ± 0.01
2014	-2.15 ± 0.01	-1.04 ± 0.01	0.09 ± 0.01
2015	-2.28 ± 0.01	-1.23 ± 0.01	-0.02 ± 0.01
2016	-2.00 ± 0.02	-1.03 ± 0.02	0.03 ± 0.02
2017	-1.66 ± 0.03	-0.84 ± 0.03	-0.17 ± 0.03
All	-2.06 ± 0.01	-1.05 ± 0.01	0.01 ± 0.01

(B) Slope of Log(S_λ) vs Log(λ) from Figure 4.27.

Season	*g-r*	*r-i*	*i-z*
2013	-2.90 ± 0.05	-2.22 ± 0.05	-2.77 ± 0.06
2014	-1.61 ± 0.05	-1.29 ± 0.05	-0.83 ± 0.05
2015	-1.92 ± 0.05	-1.37 ± 0.06	-1.29 ± 0.06
2016	-0.92 ± 0.06	-0.99 ± 0.06	-0.98 ± 0.06
2017	-0.34 ± 0.09	-0.57 ± 0.08	-1.00 ± 0.08
All	-0.57 ± 0.07	-0.58 ± 0.07	-0.83 ± 0.07

The slope of the variable component, S_λ, is also shown to change between seasons, with the 2013 season having the steepest slope between all filters and the 2017 season the flattest. The shape of the spectra here also indicates the presence of more than one spectral component, including a steep blue component but also a red component that contributes to the change of slope of the variable spectra with increasing wavelengths.

This method of decomposing into the spectra into variable and non-variable components therefore supports the assumption in the previous section that both a blue and red spectral component contribute to the overall optical emission, but it also demonstrates that both coloured components are likely to contribute to the overall variable and non-variable emission. The contribution of multiple different coloured

components could therefore explain the change in colour behaviour that is observed simultaneously with different combinations of optical DES filters.

4.7 Chapter Summary

In this chapter, I studied the multi-wavelength temporal and spectral variability of the FSRQ PKS 0027-426, using optical observations from DES (2013-2018) and VOILETTE (2018-2020) in the *griz* bands, and NIR observations from VEILS (2017-2020) in the *JKs* bands. The results are summarised below:

1. The temporal variability was studied using cross-correlation analysis of the optical and NIR light curves, and the most consistent correlation over all combination of light curves was found at ~ 0 days, which implies that the emission is simultaneous or any delay between light curves occurs on timescales smaller that the cadence of observations.

2. The spectral variability was studied for each combination of optical DES *griz* light curves using the slopes of the colour vs r magnitude plots. The overall colour trends are shown to vary when different combinations of filters are used, from RWB trends in the *g-r*, *g-i*, *g-z* and *r-i* to BWB in the *r-z* and *i-z*.

3. The spectral variability was also shown to vary over each observation season, for example, in the *g-z*, the colour behaviour follows a BWB trend in the 2013 season, a SWB trend in the 2014 and 2015 seasons and a RWB trend in the 2016 and 2017 seasons.

4. Using OzDES spectra from 2013-2018, we investigated the possible explanation for the changing colour behaviour with different combinations of filters provided by Wu et al. (2011) for 3C 345, in which emission features from the AD or BLR dominate the flux at shorter wavelengths and vary less than the non-thermal continuum, and found that my results disagreed as the emission lines were not less variable than the continuum.

5. The variations in colour behaviour across different combinations of filters was instead explained as a result of each filter containing a different ratio of the multiple different coloured components that combine to give the overall optical emission. These red and blue components are thought to vary differently, which could therefore cause the emission between filters to vary.

6. The optical and NIR spectral variability was also studied, however, as the observations were not simultaneous, one of the light curves was interpolated to extract matching epochs. This method was shown to be reliable for the DES data

after half of the observations were removed, with consistent results given within 1.5σ uncertainties.

Chapter 5

Dust Reverberation Mapping of Zw229-015

Multi-wavelength variability analysis of AGN light curves are often used to estimate the locations of different emission regions within the unresolvable inner regions, as described in Chapter 1. In the previous chapter, I applied this analysis to observations of a blazar and showed that the emission in different wavelength ranges are likely to be co-spatial or that any separations were smaller than could be detected with the cadencing of observations. In this chapter, I extend the temporal variability analysis to a RQ type 1 AGN. Specifically, this involves using dust reverberation mapping which estimates the size of the dust emitting region of type 1 AGN by measuring the delays between the IR response to variability in the optical light curves, as the dust is believed to absorb and reprocess some of the optical emission produced in the AD. I perform dust reverberation analysis on the Seyfert 1 galaxy Zw229-015 using optical ground-based and *Kepler* observations and concurrent IR *Spitzer* 3.6 and 4.5 μm light curves from 2010–2015, both using the cross correlational analysis applied to PKS 0027-426 in the previous chapter, but also use MCMC modelling of the light curves. Zw229-015 was chosen for this analysis as it is one of the brightest and most highly varying AGN in the *Kepler* field, and was therefore selected as a target to be observed with *Kepler* during Quarters 4–17 (2010–2013), resulting in one of the highest quality, most complete optical light curves of any AGN. Concurrent IR observations with *Spitzer* (2010–2015), along with additional optical observations from ground-based telescopes (2010–2015), make it ideal for dust reverberation mapping analysis over 5 years.

The structure of this chapter is as follows; in Section 5.1 I summarise dust reverberation mapping and introduce Zw229-015 and some of the previous studies performed on it. In Section 5.2 I describe the observations of Zw229-015 that will be used for the analysis in this chapter. In Sections 5.3 I present the results of temporal

variability analysis using cross correlation functions. In Sections 5.4 I describe the MCMC modelling that I perform in order to further constrain the dust emitting region of Zw229-015, and present the results. Finally, in Section 5.5 I discuss the results and their implications, and in Section 5.6 I give a summary of the conclusions of this chapter.

A journal article based on the work described in this chapter was published in the Monthly Notices of the Royal Astronomy Society as Guise et al. (2022b).

5.1 Introduction

The mean distance between the optical and IR dust emitting regions is often estimated in dust reverberation mapping (DRM) studies using cross-correlation analysis. Many of the previous works use the NIR K band ($\sim 2.2\,\mu$m) to define the inner radius of the dust emitting region (which corresponds to the radius at which the dust sublimates) of AGN with redshift $z < 1$ as it traces the peak of the hot dust emission at the inner radius of the dust emitting region with a dust sublimation temperature $T_{\rm sub} \approx 1500\,$K (e.g., Nelson, 1996; Minezaki et al., 2004; Suganuma et al., 2006; Yoshii et al., 2014; Pozo Nuñez et al., 2015; Mandal et al., 2018; Ramolla et al., 2018; Mandal et al., 2021). However, additional studies of DRM using longer wavelength IR light curves have been performed to further constrain the spatial information in the dust emitting region; for example, Lyu et al. (2019) combine MIR DRM lags from multiple quasars with $z < 0.5$ using WISE W1 ($\sim 3.4\,\mu$m) and W2 ($\sim 4.5\,\mu$m) bands with K-band results from the literature to infer the dust emission size ratios of $R_k : R_{W1} : R_{W2} = 0.6 : 1 : 1.2$. Similarly, Vazquez et al. (2015) performed DRM on the optical B and V and IR *Spitzer* channel 1 ($3.6\,\mu$m) and *Spitzer* channel 2 ($4.5\,\mu$m) light curves of NGC 6418, and measured lags between the optical continuum and the IR $3.6\,\mu$m and $4.5\,\mu$m with values of $37.2^{+2.4}_{-2.2}$ and $47.1^{+3.1}_{-3.1}$ days, respectively. They also measured a lag between the IR $3.6\,\mu$m and $4.5\,\mu$m light curves with a value of $13.9^{+0.5}_{-0.1}$ days. These studies find that the emission detected in the longer IR wavelengths of these AGN is likely dominated by the black-body peak of the emission from the cooler dust at larger radii; however, contributions to the MIR emission are also expected from the Rayleigh-Jeans tail of the hotter dust from the inner regions. In compact systems that lack the extended dust, it is therefore suggested by Hönig and Kishimoto (2011) that the emission at these wavelength ranges could predominately come from the hot dust Rayleigh-Jeans tail.

Furthermore, additional information can be obtained from modelling the IR light curves. These reprocessed IR light curves can be expressed as a convolution of the optical light curve with a dust transfer function that contains information about the geometrical and structural properties of the dust emitting region. These properties can

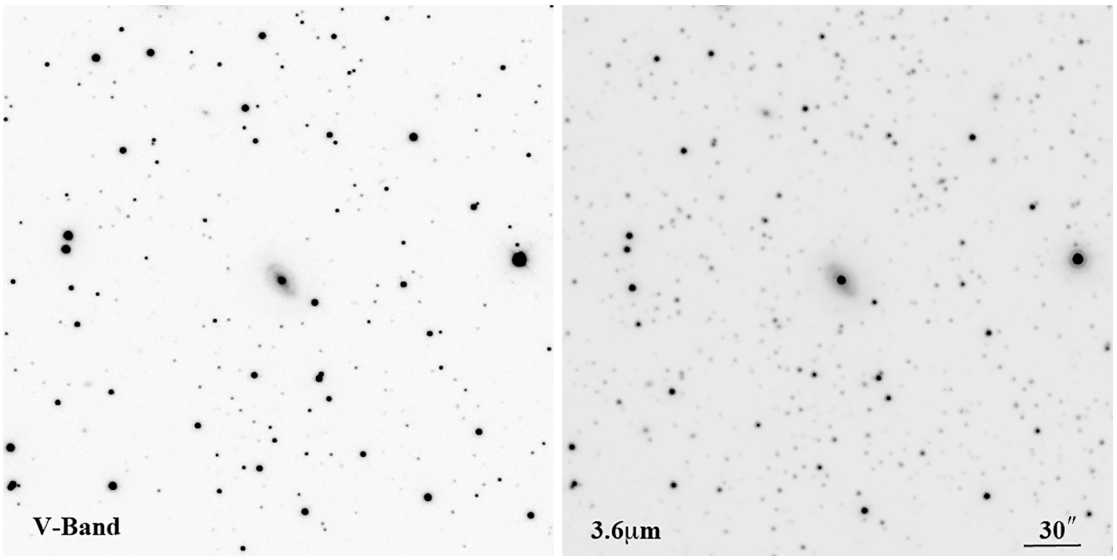

FIGURE 5.1: Stacked images of Zw229-015 from ground-based optical (V-band) imaging from the West Mountain Observatory (Barth et al., 2011) and the IR (3.6 μm) image from the *Spitzer Space Telescope.*

be constrained by fitting observed IR light curves with light curves modelled using simulated dust transfer functions convolved with observed optical light curves. Several such models of the dust emitting region have been used to constrain the inner regions of AGN; for example, Hönig and Kishimoto (2011) showed that the observed NIR K-band light curves of NGC 4151 could be well reproduced using observed optical V-band light curves convolved with simulated DTFs. Furthermore, Almeyda et al. (2017, 2020) modelled the IR response light curves to variations in the UV/optical using a torus reverberation mapping code (TORMAC), to explore geometrical and structural properties of the dusty torus.

5.1.1 Zw229-015

Zw229-015 (Figure 5.1) was first classified as a Seyfert 1 galaxy by Proust (1990). It is relatively bright and has a redshift of $z = 0.028$ (Falco et al., 1999), however due to its location within the galactic plane at galactic coordinates of longitude = 73.1 degrees and latitude = 15.5 degrees (RA = 19h 05m 25.939s, DEC = +42d 27m 39.65s (J2000)), it remained mostly unexplored until it was recognised to exist within the *Kepler* mission's field of view (Carini and Ryle, 2012). In the last decade since observations with *Kepler* were scheduled, a considerable amount of work has been performed on this object, which I will briefly summarise here.

A ground based BLR reverberation mapping campaign was carried out by Barth et al. (2011) who measured a lag of $3.86^{+0.69}_{-0.24}$ days between the Hβ and V-band continuum light curves from 2010, and additionally estimated a black hole mass of $\sim 10^7$ $M_\odot$ using the reverberation mapping results. Using this black hole mass estimate and an

estimate of the bolometric luminosity of Log(L_{Bol}) = 43.8 erg s^{-1}, they calculated an Eddington ratio of L/L_{Edd} = 0.05. Furthermore, Mandal et al. (2021) performed dust reverberation mapping on Zw229-015 with ground based observations between July 2017 - December 2018, and found significant rest frame lags between the *V*and *Ks* band light curves of $20.36^{+5.82}_{-5.68}$ days.

Raimundo et al. (2020) modelled the BLR geometry and dynamics of Zw229-015 using single-epochs of ground based optical observations and spectra to estimate an inclination angle of the AD of $i = 36.4^{+6.7}_{-6.4}$ degrees.

Additionally, fits to the PSD of Zw229-015 using *Kepler* observations have been performed by multiple authors. Mushotzky et al. (2011) and Carini and Ryle (2012) first fit the PSDs of Zw229-015 using the *Kepler* observations in the first 3 quarters only. Mushotzky et al. (2011) found a single power law of $P(f) \propto f^{-\alpha}$ with a mean slope of each individual quarter of α = 3.11±0.15. Carini and Ryle (2012) instead fit the PSD of all combined quarters and tested the fit of a single power law, broken power law in which the slope flattens to 1 after a characteristic break timescale and knee model in which the power law flattens to 0 after the characteristic break timescale. They reported an unbroken power law fit of 2.32 ± 0.26 with a confidence of 39.7% and a better fitting knee model with slope 2.88± 0.21 with a break at 92^{+27}_{-21} days with confidence of 95.6%, and broken power law with slope of 2.83±0.25 with a break at 44^{+13}_{-10} and a confidence of 95.8%. This analysis was furthered by fitting the PSD of Zw229-015 made from the entire *Kepler* light curve, and though the methods differ slightly, authors consistently report best fits of a bending/broken power law with steep slope (2-4) and a characteristic timescale of 5-16 days (e.g., Edelson et al., 2014; Smith et al., 2018a).

Furthermore, using the *Kepler* observations, Smith et al. (2018a) estimate a Eddington ratio of 0.125 and a bolometric luminosity of $\sim 10^{44}$ erg s^{-1} for Zw229-015.

Gorjian et al. (2010) requested monitoring of Zw229-015 with *Spitzer Space Telescope* to provide concurrent observations with *Kepler* and the ground based optical telescopes for dust reverberation analysis. Preliminary results were presented as Gorjian et al. (2014), though full analysis of the entire combination of data was not completed until now.

5.2 Optical and IR Light Curves of Zw229-015

Light curves of Zw229-015 were obtained from the ground based optical, *Kepler* and *Spitzer* observations by collaborators as described in Chapter 2. These observations of Zw229-015 also likely contain a substantial amount of flux from the host galaxy, the amount of which varies for each survey. This host-galaxy flux is assumed to be

constant over the entire observational period, though for consistency between the optical light curves from the ground based and *Kepler* telescopes, I subtracted a constant flux of 3.7 mJy corresponding to the mean of the difference between the overlapping ground-based V-band and *Kepler* observations to represent the difference in host galaxy contribution.

Figure 5.2 shows the optical and IR light curves of Zw229-015 in 2010–2015, with observation seasons separated by the dotted grey lines, and with overall magnitude variations (brightest − dimmest magnitude) of each light curve of $|\Delta\text{ground}| \approx 0.6$ mag, $|\Delta \textit{Kepler}| \approx 0.6$ mag, $|\Delta \textit{Spitzer 1}| \approx 0.9$ mag, and $|\Delta \textit{Spitzer 2}| \approx 0.2$ mag. The short-term variability (i.e., variability over timescales of days to months) of the individual seasons in each light curve are approximately consistent for the entire light curves, with mean overall magnitude variations of ~ 0.3, ~ 0.4, ~ 0.2, and ~ 0.1 mag in the ground-based optical, *Kepler*, and *Spitzer* channel 1 and 2 light curves, respectively. Additionally, underlying long-term variability (i.e., variability over timescales of several months to years) can be seen in the light curves, especially those that are observed in 2011–2013 as the object gets brighter, with a change of mean apparent magnitude of ~ 0.2, ~ 0.2, and ~ 0.6 mag in the ground-based optical, *Kepler*, and *Spitzer* channel 1 light curves, respectively.

These light curves in Figure 5.2 are given in Vega magnitudes, though for the upcoming analysis I convert them into fluxes.

5.3 Dust Reverberation Mapping with Cross Correlation Analysis

I interpolated and cross correlated each individual season of each combination of the optical and IR light curves, as well as the entire overlapping light curves of Zw229-015, using the interpolated cross correlation methods discussed in Chapter 3. As the light curves were interpolated using the SF, filling in the missing data in a random order to estimate the variability from different time separations, these methods were therefore repeated 10,000 times for each combination of light curves to decrease the impact of the interpolated data in each instance on the cross correlation results. When cross correlating the light curves covering more than one observation season, I first detrended the light curves as explained in Appendix B, to remove the influence of long-term variations (that were over timescales much greater than expected for DRM (e.g., Clavel et al., 1989; Glass, 1992; Suganuma et al., 2006)) from the CCFs (e.g, Welsh, 1999).

Each CCF was tested with a lag range of ± 100 days owing to the overlapping length of the individual observation seasons, except for the season starting 2011, in which the

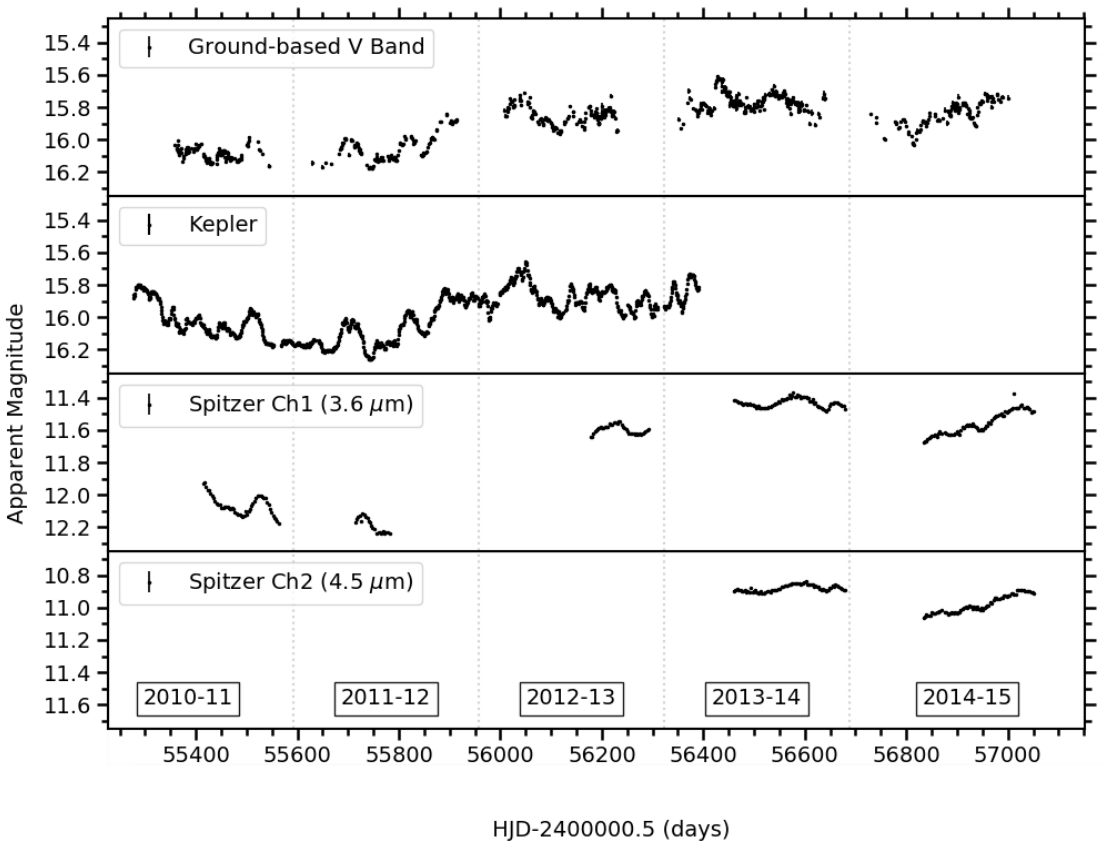

FIGURE 5.2: Light curves of Zw229-015 from the ground-based optical telescopes and *Kepler*, and from IR *Spitzer* Channel 1 (3.6 μm) and *Spitzer* Channel 2 (4.5 μm). The points represent observations, and the grey dotted lines separate each observation season.

Spitzer 1 light curve only covers a period of 67 days and hence was only tested with a range of $\pm$60 days, and the season starting in 2012 in the ground-*Spitzer* 1 CCF, in which the light curves only have overlapping periods of observation of 54 days, and hence was only tested with lags between $\pm$50 days. Potential lags that were measured from peaks on the CCFs were considered positive detections if the CCF values were > 0.5, as most nonzero peaks in the ACFs had values smaller than this. These possible lags were labelled on the plot, with the uncertainties calculated as the standard deviations of the peak of the CCF for each interpolation around the mean CCF.

5.3.1 Optical-IR Cross Correlation results

Figures 5.3 and 5.4 contain the mean CCFs and ACFs of the entire overlapping periods of the ground-*Spitzer* 1, *Kepler*-*Spitzer* 1 and ground-*Spitzer* 2 light curves, and the CCFs and ACFs of some of the individual observation seasons of the ground-*Spitzer* 1 light curves, respectively. Appendix B contains the remaining individual season CCFs of each combination of optical and IR light curve.

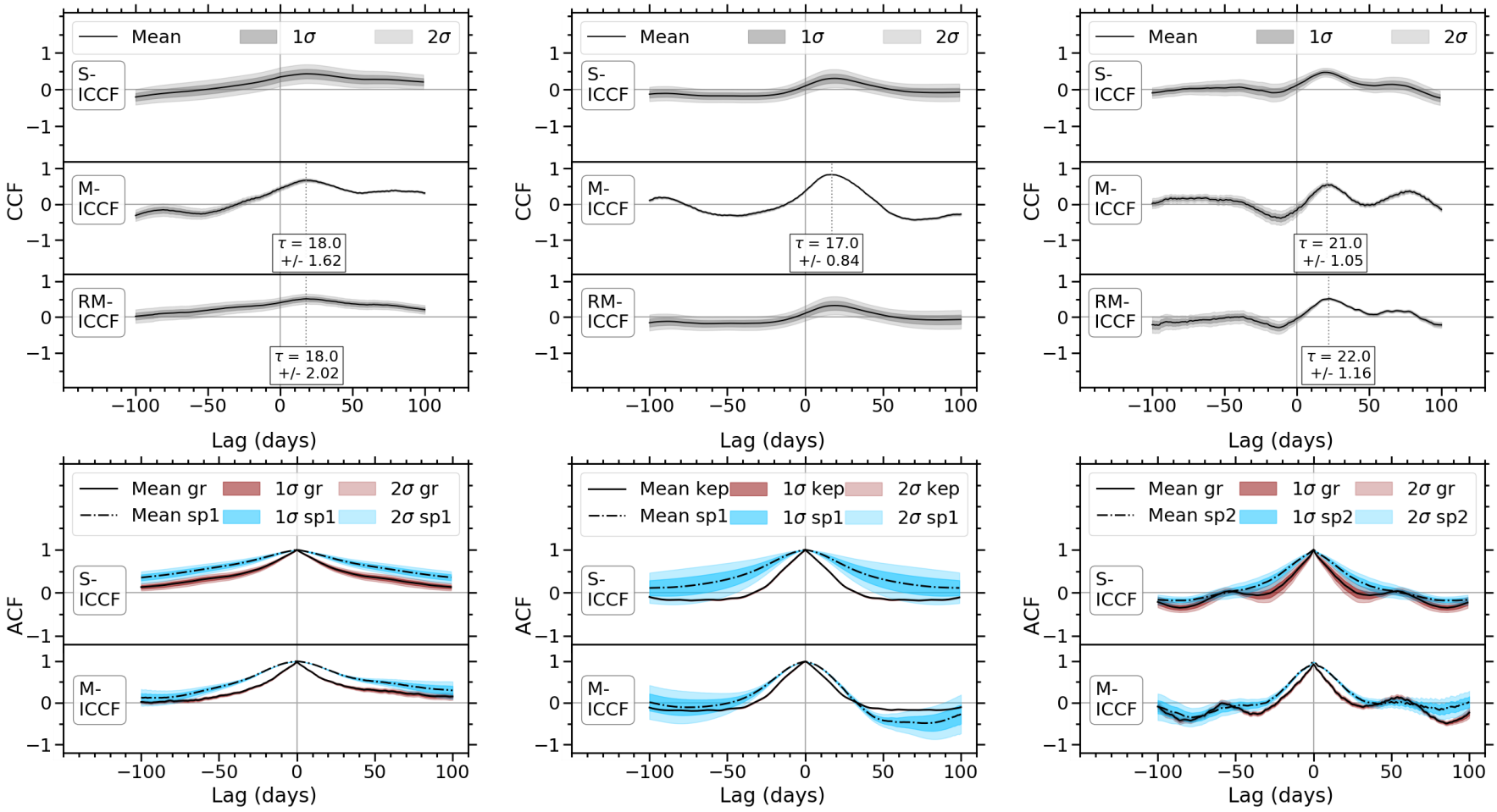

(A) CCFs and ACFs of the entire ground (gr) and *Spitzer* 1 (sp1) light curves.

(B) CCFs and ACFs of the entire *Kepler* (kep) and *Spitzer* 1 (sp1) light curves.

(C) CCFs and ACFs of the entire ground (gr) and *Spitzer* 2 (sp2) light curves.

FIGURE 5.3: CCF and ACF of each combination of the optical and IR light curves of Zw229-015 over the entire overlapping observational periods, after subtraction of long-term variability. Here, M-ICCF refers to interpolating the optical light curve and RM-ICCF refers to interpolating the IR light curve.

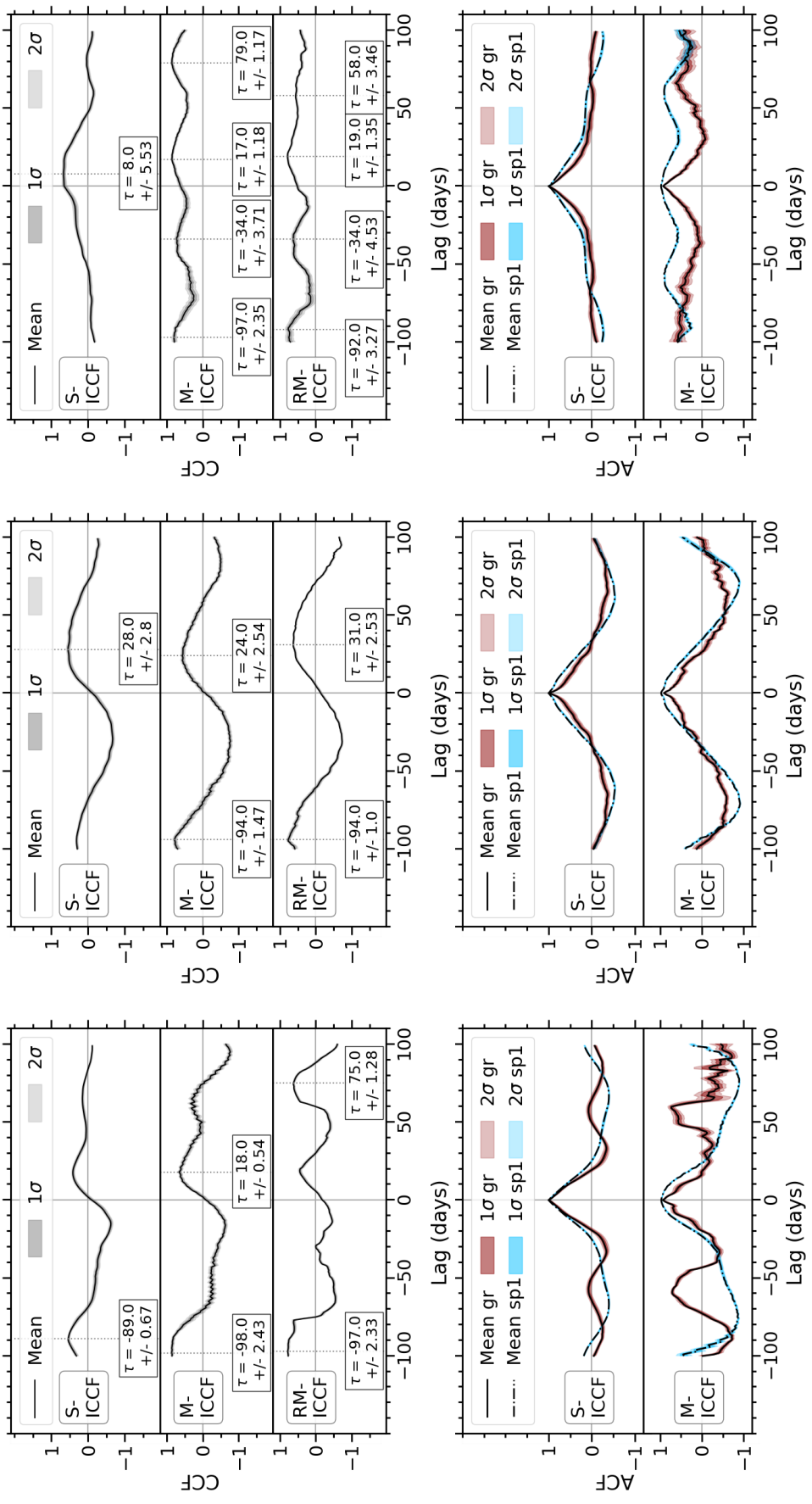

(A) CCFs and ACFs of the 2010 ground and *Spitzer* 1 light curves.

(B) CCFs and ACFs of the 2013 ground and *Spitzer* 1 light curves.

(C) CCFs and ACFs of the 2014 ground and *Spitzer* 1 light curves.

FIGURE 5.4: CCF and ACF of the ground optical (gr) and *Spitzer* 1 (sp1) light curves for some of the individual observation season light curves of Zw229-015. Here, M-ICCF refers to interpolating the ground and RM-ICCF refers to interpolating the *Spitzer* 1 light curve.

The most consistent possible lag detected occurs between $\sim$ 5 and 30 days. As there are no corresponding peaks in the ACFs at these lags, it is likely not effected by the variability of each light curve individually and instead is a potential delay between the optical and IR light curves. A positive detection of this lag is recorded in at least one method in each season and in the entire combined light curves (with the exception of the ground-*Spitzer* 2 2013 season CCF which is further discussed below). This lag is not detected in all methods of each observation season, however. For example, this lag is not detected in the S-ICCF method in the entire overlapping ground-*Spitzer* 1 CCFs in Figure 5.3a, or in the S-ICCF and M-ICCF methods of the entire overlapping *Kepler*-*Spitzer* 1 CCFs in Figure 5.3b; however, this is likely due to interpolations of the *Spitzer* 1 light curve, including in the large gap in observations between HJD 55800 and 56150.

Furthermore, potential lags between $\sim$ 55 and 80 days are detected in multiple plots, although less frequently than the $\sim$ 20 day lag. For example, they are present in either the M-ICCF or RM-ICCF methods of each combination of optical-IR in the 2010 and 2014 CCFs as shown in Figures 5.4a and 5.4c, respectively. The shape of the light curves in these seasons could be impacting the CCFs, however, as the corresponding optical ACF for each CCF that detects this lag has a secondary peak at $\sim$ 55–70 days. For example, the lag is detected in the RM-ICCF method of the 2010 season ground-*Spitzer* 1 CCF and in the corresponding ground ACFs there is a relatively high peak at $\sim \pm 60$ days, with an ACF value of $\sim$ 0.7. This means that the *Spitzer* 1 light curve would correlate with the ground light curve at the lag τ and $\tau + 60$ days (i.e., if $\tau \approx 20$, then $\tau + 60 \approx 80$ days). Furthermore, the M-ICCF and RM-ICCF methods of the 2014 season CCFs display multiple peaks separated by $\sim$ 50–60 days, as shown in Figure 5.4c for example, which could also be due to the shape of the optical and IR light curves in this season as they follow an increase with multiple distinct bumps separated by $\sim$ 50–60 days that correlate with each other. This correlation can be seen in the M-ICCF ACFs of both light curves by the peaks at $\sim \pm 60$ days with ACF values of $\sim$ 0.6 in the ground optical and 0.9 in the *Spitzer* 1 and 2. Therefore, as this $\sim$ 55–80 day lag has corresponding peaks in the optical ACFs, it is unlikely to be due to a delay between optical and IR light curves, but instead aliasing in the light curves of certain seasons. This is further explored as a potential periodicity in the optical light curves in Section 5.3.3.

Finally, possible lags between ~ -100 and -90 days are displayed in multiple methods and seasons — for example, in all methods of the ground-*Spitzer* 1 2010 season, and the M-ICCF and RM-ICCF methods of ground-*Spitzer* 1 in the 2013 and 2014 seasons displayed in Figure 5.4. These peaks in the CCFs occur only owing to a small number of overlapping data points, so are deemed less significant than other possible lags. Additionally, similar correlations are present in at least one of the

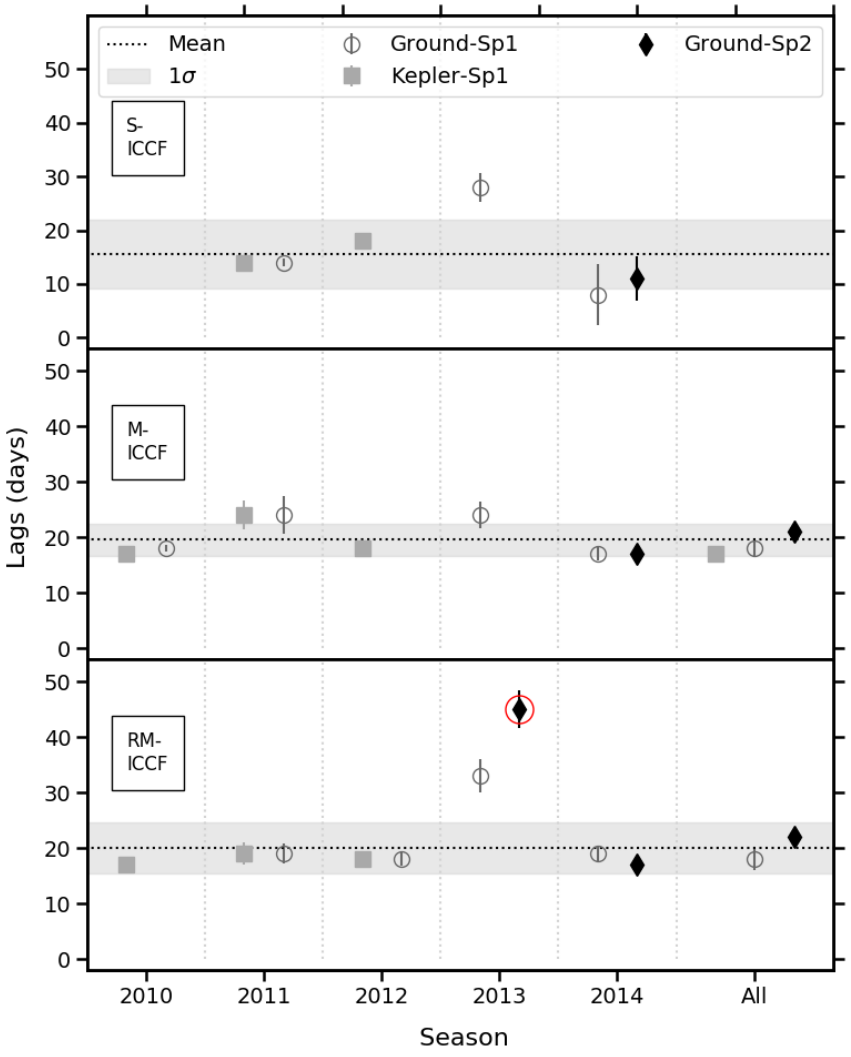

FIGURE 5.5: The lags measured between the optical and IR light curves of Zw229-015 between 0 and 50 days for each combination of optical (ground and *Kepler*) and IR (*Spitzer* 1 (sp1) and *Spitzer* 2 (sp2)) for each season and using each CCF method (S-ICCF, M-ICCF and RM-ICCF). The ground-*Spitzer* 2 RM-ICCF is circled in red as a possible outlier, and is excluded from the mean calculation.

corresponding ACFs, which further implies that the peak is not necessarily due to a lag between light curves but impacted by aliasing.

As the $\sim$ 20 day lag was deemed to be most significant, I further compared it in each season and for each combination of optical and IR light curves in Figure 5.5. This lag is found consistently with values between 8 and 30 days, with a mean of 18.8 ± 4.6 days (or 19.8 ± 7.1 days including the 2013 season RM-ICCF lag). The mean of the individual methods, S-ICCF, M-ICCF and RM-ICCF, are 15.5 ± 6.4, 19.5 ± 2.9, and 19.9 ± 4.0 days (or 22.5 ± 8.9 days including the 2013 season RM-ICCF lag) respectively, which are all consistent within 1 standard deviation of each other, and the mean of each combination of optical and IR light curve are 19.8 ± 5.7, 18.0 ± 2.5,

and 17.6 ± 3.9 days (or 22.7 ± 11.9 days including the 2013 season RM-ICCF lag) for the ground-*Spitzer* 1, *Kepler*-*Spitzer* 1 and ground-*Spitzer* 2 respectively, which are also within 1 standard deviation of each other.

The lags detected in the ground-*Spitzer* 1 CCFs in the 2013 season are found to be on the longer side with values of 24-31 days depending on CCF method. Furthermore, in the ground-*Spitzer* 2 CCFs in this season, no lag is detected in the S-ICCF or M-ICCF methods, but in the RM-ICCF method a much longer lag of ~ 50 days is measured. It can be seen in these CCFs, for example in Figure 5.4b, the shape of the CCF only contains one peak that it very broad, which is mirrored in the broadness of the ACFs. This could be due to the shape of the light curves in this season which appear almost sinusoidal in shape, especially in the IR, and therefore an increase in delay between optical and IR light curves in this season is unlikely.

5.3.2 *Spitzer* 1 - *Spitzer* 2 Cross-Correlation Results

I also cross correlated the overall combined *Spitzer* light curves and the individual seasons to measure potential lags between the 3.6 μm and 4.5 μm emission regions, as displayed in Figure 5.6. The most consistent lag is measured with value between $\sim$ 0–5 days, and is detected in each CCF, with a mean of 1.8 ± 1.7 days. Additional lags are measured in the M-ICCF methods of the 2014 season in Figure 5.6c with values of ~ 47 days and $\sim \pm 100$ days; however, as similar peaks are found in the M-ICCF ACFs at this time, the peak in the CCFs is likely a result of the shape of the light curves and not a delay between the 3.6 μm and 4.5 μm emission.

5.3.3 Potential Periodicity

A peak in the optical ACFs at $\sim 55 - 70$ days is observed in multiple seasons, which could imply a periodicity within the light curves. This peak appears predominantly in the M-ICCF ACFs, in all optical ACFs that are tested with lags of $\pm$ 100 days, except in the 2013 season. In theses ACFs, the correlation of the light curve with itself is only tested for the range of light curve that overlaps with the IR observations ($\sim 50 - 150$ days per season), so to further examine this potential periodicity, the entire *Kepler* light curves were analysed for each season and overall.

Figure 5.7 shows the ACF of the entire *Kepler* light curves in the 2010 and 2012 seasons respectively compared to the ACFs of the portion of the light curve that overlaps with the IR observations. The entire season light curve ACFs do not demonstrate a peak at ~ 60 days as is shown in the limited ACFs. Furthermore, the peak is not present in the entire *Kepler* ACF in Figure 5.3b or in the ground ACFs in the 2013 season in Figure 5.4b or entire ground ACFs in Figure 5.3a. The possible ~ 60 day periodicity is

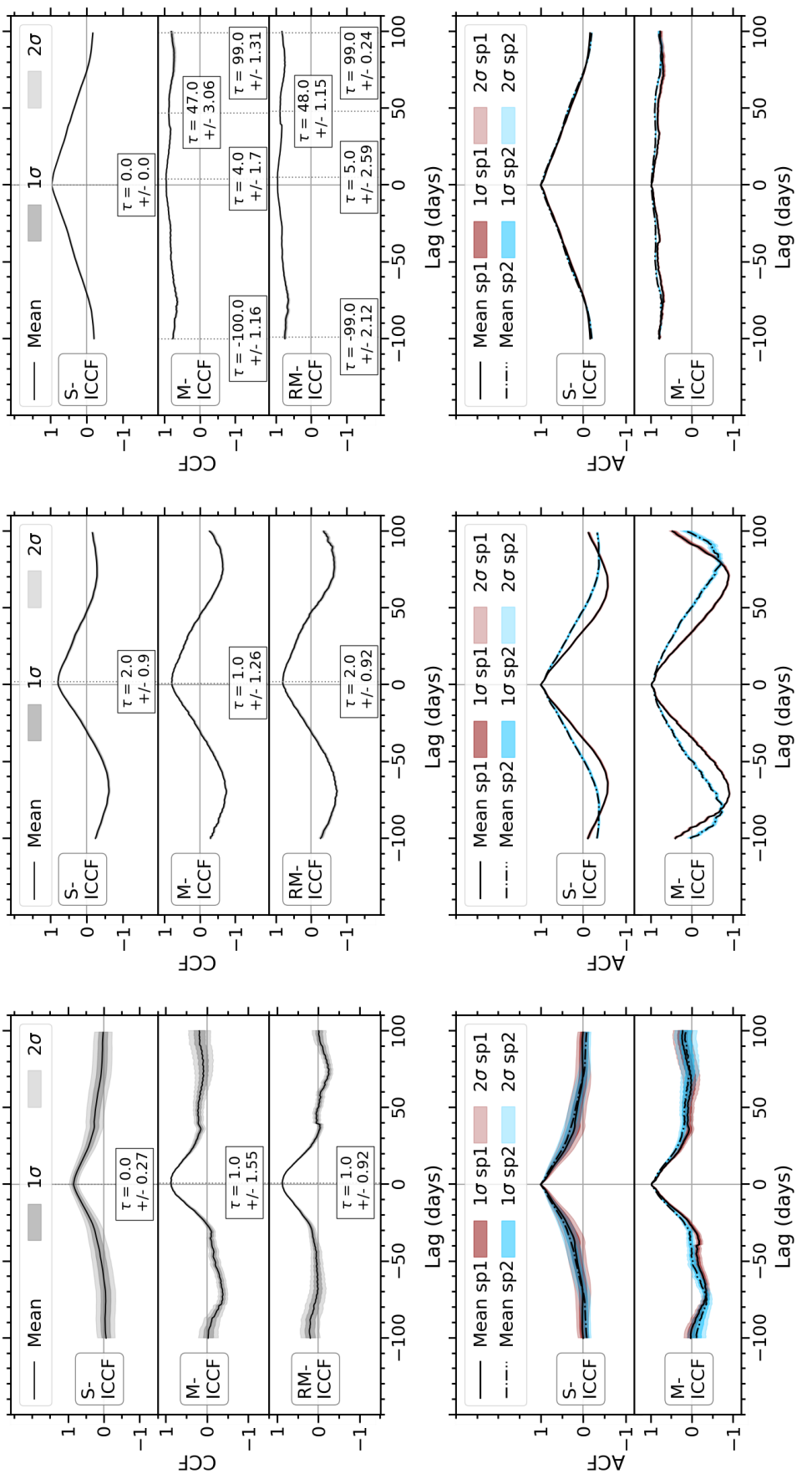

(A) CCF and ACF of the *Spitzer* 1 (sp1) and *Spitzer* 2 (sp2) light curves for the entire overlapping light curves of Zw229-015.

(B) CCFs and ACFs of the 2013 *Spitzer* 1 and *Spitzer* 2 light curves.

(C) CCFs and ACFs of the 2014 *Spitzer* 1 and *Spitzer* 2 light curves.

FIGURE 5.6: CCF and ACF of the *Spitzer* 1 (sp1) and *Spitzer* 2 (sp2) light curves for the individual observation seasons and the entire light curves of Zw229-015, made using each method of CCF, where M-ICCF refers to interpolating the *Spitzer* 1 light curve and RM-ICCF refers to interpolating the *Spitzer* 2 light curve.

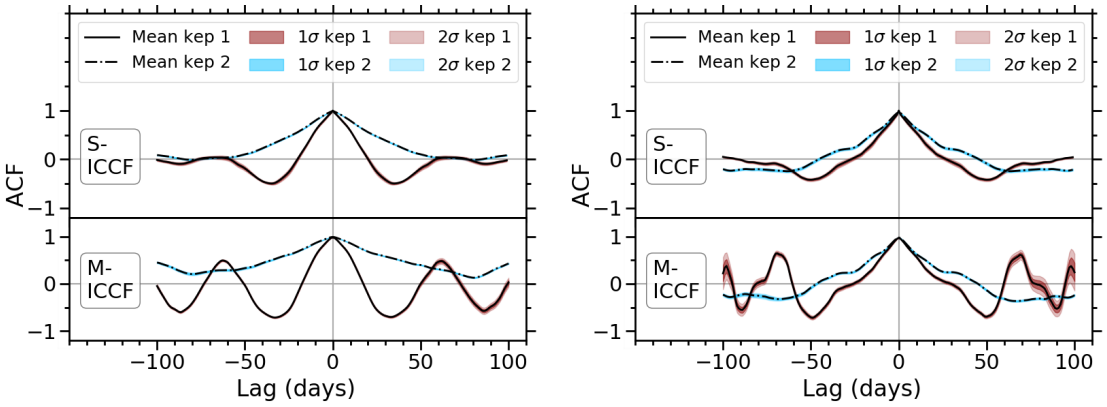

(A) ACFs of the 2010 season *Kepler* light curves.

(B) ACFs of the 2012 season *Kepler* light curves.

FIGURE 5.7: ACFs of the entire seasons *Kepler* light curves (kep 2) compared to the ACFs of the portion of *Kepler* light curves that overlap with the IR observations (kep 1), in both the S-ICCF and M-ICCF methods.

therefore not observed consistently across all optical ACFs of all lengths, which implies $\sim$ 60 days is not a characteristic timescale of Zw229-015, but a consequence of the overlapping observation epochs. This is shown further in the Lomb-Scargle periodograms in Appendix B.

5.4 Dust Reverberation Mapping with Simulations of Dust Transfer Functions

As previously mentioned, DRM with cross correlation analysis can provide a good indication of the size of the dust emitting region, however the overall delayed IR response to the optical emission actually depends on the structure and geometry of this dust emission region.

In Chapter 1 I introduced that the light curve of the reprocessed optical emission into the IR at time t can be expressed as a convolution of the optical light curve with a dust transfer function (DTF) (Peterson, 1993),

$$f_{\rm IR}^{\rm rep}(t) \;=\; \int_{-\infty}^{+\infty} \Psi(\tau')\, f_{\rm opt}(t-\tau')\, d\tau' \,. \tag{5.1}$$

Here $f_{\rm opt}(t-\tau')$ is the optical light curve at an earlier time $t-\tau'$, τ' is an arbitrary delay, $\Psi(\tau')$ is the DTF, and $f_{\rm IR}^{\rm rep}(t)$ is the reprocessed IR light curve at time t:

$$f_{\rm IR}^{\rm rep}(t) = f_{\rm IR}^{\rm obs}(t) - f_{\rm IR}^{\rm disk}(t)\,, \tag{5.2}$$

where $f_{\rm IR}^{\rm obs}(t)$ is the total observed IR light curve at time t, and $f_{\rm IR}^{\rm disk}(t)$ is the contribution to the observed IR light curve from the AD at time t, which is estimated from

$$f_{\rm IR}^{\rm disk}(t) = f_{\rm opt}(t)\left(\frac{\nu_{\rm IR}}{\nu_{\rm opt}}\right)^{\alpha_\nu}, \tag{5.3}$$

where $f_{\rm opt}(t)$ is the optical flux at time t, $\nu_{\rm IR}$ and $\nu_{\rm opt}$ are respectively the effective frequencies of the IR and optical filters, and α_ν is the power-law index which is set to the expected value of $\alpha_\nu = 1/3$ in the standard accretion-disk model (Shakura and Sunyaev, 1973a).

The DTF is not directly measurable, and finding a unique solution for it in Equation 5.1 would require high-quality data; thus, in this paper, it is estimated by first simulating the distribution of the dust in the inner regions of the AGN.

5.4.1 Simulating Dust Transfer Functions

Currently, the dust distribution in the inner regions of the AGN can only be spatially resolved using interferometry on relatively bright, nearby AGN. Therefore in this chapter I am modelling the dust distribution using updated versions of the radiative transfer models of the dust emitting region used in Hönig et al. (2006); Hönig and Kishimoto (2010, 2011), which simulates a distribution of dust clouds as described below. Note that the sizes of the dust clouds are assumed to be much smaller than the size of the overall dust distribution, so the dust clouds are treated as points in this model.

Firstly, in the equatorial plane, 10,000 clouds are distributed following a radial power law with index α, as given in Equation 5.4 below, and are uniformly distributed with azimuthal angle (ϕ) between 0 and 2π. Steep radial power-law indices (i.e., small values of α) correspond to a compact object, while in shallow radial brightness distributions, the dust is extended as shown in Figure 5.8. Figure 5.8d shows how the radial dust distribution effects the DTF, as the DTF corresponding to a compact object (e.g. α=-5.5, shown in Figure 5.8c) contains a stronger peak that tails off faster than in the extended object (e.g. α=-0.5 shown in Figure 5.8a), as the emission comes from nearer to the centre of the source.

$$r \propto \left(\frac{r'}{r_{\rm sub}}\right)^{\alpha}, \tag{5.4}$$

where $r_{\rm sub}$ is the dust sublimation radius.

The heights of the dust clouds above the equator (h) are distributed following a vertical scale height power law with index β, as given by Equation 5.5 below, where

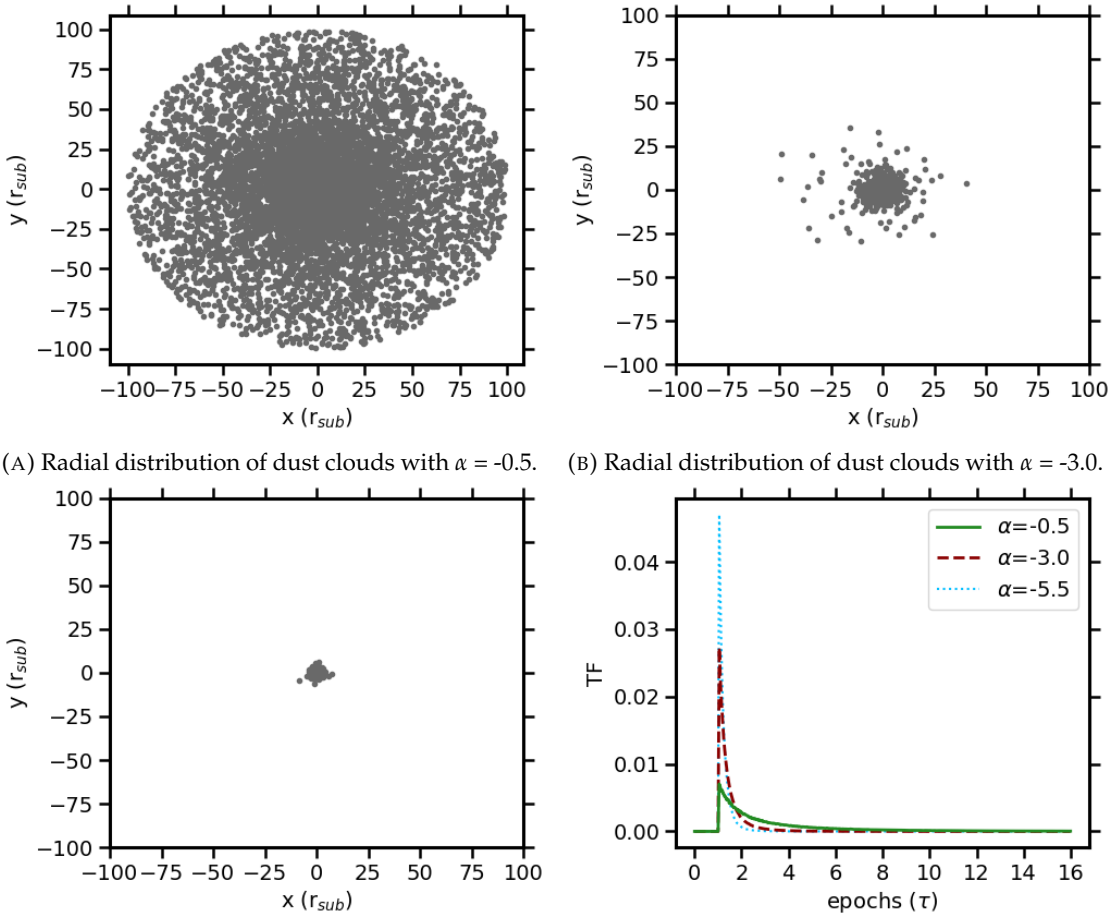

(A) Radial distribution of dust clouds with α = -0.5.

(B) Radial distribution of dust clouds with α = -3.0.

(C) Radial distribution of dust clouds with α = -5.5.

(D) Change in DTF with different values of radial power law index, α.

FIGURE 5.8: Examples of the radial distribution of 10,000 dust clouds with different values of α and the effect of radial distribution on the simulated dust transfer functions. In this figure, the inclination angle is set to i=0 degrees and the vertical scale height law index is set to $\beta = 0.05$.

values of $\beta = 0$ correspond to a flat disk, $\beta = 1$ is a flared disk of constant height to radius ratio, and $\beta > 1$ follows an outflow-like distribution as shown in Figure 5.9. The DTF also changes depending on the height of the dust clouds above the equator as shown in Figure 5.9d, as for an AGN with an inclination angle of 0 degrees, the clouds with $\beta = 2.05$ (e.g. with distribution shown in Figure 5.9c) are closer to the observer than the clouds with $\beta = 0.05$ (e.g. with distribution shown in Figure 5.9a), and therefore the DTF peaks earlier.

$$h \propto r^{\beta}\,, \tag{5.5}$$

where r is the radial position of each dust particle from Equation 5.4.

I chose to simulate the dust following this radial and vertical distribution to be consistent with interferometric studies which have observed dust within an equatorial

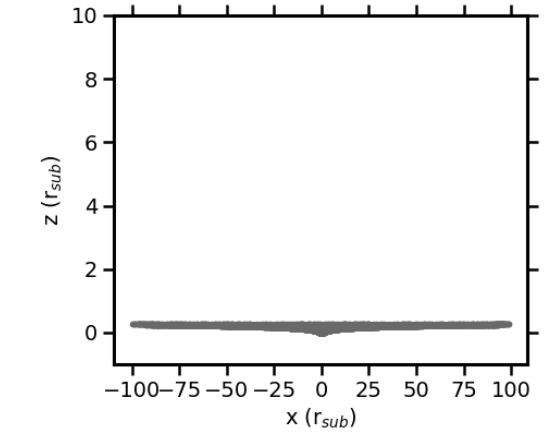

(A) Vertical distribution of dust clouds with $\beta = 0.05$.

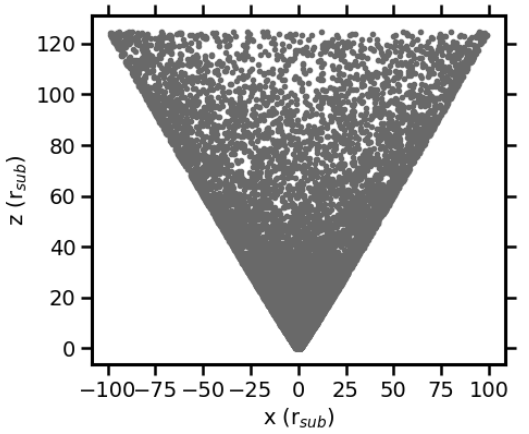

(B) Vertical distribution of dust clouds with $\beta = 1.05$.

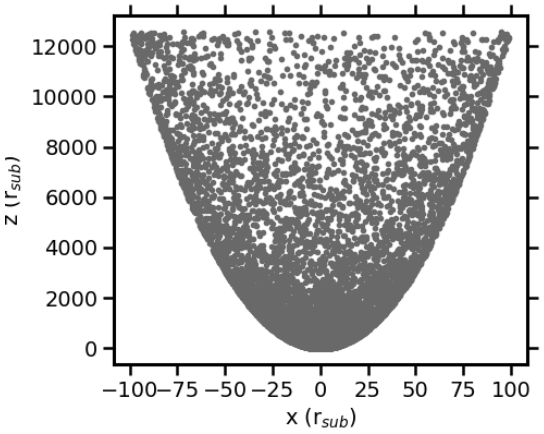

(C) Vertical distribution of dust clouds with $\beta = 2.05$.

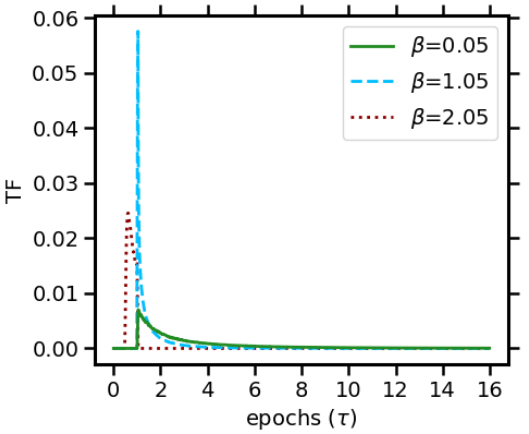

(D) Change in DTF with different values of vertical scale height power law index, β.

FIGURE 5.9: Examples of the vertical distribution of 10,000 dust clouds with different values of β and the effect of vertical distribution on the simulated dust transfer functions. In this figure, the inclination angle is set to i=0 degrees and the radial power law index is set to $\alpha = -0.5$.

disk surrounding the central engine, but also as a secondary extended polar component has also been observed in some AGN (e.g., Raban et al., 2009; Hönig et al., 2012, 2013; Leftley et al., 2018). It is also expected that close to the central region the dust would be sublimated, creating a dust sublimation radius beyond which the dust can survive. This is included in the simulated dust distributions, however occurs on sizes much smaller than the entire distribution of dust and hence is not visible in Figures 5.8 and 5.9. Furthermore, it is expected that the dust in the equatorial disk would be subject to flaring depending on the location within the equatorial plane (e.g., Manske et al., 1998; Hönig and Kishimoto, 2010; Almeyda et al., 2017), however for simplicity the height of the dust clouds within the equatorial component are assumed to be consistent.

The observed emission further depends on the angle (ψ) that describes the dust cloud's position relative to the equatorial plane and relative to the observer, as given

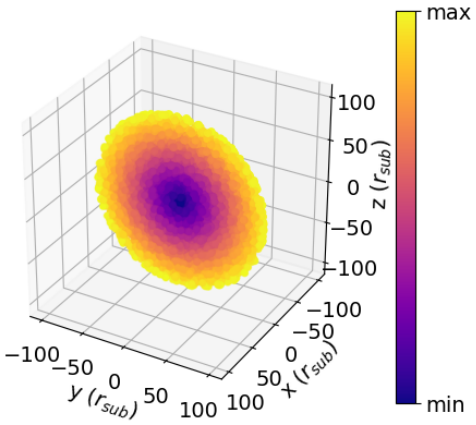

(A) Delay map for i = 0 degrees.

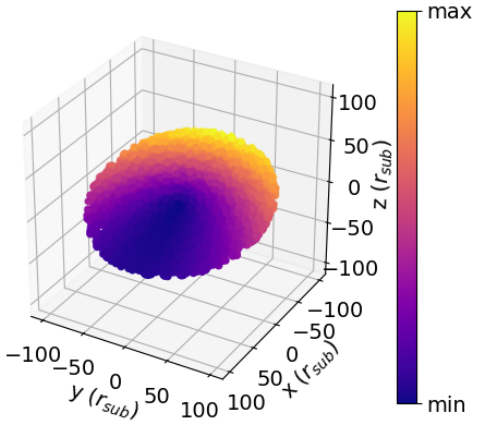

(B) Delay map for i = 69 degrees.

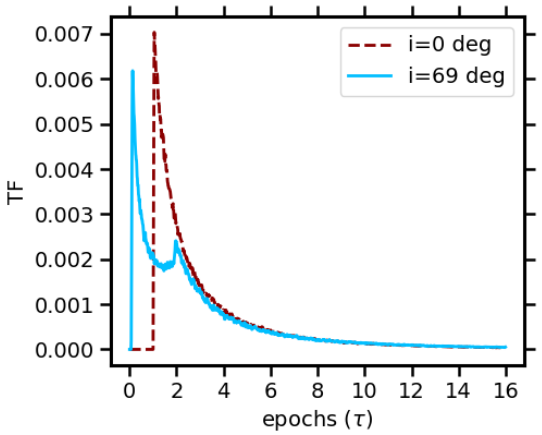

(C) Change in DTF with different values of inclination angle, i, before the illumination effects are considered.

FIGURE 5.10: Maps of the delay to each corresponding dust cloud depending on inclination angle and location of the cloud, where the line of sight of the observer is down the y axis, and the effect it has on the DTFs. 10,000 dust clouds have been plotted in this figure, with the radial power law index set to $\alpha = -0.5$ and the vertical scale height power law index set to $\beta = 0.05$.

in Equation 5.6. The observed delay for each dust cloud depending on the inclination is shown in Figure 5.10, as when the disk is tilted (e.g., represented by an angle of $i = 69$ degrees) the far-side clouds have larger delays and the near-side clouds have smaller delays relative to the dust clouds in a face-on disk (i.e., $i = 0$ degrees). This impacts the DTFs as shown in Figure 5.10c where the DTF of a tilted disk peaks at shorter lags compared to the DTF corresponding to a face on disk due to the shorter lags observed of the near-side clouds, and the DTF develops a tail towards larger lags due to the far-side clouds.

$$\cos\psi = \cos\theta\cos\phi\sin i + \sin\theta\cos i\,, \tag{5.6}$$

where θ is the complement of the polar angle and i is the inclination angle.

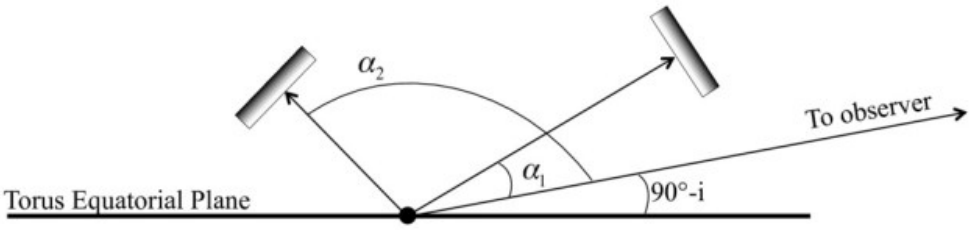

FIGURE 5.11: Example of the illumination of the dust clouds by the central engine, where the dust clouds are represented by rectangles for demonstration purposes only. Image credit: Almeyda et al. (2017).

Furthermore, these optically thick dust clouds are assumed to be directly heated from the AGN; thus, only the side facing the AGN is illuminated while the far side is not, as shown in Figure 5.11. The fraction of a dust cloud's illuminated surface that is then visible to the observer (κ) is estimated from Equation 5.7.

$$\kappa = 0.5\,(1 - \cos\psi)\,, \tag{5.7}$$

where an angle of $\psi = 180$ degrees corresponds to the entire illuminated side of the dust cloud being visible to the observer, while for an angle of $\psi = 0$ degrees, the entire nonilluminated side is visible to the observer. This is shown in Figure 5.12c as for an inclination angle of 0 degrees the clouds are all similarly partially illuminated, and therefore the shape of the DTF remains the same, but for an inclination angle of 69 degrees the surface of the nearside dust clouds that are visible to the observer are mostly not illuminated, while the far side clouds are mostly illuminated. This therefore changes the DTF, as shown in Figure 5.12c, as the first peak that is visible in Figure 5.10c for an inclination angle of $i = 69$ degrees, which corresponds to the emission from the nearside clouds, is no longer present, while the peak corresponding to the far side dust clouds remains.

The dust clouds are assumed to radiate as blackbodies, and after accounting for the illumination effects, the DTF can be estimated from the combined emission response of each dust cloud (calculated using the Planck function, $B_\nu(T(r))$, for temperature $T(r)$ at radial distance r given by Equation 5.8) to a delta-function input continuum pulse,

$$T(r) = T_{\rm sub}\left(\frac{r}{r_{\rm sub}}\right)^{\frac{-2}{4+\gamma}}, \tag{5.8}$$

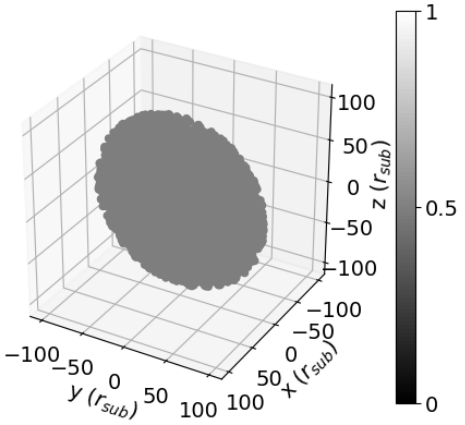

(A) Illumination map for i = 0 degrees.

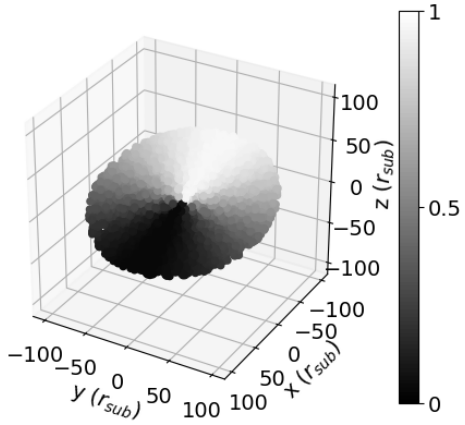

(B) Illumination map for i = 69 degrees.

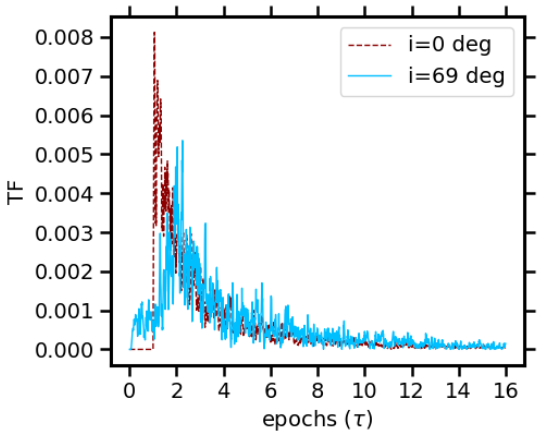

(C) Change in DTF with different values of inclination angle, i, when illumination effects are considered

FIGURE 5.12: Maps of the illumination of each corresponding dust cloud depending on inclination angle and location of the cloud, where the line of sight of the observer is down the y axis, and the effect it has on the DTFs. 10,000 dust clouds have been plotted in this figure, with the radial power law index set to $\alpha = -0.5$ and the vertical scale height power law index set to $\beta = 0.05$.

where $T_{\rm sub} = 1500\,{\rm K}$ is the sublimation temperature, and γ is the dust IR opacity power-law index, which is set to 1.6 to correspond to standard interstellar dust material dust grains (Barvainis, 1987).

Using this method, a grid of DTFs for each IR wavelength was simulated, for a range of radial power-law indices $-5.5 \leq \alpha \leq -0.5$, a range of vertical scale height power-law indices $0.05 \leq \beta \leq 2.05$, and a range of inclination angles $0 \leq i \leq 69$ degrees that approximately corresponds to the inclination angles expected for a type 1 AGN to be observed. The DTFs are calculated over (0–16) τ, where τ corresponds to the projected light-travel time between the source of the optical and IR emission.

5.4.2 MCMC Modelling of the DTFs and Light Curves

To further constrain properties of Zw229-015, the DTFs from these grids were convolved with the optical light curves to simulate the reprocessed IR light curve. The best fit DTF therefore can be found by comparing the simulated light curves to observations. Specifically, this is done in this chapter using Markov Chain Monte Carlo (MCMC) modelling to find the estimates of the values for each free parameter in the model which are described further below.

MCMC modelling is a method of sampling the parameter space by comparing generated models to data in order to constrain these parameters to those whose models match the data reasonably well. The MCMC process works here for each chain as follows.

1. It starts by choosing a random combination of values for each parameter within the defined parameter space, giving a set of parameters, θ. It then generates a model of the data using this combination of parameters, and compares the model to the data by computing the posterior probability density of this model, $P(\theta|D)$, as given by,

$$P(\theta|D) = P(D|\theta)P(\theta) \tag{5.9}$$

   where $P(\theta)$ is the probability of that model that is supplied to the MCMC as priors, and $P(D|\theta)$ is the probability of the data given the model which is defined using an estimate of the likelihood of $-\frac{1}{2}\chi^2$ where χ^2 is the value of χ^2 computed comparing the model to the data.

2. A new set of parameters is then chosen from the parameter space and a new model is generated and compared to the data as described in the previous step. The ratio of posterior probabilities of the new and previous models are then compared to an acceptance probability, P_a that is randomly drawn. If the probability ratio $P_{\rm new}/P_{\rm old} > P_a$, then the current set of parameters are updated to match the new set of parameters. If $P_{\rm new}/P_{\rm old} < P_a$ then the new model is not accepted and the MCMC continues with the previous set of parameters.

3. Step 2 is then repeated for a given number of iterations until the parameters converge.

The result is a posterior distribution for each set of parameters in each chain that represents the sample of models that reasonably describe the data, from which we can estimate values for each parameter. A number of initial iterations are excluded from the resulting distribution as "burn-in" (i.e., iterations before the chain reaches its equilibrium distribution due to the random starting value of each parameter within

the parameter space). Furthermore, the samples in the chain are not necessarily independent, which means the chain can be strongly autocorrelated. This autocorrelation can be averaged out using sufficiently long chains or by thinning the sample by excluding the results from every n^{th} step.

In this chapter, the MCMC modelling is done using an idl code emcee.pro (Hönig, 2020), adapted from the python package emcee (Foreman-Mackey et al., 2013).

For estimating properties of the dust distribution of Zw229-015, an MCMC search is performed over the parameters described in Table 5.1 to find the DTFs that result in reasonable fits of the simulated IR light curve to observations. These parameters include the radial power-law index, vertical scale height power-law index, inclination angle, and time lag that describe the parameter space of the DTF grids created in the previous section. They also include parameters such as the optical-IR amplitude conversion factor, $w_{\rm eff}$, which is a scaling factor of the amplitudes of the transfer functions to account for uncertainties such as different amounts of host-galaxy contributions in the different light curves or the accretion-disk subtraction in the IR light curves, and an additional offset that could arise as the modelling is performed on the relative light curves, $g_i(t) = f_i(t)/\langle f_i(t)\rangle - 1$ (i = IR, opt), where $\langle f_i(t)\rangle$ is the mean flux of the light curves, $f_i(t)$, over the entire observational period being modelled.

The driving optical light curve that is convolved with the best-fit DTF needs to be uniformly sampled; hence, resampled light curves were found by linearly interpolating the observations with a cadence of 4 days. While the mean of the interpolations could be used as the input optical light curve, this could underestimate the variability within the seasonal gaps, so instead the input optical light curves are treated as free model parameters with a prior range that is constrained by the data, and a simultaneous MCMC search is performed to also find the best optical light curve that when convolved with the DTF best fits the IR observations.

Additionally, as most AGN (excluding blazars) will vary annually in the IR by $\sim 10\%$ (e.g., Lyu et al. 2017), the uncertainty in the IR light curves is set to 1% of the flux, to prevent the model from trying to overfit the shorter timescale variations (i.e., the nightly/weekly variations).

I therefore modelled each combination of optical and IR light curve of Zw229-015 using the methods described above to attempt to further constrain the inner regions of the AGN. The MCMC modelling was performed using 64 chains, each with a length of 50,000 iterations, which was sufficient for the parameters to converge. The range of priors for each parameter is listed in Table 5.1, where the time lag (for example) is constrained by the results of the DRM in Section 5.3. The quality of the fit is measured using the reduced χ^2 to compare the simulated light curves to the observations.

TABLE 5.1: Descriptions of the parameters of the MCMC modelling that are used to find the best-fit dust transfer function and simulate the IR light curves.

Parameter	Definition	Priors Range
Radial power-law index, α	Power-law index which is used to describe the radial distribution of dust	$-5.5 \leq \alpha \leq -0.5$
Vertical scale height power-law index, β	Power-law index which is used to describe the vertical distribution of the dust above the equator	$0.05 \leq \beta \leq 2.05$
Time lag (days), τ	The projected time delay between optical and IR light curves	$5 \leq \tau \leq 30$
Inclination angle (degrees), i	The angle between the torus and line of sight of the observer	$1 \leq i \leq 69$
Optical-IR amplitude conversion factor, w_{eff}	The scaling factor of the amplitudes of the DTFs to account for uncertainties within the light curves, including different amounts of host-galaxy flux in the different observations and accretion-disk subtraction	$0.2 \leq w_{\text{eff}} \leq 10$
Offset	Additional offset between relative light curves	$-0.2 \leq \text{Offset} \leq 0.2$
Resampled relative optical light curve	As the observed optical light curves are not necessarily evenly sampled, they are interpolated and then treated as free parameters to find the best-fit optical light curve that, when convolved with the DTF, best fits the IR observations.	Interpolated optical light curve $\pm$ the 1σ uncertainties at that point

5.4.3 IR Light Curve Modelling Results

5.4.3.1 Modelling Entire Overlapping Light Curves

Initially, I modelled the entire overlapping light curves for each combination of optical and IR; for example, Figure 5.13a displays the model that corresponds to the maximum of the posterior distribution for the entire *Kepler-Spitzer* 1 light curves. It can be seen here that the overall variability trends of the simulated IR light curve on the order of several months to years fits the observations relatively well; however, the shape of the simulated IR light curve for the individual seasons deviates from the observations, specifically in the 2011 and 2012 seasons where the amplitude of variability appears to be overestimated. This is further demonstrated in Figure 5.13b which shows the mean subtracted simulated and observed light curves in the individual seasons.

A considerable increase in flux occurs between the 2011 and 2012 seasons, which is greater in the IR than optical and could affect the modelling, so to investigate this, only the 2010–2011 seasons were modelled in Figure 5.14a. It can be seen that this simulated light curve follows the shape of the 2011 season substantially better than Figure 5.13a, both by eye and by the reduced χ^2_{IR}, although the flux is now underestimated at the start of the 2010 season. Furthermore, the peak of the simulated light curve in Figure 5.14a at $\sim$ HJD 55525 matches the observations better than Figure 5.13a. The means of the parameters that correspond to the best-fit DTFs in each of the 64 MCMC chains are compared in Table 5.2 for the *Kepler-Spitzer* 1 model over

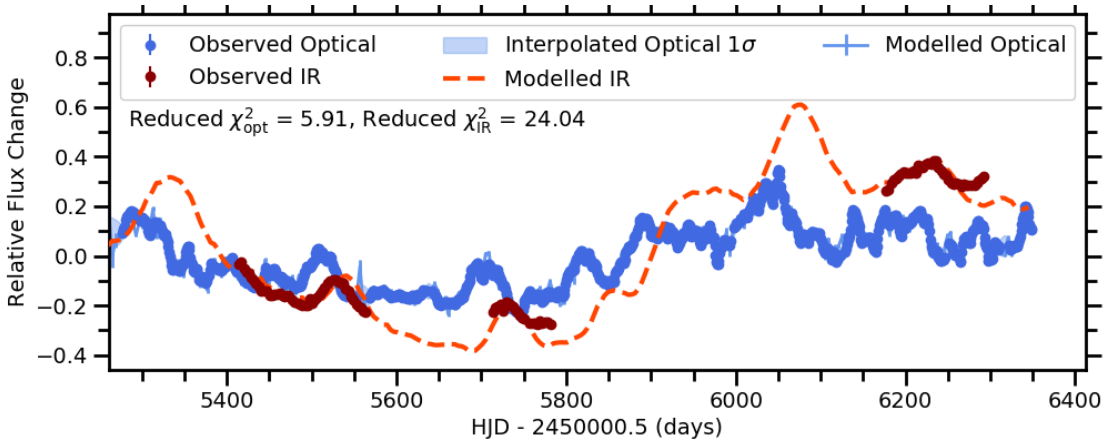

(A) Simulated light curves of *Kepler-Spitzer* 1 for the entire overlapping observational periods, plotted with the parameters that corresponded to the highest posterior distribution, with values of $\alpha = -0.50$, $\beta = 0.20$, $w_{eff} = 2.67$, $\tau = 15.94$ days, and $i = 54.08°$.

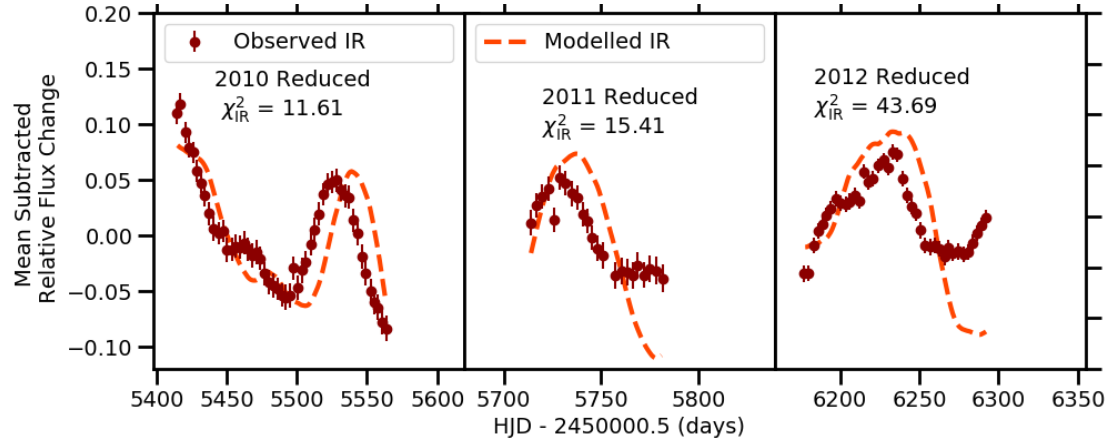

(B) Simulated light curves of Figure 5.13a mean subtracted and compared to the observations.

FIGURE 5.13: Results of the IR Modelling of the *Kepler-Spitzer* 1 for the entire overlapping observational periods.

2010–2011 and 2010–2012, and are shown to be consistent for the radial power-law index, vertical scale height power-law index, and inclination angle. However, the amplitude conversion factor is larger for the 2010–2012 simulated light curves, which explains why the variability of the 2011 season appears overestimated. Also, the time lag between optical and IR emission is $\sim$ 20 days in the 2010–2012 model compared to the $\sim$ 10 days found by only fitting the simulated light curves to the 2010–2011 seasons, which again could explain why the simulated peak at $\sim$ HJD 55525 is later than the observations in Figure 5.13a.

Furthermore, in Figure 5.14b, I convolved the best-fit DTF found for Figure 5.14a with the entire observed *Kepler* light curve. Here, the flux of the simulated light curve in the 2012 season is underestimated; however, the shape matches the observations well, which can be further seen in Figure 5.14c. This suggests that the increase in flux between the 2011 and 2012 seasons is not well modelled by a single dust component;

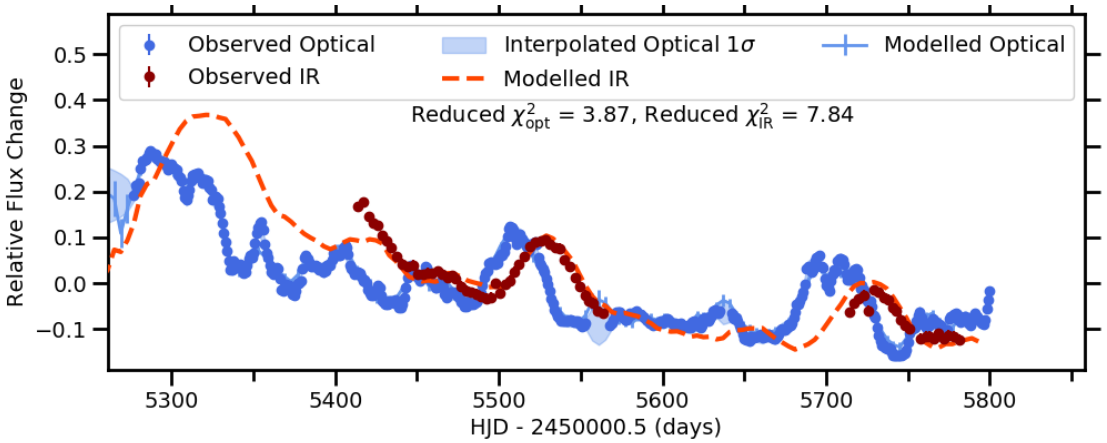

(A) Simulated light curves of *Kepler-Spitzer* 1 for the observation seasons starting 2010–2011, plotted with the parameters that corresponded to the highest posterior distribution, with values of $\alpha = -0.56$, $\beta = 0.51$, $w_{\rm eff} = 1.63$, $\tau = 12.12$ days, and $i = 45.67°$.

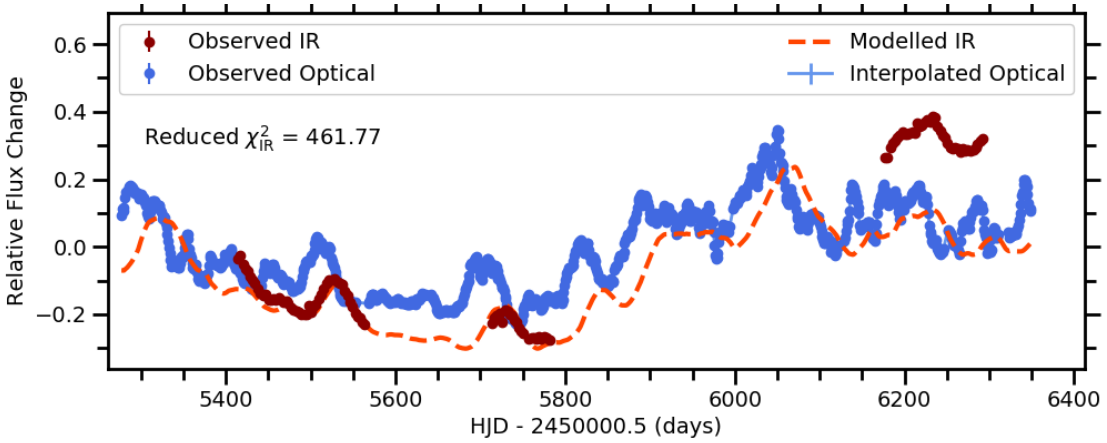

(B) Simulated IR light curve of *Kepler-Spitzer* 1 for the entire overlapping observational periods, made using the linearly interpolated *Kepler* light curve convolved with the DTF corresponding to Figure 5.14a.

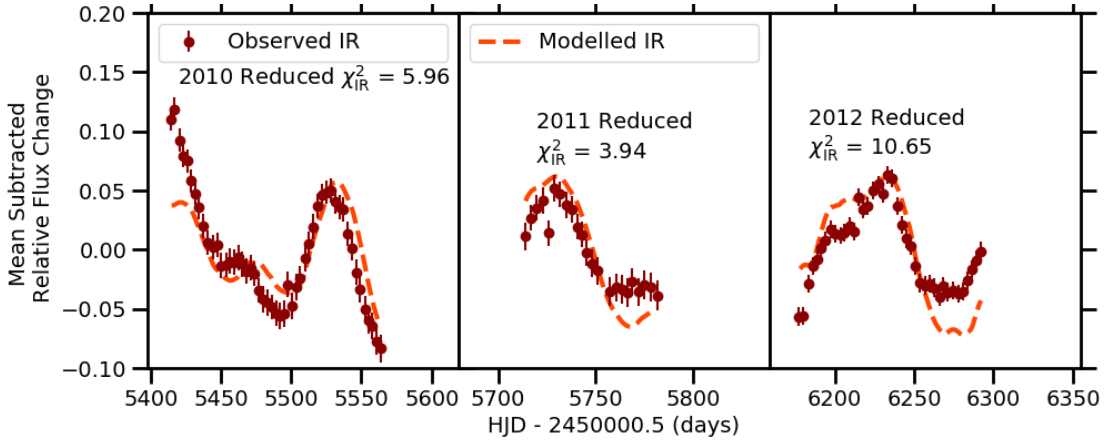

(C) Simulated light curves of Figure 5.13a mean subtracted and compared to the observations.

FIGURE 5.14: Results of the IR Modelling of the *Kepler-Spitzer* 1 for the combined 2010–2011 observation seasons.

TABLE 5.2: Mean output parameters of the MCMC modelling for each combination of optical (ground (gr) and *Kepler* (kep)) and IR (*Spitzer* 1 (sp1) and *Spitzer* 2 (sp2)) light curves covering multiple observation seasons over different combination of observation seasons. The uncertainties here represent the 1σ standard deviations of the distributions for each parameter in each model.

Light Curve Combination	Seasons Starting	Radial Power Law Index	Vertical Scale Height Power Law Index	Amplitude Conversion Factor	Lag (days)	Inclination (degrees)	Offset ($\times 10^{-2}$)	χ^2_{opt}	χ^2_{IR}
whiteGr-Sp1	2010-2014	$-0.53^{+0.03}_{-0.25}$	$0.06^{+0.16}_{-0.01}$	$1.92^{+0.09}_{-0.04}$	$25.45^{+2.50}_{-2.35}$	$45.54^{+3.45}_{-6.50}$	$-0.91^{+1.50}_{-0.43}$	6.66	12.67
whiteKep-Sp1	2010-2012	$-0.52^{+0.02}_{-0.05}$	$0.43^{+0.18}_{-0.35}$	$2.64^{+0.05}_{-0.05}$	$20.42^{+3.34}_{-2.77}$	$44.42^{+9.71}_{-2.48}$	$4.50^{+0.44}_{-0.52}$	5.91	24.04
whiteGr-Sp1	2010-2011	$-0.52^{+0.01}_{-0.11}$	$0.16^{+0.48}_{-0.10}$	$2.66^{+0.16}_{-0.21}$	$8.02^{+2.16}_{-0.55}$	$49.71^{+13.81}_{-8.83}$	$-0.74^{+0.55}_{-0.40}$	7.87	7.66
whiteKep-Sp1	2010-2011	$-0.52^{+0.02}_{-0.05}$	$0.08^{+0.51}_{-0.02}$	$1.58^{+0.12}_{-0.10}$	$10.83^{+1.05}_{-1.38}$	$46.68^{+18.81}_{-11.28}$	$0.47^{+0.38}_{-0.38}$	3.87	7.84
whiteGr-Sp1	2012-2014	$-0.52^{+0.01}_{-0.03}$	$0.23^{+0.45}_{-0.18}$	$1.65^{+0.07}_{-0.06}$	$26.67^{+2.06}_{-1.71}$	$47.76^{+20.42}_{-6.76}$	$1.19^{+0.25}_{-0.23}$	5.99	8.74
whiteGr-Sp1	2013-2014	$-0.54^{+0.03}_{-0.29}$	$0.11^{+0.56}_{-0.05}$	$1.38^{+0.07}_{-0.06}$	$27.40^{+0.99}_{-3.87}$	$42.18^{+23.81}_{-3.30}$	$0.70^{+0.34}_{-0.43}$	2.49	5.62
whiteGr-Sp2	2013-2014	$-0.53^{+0.02}_{-0.51}$	$0.08^{+0.53}_{-0.02}$	$1.21^{+0.05}_{-0.04}$	$28.54^{+0.44}_{-5.66}$	$52.09^{+15.75}_{-7.70}$	$0.95^{+0.33}_{-0.22}$	5.19	5.20

thus, to exclude any effect from the dramatic increase in flux going forward, the entire light curves are instead separated into the 2010–2011 seasons and the 2012–2014 seasons when modelling light curves that cover multiple seasons. The simulated ground-*Spitzer* 1 and ground-*Spitzer* 2 light curves are displayed in Appendix B.

Table 5.2 contains the corresponding mean and 1σ uncertainties for each parameter in the MCMC modelling that describe the best-fit DTF in each combination of optical and IR light curves. It can be seen that the results for the radial power-law index and vertical scale height power-law index are consistent over the different combinations of light curves, as each model suggests a shallow radial power-law index with a mean of $\alpha = -0.52 \pm 0.01$ and a small vertical scale height power-law index with a mean of $\beta = 0.14 \pm 0.06$. The inclination angles are less well constrained in each model than the other parameters, demonstrating large 1σ uncertainties of $\sim$ 20 –30 degrees, but they return an overall mean of $i = 49.1 \pm 2.1$ degrees. Differences in the time lag can be seen depending on the seasons modelled, as the ground-*Spitzer* 1 and *Kepler*-*Spitzer* 1 light curves over the 2010–2011 seasons find lags of $\sim$ 10 days, while the ground-*Spitzer* 1 and ground-*Spitzer* 2 light curves over the 2012–2014 and 2013–2014 seasons (respectively) find longer time lags that tend toward the upper limit of the prior range, with values of $\tau \approx$ 25-30 days. This gives an overall mean value of $\tau = 18.5 \pm 9.2$ days, but could also imply that the delay between light curves is increasing with time.

5.4.3.2 Comparing with Models of the Individual Observation Seasons

In addition to modelling the entire observed light curves, I also modelled the individual observation seasons to see whether the best fit parameters remained consistent over time as the time lag increases when modelling the multi-season light curves using only the later seasons. These individual season models are displayed in Appendix B. The means of the output DTF parameters for these individual season models are compared with the output parameters from the simulated light curves covering multiple observational seasons in Figure 5.15, for the radial power-law index, vertical scale height power-law index, time lag, and inclination angle.

It can firstly be seen that modelling of the individual seasons is not able to constrain the parameters as well as the multi-season plots, specifically for the radial power-law index and the vertical scale height power-law index which often have uncertainties that cover nearly the entire prior range $-5.5 \leq \alpha \leq -0.5$ and $0.05 \leq \beta \leq 2.05$, respectively. This could be a result of the length of the observations, especially as some individual seasons only cover a range of $\sim$ 60 days, which might not be long enough to properly constrain the parameters of the DTFs. Despite the large range in uncertainties, the overall mean is found to be $\alpha = -0.80^{+0.28}_{0.66}$ and $\beta = 0.23^{+0.35}_{-0.14}$, consistent with the multi-season models.

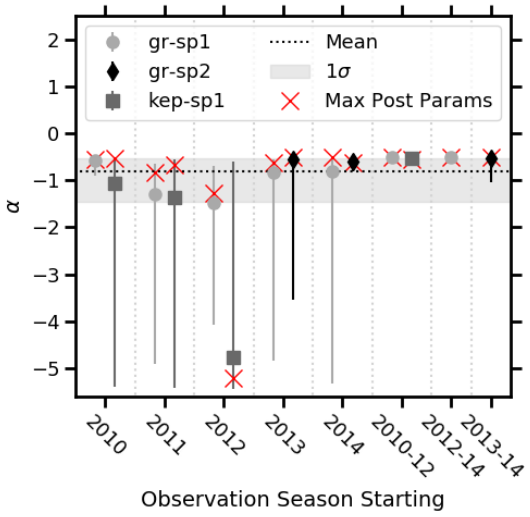

(A) Comparison between the mean output radial power-law indices.

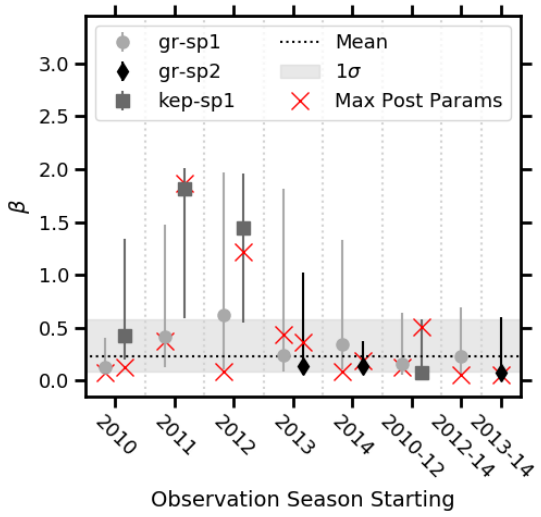

(B) Comparison between the mean output vertical scale height power-law indices.

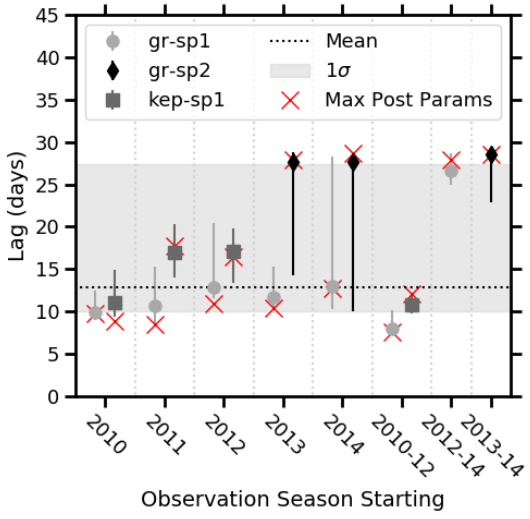

(C) Comparison between the mean time lags.

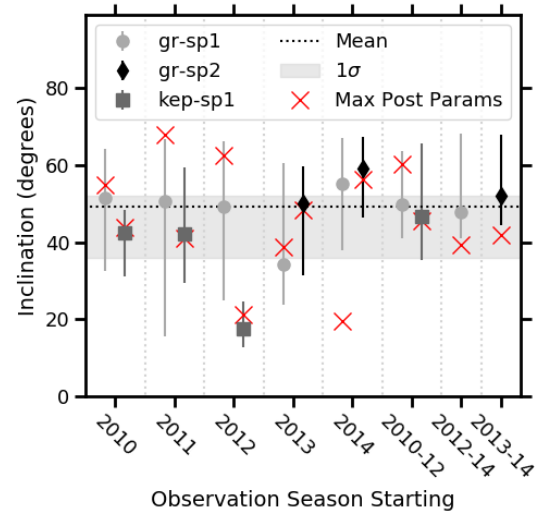

(D) Comparison between the mean output inclination angles.

FIGURE 5.15: Comparison between the mean output parameters of the MCMC modelling of each combination of optical and IR light curves, for the individual observation seasons and multiseason light curves. The values corresponding to the maximum posterior distribution are also plotted in red.

Similarly, in Figure 5.15d, the inclination angles found for the individual seasons often have a broad spread, with uncertainties covering $\sim$ 20–40 degrees, showing that they are not very well constrained. Most combinations of optical and IR light curve are shown to be consistent amongst themselves over the different observation seasons, and the overall mean inclination angle is found to be $i = 49.08^{+2.89}_{-13.17}$ degrees. However, some models deviate from this value; for example, the *Kepler-Spitzer* 1 light curves in the 2012 season find a value of $i \approx 20$ degrees, which again could be a result of the length of the individual seasons not being sufficient to properly constrain the parameters. It can also be seen that the value of the inclination angle that corresponds to the highest posterior distribution in the 2014 season of the ground-*Spitzer* 1 light curve is outside of the 1σ uncertainties, which could imply that for this season the MCMC modelling does not search the appropriate range of priors well.

Finally, in Figure 5.15c, the time lags are found to be better constrained in most of the individual observation seasons than the other parameters, especially in the earlier observation seasons. In all individual observation seasons these lags are found with values between $\sim$ 10 and 20 days for the ground-*Spitzer* 1 and *Kepler-Spitzer* 1 light curves, but the ground-*Spitzer* 2 light curves in the 2013 and 2014 seasons find a higher lag of $\sim$ 25–30 days, which could be influencing the larger lag found in ground-*Spitzer* 2 combined 2013–2014 light curves. However, the corresponding ground-*Spitzer* 1 light curves in the individual seasons all find a shorter lag with a value of 10–15 days, although the 2014 season lag has large uncertainties, while the ground-*Spitzer* 1 light curve over the combined 2012–2014 seasons finds the larger lag.

To further explore the larger uncertainties in the time lag in the later seasons, I plot the distributions of the time lag recovered in the each of MCMC models, for example Figure 5.16a contains the distribution of time lags found when modelling the 2014 ground-*Spitzer* 2 light curves. It can be seen that this actually returns a double-peaked distribution with peaks at $\sim$ 10 and 30 days. In Figures 5.16b and 5.16c I show the best fit models corresponding to the individual peak lags, and it can be seen that the model for the $\sim$ 10 day lag better replicates the shape of the variability of the IR observations, specifically the small peak at MHJD $\sim$ 56875 and the dip at MHJD $\sim$ 56950, but the larger lag has a lower reduced χ^2 value.

If the increase in time delay is then not a result of the variability in the individual seasons, the difference between the individual and multiple season models could alternatively still be impacted by modelling their long-term variability and the months-long gaps between observations. The overall mean time lag is found with a value of $\tau = 12.89^{+14.54}_{-2.83}$ days, or for each combination of optical and IR light curve, the means have values of $11.19^{+1.73}_{-2.97}$ days, $11.04^{+5.99}_{-0.29}$ days, and $27.66^{+0.47}_{-0.04}$ days for the ground-*Spitzer* 1, *Kepler-Spitzer* 1, and ground-*Spitzer* 2 light curves, respectively.

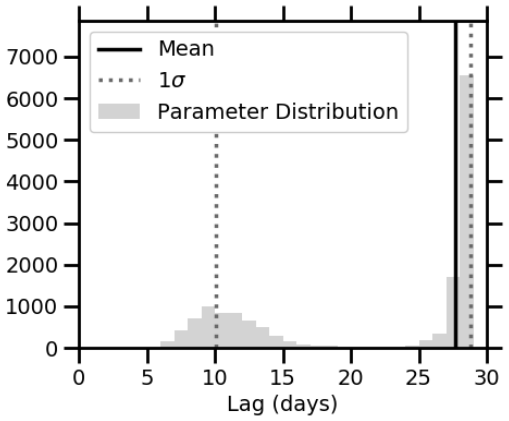

(A) Distribution of the lag found modelling the ground-Spitzer 2 light curve in the season starting 2014.

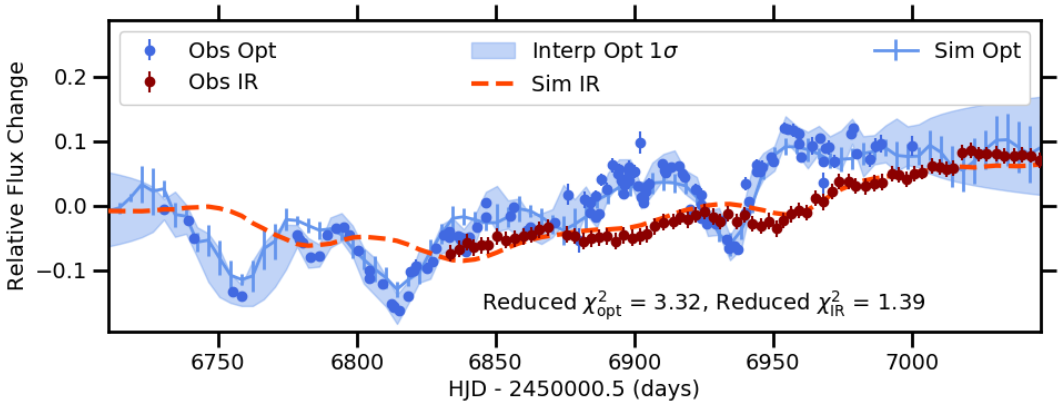

(B) Simulated light curves for ground-Spitzer 2 in the 2014 season, plotted with $\alpha = -0.59$, $\beta = 0.17$, $\tau = 11.28$ days, $i = 64.90$ degrees.

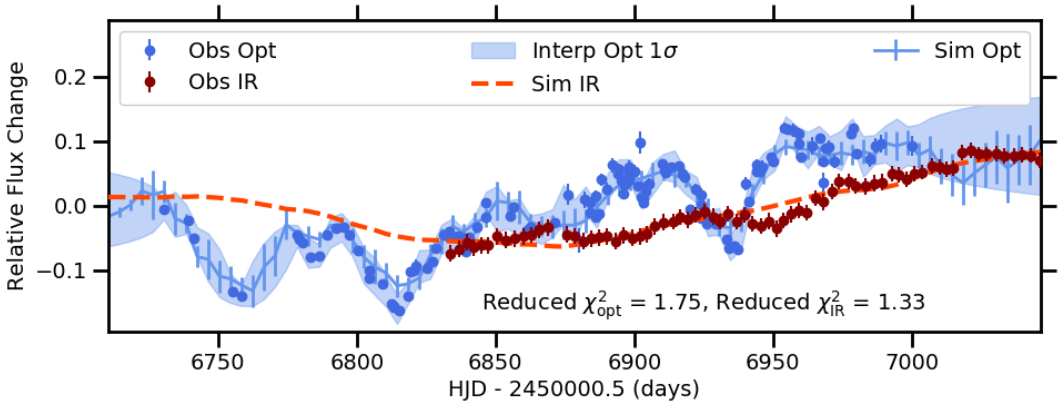

(C) Simulated light curves for ground-Spitzer 2 in the 2014 season, plotted with $\alpha = -0.62$, $\beta = 0.19$, $\tau = 28.73$ days, $i = 56.22$ degrees.

FIGURE 5.16: The distribution of time lags found modelling the ground-Spitzer 2 light curve in the 2014 seasons, and the models corresponding to each of the peaks found in the distribution.

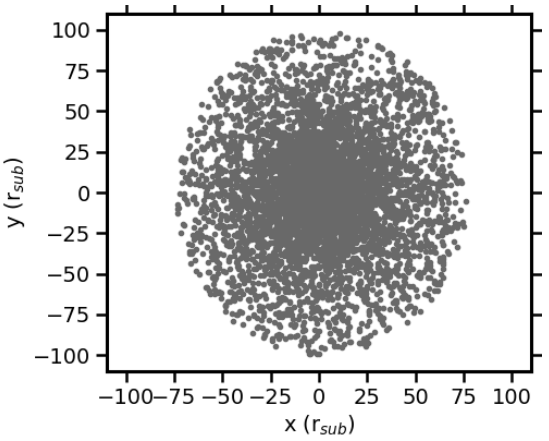

(A) Distribution of dust clouds in xy.

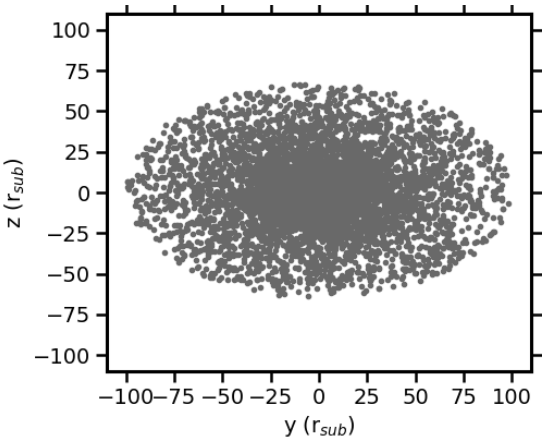

(B) Distribution of dust clouds in yz.

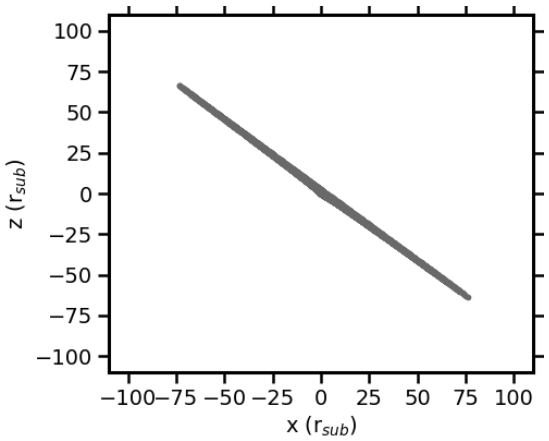

(C) Distribution of dust clouds in xz.

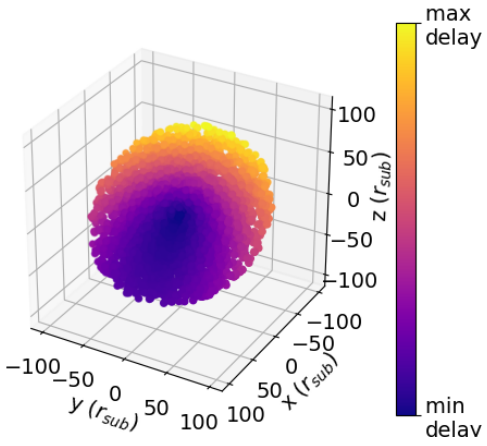

(D) Delay map for the distribution of dust clouds.

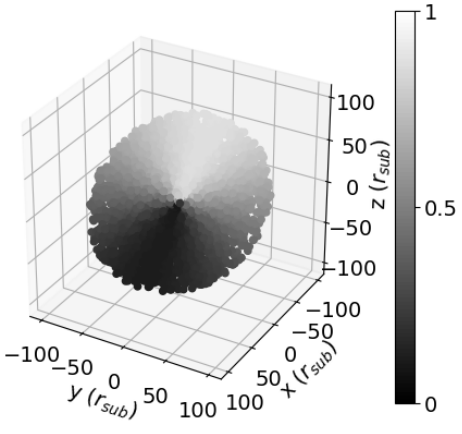

(E) Illumination map for the distribution of dust clouds.

FIGURE 5.17: Distribution of 10,000 dust clouds corresponding to the mean parameters from the MCMC modelling of the Zw229-015 light curves, and the corresponding delay and illumination maps.

Using the mean radial power-law index, vertical scale height power-law index, and inclination angle from modelling the light curves of Zw229-015, I plotted the distribution of dust clouds and the associated delay and illumination maps in Figure 5.17.

5.5 Discussion

In the previous sections, I studied optical and IR light curves of Zw229-015 to further understand the inner regions of the AGN that are not spatially resolved.

5.5.1 Dust Reverberation Mapping

The optical ground based and *Kepler* light curves were cross correlated with the IR *Spitzer* channel 1 (3.6μm) and 2 (4.5μm) light curves to determine the possible lags between them, and their corresponding dust reverberation radii. The most consistent observed lag was detected between 5 and 30 days in 70 % of the CCFs, with an overall mean of $\tau_{obs} = 18.8 \pm 4.6$ days, which corresponds to a radius of 0.016 ± 0.004 pc (or in the rest frame of Zw229-015, τ_{rest} = 18.3 ± 4.5 days, which corresponds to a radius of 0.015 ± 0.004 pc).

Additional less consistent lags were also detected in multiple seasons in the different combinations of optical - IR light curves, including a lag between 55 and 80 days, however a peak in the corresponding optical ACF in these seasons was detected at $\sim$ 60 days, implying the lag is not between optical and IR light curves but is a result of aliasing in the light curves. This peak in the optical ACFs was further investigated as a possible periodicity in Section 5.3.3, however it was found to be a result of the overlapping light curve regions used for cross correlation as the entire *Kepler* light curves for each season did not display this peak, nor did the 2013 ground light curve or the overall ground and *Kepler* light curves.

The *Spitzer* channel 1 and 2 light curves were also cross correlated with each other to look for possible lags between the emission from different IR wavelength ranges. The most consistent lag which was detected in all CCFs was found between 0-5 days, with a mean of $\tau_{obs} = 1.8 \pm 1.7$ days (= τ_{rest}). This $\sim$ 0 lag implies that the 3.6μm and 4.5μm emission is dominated by emission from the same dust component. This delay was further investigated in the ground-*Spitzer* 1 and ground-*Spitzer* 2 CCFs. In the 2013 season, a lag was only detected in the RM-ICCF method of ground-*Spitzer* 2, but comparing this with the ground - *Spitzer* 1 shows that the 4.5μm lag it is longer by $\sim$ 13 days, however this could be due to the broadness of the CCFs and the corresponding ACFs. Furthermore, comparing the lags detected in the 2014 season of

the ground - *Spitzer* 1 and ground - *Spitzer* 2 CCFs shows that they are consistent with each other in the individual methods within 1σ.

5.5.1.1 IR wavelength dependence on dust lags

The mean observed lag is found to be consistent between each combination of optical and IR light curve, and also with the rest frame delay of $20.36^{+5.82}_{-5.68}$ days measured between the *V*and *Ks* bands using observations from 2017-2018 by Mandal et al. (2021).

Lyu et al. (2019) found the radius of dust reverberation mapping with longer IR wavelengths to be larger than those of smaller IR wavelengths, as they found a ratio between the *K* (2.2 μm), W1 (3.4 μm), and W2 (4.5 μm) dust reverberation radii of $R_K : R_{W1} : R_{W2} = 0.6 : 1.0 : 1.2$ for multiple quasars. The results in this chapter show that Zw229-015 behaves anomalously to the behaviour reported in Lyu et al. (2019) however, as the lags between the optical and 3.6 μm, and the optical and 4.5 μm are shown to be consistent within the 1σ uncertainties of the rest-frame dust reverberation lag measured between the V and K_s bands using observations from 2017–2018 by Mandal et al. (2021). If we assume the *V*and *Ks* band reverberation lag remained approximately consistent between 2010-2018, the similarities between the *Ks* band (2.15μm), 3.6 μm and 4.5 μm reverberation lags indicates that in Zw229-015 they are all tracing the same regions, which corresponds to the hottest dust at the inner radius. Hönig and Kishimoto (2011) explain that the NIR emission (i.e., the *Ks* band) predominantly originates in the peak of the blackbody emission of the hot dust in the inner region, while the predominant source of MIR emission (i.e., the 3.6 and 4.5 μm bands) can either be from the peak of the blackbody emission of cooler dust at larger distances from the central engine than the hot dust, or from the Rayleigh-Jeans tail of the hot dust emission. If the object is compact, and the brightness distributions are therefore steep, the Rayleigh-Jeans tail of the hot dust emission can dominate the MIR because of the lack of extended dust. This therefore suggests that in the previous MIR reverberation studies that found a larger lag between the optical and MIR than the optical and NIR (e.g. Lyu et al. 2019), that the MIR emission is originating in the peak of the blackbody emission of the cooler dust, whereas for Zw229-015, where the lag between the optical and MIR is consistent with the lag between the optical and NIR, the 3.6 and 4.5 μm emission is dominated by the Rayleigh-Jeans tail of the hottest dust.

5.5.1.2 Comparison with BLR lags

The dust reverberation lag measured in this paper is found to be a factor of ~ 4.7 larger than the BLR reverberation lag measured by Barth et al. (2011), which is consistent with the results found by Koshida et al. (2014), in which the reverberation radius of broad emission lines is a factor of 4-5 smaller than dust reverberation radii.

Czerny and Hryniewicz (2011) proposed that some broad emission lines are formed in a failed radiatively accelerated dusty outflow (FRADO), and therefore predict the existence of a significant amount of dust within the BLR. This could be tested with the high quality optical and IR data used in this paper, which allows for the detection of lags between light curves on timescales as short as ~ 3 days, which is in line with the BLR lag measured by Barth et al. (2011). As a lag on such timescales is not measured in the high cadenced CCFs, it suggests the presence of a significant amount of dust in the BLR is unlikely.

5.5.1.3 Reverberation Lag-Luminosity Relations

Both the dust reverberation radii and BLR reverberation radii are expected to correlate with the optical luminosity of the AGN, with an approximate relationship of $r \propto L^{0.5}$. For example, Bentz et al. (2013) found the Hβ BLR radius-luminosity relation to be $R_{\rm BLR} \propto L^{0.533^{+0.035}_{-0.033}}$. Minezaki et al. (2019) fit the luminosity-dust radius relationship of dust reverberation mapped AGN, both forcing a fixed slope of 0.5 and allowing the slope to vary which resulted in a best fit to the data of $R_{\rm dust} \propto L^{0.424\pm0.026}$. Similarly, Gravity Collaboration et al. (2020) estimated the hot dust radius vs. bolometric luminosity relation using NIR interferometric measurements, and found a best fit with a flatter slope of $R_{\rm dust,int} \propto L_{\rm bol}^{0.40\pm0.04}$. It is currently unclear whether the deviations of the slope from the relationship of $r \propto L^{0.5}$ is an intrinsic effect however: Selection biases could affect the results as the brightest and most suitably variable objects are typically chosen as targets for both reverberation mapping and interferometric analysis. As it is easier to measure shorter lags in brighter objects, this could therefore lead to a biased selection on the short-lag side from the intrinsic dispersion in the correlation and, hence, flatten the observed slope. On the other hand, AGN with lower continuum luminosities are likely to contain stronger broad and narrow emission lines compared to the continuum brightness (the Baldwin effect; Baldwin et al., 1989). This could therefore mean that the continuum luminosities inferred from broad-band imaging filters for these lower luminosity objects are greater compared those predicted for the measured radii due to the extra line contributions compared to higher luminosity sources, potentially leading to a steeper relationship between luminosity and radius.

Examples of the observed radius-luminosity relationships are shown in Figure 5.18a for the $R_{\rm dust}$ vs. the V-band luminosity using the DRM lag estimated for Zw229-015 in this paper and for other AGN taken from the literature (e.g., Koshida et al., 2014; Minezaki et al., 2019). Figure 5.18b is the equivalent plot for the $R_{\rm BLR}$ vs. optical 5100 Å luminosity (Barth et al., 2011; Bentz et al., 2013). Comparing the distribution of AGN luminosities in Figures 5.18a and 5.18b, it can be seen that fewer dust lags of AGN with lower luminosity have been recorded, which suggests that the flatter slope

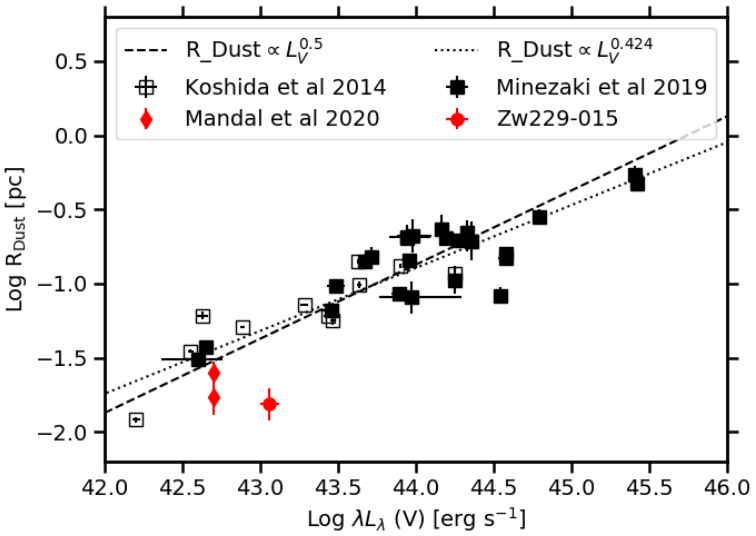

(A) Plot of the radius of the dust emitting region against *V*band luminosity for AGN from literature in the black squares (Koshida et al., 2014; Minezaki et al., 2019) and for Zw229-015 using the DRM result from this paper and from Mandal et al. (2021) in red.

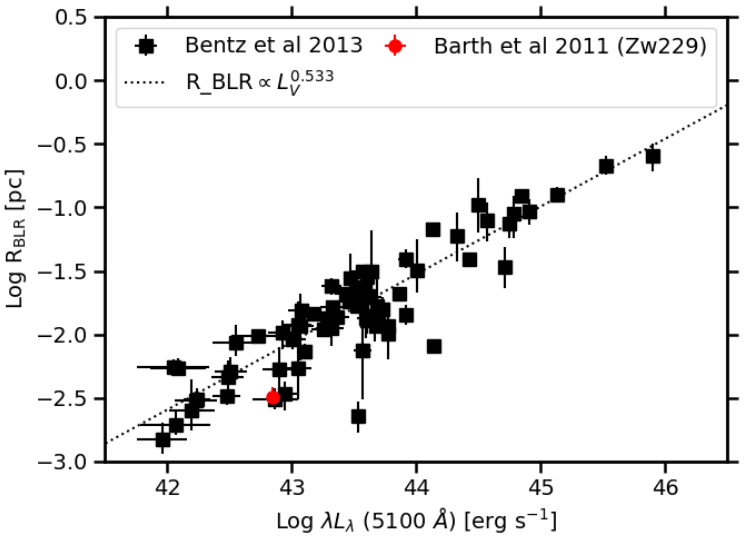

(B) Plot of the radius of the BLR against 5100Åluminosity for AGN from Bentz et al. (2013) in the black squares and for Zw229-015 using the BLR-RM result from Barth et al. (2011) in red.

FIGURE 5.18: Radius-Luminosity relations using AGN from literature compared to Zw229-015.

of this plot could be biased by selection effects from selecting mostly brighter AGN at the lower luminosity end that are easier to observe due to higher S/N and better contrast against the host galaxy.

There is some intrinsic dispersion shown about the best fit trends in both Figure 5.18a and 5.18b. Several factors have been considered to explain the dispersion in the distributions. Firstly, the accretion rate of the AGN affects the slope of the $R_{\rm BLR}$–L relationship. Du et al. (2016) showed that AGN higher accretion rates have been linked to shorter Hβ lags, which is theorised to be a result of self shadowing effects of slim ADs (Li et al., 2010). The self-shadowing region suppresses the ionizing flux seen by the BLR clouds (Wang et al., 2014), thereby reducing the ionisation parameter at a given distance compared to a normal accretion flow. This leads to a shorter time lag than implied by the luminosity based on the standard relation. Such self-shadowing is not restricted to the BLR, but would also affect dust temperature and, hence, reduce the sublimation radius. As a consequence, a high accretion rate AGN would have a shorter dust time lag. Secondly, the intrinsic scatter of the $R_{\rm dust}$–L relation could be due to the distribution of the dust, and whether it is illuminated isotropically or anisotropically by the central AGN (Kawaguchi and Mori, 2010, 2011; Almeyda et al., 2017, 2020). Kawaguchi and Mori (2010) show that for an AD emitting less radiation in the equatorial plane than towards the poles, the dust sublimation radius would be closer to the central black hole than if the emission was isotropic. Therefore, for AGN observed along angles closer to the pole, a higher luminosity would be inferred and the measured radius would be smaller compared to predictions using the this luminosity. Furthermore, most of the lags in Figure 5.18a are measured using a constant spectral index to correct the NIR fluxes for contributions from the AD, though AGN often demonstrate spectral variability as the flux variations are not necessarily consistent across different wavelength ranges (e.g., Kishimoto et al., 2008). Mandal et al. (2021) therefore suggest that use of constant spectral index could affect the estimated lags. In their analysis with a constant spectral index, their estimated lag is found to lie closer to the predicted relation as shown in Figure 5.18a. Alternatively, a significant increase in brightness of the AGN is expected to result in a change in the dust sublimation radius as the dust in the innermost region is destroyed; however, the changing sublimation radius is found to follow the brightening with a delay of a few years. For example, Kishimoto et al. (2013) found that the radius at a given time was correlated not with the instantaneous flux but with the long-term average flux of the AGN in the previous ~ 6 yr.

The results for Zw229-015, both from this chapter and from literature, were compared to the $R_{\rm dust}$–L and $R_{\rm BLR}$–L relations. To put the dust lag measurements from this chapter into context, I calculate a predicted lag using the correlation found by Minezaki et al. (2019). I determine a mean luminosity of Zw229-015 using the Galactic extinction-corrected ground-based V-band light curves. The predicted time lag was

found to be ~ 60 days, which is a factor of ~ 3 larger than the results measured in this paper. Using the theoretical $L^{0.5}$ relation leads to a similar offset. This deviation from the predictions of both the $R_{\rm dust} \propto L^{0.5}$ and $R_{\rm dust} \propto L^{0.424}$ relations can be seen in Figure 5.18a, in which $R_{\rm dust}$ is plotted against the V-band luminosity using the DRM lag estimated for Zw229-015 in this paper and for other AGN taken from the literature (e.g., Koshida et al., 2014; Minezaki et al., 2019). Furthermore, the observed IR lag-luminosity relation of Zw229-015 from Mandal et al. (2021) is also plotted, using both a varying index of the power law for each epoch to estimate the contribution of emission from the AD to the IR light curve, and using a fixed power-law index. Note that the luminosity of Zw229-015 in Mandal et al. (2021) was calculated from a modelled host-galaxy-flux-subtracted light curve, whereas the data point from this chapter is still expected to have contributions from the host-galaxy flux. Additionally, the predicted BLR time-delay estimated using the relation from Bentz et al. (2013) for the optical 5100 Å luminosity of Zw229-015 is found to be ~ 9 days, which is a factor of ~ 2.5 larger than the delay measured by Barth et al. (2011). Figure 5.18b shows that the measured BLR radius of Zw229-015 is below the $R_{\rm BLR} \propto L^{0.533}$ relation found by Bentz et al. (2013); however, other objects are also shown to have a similar offsets from this relation, which has been suspected to be Eddington ratio dependent (e.g. Du et al., 2016).

Both Figure 5.18a and 5.18b show that the Zw229-015 BLR and dust lags are consistently shorter than predicted by the canonical lag-luminosity relations. As previously mentioned, a recent change in intrinsic luminosity could cause this deviation if the sublimation radius did not adjust to this change yet. For that, I compare the fluxes used in this paper with photometric monitoring taken at earlier epochs. Zw229-015 was observed with the Catalina Real-time Transient Survey between 2005 and 2010 (e.g., Drake et al., 2009) with the observed V band photometry given in Appendix B. The observed magnitudes did not change substantially over the 5 years prior to the data used in this paper. Using the observationally inferred typical delay time for structural changes (Kishimoto et al., 2013), I conclude that a substantial increase in brightness is not responsible for the short time lags measured. Two further potential reasons for a deviation from the relation I introduce above are Eddington ratio or anisotropy. Zw229-015 has been previously estimated to have a relatively low accretion rate (Smith et al., 2018a) and an inclination angle of $i = 36.4^{+6.7}_{-6.4}$ degrees (Raimundo et al., 2020). This inclination is quite typical for type 1 AGN and Du et al. (2016) associate offsets from the BLR lag-luminosity relation to high accretion rates, not low ones. This implies that Zw229-015 is a very typical Seyfert 1 AGN. This leaves the possibility that the current sample of AGN on the lower luminosity end of the correlation may be biased towards objects with longer lags from the intrinsic dispersion of lags.

5.5.2 Light Curve Modelling

I simulated the response of the IR dust emission to the optical variability and compared it to observations for each combination of optical and IR light curve of Zw229-015 in an attempt to further constrain the properties of the inner regions of the AGN, including the distribution of dust, time lag between light curves and inclination angle. MCMC modelling was used to sample the best fit dust transfer functions (DTFs) that, when convolved with a driving optical light curve, replicated the variability of the IR emission well.

This modelling was initially performed on the entire overlapping light curves, however Figure 5.13a demonstrates that the increase in flux between the 2011 and 2012 seasons in the IR is not well replicated when modelling to fit the shape of the individual seasons in the light curves using a single dust component. The underestimation of the IR flux in the 2012 season could therefore imply that a secondary dust component is contributing to the overall emission, which has previously been seen in other AGN, for example, Gravity Collaboration et al. (2021) show that $\sim$ 5% of the total flux of NGC 3783 in the K-band is located 0.6pc away in projected distance from the central hot dust component. This offset dust cloud of NGC 3783 is explored as either a secondary SMBH or an additional cloud of dust and gas that is heated by the central engine, though the authors favour the latter interpretation.

To therefore lessen the impact of the dramatic increase in flux on the results, I instead performed the modelling on the different combinations of optical and IR light curves in the 2010-2011 seasons and the 2012-2014 seasons separately. Furthermore, to examine whether the parameters corresponding to the best fit DTFs were consistent over time, I also modelled the individual observation seasons. It was found that the parameters were less well constrained for the individual seasons compared to the multi-season plots, which could be due to the length of the observations of individual season light curves, but for the most part the results were consistent with the multi-season models.

The radial power law index was consistently found to be shallow in all of the models except the *Kepler-Spitzer* 1 2012 season, and had a mean value of -0.80$^{+0.28}_{-0.66}$, which implies the dust distribution is extended. This result contradicts the results from dust reverberation mapping which suggested that the dust should be compact as the MIR and NIR lag the optical with similar delays, implying that they are tracing the same hot dust region. An additional contribution to the total IR emission from another dust component located further away from the central source could explain this, as the modelling could be influenced by the extended nature of the second component and therefore find the overall dust distribution to be extended. For example, multiple dust components were found by Lyu and Rieke (2021), who analysed dust reverberation signals over a wavelength range of 1-40μm for NGC 4151, and detected lags

corresponding to the sublimation radii of carbon and silicate dust, as well as a lag for cooler dust located further from the central source.

A low value was consistently found for the vertical scale height power law index in a majority of models, with a mean value of $\beta = 0.23^{+0.35}_{-0.14}$, which indicates the dust is distributed in a relatively flat disk. García-Burillo et al. (2021) showed that AGN with low Eddington ratios and/or luminosities are dominated by the disk and thought to display little to no polar dust emission as the radiative pressures are not enough to drive winds, which is observationally confirmed by Alonso-Herrero et al. (2021). Zw229-015 has an Eddington ratio of 0.125 and a bolometric luminosity of $\sim 10^{44}$ erg s^{-1} (Smith et al., 2018a), which is therefore consistent with a small vertical scale height power law index obtained from the modelling.

The time delay that corresponds to the light travel time between the source of the optical and IR dust emission was consistently measured for a majority of models with values between $\sim 10 - 20$ days, and the overall mean time lag was found to be $12.89^{+14.54}_{-2.83}$ days, which is consistent with the result found with the DRM in Section 5.3. However, it was also found that all of the simulated ground-*Spitzer* 2 light curves and the ground-*Spitzer* 1 light curve that covered a combination of observation seasons between 2012-2014 detected larger time lags with values approaching the upper limit of the prior range of ~ 25 days. The larger lags in the ground-*Spitzer* 2 models could imply that the lag is different for the 3.6μm and 4.5μm light curves, however, for the individual seasons the uncertainties cover a broad range of lags. These large uncertainties were explored and were shown to be due to a double peaked distribution, with peaks at ~ 10 and 30 days. A similar double peaked distribution of lags is also found in the ground-*Spitzer* 1 light curve in the 2013 season, however the ~ 10 day peak is stronger for this model. In Figure 5.16, both best fit models corresponding to each of the peaks in the lag distribution of the ground-*Spitzer* 2 2014 season are plotted, and it is shown that the model corresponding to the ~ 10 day lag follows the shape of the variability of the IR observations better, though the reduced χ^2 are smaller for the ~ 30 day lag model. The larger lag found in some of the individual season models, especially in the ground-*Spitzer* 2 but also in the 2013 ground-*Spitzer* 1 light curve, could therefore influence the larger lag found in the multi-season models between 2012–2014. Additionally, the modelling over these seasons could still be impacted by the long-term variability, or as a result of the large gaps between observations.

Finally, the mean inclination angle found by modelling the light curves was $49.08^{+2.89}_{-13.17}$ degrees which is consistent with the inclination angle measured by Raimundo et al. (2020) of $i = 36.4^{+6.7}_{-6.4}$ degrees within 1σ.

5.6 Chapter Summary

In this chapter I studied the optical and IR variability of Zw229-015, a Seyfert 1 galaxy at $z = 0.028$, using observations from optical ground-based telescopes and the *Kepler* space telescope, and concurrent IR observations from the *Spitzer Space Telescope* in 3.6 μm and 4.5 μm. The results are summarised below.

1. I used multiple methods of cross correlation to measure dust reverberation lags, and found a mean rest frame lag of 18.3 ± 4.5 days for all combinations of optical and IR light curves, over the entire observation periods and the individual observation seasons.

2. No obvious difference was found between the DRM lags recovered using the *Spitzer* 1 (3.6 μm) or *Spitzer* 2 (4.5 μm) light curves, and furthermore, these lags were consistent with the result found between the *V*and *Ks* bands measured by Mandal et al. (2021), which implies that the different IR wavelength ranges are dominated by dust within the same emission regions.

3. Measured lags of Zw229-015 are consistently smaller than predictions from the lag-luminosity relations, for both IR dust lags and the BLR lag from Barth et al. (2011). I argue that this is not because of Zw229-015 being unusual, but speculate that the current reverberation mapped sample on the low luminosity end may be biased towards objects with longer lags, hence artificially flatting the dust lag-luminosity relation.

4. By simulating the distribution of dust, I explored the response of the IR dust emission to the optical variability using MCMC modelling to further constrain parameters of the inner regions of the AGN that are not directly observable.

5. A dramatic increase in flux between the 2011-2012 observation seasons, which is more extreme in the IR light curve than the optical, was shown to not be modelled well by a single dust component, which could therefore imply multiple dust components are contributing to the overall emission.

6. The MCMC modelling consistently found that the dust was distributed with a shallow radial power law index and a relatively small vertical scale height power law index which implies an extended, flat dust distribution.

7. The modelling also estimated a mean inclination angle of $49.08^{+2.89}_{-13.17}$ degrees, which is consistent with the inclination angle found by Raimundo et al. (2020) within 1σ uncertainties, and also detected a mean projected time lag of $12.89^{+14.54}_{-2.83}$ days, which is consistent with the result found for the DRM.

Chapter 6

Simulations of Optical AGN Variability Analysis with LSST

In Chapter 1, I explained that variability is a ubiquitous property of the emission of AGN, and is observed over the entire electromagnetic spectrum, with timescales ranging from minutes to years (e.g., Ulrich et al., 1997). In the previous two chapters, I performed detailed analysis of the variability of the individual AGN; PKS 0027-426 and Zw229-015. While studying individual objects is useful for expanding our knowledge, constraining properties of a large sample is also necessary for understanding the behaviours of AGN as a whole. With the current proposed observation strategy, it is predicted that LSST will provide hundreds of observations for up to 10 million quasars with redshifts up to 7 (LSST Science Collaboration et al., 2009). This therefore has the potential of allowing variability analysis of AGN in the optical to be expanded significantly, though limitations will arise due to the schedule of observations.

One tool that is commonly used to study the variability of AGN is the PSD which describes the amount of variability power observed over different timescales. This therefore makes PSDs a useful probe of the emission processes in regions that are unresolvable. As such, this chapter will explore the extent to which PSD analysis in the optical could be possible using LSST cadenced light curves.

The structure of this chapter is as follows; in Section 6.1 I will introduce the need for large scale variability analysis of AGN light curves in understanding physical processes and dynamics occurring within unresolvable regions of the AGN. In Section 6.2 I will describe the simulation of mock AGN light curves that will be used within this chapter. The methods, results and implications of these results for recovering properties of input PSDs will be described in Sections 6.3, 6.4, and 6.5, for the DRW model, varying power laws, and including quasi-periodicities respectively. Finally, in Section 6.6 I will summarise the conclusions of this chapter.

6.1 Introduction

The AD surrounding the SMBH is widely accepted to be responsible for the majority of thermal emission observed in AGN, however our understanding of the AD itself is still limited. The variable nature of the emission observed, which is mostly stochastic and aperiodic, should provide indirect information into the dynamics and processes occurring within such unresolvable components of AGN. For example, comparing the timescales over which the optical emission varies to the different physical timescales described in Chapter 1 would allow insight into the physical mechanisms driving the AD variability.

Kelly et al. (2009) attempted to describe the optical variability of AGN light curves by modelling stochastic turbulent processes in a DRW model. This model corresponds to PSD slopes of $\alpha = 2$ and depends on two parameters; the characteristic timescale, $\tau_{\rm DRW}$, after which the flux variations become uncorrelated, and the variability, $\hat{\sigma}_{\rm DRW}$, of the time series on timescales smaller than $\tau_{\rm DRW}$. In their analysis, Kelly et al. (2009) further describe that the characteristic timescales were consistent with dynamical or thermal timescales. Several authors reported that this DRW model fit observed AGN light curves well (e.g. Kozłowski et al., 2010; MacLeod et al., 2010; Zu et al., 2013) and furthermore found correlations between the parameters $\tau_{\rm DRW}$ and $\hat{\sigma}_{\rm DRW}$ and physical properties of the AGN including black hole mass and luminosity (e.g., Kelly et al., 2009; Kozłowski et al., 2010; MacLeod et al., 2010). However, deviations from this DRW model have been found in many observed optical PSDs of AGN. For example, the *Kepler* AGN are found to be best fit with single power laws that have a range of slopes which are often much steeper than $\alpha = 2$ (e.g. Mushotzky et al., 2011; Kasliwal et al., 2015; Caplar et al., 2017; Smith et al., 2018a). Furthermore, some quasars have PSDs that are best fit using broken power laws with characteristic break timescales (e.g. Edelson et al., 2014; Simm et al., 2016; Smith et al., 2018a). Larger samples of AGN light curves are therefore necessary to further constrain the shapes of the PSDs and in turn, attempt to explain the physical processes responsible for the observations.

Additionally, while most quasar light curves are characterized by their stochastic variability, some have been flagged as having potential quasi-periodicity within them. The first short timescale quasi-periodic oscillations (e.g. on the order of $\sim$ minutes to days) in AGN was discovered by Gierliński et al. (2008), who reported a $\sim$ 1 hour X-ray quasi-periodicity in the AGN REJ1034+396 (later confirmed by Alston et al. 2014). This quasi-periodicity is believed to be analogous to the QPOs commonly seen in the X-ray power spectra of stellar mass black hole candidates in X-ray binaries (Middleton and Done, 2010), which are thought to occur close to the black hole, and can provide possible insights into behaviour within the AD. Since the QPO discovery of REJ1034+396, there have been several other reports of potential short timescale QPOs detected in the X-ray emission of other AGN (e.g. Alston et al., 2015; Zhang

et al., 2017, 2018; Ashton and Middleton, 2021). Furthermore, Smith et al. (2018b) report evidence for a potential QPO in the *Kepler* optical light curve of KIC 9650712 corresponding to a quasi-period of ~ 44 days. A linear correlation between the mass of the black hole and frequency of the QPO has been found to extend from stellar mass black holes to SMBHs (e.g. Abramowicz et al., 2004; Zhou et al., 2015), which could be significant as it could imply a link between the accretion processes over large scales. This correlation could potentially be used to estimate the mass of black holes.

Possible longer timescale ($\sim$ months - years) quasi-periodicities have also been detected in AGN, which are often considered to be the result of a SMBHB system with sub-parsec separation. Detections of potential SMBHB candidates have been reported in both radio-loud (e.g. Liu et al., 2015; Bhatta et al., 2016) and radio-quiet AGN (e.g. Zheng et al., 2016), with the best-known candidate being the blazar OJ 287 (e.g., Sillanpaa et al., 1988; Valtonen et al., 1988; Dey et al., 2019) which is associated with 2 quasi-periodicities at ~ 12 and ~ 60 years.

Detecting potential quasi-periodic oscillations in AGN light curves can be difficult however, as red-noise processes can mimic quasi-periodic behaviour (Vaughan et al., 2016). Furthermore, limitations arise due to the the lack of observations of AGN over timescales long enough to detect these quasi-periodicities, and in fact, many of the reported quasi-periodicities are based on very few observation cycles of the periods.

Upcoming large-scale photometric surveys will therefore be vital in providing large enough samples of AGN to allow more in depth studies into the variability, and thereby allowing indirect analysis of the processes and dynamics occurring within the unresolvable inner regions. In particular, LSST is expected to provide hundreds of observations for up to 10 million quasars with redshifts up to 7 (LSST Science Collaboration et al., 2009). Previous studies such as Witt et al. (2021) have explored recoverability of underlying PSDs in LSST-like light curves and potential quasi-periodicity detections, but limitations arise due to the assumptions and differences in methodology. These limitations, which will be discussed later in this chapter, leave this an area of interest still.

6.2 Simulating AGN Light Curves

6.2.1 Creating a Mock AGN Sample

For the following analysis, a realistic mock sample of AGN was needed. I estimated the number, luminosity and redshift distributions of all unobscured AGN within a 10 square degree area (to replicate the field of view of LSST) up to a redshift of 5, using codes by Shankar (2022) that utilised the optical quasar luminosity functions from Palanque-Delabrouille et al. (2013) and Ross et al. (2013).

The quasar luminosity function, $\Phi(L, z)$, measures the comoving number density of quasars as a function of luminosity and redshift. It is typically modelled by a double power law, either in terms of luminosity, or magnitude as shown in Equation 6.1 (e.g. Boyle et al., 2000).

$$\Phi(M_g, z) = \frac{\Phi^*}{10^{0.4(\gamma_1+1)(M_g - M_g^*(z))} + 10^{0.4(\gamma_2+1)(M_g - M_g^*(z))}} \tag{6.1}$$

where Φ^* is the comoving density normalization, $M_g^*(z)$ is the break luminosity, γ_1 and γ_2 are the faint-end and bright-end slopes respectively.

The AGN in this sample were then assigned a black hole mass using the luminosity, Eddington luminosity, and Eddington ratio, as shown in Equations 6.2 (Woo and Urry, 2002) and 6.3 (Shankar et al., 2009).

$$L_{\rm Edd} = 1.26 \times 10^{38} \frac{M_{\rm BH}}{M_\odot} \tag{6.2}$$

$$\lambda_{\rm Edd} = \frac{L}{L_{\rm Edd}} = \dot{m} f_{0.1} \tag{6.3}$$

where $\dot{m}$ is the mass Eddington ratio given in Equation 6.4, and $f_{0.1}$ is the radiative efficiency.

$$\dot{m} = 0.445 \times \left(\frac{M_{\rm BH}}{10^9 M_\odot} \right)^{0.5} \tag{6.4}$$

The initial sample contained 7730 AGN, with luminosity, redshift, magnitude and black hole mass distributions shown in Figure 6.1.

6.2.2 Simulating AGN Light Curves with LSST cadencing

I used the Timmer and Koenig (1995) algorithm described in Chapter 3 to generate artificial AGN light curves with 1 day cadencing using simulated PSDs that will be described in each of the following sections. Specifically, I used the IDL function timmerlc[1] to simulate the light curves, which takes the PSD as an input. This function additionally had inputs of the mean magnitude of each light curve, which was given as the magnitude assigned to each mock AGN as described previously, and the standard deviation of the light curve.

To simulate realistic AGN light curves, I chose to create them with initial lengths of $\sim$ 4000 days to account for the effects of red-noise leakage that occurs as, for steep

[1] http://astro.uni-tuebingen.de/software/idl/aitlib/timing/timmerlc.pro

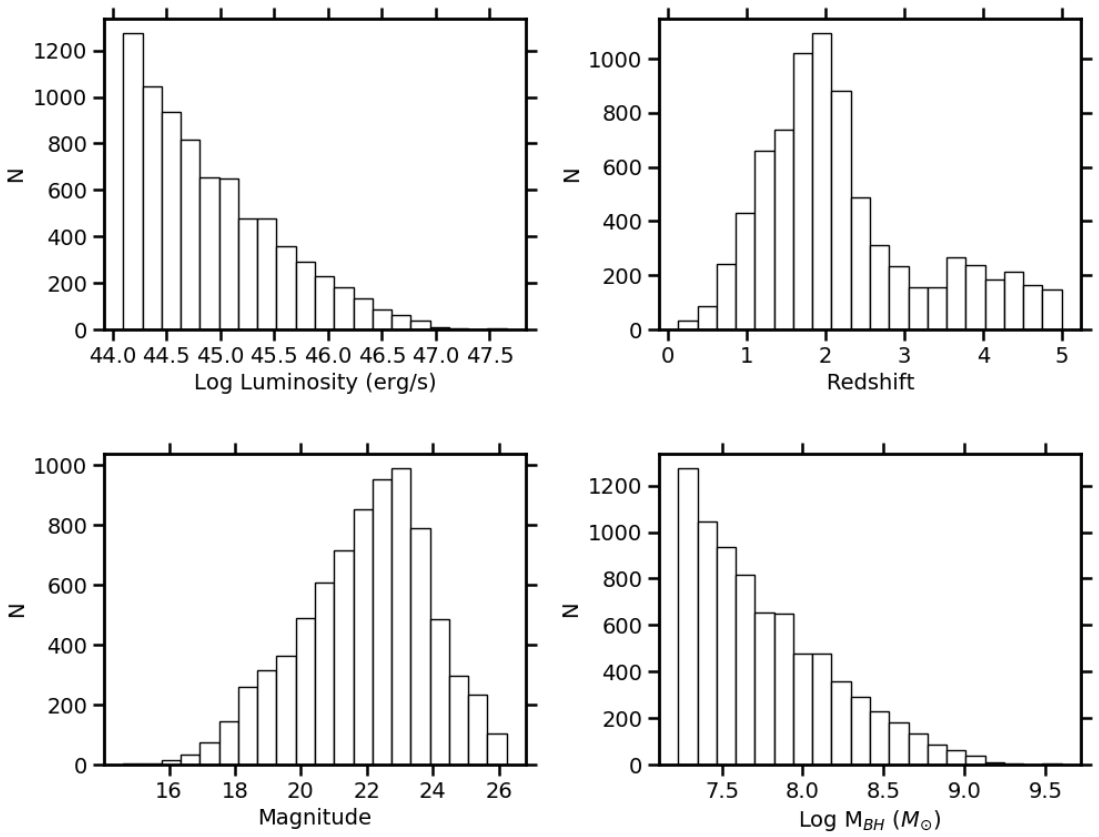

FIGURE 6.1: Distributions of the parameters of the AGN made in the mock sample, including luminosity, redshift, mean apparent *r* band magnitude and mass of the SMBH.

PSDs especially, the variance can be dominated by the long-term variations. This therefore means that shorter light curves can be impacted by the slower, long-term trends.

The photometric uncertainty of the light curves was calculated using the expected photometric error equation from Ivezić et al. (2019), given in Equation 6.5.

$$\sigma^2_{LSST} = \sigma^2_{\text{sys}} + \sigma^2_{\text{rand}} \tag{6.5}$$

This is a combination of the random photometric error, σ^2_{rand}, summarised in Equation 6.6, and the systematic photometric error due to imperfect modelling of the PSF, σ^2_{sys} (= 0.005).

$$\sigma^2_{\text{rand}} = (0.04 - \gamma)x + \gamma x^2 \tag{6.6}$$

where $x = 10^{0.4(m-m_5)}$ and m_5 is the 5σ depth in a given observation band (m_5 = 24.7 for *r* band) and γ depends on the sky brightness and readout noise (γ = 0.039 for *r* band).

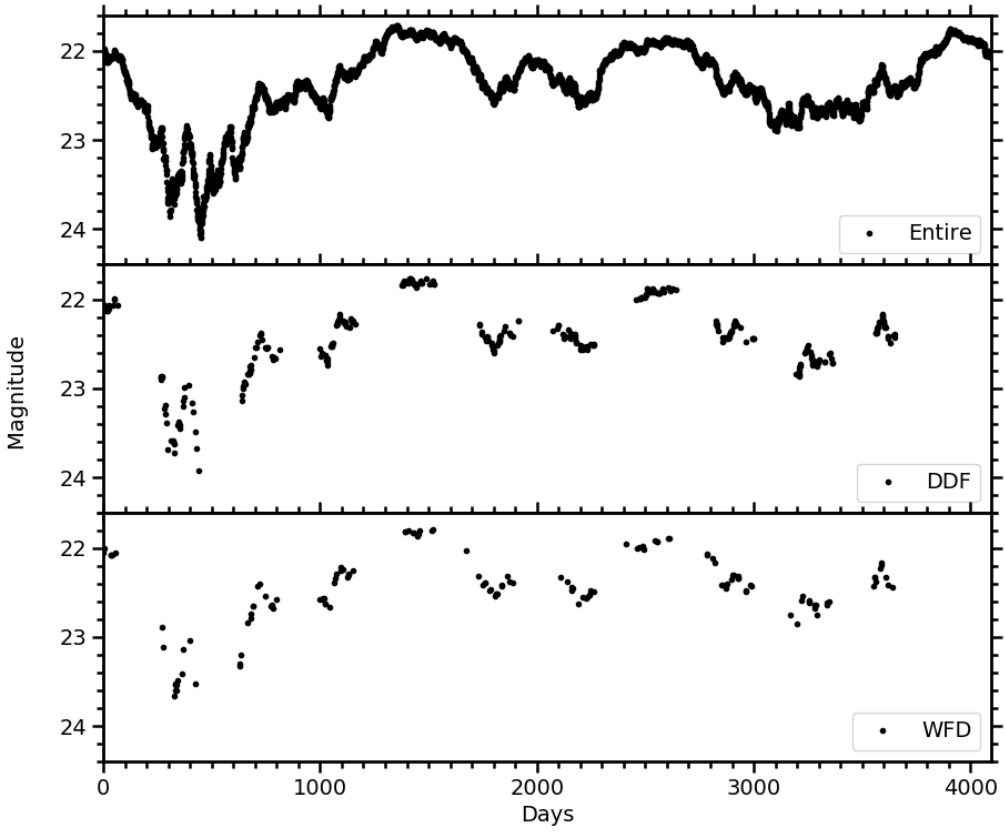

FIGURE 6.2: Examples of an artificial AGN *r* band light curve and the extracted DDF and WFD cadenced light curves using simulated observations from one pointing in the FBS 1.7 DDF OpSim and from the FBS 1.7 baseline OpSim run respectively.

The continuous light curves were then sampled with simulated LSST cadences obtained using OpSim 1.7[2], using the code described in Kovačević et al. (2021). Though not yet finalised, the current LSST observing strategy has been optimised to fulfil a wide range of scientific objectives, and as such the observing time will be divided between the main survey, commonly referred to as the WFD survey, and other mini-surveys, including the DDFs as described in Chapter 2. The WFD survey intends to repeatedly image the entire visible sky (covering $\sim$ 18,000 deg^2) every few nights, alternating between 6 filters in the *ugrizY* bands. The DDF survey will have more frequent sampling of 5-10 observation fields than for the rest of the sky to allow deeper coverage. I chose to perform the following analysis with cadencing from one pointing in the Elias South field in the FBS 1.7 DDF OpSim run in the *r* band, as the DDF is thought to be the most relevant for AGN research due to the more frequent observations. I then compared the results against one pointing in WFD region using the FBS 1.7 baseline OpSim run which will cover a much larger area of sky and hence observe many more AGN. Examples of these WFD and DDF cadenced light curves are shown in Figure 6.2.

[2] https://epyc.astro.washington.edu/~lynnej/opsim_downloads/fbs_1.7/

Any epoch of any of the mock AGN light curves that was below the 5σ detection limit of LSST was excluded at this stage.

6.3 Recovering Properties of the DRW PSDs

As the DRW model introduced by Kelly et al. (2009) is often used to model optical AGN variability and has been shown to be consistent with many AGN observations (e.g., Kozłowski et al., 2010; MacLeod et al., 2010; Zu et al., 2013), I first explored the recoverability of the parameters of this model using the simulated LSST cadenced light curves.

6.3.1 Simulating Damped Random Walk PSDs and Light Curves

For each AGN in the mock sample described in Section 6.2.1, the power spectra of the DRW process, $P(f)$, for a range of frequencies was calculated using Equation 6.7 (Kelly et al., 2009).

$$P(f) = \frac{2\hat{\sigma}^2_{\rm DRW}\tau^2_{\rm DRW}}{1 + (2\pi\tau_{\rm DRW}f)^2} \tag{6.7}$$

where the parameters $\tau_{\rm DRW}$ and $\hat{\sigma}_{\rm DRW}$ were assigned to each mock AGN using the relation to the luminosity, λL_λ, and redshift, z, of the AGN given in Equations 6.8 and 6.9 respectively (Kelly et al., 2009).

$$\text{Log } \tau_{\rm DRW} = (-8.13 \pm 0.12) + (0.24 \pm 0.12)\ \text{Log } \lambda L_\lambda + (0.34 \pm 0.58)\ \text{Log } (1+z) \tag{6.8}$$

$$\text{Log } \hat{\sigma}^2_{\rm DRW} = (8.00 \pm 3.29) - (0.27 \pm 0.07)\ \text{Log } \lambda L_\lambda + (0.47 \pm 0.33)\ \text{Log } (1+z) \tag{6.9}$$

The values of $\tau_{\rm DRW}$ and $\hat{\sigma}^2_{\rm DRW}$ calculated here were then converted to the observational frame by multiplying and dividing by (1+z) respectively. Figure 6.3 contains the distribution of $\tau_{\rm DRW}$ and $\hat{\sigma}_{\rm DRW}$ for the mock sample of AGN defined in Section 6.2.1.

As explained in Section 1.4.1, the variance of the light curves is given by the integral of the PSD over the timescales of the light curve, and therefore for large timescales in the DRW PSDs, it is given by $\sigma^2_{\rm DRW} = \hat{\sigma}^2_{\rm DRW}\tau_{\rm DRW}/2$.

Using these estimated DRW PSDs, light curves for each mock AGN in the sample were then simulated and cadenced to replicate the LSST observations as described in Section 6.2.

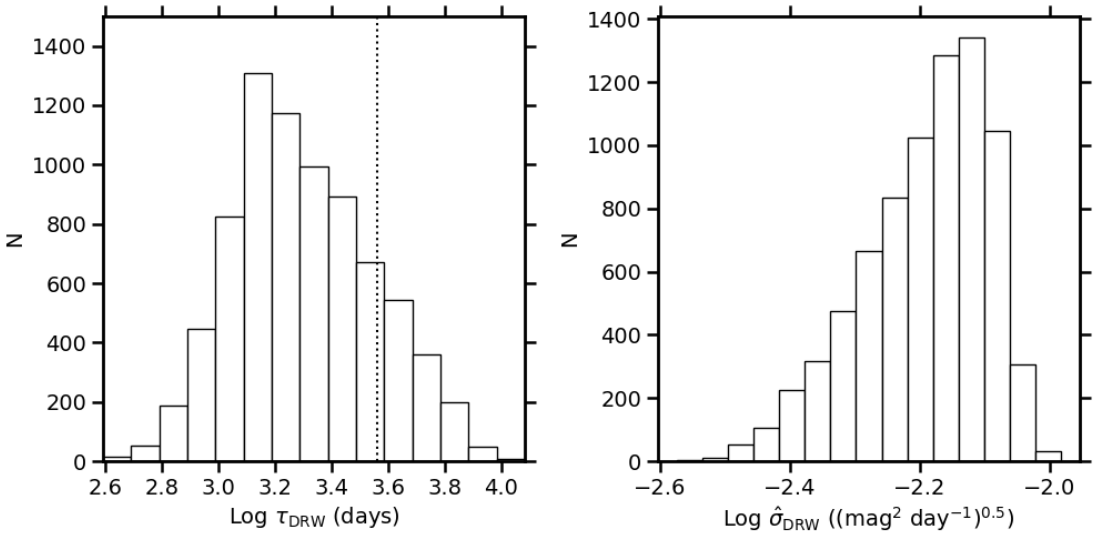

FIGURE 6.3: Distribution of the parameters of the DRW model (Kelly et al., 2009) for each AGN in the mock sample. The dotted line in the distribution of τ_{DRW} represents the expected baseline of LSST's observations.

6.3.2 Methods for Recovering Properties of DRW PSDs

I chose to use JAVELIN (Zu et al., 2011, 2013), which is a popular tool used when modelling AGN light curves as DRW processes, to estimate the input properties τ_{DRW} and σ_{DRW} (i.e. the standard deviation of the light curve, not the characteristic amplitude, $\hat{\sigma}_{DRW}$).

JAVELIN works by performing an MCMC search to find the most likely values of τ_{DRW} and σ_{DRW} to be used to fit a DRW model to the light curve. Specifically, this MCMC modelling was done over 10,000 iterations (5,000 of which are excluded from the final distribution as burn-in), using uniform logarithmic priors for each parameter. JAVELIN returns a posterior distribution for each parameter as shown in Figure 6.4. The mean of these posterior distributions are then used as the estimate for the parameters τ_{DRW} and σ_{DRW}, and their uncertainties are given as their standard deviations.

6.3.3 Results

Deep Drilling Field The ability to recover the parameters of the DRW model for the DDF cadenced light curves were explored first. Of the 7730 AGN in the mock sample, 7229 (∼94%) were able to be fit using JAVELIN. The accuracy of these recovered parameters was then explored by evaluating the means of the posterior distributions that were consistent with the inputs within their standard deviations. It was found that for these AGN, 1492 (∼ 21%) recovered values of τ_{DRW} consistent with the input values within 1σ, and 3277 (∼ 45%) and 4838 (∼ 67%) were found consistently within

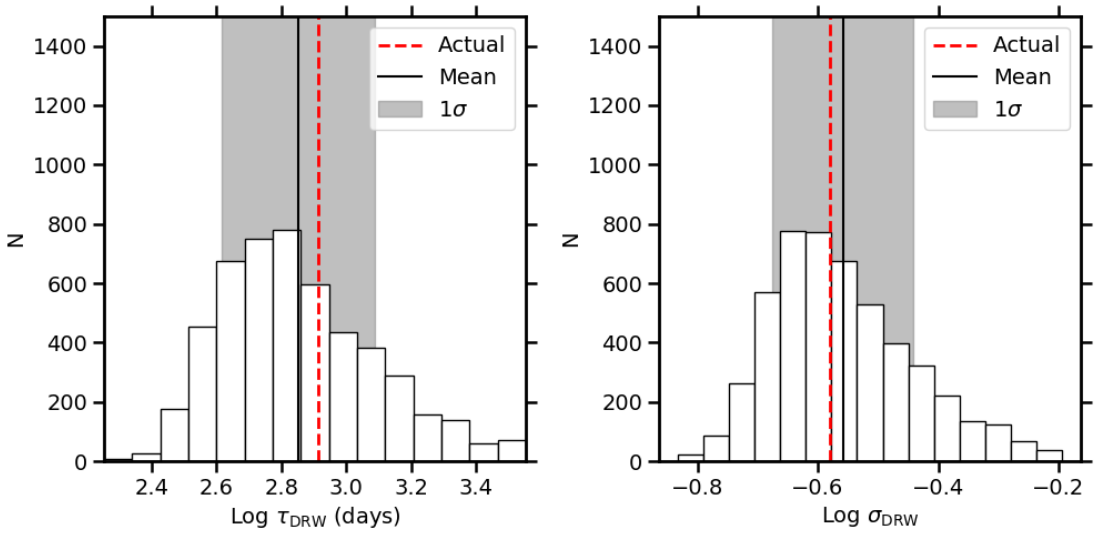

FIGURE 6.4: Examples of the posterior distributions of parameters τ_{DRW} and σ_{DRW} returned when modelling the PSDs of the AGN light curves with JAVELIN.

2σ and 3σ respectively. For the standard deviation of the light curve, the recovered parameters were found successfully within 1σ, 2σ, and 3σ for 5106 ($\sim$ 71%), 6751 ($\sim$ 93%) and 6994 ($\sim$ 97%) AGN respectively.

Figure 6.5 displays the distribution of input values of τ_{DRW} and σ_{DRW} that were successfully recovered within the 1σ, 2σ, and 3σ uncertainties. It can be seen that shorter decorrelation timescales are easier recovered which is to be expected as the baseline of the light curves will provide enough information to probe these timescales. Furthermore, smaller values of the standard deviation are also shown to be easier recovered.

To further explore the AGN corresponding to the successfully recovered parameters of the DRW model with JAVELIN within the 1σ standard deviations, colour maps are plotted in Figure 6.6 to search for correlations between luminosity and redshift. As the mock AGN sample is not distributed evenly across luminosity and redshift space but instead calculated using the quasar luminosity function, the colour maps are divided into bins that contain similar numbers of AGN. The distribution of AGN per bin is shown in Figure 6.6a, where the colour corresponds to the number of AGN. It can be seen that most bins have $\sim$ 60-90, though some of the bins at the edges have higher or lower values.

Figure 6.6b shows how many of the mock AGN in the same luminosity-redshift space had parameters that could not be recovered using JAVELIN as described above, where the colour of each bin corresponds to the percent of AGN within that bin deemed unrecoverable. It can be seen that the majority of unrecoverable AGN are those with high redshifts and low luminosities. These AGN are found to be those that have light

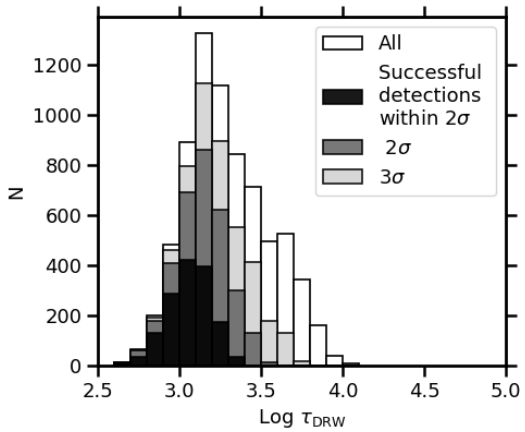

(A) Distribution of Log τ_{DRW}.

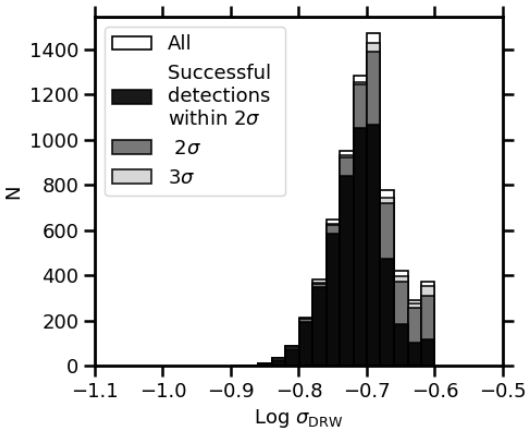

(B) Distribution of Log σ_{DRW}.

FIGURE 6.5: Distribution of parameters of the DRW model that are successfully recovered for DDF light curves using JAVELIN compared to the overall distribution. The parameters are in observed frame.

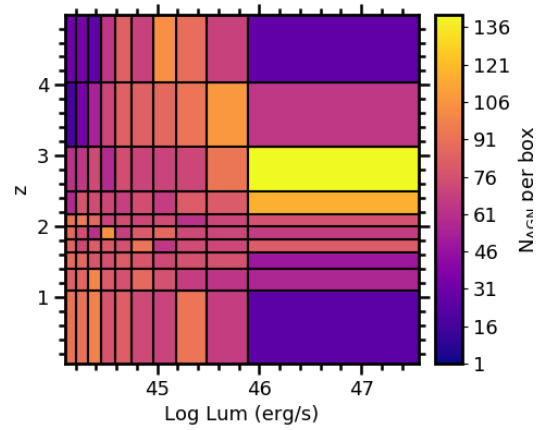

(A) Number of AGN per bin for the luminosity-redshift colour plots.

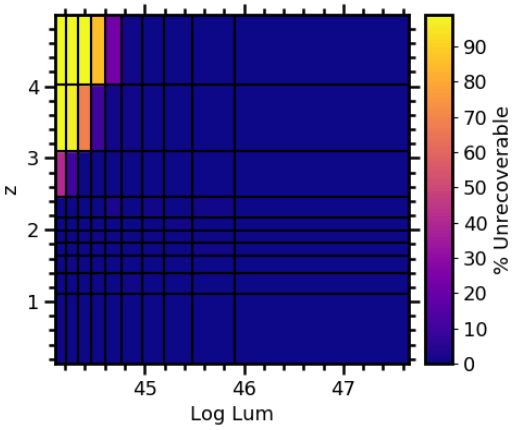

(B) The percentage of AGN whose power law could not be fit using JAVELIN.

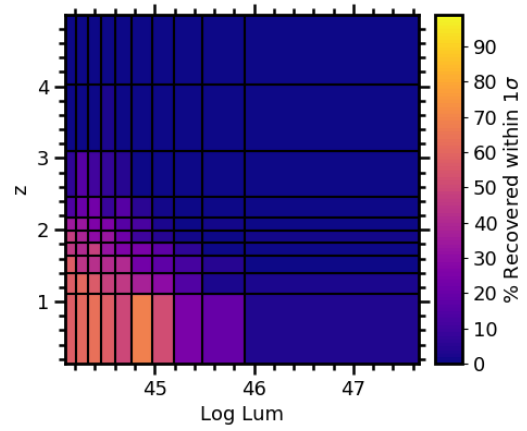

(C) Distribution of successful recovery of the decorrelation timescale within 1σ uncertainties.

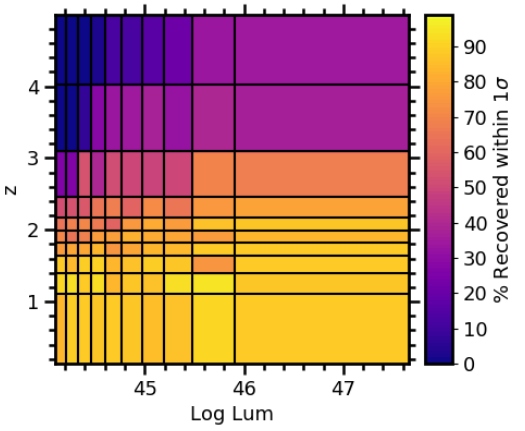

(D) Distribution of successful recovery of the standard deviation of the light curves within 1σ uncertainties.

FIGURE 6.6: Colour maps depicting the ability to recover the parameters of the DRW model using DDF cadenced light curves depending on combinations of luminosity and redshift of the AGN.

curves in which many of the epochs are below the single epoch 5σ detection limits of LSST, and therefore have limited information available to classify the parameters.

Figures 6.6c and 6.6d show the percent of AGN within the same luminosity-redshift space whose decorrelation timescales and standard deviations were successfully recovered within the 1σ uncertainties respectively, where the colours again corresponds to the percent of AGN with successfully recovered parameters within each bin. The recovery of the decorrelation timescale is shown in Figure 6.6c to depend on both the luminosity and redshift, with lower redshift and lower luminosity AGN recovering the parameters better as shown by the higher percent being successfully recovered. This is expected given the correlation of the decorrelation timescale with luminosity and redshift, as the low redshift and lower luminosity AGN will have smaller values of decorrelation timescale, therefore the white noise portion of the power spectrum will be probed sufficiently. Figure 6.6d shows that the standard deviation of the light curve is better recovered for the lower redshift objects, however the recovery is shown to be approximately uniform over the different values of luminosity.

Appendix C contains similar colour maps for the AGN successfully recovered within 2σ and 3σ.

Wide Fast Deep The recoverability of the parameters of the DRW model using JAVELIN on the WFD cadenced light curves were also explored here. From the initial sample of 7730 AGN, 7220 ($\sim$ 93%) were able to be fit using JAVELIN. It was found that for these AGN, 1320 ($\sim$ 18%) recovered values of $\tau_{\rm DRW}$ consistent with the input values within 1σ, and 3162 ($\sim$ 44%) and 4765 ($\sim$ 66%) were found consistently within 2σ and 3σ respectively. For the standard deviation of the light curve, the recovered parameters were found successfully within 1σ, 2σ, and 3σ for 5109 ($\sim$ 71%), 6765 ($\sim$ 94%) and 6982 ($\sim$ 97%) AGN respectively. Fewer AGN have parameters that are reasonably recovered using WFD light curves than those recovered using the DDF cadenced light curves, but the distribution of recovered parameters are similar as shown in Figure 6.7, and furthermore Appendix C shows that the colour maps for the recovery of these parameters are also similar. This could be explained as though reduced cadencing will limit the total number of data points available and therefore result in fewer correctly recovered parameters, for many light curves the low frequency region of the WFD PSDs could still be sufficiently sampled, allowing similar recovery of parameters as seen in the DDF light curves.

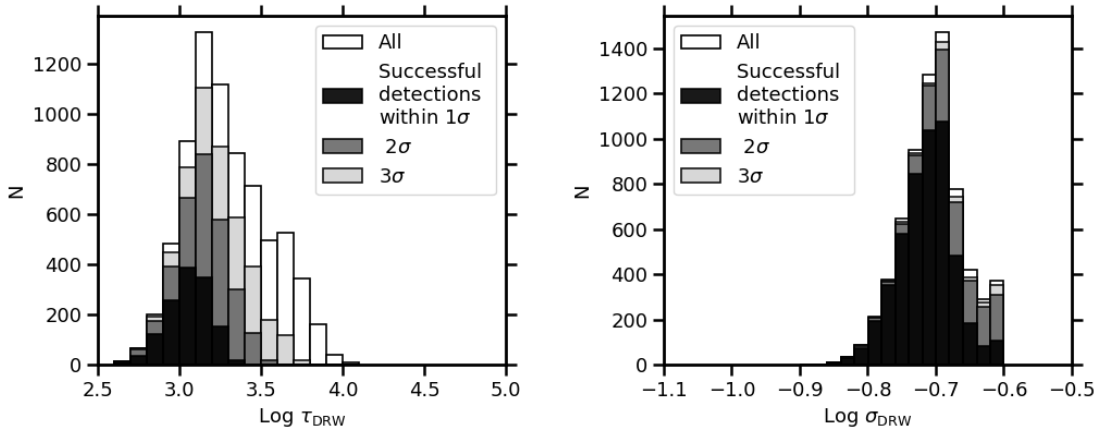

(A) Distribution of Log τ_{DRW} that are successfully recovered using JAVELIN compared to the overall distribution.

(B) Distribution of Log σ_{DRW} that are successfully recovered using JAVELIN compared to the overall distribution.

FIGURE 6.7: Distribution of parameters of the DRW model that are successfully recovered for WFD light curves using JAVELIN compared to the overall distribution. The parameters are in observed frame.

6.3.4 Discussion

In this section, I explored the recoverability of the parameters of the DRW model of optical AGN variability introduced by Kelly et al. (2009) for mock AGN light curves with simulated LSST cadencing using JAVELIN (Zu et al., 2011, 2013).

Firstly, for the mock DDF cadenced light curves, the decorrelation timescales and standard deviations of the light curves were successfully recovered for 21% and 71% respectively within the 1σ uncertainties. It was found that smaller decorrelation timescales were best recovered, which corresponds to low luminosity and low redshift AGN. This result is not unexpected as for larger timescales, the overall length of the light curve observed with LSST does not probe the white noise part of the power spectrum which is necessary for constraining the decorrelation timescale. Indeed, Kozłowski (2016) found that observations over a baseline smaller than $\sim 10\,\tau_{DRW}$ were insufficient to measure the decorrelation timescales. Witt et al. (2021) report similar results from modelling simulated DRW light curves. Additionally, smaller light curve standard deviations were also better recovered, and the recovery was shown to largely depend on the redshift, where AGN with lower redshifts were more likely to recover values of the standard deviation, while no clear dependence was found on luminosity. This again can be expected from the dependences of the parameters on luminosity and redshift given in Equations 6.8 and 6.9.

For those mock AGN that did not have the decorrelation timescales and standard deviations of the light curves successfully recovered within the uncertainties, often the posterior distributions of the MCMC process used in JAVELIN were shown to not converge well. It is difficult to define the convergence of an MCMC process, and for

such a large number of AGN that are expected to be observed with LSST, individually checking how well each MCMC process converges would be time-consuming. However citing the output of a process that has not converged could lead to uncertainties in any conclusions drawn from the results. Therefore, if similar analysis is performed on the real sample of AGN that will be observed with LSST, caution will be needed when inferring behaviour from the results.

Finally, it was found that exploring the DRW model with WFD cadenced light curves instead of DDF light curves return a slightly smaller number of well-recovered parameters, but contain a similar distribution. The WFD cadenced light curves have PSDs that contain fewer data points, but this has a greater impact on the higher frequency portion, meaning the low frequency range is similarly probed. As the recovery of the decorrelation timescales is found to be largely dependent on the light curves probing the white noise part of the power spectrum at the lower frequencies, this likely explains why the difference in recovery is not extreme when using WFD and DDF cadenced light curves. This therefore suggest that the difference between observation strategies for the DDF and WFD regions does not greatly impact the analysis of these objects, and therefore suggests many more AGN will be able to be studied as the WFD survey covers a much larger region of sky.

6.4 Recovering Properties of Various PSD Slopes and Shapes

Section 6.3 explored the recoverability of parameters in the DRW model using simulated LSST cadenced light curves, however previous studies have shown that the optical PSD of some AGN deviate from the DRW model. For example, the PSDs of many *Kepler* AGN have yielded power law slopes ranging from 2 to 3.3 (e.g. Mushotzky et al., 2011; Smith et al., 2018a), and furthermore, Caplar et al. (2017) found the PSDs of 2,200 AGN in the PTF/iPTF survey were best fit with slopes ranging between $1.5 < \alpha < 4$.

In addition, some studies have also found that the optical PSDs are best fit using broken power laws (BPLs). For example, Edelson et al. (2014) find that the *Kepler* PSD of Zw229-015 shows a break in the power law slope of ~ 2 to ~ 4 at timescales smaller than ~ 5 days. Simm et al. (2016) found that the optical PSDs all 90 of their sources observed in the Pan-STARRS1 survey are consistent with BPLs, with the low-frequency slope consistent with a value of 1 and a high-frequency slope between 2 and 4, with the break occurring at timescales between ~ 100 and ~ 300 days. Furthermore, Smith et al. (2018a) found that 6 of the 21 *Kepler* AGN in their sample were best fit with BPLs with flattening at the lower frequencies with the break occurring at temporal frequencies corresponding to timescales of ~ 10 to ~ 50 days.

Therefore, in this section, I explore how properties of various power laws are recovered using simulated LSST cadenced light curves, including both single and broken power laws.

6.4.1 Simulating PSDs with Varying Power Laws

Single Power Laws First, to explore how the different PSD slopes are recovered with simulated LSST observations, I created light curves for each AGN in the mock sample with a SPL that has a random slope chosen uniformly between $1.0 \leq \alpha \leq 3.0$. Here the upper limit is set due to the inability to distinguish PSDs with red-noise leakage for steeper slopes as shown in Section 6.4.2, and the lower limit is chosen to be consistent with observed PSD slopes and because slopes closer to 0 represent white noise as opposed to the red noise behaviour observed in AGN.

Figure 6.8 demonstrates how artificial light curves created from SPLs with different slopes can differ. It can be seen that in the light curve created with the steeper power law (e.g. α=2.5), more power is given to the long term variability, while in the light curve corresponding to the shallower PSD (e.g. α=1.5), the short term variability is more powerful.

Broken Power Laws Light curves were also created for the AGN in the mock sample using a BPL with a random low-frequency slope between $1.0 \leq \alpha \leq 1.8$ and high-frequency slope between $2.2 \leq \beta \leq 3.0$. The overall upper and lower limits of the power law slopes were set to 1.0 and 3.0 as described for the SPLs above, and the individual limits of $\alpha \leq 1.8$ and $\beta \geq 2.2$ were chosen to provide a clear distinction between the low-frequency and high-frequency power laws. A random value for the characteristic break timescale was then chosen between $1.3 \leq \mathrm{Log}(t_{\mathrm{br}}) \leq 2.3$, where the upper limit of t_{br} is due to the number of data points available when binning the periodogram which is explained further in Section 6.4.2, and the lower limit is set such that there are sufficient data points for the high frequency power law slope to be observed between this limit and the mean cadence of observations.

Figure 6.9 shows how the light curves created from BPLs can differ depending on the location of the break timescale, as a shorter break timescale means more power is given to the shallower slope and thus the light curve is more dominated by short term variations.

In both the SPL and BPL PSDs, the power would be expected to taper off towards lower frequencies as the variability becomes uncorrelated, however for simplicity, in these simulations it is assumed to occur at timescales much greater than the length of observations and therefore is not included.

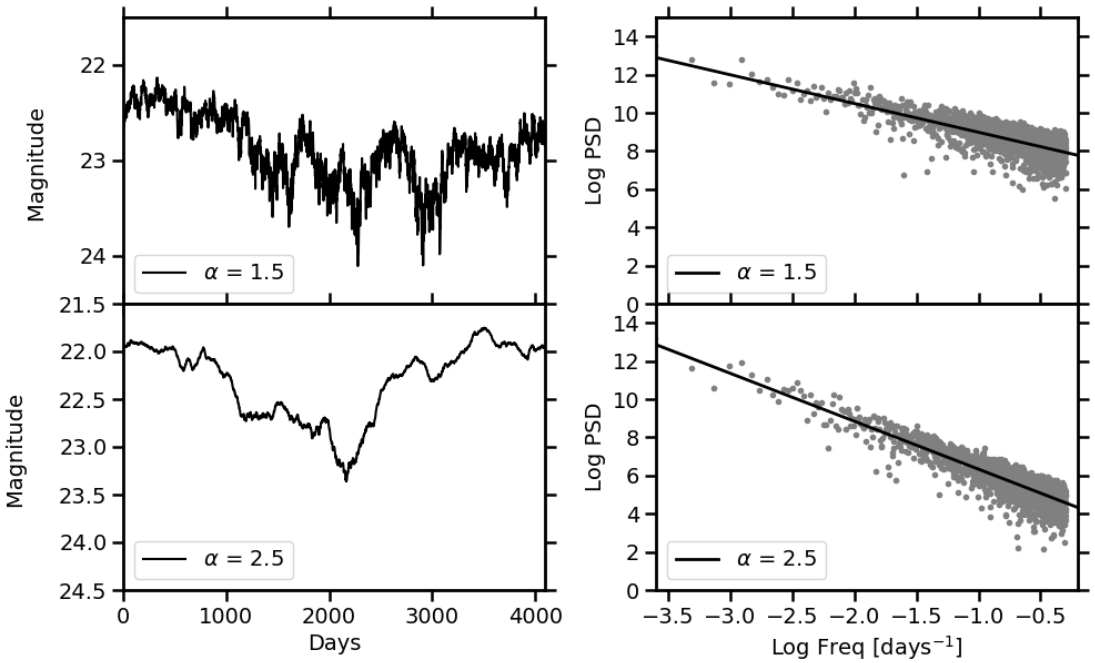

FIGURE 6.8: Examples of light curves made from single power law PSDs with different power law indices.

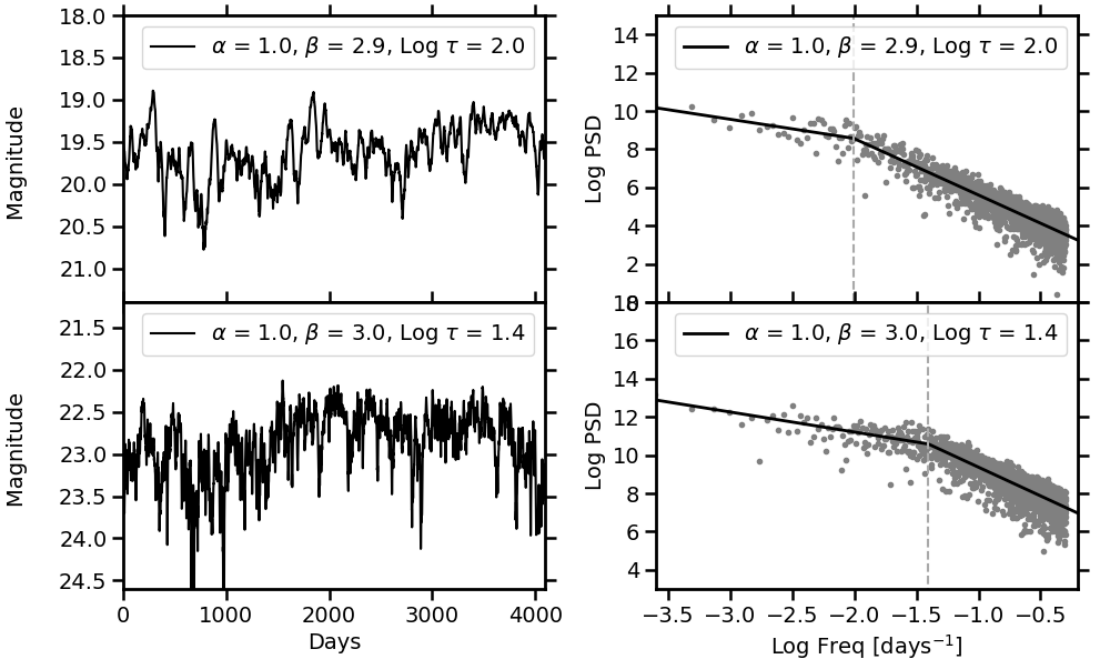

FIGURE 6.9: Examples of light curves made from broken power law PSDs with different break frequencies.

6.4.2 Methods for Recovering Properties of PSDs

The PSD of the light curves made using various input slopes/shapes as described in Section 6.4.1 could be estimated using a discrete Fourier transform (DFT) of the light curve to create a periodogram as described in Section 3.4. The DFT requires evenly sampled data however, so the simulated LSST cadenced light curves needed to be interpolated first. In the interest of creating a time-effective pipeline, I chose to perform linear interpolation instead of other methods such as interpolation using the SF. Though linear interpolation could lead to inaccuracies in the estimated periodograms as it does not replicate the variability of AGN, similar underestimation of the variability should be present in the Monte Carlo fitting of the slopes using the PSRESP method described in Section 3.4 as the method of interpolation is kept consistent.

These periodograms were then resampled into evenly spaced log frequency bins to give an estimate of the mean PSD of the object. Each bin was required to have at least 3 data points, and as a result the PSDs are limited to timescales less than ~ 300 days. As the high-frequency data is provided by the linear interpolation, the PSDs are also further restricted to only show information for timescales greater than the mean sampling rate of the individual observation seasons of the light curves.

Additionally, at high frequencies the power spectra flattens to white noise as it becomes dominated by measurement errors. To quantify this expected noise, $P_{\rm noise}$, assuming the light curve measurement errors are Gaussian and considering the normalization factor of the periodogram given in Equation 3.4, I use Equation 6.10 (Vaughan et al., 2003).

$$P_{\rm noise} = \frac{2\Delta T\, \overline{\sigma_{err}^2}}{\bar{x}^2} \tag{6.10}$$

where ΔT is the sampling, $\bar{x}^2$ is the mean flux and $\overline{\sigma_{err}^2}$ is the mean square light curve measurement error.

As described in Chapter 3, the observed periodogram is often distorted from the underlying input PSD due to effects such as cadences of observations, rebinning of the PSD and red-noise leakage. An example of the effect of red-noise leakage is displayed in Figure 6.10, which shows the change in power law with the effects of red-noise leakage in the right panel. Additionally, the left panel of Figure 6.10 displays how slopes, especially those that are steeper, often become indistinguishable within their uncertainties because of this phenomenon. Therefore the observed PSD is fit using the PSRESP method introduced by Uttley et al. (2002) also described in Chapter 3.

Uttley et al. (2002) suggest that the number of light curves simulated for each known underlying PSD needs to be large, between 100-1000. I varied the number of

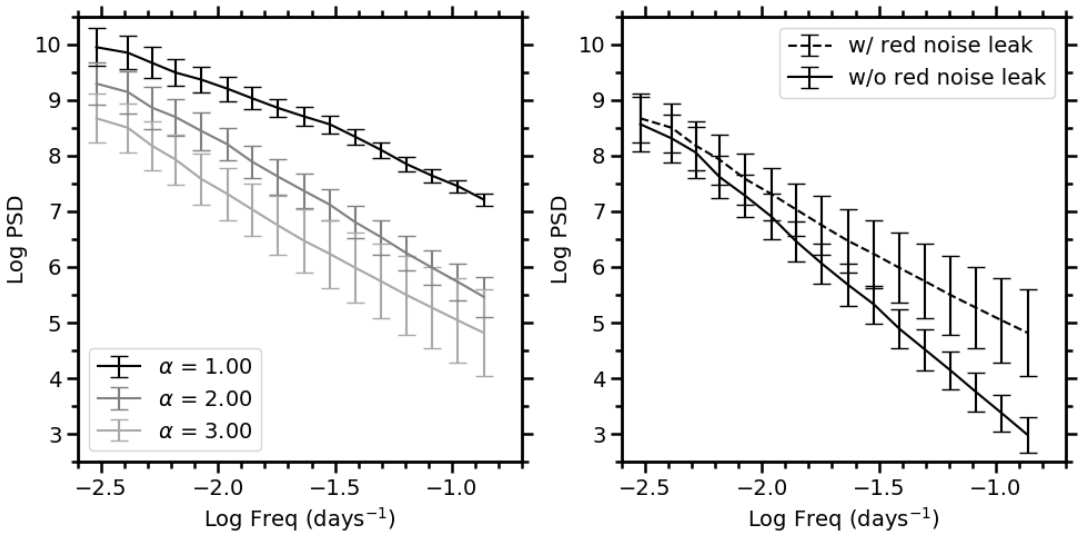

FIGURE 6.10: Demonstration of the effects of red-noise leakage of the observed single power laws PSD with different slopes. The right panel shows the difference between power laws observed with and without red-noise leak for a single power law with slope 3, and the left panel displays how steeper slopes often become indistinguishable within their uncertainties because of this phenomenon.

simulated light curves for a sub-sample of 100 mock AGN to find the most appropriate number to use so that it would give the best accuracy of PSD recovery while not taking excessive time to compute. The results of this are plotted in Figure 6.11, which shows that the mean difference between the actual and recovered best fit PSD is approximately consistent over the entire range, but the confidence with which we can reject the model decreases slightly up to ~ 100 simulated light curves, after which it plateaus. As a result, the following analysis is performed using 100 simulated light curves.

Figure 6.12 displays an example of the confidence of rejection for the different model PSD slopes compared to an observed PSD, with the best fit PSD plotted as a comparison to the data. It can be seen that the confidence of rejection for the example is 100% at slopes much shallower than the actual slope, but is less than 100% for steeper slopes. This is due to both the rms spread of the model PSDs, which are larger for steeper slopes than for the shallow slopes, and red-noise leakage which has a larger impact on the steep slopes, as shown in Figure 6.10.

This Monte Carlo technique would be ideally repeated for the entire range of PSD slopes that are being tested, and the power law that can be rejected with the least confidence would be considered the best fit as shown in Figure 6.12. However, this is a time-consuming process as it needs to be calculated for each AGN separately. Testing the entire range for each AGN is not feasible due to the time it would take, especially when considering the much larger sample that will be observed with LSST, therefore I

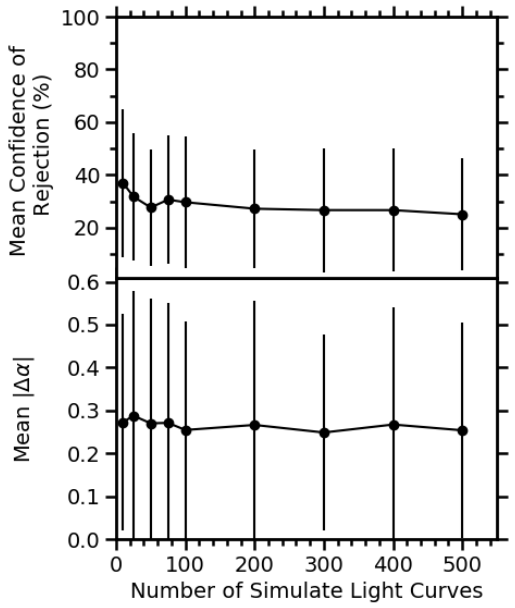

FIGURE 6.11: An exploration of the appropriate number of simulated light curves necessary for PSRESP analysis. *Upper panels:* The mean confidence of rejection for different number of simulated light curves. *Lower panels:* The mean difference between input slope and recovered slope for different number of simulated light curves. This analysis was performed on a sub-sample of 100 AGN from the AGN mock sample.

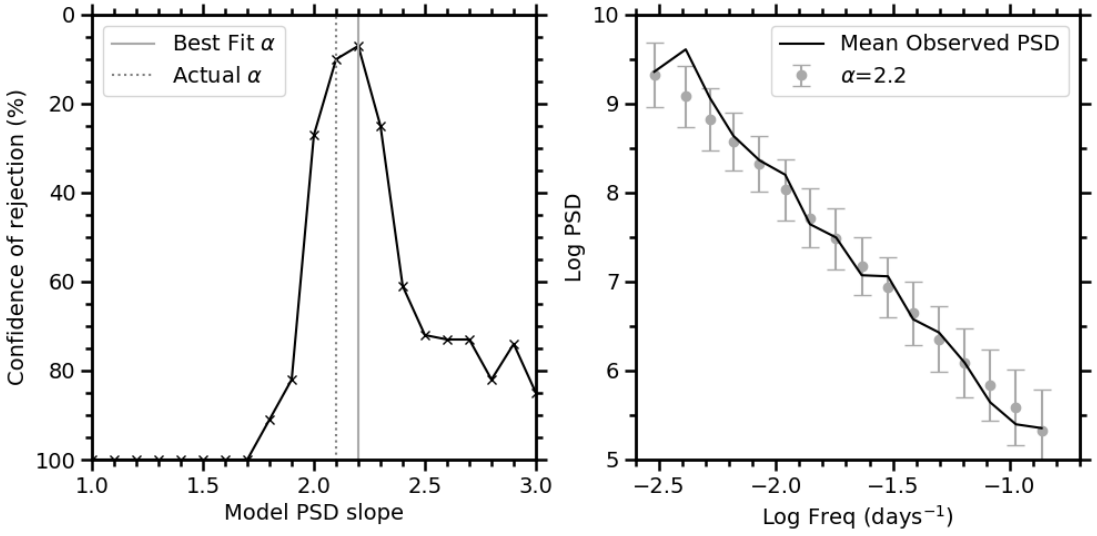

FIGURE 6.12: Example of the PSRESP method of recovering power law slopes, with the left panel displaying the confidence of rejection found for each slope explored, and the right panel displaying the best fit power law compared to the data.

instead perform this analysis using a stochastic hillclimbing algorithm which is described in more detail in the following.

Single Power Law For the SPL PSD recovery, the hillclimbing algorithm works by taking a random initial guess for the best fit power law slope, and computes the confidence with which we can reject this model as explained previously. It then computes the confidence of rejection for the model with slope above and below the initial guess within a defined step size (=0.1), and compares these to the initial guess. If the confidence with which either of the new PSD models can be rejected is less than or equal to that of the previous, it assigns that as the new best solution and repeats the process until the confidence of rejection stops improving. To prevent local minima being selected as the best solution, it also compares the current best guess to a randomly chosen point at every iteration, and updates the best guess accordingly.

In order to find the best solution most efficiently, I again performed this technique on the sub-sample of 100 AGN using a different number of minimum required guesses, as shown in Figure 6.13. It can be seen that the mean difference between the input and recovered power law slope, and the confidence with which we can reject the model both improve with a minimum number of iterations of the stochastic hillclimbing algorithm up to 7, and then is approximately consistent, hence the minimum number of guesses is set to 7.

Broken Power Laws For the BPL PSD recovery, the hillclimbing algorithm works similarly to the SPL PSD recovery, however it now has three parameters to fit. Therefore, it takes a random combination of these three parameters as the initial guess, then cycles through to find the best fit for the first parameter while keeping the other two constant, before moving on to the second and then the third. As it only finds the best guess of each parameter while keeping the other two fixed, it continues cycling through all three parameters until none of them change. Again, to avoid local minima, it compares each best combination to a random combination at every iteration.

The minimum number of combinations that need to be tested before accepting the best fit solution was also explored to improve the accuracy of detection while remaining efficient. It can be seen in Figure 6.14 that the mean rms difference of the three recovered parameters from the input parameters used to make the light curves is approximately consistent over the range of minimum combinations tested. The confidence of rejection decreases between 25 and 100 combinations before plateauing, therefore the minimum number of guesses used in this hillclimbing algorithm is set to 100.

Furthermore, in some cases a fit to the observed PSD cannot be recovered, and as such the confidence of which the model can be rejected is consistently 100%. As it is time

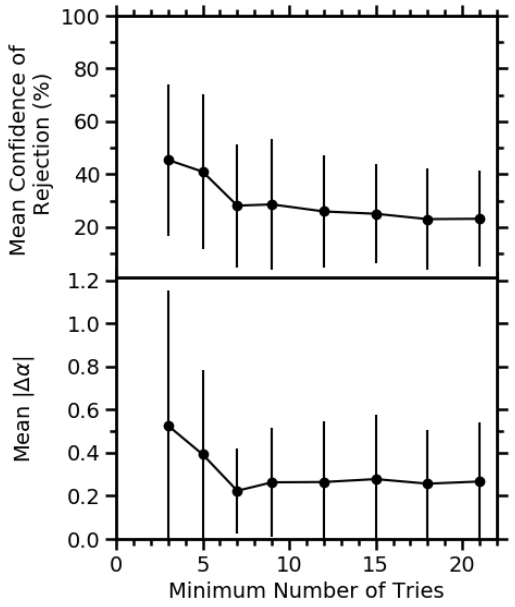

FIGURE 6.13: An exploration of the minimum number of power law slopes that need to be sampled for good recoverability of the underlying PSD for SPLs. *Upper panels:* The mean confidence of rejection for different number of simulated light curves. *Lower panels:* The mean difference between input slope and recovered slope for different number of simulated light curves. This analysis was performed on a sub-sample of 100 AGN from the AGN mock sample.

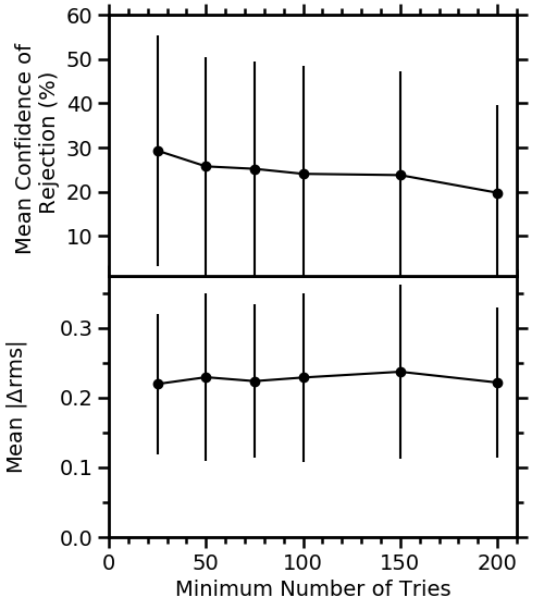

FIGURE 6.14: Same as Figure 6.13 but for BPLs.

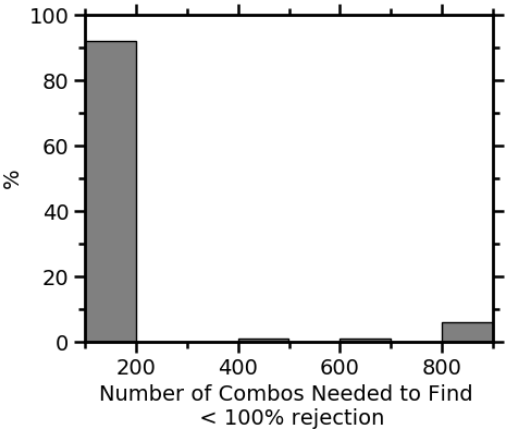

FIGURE 6.15: An exploration of the maximum number of power law slopes that need to be sampled before it can be assumed that a fit for the broken power law cannot be found.

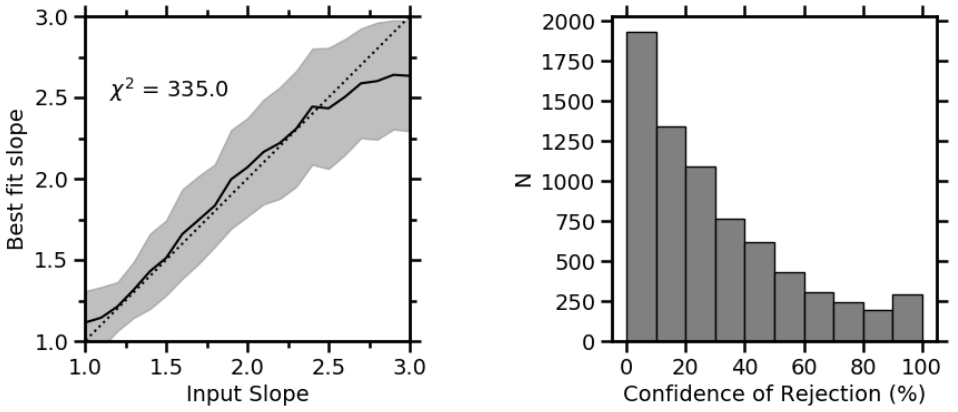

(A) Mean and standard deviations of the best fit slopes found for each input PSD slope.

(B) Distribution of the confidence of rejection for the SPL PSD recovery.

FIGURE 6.16: Results of the successfully recovered single power law fits using DDF cadenced light curves.

consuming to test all possible combinations of the parameters, I also defined a maximum number of attempts before it is likely to not be able to recover a power law fit. Figure 6.15 shows the distribution of the number of tries needed to recover a fit. It can be seen that > 90 mock AGN in the sample can be fit with less than 200 combinations, and only 2 mock AGN needed between 400-700 combinations to find the best fit, while for the remainder a fit to the PSD could not be recovered. I therefore chose to set the maximum number of tries to 200 so that the majority of the sample could find a fit without it taking unnecessarily large amounts of time. The parameters corresponding to the light curves whose PSDs could not be recovered within this number of tries are also further explored in the following sections.

6.4.3 Single Power Law PSD Recovery Results

Deep Drilling Field The SPL PSD slope recovery was first explored for the mock DDF cadenced light curves created using the SPL as described in Section 6.4.1. Out of the initial 7730 objects in the mock AGN sample, a best fit power law could be recovered for 7214 ($\sim$93%), which are evaluated in the following. The remaining $\sim$ 7% of the mock AGN were deemed unrecoverable and are also explored below in Figure 6.17a.

Firstly, the mean best fit slope and the standard deviation found for the range of input power law slopes is plotted in Figure 6.16a, and shows that overall, most best fit PSDs match the input power law well. However, it can be seen that there is an underestimation of the best fit towards steeper slopes with a larger standard deviation, which shows that the recovery of the steeper power law slopes is less reliable. This same underestimation of the steepest slopes can be seen in Appendix C

for the recovery of parameters using the 1 day cadenced light curves covering the baseline of LSST, which therefore suggests that it could be due to the effects including red-noise leakage on the light curves, and not solely the results of the LSST cadencing. Red-noise leakage has been shown to have a stronger impact on the steeper slopes (e.g., Uttley et al., 2002) as more power is given to the high frequencies from the lower frequency variability.

The distribution of confidences with which the best fitting PSD can be rejected for each mock AGN is shown in Figure 6.16b. It can be seen that the majority of objects have a low confidence of rejection, meaning the method finds reasonably good fits of the model power laws to the mock 'observed' PSDs.

Additionally, Figure 6.17 displays colour maps depicting the success of the recovery of the input PSD slope depending on properties of the AGN such as the luminosity, redshift, and input power law slope. As described in Section 6.3, the colour maps were divided into unevenly sized bins in order to display the results for approximately similar numbers of AGN in each bin, which is demonstrated in Appendix C.

Figure 6.17a displays the number of mock AGN in each luminosity-redshift bin whose best fit power law slope could not be recovered as the confidence of rejection was consistently 100%, where the colour corresponds to the percentage of mock AGN within each bin whose power law slope could not be recovered. It can be seen that the AGN with low luminosities and high redshifts were mostly unrecoverable, which is likely due to the objects having observations that were below the 5σ single epoch detection limits of LSST.

Furthermore, Figure 6.17b displays the mean difference in input and recovered slope for the mock AGN in luminosity-redshift space that could recover a best fit PSD. In this colour map, the darker colour corresponds to a smaller difference and the lighter corresponding to a larger difference between input and recovered values of the PSD slope. It can be seen that the high redshift and low luminosity AGN were more likely to recover power laws that were different to the inputs as the mean difference between the best fit and input slope is largest, while the remainder of the AGN distribution consistently had a mean difference between best fit and input slope of $\lesssim 0.5$.

Similarly to Figure 6.17a, Figures 6.17c and 6.17e display the number of mock AGN in each input power law slope-luminosity and input power law slope-redshift bins respectively whose best fit power law slope could not be recovered. It can be seen that the high redshift and low luminosity AGN struggle to find a best fit slope, regardless of the input slope, which again is likely due to observations being too dim for detection with LSST.

Additionally, Figures 6.17d and 6.17f display the mean difference in input and recovered slope for the mock AGN in input power law slope-luminosity and input

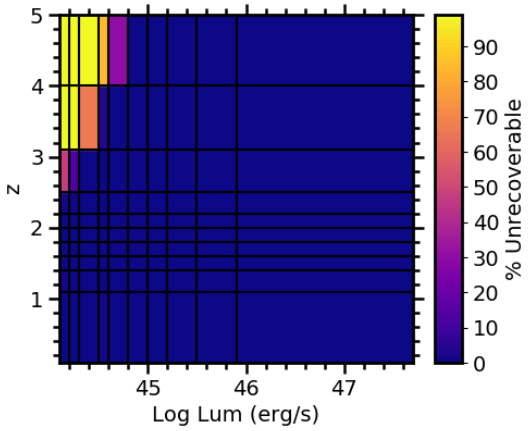

(A) The percentage of AGN of a given luminosity and redshift whose power law could not be fit using these methods.

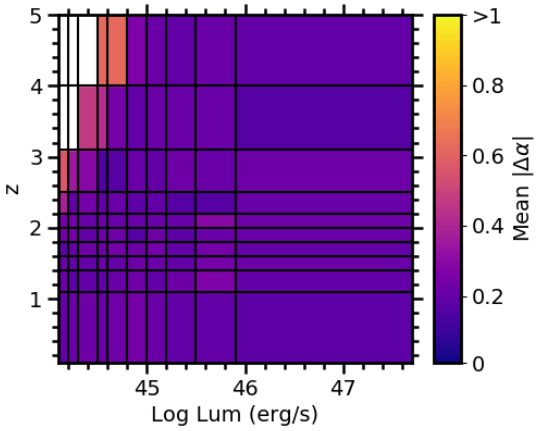

(B) The mean difference found for the power law slope of AGN of a given luminosity and redshift.

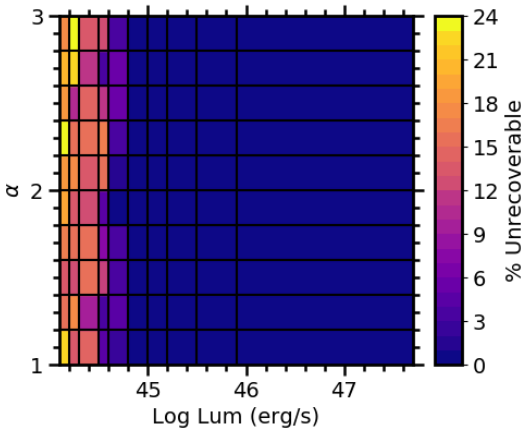

(C) The percentage of AGN of a given luminosity and input power law slope whose power law could not be fit using these methods.

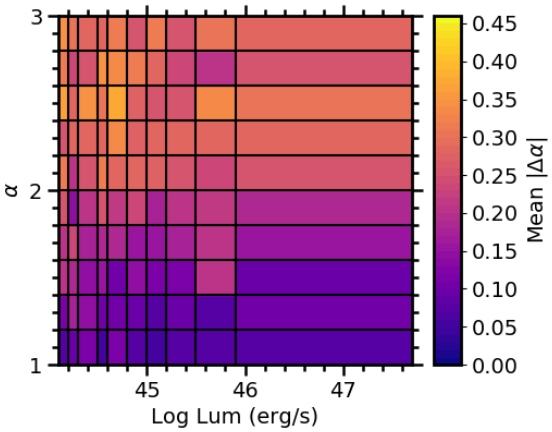

(D) The mean difference found for the power law slope of AGN of a given luminosity and input power law slope.

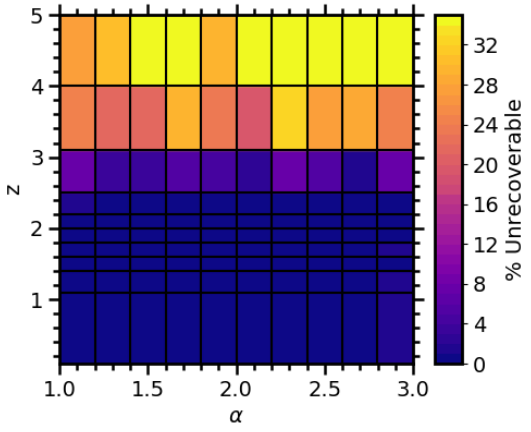

(E) The percentage of AGN of a given input power law slope and redshift whose power law could not be fit using these methods.

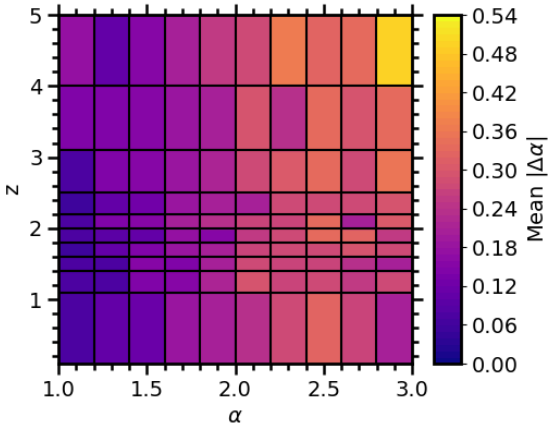

(F) The mean difference found for the power law slope of AGN of a given input power law slope and redshift.

FIGURE 6.17: Colour maps depicting the ability to recover the input SPL PSD using DDF cadenced light curves depending on combination of the power law slope, luminosity and redshift of the AGN. Each plot is divided such that each rectangle contains similar numbers of AGN, with the distributions given in Appendix C.

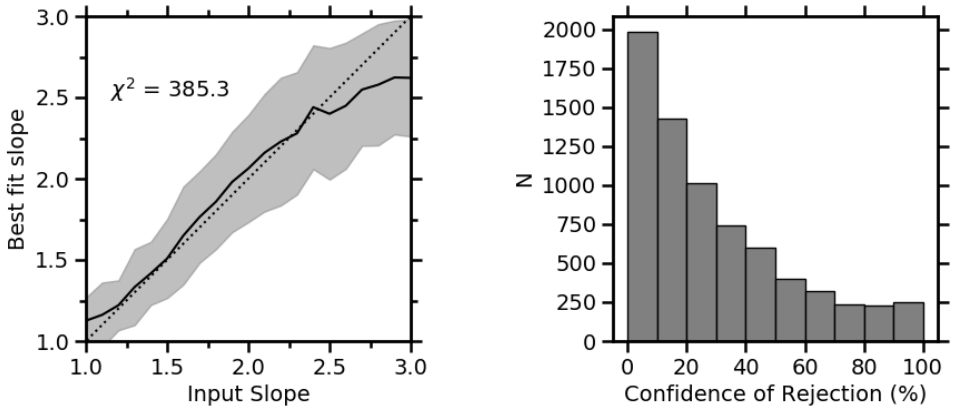

(A) Mean and standard deviations of the best fit slopes found for each input PSD slope.

(B) Distribution of the confidence of rejection for the SPL PSD recovery.

FIGURE 6.18: Results of the successfully recovered single power law fits using WFD cadenced light curves.

power law slope-redshift space respectively, similar to Figure 6.17b. These colour maps imply that the steeper slopes are more difficult to recover accurately, especially with decreasing luminosity or increasing redshift. This can be seen as the mean difference between the best fit and input slope reaches ~ 0.5, while for the shallower slopes the mean difference between the best fit and input slope is $\lesssim 0.3$. This could be a result of red-noise leakage again having more of an impact on the steeper slopes, or could be due to the cadencing of the DDF observations, as steeper slopes have more variability in longer timescales which are not probed as much as the shorter timescale variations.

Wide Fast Deep The SPL PSD slope recovery was also explored using the WFD cadenced light curves, where out of the initial 7730 mock AGN, a best fit power law could be recovered for 7200 ($\sim 93\%$). The mean best fit slope with the 1σ standard deviation is plotted for the range of input PSD slopes in Figure 6.18a, which displays a similar shape to Figure 6.16a, though the χ^2 is slightly worse with values of 335.0 and 385.3 for the DDF and WFD cadenced light curves respectively. Similarly, the distribution of the confidence of rejection is plotted in Figure 6.18b, which also shows a similar shape to Figure 6.16b. The dependence of recoverability on input parameters of the WFD AGN light curves are explored further in Appendix C, and are found to be similar to the results for DDF cadenced light curves. These results suggest that though the PSDs of the WFD light curves contain fewer data points, they still mostly contain sufficient information for recovering the underlying power law slope, therefore suggesting that reasonable single power law recovery can be expected for the less frequently observed AGN light curves in the WFD region. This therefore means that this analysis will be able to be performed on many more AGN observed with LSST.

6.4.4 Broken Power Law PSD Recovery Results

The recoverability of the parameters of the BPLs in the simulated LSST cadenced light curves were also explored using the methods described in Section 6.4.2.

Deep Drilling Field From the initial sample of 7730 mock AGN, best fit BPLs of the DDF cadenced light curves could be recovered for 7231 ($\sim$ 94%). Figure 6.19 displays the mean recovered parameters compared to the input parameters, as well as the distribution of the confidence with which we can reject the best fit model. It can be seen in Figure 6.19a that the mean recovered low-frequency power law slope, α, generally correlates well with the input parameter, however the uncertainty on the mean shows that the lower values are overestimated and the higher values are slightly underestimated. Figure 6.19b shows that the mean recovered values of the higher frequency power law slope, β, is consistently found to lie around $\sim$ 2.5 - 2.6. The characteristic break timescale is shown in Figure 6.19c to be reasonably well recovered, though values towards the limits deviate more, which is most likely the result of one power law dominating the PSD while the other likely has fewer data points to characterise it. A similar behaviour is shown in Appendix C for the results of the 1 day cadenced light curves for the recovery of the low-frequency power law slope and characteristic break timescale, however the high-frequency power law slope is much better recovered for the 1 day cadenced light curves which suggests that the DDF cadencing impacts the ability to recover the high-frequency slopes. Finally in Figure 6.19d, the confidence with which the best fit model can be rejected is shown to be small for the majority of AGN light curves.

Colour maps depicting the success of the recovery of the parameters of the BPL PSD are shown for the different combinations of AGN properties including luminosity, redshift, input values of power law slopes α and β, and timescales corresponding to the characteristic break frequencies, $t_{\rm br}$, in Figure 6.20.

Figure 6.20a displays the distribution of the mock AGN corresponding to those whose power law could not be fit within luminosity-redshift space, where the colour corresponds to the percentage of mock AGN in each bin that did not recover a power law. Figure 6.20b displays the mean rms difference of each parameter (α, β and $t_{\rm br}$) for the mock AGN light curve in luminosity-redshift space, where lighter colours correspond to larger rms differences. In both of these plots, similar distributions are found to the SPL recovery results where the low luminosity-high redshift AGN are more likely to not be able to recover a best fit PSD or to recover a best fit PSD with parameters that are most different from the inputs, likely as a result of observations being below the single epoch 5σ detection limits of LSST.

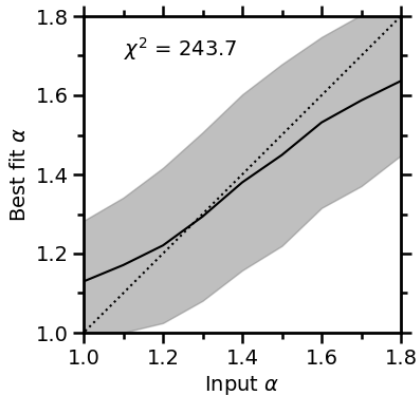

(A) Mean and standard deviations of the best fit low-frequency slopes found for each input low-frequency PSD slope.

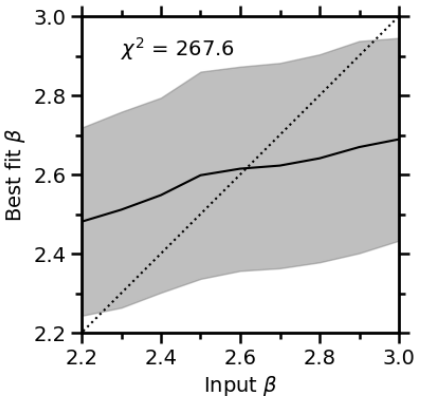

(B) Mean and standard deviations of the best fit high-frequency slopes found for each input high-frequency PSD slope.

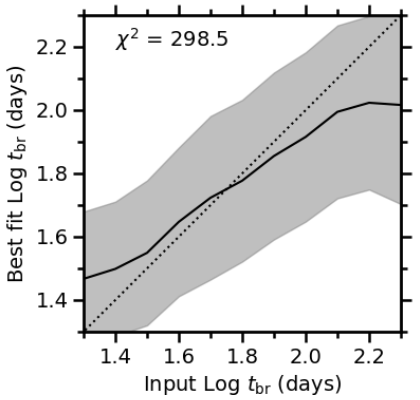

(C) Mean and standard deviations of the best fit break timescale found for each input break timescale.

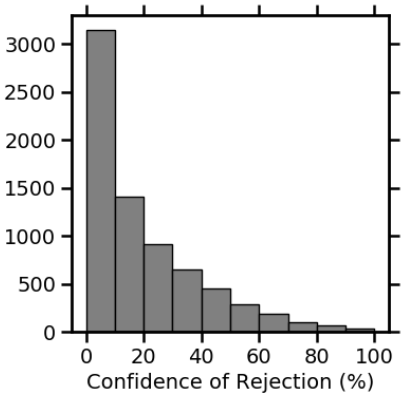

(D) Distribution of the confidence of rejection for the BPL PSD recovery.

FIGURE 6.19: Results of the successfully recovered broken power law fits using DDF cadenced light curves.

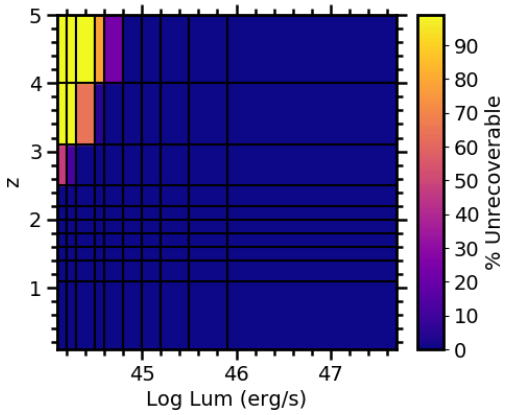

(A) The percentage of AGN of a given luminosity and redshift whose power law could not be fit using these methods.

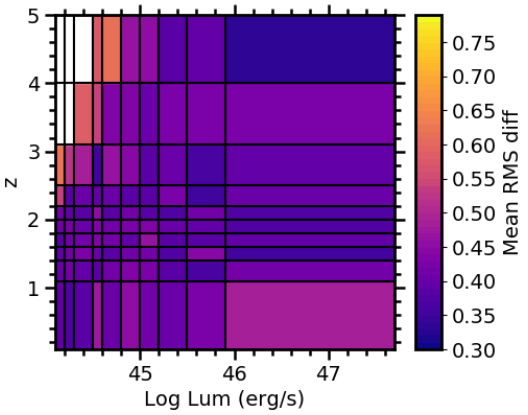

(B) The mean difference found between the recovered parameters and input parameters for the AGN of a given luminosity and redshift.

FIGURE 6.20: Colour maps depicting the ability to recover the input BPL PSD using DDF cadenced light curves depending on combination of parameters of the AGN. Each plot is divided such that each rectangle contains similar numbers of AGN, with the distributions given in Appendix C.

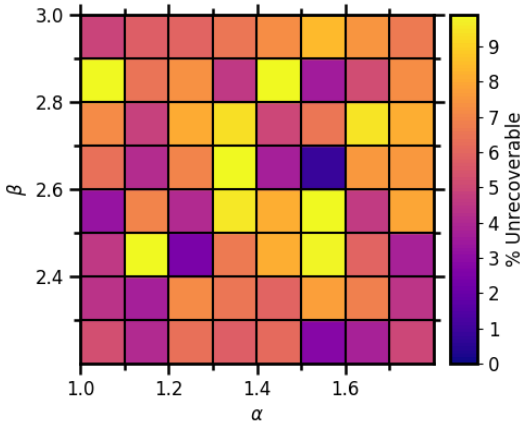

(C) The percentage of AGN of given power law slopes whose power law could not be fit using these methods.

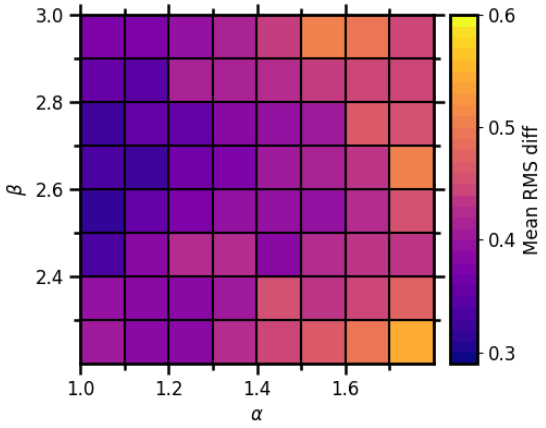

(D) The mean difference found between the recovered parameters and input parameters for the AGN of given input power law slopes.

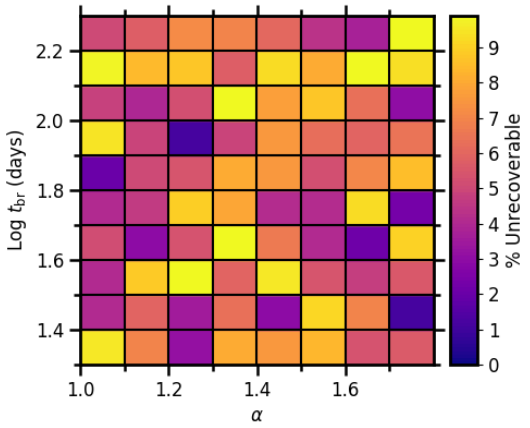

(E) The percentage of AGN of given low-frequency power law slope and break timescale whose power law could not be fit using these methods.

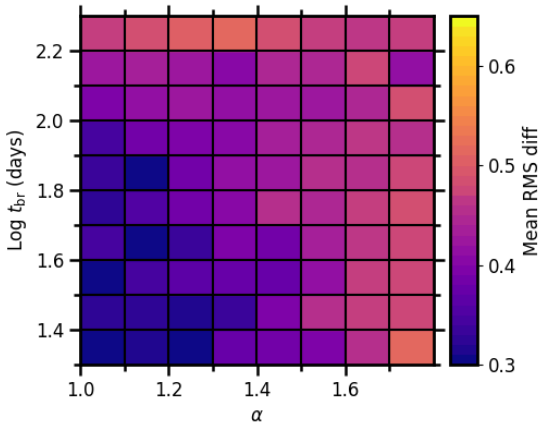

(F) The mean difference found between the recovered parameters and input parameters for the AGN of given low-frequency power law slope and break timescale.

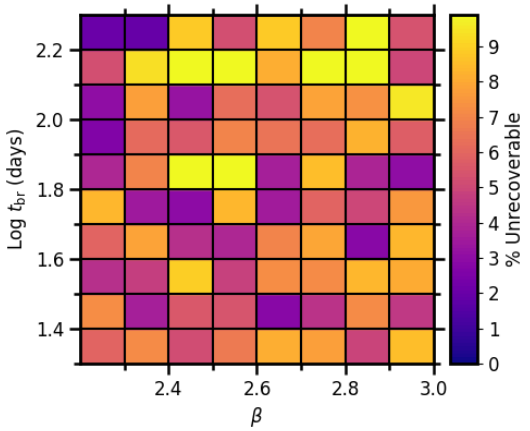

(G) The percentage of AGN of given high-frequency power law slope and break timescale whose power law could not be fit using these methods.

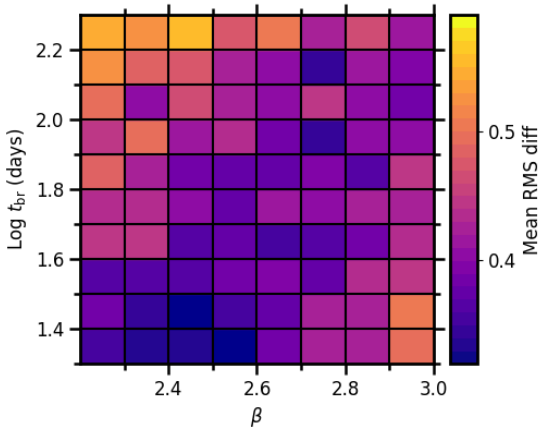

(H) The mean difference found between the recovered parameters and input parameters for the AGN of given high-frequency power law slope and break timescale.

FIGURE 6.20: Continued.

Figures 6.20c, 6.20e, and 6.20g show the number of AGN whose power laws could not be fit in terms of input power laws and characteristic break timescale space, similar to Figure 6.20a. These plots all show little dependence on the input values of the power law slopes and characteristic break timescales on the ability to recover best fits.

Similar to Figure 6.20b, Figures 6.20d, 6.20f, and 6.20h display the rms difference of the input parameters to the best fits, but in terms of input power laws and characteristic break timescale space. Figure 6.20d shows that shallower low-frequency power law slopes are better recovered than the steeper slopes and that the mean rms difference between input and best fit parameters is lowest when the high-frequency power law slope is in the range $\sim$ 2.4 - 2.8, however this is expected as Figure 6.19b demonstrated that most AGN light curves were found to be best modelled by high-frequency power laws in this range. Figure 6.20f shows that the combination of shallow low-frequency power law slope and small break timescales are best recoverable, which would be expected as those with smaller break timescales are mostly dominated by the low-frequency power law slope, meaning there would be more information available to recover values of α. Finally, Figure 6.20h shows a weak potential correlation between the high-frequency power slope and break timescales.

Additional plots of the dependence of different combinations of parameters on the success of recovering the parameters of the BPL PSDs are given in Appendix C.

Wide Fast Deep Additionally, the recoverability of the BPLs in the WFD cadenced light curves was explored. From the initial sample of 7730 mock AGN, a best fit broken power law was found for 7217 ($\sim$ 93%). The mean recovered parameters for these light curves compared to the input parameters are displayed in Figure 6.21. It can be seen that the shapes of these plots follow a similar shape to Figure 6.19, however the scatter is worse as shown by the values of χ^2. The distribution of confidence of rejection is plotted in Figure 6.21d and also has a similar spread to Figure 6.19d. The dependence of recoverability on input parameters of the WFD AGN light curves are explored further in Appendix C, and are found to be similar to the results for DDF cadenced light curves.

6.4.5 Exploring PSD Shape Classifications

In addition to exploring how well the parameters of the underlying PSDs could be recovered from simulated LSST cadenced light curves, I also investigated the ability to correctly identify the shape of the underlying PSD. This is necessary as incorrectly identified PSDs can confuse the overall results and make it more difficult to explain the observed behaviours. For example, BPLs have a characteristic timescale at which the power law slope changes which would be expected to be related to physical

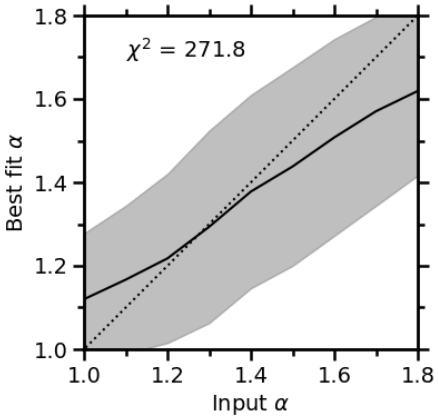

(A) Mean and standard deviations of the best fit low-frequency slopes found for each input low-frequency PSD slope.

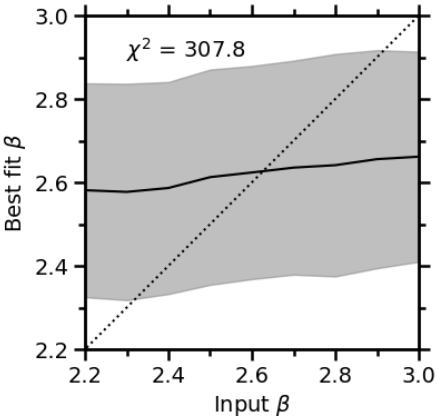

(B) Mean and standard deviations of the best fit high-frequency slopes found for each input high-frequency PSD slope.

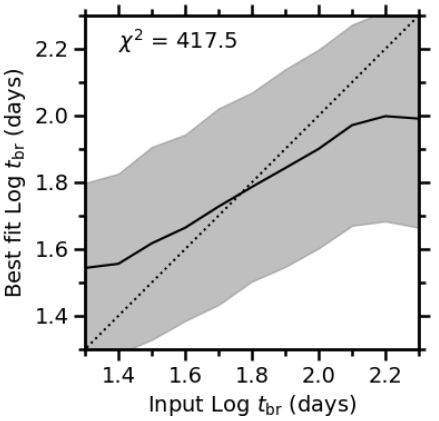

(C) Mean and standard deviations of the best fit break timescale found for each input break timescale.

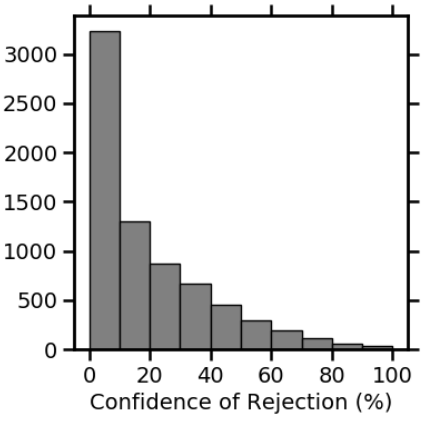

(D) Distribution of the confidence of rejection for the BPL PSD recovery.

FIGURE 6.21: Results of the successfully recovered broken power law fits using WFD cadenced light curves.

processes within the emission, however if SPLs are incorrectly classified as BPLs, then it would be harder to constrain any correlations of this characteristic timescale.

Therefore, in order to investigate this, I also used the SPL and BPL PSD slope recovery methods on the mock AGN light curves made from BPLs and SPLs respectively to estimate how often it should be expected that the shape of the PSD is incorrectly classified.

Deep Drilling Field I first tested these methods using the DDF cadenced light curves. Figure 6.22 shows a comparison between the distribution of the confidence with which the best fit PSD can be rejected for the mock AGN light curves made with the SPL and BPL. It can be seen in Figure 6.22a that the confidence of rejection peaks at $\sim 0\%$ when the input SPLs are fit with SPLs and it decreases towards high confidences

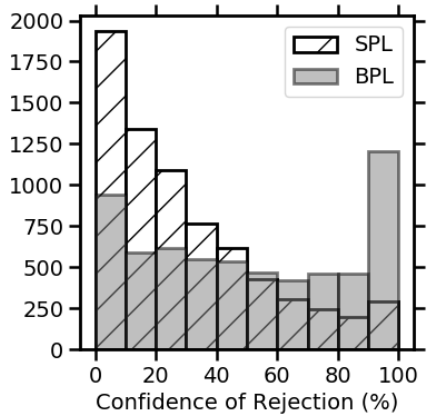

(A) Distributions of the confidence of rejection for the input SPL PSD recovery.

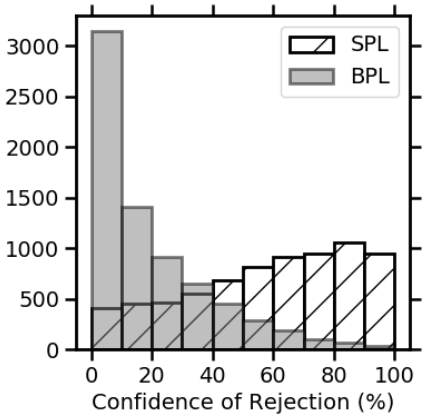

(B) Distributions of the confidence of rejection for the input BPL PSD recovery.

FIGURE 6.22: Comparison between the distributions of the confidence of rejections when using both the SPL and BPL recovery methods on both the input SPL and BPL DDF cadenced light curves.

TABLE 6.1: Number of DDF cadenced AGN light curves whose shapes are correctly and incorrectly classified.

Input ↓ Best Fit →	SPL	BPL	Not Recoverable
SPL	5627 ($\sim$ 73%)	1587 ($\sim$ 21%)	516 ($\sim$ 6%)
BPL	657 ($\sim$ 9%)	6574 ($\sim$ 85%)	499 ($\sim$6%)

of rejection. Whereas when the SPLs are fit with BPLs there is a strong peak at $\sim$ 100% which shows that the incorrect PSD shape is more often unable to find a good fit for the 'observed' PSD, however beyond this there is also a slight increase in confidence which suggests that some BPLs models are reasonably fit. Figure 6.22b similarly shows the peak in confidence of rejection at $\sim$0% which decreases towards higher confidences for the BPLs modelled as BPLs. When the BPLs are modelled as SPLs, the distribution increases with increasing confidence, however there is not as strong a peak at $\sim$ 100% which suggests that fewer 'observed' PSDs can't find a good fit at all.

For each mock AGN light curve, the confidence of rejection for the best fitting model PSD found with a SPL and BPL were compared in order to classify the shape of the PSD. For example, if the confidence of rejection for the SPL best fit PSD was smaller, then the underlying PSD used to create that AGN light curve is assumed to be a SPL. The percentage of the entire sample that were correctly or incorrectly classified, as well as those that could not be fit by either model, are summarised in Table 6.1.

It can be seen that the majority of AGN light curves created using BPLs are correctly identified, with 85% being detected as BPLs, while only $\sim$ 9% of the BPLs were falsely identified as SPLs. However the AGN light curves created using SPLs are shown to be more likely to be incorrectly identified, with $\sim$ 73% correctly identified as SPLs and 21% falsely classified as BPLs. 6% of the light curves are not well fit by either a SPL or

BPL model PSD, though these correspond to the light curves that had many observations that were below the 5σ detection limits of LSST.

To further explore the input PSD slopes of the AGN light curves that were incorrectly identified, I have plotted the corresponding distributions of the properties of the mock AGN. For example, the distribution of luminosity, redshift and input power law slope of the AGN light curves made using SPLs are shown in Figure 6.23. In Figures 6.23a and 6.23b, the shape of the luminosity and redshift distributions are shown to remain approximately consistent for the correct and incorrect classifications, which implies that these does not impact the results. However the shape of the distribution of the input power law slope is shown to differ in Figure 6.23c. Specifically, most of the incorrect classifications correspond to the light curves made from input power law slopes of $\sim$ 1.5-2.5.

Similarly the distribution of the parameters for the AGN light curves made with BPL PSDs are displayed in Figure 6.24 for α, β, $t_{\rm br}$. It can be seen in Figure 6.24a that the input α of the BPLs that are incorrectly recovered as SPLs seems to have the strongest impact as they are mostly found in the upper limit. Figure 6.24b shows that there is a weaker preference for a smaller values of β in those that are falsely classified, and Figure 6.24c shows that there is a small peak at the lower limit for $t_{\rm br}$ in the distribution of mock AGN that are falsely classified.

Figure 6.25 then shows the distribution of best fit parameters recovered for the SPLs incorrectly classified as BPLs. Figure 6.25a shows that the majority of recovered αs are found at the upper limit, while Figure 6.25b shows that the majority of recovered βs at the lower limit. Furthermore, Figure 6.25c shows that the recovered values of $t_{\rm br}$ are most often found at either the upper or lower limits, which suggests that these BPLs are mostly dominated by either the α or β components. This could imply that the BPL shape is difficult to distinguish from SPLs given the scatter on the observed PSDs, and therefore could explain the confusion of the classifications.

Furthermore, the slopes of the SPLs that are falsely found to best fit the BPLs are given in Figure 6.26, which shows that they are mostly found with values between 1 and 2.

Wide Fast Deep The ability to correctly recover the shape of the PSD was also tested for the WFD cadenced light curves. Figure 6.27 displays a comparison of the distribution of confidence of rejection for the mock AGN light curves, where it can be seen that the input SPL have a similar distribution as shown in Figure 6.22, however more AGN are detected with BPL PSDs with a smaller confidence of rejection. The distribution for the input BPLs with SPL fits are shown to be detected with almost even numbers for each confidence of rejection. This differs from Figure 6.22 which has an increase from low to high confidence of rejections, and therefore suggests that the WFD cadenced light curves cannot be as confidently rejected.

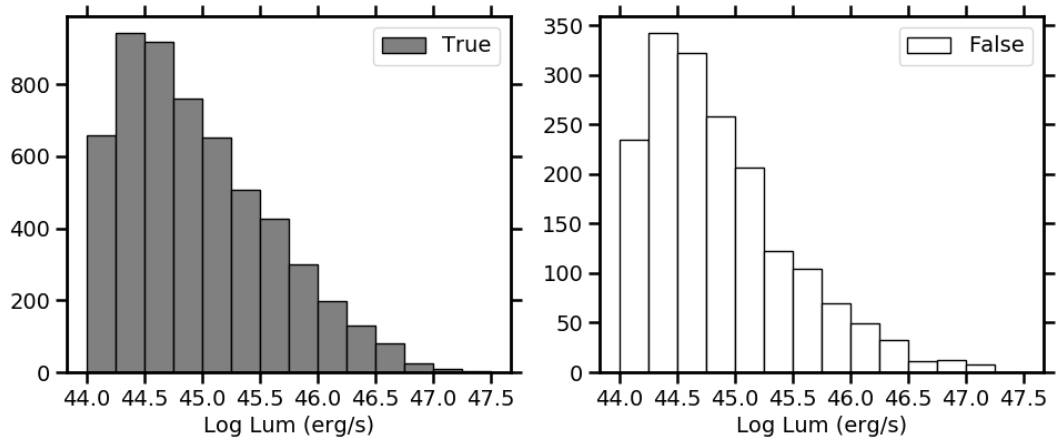

(A) Distributions of luminosity corresponding to the SPL light curves that are correctly and incorrectly identified as SPLs.

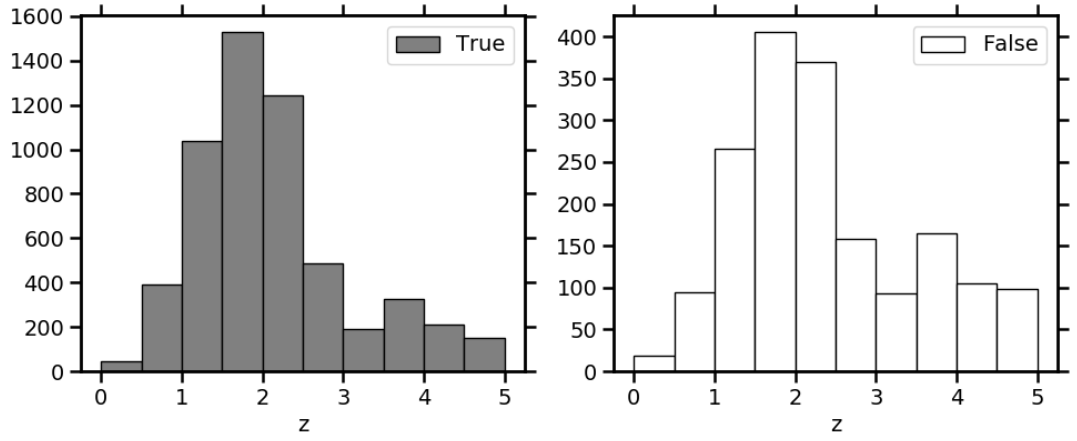

(B) Distributions of redshift corresponding to the SPL light curves that are correctly and incorrectly identified as SPLs.

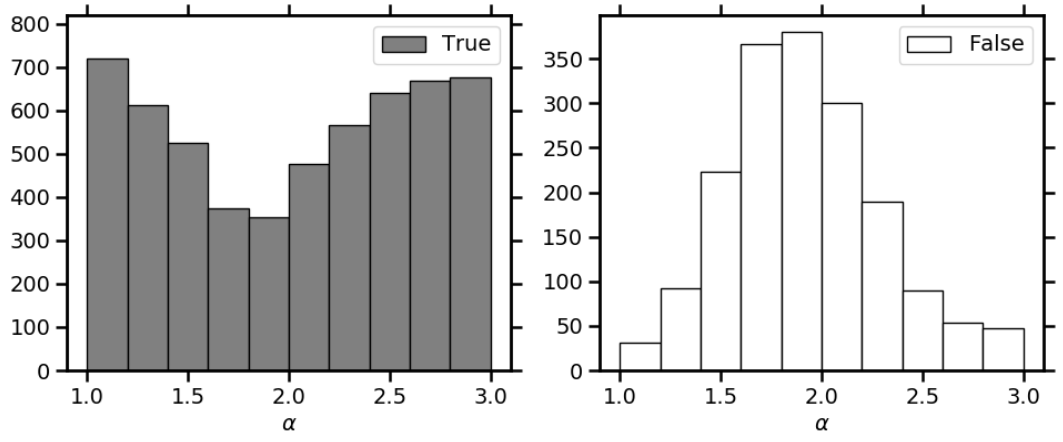

(C) Distributions of input power law slope corresponding to the SPL light curves that are correctly and incorrectly identified as SPLs.

FIGURE 6.23: Distributions of parameters corresponding to the SPL DDF cadenced light curves that are correctly and incorrectly identified as SPLs.

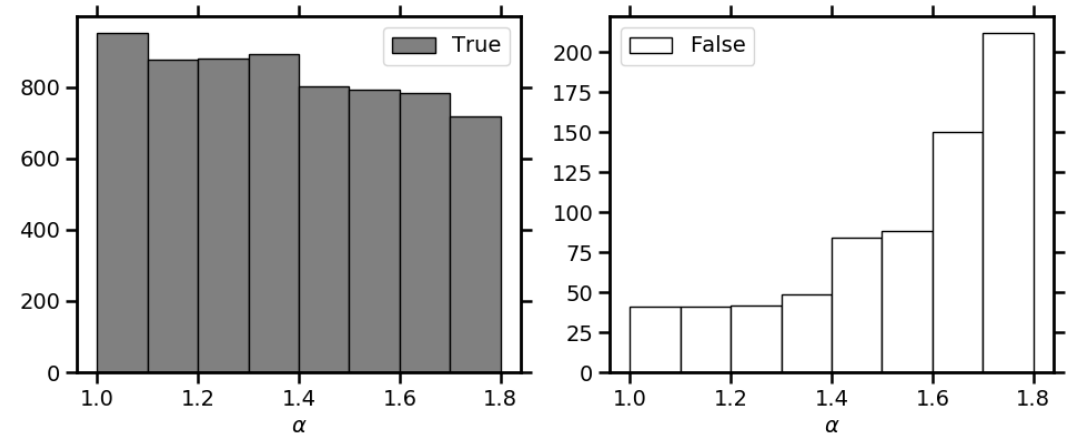

(A) Distributions of low-frequency power law slope corresponding to the BPL light curves that are correctly and incorrectly identified as BPLs.

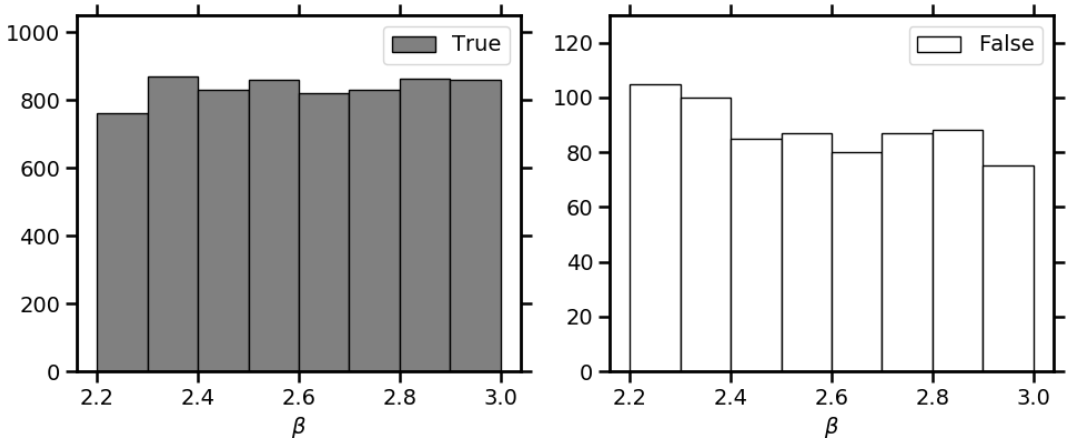

(B) Distributions of high-frequency power law slope corresponding to the BPL light curves that are correctly and incorrectly identified as BPLs.

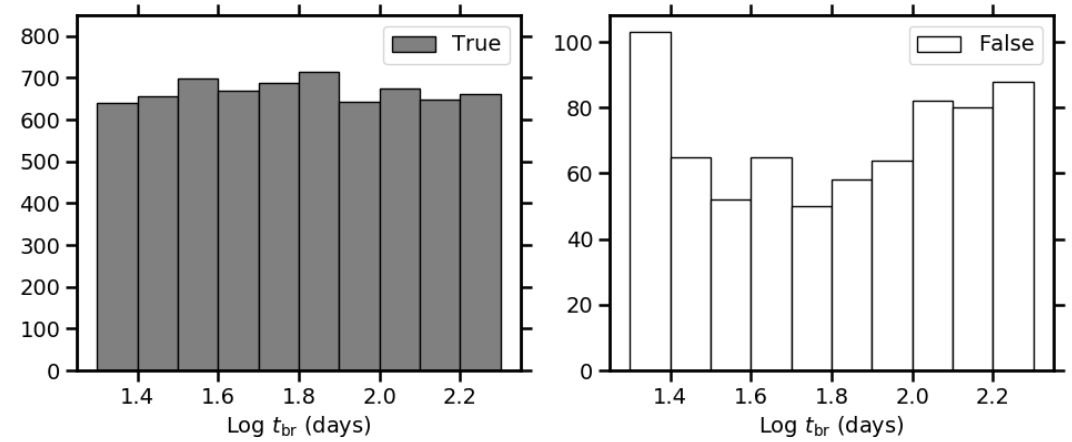

(C) Distributions of break timescale corresponding to the BPL light curves that are correctly and incorrectly identified as BPLs.

FIGURE 6.24: Distributions of parameters corresponding to the BPL DDF cadenced light curves that are correctly and incorrectly identified as BPLs.

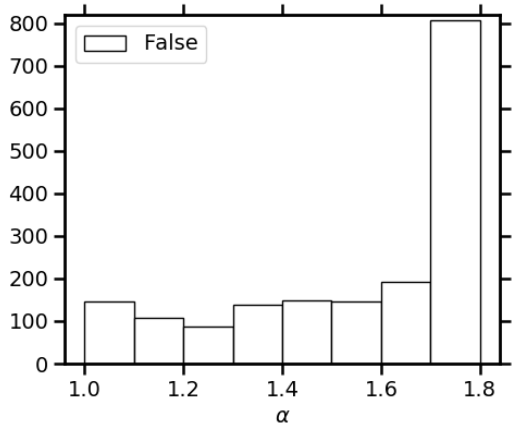

(A) Distributions of the low-frequency power law slope found for the SPL light curves that are incorrectly identified as BPLs.

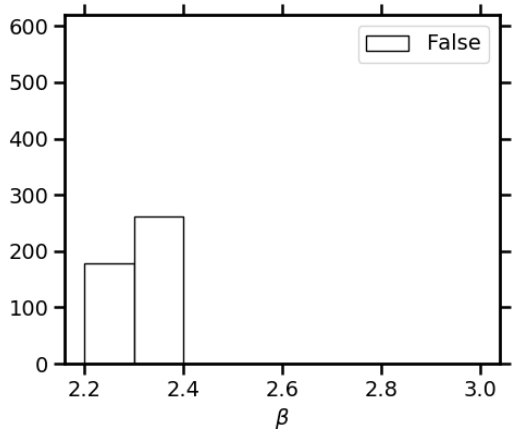

(B) Distributions of the high-frequency power law slope found for the SPL light curves that are incorrectly identified as BPLs.

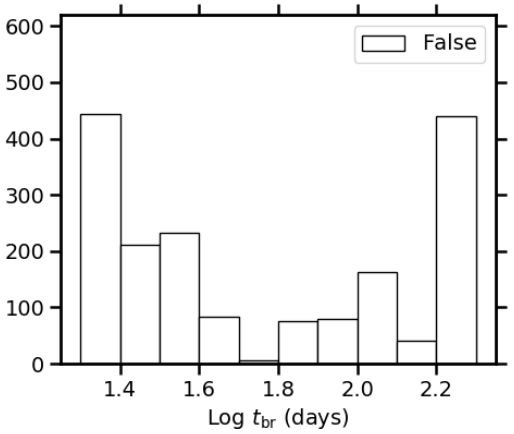

(C) Distributions of the break timescale found for the SPL light curves that are incorrectly identified as BPLs.

FIGURE 6.25: Distributions of the BPL parameters found to best fit the SPL DDF cadenced light curves that are incorrectly identified as BPLs.

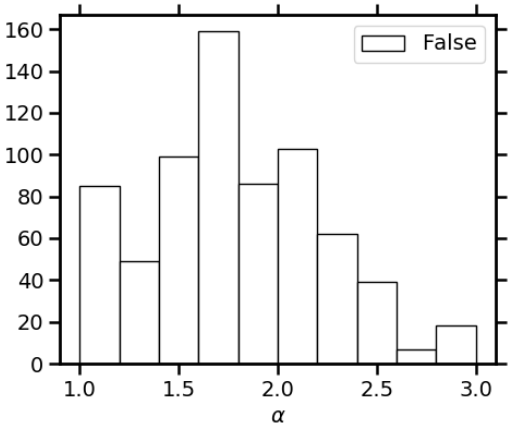

FIGURE 6.26: Distributions of the power law slope of the SPL that is found to best fit the BPL DDF cadenced light curves that are incorrectly identified as SPLs.

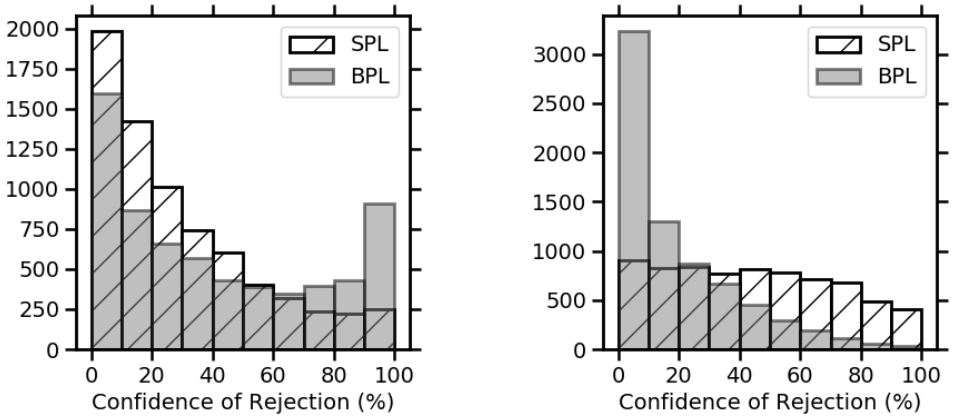

(A) Distributions of the confidence of rejection for the input SPL PSD recovery.

(B) Distributions of the confidence of rejection for the input BPL PSD recovery.

FIGURE 6.27: Comparison between the distributions of the confidence of rejections when using both the SPL and BPL recovery methods on both the input SPL and BPL WFD cadenced light curves.

TABLE 6.2: Number of WFD cadenced AGN light curves whose shapes are correctly and incorrectly classified.

Input ↓ Best Fit →	SPL	BPL	Not Recoverable
SPL	4556 (∼59%)	2645 (∼34%)	529 (∼7%)
BPL	928 (∼12%)	6289 (∼81%)	513 (∼7%)

Table 6.2 shows the number of mock AGN that are detected with real and false PSD shapes. $\sim$ 7% of the light curves were not able to be fit with either SPLs or BPLs, which correspond to those whose emission is mostly not detectable within the 5σ detection limit of LSST. The success of detection of input BPL PSDs is approximately consistent for WFD cadenced light curves and DDF cadenced light curves, with $\sim$ 81% and 85% being correctly classified as BPLs respectively, however the SPL detection is much worse for the WFD cadenced light curves as only $\sim$ 59% are correctly identified as SPLs compared to the $\sim$ 73% for the DDF cadenced light curves.

To further investigate this, the distributions of input parameters that correspond to true and false classifications were also explored in Figure 6.28. Figure 6.28a contains the distributions of input parameters of the light curves made using input SPLs that are detected as SPL and BPL, and Figures 6.28b, 6.28c and 6.28d contain the distribution of the best fit BPL parameters; α, β and $t_{\rm br}$, that are recovered. Most of the incorrectly classified PSDs are shown in Figure 6.28a to be those whose input power law slope is between 1.5 and 2.5, and these are detected as BPLs with small or large values of $t_{\rm br}$ which means the BPL is dominated by either the low-frequency or high-frequency slope. This differs from the DDF cadenced light curves as more of the flatter input power laws are falsely detected as BPL here, which could be due to the reduced cadence of the WFD light curves as shallower power laws have more emphasis on the short-term variations.

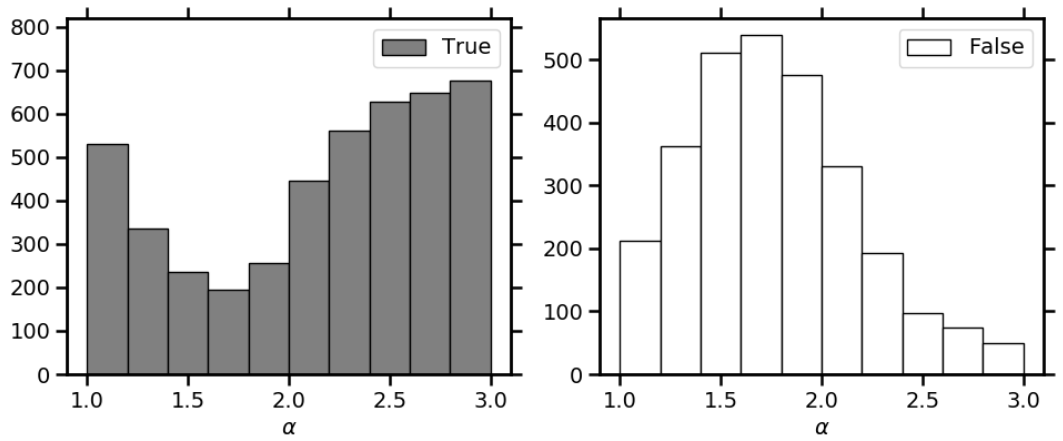

(A) Distributions of input power law slope corresponding to the SPL light curves that are correctly and incorrectly identified as SPLs.

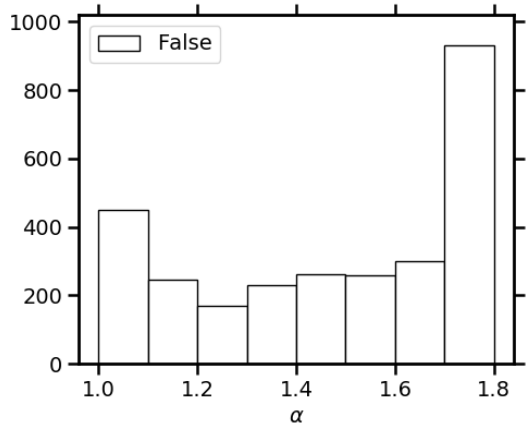

(B) Distributions of the low-frequency power law slope found for the SPL light curves that are incorrectly identified as BPLs.

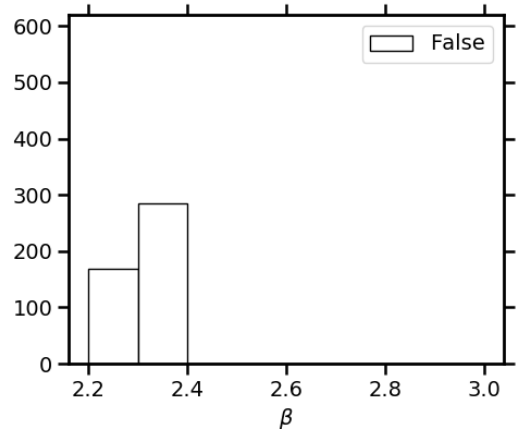

(C) Distributions of the high-frequency power law slope found for the SPL light curves that are incorrectly identified as BPLs.

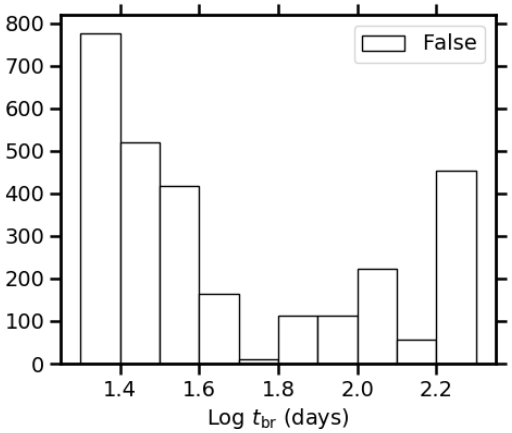

(D) Distributions of the break timescale found for the SPL light curves that are incorrectly identified as BPLs.

FIGURE 6.28: Distributions of the BPL parameters found to best fit the SPL WFD cadenced light curves that are incorrectly identified as BPLs.

Additionally, the parameters for the WFD BPL light curves that are correctly and incorrectly classified are displayed in Appendix C and are shown to be similar to results for the DDF cadenced light curves.

6.4.6 Discussion

In this Section, I explored the recoverability of properties of both single power law PSDs and broken power law PSDs using stochastic hillclimbing algorithms that used the PSRESP method described by Uttley et al. (2002) of fitting power law slopes to observed PSDs.

Recovering Underlying PSD Slopes and Break Frequencies For the SPLs, a fit could be found for 7214 of the initial 7730 AGN DDF cadenced light curves. Furthermore the recovered slopes were found to be consistent with the inputs, though a slightly larger deviation from the input power law slope was found for steeper slopes. As this behaviour was similarly shown in Appendix C for the 1 day cadenced light curves, it therefore suggests that the cadencing of LSST was not responsible, but it is likely due to effects such as red-noise leakage.

For the BPL recovery using DDF cadenced light curves, fits were found for 7231 of the initial AGN sample. These fits were also shown to be reasonable for the low-frequency power law slope though the same deviation was seen for steeper slopes. Additionally, the characteristic break timescale was also shown to be reasonably well fit, though a slightly worse recovery was found for characteristic break timescales at either limit which correspond to PSDs that are dominated by either the high-frequency or low-frequency power law. Furthermore, the mean high-frequency power law slope recovered for each input value was shown to be found between 2.5-2.6 for all input slopes, with an increase from shallow to steeper slopes. This behaviour for the high-frequency power law slope recovery is not seen in the results of the recovery of the parameters of the 1 day cadenced light curves given in Appendix C, which therefore suggests that the LSST cadencing does limit the ability to recover the behaviour at higher frequencies.

To assess the recovery of the parameters in these models, the values of the power law slopes were limited to < 3 as a result of red-noise leakage having a larger impact on steeper slopes, which therefore excludes analysis of steeper PSD slopes that have been reported by several authors (e.g., Mushotzky et al., 2011; Caplar et al., 2017; Smith et al., 2018a). For both models, further analysis showed that the recovery of the power law slope was found to be better for high luminosities, low redshifts and shallower power law slopes. The recovered values corresponding to the steeper slopes were also shown to be more likely to deviate for both models which is believed to be due to the

effects of red-noise leakage which has been shown to distort slopes of $\alpha > 2$ towards $\alpha = 2$ (e.g., Uttley et al., 2002). Future analysis of steeper slopes could potentially be explored using alternate methods that attempt to overcome the issue of red-noise leakage, include the normalized leakage spectrum introduced by Zhu and Xue (2016), which described the effects of red-noise leakage power on the observed PSD in order to constrain the underlying PSD.

For the BPLs, the location of the break-frequency was limited to values corresponding to observed timescales of $\sim$ 20-200 days as a result of binning of the periodograms. Observing smaller observed break timescales is not possible with the current proposed cadence of LSST observations, and potential longer timescales within the baseline of LSST observations would require alternate methods or different binning in the analysis.

Finally in this section, only SPL and BPL PSD shapes were explored, though several authors have also reported optical AGN PSD fits using bending power laws instead of broken (e.g., Carini and Ryle, 2012; Smith et al., 2018a). Further analysis of the recoverability of these models separate for the simpler SPL and BPL models could therefore be explored in the future.

Classifying Underlying PSD shape Additionally, identification of each type of power law was explored by comparing the confidence with which both models could be rejected for each AGN light curve. It was found that the input BPLs had a higher rate of being correctly identified as BPLs, with 85% of the DDF cadenced light curves having a lower confidence of rejection with a BPL fit than SPL fit. The distribution of parameters of the BPLs that were incorrectly identified were shown to have a strong dependence on low-frequency power law slope and weak dependences on high-frequency slope and characteristic break timescale, where most false detections corresponded to steep low-frequency power laws slopes, shallower high-frequency power law slopes, and break frequencies located towards either limit. Furthermore, these BPLs were often detected as SPLs with power law slopes between 1.5 and 2.5.

The SPLs were more likely to be confused with BPLs, with a correct identification rate of 73% for the DDF cadenced light curves, and 21% being falsely identified as BPLs. The false identifications were more likely to occur for input single power law slopes around 1.5 and 2.5. Furthermore, the incorrectly classified SPLs are mostly found to be better fit by steep low-frequency power law slopes and shallow high-frequency power law slopes, with characteristic break timescales corresponding to the upper and lower limits which means the BPL is mostly dominated by either the higher or lower frequency slope.

The rate of false classifications found here could create inaccuracies and impact on any conclusions drawn from the AGN that will be observed with LSST, so alternative

methods might be needed to distinguish between the different types of underlying power law. Alternatively, a limit could be applied to the accepted confidences of rejection, where those AGN that have best fits with a higher confidence of rejection than the specified limit will be excluded from the overall analysis.

Finally, similar results were found when analysing light curves cadenced to match the WFD region which again implies the differences between observations of these regions has very little impact on the overall results and the analysis could be performed on a greater sample of AGN that will be observed in these regions.

6.5 Recovering Quasi-Periodicities within the PSDs

While most AGN light curves are consistent with stochastic variability, quasi-periodicity has been reported in some (e.g., Sillanpaa et al., 1988; Valtonen et al., 1988; Gierliński et al., 2008; Alston et al., 2014, 2015; Graham et al., 2015; Liu et al., 2015; Bhatta et al., 2016; Zheng et al., 2016; Zhang et al., 2017, 2018). This could be the result of red-noise processes mimicking periodic behaviour, or alternatively, QPOs and SMBHB systems can also potentially create this observed quasi-periodicity as described in Section 1.4.3.

Identifying quasi-periodicities within AGN light curves has been difficult due to factors including the baselines of current available observation campaigns for AGN (e.g. Vaughan and Uttley, 2005), which makes it interesting to predict what could be detected from such a large sample of AGN that will be observed with LSST.

6.5.1 Simulating Quasi-periodicities in PSDs

I simulated light curves for each mock AGN described in Section 6.2.1 with quasi-periodicities that are represented by a Lorentzian function, as described by Equation 6.11 (Vaughan and Uttley, 2005), superimposed onto a random SPL PSD with power law slope between $1.0 \leq \alpha \leq 3.0$.

$$L(f) = \frac{R^2 Q f_0 / \pi}{f_0^2 + Q^2 (f - f_0)^2} \tag{6.11}$$

where f_0 is the centroid frequency of the peak, Q is the quality factor that characterises the coherence of the QPO ($Q = f_0/\text{FWHM}$, where FWHM is the full width half maximum of the peak), and R is the normalisation factor that gives the strength of the quasi-periodic component, which can be approximated as the fractional rms amplitude of the Lorentzian component.

Low frequency QPOs are the most likely to be detected with LSST sampling due to the predicted QPO frequency ranges that correspond to rest frame timescales of $\sim$ 1-1000 days for the AGN in the mock sample. These QPOs have been observed with quality factors and rms amplitudes ranging from $Q \lesssim 3$ and a few percent respectively, to $Q \gtrsim 8$ and R $\lesssim$ 20% depending on the subclass (e.g Ingram and Motta, 2019). As there are no confirmed SMBHBs, the corresponding parameters for the Lorentzian component are not well-constrained. Therefore, I chose to explore the possible quasi-periodicity detection with LSST cadencing using centroid frequencies that corresponded to observed quasi-period timescales of $1.0 \leq \text{Log } t_0[\text{days}] \leq 3.5$, which approximately covered the mean cadencing of each observation season up to the baseline of LSST's observations. I assigned each AGN in the mock sample a random quasi-period from this range, and also assigned them a random quality factor from the range $0 \leq Q \leq 15$ and a random normalization factor between $0 \leq R \leq 30\%$.

Figure 6.29 displays examples of light curves made with different quasi-periodicities superimposed on the SPL PSDs.

6.5.2 Methods for Recovering properties of PSDs with QPOs

In Section 6.4, classical periodograms were used to estimate the PSDs. These periodograms rely on evenly sampled data, and therefore the light curves were first interpolated. However, for quasi-periodicity detection this interpolation can distort the results, so instead I used the Lomb-Scargle periodogram (LSP, Lomb 1976; Scargle 1982) described in Section 3.4, which is a well known algorithm used in astronomy for detecting quasi-periodicity in unevenly sampled data. To quantify the significance of a quasi-periodicity detection, simulated LSPs are used to create significance contours.

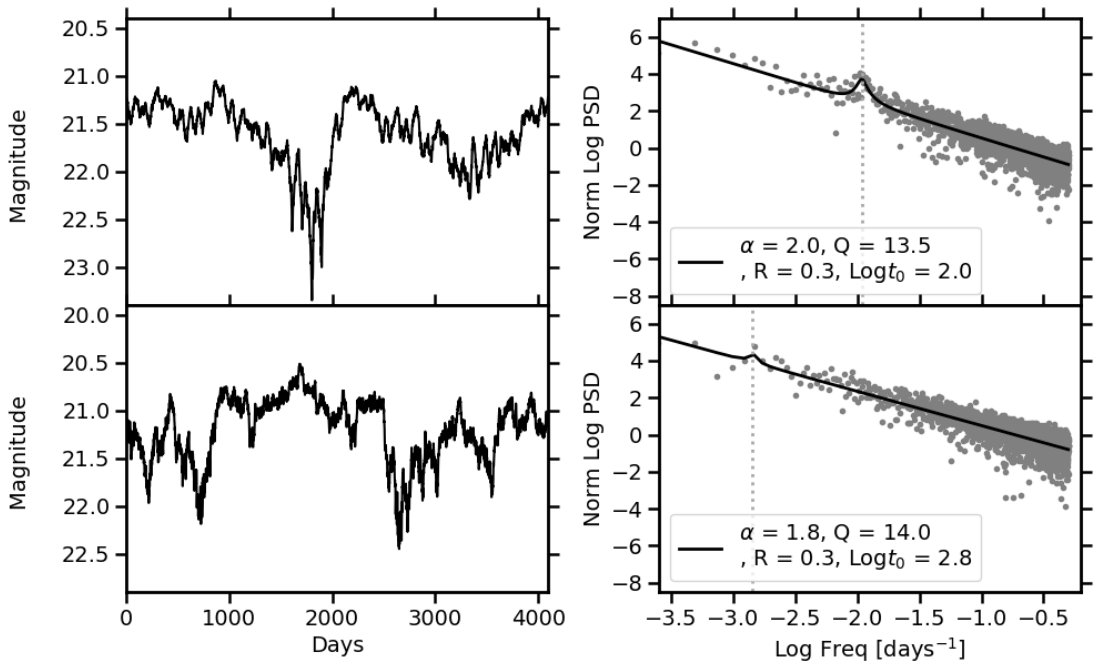

FIGURE 6.29: Examples of light curves made from single power law PSDs with QPO superimposed, with different quasi-periodicities.

Both the observed LSP and the significance contour were binned in log frequency space to remove multiple peak detections due to oversampling at the higher frequencies, and any peak in the observed LSP greater than the significance contours was deemed a significant quasi-periodicity detection. Note that here I decided not to use the requirement of each frequency bin to have a minimum of 3 data points so that the detection of quasi-periodic behaviour at lower frequencies could still be explored.

Examples of this method of quasi-periodicity detection are given in Figure 6.30, using both a cadenced light curve and a continuous light curve to demonstrate how the sampling can affect the quasi-periodicity detection. Figure 6.30b contains the LSP created using a continuous light curve, where the significance contours are shown to be approximately a smooth line. In contrast, the LSP in Figure 6.30c shows significance contours where multiple peaks can be seen, demonstrating how sampling of the light curve can lead to false quasi-periodic detections. Additionally, a significant peak is detected in Figure 6.30b, however due to the sampling of the cadenced light curve there is no corresponding peak in Figure 6.30c. Furthermore, the effect of red-noise leakage is also evident in the cadenced LSP.

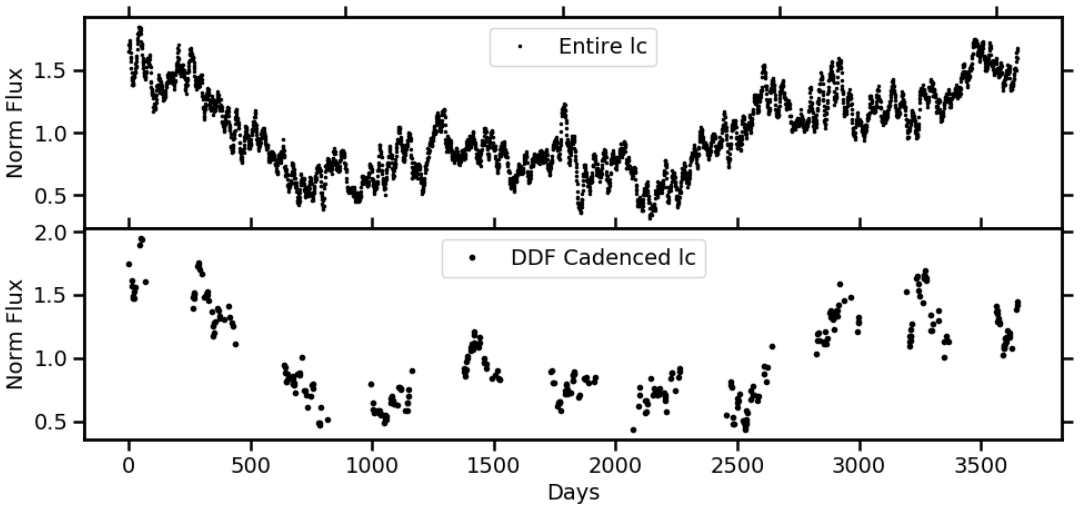

(A) Light Curves with 1-day cadencing and DDF cadencing.

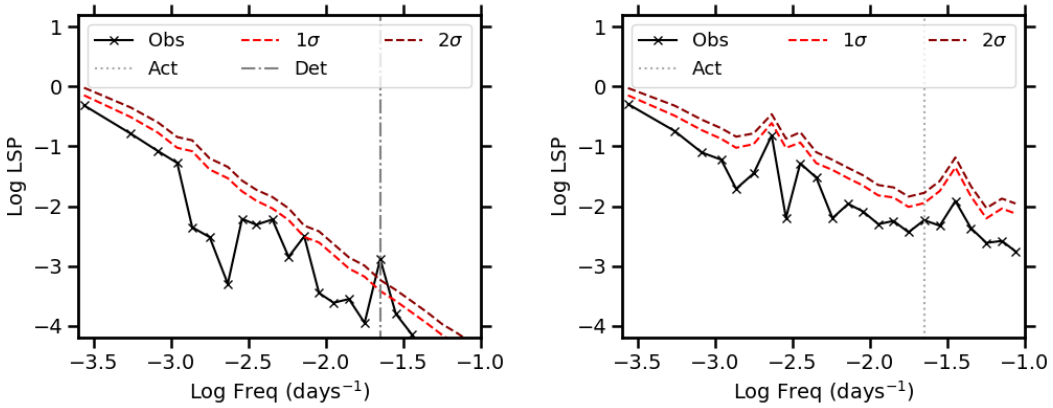

(B) Example of the Lomb-Scargle periodograms for the 1-day cadenced light curves.

(C) Example of the Lomb-Scargle periodograms for the DDF cadenced light curves.

FIGURE 6.30: Examples of Lomb-Scargle periodograms created from light curves with different cadencing.

6.5.3 Results of the Quasi-Periodicity Detection

Entire Light Curves To test the significance detection of the peaks in the LSP, I first tried the method described above on the continuous, 1 day cadenced light curves for the observations up to 10 years. For this test, I calculated the significance contours by simulating light curves with underlying PSD using the true input power law slopes to simulate the best case scenario of the recovery.

From the initial 7730 AGN in the mock sample, 4681 had quasi-periodicities detected above the 1σ significance contour, and 2969 detected above the 2σ significance contour. Note that some light curves resulted in detections of more than one quasi-periodicity due to multiple peaks in the LSP, and therefore the overall number of quasi-periodicities detected above the 1σ and 2σ significance contours were 5852 and 3469 respectively.

For the detection to be classified as true, I required the peak log frequency to be within 0.1 of the input peak due to the widths of the resampled bins chosen. Thus from the 1σ detected peaks, 2209 and 3643 were classified as true and false detections respectively, and for the 2σ detected peaks, 1607 and 1862 were classified as true and false detections respectively. This shows that in both cases, more false detections were recovered than true.

Figure 6.31 further explores the parameter spaces that correspond to these true and false quasi-periodicities detected. For the most part, the 1σ and 2σ detections have similar distributions of parameters.

Firstly, it can be seen in Figure 6.31a that the quasi-periodicities that are falsely detected have a different distribution to those that are true detections as the true detections mostly consists of shorter quasi-periodicities while the false quasi-periodicities has a peak at ~ 3. This is likely due to the small number of data points binned in the LSP at low frequencies. The shorter quasi-periods are also expected to be easier to detect than the longer quasi-periods as more cycles are covered in the light curves.

Figure 6.31b shows that the false quasi-periodicities that are detected are distributed approximately evenly across the different input power law slopes, especially for the 1σ detections, though there could be a weak trend of more detections for steeper slopes for the 2σ detections. The true detections appear to have a strong dependence power law slope, with detections more likely for steeper power laws. Shorter quasi-periodicities are likely to be easier to detect in the light curves corresponding to steep slopes as the steeper slopes usually have more power in the longer term variations, therefore the additional short-term quasi-periodicities could be easier to distinguish.

Figure 6.31c shows that the strength of the QPO is approximately evenly distributed for the false detections, while the true detections are more likely for stronger QPOs which is likely because the QPO is easier to distinguish from the underlying SPL.

Finally a weak preference is seen for narrower QPOs in the true detections in Figure 6.31d, which is likely due to the binning of the LSP, meaning the width is not really distinguishable.

Appendix C contains additional colour maps of the distribution of recovered quasi-periodicities depending on combinations of parameters. No clear relation is seen between luminosity and redshift, though the detections peak as expected from the 1D histograms shown in Figure 6.31.

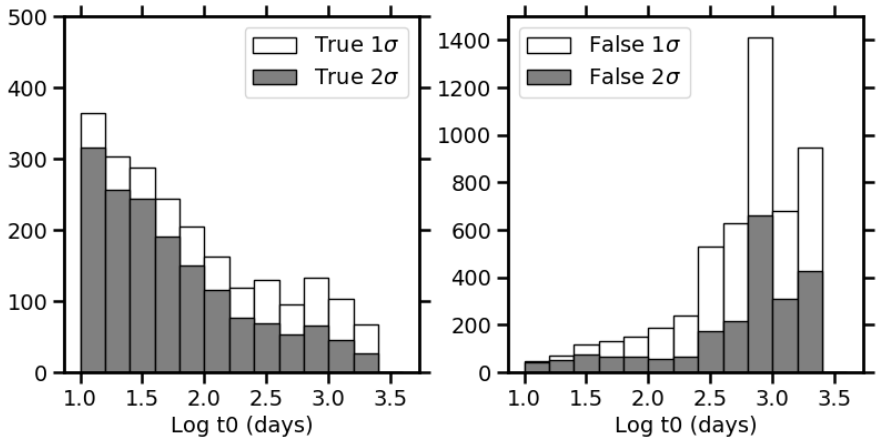

(A) Distributions of the quasi-periodicity of the AGN light curves corresponding to true and false quasi-periodicity detections. Note that the scale of the false detection histograms is a factor of 3 greater than of the true detections.

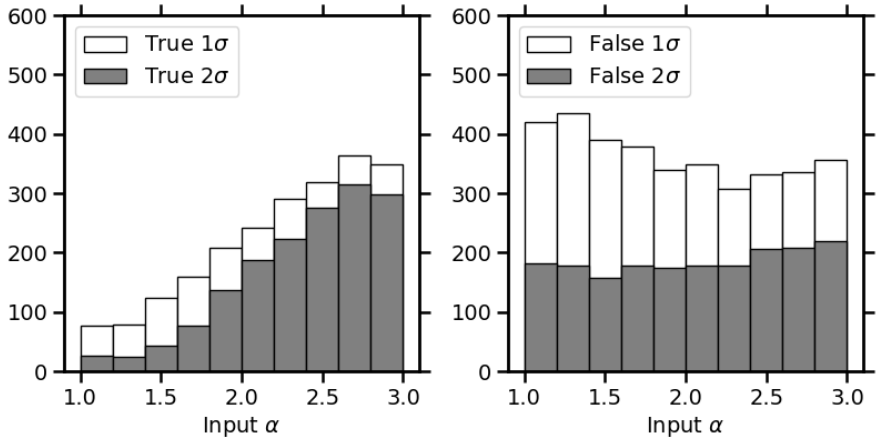

(B) Distributions of the PSD power law slope of the AGN light curves corresponding to true and false quasi-periodicity detections.

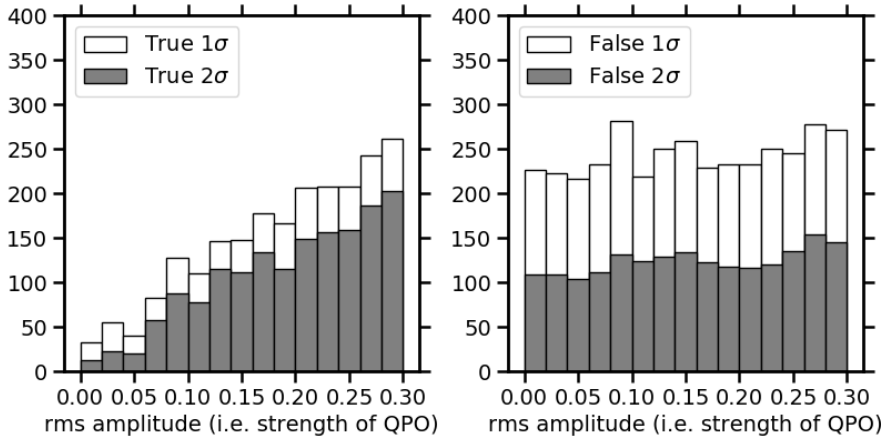

(C) Distributions of the strength of the QPO of the AGN light curves corresponding to true and false quasi-periodicity detections.

FIGURE 6.31: Distributions of the parameters of the AGN light curves corresponding to true and false quasi-periodicity detections.

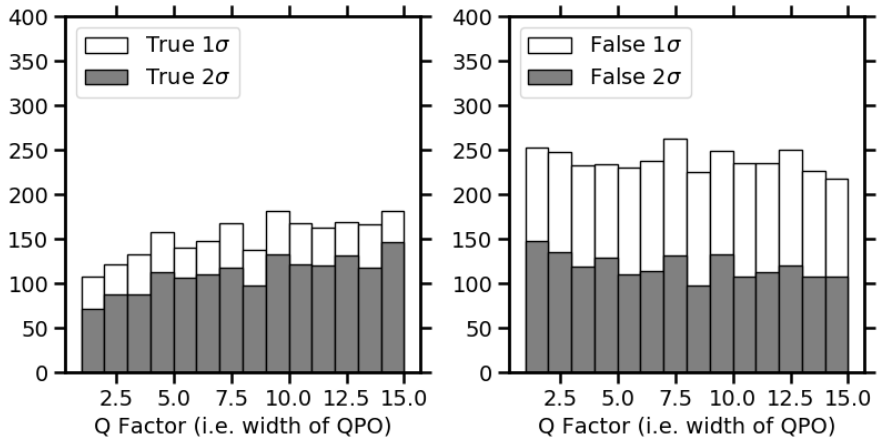

(D) Distributions of the width of the QPO of the AGN light curves corresponding to true and false quasi-periodicity detections.

FIGURE 6.31: Continued.

Deep Drilling Field Significant quasi-periodicity detection was then explored with the DDF cadenced light curve LSPs. Here the significance contours used to define quasi-periodicity detection were calculated using simulated light curves whose power law slope corresponded to the best fit power law of the SPL recovery analysis explained above.

3067 quasi-periodicities were detected above 1σ significance contours, and 1369 of these were significant above the 2σ confidence contours, however of these quasi-periodicities, only 429 and 158 were classified as true detections as described above, and 2834 and 1231 were false detections for the 1σ and 2σ detections respectively.

Figure 6.32 explores the input parameters that correspond to the true and false quasi-periodicity detections for these light curves. It can be seen that the true and false detections follow similar distributions to each other for all parameters including quasi-periodicity, power law slope, strength of QPO, and width of QPO in Figures 6.32a, 6.32b, 6.32c, and 6.32d respectively, though the true detections have slightly more scatter probably due to the small number of objects in each bin.

Wide Fast Deep Furthermore, quasi-periodicity detection with WFD cadenced light curves was also explored using these methods, and the results found 3293 AGN with quasi-periodicities detected above 1σ significance contours, and 1359 of these were significant above the 2σ confidence contours. Of these quasi-periodicities, only 425 and 164 were classified as true detections as described above, and 3068 and 1216 were false detections for the 1σ and 2σ detections respectively. This shows that fewer quasi-periodicities were correctly identified for the less well observed light curves, but Appendix C shows that the distribution of the true detections is similar to Figure 6.32.

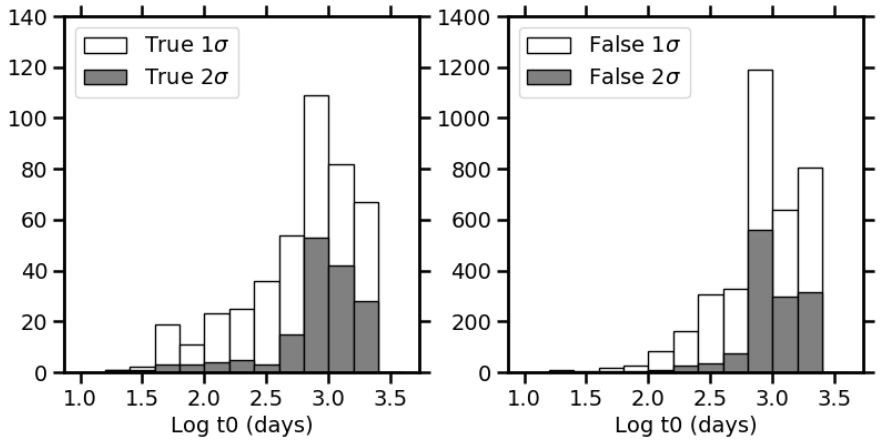

(A) Distributions of the quasi-periodicity of the AGN light curves corresponding to true and false quasi-periodicity detections. Note that the scale of the false detection histograms is a factor of 10 greater than of the true detections.

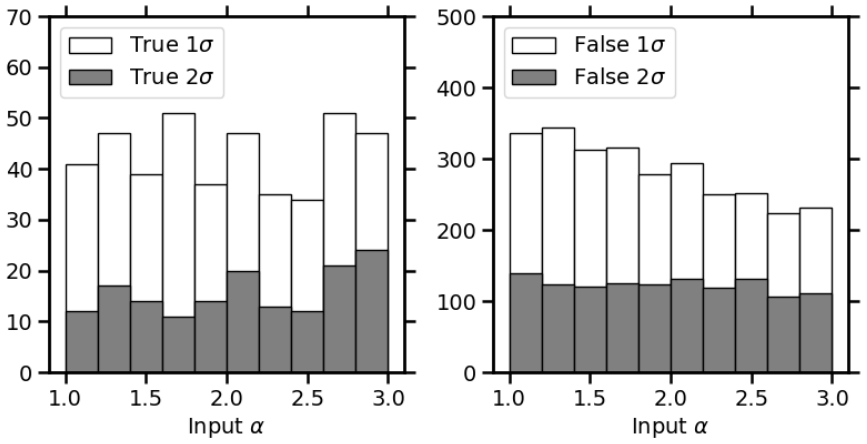

(B) Distributions of the PSD power law slope of the AGN light curves corresponding to true and false quasi-periodicity detections. Note that the scale of the false detection histograms is a factor of ~ 7 greater than of the true detections.

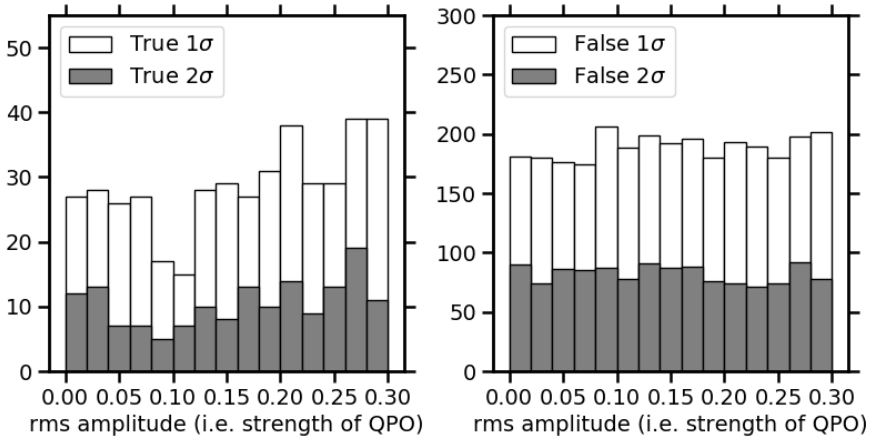

(C) Distributions of the strength of the QPO of the AGN light curves corresponding to true and false quasi-periodicity detections. Note that the scale of the false detection histograms is a factor of ~ 6 greater than of the true detections.

FIGURE 6.32: Distributions of the parameters of the DDF cadenced AGN light curves corresponding to true and false quasi-periodicity detections.

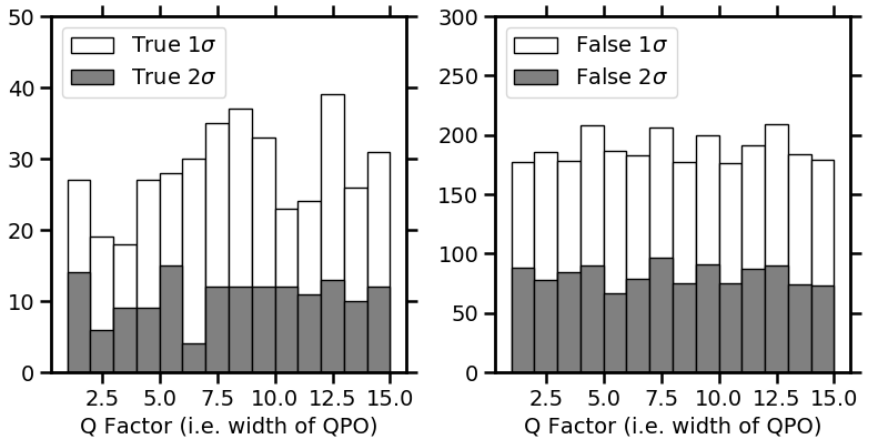

(D) Distributions of the width of the QPO of the AGN light curves corresponding to true and false quasi-periodicity detections. Note that the scale of the false detection histograms is a factor of ~ 6 greater than of the true detections.

FIGURE 6.32: Continued.

False Quasi-Periodicity Detections within Single and Broken Power Law Light Curves To further explore the false quasi-periodicity detection using these methods, I searched for quasi-periodicities in the DDF cadenced light curves made with only SPL and BPL PSDs (i.e., without QPOs).

2925 of the 7730 SPL light curves detected quasi-periodicities over the 1σ significance contours, and 1298 of these were above the 2σ significance contours. The distributions of false quasi-periodicities detected and the corresponding power law slopes of the PSDs used to created light curves for these AGN are given in Figure 6.33. In Figure 6.33a, similar distributions of false quasi-periodicities can be seen to the distributions found for the false detections in Figure 6.32. In Figure 6.33b, there is a slight preference for a shallower input power law slope in for the false detections above the 1σ significance contour, however no clear distinction can be seen for the false detections above the 2σ significance contours.

For the BPL quasi-periodicity detection, 4294 and 2014 light curves detected quasi-periodicities above the 1σ and 2σ significance contours respectively, which is much greater than the number of false quasi-periodicities detected within the SPL QPO light curves. This is likely due to the simulation of the light curves that define the significance contours as these are simulated using the best fitting results from the SPL fits. The distributions of the parameters of these PSDs that detect the false quasi-periodicities are given in Figure 6.34, where it can be seen in Figure 6.34b that the quasi-periodicities that are falsely detected are distributed similarly to Figures 6.33 and Figure 6.32. Furthermore, there appears to be no clear dependence on the value of the high-frequency slope as shown in Figure 6.34c, though Figure 6.34b demonstrates that shallower low-frequency slopes are more likely to return a false quasi-periodicity. Finally, Figure 6.34a shows that there may be a weak dependence on the location of the

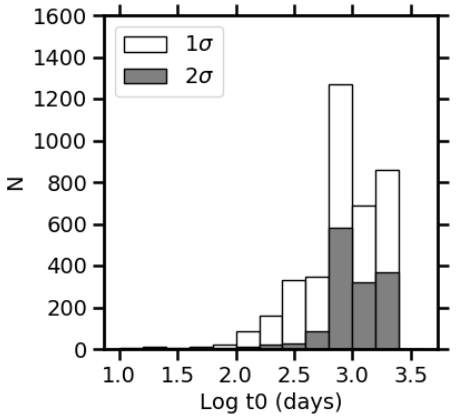

(A) Distributions of the false quasi-periodicities recovered from the SPL light curves.

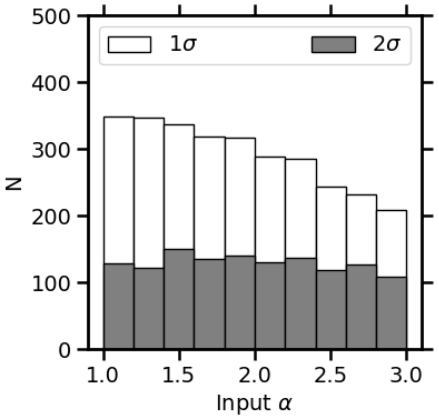

(B) Distributions of the power law slopes that correspond to the SPL AGN that recovered false quasi-periodicities.

FIGURE 6.33: Distributions of the SPL parameters that correspond to the AGN with false quasi-periodicity detection.

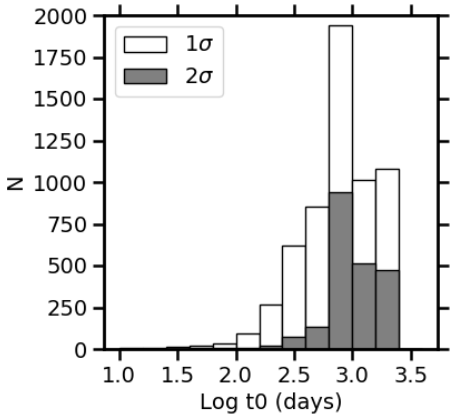

(A) Distributions of the false quasi-periodicities recovered from the BPL light curves.

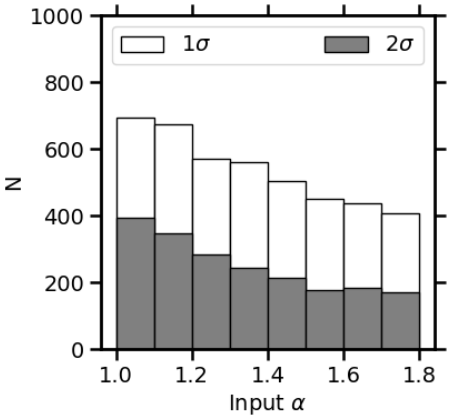

(B) Distributions of the low-frequency power law slopes that correspond to the BPL AGN that recovered false quasi-periodicities.

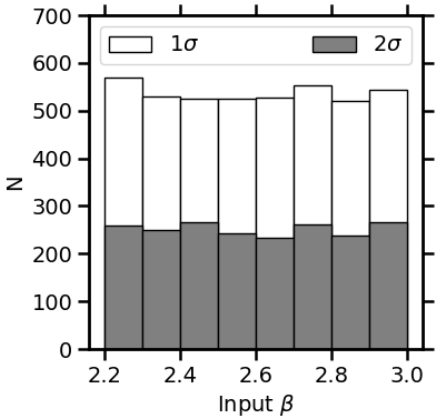

(C) Distributions of the high-frequency power law slopes that correspond to the BPL AGN that recovered false quasi-periodicities.

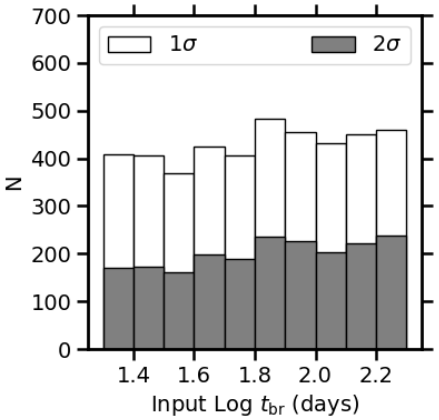

(D) Distributions of the break timescales of the power laws that correspond to the BPL AGN that recovered false quasi-periodicities.

FIGURE 6.34: Distributions of the BPL parameters that correspond to the AGN with false quasi-periodicity detection.

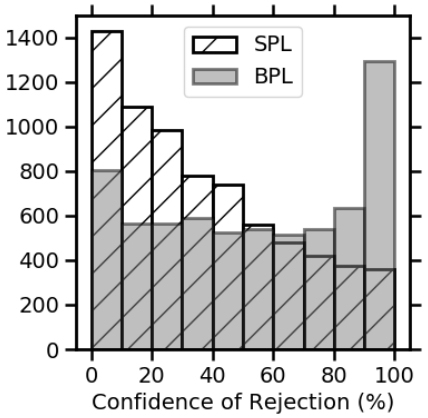

(A) Distributions of the confidence of rejection for the input QPO PSD recovery using DDF cadenced light curves.

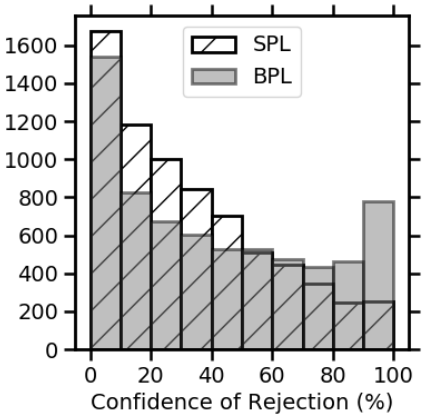

(B) Distributions of the confidence of rejection for the input QPO PSD recovery using WFD cadenced light curves.

FIGURE 6.35: Comparison between the distributions of the confidence of rejections when using both the SPL and BPL recovery methods on the light curves made with QPOs, for both the DDF and WFD cadenced light curves.

TABLE 6.3: Number of cadenced QPO SPL AGN light curves whose underlying shapes are correctly and incorrectly classified.

Cadencing ↓ Best Fit →	SPL	BPL	Not Recoverable
DDF	5242 (∼68%)	1972 (∼26%)	516 (∼7%)
WFD	4241 (∼55%)	2961 (∼38%)	528 (∼7%)

break timescale, with high break timescales returning more false quasi-periodicities. The increase in false quasi-periodicity detections could be a results of the fit of the SPL to the light curve PSD being poor, which would result in incorrect light curves being simulated and therefore the significance contours could be poorly defined.

6.5.4 Classifying Underlying PSD Slopes of Light Curves with QPOs

Finally, in addition to detecting the quasi-periodicity in QPOs light curves, I also explored how the presence of a QPO impacted the detection of the underlying PSD by comparing the recovery of SPL and BPL parameters as described previously.
Figure 6.35 displays the distribution of the confidence of rejection when fitting each cadenced light curve with a SPL or BPL. The distributions are shown to be similar to those given for the solely SPL PSD recoveries in Figures 6.22a and 6.27a, though the number of WFD cadenced AGN light curves with the lowest confidence of rejection with the BPL fitting is slightly higher than the SPL fitting, which suggests more AGN light curves become confused with the BPLs. The number of AGN best fit with each model are given in Table 6.3, where it can be seen that more AGN are incorrectly identified, with $\sim$ 26% and $\sim$ 38% of the DDF and WFD cadenced light curves respectively, compared to the SPL recovery which falsely identified $\sim$ 21% and $\sim$ 34%

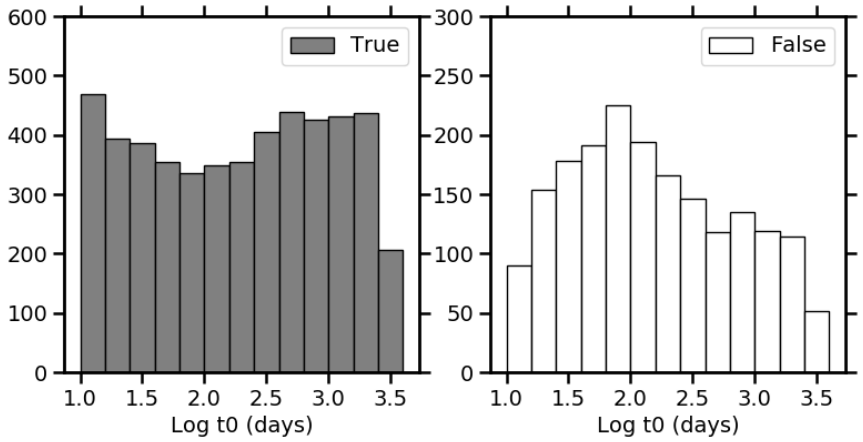

(A) Distributions of the quasi-periodicity of the AGN light curves corresponding to correct and incorrect underlying power law classifications.

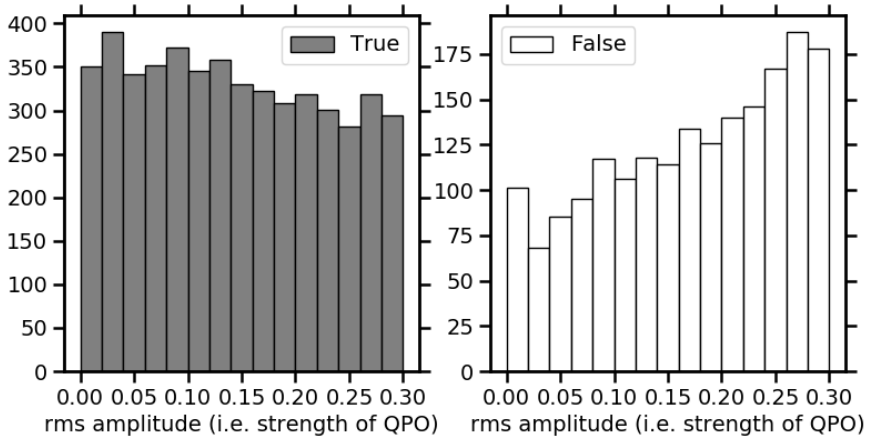

(B) Distributions of the strength of the QPO of the AGN light curves corresponding to correct and incorrect underlying power law classifications.

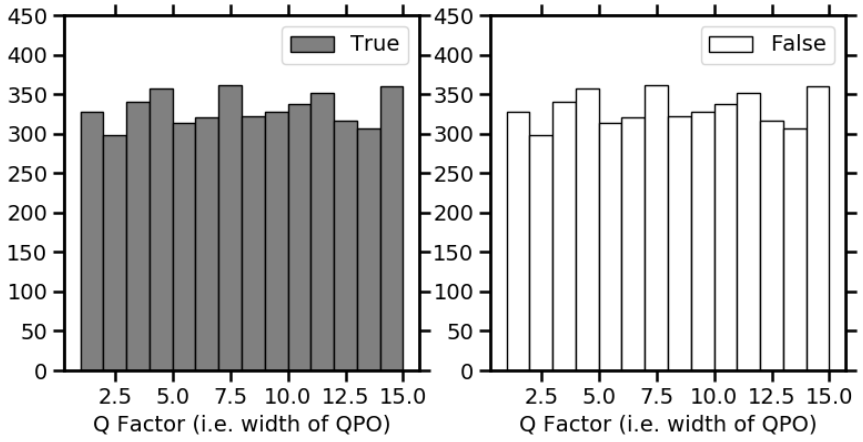

(C) Distributions of the width of the QPO of the AGN light curves corresponding to correct and incorrect underlying power law classifications.

FIGURE 6.36: Distributions of the parameters of the QPO of the AGN light curves corresponding to correct and incorrect underlying power law classifications.

respectively. This therefore implies that the QPO light curves make it more difficult to distinguish the shape of the underlying power law.

The distribution of parameters of the AGN whose underlying power law is correctly and incorrectly identified are given in Appendix C and show similar distributions to the SPL only distributions. Furthermore, Figure 6.36 displays the distribution of the properties of the QPOs that correspond to the correct and incorrect classifications. It can be seen in Figure 6.36c that the width of the QPO has no strong correlation with success of the classification of the underlying PSD. Figure 6.36b however shows that there is an increase in false classification when stronger QPOs are present. Furthermore, Figure 6.36a shows that quasi-periodicities of $1.5 \lesssim \mathrm{Log}t_0 \lesssim 2.5$ correspond to more false classifications.

6.5.5 Discussion

In this section, quasi-periodicity detection in AGN light curves observed with proposed LSST cadencing was explored for possible quasi-periodicities covering potential QPOs and SMBHBs.

It was found that for idealised light curves with 1 day cadencing over the duration of LSST's observations, the recovery of quasi-periodicities depend on parameters including the slope of the underlying power law, with more detections found for steeper PSD slopes, and the strength and quasi-periodicity of the QPO. Furthermore, a high number of false detections were found, mostly corresponding to large quasi-periodicities which would have a limited number of cycles observed. The dependence of the parameters on the false detections differ from the true detections making them somewhat distinguishable.

When considering both the DDF and WFD cadenced LSST light curves however, the number of detections of true quasi-periodicity drastically decreases, and furthermore, the distribution of parameter space corresponding to the true and false detections are similar, which makes them difficult to distinguish. The decrease in true quasi-periodicity detection stems from the loss of information from only using a small number of observations, but is partly due to the inability to classify the detection as significant because the sampling of the observations can mimic quasi-periodic behaviour in red-noise light curves (Vaughan et al., 2016).

The false detection of quasi-periodicity was also explored for the light curves created using only SPL and BPL, and it was shown that the false detection for SPL was similar to that of the SPL+QPO light curves, however an increased number were detected when using the BPL light curves. This could be a result of fitting a SPL in order to estimate the significance contours for the quasi-periodicity detection.

While these results show that the cadencing of LSST in both the DDF and WFD regions limit the detection of quasi-periodicity in AGN emission, this detection is performed only for light curves in a single filter. The total number of observations of each field are expected to be more regular, however these observations are planned to rotate between different filters. Combining the data from different filters could significantly improve the detection of quasi-periodicities within the light curves, and indeed a multi-band LSP was developed by VanderPlas and Ivezić (2015) in order to construct a periodogram from all filters available. This has been shown to be more successful for quasi-periodicity detections in simulations of different objects with LSST cadences (e.g., Johnson et al., 2019). However, the underlying bluer when brighter behaviour observed in AGN makes it more complicated to use as the colour-dependence of the variability would need to be taken into account before light curves from different filters could be combined.

Previous studies have found more promising results for potential SMBHB quasi-periodicity detection within LSST observations, however this is likely due to the assumptions and methods used for the simulations and detections.

For example, Witt et al. (2021) found that the periodicity was recovered well for their simulated LSST light curves, however numerous assumptions were made which could impact their results. Firstly, they simulate AGN light curves using only a DRW model and include the periodicity as a sinusoidal signal with amplitude in the range [0.05, 0.5] mags (as opposed to the Lorentzian function superimposed on the PSD that I use to represent quasi-periodicity). Specifically, the AGN light curves are modelled using a DRW with parameters $\sigma_{\rm DRW}$ and $\tau_{\rm DRW}$ drawn from log-uniform distributions of [-1.6, -0.25] and $[10^{-3}T, 15T]$ respectively, where $T = 10$ years is the LSST observational baseline, as they were exploring the capabilities of the surveys as opposed to exploring a representative distribution of AGN. Furthermore, introducing the periodicity as a sinusoidal signal could represent an idealistic scenario as it is expected that the Keplerian binary motion of a SMBHB system could induce periodic accretion perturbations, resulting in a quasi-periodic signal observed within the emission (e.g., Hayasaki et al., 2007; MacFadyen and Milosavljević, 2008; D'Orazio et al., 2013; Farris et al., 2014). Pure periodic signals are likely to be easier to detect than quasi-periodic as they are observed as sharp, narrow peaks on the PSD whereas quasi-periodic signals have the power spread over a range of frequencies.

Secondly, when cadencing their light curves, Witt et al. (2021) do not use OpSim simulations of expected cadences from LSST, but instead choose to create "idealized" LSST-like light curves that ignore the rotations of filters, and furthermore do not take into account the gaps between observation seasons. Their resulting LSST-like light curves are therefore created assuming cadences of ~ 7 days with deviations of 1 day. Though in addition to the mock LSST light curves, Witt et al. (2021) also simulated light curves with a baseline of 8 years with sampling from Catalina Real-time

Transient Survey (CRTS) that had average differences of $\sim$ 20 days between observations and gaps of $\sim$ 200 days between observation seasons.

In order to detect quasi-periodic behaviour, Witt et al. (2021) use MCMC modelling to find the fits of DRW only light curves and light curves made using DRW with sinusoidal quasi-periodicities. They found that the periodicity was recovered well for their light curves, and furthermore found that the MCMC modelling was able to distinguish between input DRW and DRW+sinusoid light curves reasonably well. The false positive rates of classifying the light curves increased for the simulated CRTS light curves compared to the simulated LSST light curves, which suggests that the detection depends on the quality of the light curves, however they found the true positive rates to be similar in both sets of light curves.

MCMC modelling could have the potential to improve the poor detection rates found in this chapter, and furthermore this method could fit properties such as the width and strength of the QPO. However this is a much more time-consuming process and given the large number of objects expected to be observed with LSST, this might not be reasonable.

Additionally, Kovačević et al. (2021) simulated LSST-like light curves using DRW models and represented the underlying quasi-periodic signal resembling the case of PG 1302-102. The simulated light curves were cadenced using OpSim 1.5 and 1.6 for both DDF and WFD cadenced light curves, as well as "idealized" light curves. They used these simulated light curves to create a statistical proxy to measure the effect of cadencing on the recoverability of observable features including quasi-periodicities using structure functions, and found that SFs with quasi-periodicity are sensitive to the cadences. Again, these results could be impacted by the assumptions and methods used, for example the use the DRW model to simulate the underlying light curves could lead to inaccuracies as many AGN have been found to deviate from this model. Furthermore, by only modelling the periodic signal to resemble the case of PG 1302-102, the analysis is not necessarily applicable to a wider range of potential periodicities linked to SMBHBs.

Finally, the impact of a QPO on the classification of the underlying power law was explored using the methods in Section 6.4.2. It was found that a larger number of AGN were incorrectly classified as having underlying BPL PSDs instead of SPLs, with increases in false detections from $\sim$ 21% to $\sim$ 26% in the DDF cadenced light curves, and from $\sim$ 34% to $\sim$ 38% when the QPO is included. These results suggest that the presence of a quasi-periodicity could create uncertainties in the classification of the underlying power law, which could imply that alternative methods excluding the AGN associated with quasi-periodicities from the sample are needed to prevent inaccurate results. However, the number of AGN that are expected to have detectable

periodicities are limited, for example, current time-domain surveys detect SMBHB candidates in 1/1000 AGN (e.g., Witt et al., 2021).

6.6 Chapter Summary

In this chapter, I explored the capabilities and limitations of optical PSD variability analysis of AGN with expected LSST cadenced light curves. To do this, I simulated a mock sample of AGN and created light curves for this sample using the Timmer and Koenig (1995) algorithm with a variety of different underlying PSDs. These underlying PSDs included the DRW model, single power laws with varying slopes, broken power laws with varying slopes and break frequencies, and single power laws with varying slopes that had quasi-periodic oscillations superimposed. The results are summarised below.

1. I recovered the parameters of the DRW model with JAVELIN which uses MCMC modelling to determine reasonable fits for the parameters. Overall I found that the shorter characteristic timescales and smaller amplitudes of variability were easier to recover, which is consistent with previous studies.

2. I used a stochastic hillclimbing version of the PSRESP method introduced by Uttley et al. (2002) to fit the SPL and BPL PSDs. I found that the properties of the underlying SPL PSDs could be recovered well, however the effects of red-noise leakage had more of an impact on the steeper power law slopes and made them harder to distinguish. For the BPL PSDs, the low-frequency power law slopes and characteristic break timescales were similarly reasonably well recovered, however the LSST cadencing was shown to impact the ability to recover the high-frequency power law slopes. Furthermore, I found that recoverability was improved for AGN with low redshifts, high luminosities and shallow power laws.

3. I also explored the classification of the underlying PSD for the SPLs and BPLs, and found correct identifications were more common than incorrect, however SPLs were shown to be more likely to be confused with BPLs with characteristic break timescales at the upper and lower limits.

4. I explored quasi-periodicity detection using the Lomb-Scargle periodogram, firstly for idealised 1-day cadenced light curves. I found that the number of successful true-periodicity detections was anti-correlated with timescale of the quasi-periodicity, and was correlated with slope of the underlying power law and amplitude of the QPO. However, I also found that a larger number of false quasi-periodicities were detected, though these mostly corresponded to longer

timescales and showed no obvious correlation with slope of the underlying power law.

5. The quasi-periodicity detection was then explored for the LSST cadenced light curves, however the number of true quasi-periodicities detected significantly decreased, and furthermore, the distributions of the parameters corresponding to the true and false quasi-periodicities detected were found to be similar which makes them difficult to distinguish.

6. The false quasi-periodicity detection was further explored using the detection methods on the red-noise only SPL and BPL light curves, where it was found that many more false quasi-periodicities were detected for the BPLs, likely due to the assumption of a SPL shape used when estimating the significance of the detection.

7. The impact of the presence of quasi-periodicities on the ability to recover the underlying power law was also studied, where it was found that more PSDs were incorrectly identified as BPLs.

8. Finally, all of the above analysis was performed using both DDF and WFD cadenced light curves, and the results all found that there was a slight decrease in the ability to recover the properties of the underlying PSDs with less observations, but this decrease was not significant. This therefore suggests analysis of the PSD of objects observed with LSST will be able to be performed on a much larger sample of AGN than if just the AGN within the DDFs were explored.

Chapter 7

Summary and Future Work

The extreme luminosity and strong variability of AGN emission makes them particularly interesting for us to observe, however their large distances and compact sizes limit our ability to study the inner regions. As a result, indirect methods are required to instead probe the physical processes occurring within. Such indirect methods often invoke various variability analyses, some of which are described below.

Power spectrums are commonly used tools for studying the variable nature of AGN emission. Light curves of AGN are typically characterized by stochastic, aperiodic variability, though the physical processes responsible for these variations are not clear. Features within the observed PSDs could be used to infer various properties of the emission mechanisms, for example authors frequently try to link characteristic timescales observed within the power spectra to physical timescales such as thermal, orbital or viscous timescales (e.g., Smith et al., 2018b). Furthermore, recent claims of periodicities within AGN light curves have been reported (e.g., Gierliński et al., 2008; Alston et al., 2014, 2015; Graham et al., 2015; Liu et al., 2015; Bhatta et al., 2016; Zheng et al., 2016; Zhang et al., 2017, 2018), which can be detected within the PSDs. The origin of these oscillations could provide further understanding of the central regions, with current theories expecting SMBHBs or QPOs to present such quasi-periodicities.

Temporal variability analysis is often used to probe the locations of different emission regions within the unresolvable central regions of the AGN. The emission from AGN observed in different wavelength ranges is commonly believed to originate in different components within the AGN, each located at different distances from the central source. Currently, only the largest components can be spatially resolved with single dish telescopes and interferometry, however reverberation mapping analysis is often employed in order to estimate the distances between these different components, using the assumption that some of the emission from the central engine is reprocessed by the different components (Blandford and McKee, 1982). The reprocessed emission is therefore expected to vary similarly to the driving emission,

but would be observed following a delay that corresponds to the light travel time between the different emission regions. These reverberation mapping methods have been successfully applied to type 1 AGN to explore the sizes of the BLR (e.g., Bentz and Katz, 2015; Grier et al., 2017) and dust emitting regions (e.g., Barvainis, 1987; Nelson, 1996; Oknyanskij and Horne, 2001; Minezaki et al., 2004; Suganuma et al., 2006; Yoshii et al., 2014; Pozo Nuñez et al., 2015; Mandal et al., 2018; Ramolla et al., 2018; Mandal et al., 2021), and in both cases, the size of the regions have been found to correlate with luminosity of the AGN (e.g., Kaspi et al., 2000; Oknyanskij and Horne, 2001; Minezaki et al., 2004; Peterson and Horne, 2004; Suganuma et al., 2006).

Spectral variability analysis uses the dependence of variability of AGN emission with wavelength in order to investigate different emission mechanisms contributing to the overall observed light curves (e.g., Marscher and Gear, 1985). The optical emission of RQ type 1 AGN is typically found to follow a BWB trend (e.g., Giveon et al., 1999; Webb and Malkan, 2000; Vanden Berk et al., 2004; Sakata et al., 2010; Schmidt et al., 2012), which is frequently attributed to contributions from a non-varying red component (commonly believed to be emission from the host galaxy) and a variable blue component (the AGN continuum emission) that dominates as the object gets brighter (e.g., Sakata et al., 2010). Furthermore, in blazars whose relativistic jets are orientated less than 10 degrees to our line of sight, contributions to the optical light curves are expected from the non-thermal Synchrotron radiation originating in the jet, and thermal emission from the AD. Studying the spectral variability of blazars can therefore allow us to explore how each component contributes to the overall emission, where BWB trends can imply that the thermal (bluer) emission is varying faster than the Synchrotron (redder) emission, or vice versa for RWB trends (e.g., Fiorucci et al., 2004; Bonning et al., 2012; Agarwal et al., 2019). Alternatively, one component synchrotron models can also suggest that these colour behaviours can be used to infer processes occurring within the jet, for example, shock-in-jet model have been used to explain observed BWB trends. (e.g., Kirk et al., 1998; Agarwal et al., 2019).

This thesis was therefore motivated to further expand on our understanding of the inner regions of AGN using these methods, both with in depth analysis performed on individual objects, and by exploring the possibilities of applying some of the variability analysis to the large influx of objects that will soon be observed with upcoming large scale surveys. The main results of this thesis are summarised in the next section, and possible methods for expansion upon this work are discussed in Section 7.2.

7.1 Summary of the Results of this Thesis

Multi-wavelength Variability Studies of the Blazar, PKS 0027-426 In Chapter 4, I explored multi-wavelength spectral and temporal variability analysis of the FSRQ PKS 0027-426 using optical *griz* observations from DES between 2013-2018 and VOILETTE between 2018-2020 and NIR *JKs* observations from VEILS between 2017-2020.

I used cross correlational analysis to quantitatively measure the inter-band temporal variability, and the results consistently suggested either simultaneous emission or delays between emission regions on timescales smaller than the cadences of observations. Further analysis was performed to determine the significance of a potential periodicity detected in multiple observation seasons, however the results showed that this was not significant compared to false detections from simulated red-noise light curves.

I then used colour-magnitude diagrams to investigate the spectral variability behaviour between each combination of filters, and the results were shown to demonstrate complex colour behaviour that changes between BWB, SWB and RWB trends over different timescales and using different combinations of filters. This was further investigated using additional analysis of the optical spectra to explain the change in colour behaviour as the result of the light curves in each filter containing a different ratio of multiple different coloured components that combine to give the overall optical emission.

Dust Reverberation Mapping of Zw229-015 In Chapter 5, I performed dust reverberation mapping analysis of the Seyfert 1 galaxy Zw229-015, using optical ground-based and *Kepler* light curves and concurrent IR *Spitzer* 3.6 and 4.5 μm light curves from 2010–2015.

I first used cross correlational analysis to estimate the mean distance between optical and IR emitting regions, and found an overall mean rest-frame lag of 18.3 ± 4.5 days. Each combination of optical and IR light curve returned lags that were consistent with each other within 1σ, and these were shown to be further consistent with dust reverberation mapping performed by Mandal et al. (2021) using a combination of *V* band and *Ks* band light curves, which implies that the different IR wavelengths are dominated by the same hot dust emission. Furthermore, I compared the dust reverberation lags detected with the BLR lag measured by Barth et al. (2011), and showed that both lags were consistently smaller than predictions using recent estimates of the lag-luminosity relationships.

I further attempted to constrain properties of the dust emitting region of Zw229-015 using MCMC modelling, as the overall IR response to the optical emission actually

depends on the geometry and structure of this dust emitting region. Models of the IR light curves were created by convolving optical driving light curves with simulated dust transfer functions, and these models were compared to observations to find the parameters of the dust transfer function that best fit the data. The results firstly showed that a large increase in flux between the 2011–2012 observation seasons, which is more dramatic in the IR light curve, is not well simulated by a single dust component. When excluding this increase in flux, the results of the MCMC modelling consistently suggests that the dust is distributed in an inclined extended flat disk.

Simulations of Optical AGN Variability Analysis with LSST In Chapter 6, I investigated the ability to recover properties of the underlying PSDs of simulated AGN with light curves, in order to understand the capabilities and limitations of performing this analysis on the objects that will be observed with the upcoming LSST survey. I simulated optical light curves for a mock sample of unobscured AGN with $z < 5$ for a 10 square degree FOV using a variety of underlying PSDs explained below, and then cadenced these light curves using OpSim 1.7 to replicate an example observing pattern in both the DDF and WFD surveys to compare what can be recovered with each.

I started by exploring the recovery of parameters of the DRW model introduced by Kelly et al. (2009) using the MCMC modelling of JAVELIN (Zu et al., 2011, 2013), and found that shorter characteristic timescales and smaller amplitudes of variability were more often recovered, both for the DDF and WFD light curves.

As there are discrepancies between the DRW model and some observed AGN PSDs, I also explored the ability to recover SPLs with varying slopes and BPLs with varying slopes and break frequencies, using LSST-like light curves. The results here showed that for the SPL PSDs, properties of the underlying PSD were generally recovered well, however the steeper power law slopes were impacted by the effects of red-noise leakage. For BPL PSDs, the low-frequency power law slope was similarly well recovered, and the location of the characteristic break timescale was also reasonably recovered, however the ability to recover the high-frequency power slope was shown to be affected by the proposed LSST cadencing. Furthermore, I found that the shape of the underlying PSDs were mostly identified correctly, though SPLs were more likely to be confused with BPLs.

Additionally, I also explored the ability to detect different quasi-periodicities with LSST-cadenced light curves by simulating light curves from varying SPLs with quasi-periodicities superimposed. For the LSST cadenced light curves, very few true periodicities were detected and furthermore, the distributions of these AGN with true periodicities were difficult to distinguish from the distribution of false periodicities detected.

Finally, in all of these analyses, I found that the parameters of the underlying PSDs were slightly better recovered using the higher cadenced DDF light curves than the less observed WFD light curves, however these differences were not great and the distributions of the results were shown to be similar. This suggests that it would be reasonable to perform the analysis used here on the much larger sample of AGN that will be detected in the WFD portion of the survey.

7.2 Future work

7.2.1 Dust Reverberation Mapping using Observations from DES, VEILS and VOILETTE

As previously described in Chapter 2, one of the primary science goals of VEILS is to perform dust reverberation mapping analysis on the sample of AGN that were repeatedly observed in the optical and NIR between 2017-2021. Indeed, we plan to do so using the cross correlation analysis methods described in this thesis in order to estimate the mean reverberation lags for these objects. Hönig et al. (2017) performed simulations of recovering dust time lags with the VEILS survey, and found that for AGN within a redshift range of $0.1 < z < 1.2$, lags could be recovered for ~ 450 objects. This therefore has the potential to increase the number of *Ks* band dust reverberation mapped AGN by a factor of 10 (Mandal et al. 2021 and references within).

The potential for using AGN dust reverberation lags for cosmology has been suggested based on the correlations found between lag and luminosity (e.g., Oknyanskij and Horne, 2001; Hönig et al., 2014; Yoshii et al., 2014; Hönig et al., 2017). Hönig et al. (2017) further demonstrated that the AGN observed with VEILS could potentially be used for this purpose, using simulations to create the Hubble diagram displayed in Figure 7.1.

Furthermore, we plan to apply the MCMC modelling used to constrain properties of the dust emitting region of Zw229-015 in Chapter 5 to this sample of AGN observed with DES, VOILETTE and VEILS. In addition to constraining information for the individual AGN, this provides the opportunity to further explore correlations between the parameters of the models and properties of the different AGN.

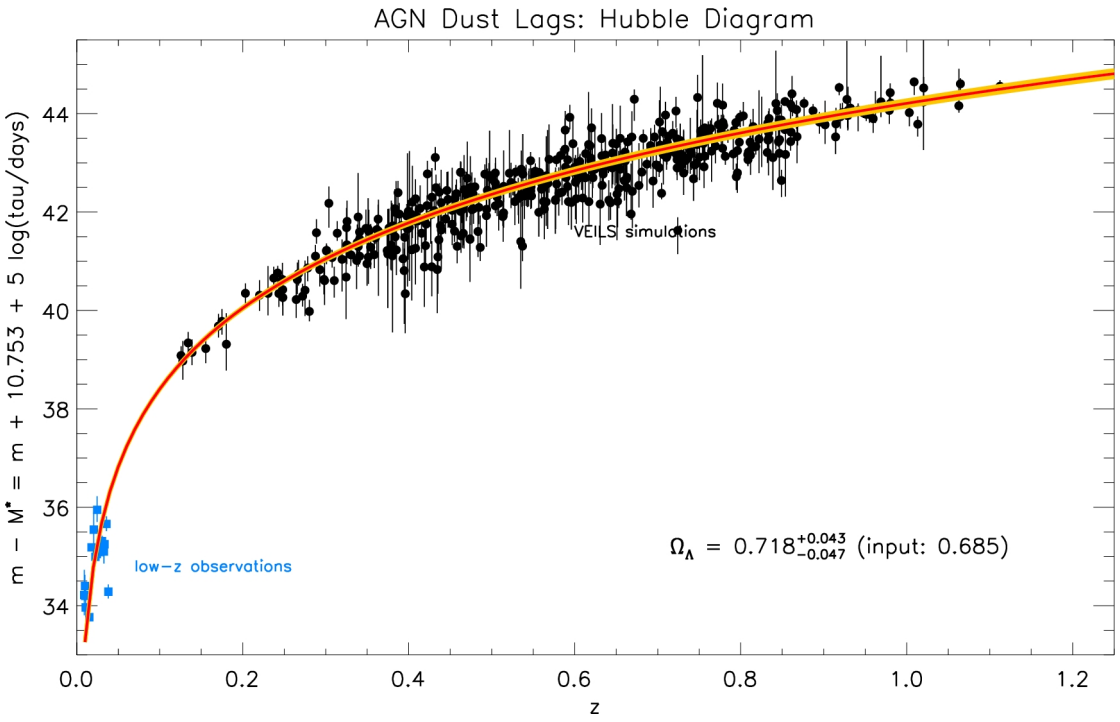

FIGURE 7.1: Hubble diagram created using AGN dust reverberation time lags from simulations of AGN light curves observed with VEILS and an optical counterpart. Image Credit: Hönig et al. (2017).

7.2.2 Further Exploration of the Recoverability of Properties of AGN Light Curves with LSST

In Chapter 6 I explored the possibility of recovering the underlying PSDs of simulated AGN light curves that are observed with LSST-like cadencing, however this work has many possible paths for expansion, some of which are considered below.

LSST Observing Strategy Firstly, the observational strategy of LSST has yet to be finalised, and therefore the analysis performed with the OpSim 1.7 proposed cadences might not reflect the true observation patterns of LSST. Furthermore, in this work, I only consider an example of the observations for the DDF and WFD regions, however alternative observing strategies have been proposed. This includes observing strategies that utilise a "rolling cadence", in which observations will observe certain pointings with a higher cadence one year, followed by a reduced cadence in the next. If this strategy is in fact chosen, the results of the different parameter recoveries here might not be consistent. Additionally, this analysis does not need to be limited to only LSST, but could be performed on other upcoming observation surveys.

I will therefore update the results of the analysis for LSST when the WFD and DDF observing patterns are finalised, but also plan to obtain a more comprehensive understanding of the capabilities of the underlying PSD recovery as a result of

sampling by extending the analysis to AGN light curves of different types of sampling patterns. This could be used not only to explore what can be recovered with the cadencing of different surveys, but also to help select ideal cadencing strategies when planning future observational surveys.

Underlying PSD Identification The types of underlying PSD that were simulated for the analysis in Chapter 6 were limited to the DRW model, single power laws with slopes between $1 \leq \alpha \leq 3$, and broken power laws with low-frequency power law slopes of $1 \leq \alpha \leq 1.8$, and high-frequency power law slopes of $2.2 \leq \beta \leq 3$, with only one break frequency located with corresponding timescales between $1.3 \leq \mathrm{Log}t_{\mathrm{br}} \leq 2.3$.

PSD studies of real AGN observations have reported different results than explored in this study, including steeper slopes (e.g, Mushotzky et al., 2011; Caplar et al., 2017; Smith et al., 2018b), but also both longer and shorter characteristic break timescales (e.g Caplar et al., 2017; Smith et al., 2018b). The choice of power law slope was motivated by the effects of red-noise leakage which has a greater impact on steeper slopes (e.g., Uttley et al., 2002), so employing alternate analysis methods such as the normalized leakage spectrum introduced by Zhu and Xue (2016) will allow for more in depth analysis from the objects observed with LSST. The possible range of break frequencies explored were limited by the sampling of observations with LSST and the binning of the periodograms used in the analysis, where the longer timescales had relatively few data points as a result of the analysis being performed in Fourier space. I plan to explore alternative methods including structure function analysis to potentially combat this problem.

Furthermore, the SPL and BPL models used the assumption that the timescales of decorrelation of the variability were longer than the baseline of LSST observations, however studies that successfully apply the DRW model to observations show that AGN can have decorrelation timescales shorter than this (e.g., Kozłowski et al., 2010; MacLeod et al., 2010; Zu et al., 2013). Therefore this work would be expanded by exploring the detection efficiency of AGN PSDs that do become uncorrelated within the entire observational period of LSST observations. Furthermore, some studies of observed optical PSDs find the best fits are described by alternative models, including bending power laws instead of broken (e.g., Carini and Ryle, 2012; Smith et al., 2018b), which could be used to further the analysis of this thesis.

Periodicity Detection In Chapter 6, I showed that using the Lomb-Scargle periodogram on simulated AGN light curves with proposed LSST cadences returned very few correctly identified quasi-periodicities, though many false periodicities were detected, especially for long timescales. This result is unfortunate as many past

authors expected the regular observations and long baselines of LSST to expand upon periodicity detection in AGN emission, and potentially to identify QPOs or SMBHBs within the sample of AGN.

The limitations of the detections in this thesis likely stem from the loss of information from the cadencing, but also as a result of the sampling of the observations resulting in pure red-noise light curves mimicking periodic behaviour and therefore making it hard to distinguish true periodicities. As mentioned previously, a multi-band Lomb-Scargle periodogram was introduced in order to combine observations from different filters to provide more data in order to detect periodicities. Though combining observations of AGN from different filters is more complicated because of the observed spectral variability that often accompanies flux variations, I will consider using models of spectral variability to overcome this.

Furthermore, the large number of false periodicities detected for longer timescales likely stems from the minimal number of data points available at those locations within the periodogram. Again, this is a result of analysing the data in Fourier space, so it could be advantageous to instead explore the results in linear space such as searching for dips in the structure function corresponding to quasi-periodicities instead.

Additionally, Witt et al. (2021) showed that MCMC modelling of simulated light curves was successful at recovering periodicities superimposed on DRW light curves as sinusoids. A similar method could therefore be applied to the quasi-periodic AGN light curves simulated in this thesis as an alternative method of detecting periodicities, however this is a time-consuming process and not necessarily applicable to the large number of objects that would be observed with LSST. Instead, I propose that alternative methods of periodicity detection considered above be explored first, and this MCMC modelling of the PSDs be used for constraining the parameters of the QPOs for AGN light curves that do detect potential periodicities.

Appendix A

Multi-wavelength Variability Studies of the Blazar, PKS 0027-426

A.1 Light Curves

Calibrating the Light Curves of PKS 0027-426 with Nearby, Non-Varying Objects Nearby non-varying sources were used to calibrate the observations of PKS 0027-426 to create the light curves shown in Figure 4.3. Table A.1 contains the list of objects within the same detector that were used to correct the light curves of PKS 0027-426, including their position in RA and Dec (J2000), mean magnitude over the entire observational period in each filter, and standard deviation of the magnitudes in each night from the mean. The object had to be detected in every epoch observed for PKS 0027-426 for it to be included, which is why some objects were only used as reference stars in some of the filters. As the NIR observations contained inconsistencies across the detector, the non-varying objects used to correct the NIR light curves were further restricted to within $\sim$ 200 pixels of PKS 0027-426.

A.2 Temporal Variability

More CCFs of the Individual Observation Seasons The *r* and *i* band CCFs of the individual seasons starting 2013-2016 and 2018 are displayed in Figure A.1 for each CCF method, along with their corresponding ACFs. Each CCF detects a correlation at $\sim$ 0 days, except the 2016 season which instead contains a small peak at $\sim$ 0 days with a value of less than 0.5 in the S-ICCF and M-ICCF methods, and was therefore not counted. The CCFs from 2016 are relatively level, especially in the S-ICCF method, implying that there is no distinctive lag observed in this season, which could be due to the shape of the 2016 light curves, which contain multiple peaks and troughs that

would all correlate with each other. The 2018 season CCFs of the *J* and *Ks* band light curves and the *r* and *Ks* band light curves are displayed in Figures A.2a and A.3a respectively.

Lomb-Scargle Periodograms for PKS 0027-426 As a peak in the ACFs at $\sim$ 75 days was detected in multiple light curves in multiple observation seasons, the significance of this peak as a periodicity was explored. In Chapter 4 I investigated the significance of this 75 day timescale by exploring the structure function. To further this investigation, I also plotted the Lomb-Scargle periodogram as discussed in Chapter 3 in Figure A.4 for both the entire *r* band light curve, and for the 2017-2019 season which correspond to the seasons that detect this peak in the ACFs. Significance contours are also plotted corresponding to simulated light curves made from single power laws whose slope was calculated following the PSRESP method described by Uttley et al. (2002). It can be seen that in both periodograms, a peak is detected at $\sim$ 75 days, but is smaller than the 2 and 3 σ significance contours which suggests that this isn't a significant periodicity detection.

A.3 Spectral Variability

DES Colour - Magnitude Plots for Individual Observation Seasons The optical colour-magnitude plots for each season of each combination of DES *griz* filters, *g-r*, *g-i*, *r-i*, *r-z* and *i-z* are plotted in Figure A.5, and the corresponding tables containing the slopes, Spearman rank correlation coefficients and probability of no correlation are given in Table A.2, to demonstrate how the spectral behaviour changes over time.

DES Outliers The colour-magnitude plots made in the previous section excluded the outliers which are displayed in Figure A.6 for the 2013-2016 seasons of DES. The differences in slope between when the outliers are included and excluded is given in Table A.3.

Optical-NIR Colour - Magnitude Plots from 2017-18, with Gap in Observations Figure A.7 display histograms of the measured slopes of the 2017-2018 optical-NIR colour vs r magnitude plots, from each interpolated light curve, with the $\sim$ month long break in observations between MJD 57993 and 58044. The measured slope from each light curve are no longer consistent with each other in this scenario, which is assumed to be due the the peak that occurs in the optical light curve within this period. When the optical light curve is interpolated, the results are similar to Figure 4.22, however, when the NIR light curve is interpolated, the results are shown to be more positive as the interpolations in the NIR light curve in this gap will not be

as drastically variable as the optical light curve within this period. This means that the overall slope will be shifted to be positive as the optical light curve will be a lot more variable in this period.

Decomposition of the OzDES Spectra into Variable and Non-Variable Components In Figure A.8, the OzDES spectra are decomposed into their variable and non-variable components using Equation 4.7. The behaviour of the OzDES components is similar to the behaviour seen in Figure 4.27 for the broadband DES spectra, although it is worth noting that the 2017 OzDES spectra were not observed during the brightest epochs of the DES observations. The shape of the A_λ component remains similar over all seasons, and is steeper towards the bluer wavelengths, flattening towards the redder wavelengths. The S_λ component also behaves similarly to Figure 4.27 however the lack of spectra during the brightest, most variable flare of the DES observations is reflected in the 2017 season. There is a noticeable bump in the $\log(S_\lambda)$ vs $\log(\lambda_{\text{rest}})$ plots especially at $\log(\lambda_{\text{rest}}) \sim 3.58$ which corresponds to the split between the red and blue arms of the spectrograph as explained in Hoormann et al. (2019).

Broadband Spectra from DES for each Observation Season In Chapter 4, only the mean brightest and dimmest broadband spectra are shown. Figure A.9 displays the broadband spectra for each DES epoch in each observation season, coloured according to the observation epoch, to demonstrate how it changes between the brightest and dimmest states.

Additional Models of the Broadband Spectra of DES Figure A.10 displays the modelled broadband spectra for the 2015 season and for the entire DES observational period.

In Chapter 4, the broadband spectra are fit using models of blue and red components, however, the models displayed are not unique, and the overall broadband spectra can be fit using a variety of spectral indices for the blue and red emission. In Figure A.11, more examples of the change in spectral slope are displayed for the 2014 season of DES, including models in which the blue component is fixed and the red emission varied.

TABLE A.1: List of non-varying objects used to calibrate the light curves of PKS 0027-426.

RA (deg)	Dec (deg)	Mean g mag	1σ (g mag)	Mean r mag	1σ (r mag)	Mean i mag	1σ (i mag)	Mean z mag	1σ (z mag)	Mean J mag	1σ (J mag)	Mean Ks mag	1σ (Ks mag)
7.50	-42.41	-	-	-	-	-	-	-	-	18.91	0.02	-	-
7.51	-42.43	-	-	-	-	-	-	-	-	19.06	0.02	-	-
7.51	-42.44	-	-	-	-	-	-	-	-	19.61	0.03	-	-
7.51	-42.37	-	-	-	-	-	-	-	-	19.58	0.02	-	-
7.53	-42.41	-	-	-	-	-	-	-	-	-	-	17.10	0.03
7.53	-42.44	-	-	-	-	-	-	-	-	18.86	0.02	19.08	0.04
7.54	-42.38	-	-	-	-	-	-	-	-	20.20	0.03	-	-
7.54	-42.35	-	-	-	-	-	-	-	-	18.58	0.02	-	-
7.54	-42.42	-	-	-	-	-	-	-	-	18.33	0.02	18.52	0.04
7.55	-42.43	-	-	-	-	-	-	-	-	-	-	16.74	0.03
7.55	-42.38	-	-	-	-	-	-	-	-	19.52	0.02	19.85	0.13
7.56	-42.50	-	-	18.48	0.09	18.19	0.09	-	-	-	-	-	-
7.56	-42.40	20.75	0.03	20.32	0.07	-	-	-	-	-	-	-	-
7.56	-42.51	-	-	18.38	0.07	17.84	0.08	-	-	-	-	-	-
7.57	-42.58	-	-	20.59	0.09	19.78	0.11	-	-	-	-	-	-
7.57	-42.49	-	-	-	-	20.28	0.10	20.17	0.04	-	-	-	-
7.57	-42.41	20.67	0.05	20.06	0.07	19.80	0.08	-	-	-	-	-	-
7.57	-42.44	-	-	-	-	-	-	20.51	0.04	-	-	-	-
7.57	-42.53	19.90	0.06	19.77	0.05	19.66	0.05	19.50	0.04	-	-	-	-
7.57	-42.39	-	-	18.00	0.06	17.70	0.05	-	-	-	-	-	-
7.57	-42.55	17.91	0.03	18.88	0.06	17.56	0.06	17.02	0.02	-	-	-	-
7.57	-42.34	-	-	17.31	0.05	17.04	0.05	18.64	0.05	-	-	-	-
7.58	-42.52	18.48	0.01	20.77	0.13	20.22	0.10	-	-	-	-	-	-
7.58	-42.61	19.88	0.09	18.02	0.05	-	-	-	-	-	-	-	-
7.58	-42.56	-	-	18.22	0.10	17.79	0.03	-	-	-	-	-	-
7.58	-42.34	-	-	19.78	0.05	17.10	0.13	18.93	0.04	18.41	0.02	-	-
7.58	-42.60	-	-	-	-	19.13	0.05	-	-	-	-	-	-

TABLE A.1: Continued

RA (deg)	Dec (deg)	Mean g mag	1σ (g mag)	Mean r mag	1σ (r mag)	Mean i mag	1σ (i mag)	Mean z mag	1σ (z mag)	Mean J mag	1σ (J mag)	Mean Ks mag	1σ (Ks mag)
7.59	-42.53	-	-	20.70	0.12	19.47	0.04	-	-	-	-	-	-
7.59	-42.46	-	-	20.79	0.04	20.31	0.18	20.48	0.11	-	-	-	-
7.59	-42.55	-	-	-	-	-	-	19.32	0.02	-	-	-	-
7.59	-42.59	-	-	-	-	-	-	17.63	0.01	-	-	-	-
7.59	-42.34	-	-	19.51	0.07	19.76	0.04	20.37	0.07	-	-	-	-
7.59	-42.54	20.61	0.03	20.59	0.06	18.24	0.07	20.19	0.06	-	-	-	-
7.60	-42.34	-	-	-	-	-	-	19.95	0.03	-	-	-	-
7.60	-42.44	20.06	0.01	20.88	0.06	20.27	0.06	18.51	0.02	-	-	-	-
7.60	-42.59	-	-	19.28	0.06	18.73	0.06	19.25	0.03	-	-	-	-
7.60	-42.60	-	-	-	-	-	-	17.21	0.00	-	-	-	-
7.61	-42.50	20.77	0.01	18.51	0.02	-	-	-	-	-	-	-	-
7.61	-42.45	-	-	20.09	0.07	19.05	0.09	18.92	0.09	-	-	-	-
7.61	-42.62	20.54	0.01	20.74	0.27	19.52	0.14	18.67	0.01	-	-	-	-
7.61	-42.34	20.21	0.02	19.46	0.03	18.91	0.02	19.01	0.01	-	-	-	-
7.61	-42.43	-	-	19.99	0.03	19.32	0.02	-	-	-	-	-	-
7.61	-42.35	17.73	0.01	-	-	-	-	-	-	-	-	-	-
7.61	-42.32	-	-	19.41	0.06	-	-	19.99	0.08	-	-	-	-
7.61	-42.42	-	-	-	-	-	-	-	-	-	-	-	-
7.62	-42.51	-	-	20.98	0.05	-	-	19.82	0.03	-	-	-	-
7.62	-42.45	18.56	0.02	17.27	0.05	20.44	0.12	-	-	-	-	-	-
7.62	-42.59	-	-	-	-	19.47	0.02	-	-	-	-	-	-
7.62	-42.32	19.37	0.04	20.77	0.04	18.34	0.02	18.03	0.02	-	-	-	-
7.62	-42.55	19.57	0.02	18.68	0.04	18.01	0.02	-	-	-	-	-	-
7.63	-42.38	20.42	0.04	18.19	0.02	18.68	0.10	18.42	0.02	-	-	-	-
7.63	-42.33	-	-	18.95	0.10	-	-	-	-	-	-	-	-
7.63	-42.47	-	-	-	-	18.13	0.04	16.74	0.03	-	-	-	-

TABLE A.1: Continued

RA (deg)	Dec (deg)	Mean g mag	1σ (g mag)	Mean r mag	1σ (r mag)	Mean i mag	1σ (i mag)	Mean z mag	1σ (z mag)	Mean J mag	1σ (J mag)	Mean Ks mag	1σ (Ks mag)
7.63	-42.58	17.49	0.02	18.57	0.05	17.39	0.03	20.08	0.06	-	-	-	-
7.63	-42.51	18.52	0.02	18.79	0.04	-	-	20.40	0.10	-	-	-	-
7.63	-42.28	18.38	0.05	-	-	-	-	-	-	-	-	-	-
7.64	-42.34	-	-	-	-	16.42	0.07	17.65	0.02	-	-	-	-
7.64	-42.31	-	-	16.72	0.08	17.69	0.01	16.60	0.04	-	-	-	-
7.65	-42.57	-	-	17.94	0.02	-	-	17.99	0.01	-	-	-	-
7.65	-42.35	-	-	-	-	-	-	-	-	-	-	-	-
7.65	-42.36	-	-	-	-	19.50	0.06	-	-	-	-	-	-
7.66	-42.59	19.09	0.03	-	-	20.19	0.09	16.92	0.02	-	-	-	-
7.66	-42.41	-	-	-	-	16.96	0.04	-	-	-	-	-	-
7.66	-42.36	19.10	0.01	17.23	0.05	18.47	0.03	-	-	-	-	-	-
7.66	-42.31	-	-	18.86	0.04	17.21	0.08	19.36	0.01	-	-	-	-
7.66	-42.40	19.86	0.03	17.77	0.07	20.10	0.03	-	-	-	-	-	-
7.66	-42.44	-	-	-	-	16.82	0.03	-	-	-	-	-	-
7.66	-42.51	19.53	0.02	17.61	0.04	16.69	0.06	19.09	0.00	-	-	-	-
7.67	-42.43	20.61	0.05	-	-	19.10	0.01	-	-	-	-	-	-
7.67	-42.51	-	-	19.36	0.02	19.59	0.03	16.40	0.02	-	-	-	-
7.68	-42.46	21.06	0.06	20.75	0.02	16.87	0.02	16.36	0.01	-	-	-	-
7.68	-42.28	-	-	17.90	0.04	16.37	0.01	-	-	-	-	-	-
7.69	-42.55	21.17	0.06	16.59	0.03	18.12	0.02	19.05	0.01	-	-	-	-
7.69	-42.50	-	-	19.09	0.02	19.33	0.03	18.31	0.01	-	-	-	-
7.69	-42.32	18.17	0.03	19.96	0.03	18.71	0.02	19.42	0.04	-	-	-	-
7.70	-42.50	18.85	0.01	19.58	0.02	-	-	-	-	-	-	-	-
7.70	-42.41	17.75	0.00	-	-	-	-	19.18	0.02	-	-	-	-
7.70	-42.37	-	-	20.87	0.06	19.35	0.02	17.93	0.02	-	-	-	-
7.70	-42.43	-	-	19.77	0.02	19.40	0.05	16.83	0.01	-	-	-	-

TABLE A.1: Continued

RA (deg)	Dec (deg)	Mean *g* mag	1σ (*g* mag)	Mean *r* mag	1σ (*r* mag)	Mean *i* mag	1σ (*i* mag)	Mean *z* mag	1σ (*z* mag)	Mean *J* mag	1σ (*J* mag)	Mean *Ks* mag	1σ (*Ks* mag)
7.70	-42.44	20.83	0.04	-	-	17.87	0.06	-	-	-	-	-	-
7.70	-42.40	-	-	17.55	0.03	17.04	0.02	19.16	0.03	-	-	-	-
7.71	-42.49	18.93	0.00	17.22	0.02	16.96	0.02	19.26	0.05	-	-	-	-
7.71	-42.39	-	-	-	-	19.99	0.05	20.46	0.07	-	-	-	-
7.71	-42.30	-	-	20.49	0.04	-	-	-	-	-	-	-	-
7.71	-42.32	-	-	20.58	0.04	-	-	-	-	-	-	-	-
7.72	-42.31	-	-	20.75	0.05	20.16	0.05	18.38	0.03	-	-	-	-
7.72	-42.33	17.31	0.02	17.50	0.03	16.76	0.03	-	-	-	-	-	-
7.74	-42.50	-	-	18.65	0.04	18.41	0.03	-	-	-	-	-	-
7.74	-42.42	-	-	-	-	19.77	0.15	18.18	0.01	-	-	-	-

TABLE A.2: The slopes, Spearman rank coefficients, probability of no correlation and colour trend for each season of DES in each combination of filters plotted in Figure A.5.

(A) From the *g*-*r* colour vs *r* magnitude plots in Figure A.5a.

Season	Slope of *g*-*r* vs *r* mag	ρ-value	p-value	Trend
2013	0.16 ± 0.05	0.54	3.86×10^{-3}	BWB
2014	-0.19 ± 0.05	-0.56	2.02×10^{-3}	RWB
2015	-0.19 ± 0.07	-0.4	0.03	SWB
2016	-0.27 ± 0.02	-0.93	1.26×10^{-13}	RWB
2017	-0.32 ± 0.02	-0.87	1.09×10^{-8}	RWB

(B) From the *g*-*i* colour vs *r* magnitude plots in Figure A.5b.

Season	Slope of *g*-*i* vs *r* mag	ρ-value	p-value	Trend
2013	0.38 ± 0.07	0.63	4.73×10^{-4}	BWB
2014	-0.14 ± 0.07	-0.33	0.09	SWB
2015	-0.14 ± 0.12	-0.11	0.57	SWB
2016	-0.29 ± 0.03	-0.92	1.30×10^{-12}	RWB
2017	-0.38 ± 0.03	-0.84	1.67×10^{-7}	RWB

(C) From the *r*-*i* colour vs *r* magnitude plots in Figure A.5c.

Season	Slope of *r*-*i* vs *r* mag	ρ-value	p-value	Trend
2013	0.21 ± 0.03	0.7	3.11×10^{-5}	BWB
2014	0.06 ± 0.03	0.34	0.09	SWB
2015	0.07 ± 0.05	0.35	0.06	SWB
2016	0.01 ± 0.02	-0.33	0.08	SWB
2017	-0.06 ± 0.01	-0.71	5.45×10^{-5}	RWB

(D) From the *r*-*z* colour vs *r* magnitude plots in Figure A.5d.

Season	Slope of *r*-*z* vs *r* mag	ρ-value	p-value	Trend
2013	0.58 ± 0.03	0.88	1.56×10^{-19}	BWB
2014	0.23 ± 0.03	0.58	3.81×10^{-6}	BWB
2015	0.31 ± 0.05	0.67	1.03×10^{-9}	BWB
2016	0.13 ± 0.01	0.75	1.02×10^{-11}	BWB
2017	0.06 ± 0.01	0.36	9.58×10^{-3}	BWB

(E) From *i*-*z* colour vs *r* magnitude plots in Figure A.5e.

Season	Slope of *i*-*z* vs *r* mag	ρ-value	p-value	Trend
2013	0.37 ± 0.02	0.9	1.03×10^{-20}	BWB
2014	0.17 ± 0.02	0.65	1.73×10^{-7}	BWB
2015	0.25 ± 0.03	0.77	3.68×10^{-13}	BWB
2016	0.15 ± 0.01	0.9	3.07×10^{-22}	BWB
2017	0.12 ± 0.01	0.89	9.82×10^{-19}	BWB

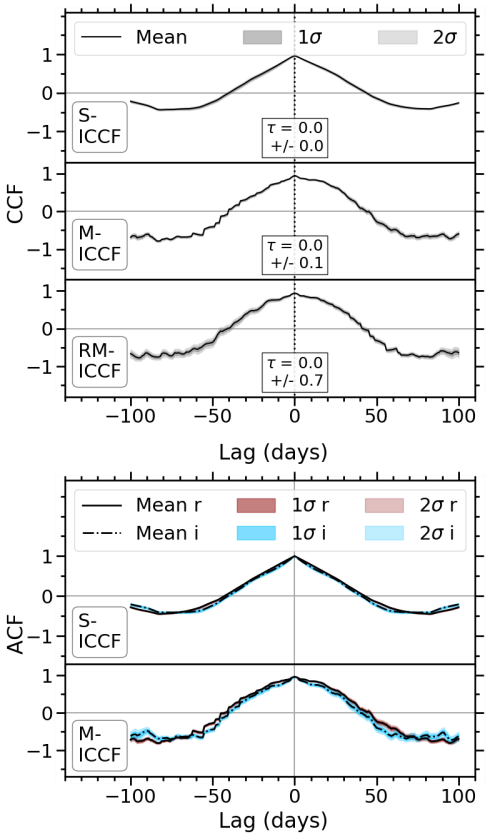

(A) CCFs and ACFs of the 2013 *r* and *i* light curves.

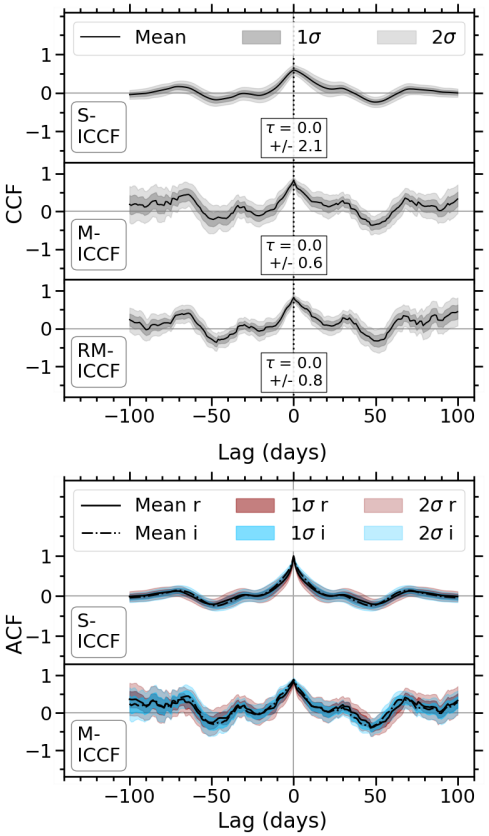

(B) CCFs and ACFs of the 2014 *r* and *i* light curves.

FIGURE A.1: *Top Panels*: Mean CCFs of the *r* and *i* light curves of the individual years of PKS 0027-426 between 2013-2016 and 2018, made using each method of CCF. *Lower Panels*: The corresponding ACFs . In these CCFs, the M-ICCF method refers to the interpolated *r* band, and the RM-ICCF method refers to the interpolated *i* band.

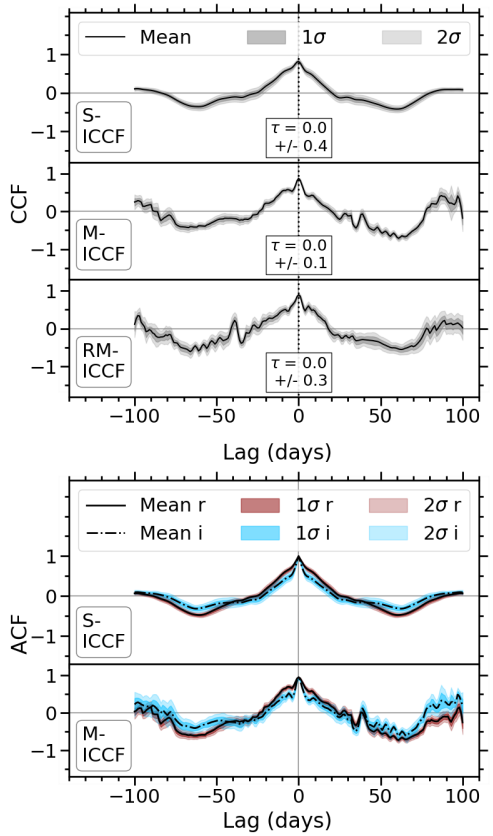

(C) CCFs and ACFs of the 2015 r and i light curves.

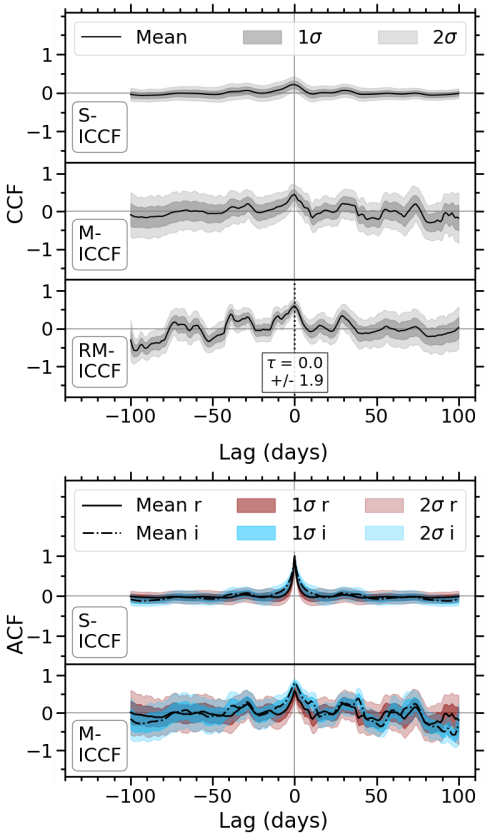

(D) CCFs and ACFS of the 2016 r and i light curves.

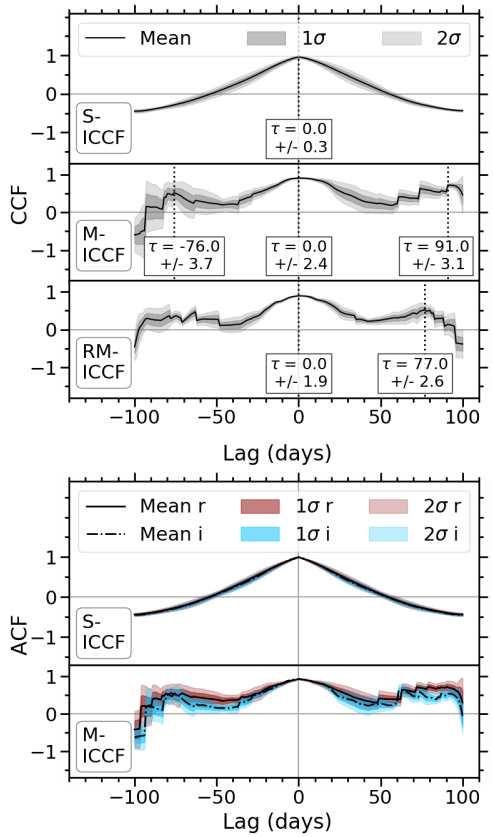

(E) CCFs and ACFs of the 2018 r and i light curves.

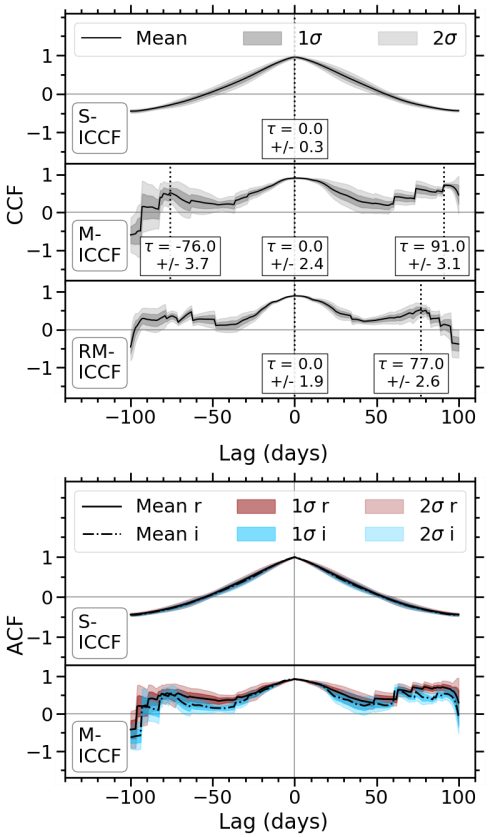

(F) CCFs and ACFs of the 2019 r and i light curves.

FIGURE A.1: Continued.

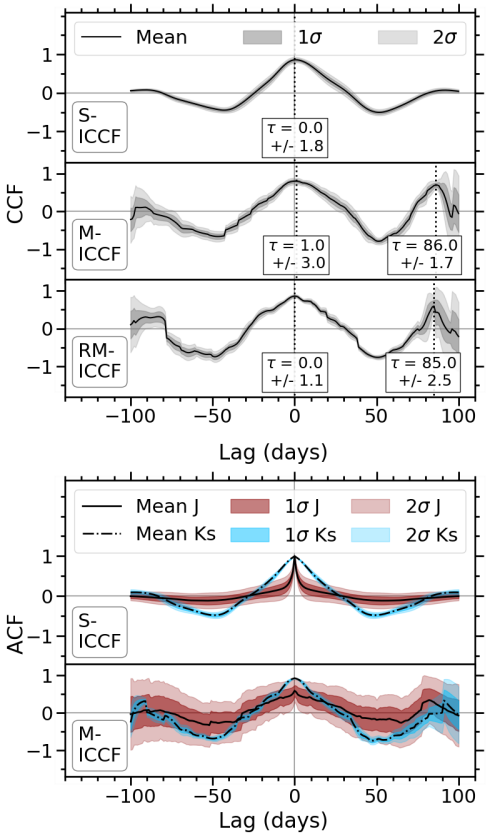

(A) CCFs and ACFs of the 2018 *J* and *Ks* light curves.

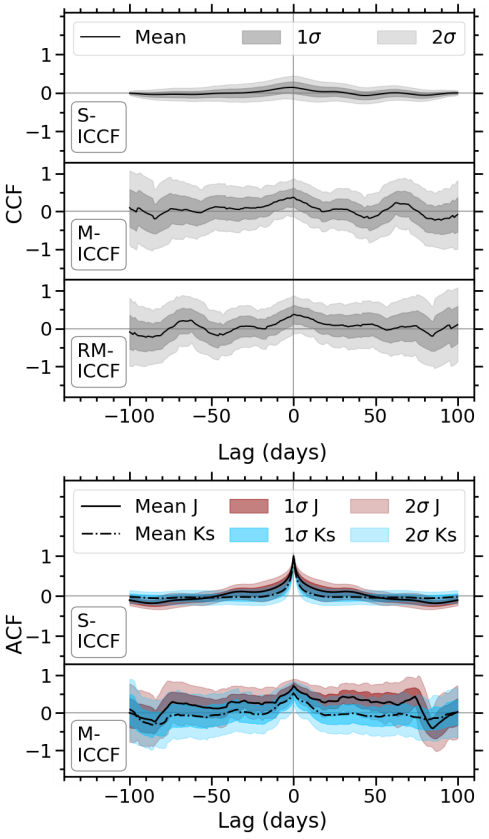

(B) CCFs and ACFs of the 2019 *J* and *Ks* light curves.

FIGURE A.2: *Top Panels*: Mean CCFs of the *J* and *Ks* light curves of the individual years of PKS 0027-426 for the seasons starting 2018 and 2019, made using each method of CCF. *Lower Panels*: The corresponding ACFs . In these CCFs, the M-ICCF method refers to the interpolated *J* band, and the RM-ICCF method refers to the interpolated *Ks* band.

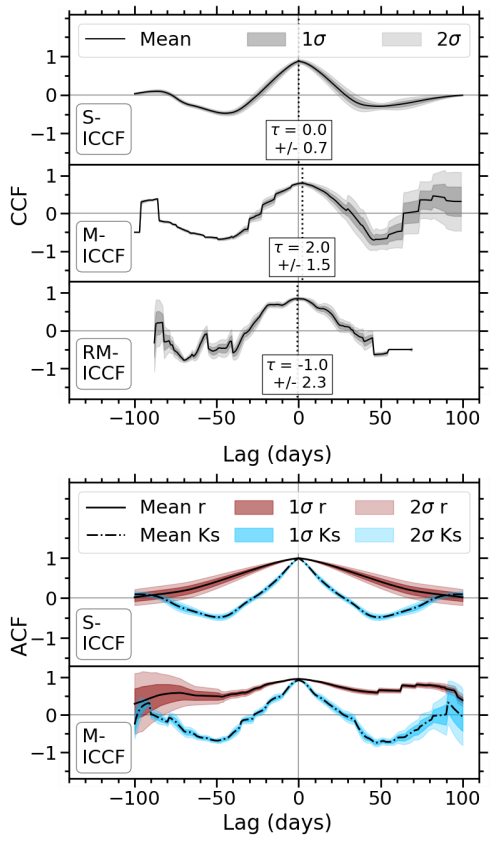

(A) CCFs and ACFs of the 2018 *r* and *Ks* light curves.

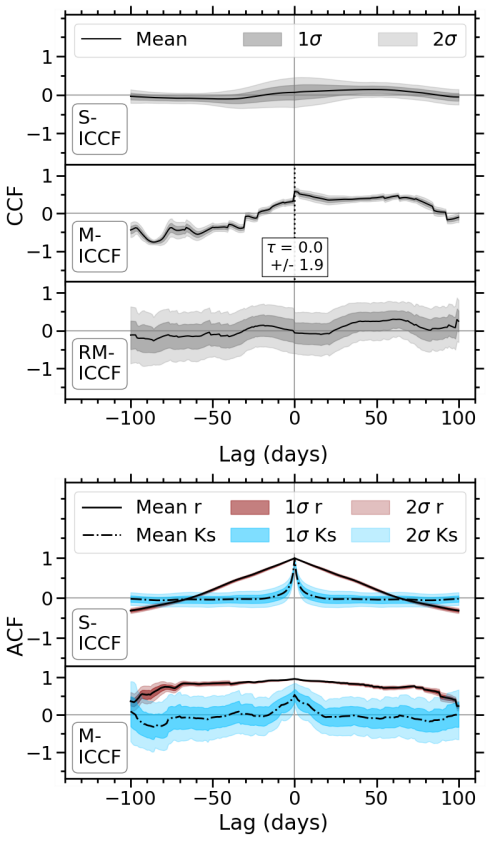

(B) CCFs and ACFs of the 2019 *r* and *Ks* light curves.

FIGURE A.3: *Top Panels*: Mean CCFs of the *r* and *Ks* light curves of the individual years of PKS 0027-426 for the seasons starting 2018 and 2019, made using each method of CCF. *Lower Panels*: The corresponding ACFs . In these CCFs, the M-ICCF method refers to the interpolated *r* band, and the RM-ICCF method refers to the interpolated *Ks* band.

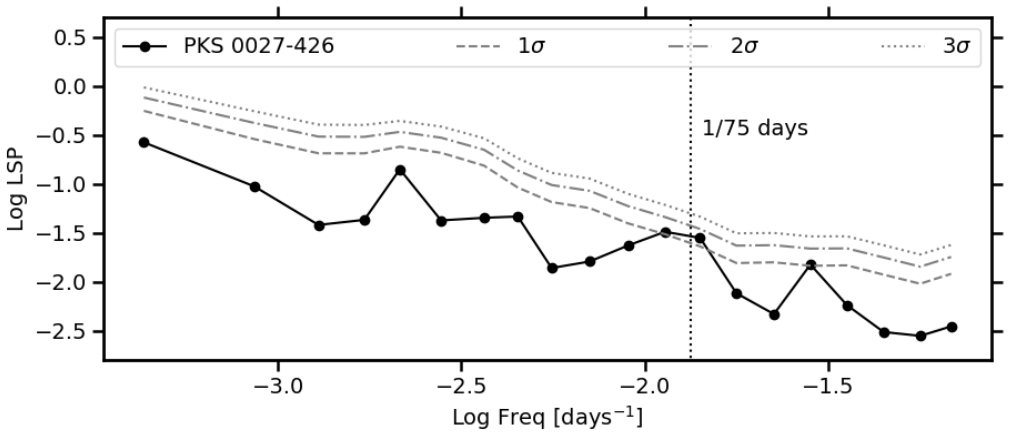

(A) Lomb-Scargle periodogram of the 2017-2019 observation seasons of PKS 0027-426 in the *r* band.

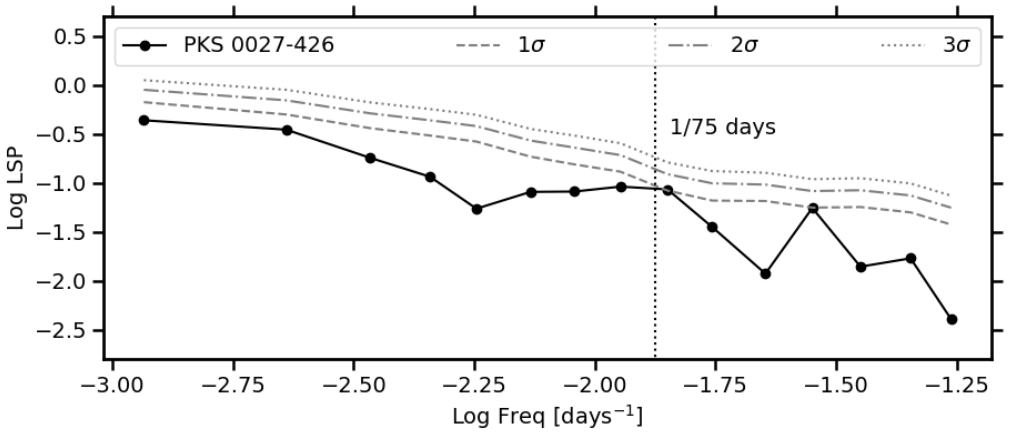

(B) Lomb-Scargle periodogram of the entire observational period of PKS 0027-426 in the *r* band.

FIGURE A.4: Lomb-Scargle periodograms of PKS 0027-426.

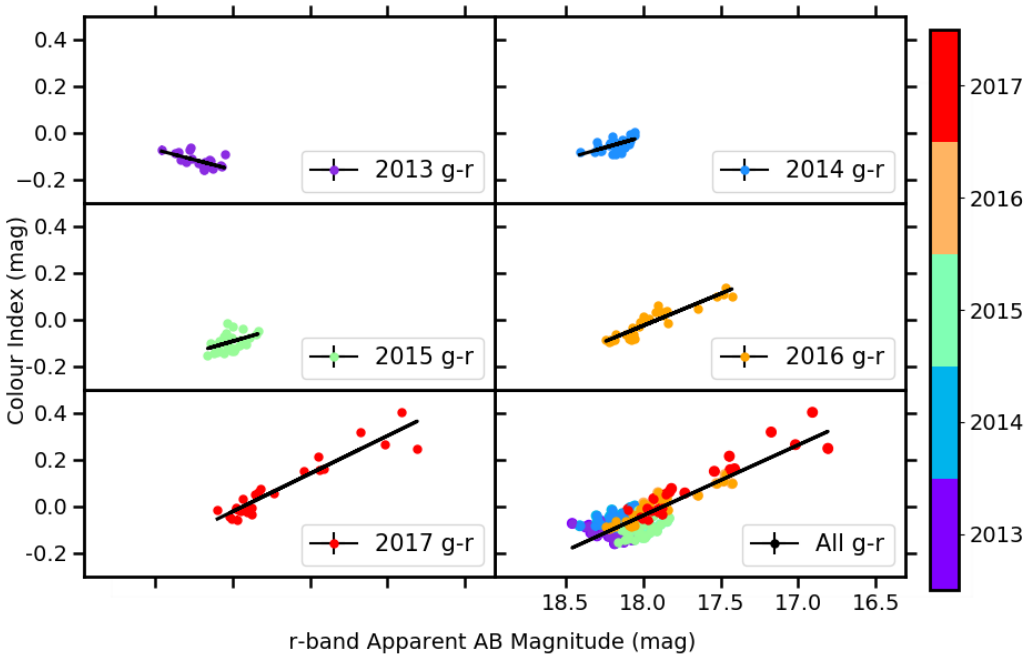

(A) Optical *g-r* colour variability for each observation season of DES.

FIGURE A.5: Optical colour variability for each combination of filters in each observation season of DES, where the colour of the data points corresponds to the observation season.

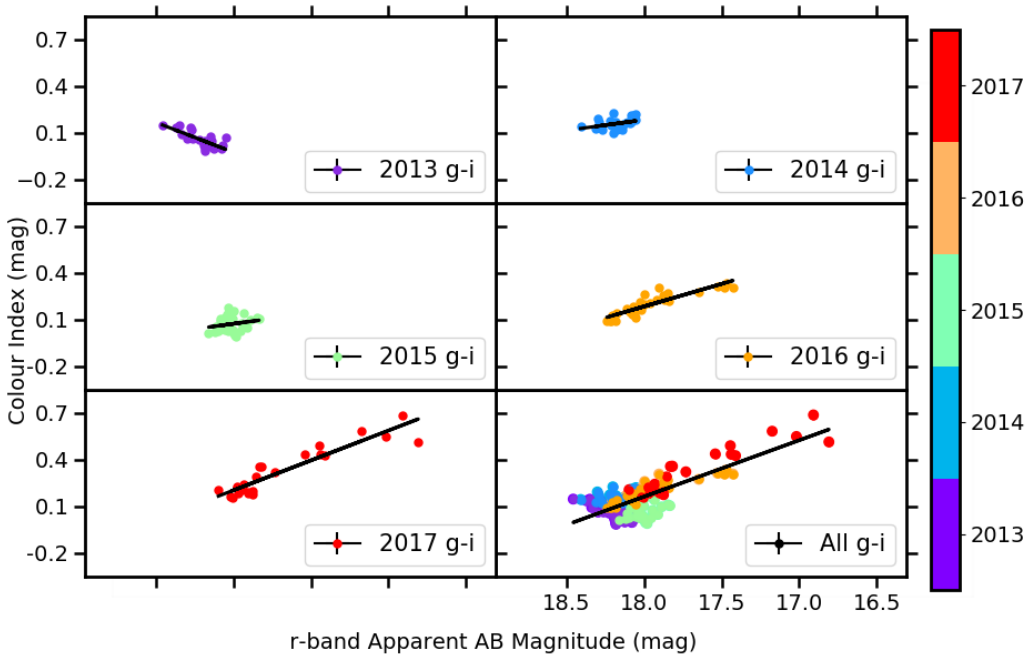

(B) Optical *g-i* colour variability for each observation season of DES.

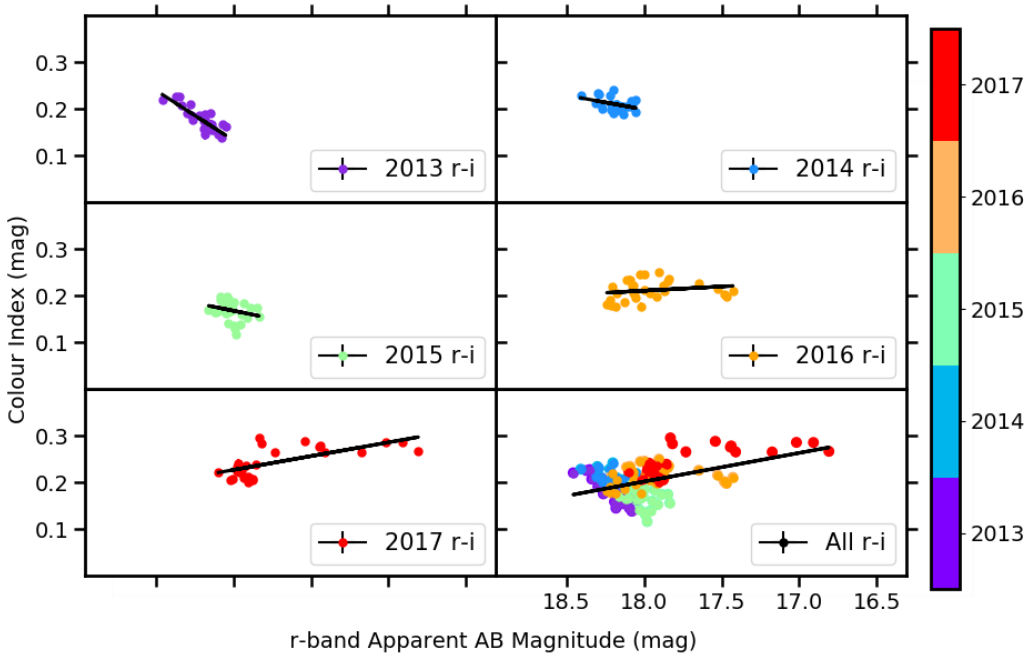

(C) Optical *r-i* colour variability for each observation season of DES.

FIGURE A.5: Continued

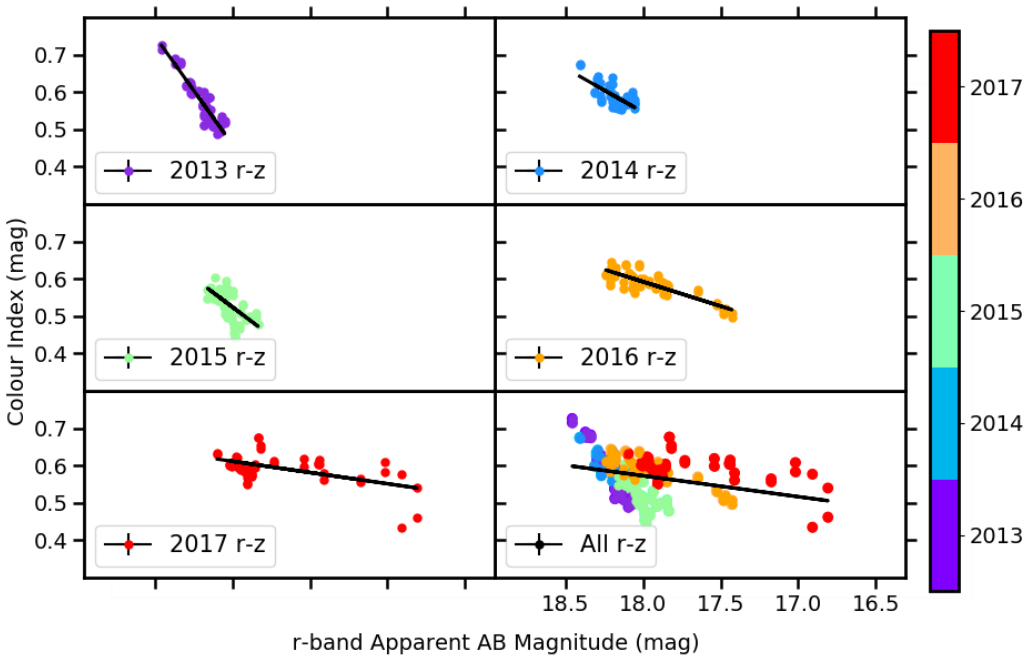

(D) Optical *r-z* colour variability for each observation season of DES.

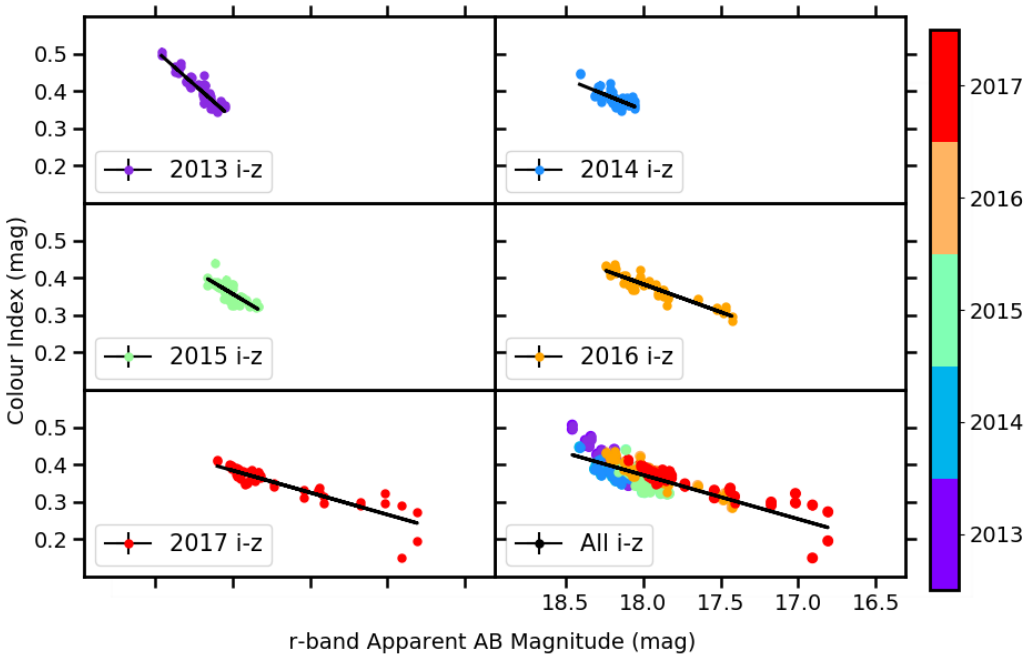

(E) Optical *i-z* colour variability for each observation season of DES.

FIGURE A.5: Continued.

TABLE A.3: The change in slope after the outliers are excluded.

(A) The 2013 season after the outliers on MJD 56590 are excluded.

Colour	Slope with All Epochs	Slope Without Outlier
g-r	0.15 ± 0.05	0.16 ± 0.05
g-i	0.39 ± 0.07	0.38 ± 0.07
g-z	0.85 ± 0.07	0.74 ± 0.05
r-i	0.22 ± 0.03	0.22 ± 0.03
r-z	0.69 ± 0.06	0.58 ± 0.03
i-z	0.45 ± 0.05	0.36 ± 0.02

(B) The 2014 season after the outliers on MJD 56916 are excluded.

Colour	Slope with All Epochs	Slope Without Outlier
g-r	-0.2 ± 0.05	-0.19 ± 0.05
g-i	-0.2 ± 0.09	-0.14 ± 0.08
g-z	0.03 ± 0.06	0.06 ± 0.06
r-i	0.01 ± 0.06	0.06 ± 0.03
r-z	0.22 ± 0.03	0.23 ± 0.03
i-z	0.21 ± 0.03	0.17 ± 0.02

(C) The 2015 season after the outliers on MJD 57281 are excluded.

Colour	Slope with All Epochs	Slope Without Outliers
g-r	-0.31 ± 0.09	-0.19 ± 0.08
g-i	-0.48 ± 0.18	-0.14 ± 0.13
g-z	-0.49 ± 0.20	0.12 ± 0.09
r-i	-0.14 ± 0.10	0.07 ± 0.05
r-z	-0.18 ± 0.16	0.31 ± 0.05
i-z	-0.04 ± 0.11	0.24 ± 0.03

(D) The 2016 season after the outliers on MJD 57627 are excluded.

Colour	Slope with All Epochs	Slope Without Outliers
g-r	-0.27 ± 0.02	-0.27 ± 0.02
g-i	-0.29 ± 0.03	-0.29 ± 0.03
g-z	-0.14 ± 0.02	-0.14 ± 0.02
r-i	0.31 ± 0.15	-0.02 ± 0.02
r-z	0.42 ± 0.09	0.13 ± 0.01
i-z	0.11 ± 0.01	0.15 ± 0.01

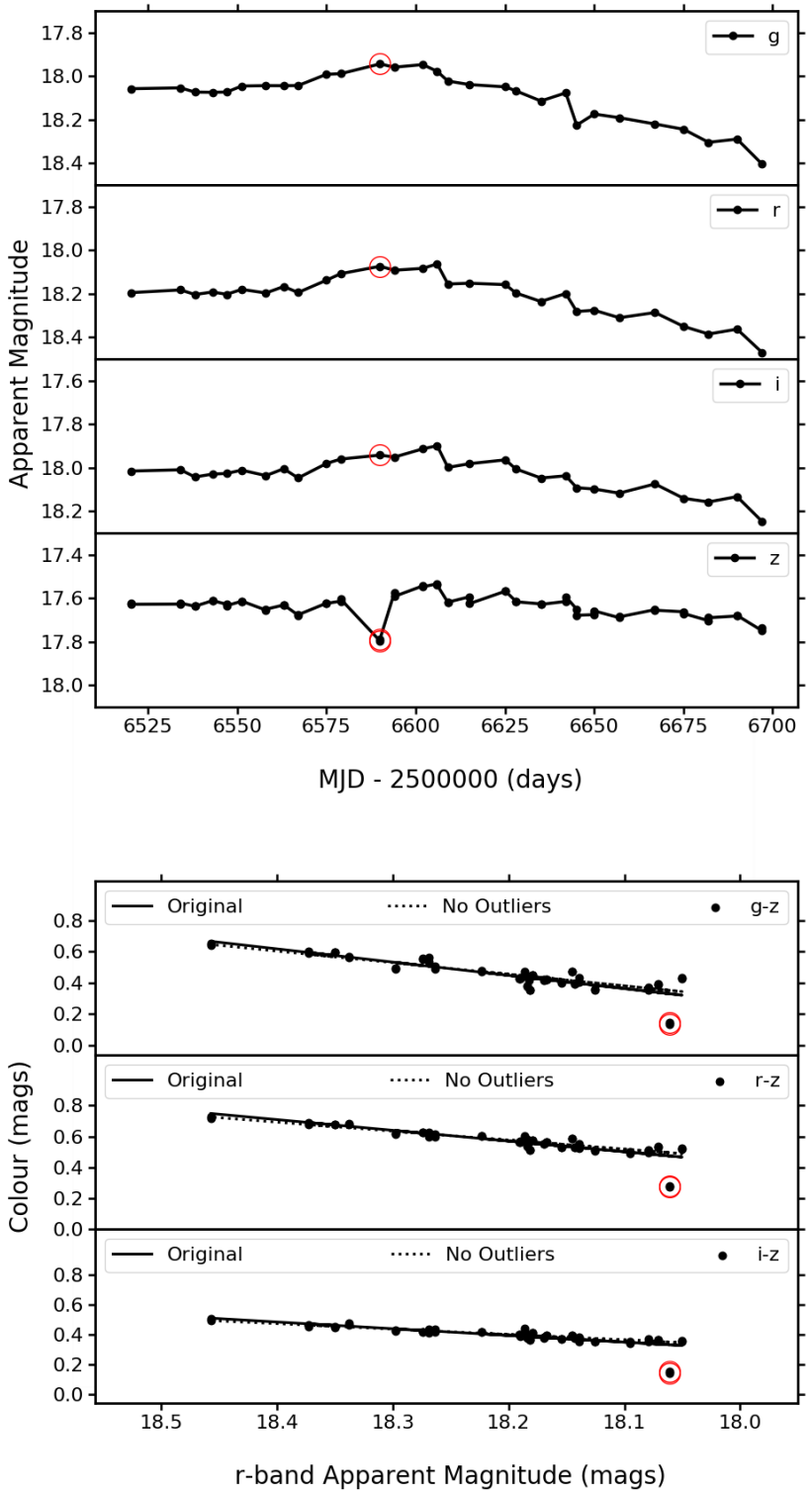

(A) Outlier of the optical colour variability in the 2013 season.

FIGURE A.6: Outliers in the DES light curves of PKS 0027-426 and the optical colour variability.

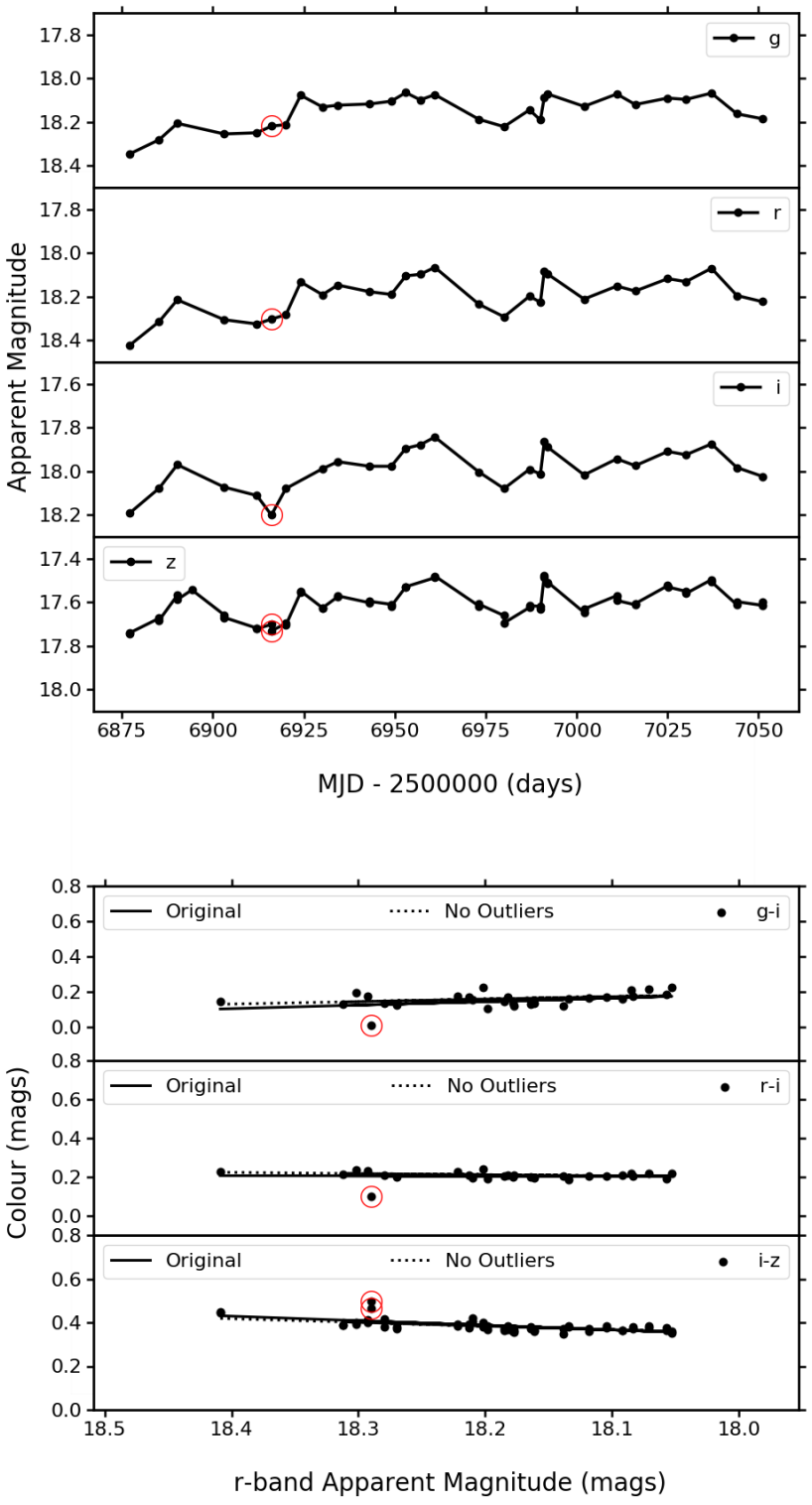

(B) Outlier of the optical colour variability in the 2014 season.

FIGURE A.6: Continued.

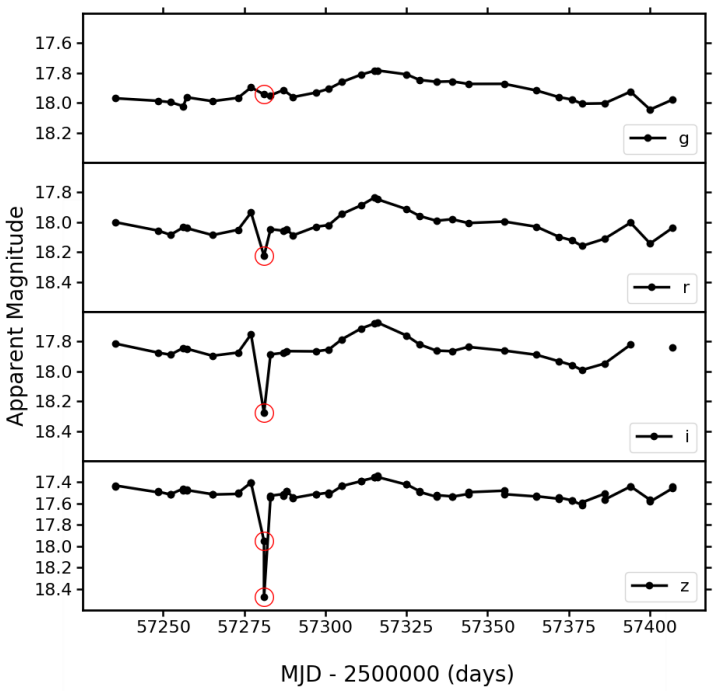

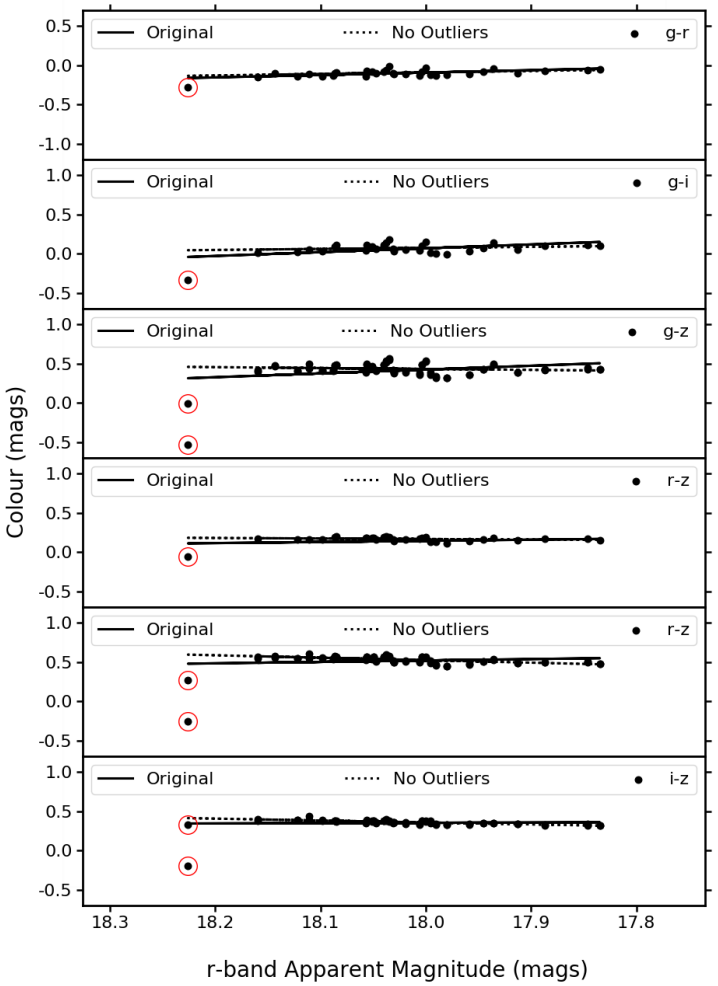

(C) Outlier of the optical colour variability in the 2015 season.

FIGURE A.6: Continued.

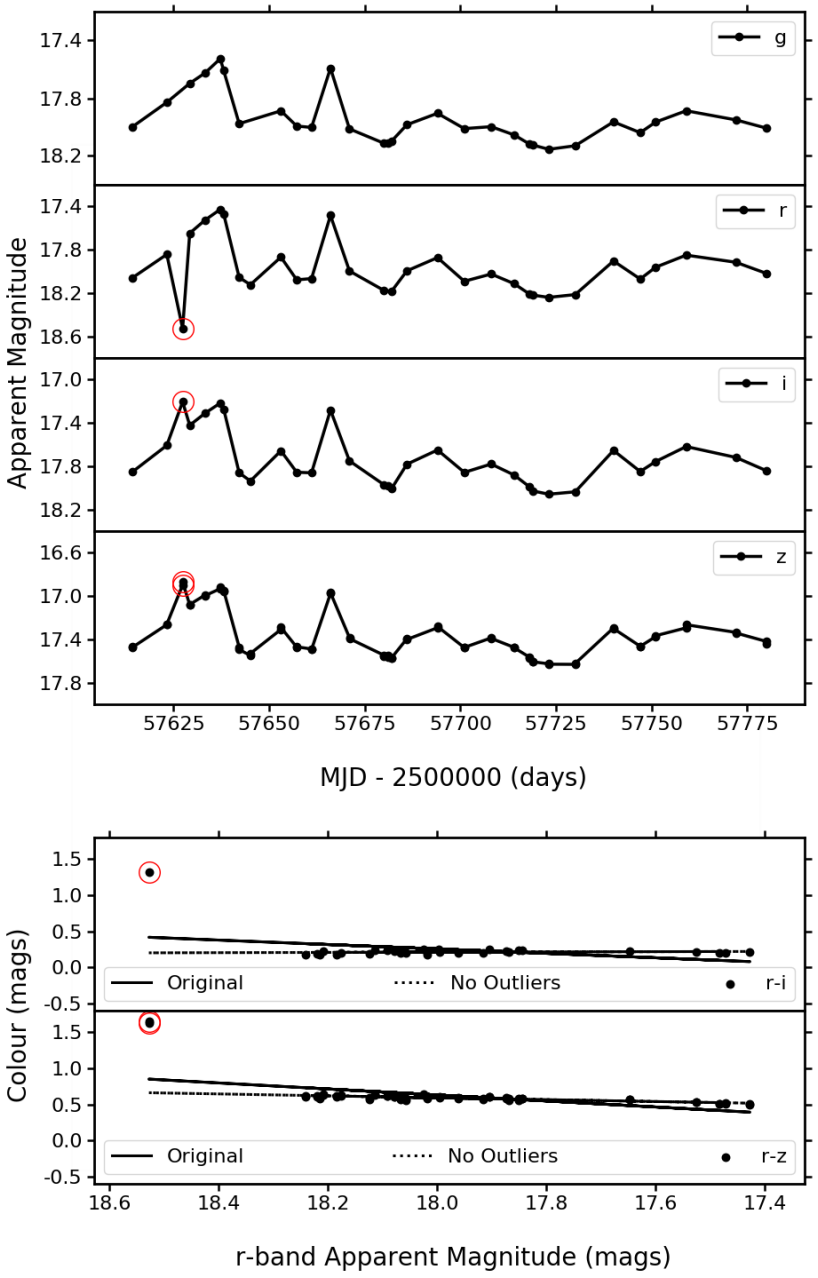

(D) Outlier of the optical colour variability in the 2016 season.

FIGURE A.6: Continued.

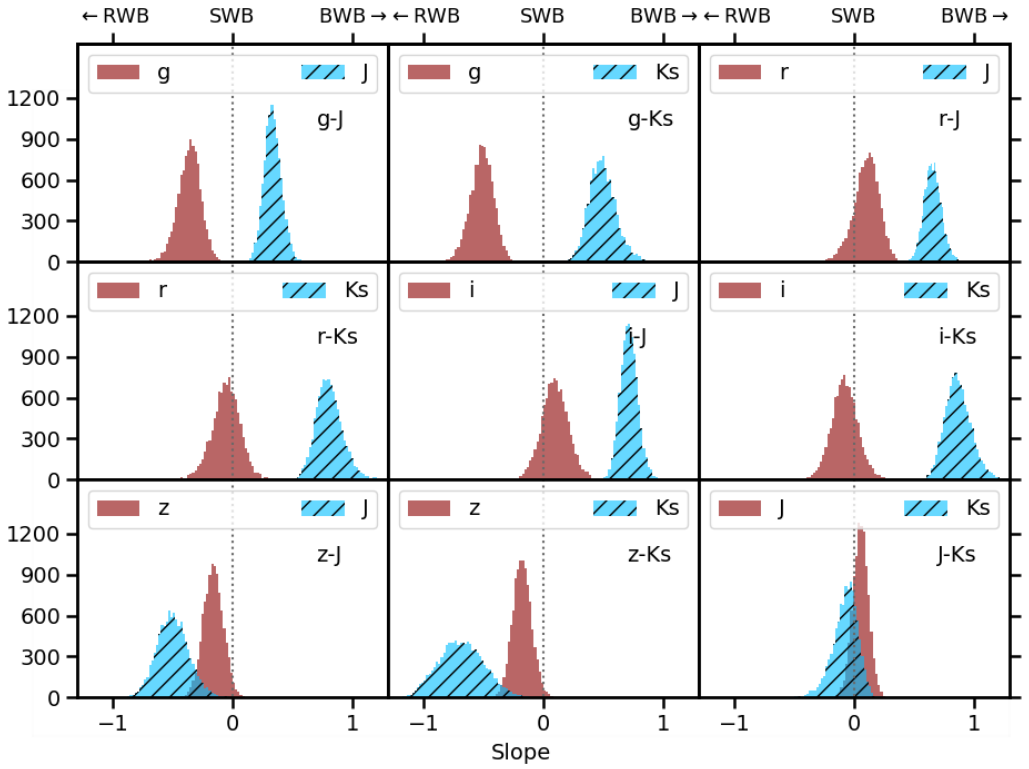

FIGURE A.7: The slopes measured for each combination of the Optical-NIR colour vs r magnitude plots in the 2017 season, for the entire light curve, which includes a ∼ month long gap in the NIR light curve between MJD 57993 and 58044.

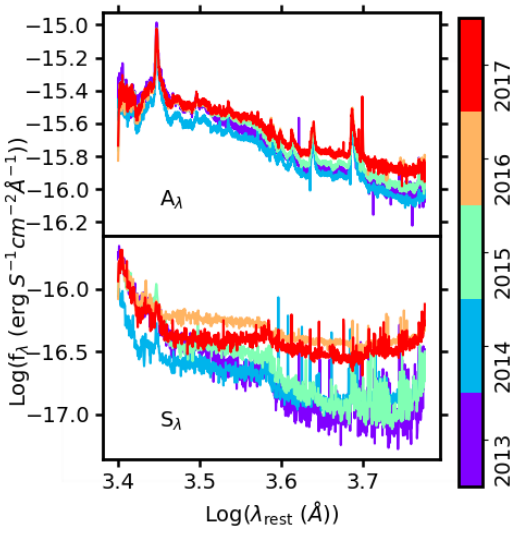

FIGURE A.8: Decomposition of the OzDES spectra into the variable (S_λ) and non-variable (A_λ) components for each season of DES. The S_λ spectra are smoothed in this plot so that they are easier to see.

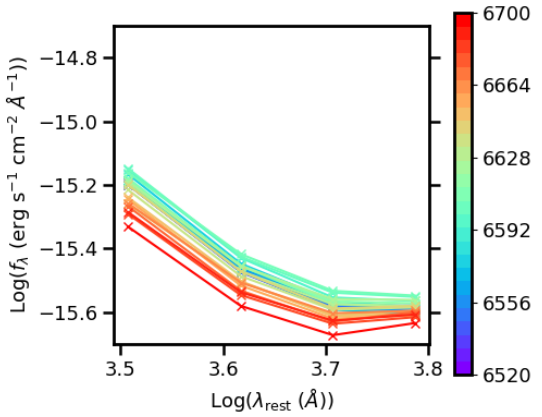

(A) Broadband Spectra of the 2013 Season.

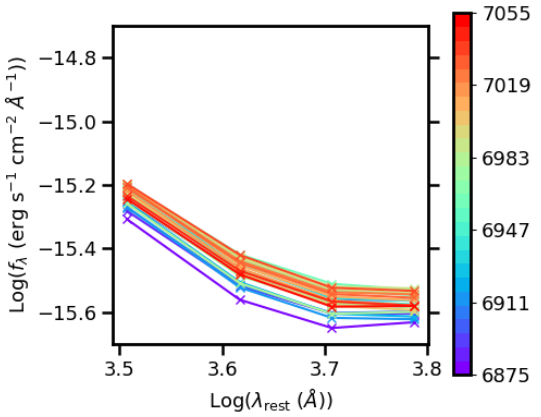

(B) Broadband Spectra of the 2014 Season.

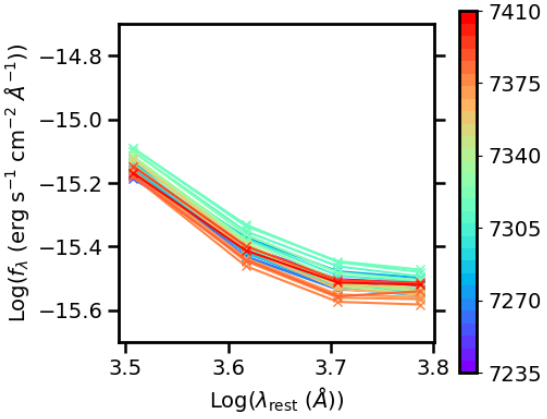

(C) Broadband Spectra of the 2015 Season.

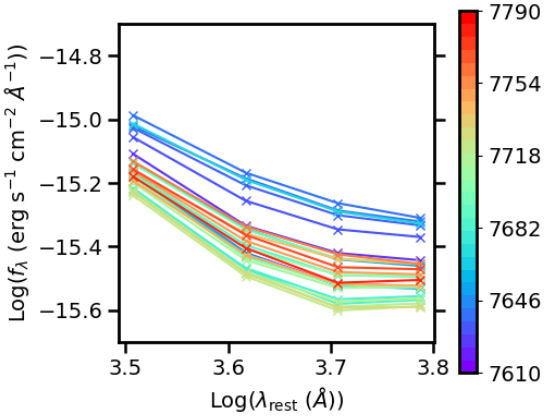

(D) Broadband Spectra of the 2016 Season.

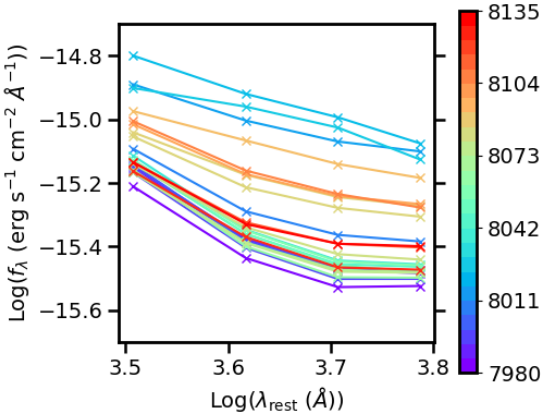

(E) Broadband Spectra of the 2017 Season.

FIGURE A.9: All broadband spectra in each observation season of DES, coloured according to observation epoch.

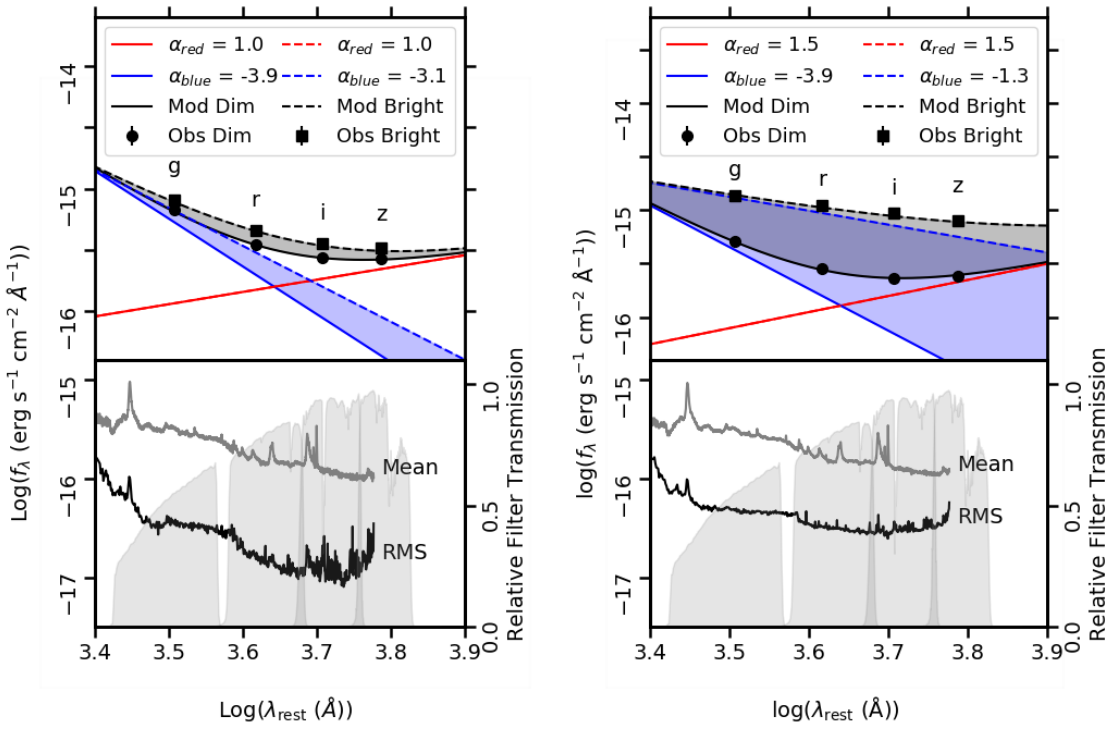

(A) Modelled Spectra of the 2015 Season.

(B) Modelled Spectra of the Entire DES Observation Period.

FIGURE A.10: *Upper panel*: Modelled broadband spectra of the red and blue emission that combine to match the average brightest and dimmest epochs in the 2015 observation season and the entire observational period compared to the observed broadband spectra. The solid lines correspond to the modelled spectra of the dimmest epochs, and the dashed lines correspond to the modelled spectra of the brightest epochs. *Lower panel*: Mean and smoothed RMS OzDES spectra for each season plotted over the DES filter Transmissions.

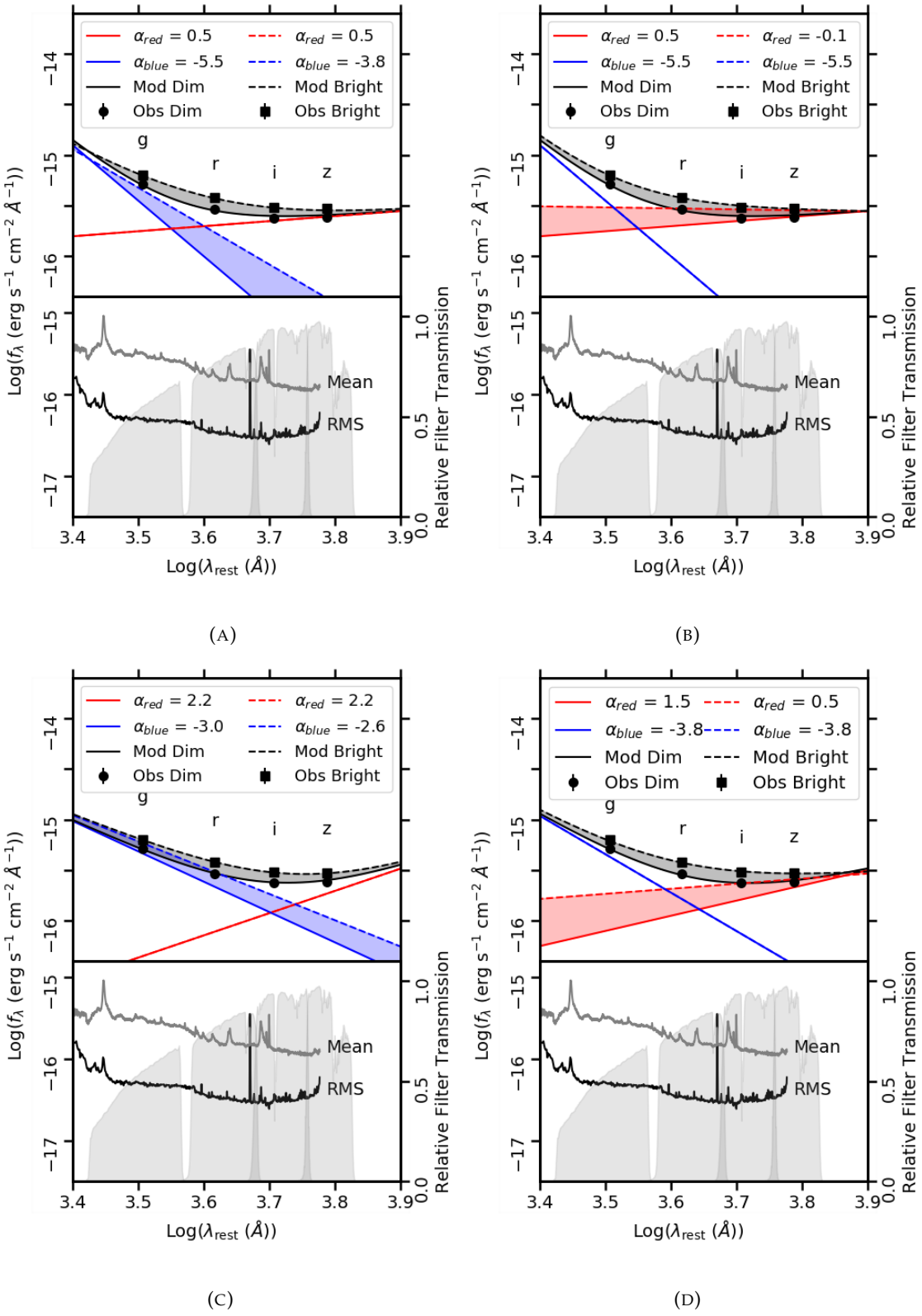

FIGURE A.11: *Upper panel*: Alternative examples of the modelled broadband spectra of the blue and red emission to match the average observed brightest and dimmest epochs in the 2014 season. The solid lines correspond to the modelled spectra of the dimmest epochs, and the dashed lines correspond to the modelled spectra of the brightest epochs. *Lower panel*: Mean and smoothed RMS OzDES spectra for each season plotted over the DES filter Transmissions.

Appendix B

Dust Reverberation Mapping of Zw229-015

B.1 Earlier Observations of Zw229-015

Table B.1 contains the mean photometric measurements of Zw229-015 from each epoch observed with the Catalina Real-time Transient Survey between 2005 and 2010. Note that this data likely contains a different amount of host galaxy flux contribution to the observations used in this thesis.

B.2 Cross Correlations

The remaining CCFs and the corresponding ACFs of each combination of optical and IR light curve in each observation season are displayed in Figures B.1, B.2 and B.3 for the ground-Spitzer 1, *Kepler*-Spitzer 1 and ground-Spitzer 2 light curves respectively, for each method of cross correlation. Unless otherwise stated, each CCF is tested with a lag range of $\pm$ 100 days due to the length of the light curves in the individual seasons. Potential lags are measured from the peaks of the CCFs and are considered positive detections if the values are greater than 0.5 as discussed in Chapter 5, and are labelled on the plots.

Figure B.1 contains the CCFs of the ground-Spitzer 1 light curves in the 2011 and 2012 seasons, where the CCFs are only tested with lags between $\pm$ 60 days and $\pm$ 50 days for the 2011 and 2012 seasons respectively due to the length or overlapping regions of the light curves. Each method of CCF for the season starting in 2011 detects a lag at $\sim$ 20 days, as does the RM-ICCF method of the 2012 season, however the S-ICCF and M-ICCF methods in the 2012 season do not detect lags, which is likely due to the sampling of the light curves.

Figure B.2 contains the *Kepler*-Spitzer 1 CCFs for the individual seasons. The 2011 CCFs are only tested with a lag range of $\pm$ 60 days due to the length of the *Spitzer* 1 light curve in that season. Each method of CCF in the 2011 and 2012 seasons detects the lag at $\sim$ 20 days, as does the M-ICCF and RM-ICCF methods of the 2010 season. The S-ICCF method of the 2010 season does not detect a lag at $\sim$ 20 days, but it does display a peak at that time with a value < 0.5, which could imply the interpolations are diluting the correlations. Additional lags are measured at $\sim$ 75 days in the M-ICCF and RM-ICCF methods of the 2010 and 2012 seasons, which could be due to aliasing of the light curves as peaks at $\sim$ 50-60 days are found in the corresponding optical ACFs. Finally, lags at $\sim$ -90 days are found in some of the CCF methods in the 2010 and 2012 seasons, but as described in Chapter 5, these are deemed unlikely as they occur only due to a small number of overlapping data points.

Figure B.3 contains the ground-Spitzer 2 CCFs for the seasons starting 2013 and 2014. The 2014 season detects a lag at $\sim$ 15 days in each method of CCF, but also detects possible lags at additional intervals of $\sim$ 60 days which could be due to aliasing in the light curves. The 2013 season only detects a possible positive lag in the RM-ICCF method with a value of 48.00$\pm$2.95 days, which is much larger than the positive lags detected below 50 days in the other seasons and other combinations of optical and IR light curves. The M-ICCF and RM-ICCF also detect a possible lag at $\sim$ -95 days, however as this occurs due to a small number of overlapping data points in the light curves, this is deemed unlikely.

Detrending Multi-Season Light Curves The long term variations (i.e. the variability on the timescales of $\sim$ months-years) could impact the CCFs as shown in Figure B.5 for example, as in the *Spitzer* 1 light curve in Figure 5.2 the seasons starting 2012 onward are $\sim$ 0.5 mag brighter than the seasons starting 2010 and 2011 which can result in a CCF that is entirely positive. Therefore to reduce the impact of the long term variations, I detrended each light curve by fitting a third order polynomial and subtracting it, as shown in Figure B.4.

***Kepler* Lomb-Scargle Periodograms** To further explore the peaks detected in the optical ACFs at $\sim$ 50-70 days, I also plotted the Lomb-Scargle periodograms as described in Chapter 3 in Figure B.6. A significant peak is only detected for the periodogram made with the *Kepler* light curve during the period of time that overlaps with the *Spitzer* channel 1 light curves in 2010, therefore implying this is not a true periodicity.

B.3 Light Curve Modelling

Additional Multi-Season Modelling Figures B.7 and B.8 display the simulated light curves made using the MCMC model described in Chapter 5 for the entire ground-Spitzer 1 and ground-Spitzer 2 light curves respectively. The ground-Spitzer 1 light curves were divided into the 2010-2011 seasons and the 2012-2014 seasons as the dramatic increase in flux between 2011 and 2012 was shown to be poorly fit by a single dust component model.

Figure B.7b shows the model matching the highest posterior distribution of the 2010-2011 seasons of the ground-Spitzer 1 light curves. Overall, the shape of the simulated IR light curve is shown to follow the variability of the observed light curve quite well, however, the amplitude of the 2011 season still appears to be overestimated here, and furthermore, the start of the 2010 season is underestimated in the simulated light curve.

Figure B.7c shows the model of the ground-Spitzer 1 light curve in the seasons starting 2012-2014. The overall variability is once again modelled quite well by the simulated light curve, however there are portions that deviate from the observed light curve. For example, the end of the 2012 season is overestimated, and the peak at the end of the 2013 season is not visible in the simulated light curve, however both of these correspond to periods where there are very few, if any, observations in the optical and therefore the IR is simulated here based on the optical interpolations. Additionally, there is a dip in the 2014 season IR observed light curve that is not replicated by the simulated light curve.

Figure B.8 contains the simulated and observed ground-Spitzer 2 light curves for the observation seasons starting in 2013-2014. Like Figure B.7c, the simulated light curve does not replicate the peak in the IR observations at the end of the 2013 season, or the dip in the 2014 season, and it also slightly overestimates the flux between HJD 56450 and 56500 and underestimates the flux between HJD 56550 and 56625, making the variability of the 2013 flatter than the observations. As a comparison, the ground-Spitzer 1 light curves in the seasons starting 2013-2014 were also modelled in Figure B.9.

Individual Observation Season Modelling The MCMC model described in Chapter 5 was also applied to each individual observation seasons for each combination of optical and IR light curves to test whether the best fit parameters remained consistent over time and to lessen the impact of the gaps between observation seasons. The models corresponding to the highest posterior distribution are displayed in Figure B.10, and the mean and their 1σ uncertainties for each parameter are listed in Table B.2.

Overall, the simulated light curves for the individual seasons are shown to fit the observations quite well, and the best fit parameters found are largely consistent with each other and the results found from modelling multiple seasons. However, a lot of the parameters are not constrained well, specifically the radial power law indices and the vertical scale height power law indices are often returned with uncertainties that cover nearly the entire prior range, and the inclination angles are often found with 1σ uncertainties that cover 20-40 degrees. This is thought to be due to the length of the observation seasons not being long enough to properly constrain a best-fit DTF.

Furthermore, some observation seasons find different results depending on the combination of optical and IR light curve used. Specifically, the ground-Spitzer 2 light curves differ from the ground-Spitzer 1 in the season starting in 2013 and 2014, as the ground-Spitzer 1 light curves find a lag of $\sim$ 10 days while the ground-Spitzer 2 light curves find a larger lag of $\sim$ 30 days and a larger inclination angle. However, the lags in these models are not as well constrained as the earlier seasons, returning 1σ uncertainties of $\sim$ 15-20 days. These larger uncertainties occur as the distribution of the lags found are actually double peaked at $\sim$ 10 and 30 days.

TABLE B.1: Mean photometry of Zw229-015 from the Catalina Real Time Transient Survey (Drake et al., 2009).

MJD–2,450,000.5 (days)	V (mag)	Uncertainty in mag
3524.4	14.71	0.06
3669.1	14.65	0.06
4586.4	14.66	0.06
5104.2	14.74	0.06
5339.4	14.70	0.06
5366.4	14.69	0.06
5369.3	14.69	0.06

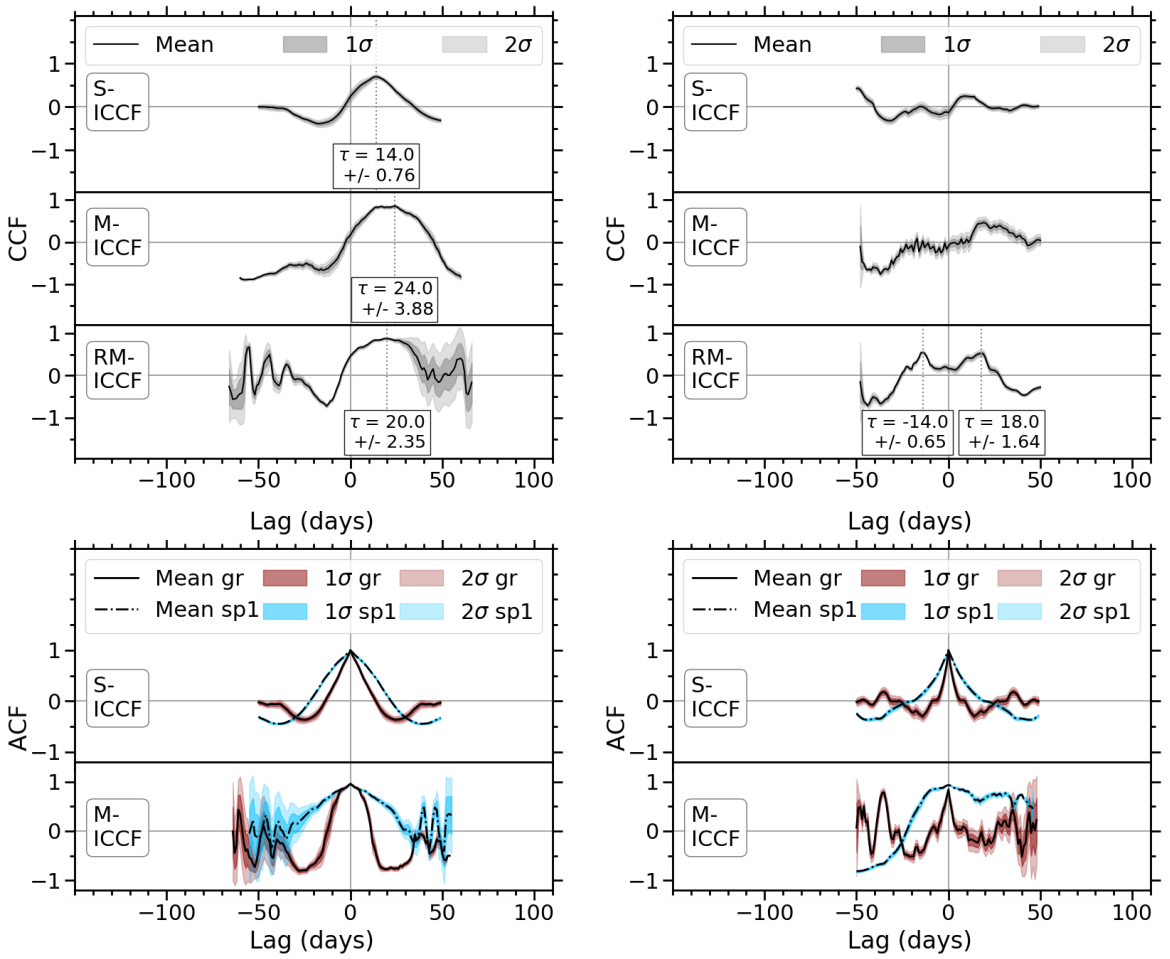

(A) CCFs and ACFs of the 2011 ground and *Spitzer* 1 light curves.

(B) CCFs and ACFs of the 2012 ground and *Spitzer* 1 light curves.

FIGURE B.1: CCF and ACF of the ground optical (gr) and *Spitzer* 1 (sp1) light curves for some of the individual observation seasons of Zw229-015, made using each method of CCF, where M-ICCF refers to interpolating the ground light curve and RM-ICCF refers to interpolating the *Spitzer* 1 light curve.

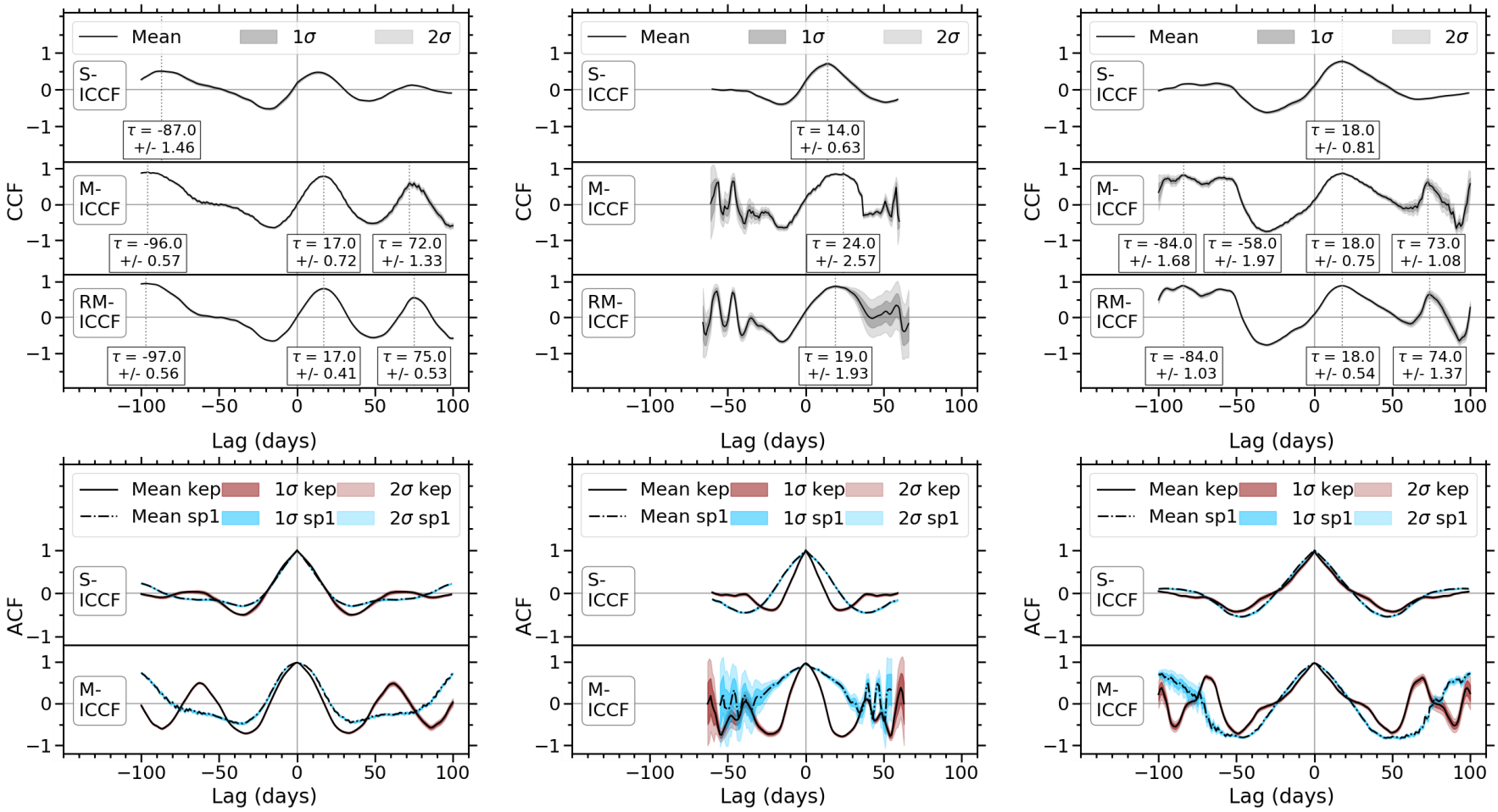

(A) CCFs and ACFs of the 2010 *Kepler* and *Spitzer* 1 light curves.

(B) CCFs and ACFs of the 2011 *Kepler* and *Spitzer* light curves.

(C) CCFs and ACFs of the 2012 *Kepler* and *Spitzer* 1 light curves.

FIGURE B.2: CCF and ACF of the *Kepler* (kep) and *Spitzer* 1 (sp1) light curves for the individual observation seasons of Zw229-015, made using each method of CCF, where M-ICCF refers to interpolating the *Kepler* light curve and RM-ICCF refers to interpolating the *Spitzer* 1 light curve.

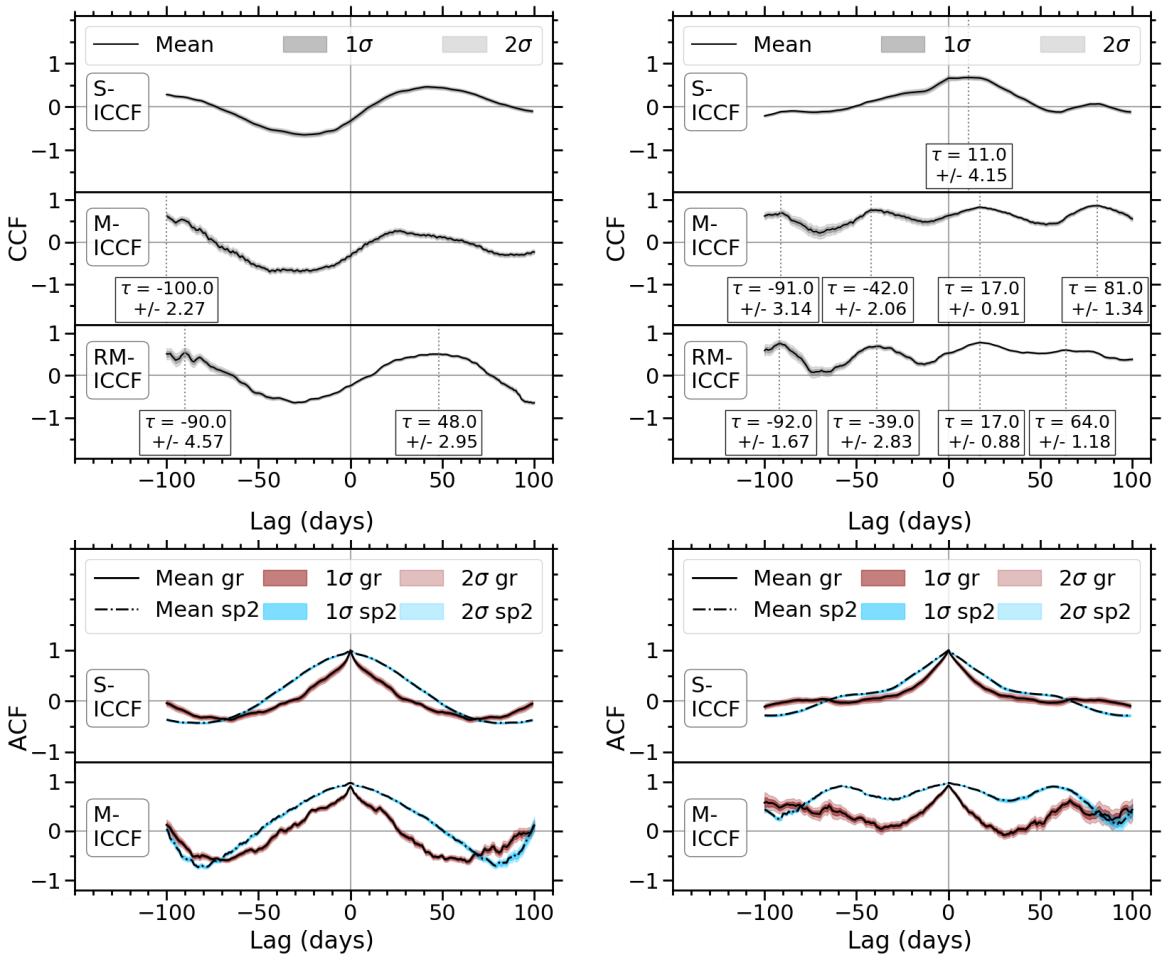

(A) CCFs and ACFs of the 2013 ground and *Spitzer* 2 light curves.

(B) CCFs and ACFs of the 2014 ground and *Spitzer* 2 light curves.

FIGURE B.3: CCF and ACF of the ground optical (gr) and *Spitzer* 2 (sp2) light curves for the individual observation seasons and the entire light curves of Zw229-015, made using each method of CCF, where M-ICCF refers to interpolating the ground light curve and RM-ICCF refers to interpolating the *Spitzer* 2 light curve.

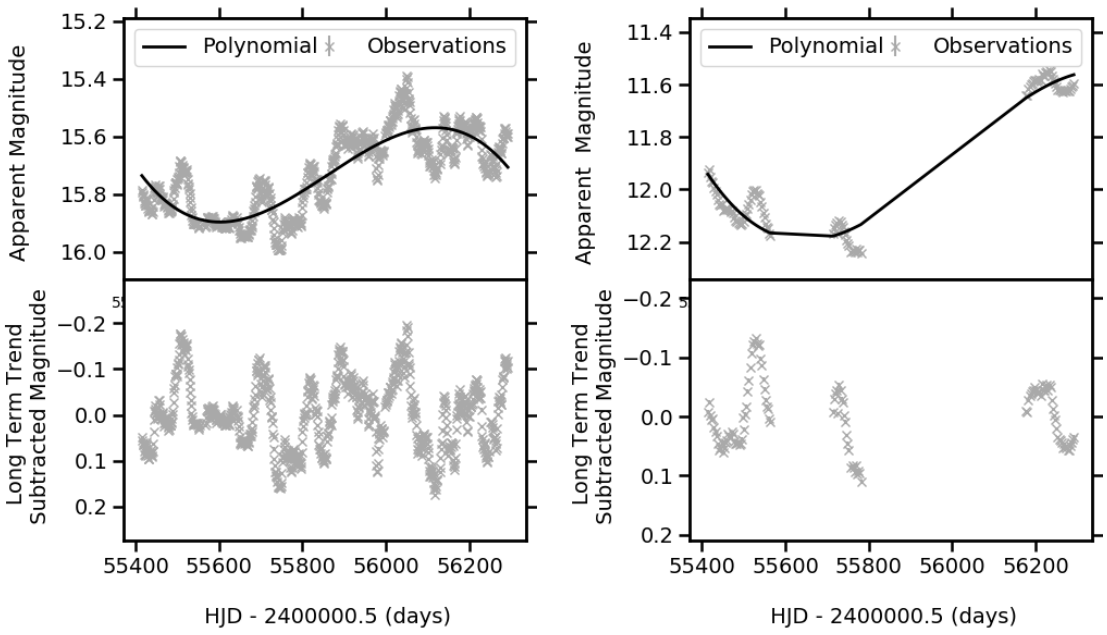

(A) Long-term variability detrended *Kepler* light curve.

(B) Long-term variability detrended *Spitzer* 1 light curve.

FIGURE B.4: *Upper Panels:* Examples of the polynomials fitted to the light curves of Zw229-015 for the 2010-2012 observation seasons that demonstrated the long term trends. *Lower Panels:* Examples of the light curves of Zw229-015 detrended of the long-term variations by subtracting the polynomial that was fitted to the data.

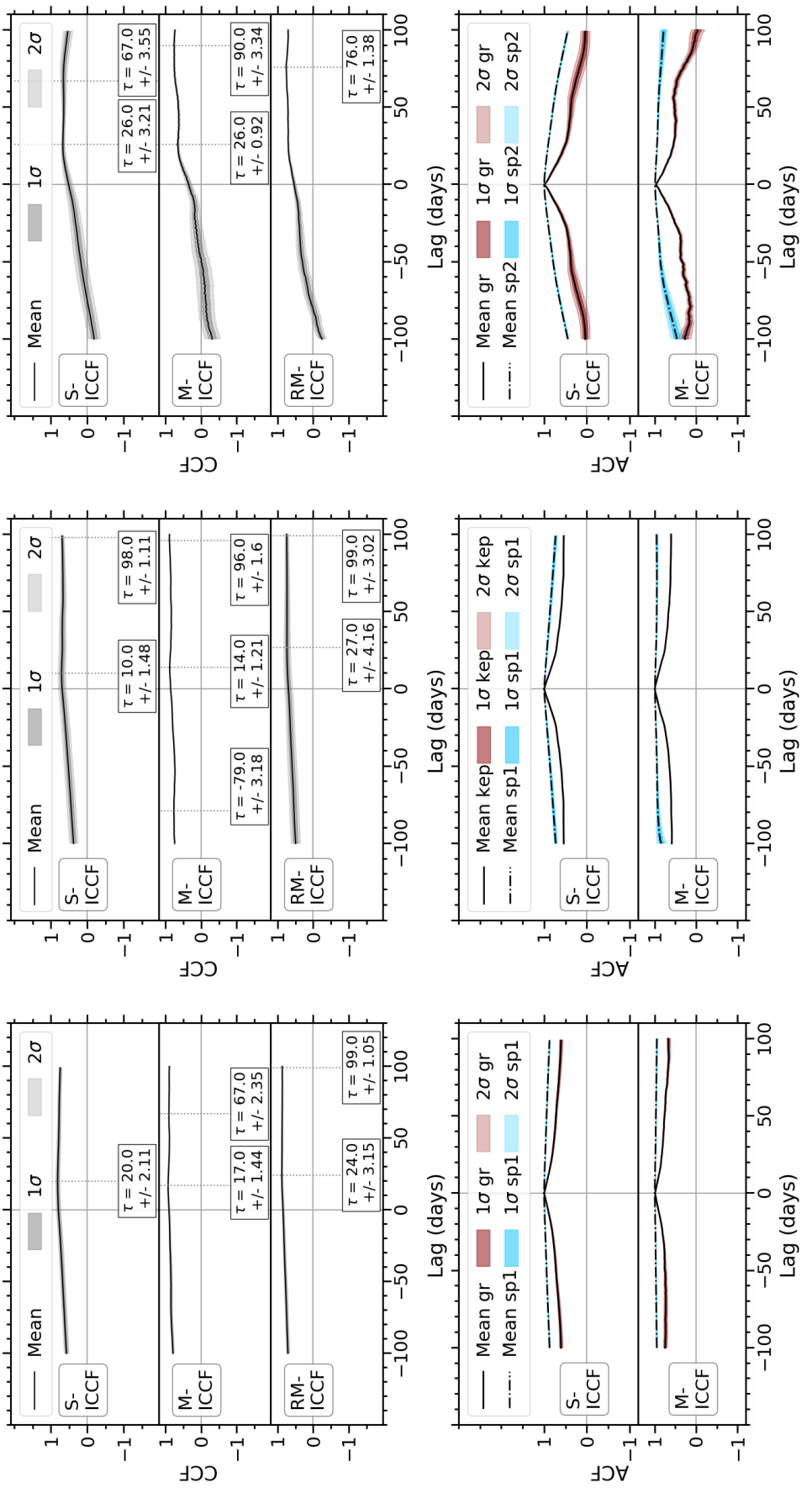

(A) CCFs and ACFs of the entire ground (gr) - *Spitzer* 1 (sp1) light curves

(B) CCFs and ACFs of the entire *Kepler* (kep) - *Spitzer* 1 (sp1) light curves

(C) CCFs and ACFs of the entire ground (gr) - *Spitzer* 2 (sp2) light curves

FIGURE B.5: CCF and ACF of each combination of the optical and IR light curves of Zw229-015 over the entire overlapping observational periods, without subtraction of long-term variability.

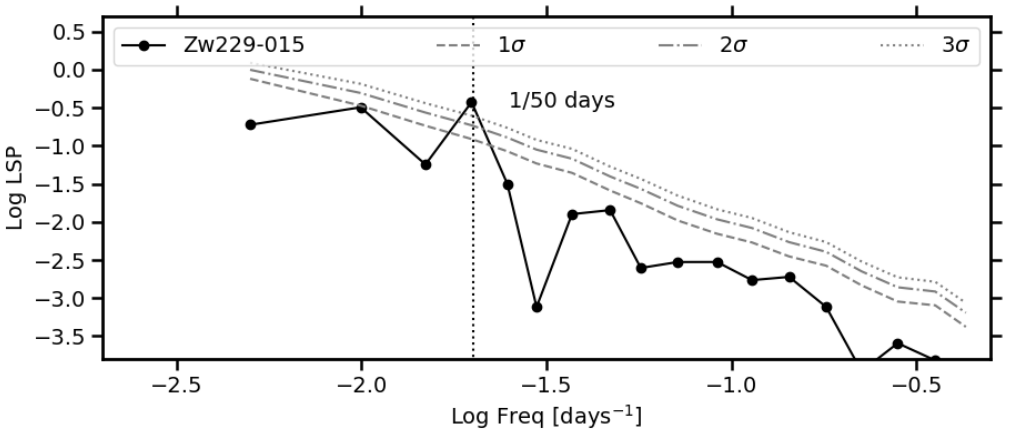

(A) *Kepler* Lomb-Scargle Periodogram for the time that overlaps with the *Spitzer* channel 1 light curves in 2010.

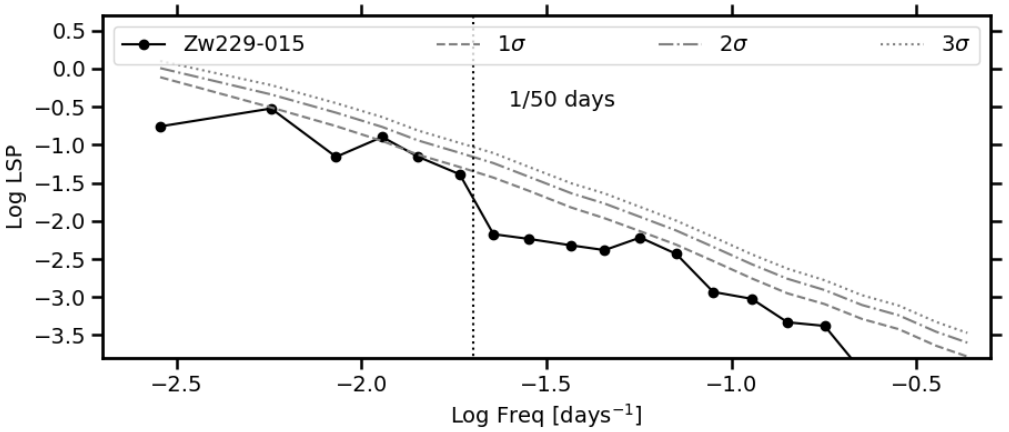

(B) *Kepler* Lomb-Scargle Periodogram for the entire 2010 observation season.

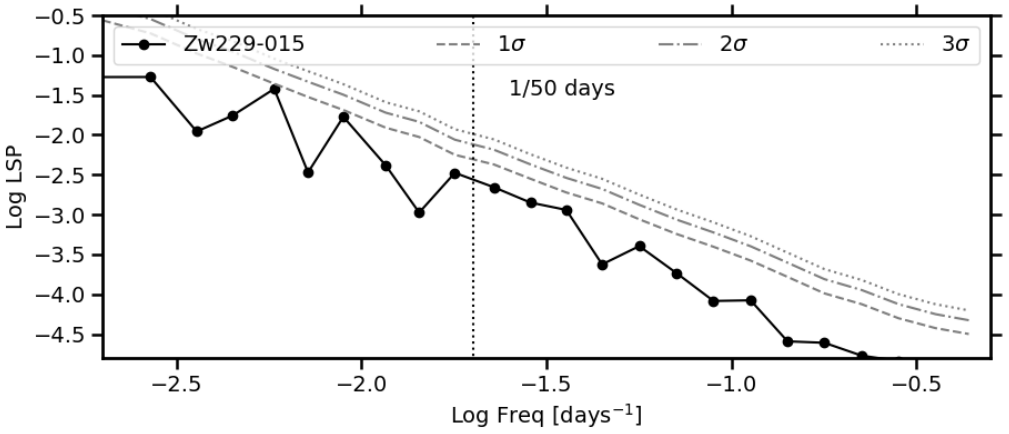

(C) *Kepler* Lomb-Scargle Periodogram for the entire light curve.

FIGURE B.6: *Kepler* fLomb-Scargle Periodograms

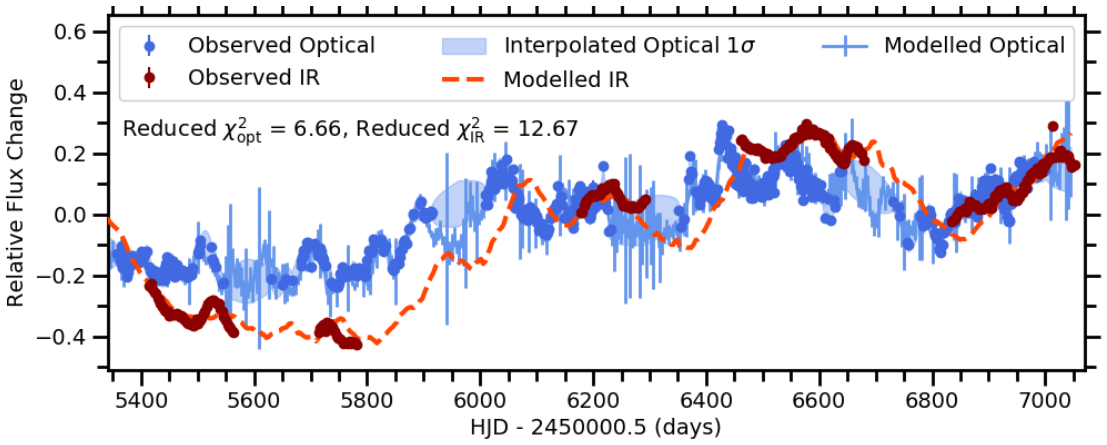

(A) Simulated light curve of ground-Spitzer 1 for the entire overlapping light curves, plotted with the parameters that corresponded to the highest posterior distribution, with values of $\alpha = -0.51$, $\beta = 0.05$, $\tau = 23.05$ days, $i = 47.85$ degrees.

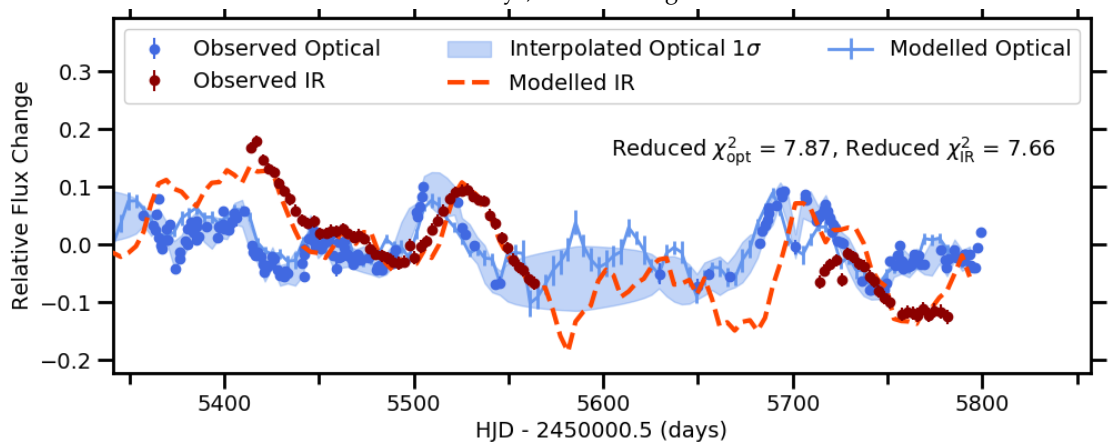

(B) Simulated light curves for ground-Spitzer 1 in the 2010-2011 season, plotted with $\alpha = -0.51$, $\beta = 0.13$, $\tau = 7.62$ days, $i = 60.32$ degrees.

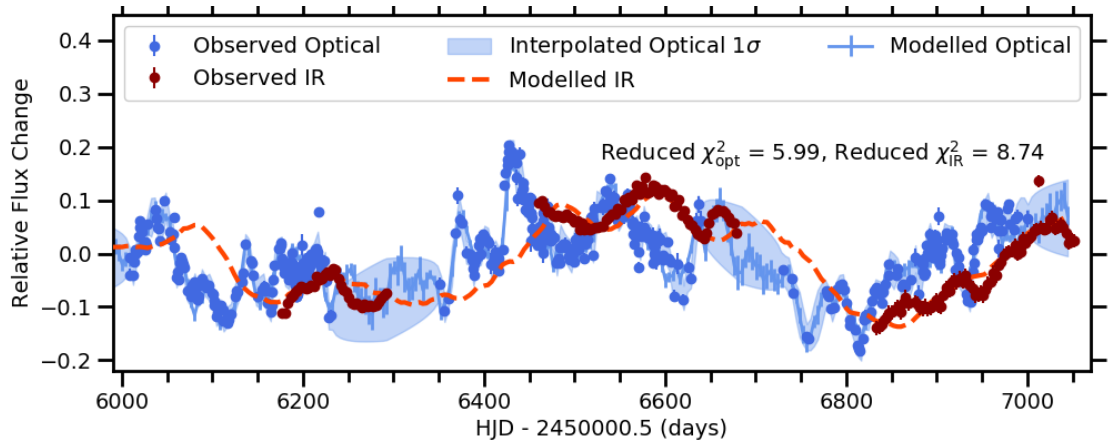

(C) Simulated light curves for ground-Spitzer 1 in the 2012-2014 season, plotted with $\alpha = -0.51$, $\beta = 0.06$, $\tau = 27.92$ days, $i = 39.34$ degrees.

FIGURE B.7: Simulated light curves of the ground-Spitzer 1 observations, for the entire overlapping light curves and the light curves separated into the 2010-2011 seasons and 2012-2014 seasons, plotted with the parameters listed that corresponded to the highest posterior distribution.

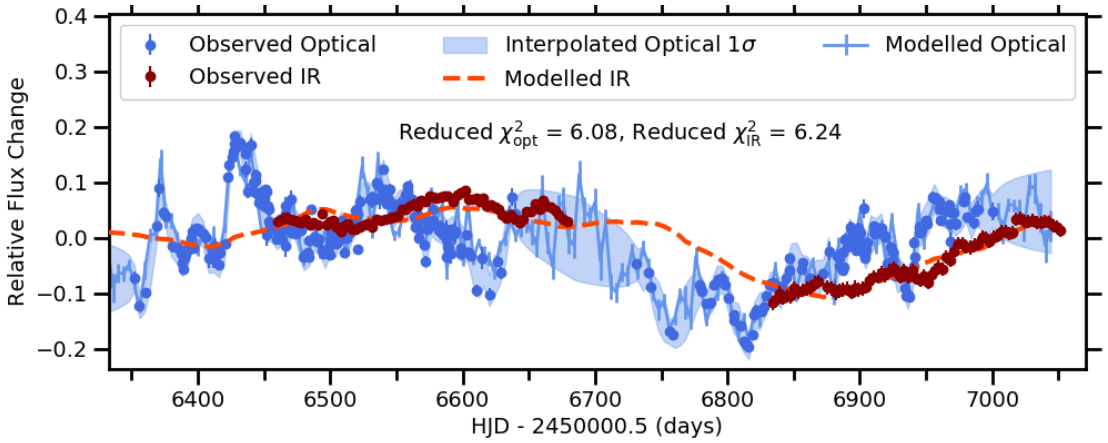

FIGURE B.8: Simulated light curve of ground-Spitzer 2 for the observation seasons starting 2013-2014, plotted with the parameters that corresponded to the highest posterior distribution, with values of $\alpha = -0.52$, $\beta = 0.05$, $\tau = 28.53$ days, $i = 41.94$ degrees.

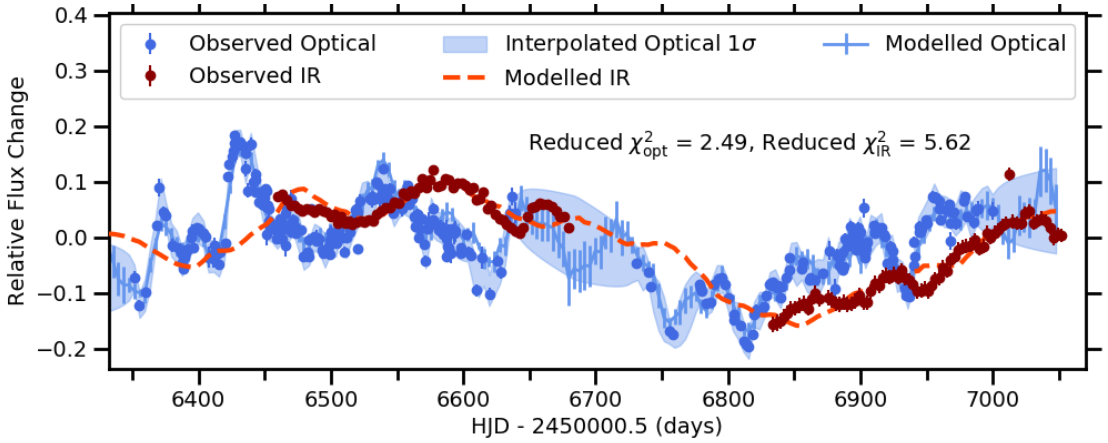

FIGURE B.9: Simulated light curve of ground-Spitzer 1 for the observation seasons starting 2013-2014, plotted with the parameters that corresponded to the highest posterior distribution, with values of $\alpha = -0.51$, $\beta = 0.06$, $\tau = 19.66$ days, $i = 61.02$ degrees.

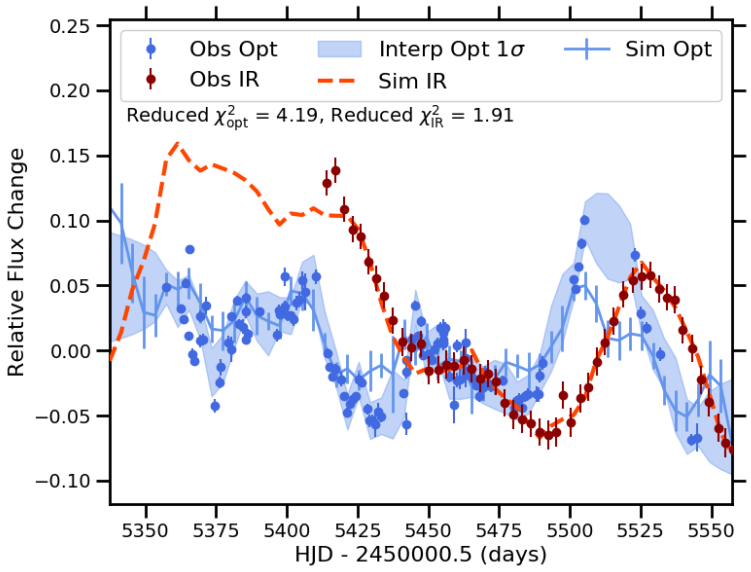

(A) Simulated light curves for ground-Spitzer 1 in the 2010 season, plotted with $\alpha = -0.55$, $\beta = 0.07$, $\tau = 9.74$ days, $i = 54.97$ degrees.

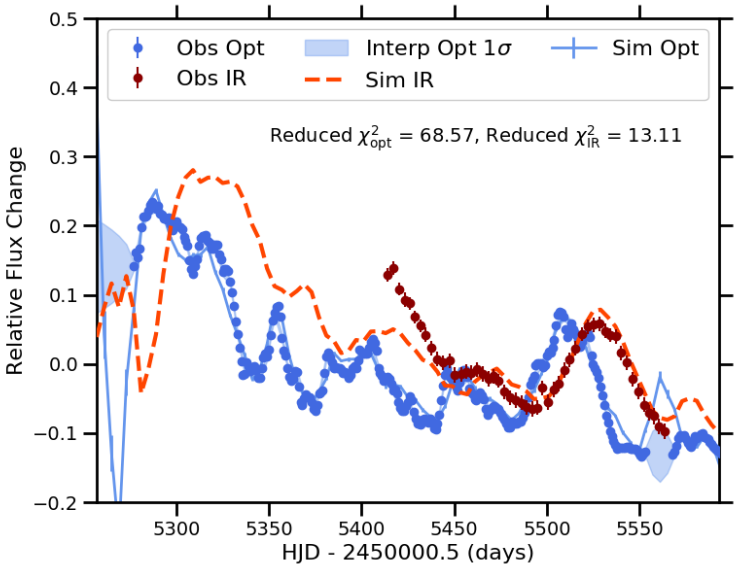

(B) Simulated light curves for *Kepler*-Spitzer 1 in the 2010 season, plotted with $\alpha = -0.52$, $\beta = 0.13$, $\tau = 8.82$ days, $i = 43.76$ degrees.

FIGURE B.10: Simulated optical and IR light curves for the individual observations seasons, plotted with the specified values corresponding to the maximum posterior model.

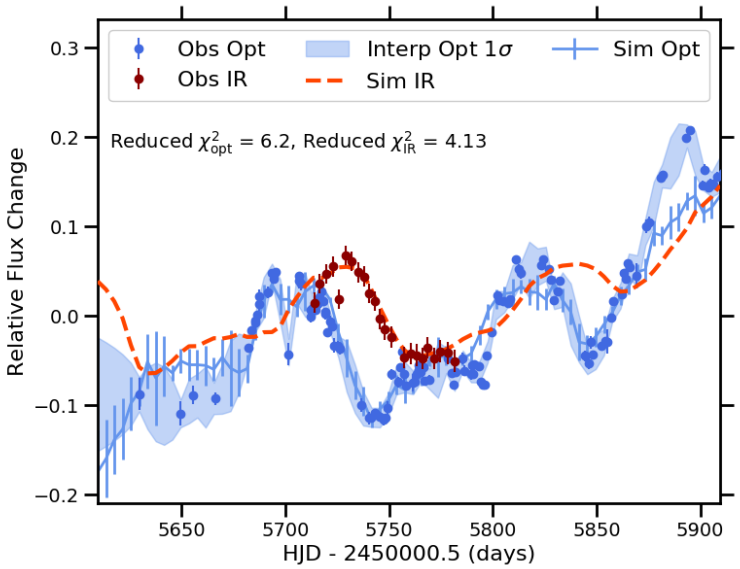

(C) Simulated light curves for ground-Spitzer 1 in the 2011 season, plotted with $\alpha = -0.83$, $\beta = 0.37$, $\tau = 8.43$ days, $i = 68.00$ degrees.

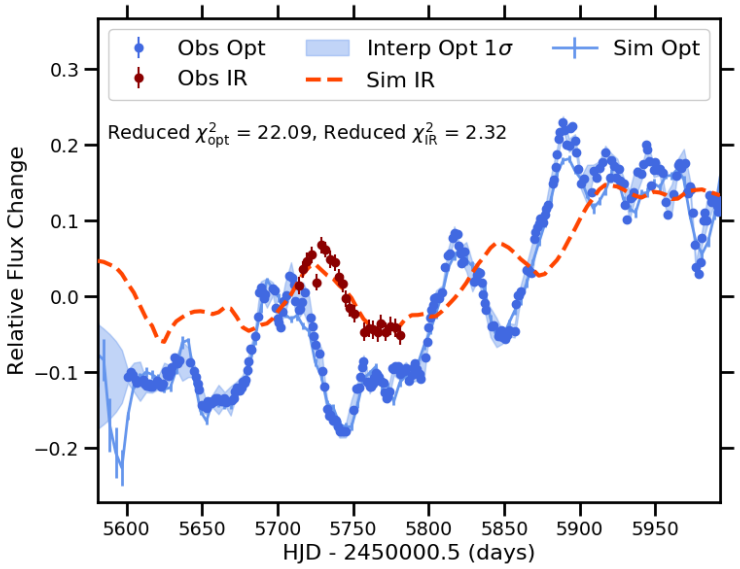

(D) Simulated light curves for *Kepler*-Spitzer 1 in the 2011 season, plotted with $\alpha = -0.66$, $\beta = 1.87$, $\tau = 17.77$ days, $i = 40.98$ degrees.

FIGURE B.10: Continued.

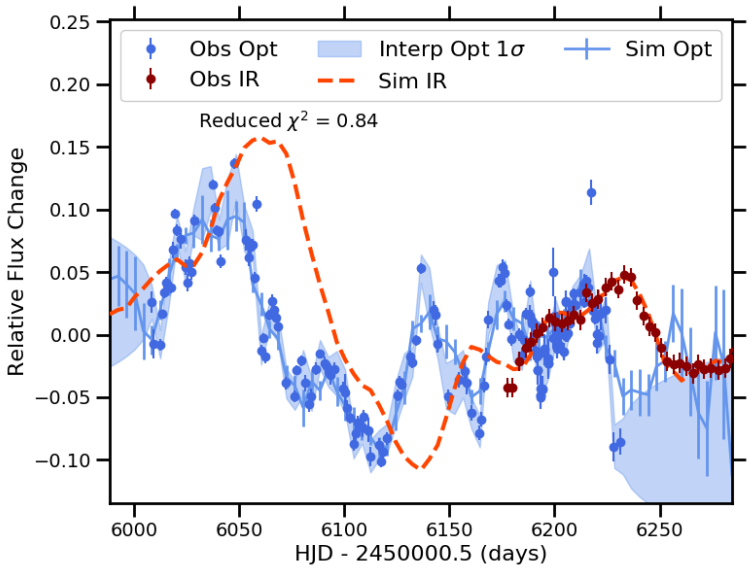

(E) Simulated light curves for ground-Spitzer 1 in the 2012 season, plotted with $\alpha = -1.28$, $\beta = 0.08$, $\tau = 10.92$ days, $i = 62.64$ degrees.

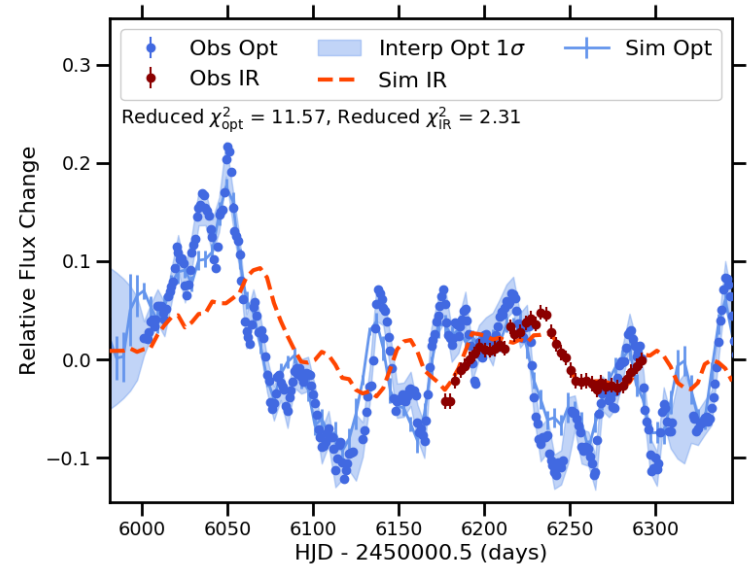

(F) Simulated light curves for *Kepler*-Spitzer 1 in the 2012 season, plotted with $\alpha = -5.21$, $\beta = 1.22$, $\tau = 16.45$ days, $i = 21.22$ degrees.

FIGURE B.10: Continued.

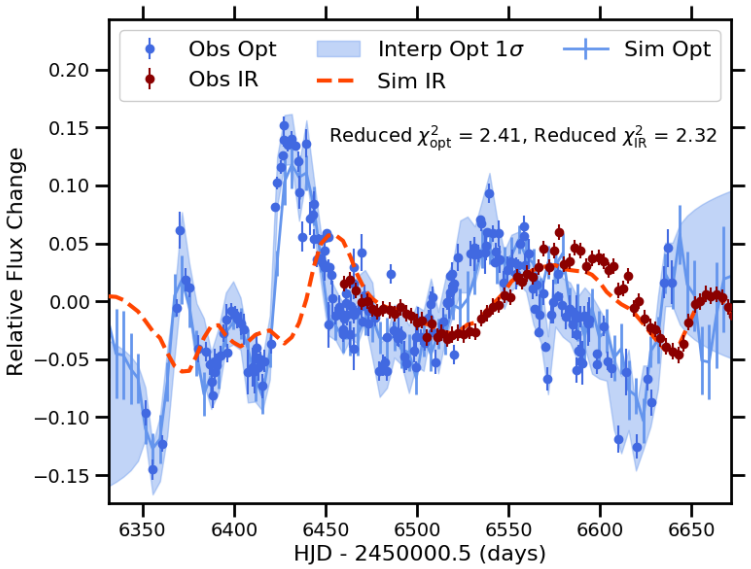

(G) Simulated light curves for ground-Spitzer 1 in the 2013 season, plotted with $\alpha = -0.62$, $\beta = 0.43$, $\tau = 10.44$ days, $i = 38.89$ degrees.

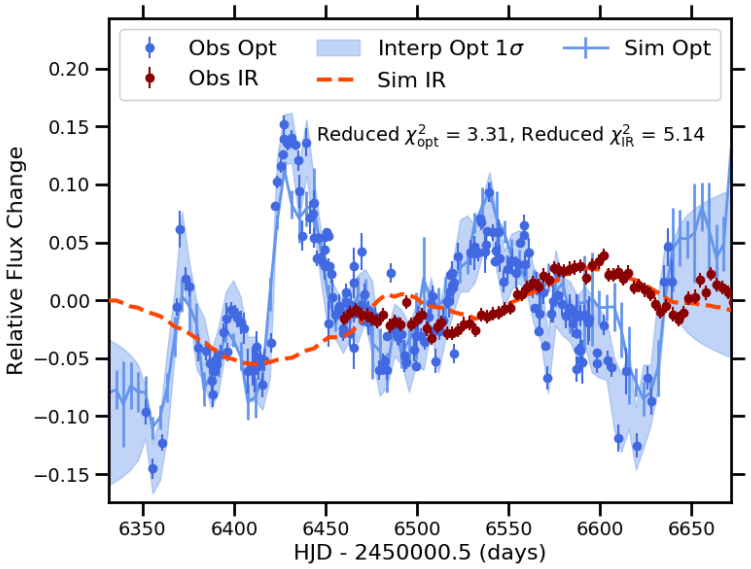

(H) Simulated light curves for ground-Spitzer 2 in the 2013 season, plotted with $\alpha = -0.51$, $\beta = 0.37$, $\tau = 27.94$ days, $i = 48.41$ degrees.

FIGURE B.10: Continued.

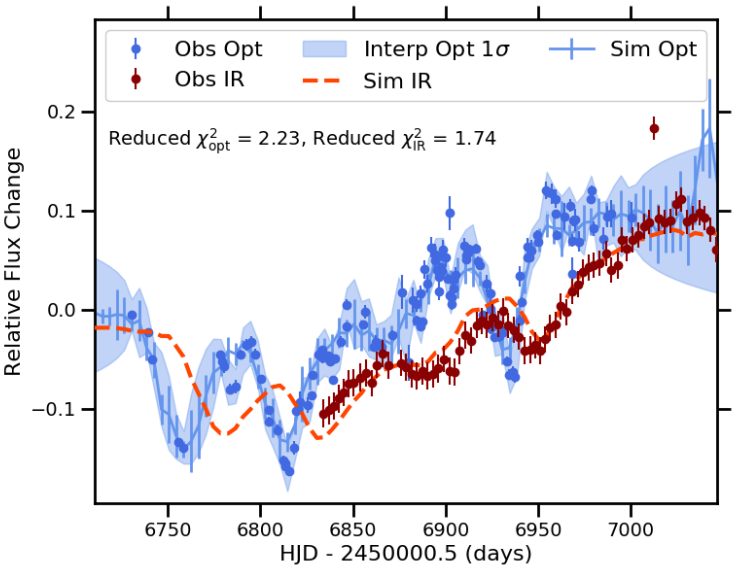

(A) Simulated light curves for ground-Spitzer 1 in the 2014 season, plotted with $\alpha = -0.51$, $\beta = 0.09$, $\tau = 12.70$ days, $i = 19.45$ degrees.

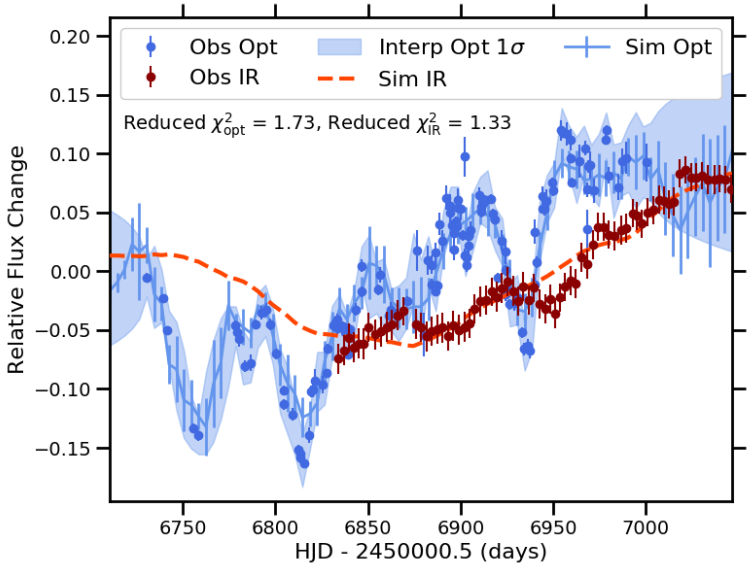

(B) Simulated light curves for ground-Spitzer 2 in the 2014 season, plotted with $\alpha = -0.62$, $\beta = 0.19$, $\tau = 28.73$ days, $i = 56.22$ degrees.

FIGURE B.11: Continued.

TABLE B.2: Mean output parameters corresponding to the best fit DTFs found by MCMC modelling the individual observation seasons for each combination of optical and IR light curve, and the quality of their fits described by reduced χ^2.

Light Curve Combination	Season Starting	Radial Power Law Index	Vertical Scale Height Power Law Index	Amplitude Conversion Factor	Lag (days)	Inclination (degrees)	Offset ($\times 10^{-2}$)	χ^2_{opt}	χ^2_{IR}
whiteGr-Sp1	2010	$-0.58^{+0.06}_{-0.33}$	$0.13^{+0.28}_{-0.06}$	$3.23^{+0.46}_{-0.50}$	$9.90^{+2.59}_{-0.86}$	$51.57^{+12.52}_{-18.91}$	$1.17^{+0.76}_{-0.88}$	4.19	1.91
whiteKep-Sp1	2010	$-1.07^{+0.55}_{-4.33}$	$0.43^{+0.92}_{-0.23}$	$1.30^{+0.29}_{-0.20}$	$11.04^{+3.89}_{-1.71}$	$42.50^{+5.91}_{-11.50}$	$3.49^{+0.47}_{-0.68}$	68.57	13.11
whiteGr-Sp1	2011	$-1.29^{+0.65}_{-3.61}$	$0.41^{+1.06}_{-0.29}$	$0.91^{+0.23}_{-0.14}$	$10.64^{+4.62}_{-1.97}$	$50.64^{+35.21}_{-15.96}$	$2.85^{+0.86}_{-0.66}$	6.20	4.13
whiteKep-Sp1	2011	$-1.37^{+0.82}_{-4.04}$	$1.81^{+0.20}_{-1.22}$	$0.68^{+0.08}_{-0.08}$	$16.96^{+3.36}_{-2.99}$	$42.26^{+17.28}_{-12.81}$	$5.19^{+0.85}_{-0.67}$	22.09	2.33
whiteGr-Sp1	2012	$-1.48^{+0.79}_{-2.60}$	$0.62^{+1.34}_{-0.52}$	$1.30^{+0.36}_{-0.22}$	$12.89^{+7.52}_{-1.34}$	$49.08^{+17.21}_{-24.12}$	$1.54^{+0.47}_{-0.39}$	4.82	0.84
whiteKep-Sp1	2012	$-4.77^{+4.17}_{-0.66}$	$1.45^{+0.52}_{-0.89}$	$0.55^{+0.09}_{-0.06}$	$17.15^{+2.68}_{-3.82}$	$17.46^{+7.27}_{-4.70}$	$0.93^{+0.28}_{-0.26}$	11.57	2.31
whiteGr-Sp1	2013	$-0.84^{+0.28}_{-4.00}$	$0.24^{+1.57}_{-0.15}$	$0.74^{+0.12}_{-0.12}$	$11.75^{+3.55}_{-1.54}$	$34.11^{+26.54}_{-10.29}$	$0.61^{+0.21}_{-0.23}$	3.98	3.02
whiteGr-Sp2	2013	$-0.55^{+0.04}_{-2.98}$	$0.14^{+0.88}_{-0.08}$	$0.83^{+0.22}_{-0.63}$	$27.65^{+1.17}_{-13.40}$	$49.97^{+9.82}_{-18.69}$	$0.12^{+0.17}_{-0.20}$	3.51	5.14
whiteGr-Sp1	2014	$-0.80^{+0.25}_{-4.52}$	$0.34^{+0.98}_{-0.23}$	$1.09^{+0.16}_{-0.10}$	$12.93^{+15.32}_{-2.59}$	$55.29^{+11.72}_{-17.45}$	$2.09^{+2.59}_{-0.78}$	2.23	1.74
whiteGr-Sp2	2014	$-0.61^{+0.08}_{-0.20}$	$0.13^{+0.24}_{-0.06}$	$1.13^{+0.20}_{-0.27}$	$27.68^{+1.11}_{-17.63}$	$58.98^{+8.25}_{-12.67}$	$0.82^{+0.67}_{-0.24}$	1.73	1.33

Appendix C

Simulations of Optical AGN Variability Analysis with LSST

C.1 Recovering Parameters of the DRW Model from LSST Cadenced Light Curves

In Chapter 6 I displayed the dependence of the successful recovery of the parameters of the DRW model with JAVELIN within the 1σ uncertainties for the DDF cadenced light curves. Figure C.1 contains the corresponding colour maps for the successful recovery within the 2σ and 3σ uncertainties respectively. Furthermore, corresponding plots for the WFD cadenced light curves are given in Figure C.2. All of these show similar relations for luminosity and redshift as described in Chapter 6.

C.2 Recovery Parameters of the Varying Power Laws

Recovering Properties of underlying PSD with 1 day cadenced light curves In Chapter 6, I focus on the recoverability of the parameters using simulated LSST cadenced light curves, however to understand the full extent of which the choice of observational sampling effects the results, I also applied the same analysis to simulated light curves with 1 day cadencing that covered the expected baseline of LSST observations. Figures C.3 and C.4 display plots of the mean best fit of each input parameter against the input value and the distributions of confidence with which each best fit model can be rejected, for SPL and BPL PSD recovery respectively.

SPL Colour Maps As the distribution of AGN in luminosity and redshift space was not uniform, the colour maps were plotted with different sized bins so that each bin

contained similar numbers of AGN. The distributions of AGN for the colour maps plotted in Figure 6.17 are displayed in Figure C.5.

Colour maps depicting the recoverability of the input SPL PSDs for the WFD cadenced AGN light curves depending on properties including luminosity, redshift and input power law slope are given in Figure C.6. The results are shown to be similar to those given in Chapter 6 for the DDF cadenced light curves, with the lower luminosity, higher redshift AGN being more likely to not find a reasonable fit or to fit poorly compared to the rest. Furthermore, the a similar dependence on input power law slope is also seen. The distributions of AGN for the colour maps plotted in Figure C.6 are displayed in Figure C.7.

BPL Colour Maps In Chapter 6 I displayed examples of the dependence of the successful recovery of the parameters of the BPL model on luminosity and redshift and on the power law slopes and locations of the break frequencies. Additional colour maps are given in Figure C.8 for different combination of parameters. Furthermore, colour maps depicting the recoverability of the input BPL PSDs for the WFD cadenced AGN light curves are displayed in Figure C.10.

Classifications of the Underlying PSD shape Chapter 6 explores how often the underlying PSD of light curves made from SPL and BPLs are incorrectly classified for the LSST cadenced light curves. Figure C.13 displays the distributions of the WFD cadenced light curves made with BPLs that are correctly and incorrectly identified, with the distributions of the incorrect SPL parameters recovered in Figure C.14. The distributions are shown to be similar to the results from DDF cadenced light curves.

C.3 Detecting Quasi-Periodicity in LSST Light Curves

Figure C.15 displays colour maps of the AGN corresponding to true and false periodicity detections using 1-day cadenced light curves to display any correlations between parameters. It can be seen that the true and false detections have different distributions, as shown in Chapter 6.

Figure C.16 contains the distributions of the parameters of the WFD AGN light curves that correspond to the true and false detections of periodicity, and are shown to follow similar shapes to the DDF cadenced light curves given in Chapter 6.

Classifying the Underlying PSD shape Finally, the classification of the underlying power laws of light curves made from SPLs with QPOs superimposed were explored

to see how the presence of a QPO impacted on the success of the identification. The distribution of parameters of the AGN whose underlying power law was correctly and incorrectly identified are given in Figure C.17 and show similar distributions to the SPL only distributions.

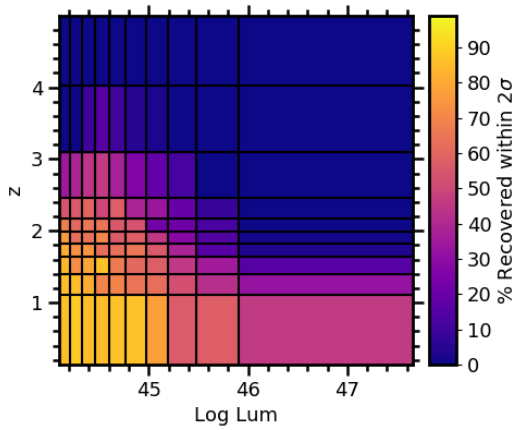

(A) The percentage of AGN of a given luminosity and redshift that successfully recovered the characteristic timescale of the DRW model within 2σ uncertainties.

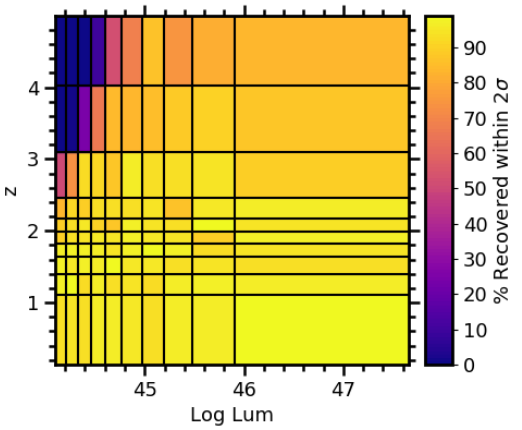

(B) The percentage of AGN of a given luminosity and redshift that successfully recovered the standard deviation of the light curves within 2σ uncertainties.

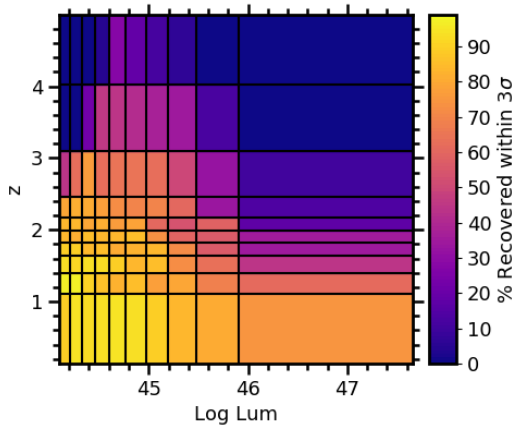

(C) The percentage of AGN of a given luminosity and redshift that successfully recovered the characteristic timescale of the DRW model within 3σ uncertainties.

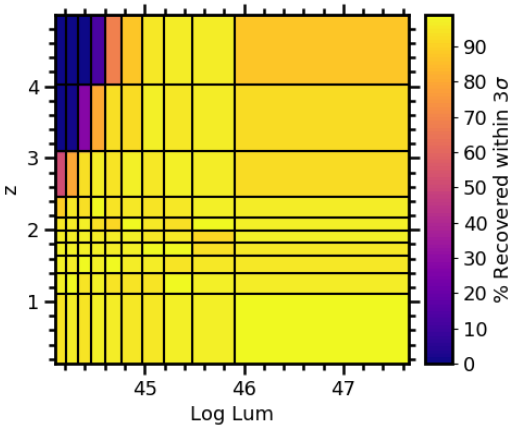

(D) The percentage of AGN of a given luminosity and redshift that successfully recovered the standard deviation of the light curves within 3σ uncertainties.

FIGURE C.1: Colour maps depicting the ability to recover the parameters of the DRW model using DDF cadenced light curves depending on combinations of luminosity and redshift of the AGN.

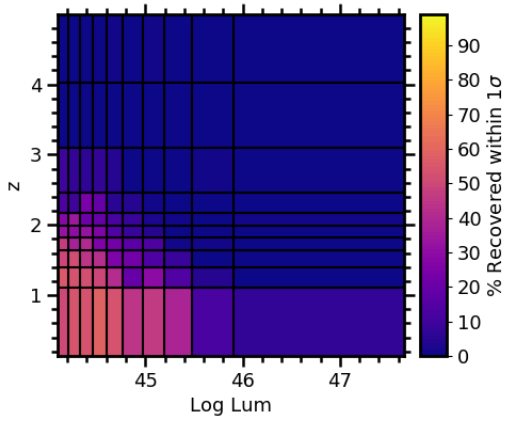

(A) The percentage of AGN of a given luminosity and redshift that successfully recovered the characteristic timescale of the DRW model within 1σ uncertainties.

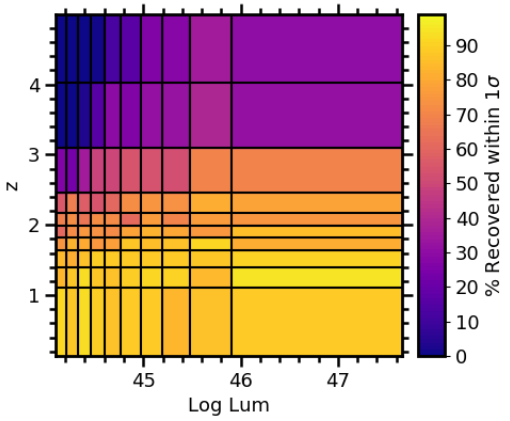

(B) The percentage of AGN of a given luminosity and redshift that successfully recovered the standard deviation of the light curves within 1σ uncertainties.

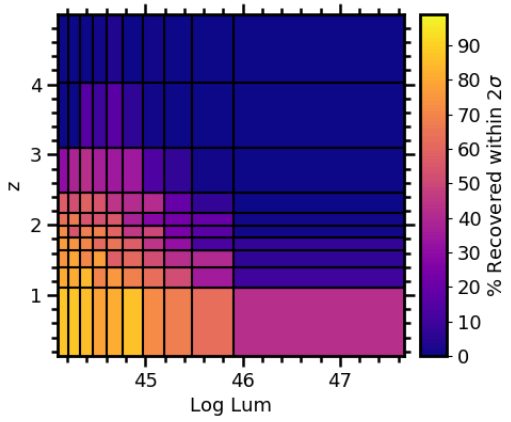

(C) The percentage of AGN of a given luminosity and redshift that successfully recovered the characteristic timescale of the DRW model within 2σ uncertainties.

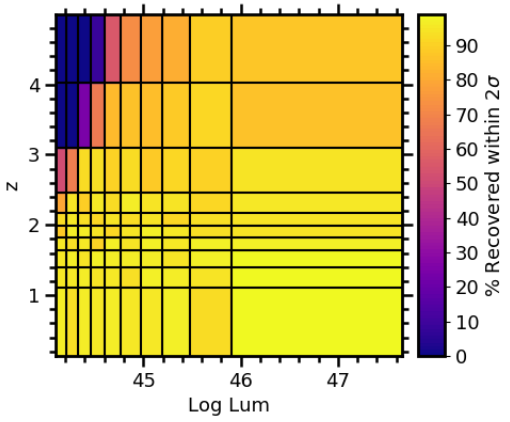

(D) The percentage of AGN of a given luminosity and redshift that successfully recovered the standard deviation of the light curves within 2σ uncertainties.

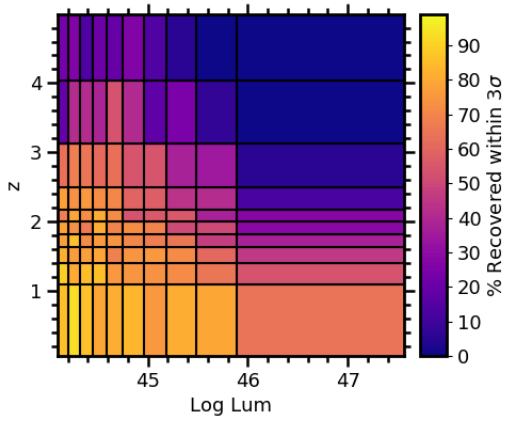

(E) The percentage of AGN of a given luminosity and redshift that successfully recovered the characteristic timescale of the DRW model within 3σ uncertainties.

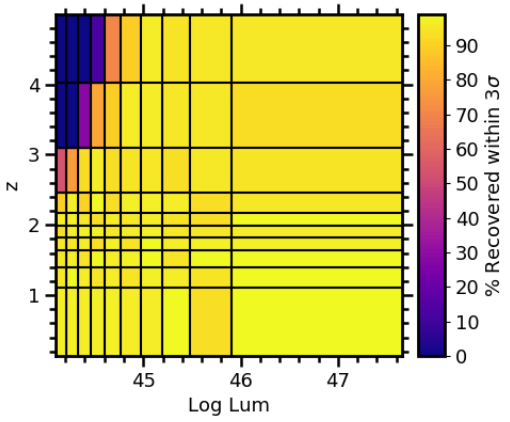

(F) The percentage of AGN of a given luminosity and redshift that successfully recovered the standard deviation of the light curves within 3σ uncertainties.

FIGURE C.2: Colour maps depicting the ability to recover the parameters of the DRW model using WFD cadenced light curves.

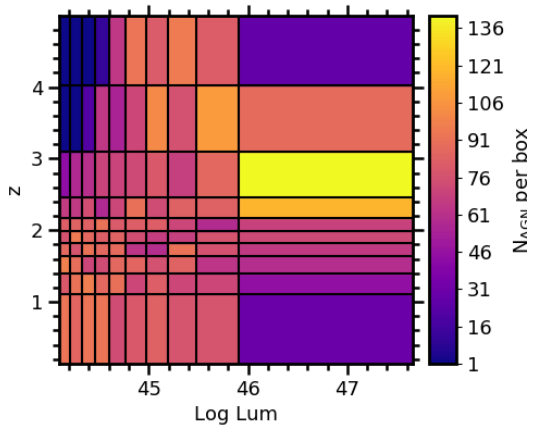

(G) Number of AGN per bin for the luminosity-redshift colour plots.

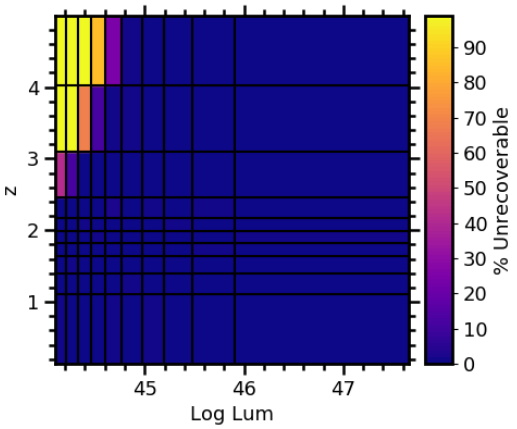

(H) The percentage of AGN of a given luminosity and redshift whose power law could not be fit using JAVELIN.

FIGURE C.2: Continued.

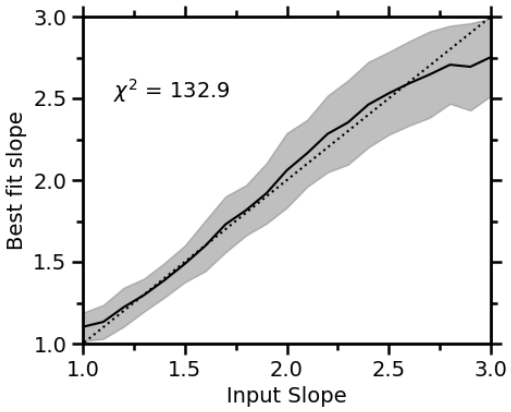

(A) Mean and standard deviations of the best fit slopes found for each input PSD slope.

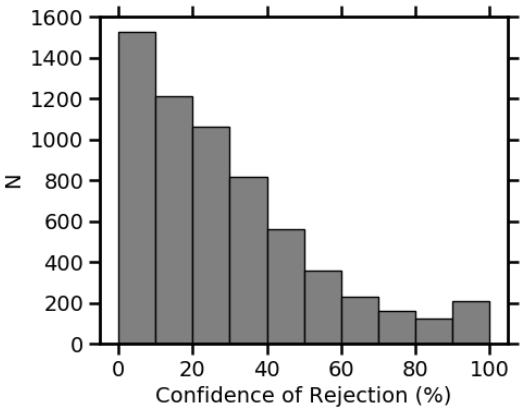

(B) Distribution of the confidence of rejection for the SPL PSD recovery.

FIGURE C.3: Results of recovering single power law fits using 1 day cadenced light curves.

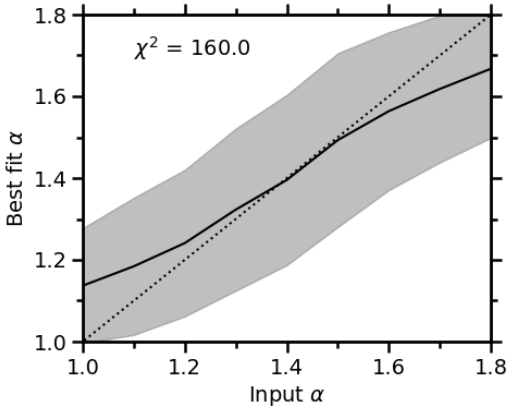

(A) Mean and standard deviations of the best fit low-frequency slopes found for each input low-frequency PSD slope.

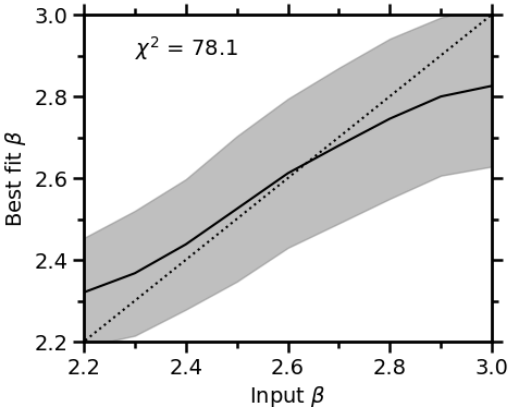

(B) Mean and standard deviations of the best fit high-frequency slopes found for each input high-frequency PSD slope.

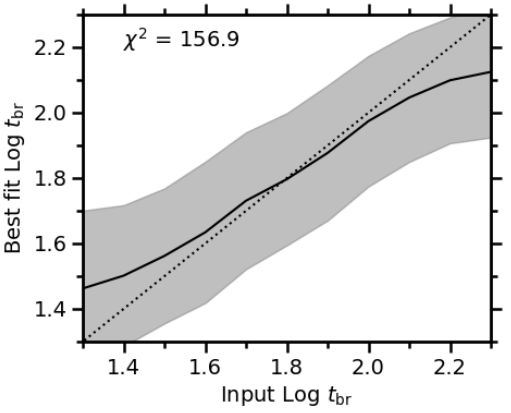

(C) Mean and standard deviations of the best fit break timescale found for each input break timescale.

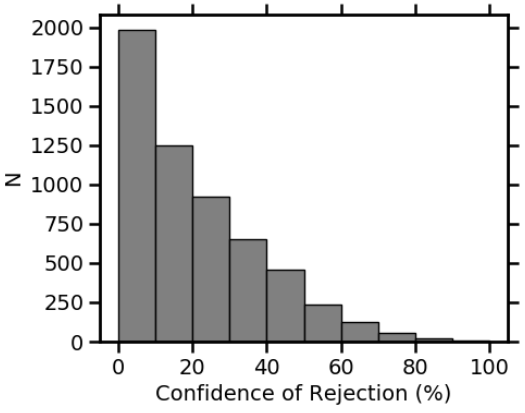

(D) Distribution of the confidence of rejection for the BPL PSD recovery.

FIGURE C.4: Results of recovering broken power law fits using 1 day cadenced light curves.

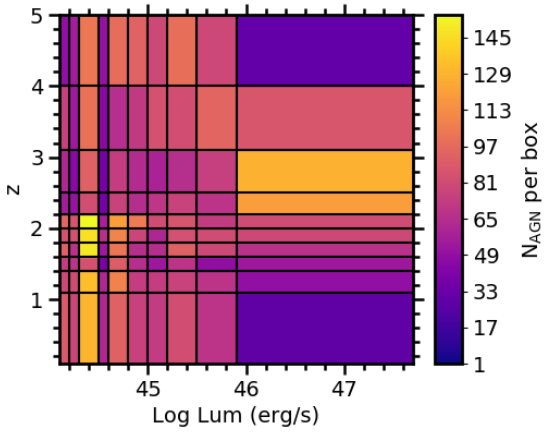

(A) Number of AGN per bin for the luminosity-redshift colour plots.

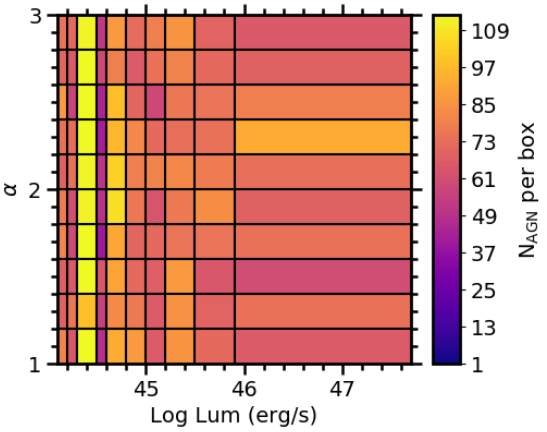

(B) Number of AGN per bin for the luminosity-input power law slope colour plots.

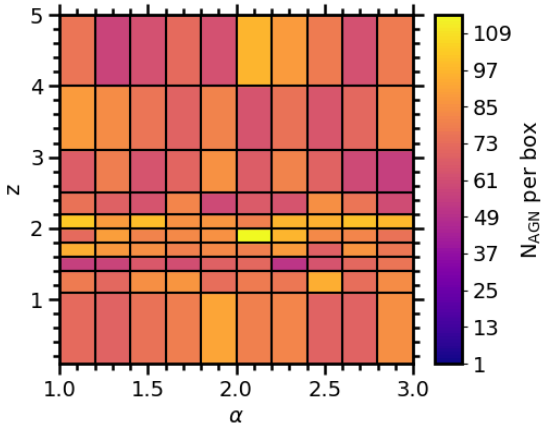

(C) Number of AGN per bin for the input power law slopes-redshift colour plots.

FIGURE C.5: Number of AGN per bin for the colour maps given in Figure 6.17.

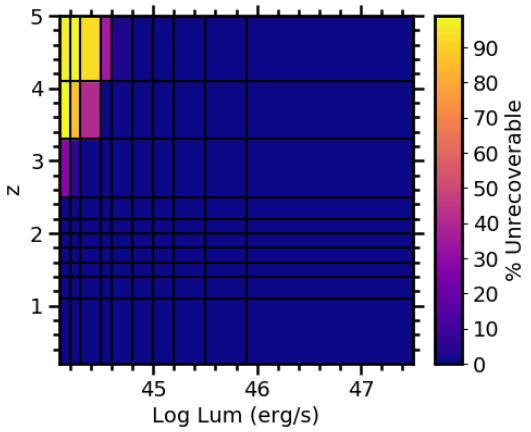

(A) The percentage of AGN of a given luminosity and redshift whose power law could not be fit using these methods.

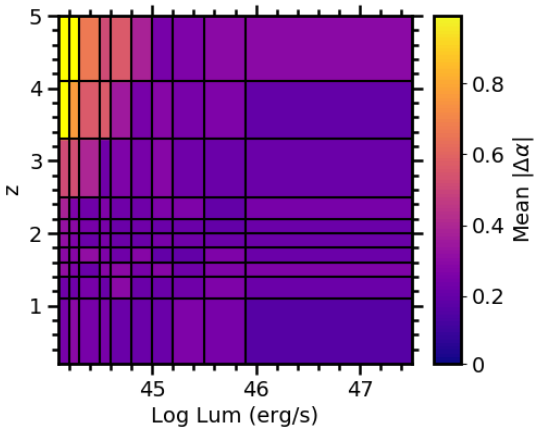

(B) The mean difference found for the power law slope of AGN of a given luminosity and redshift.

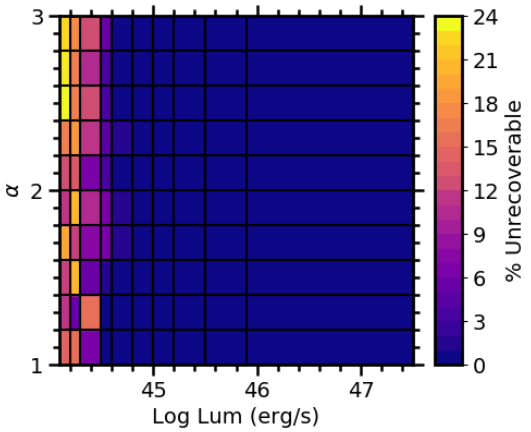

(C) The percentage of AGN of a given luminosity and input power law slope whose power law could not be fit using these methods.

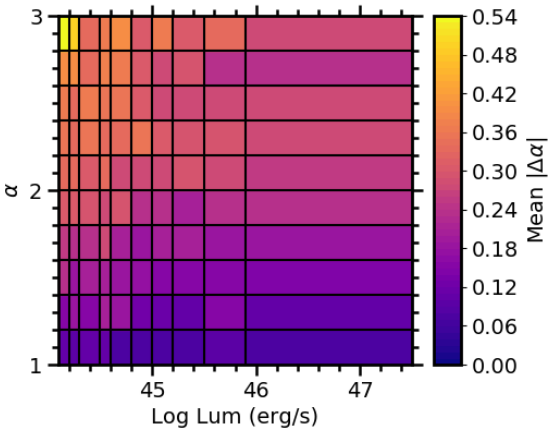

(D) The mean difference found for the power law slope of AGN of a given luminosity and input power law slope.

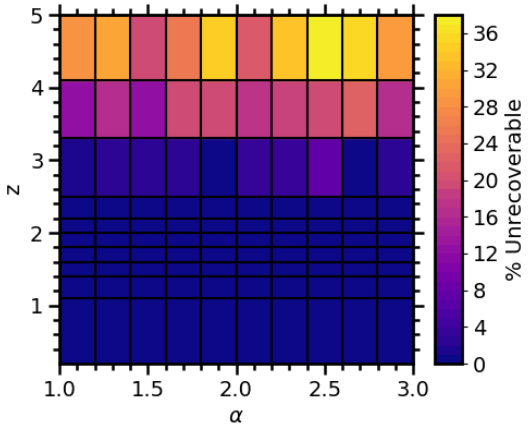

(E) The percentage of AGN of a given input power law slope and redshift whose power law could not be fit using these methods.

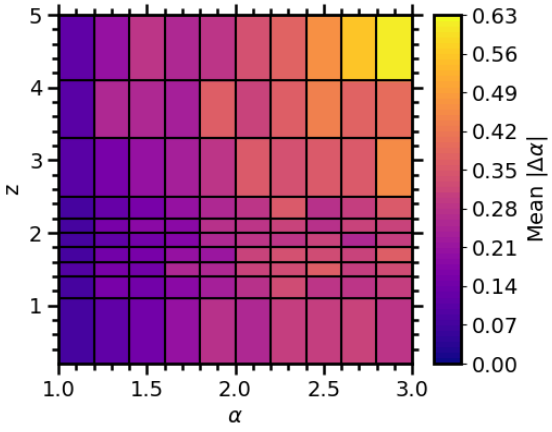

(F) The mean difference found for the power law slope of AGN of a given input power law slope and redshift.

FIGURE C.6: Colour maps depicting the ability to recover the input SPL PSD using WFD cadenced light curves depending on combination of the power law slope, luminosity and redshift of the AGN. Each plot is divided such that each rectangle contains similar numbers of AGN, with the distributions given in Figure C.7.

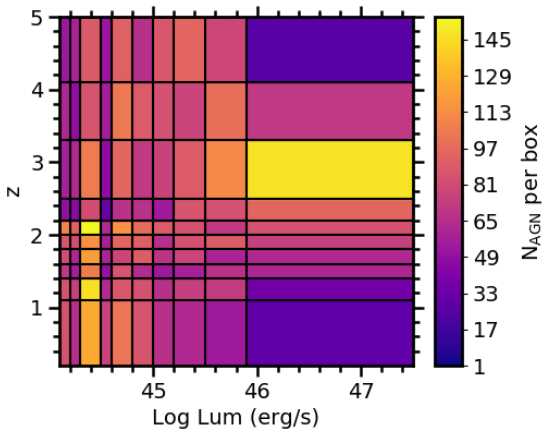

(A) Number of AGN per bin for the luminosity-redshift colour plots.

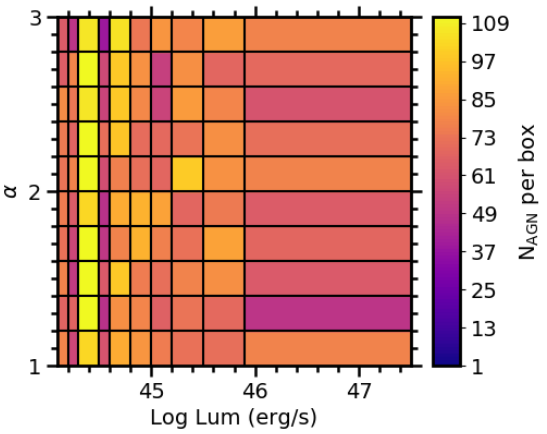

(B) Number of AGN per bin for the luminosity-input power law slope colour plots.

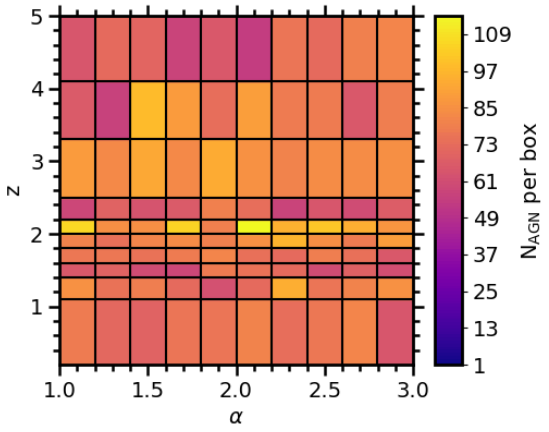

(C) Number of AGN per bin for the input power law slope-redshift colour plots.

FIGURE C.7: Number of AGN per bin for the colour maps given in Figure C.6.

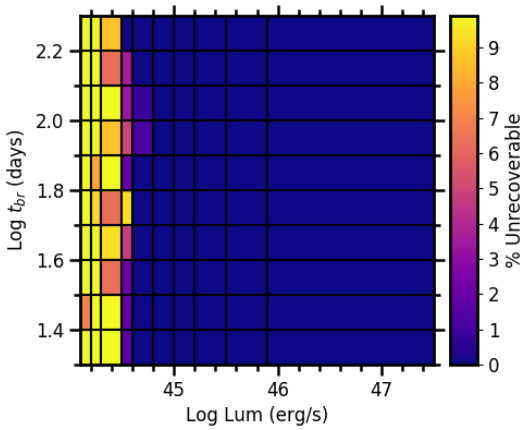

(A) The percentage of AGN of a given luminosity and break timescale whose power law could not be fit using these methods.

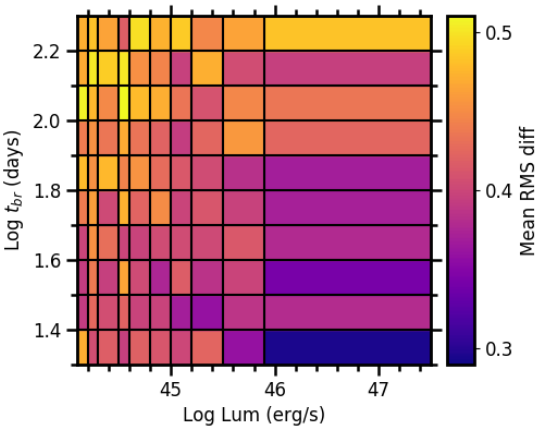

(B) The mean rms difference found between the recovered parameters with the inputs for the AGN of a given luminosity and break timescale.

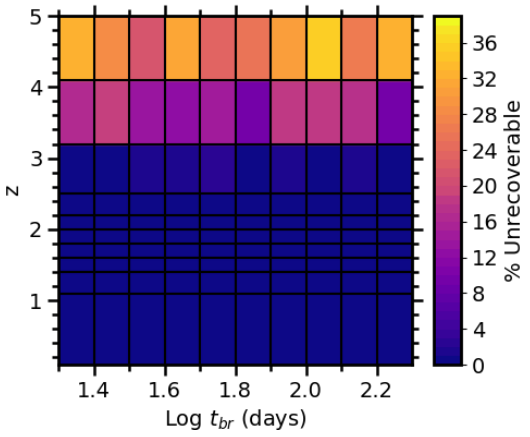

(C) The percentage of AGN of a given break timescale and redshift whose power law could not be fit using these methods.

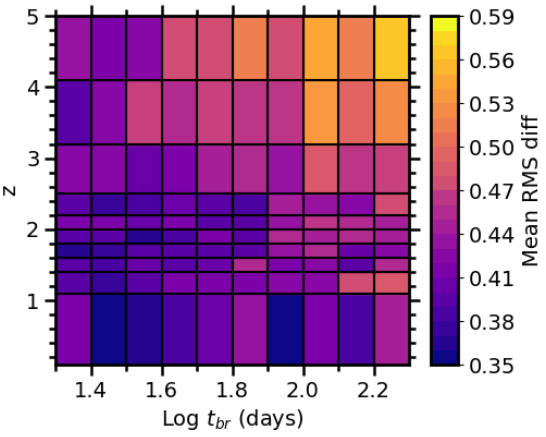

(D) The mean rms difference found between the recovered parameters with the inputs for the AGN of a given break timescale and redshift.

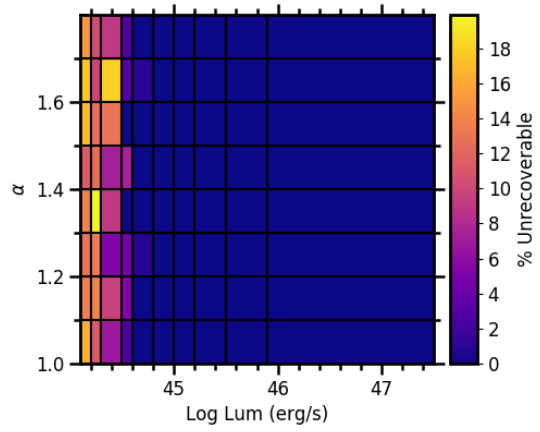

(E) The percentage of AGN of a given luminosity and low-frequency power law slope whose power law could not be fit using these methods.

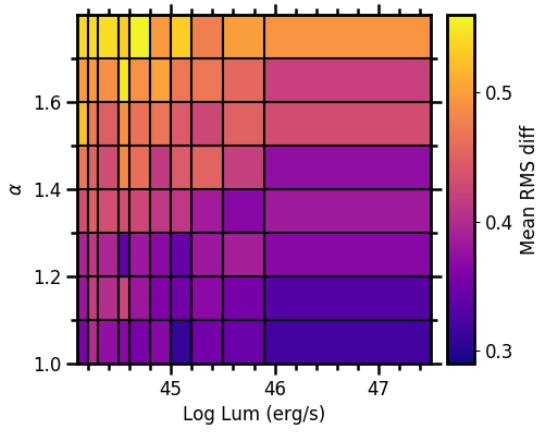

(F) The mean rms difference found between the recovered parameters with the inputs for the AGN of a given luminosity and low-frequency PSD slope.

FIGURE C.8: Colour maps depicting the ability to recover the input BPL PSD using DDF cadenced light curves depending on combination of the power law slopes, break frequencies, luminosity and redshift of the AGN.

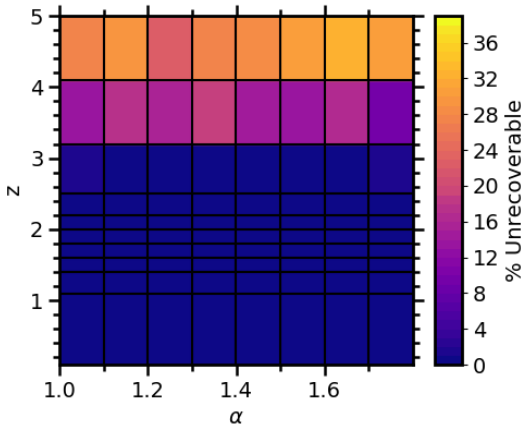

(G) The percentage of AGN of a given low-frequency PSD slope and redshift whose power law could not be fit using these methods.

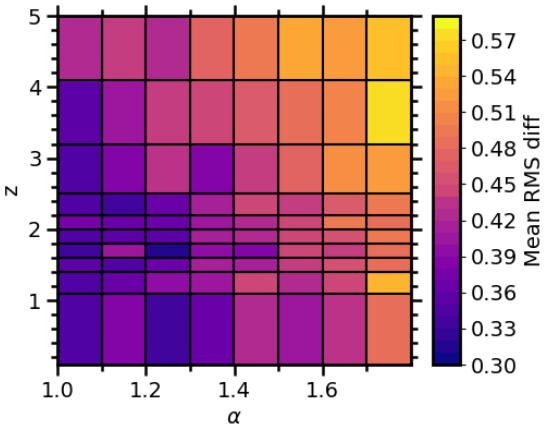

(H) The mean rms difference found between the recovered parameters with the inputs for the AGN of a given low-frequency PSD slope and redshift.

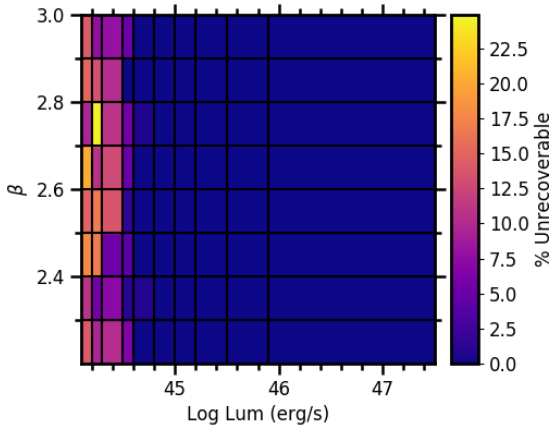

(I) The percentage of AGN of a given luminosity and high-frequency power law slope whose power law could not be fit using these methods.

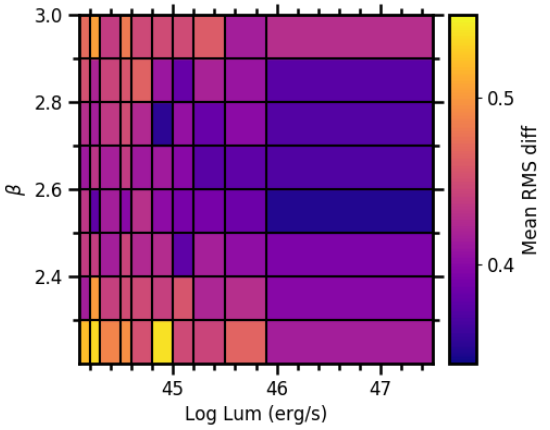

(J) The mean rms difference found between the recovered parameters with the inputs for the AGN of a given luminosity and high-frequency PSD slope.

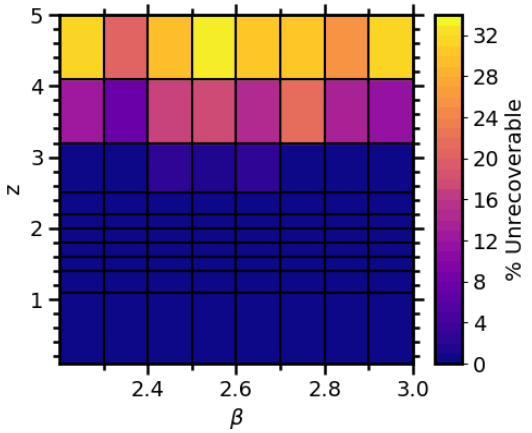

(K) The percentage of AGN of a given high-frequency power law slope and redshift whose power law could not be fit using these methods.

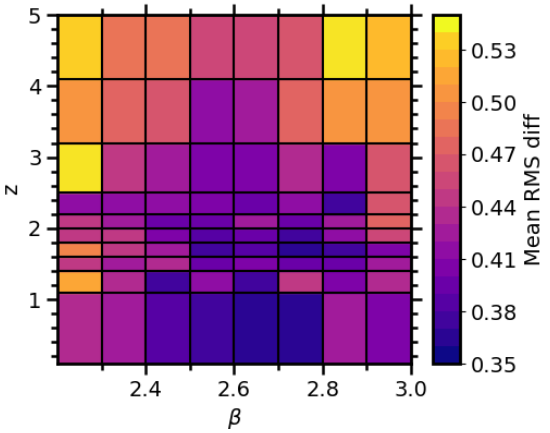

(L) The mean rms difference found between the recovered parameters with the inputs for the AGN of a given high-frequency PSD slope and redshift.

FIGURE C.8: Continued.

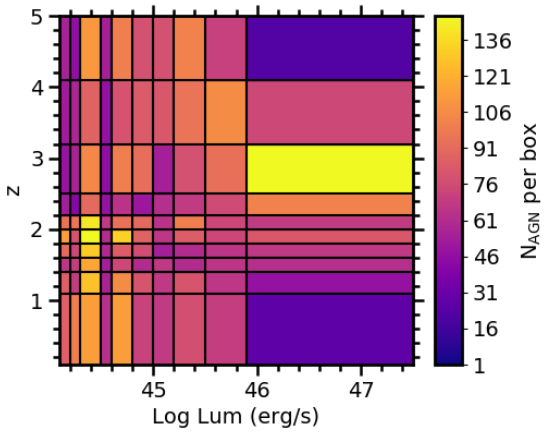

(A) Number of AGN per bin for the luminosity-redshift colour plots.

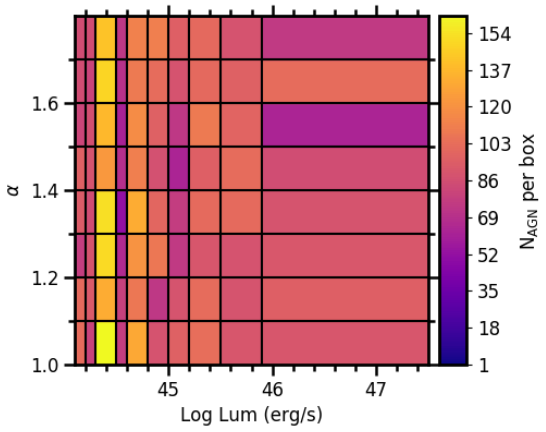

(B) Number of AGN per bin for the luminosity-input low-frequency power law slope colour plots.

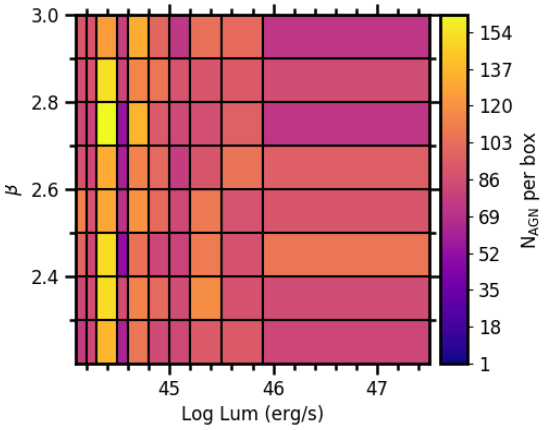

(C) Number of AGN per bin for the luminosity-input high-frequency power law slope colour plots.

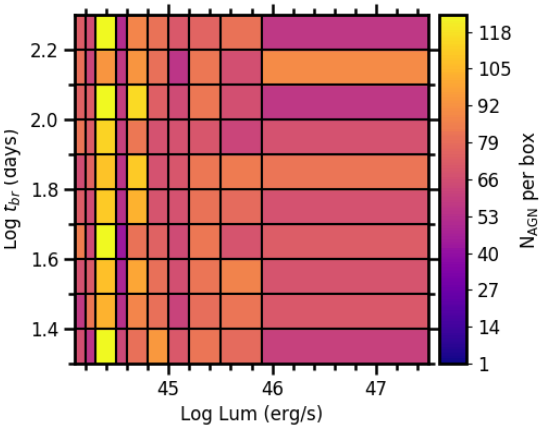

(D) Number of AGN per bin for the luminosity-break timescale colour plots.

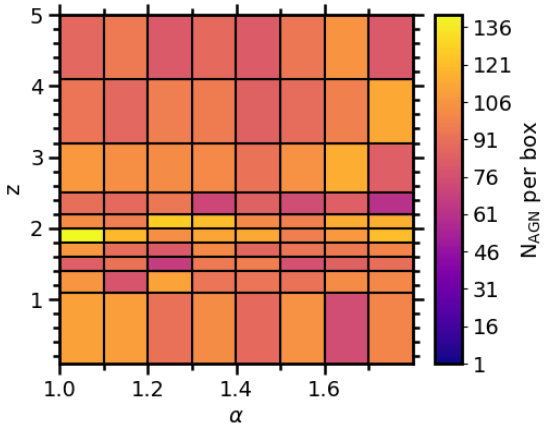

(E) Number of AGN per bin for the input low-frequency power law slope-redshift colour plots.

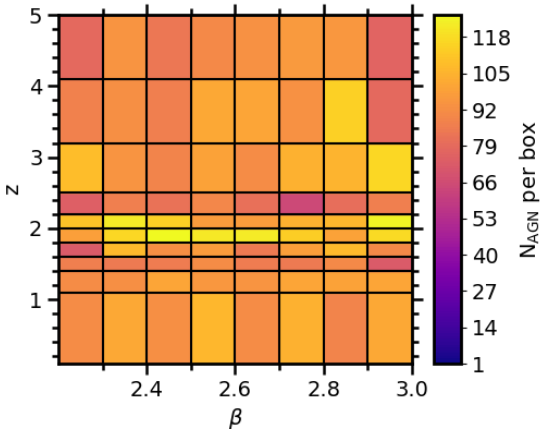

(F) Number of AGN per bin for the input high-frequency power law slope-redshift colour plots.

FIGURE C.9: Number of AGN per bin for the colour maps given in Figure C.8.

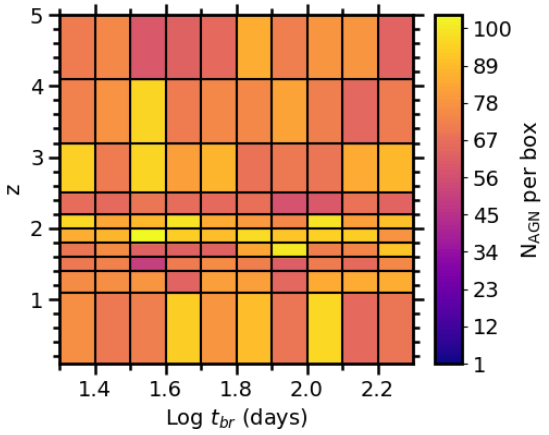

(G) Number of AGN per bin for the break timescale-redshift colour plots.

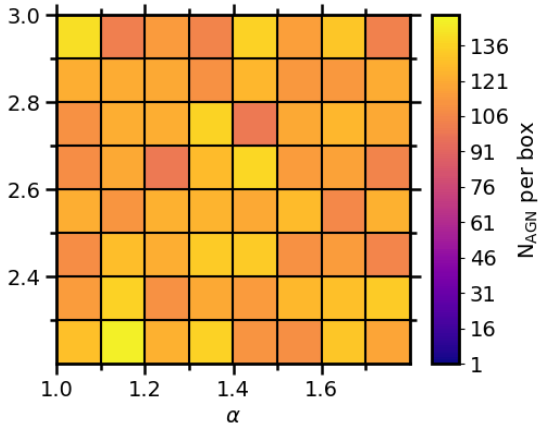

(H) Number of AGN per bin for the input power law slope colour plots.

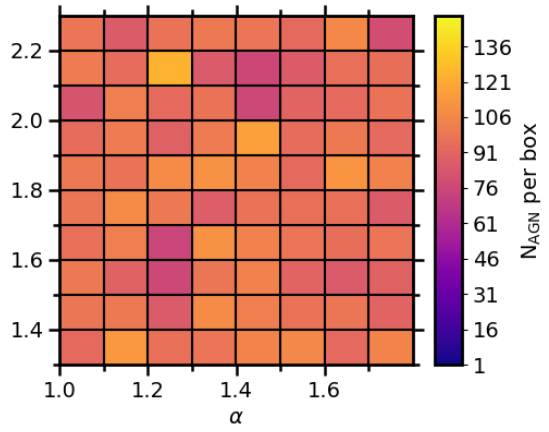

(I) Number of AGN per bin for the low-frequency slope-break timescale colour plots.

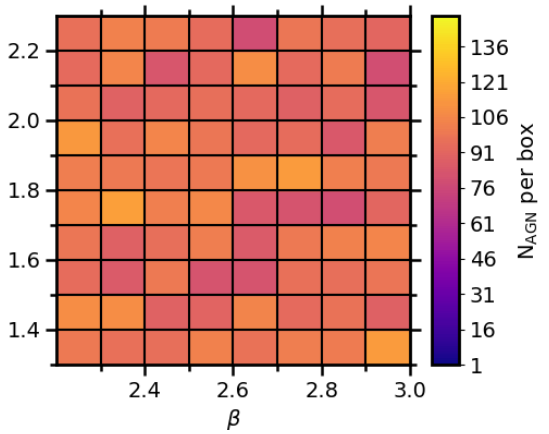

(J) Number of AGN per bin for the high-frequency slope-break timescale colour plots.

FIGURE C.9: Continued.

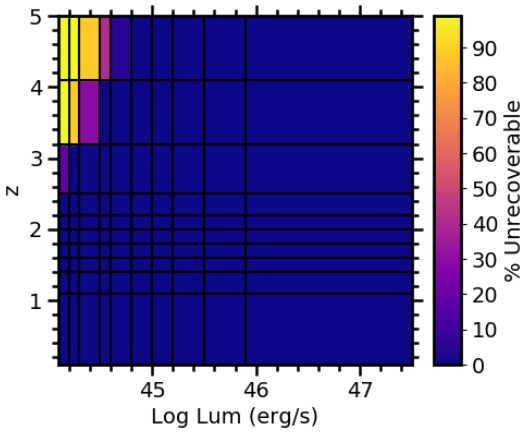

(A) The percentage of AGN of a given luminosity and redshift whose power law could not be fit using these methods.

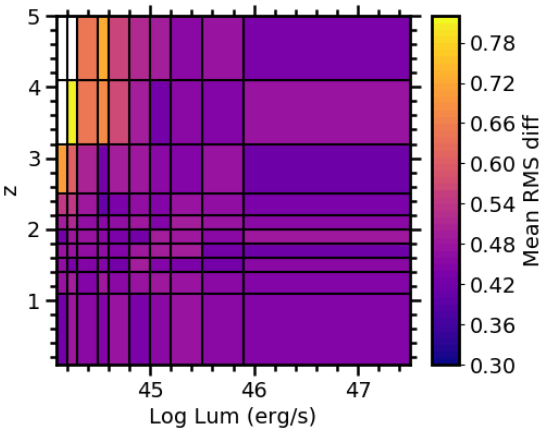

(B) The mean rms difference found between the recovered parameters with the inputs for the AGN of a given luminosity and redshift.

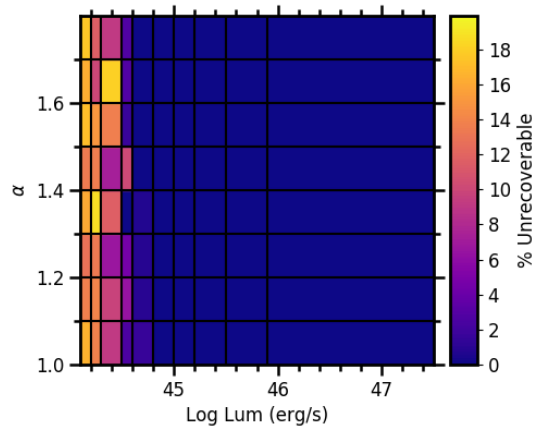

(C) The percentage of AGN of a given luminosity and low-frequency power law slope whose power law could not be fit using these methods.

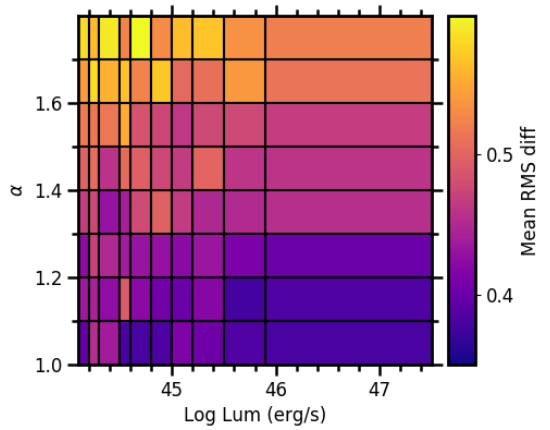

(D) The mean rms difference found between the recovered parameters with the inputs for the AGN of a given luminosity and low-frequency PSD slope.

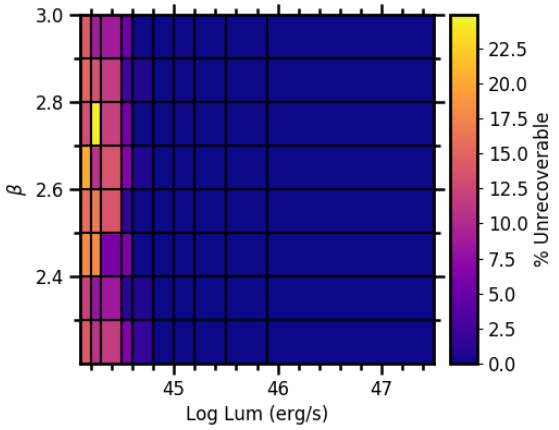

(E) The percentage of AGN of a given luminosity and high-frequency power law slope whose power law could not be fit using these methods.

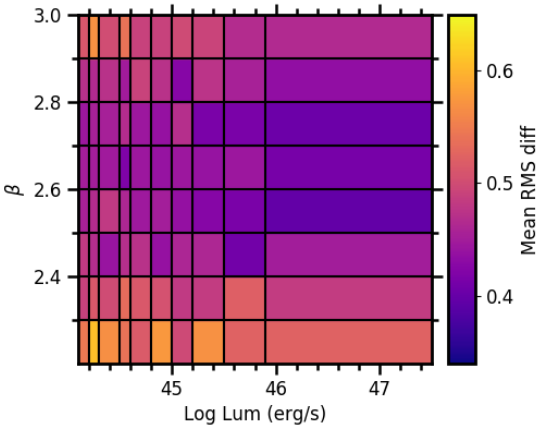

(F) The mean rms difference found between the recovered parameters with the inputs for the AGN of a given luminosity and high-frequency PSD slope.

FIGURE C.10: Colour maps depicting the ability to recover the input BPL PSD using WDF cadenced light curves depending on combination of the power law slopes, break frequencies, luminosity and redshift of the AGN.

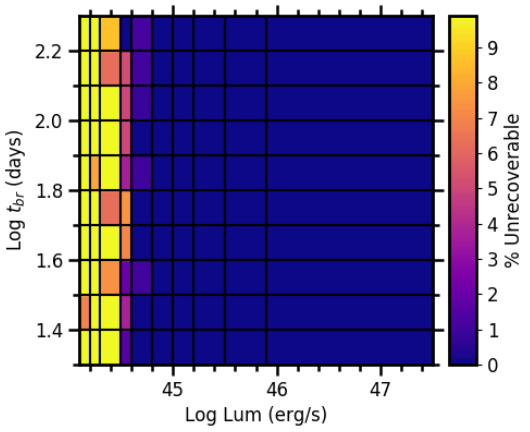

(A) The percentage of AGN of a given luminosity and break timescale whose power law could not be fit using these methods.

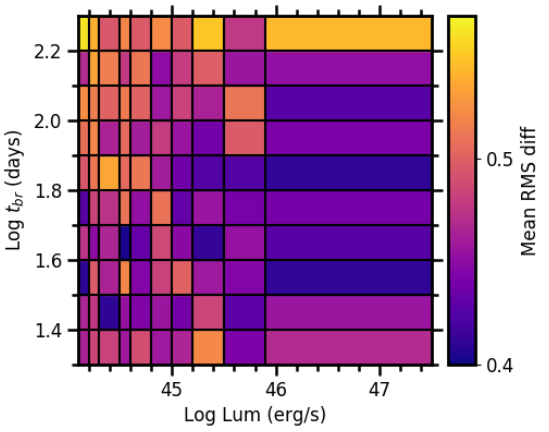

(B) The mean rms difference found between the recovered parameters with the inputs for the AGN of a given luminosity and break timescale.

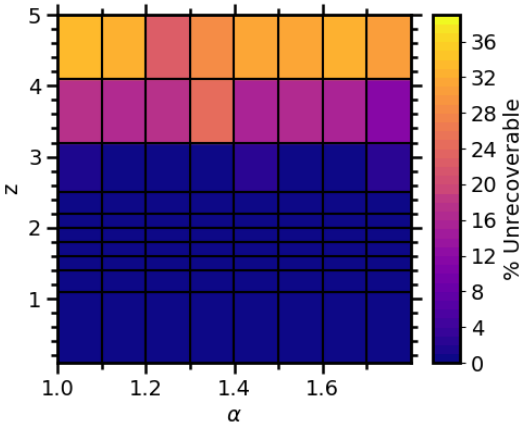

(C) The percentage of AGN of a given low-frequency PSD slope and redshift whose power law could not be fit using these methods.

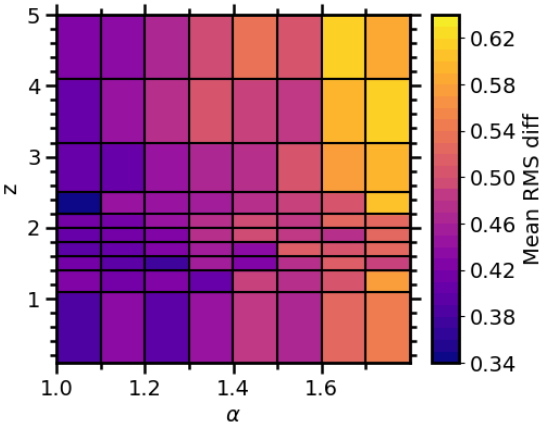

(D) The mean rms difference found between the recovered parameters with the inputs for the AGN of a given low-frequency PSD slope and redshift.

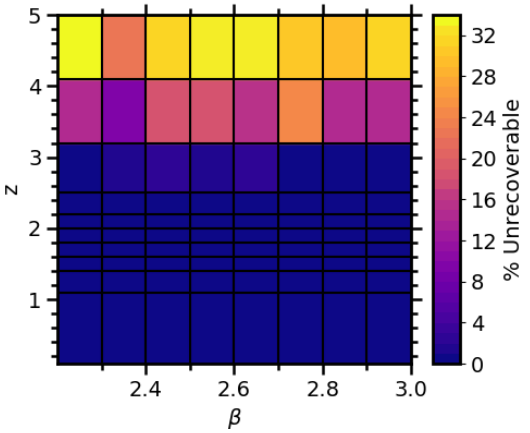

(E) The percentage of AGN of a given high-frequency power law slope and redshift whose power law could not be fit using these methods.

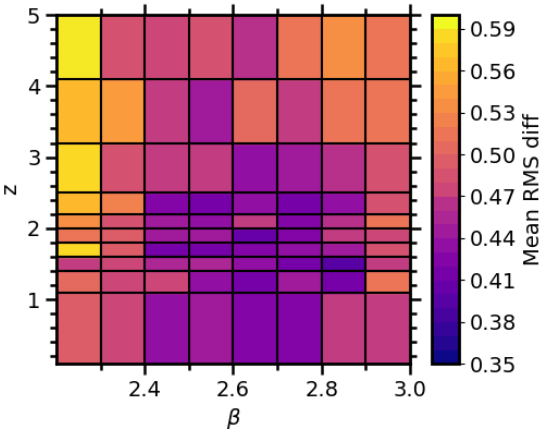

(F) The mean rms difference found between the recovered parameters with the inputs for the AGN of a given high-frequency PSD slope and redshift.

FIGURE C.11: Continued.

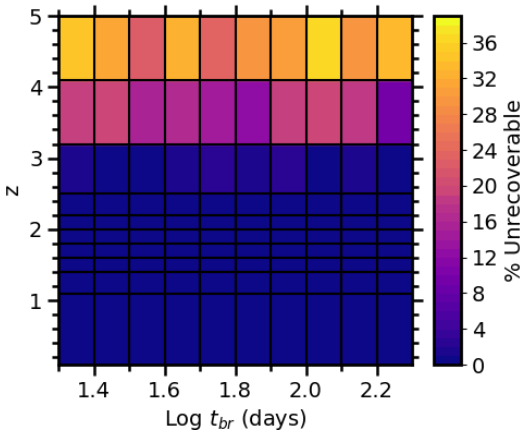

(G) The percentage of AGN of a given break timescale and redshift whose power law could not be fit using these methods.

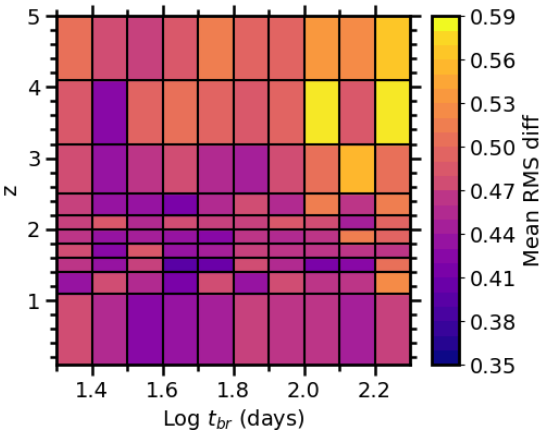

(H) The mean rms difference found between the recovered parameters with the inputs for the AGN of a given break timescale and redshift.

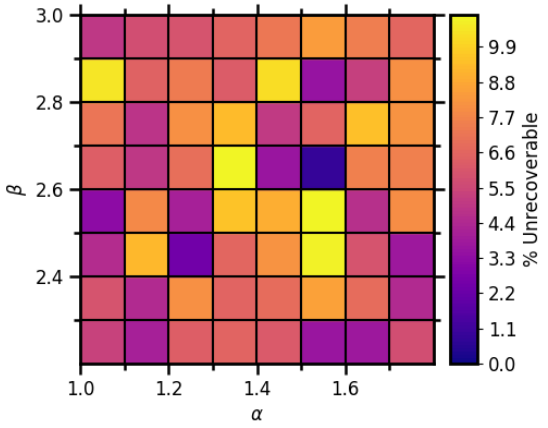

(I) The percentage of AGN of given power law slopes whose power law could not be fit using these methods.

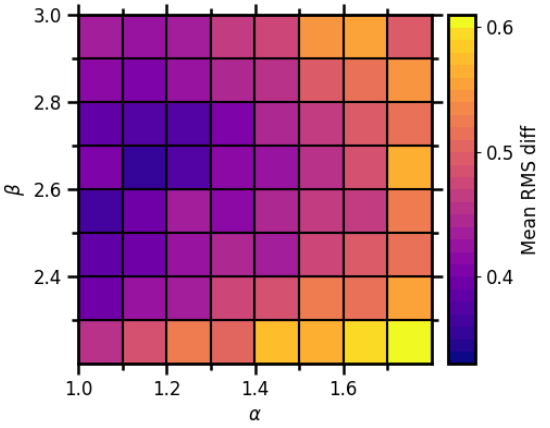

(J) The mean rms difference found between the recovered parameters with the inputs for the AGN of given PSD slopes.

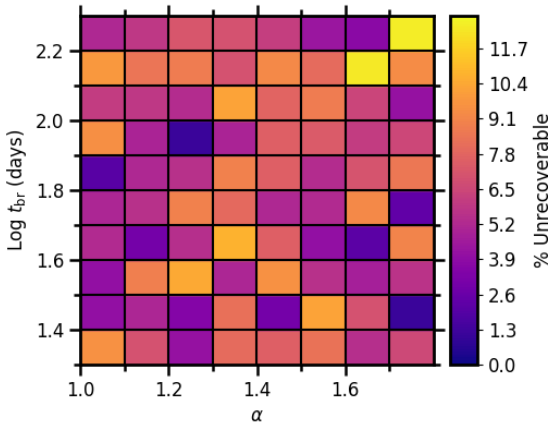

(K) The percentage of AGN of a given low-frequency power law slope and break timescale whose power law could not be fit using these methods.

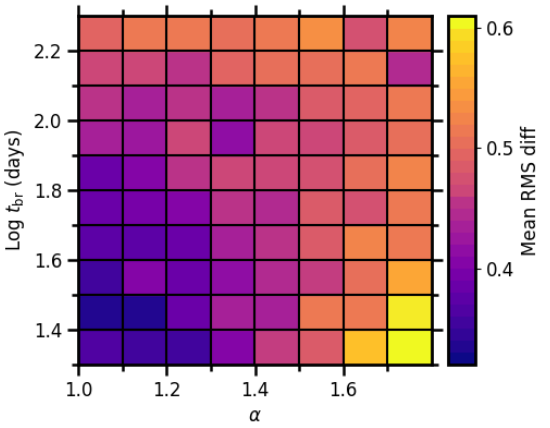

(L) The mean rms difference found between the recovered parameters with the inputs for the AGN of a given low-frequency PSD slope and break timescale.

FIGURE C.11: Continued.

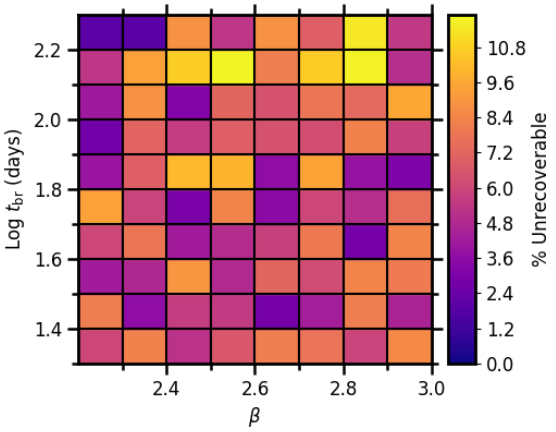

(M) The percentage of AGN of a given high-frequency power law slope and break timescale whose power law could not be fit using these methods.

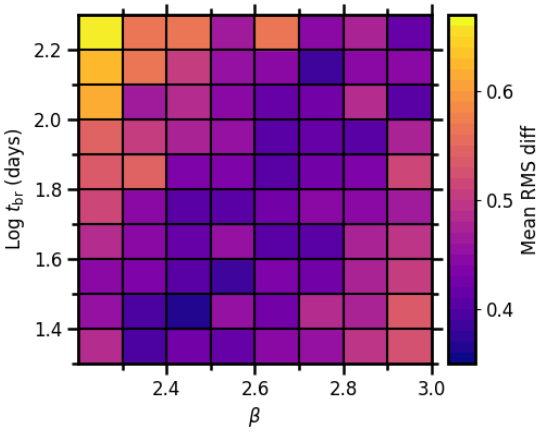

(N) The mean rms difference found between the recovered parameters with the inputs for the AGN of a given high-frequency PSD slope and break timescale.

FIGURE C.11: Continued.

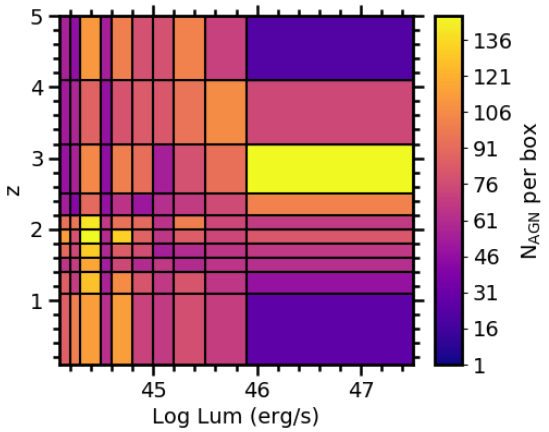

(A) Number of AGN per bin for the luminosity-redshift colour plots.

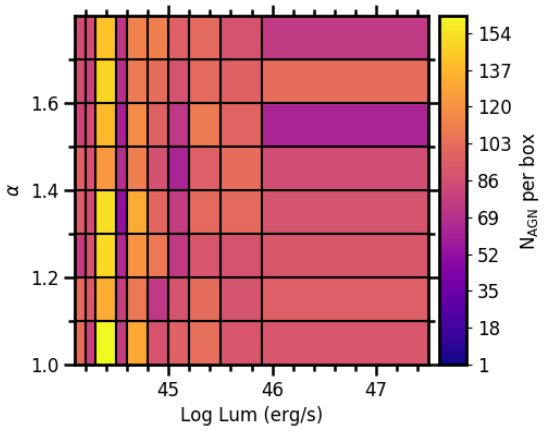

(B) Number of AGN per bin for the luminosity-input low-frequency power law slope colour plots.

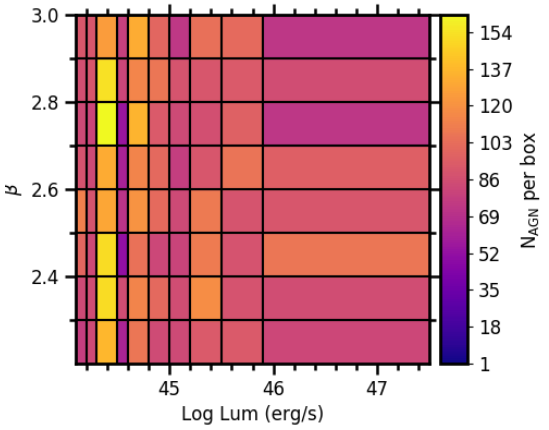

(C) Number of AGN per bin for the luminosity-input high-frequency power law slope colour plots.

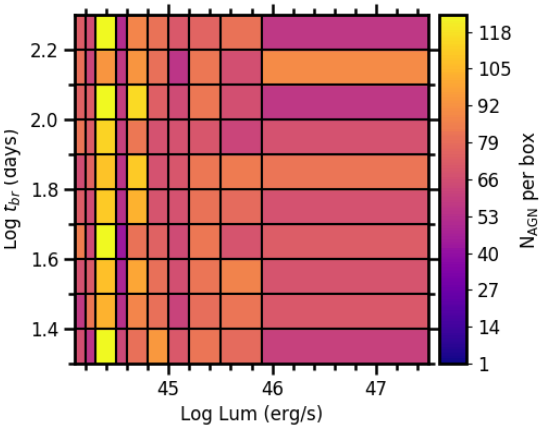

(D) Number of AGN per bin for the luminosity-break timescale colour plots.

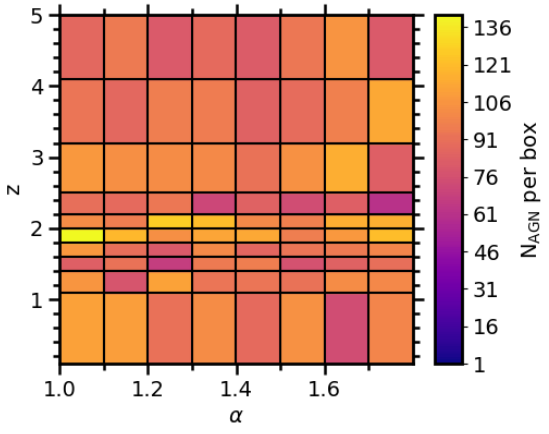

(E) Number of AGN per bin for the input low-frequency power law slope-redshift colour plots.

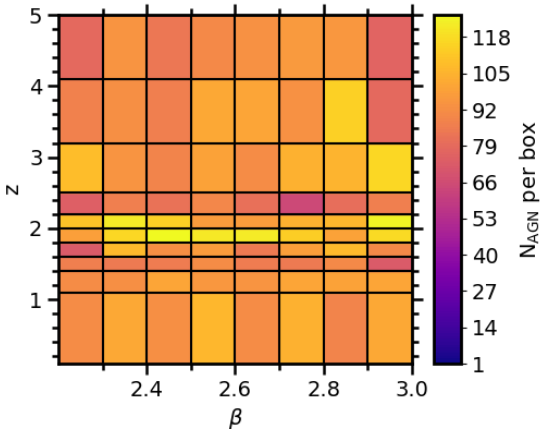

(F) Number of AGN per bin for the input high-frequency power law slope-redshift colour plots.

FIGURE C.12: Number of AGN per bin for the colour maps given in Figure C.10.

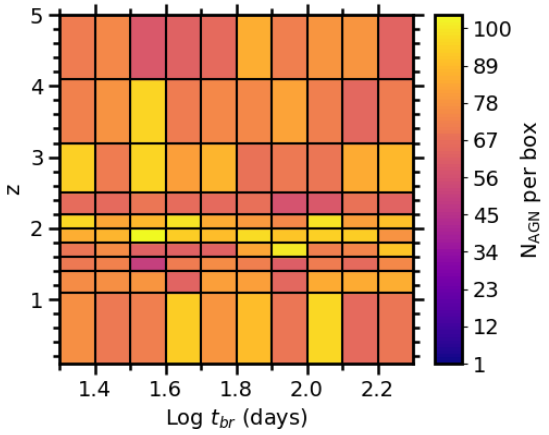

(G) Number of AGN per bin for the break timescale-redshift colour plots.

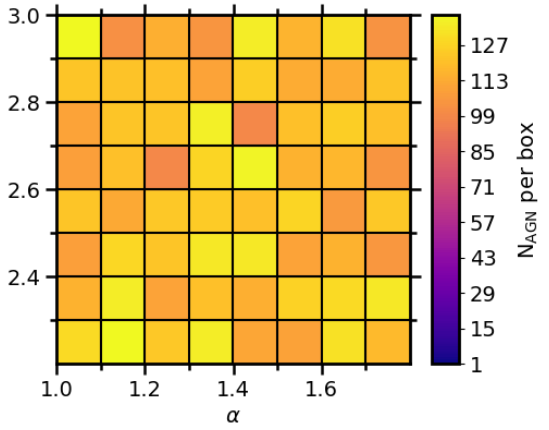

(H) Number of AGN per bin for the input power law slope colour plots.

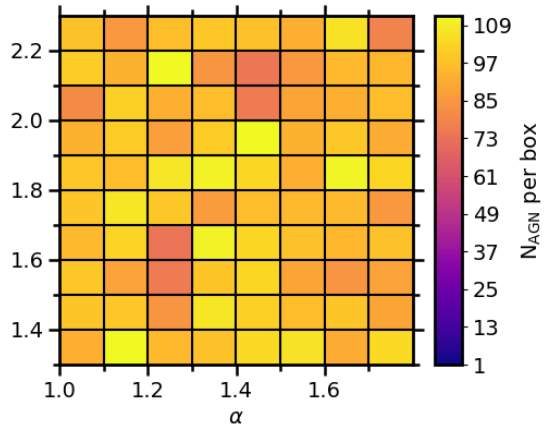

(I) Number of AGN per bin for the low-frequency slope-break timescale colour plots.

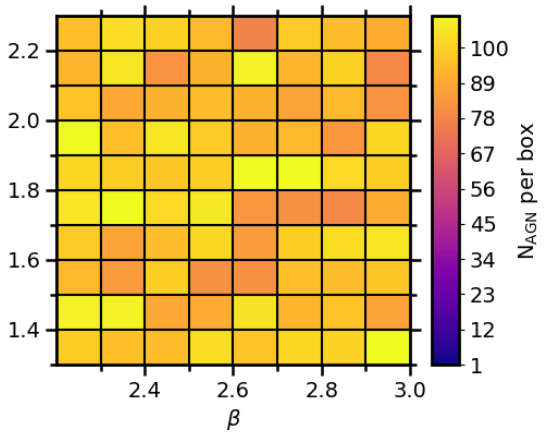

(J) Number of AGN per bin for the high-frequency slope-break timescale colour plots.

FIGURE C.12: Continued.

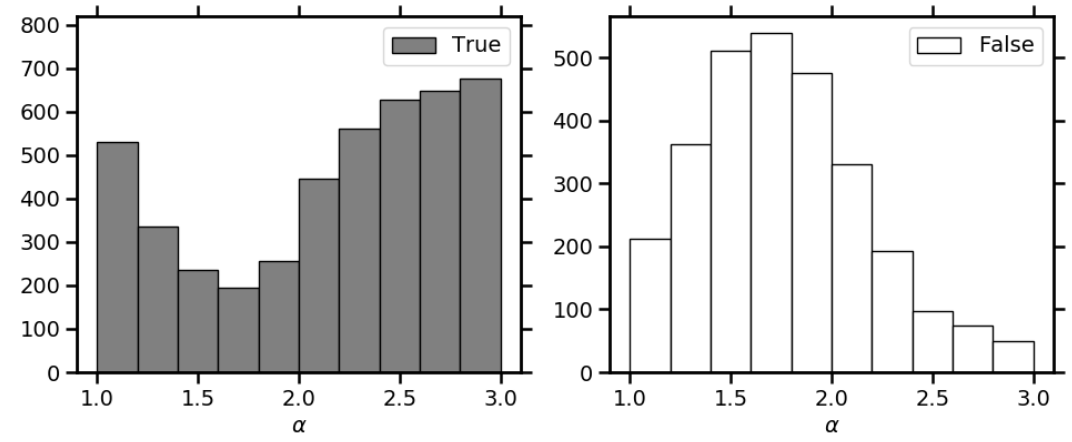

(A) Distributions of low-frequency power law slope corresponding to the BPL light curves that are correctly and incorrectly identified as BPLs.

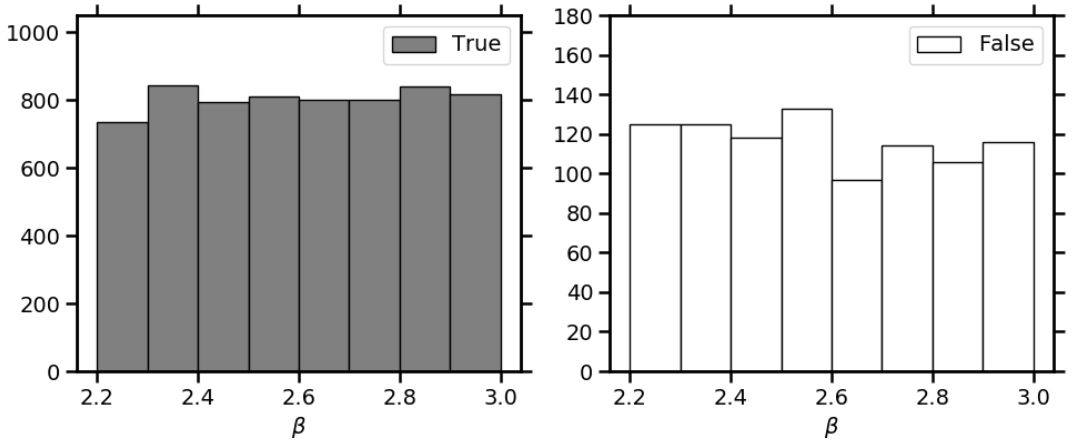

(B) Distributions of high-frequency power law slope corresponding to the BPL light curves that are correctly and incorrectly identified as BPLs.

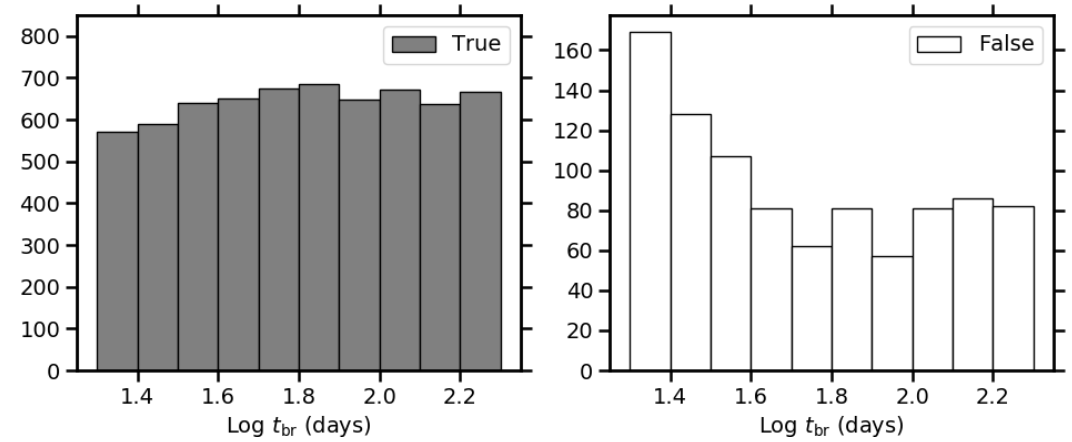

(C) Distributions of break timescale corresponding to the BPL light curves that are correctly and incorrectly identified as BPLs.

FIGURE C.13: Distributions of parameters corresponding to the BPL light curves that are correctly and incorrectly identified as BPLs.

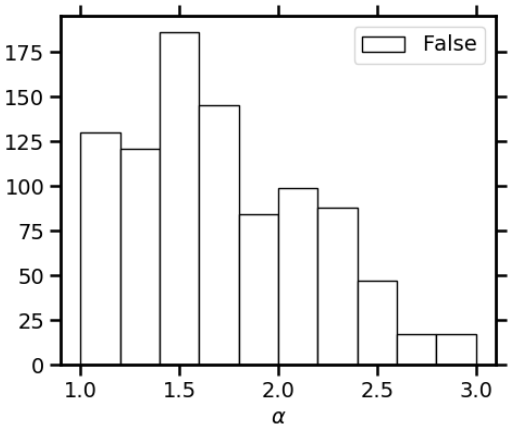

FIGURE C.14: Distributions of the power law slope of the SPL that is found to best fit the BPL light curves that are incorrectly identified as SPLs.

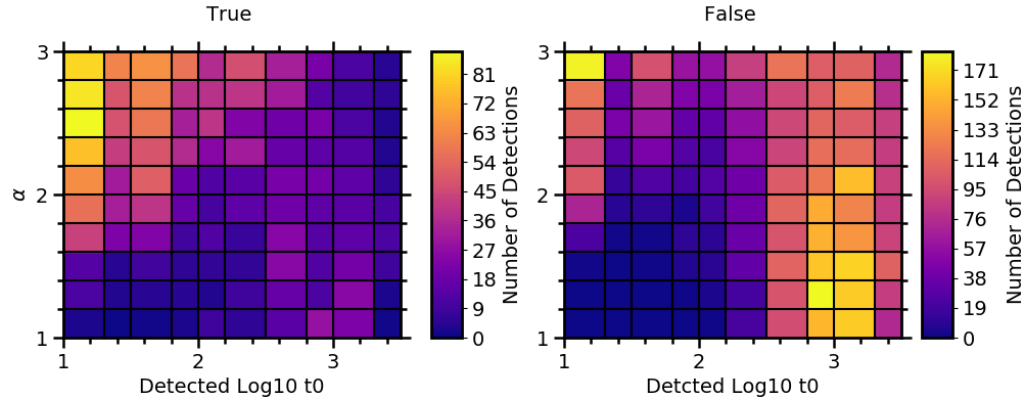

(A) Number of AGN for a given power law slope and periodicity corresponding to the true and false periodicity detections.

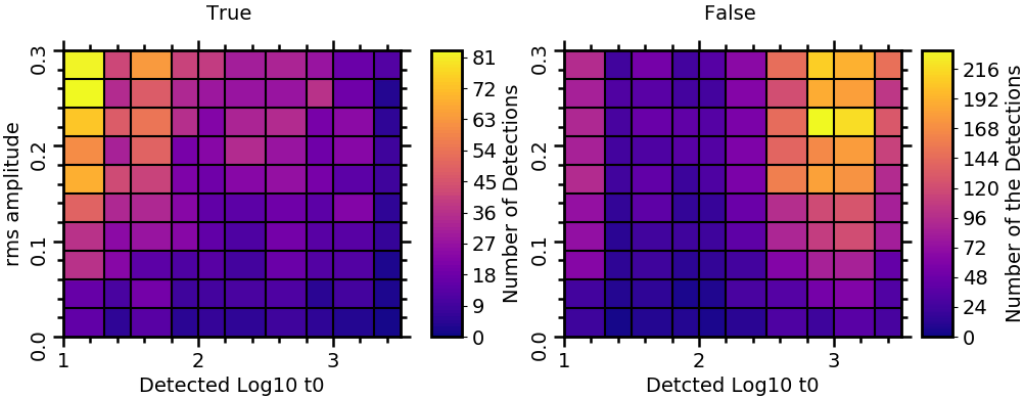

(B) Number of AGN for a given strength of QPO and periodicity corresponding to the true and false periodicity detections.

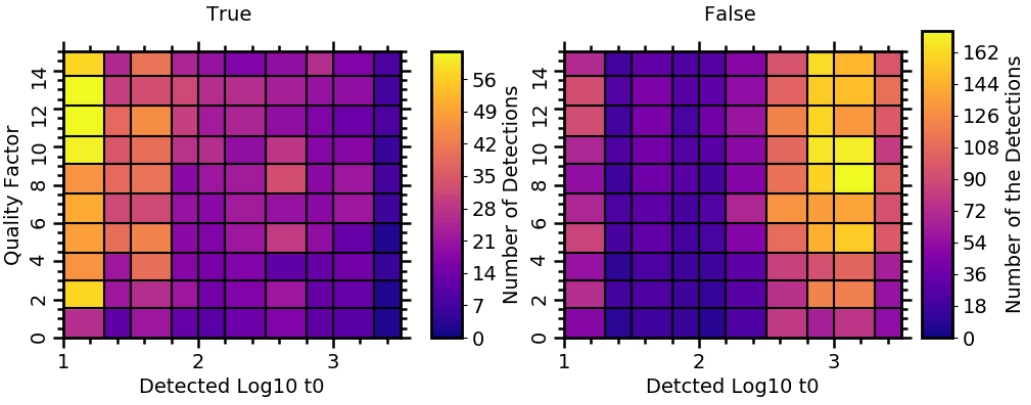

(C) Number of AGN for a given width of QPO and periodicity corresponding to the true and false periodicity detections.

FIGURE C.15: Number of AGN for a given a given set of parameters corresponding to the true and false periodicity detections.

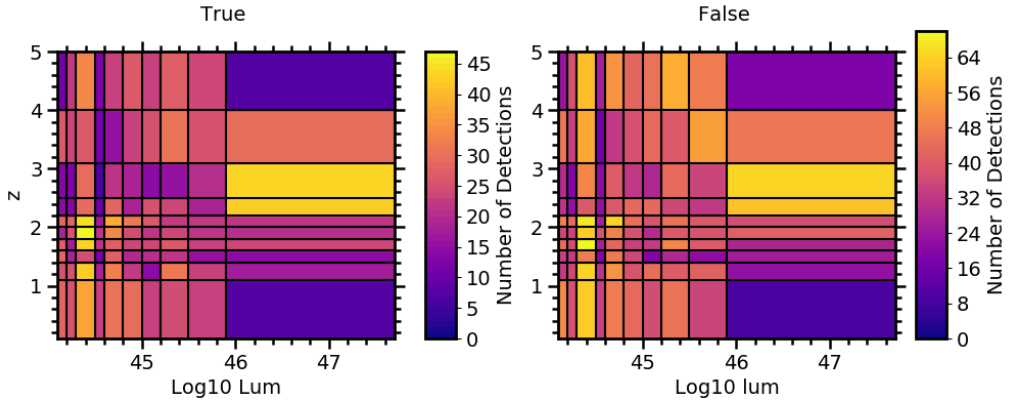

(D) Number of AGN for a given luminosity and redshift corresponding to the true and false periodicity detections.

FIGURE C.15: Continued.

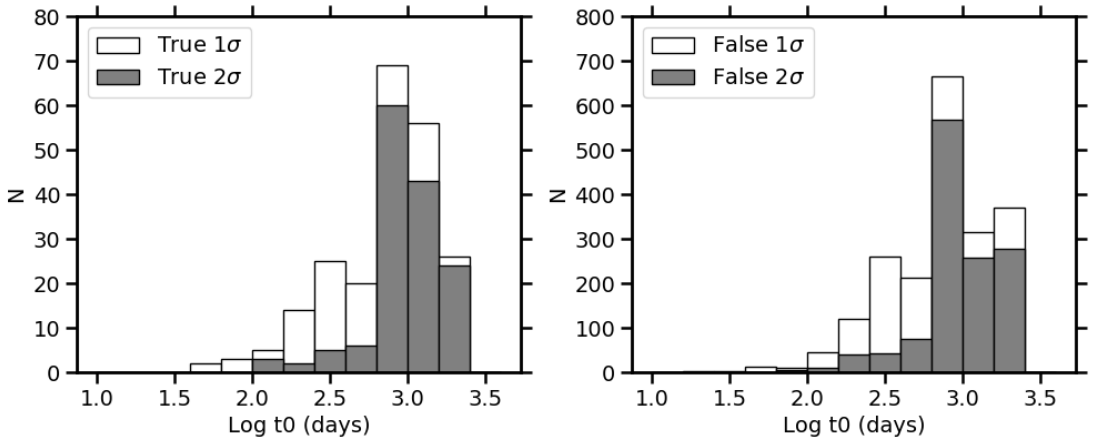

(A) Distributions of the periodicity of the AGN light curves corresponding to true and false quasi-periodicity detections.

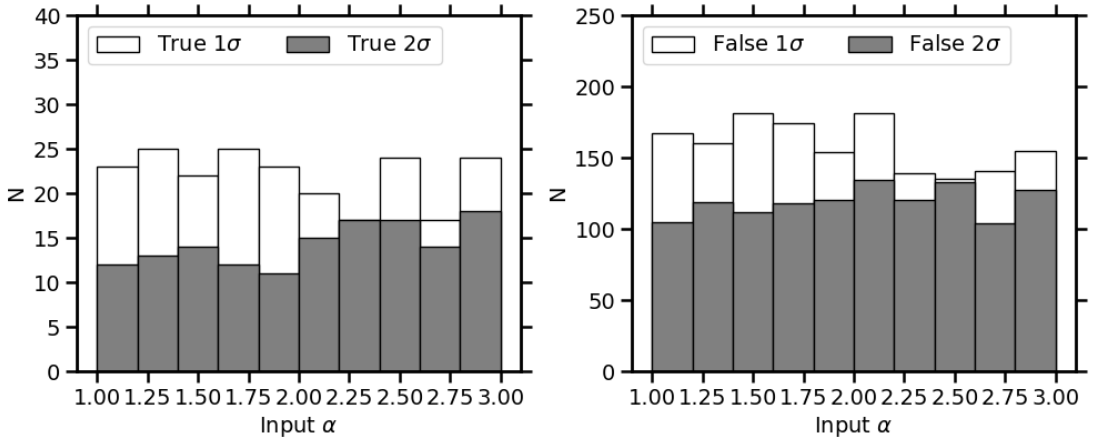

(B) Distributions of the PSD power law slope of the AGN light curves corresponding to true and false quasi-periodicity detections.

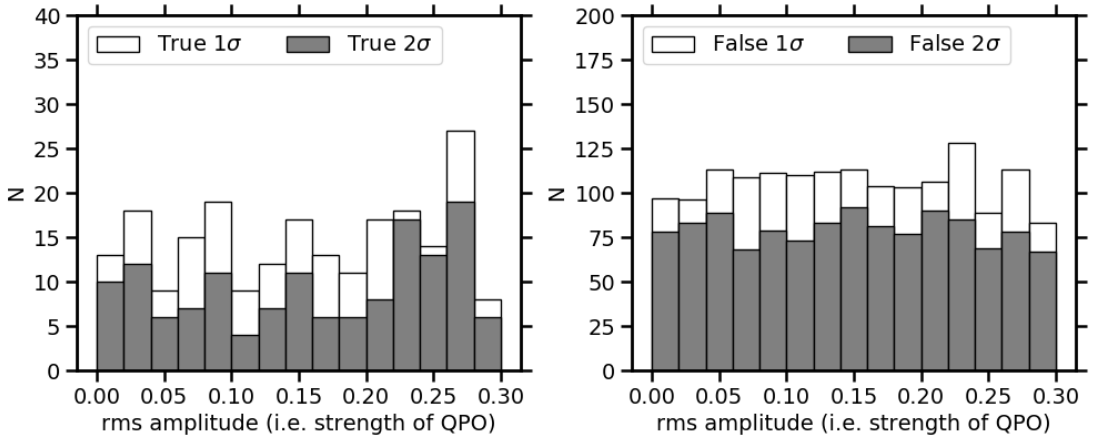

(C) Distributions of the periodicity of the AGN light curves corresponding to true and false quasi-periodicity detections.

FIGURE C.16: Distributions of the strength of the QPO of the AGN light curves corresponding to true and false quasi-periodicity detections.

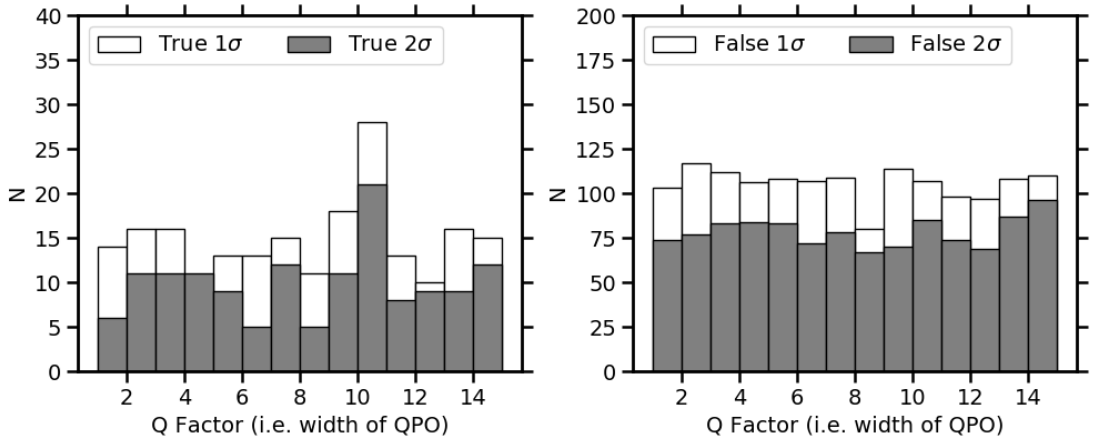

(D) Distributions of the width of the QPO of the AGN light curves corresponding to true and false quasi-periodicity detections.

FIGURE C.16: Continued.

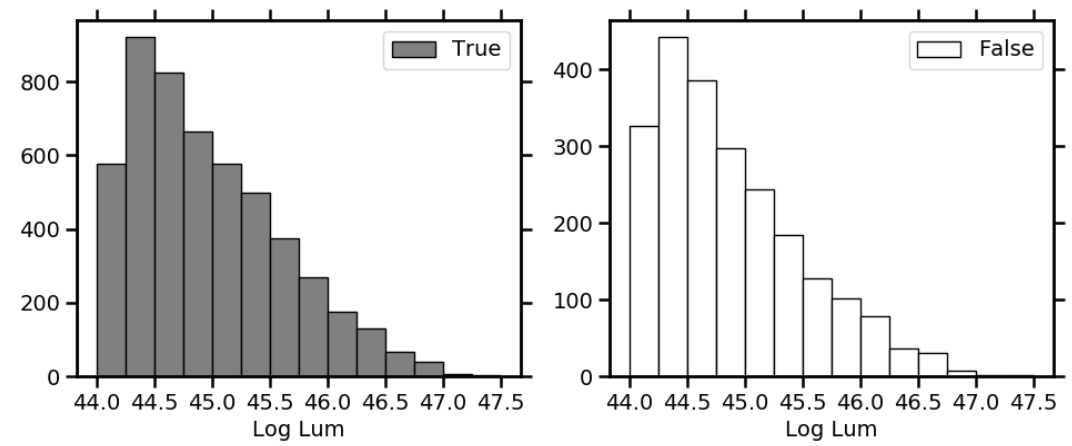

(A) Distributions of luminosity corresponding to the QPO light curves whose underlying power laws are correctly and incorrectly identified as SPLs.

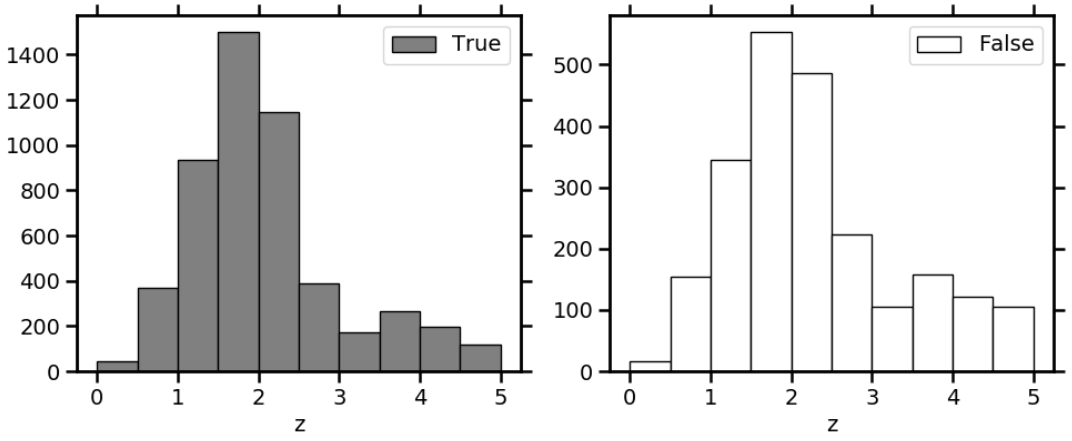

(B) Distributions of redshift corresponding to the QPO light curves whose underlying power laws are correctly and incorrectly identified as SPLs.

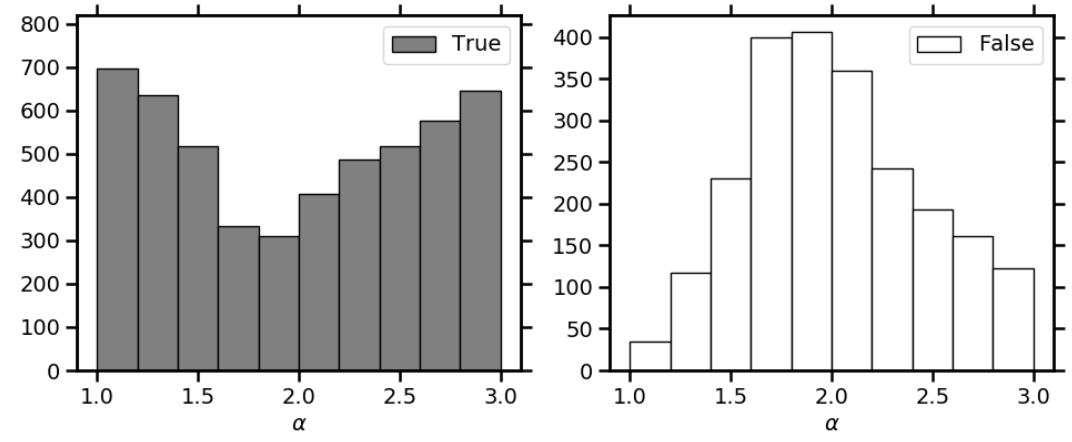

(C) Distributions of input power law slope corresponding to the QPO light curves whose underlying power laws are correctly and incorrectly identified as SPLs.

FIGURE C.17: Distributions of parameters corresponding to the QPO SPL light curves whose underlying power laws are correctly and incorrectly identified as SPLs.

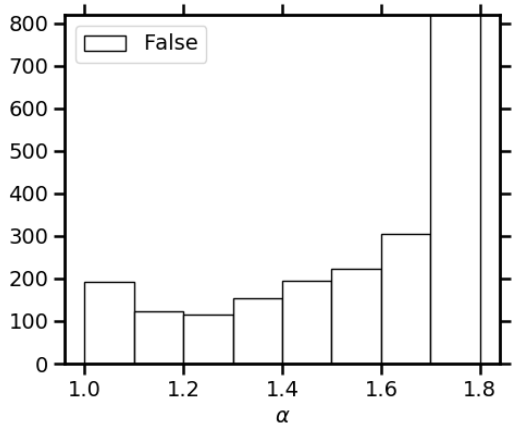

(A) Distributions of the low-frequency power law slope found for the QPO light curves that are incorrectly identified as BPLs.

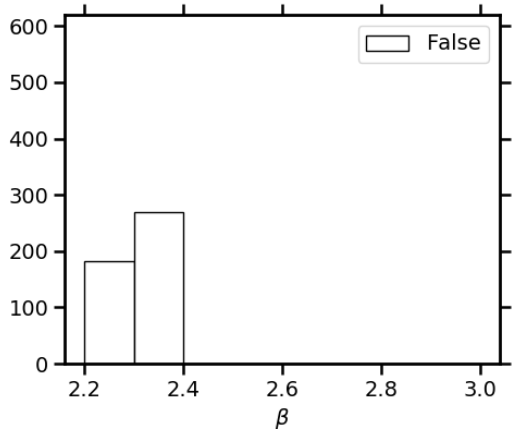

(B) Distributions of the high-frequency power law slope found for the QPO light curves that are incorrectly identified as BPLs.

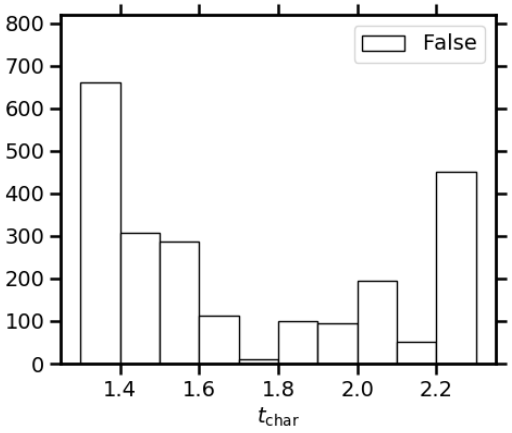

(C) Distributions of the break timescale found for the QPO light curves that are incorrectly identified as BPLs.

FIGURE C.18: Distributions of the BPL parameters found to best fit the QPO light curves that are incorrectly identified as BPLs.

References

T. M. C. Abbott et al. The Dark Energy Survey: Data Release 1. *Astrophysical Journal, Supplement*, 239(2):18, Dec 2018. .

Marek A. Abramowicz, Włodek Kluźniak, Jeffrey E. McClintock, and Ronald A. Remillard. The Importance of Discovering a 3:2 Twin-Peak Quasi-periodic Oscillation in an Ultraluminous X-Ray Source, or How to Solve the Puzzle of Intermediate-Mass Black Holes. *Astrophysical Journal, Letters*, 609(2):L63–L65, July 2004. .

Jose Acosta-Pulido, Noel Castro Segura, Maria Carnerero, and Claudia Raiteri. A New Statistical Approach to the Optical Spectral Variability in Blazars. *Galaxies*, 5(1):1, January 2017. .

Thomas F. Adams. A Survey of the Seyfert Galaxies Based on Large-Scale Image-Tube Plates. *Astrophysical Journal, Supplement*, 33:19, January 1977. .

Aditi Agarwal et al. Multiband optical variability of 3C 279 on diverse time-scales. *Monthly Notices of the RAS*, 488(3):4093–4105, September 2019. .

Iván Agudo et al. On the Location of the γ-Ray Outburst Emission in the BL Lacertae Object AO 0235+164 Through Observations Across the Electromagnetic Spectrum. *Astrophysical Journal, Letters*, 735(1):L10, July 2011. .

D. M. Alexander and R. C. Hickox. What drives the growth of black holes? *New Astronomy Review*, 56(4):93–121, June 2012. .

Triana Almeyda. VEILS light curve extraction codes. Private Communication, 2019.

Triana Almeyda, Andrew Robinson, Michael Richmond, Billy Vazquez, and Robert Nikutta. Modeling the Infrared Reverberation Response of the Circumnuclear Dusty Torus in AGNs: The Effects of Cloud Orientation and Anisotropic Illumination. *Astrophysical Journal*, 843(1):3, July 2017. .

Triana Almeyda, Andrew Robinson, Michael Richmond, Robert Nikutta, and Bryanne McDonough. Modeling the Infrared Reverberation Response of the Circumnuclear Dusty Torus in AGNs: An Investigation of Torus Response Functions. *Astrophysical Journal*, 891(1):26, March 2020. .

A. Alonso-Herrero et al. The Galaxy Activity, Torus, and Outflow Survey (GATOS). II. Torus and polar dust emission in nearby Seyfert galaxies. *Astronomy and Astrophysics*, 652:A99, August 2021. .

W. N. Alston, J. Markeviciute, E. Kara, A. C. Fabian, and M. Middleton. Detection of a QPO in five XMM-Newton observations of RE J1034+396. *Monthly Notices of the RAS*, 445:L16–L20, November 2014. .

W. N. Alston, M. L. Parker, J. Markevičiūtė, A. C. Fabian, M. Middleton, A. Lohfink, E. Kara, and C. Pinto. Discovery of an ∼2-h high-frequency X-ray QPO and iron Kα reverberation in the active galaxy MS 2254.9-3712. *Monthly Notices of the RAS*, 449 (1):467–476, May 2015. .

R. R. J. Antonucci. Optical spectropolarimetry of radio galaxies. *Astrophysical Journal*, 278:499–520, March 1984. .

Robert Antonucci. Unified models for active galactic nuclei and quasars. *Annual Review of Astron and Astrophys*, 31:473–521, January 1993. .

I. Aretxaga and R. Terlevich. On the possible stellar origin of the optical variability of NGC 4151. *Monthly Notices of the RAS*, 269:462–474, July 1994. .

P. Arévalo and P. Uttley. Investigating a fluctuating-accretion model for the spectral-timing properties of accreting black hole systems. *Monthly Notices of the RAS*, 367(2):801–814, April 2006. .

P. Arévalo, P. Uttley, S. Kaspi, E. Breedt, P. Lira, and I. M. McHardy. Correlated X-ray/optical variability in the quasar MR2251-178. *Monthly Notices of the RAS*, 389 (3):1479–1488, September 2008. .

Dominic I. Ashton and Matthew J. Middleton. Searching for energy-resolved quasi-periodic oscillations in AGN. *Monthly Notices of RAS*, 501(4):5478–5499, March 2021. .

J. A. Baldwin, E. Joseph Wampler, and C. Martin Gaskell. Emission-Line Properties of Optically and Radio-selected Complete Quasar Samples. *Astrophysical Journal*, 338: 630, March 1989. .

James M. Bardeen and Jacobus A. Petterson. The Lense-Thirring Effect and Accretion Disks around Kerr Black Holes. *Astrophysical Journal, Letters*, 195:L65, January 1975. .

Aaron J. Barth et al. Broad-line Reverberation in the Kepler-field Seyfert Galaxy Zw 229-015. *Astrophysical Journal*, 732(2):121, May 2011. .

Richard Barvainis. Hot Dust and the Near-Infrared Bump in the Continuum Spectra of Quasars and Active Galactic Nuclei. *Astrophysical Journal*, 320:537, September 1987. .

Robert H. Becker, Richard L. White, and David J. Helfand. The FIRST Survey: Faint Images of the Radio Sky at Twenty Centimeters. *Astrophysical Journal*, 450:559, September 1995. .

Volker Beckmann and Chris R. Shrader. *Active Galactic Nuclei*. John Wiley & Sons, 2012.

N. Bennert, B. Jungwiert, S. Komossa, M. Haas, and R. Chini. Size and properties of the narrow-line region in Seyfert-1 galaxies from spatially-resolved optical spectroscopy. *Astronomy and Astrophysics*, 459(1):55–69, November 2006. .

Misty C. Bentz and Sarah Katz. The AGN Black Hole Mass Database. *Publications of the ASP*, 127(947):67, January 2015. .

Misty C. Bentz et al. The Low-luminosity End of the Radius-Luminosity Relationship for Active Galactic Nuclei. *Astrophysical Journal*, 767(2):149, April 2013. .

G. Bhatta et al. Detection of Possible Quasi-periodic Oscillations in the Long-term Optical Light Curve of the BL Lac Object OJ 287. *Astrophysical Journal*, 832(1):47, November 2016. .

R. D. Blandford and C. F. McKee. Reverberation mapping of the emission line regions of Seyfert galaxies and quasars. *Astrophysical Journal*, 255:419–439, April 1982. .

Louis A. Bloomfield. *How Things Work: The Physics of Everyday Life, 2nd Edition*. John Wiley & Sons, 2000.

E. W. Bonning, L. Cheng, G. A. Shields, S. Salviander, and K. Gebhardt. Accretion Disk Temperatures and Continuum Colors in QSOs. *Astrophysical Journal*, 659(1): 211–217, April 2007. .

Erin Bonning et al. SMARTS Optical and Infrared Monitoring of 12 Gamma-Ray Bright Blazars. *Astrophysical Journal*, 756(1):13, Sep 2012. .

William J. Borucki et al. Kepler Planet-Detection Mission: Introduction and First Results. *Science*, 327(5968):977, Feb 2010. .

Markus Böttcher. Modeling the emission processes in blazars. *Astrophysics and Space Science*, 309(1-4):95–104, June 2007. .

Dennis B. Bowen, Vassilios Mewes, Manuela Campanelli, Scott C. Noble, Julian H. Krolik, and Miguel Zilhão. Quasi-periodic Behavior of Mini-disks in Binary Black Holes Approaching Merger. *Astrophysical Journal, Letters*, 853(1):L17, January 2018. .

B. J. Boyle, T. Shanks, S. M. Croom, R. J. Smith, L. Miller, N. Loaring, and C. Heymans. The 2dF QSO Redshift Survey - I. The optical luminosity function of quasi-stellar objects. *Monthly Notices of the RAS*, 317(4):1014–1022, October 2000. .

E. Breedt, I. M. McHardy, P. Arévalo, P. Uttley, S. G. Sergeev, T. Minezaki, Y. Yoshii, Y. Sakata, P. Lira, and N. G. Chesnok. Twelve years of X-ray and optical variability in the Seyfert galaxy NGC 4051. *Monthly Notices of the RAS*, 403(2):605–619, April 2010. .

E. Breedt et al. Long-term optical and X-ray variability of the Seyfert galaxy Markarian 79. *Monthly Notices of the RAS*, 394(1):427–437, March 2009. .

Brendon J. Brewer, Tommaso Treu, Anna Pancoast, Aaron J. Barth, Vardha N. Bennert, Misty C. Bentz, Alexei V. Filippenko, Jenny E. Greene, Matthew A. Malkan, and Jong-Hak Woo. The Mass of the Black Hole in Arp 151 from Bayesian Modeling of Reverberation Mapping Data. *Astrophysical Journal, Letters*, 733(2):L33, June 2011. .

S. Britzen et al. OJ287: deciphering the 'Rosetta stone of blazars. *Monthly Notices of the RAS*, 478(3):3199–3219, August 2018. .

T. M. Brown et al. Las Cumbres Observatory Global Telescope Network. *Publications of the ASP*, 125(931):1031, September 2013. .

Neven Caplar, Simon J. Lilly, and Benny Trakhtenbrot. Optical Variability of AGNs in the PTF/iPTF Survey. *Astrophysical Journal*, 834(2):111, January 2017. .

M. T. Carini and Wesley T. Ryle. Kepler Observations of the Seyfert 1 Galaxy II ZW 229.015. *Astrophysical Journal*, 749(1):70, April 2012. .

Régis Cartier et al. The QUEST-La Silla AGN Variability Survey. *Astrophysical Journal*, 810(2):164, September 2015. .

M. Charisi, I. Bartos, Z. Haiman, A. M. Price-Whelan, M. J. Graham, E. C. Bellm, R. R. Laher, and S. Márka. A population of short-period variable quasars from PTF as supermassive black hole binary candidates. *Monthly Notices of the RAS*, 463(2): 2145–2171, December 2016. .

Maria Charisi, Zoltán Haiman, David Schiminovich, and Daniel J. D'Orazio. Testing the relativistic Doppler boost hypothesis for supermassive black hole binary candidates. *Monthly Notices of the RAS*, 476(4):4617–4628, June 2018. .

M. J. Childress et al. OzDES multifibre spectroscopy for the Dark Energy Survey: 3-yr results and first data release. *Monthly Notices of the RAS*, 472(1):273–288, November 2017. .

Yumi Choi, Robert R. Gibson, Andrew C. Becker, Željko Ivezić, Andrew J. Connolly, Chelsea L. MacLeod, John J. Ruan, and Scott F. Anderson. Variability-based Active Galactic Nucleus Selection Using Image Subtraction in the SDSS and LSST Era. *Astrophysical Journal*, 782(1):37, February 2014. .

S. Ciprini, G. Tosti, C. M. Raiteri, M. Villata, M. A. Ibrahimov, G. Nucciarelli, and L. Lanteri. Optical variability of the BL Lacertae object GC 0109+224. Multiband behaviour and time scales from a 7-years monitoring campaign. *Astronomy and Astrophysics*, 400:487–498, March 2003. .

J. Clavel, W. Wamsteker, and I. S. Glass. Hot Dust on the Outskirts of the Broad-Line Region in Fairall 9. *Astrophysical Journal*, 337:236, February 1989. .

J. Clavel et al. Steps toward Determination of the Size and Structure of the Broad-Line Region in Active Galactic Nuclei. I. an 8 Month Campaign of Monitoring NGC 5548 with IUE. *Astrophysical Journal*, 366:64, January 1991. .

Julia M. Comerford, Brian F. Gerke, Daniel Stern, Michael C. Cooper, Benjamin J. Weiner, Jeffrey A. Newman, Kristin Madsen, and R. Scott Barrows. Kiloparsec-scale Spatial Offsets in Double-peaked Narrow-line Active Galactic Nuclei. I. Markers for Selection of Compelling Dual Active Galactic Nucleus Candidates. *Astrophysical Journal*, 753(1):42, July 2012. .

B. Czerny and K. Hryniewicz. The origin of the broad line region in active galactic nuclei. *Astronomy and Astrophysics*, 525:L8, January 2011. .

F. D'Ammando et al. AGILE detection of extreme γ-ray activity from the blazar PKS 1510-089 during March 2009. Multifrequency analysis. *Astronomy and Astrophysics*, 529:A145, May 2011. .

F. D'Ammando et al. Long-term monitoring of PKS 0537-441 with Fermi-LAT and multiwavelength observations. *Monthly Notices of the RAS*, 431(3):2481–2492, May 2013. .

Dark Energy Survey Collaboration et al. The Dark Energy Survey: more than dark energy - an overview. *Monthly Notices of the RAS*, 460(2):1270–1299, August 2016. .

Kris Davidson and Hagai Netzer. The emission lines of quasars and similar objects. *Reviews of Modern Physics*, 51(4):715, 1979.

Charles D. Dermer and Reinhard Schlickeiser. Model for the High-Energy Emission from Blazars. *Astrophysical Journal*, 416:458, October 1993. .

Jason Dexter and Eric Agol. Quasar Accretion Disks are Strongly Inhomogeneous. *Astrophysical Journal, Letters*, 727(1):L24, January 2011. .

Lankeswar Dey, Achamveedu Gopakumar, Mauri Valtonen, Stanislaw Zola, Abhimanyu Susobhanan, Rene Hudec, Pauli Pihajoki, Tapio Pursimo, Andrei Berdyugin, Vilppu Piirola, Stefano Ciprini, Kari Nilsson, Helen Jermak, Mark Kidger, and Stefanie Komossa. The Unique Blazar OJ 287 and Its Massive Binary Black Hole Central Engine. *Universe*, 5(5):108, May 2019. .

Daniel J. D'Orazio, Zoltán Haiman, and Andrew MacFadyen. Accretion into the central cavity of a circumbinary disc. *Monthly Notices of the RAS*, 436(4):2997–3020, December 2013. .

A. J. Drake, S. G. Djorgovski, A. Mahabal, E. Beshore, S. Larson, M. J. Graham, R. Williams, E. Christensen, M. Catelan, A. Boattini, A. Gibbs, R. Hill, and R. Kowalski. First Results from the Catalina Real-Time Transient Survey. *Astrophysical Journal*, 696(1):870–884, May 2009. .

Pu Du et al. Supermassive Black Holes with High Accretion Rates in Active Galactic Nuclei. V. A New Size-Luminosity Scaling Relation for the Broad-line Region. *Astrophysical Journal*, 825(2):126, July 2016. .

J. S. Dunlop, G. L. Taylor, D. H. Hughes, and E. I. Robson. Infrared imaging of the host galaxies of radio-loud and radio-quiet quasars. *Monthly Notices of the RAS*, 264: 455–488, September 1993. .

M. Durant, P. Gandhi, T. Shahbaz, H. H. Peralta, and V. S. Dhillon. Multiwavelength spectral and high time resolution observations of SWIFTJ1753.5-0127: new activity? *Monthly Notices of the RAS*, 392(1):309–324, January 2009. .

R. Edelson et al. Discovery of a ~5 Day Characteristic Timescale in the Kepler Power Spectrum of Zw 229-15. *Astrophysical Journal*, 795(1):2, Nov 2014. .

R. A. Edelson and J. H. Krolik. The Discrete Correlation Function: A New Method for Analyzing Unevenly Sampled Variability Data. *Astrophysical Journal*, 333:646, October 1988. .

Rick Edelson and Kirpal Nandra. A Cutoff in the X-Ray Fluctuation Power Density Spectrum of the Seyfert 1 Galaxy NGC 3516. *Astrophysical Journal*, 514(2):682–690, April 1999. .

J. Emerson, A. McPherson, and W. Sutherland. Visible and Infrared Survey Telescope for Astronomy: Progress Report. *The Messenger*, 126:41–42, December 2006.

D. Emmanoulopoulos, I. M. McHardy, and I. E. Papadakis. Generating artificial light curves: revisited and updated. *Monthly Notices of the RAS*, 433(2):907–927, August 2013. .

Event Horizon Telescope Collaboration et al. First M87 Event Horizon Telescope Results. I. The Shadow of the Supermassive Black Hole. *Astrophysical Journal, Letters*, 875(1):L1, April 2019. .

Emilio E. Falco et al. The Updated Zwicky Catalog (UZC). *Publications of the ASP*, 111 (758):438–452, April 1999. .

Brian D. Farris, Paul Duffell, Andrew I. MacFadyen, and Zoltan Haiman. Binary Black Hole Accretion from a Circumbinary Disk: Gas Dynamics inside the Central Cavity. *Astrophysical Journal*, 783(2):134, March 2014. .

G. G. Fazio et al. The Infrared Array Camera (IRAC) for the Spitzer Space Telescope. *Astrophysical Journal, Supplement*, 154(1):10–17, Sep 2004. .

Laura Ferrarese and Holland Ford. Supermassive Black Holes in Galactic Nuclei: Past, Present and Future Research. *Space Science Reviews*, 116(3-4):523–624, February 2005. .

Alexei V. Filippenko, W. D. Li, R. R. Treffers, and Maryam Modjaz. The Lick Observatory Supernova Search with the Katzman Automatic Imaging Telescope. In Bohdan Paczynski, Wen-Ping Chen, and Claudia Lemme, editors, *IAU Colloq. 183: Small Telescope Astronomy on Global Scales*, volume 246 of *Astronomical Society of the Pacific Conference Series*, page 121, January 2001.

M. Fiorucci, S. Ciprini, and G. Tosti. The continuum spectral features of blazars in the optical region. *Astronomy and Astrophysics*, 419:25–34, May 2004. .

B. Flaugher et al. The Dark Energy Camera. *Astronomical Journal*, 150:150, November 2015. .

Daniel Foreman-Mackey, David W. Hogg, Dustin Lang, and Jonathan Goodman. emcee: The MCMC Hammer. *Publications of the ASP*, 125(925):306, March 2013. .

G. Fossati, L. Maraschi, A. Celotti, A. Comastri, and G. Ghisellini. A unifying view of the spectral energy distributions of blazars. *Monthly Notices of the RAS*, 299(2): 433–448, September 1998. .

P. Gandhi et al. Rapid optical and X-ray timing observations of GX339-4: multicomponent optical variability in the low/hard state. *Monthly Notices of the RAS*, 407(4):2166–2192, October 2010. .

S. García-Burillo et al. The Galaxy Activity, Torus, and Outflow Survey (GATOS). I. ALMA images of dusty molecular tori in Seyfert galaxies. *Astronomy and Astrophysics*, 652:A98, August 2021. .

C. Martin Gaskell. What broad emission lines tell us about how active galactic nuclei work. *New Astronomy Review*, 53(7-10):140–148, July 2009. .

G. Ghisellini, F. Tavecchio, L. Foschini, G. Ghirlanda, L. Maraschi, and A. Celotti. General physical properties of bright Fermi blazars. *Monthly Notices of the RAS*, 402 (1):497–518, February 2010. .

G. Ghisellini, C. Righi, L. Costamante, and F. Tavecchio. The Fermi blazar sequence. *Monthly Notices of the RAS*, 469(1):255–266, July 2017. .

Gabriele Ghisellini. Extragalactic relativistic jets. In Felix A. Aharonian, Werner Hofmann, and Frank M. Rieger, editors, *25th Texas Symposium on Relativistic AstroPhysics (Texas 2010)*, volume 1381 of *American Institute of Physics Conference Series*, pages 180–198, September 2011. .

Marek Gierliński, Matthew Middleton, Martin Ward, and Chris Done. A periodicity of ~1hour in X-ray emission from the active galaxy RE J1034+396. *Nature*, 455(7211): 369–371, September 2008. .

Uriel Giveon, Dan Maoz, Shai Kaspi, Hagai Netzer, and Paul S. Smith. Long-term optical variability properties of the Palomar-Green quasars. *Monthly Notices of the RAS*, 306(3):637–654, July 1999. .

I. S. Glass. Infrared variability of the Seyfert galaxy NGC 3783. *Monthly Notices of the RAS*, 256:23P–27, May 1992. .

Varoujan Gorjian, Matthew Malkan, Aaron Barth, Alex Filippenko, and Joshua Bloom. Spitzer, Kepler, and Ground Based Reverberation Mapping of 3 Active Galactic Nuclei. Spitzer Proposal, June 2010.

Varoujan Gorjian et al. Spitzer and Kepler Space Telescope Detection of Reverberation in the Seyfert 1 Galaxy Zw 229-015. In *American Astronomical Society Meeting Abstracts #223*, volume 223 of *American Astronomical Society Meeting Abstracts*, page 251.08, January 2014.

Alister W. Graham. Galaxy Bulges and Their Massive Black Holes: A Review. In Eija Laurikainen, Reynier Peletier, and Dimitri Gadotti, editors, *Galactic Bulges*, volume 418 of *Astrophysics and Space Science Library*, page 263, January 2016. .

Matthew J. Graham, S. G. Djorgovski, Daniel Stern, Andrew J. Drake, Ashish A. Mahabal, Ciro Donalek, Eilat Glikman, Steve Larson, and Eric Christensen. A systematic search for close supermassive black hole binaries in the Catalina Real-time Transient Survey. *Monthly Notices of the RAS*, 453(2):1562–1576, October 2015. .

Gravity Collaboration et al. The resolved size and structure of hot dust in the immediate vicinity of AGN. *Astronomy and Astrophysics*, 635:A92, March 2020. .

Gravity Collaboration et al. The central parsec of NGC 3783: a rotating broad emission line region, asymmetric hot dust structure, and compact coronal line region. *Astronomy and Astrophysics*, 648:A117, April 2021. .

A. R. Green, I. M. McHardy, and H. J. Lehto. On the nature of rapid X-ray variability in active galactic nuclei. *Monthly Notices of the RAS*, 265:664–680, December 1993. .

C. J. Grier et al. The Sloan Digital Sky Survey Reverberation Mapping Project: Hα and Hβ Reverberation Measurements from First-year Spectroscopy and Photometry. *Astrophysical Journal*, 851(1):21, December 2017. .

M. F. Gu and Y. L. Ai. The optical variability of flat-spectrum radio quasars in the SDSS stripe 82 region. *Astronomy and Astrophysics*, 528:A95, Apr 2011. .

M. F. Gu, C. U. Lee, S. Pak, H. S. Yim, and A. B. Fletcher. Multi-colour optical monitoring of eight red blazars. *Astronomy and Astrophysics*, 450(1):39–51, Apr 2006. .

E. Guise et al. Multiwavelength optical and NIR variability analysis of the Blazar PKS 0027-426. *Monthly Notices of the RAS*, 510(3):3145–3177, March 2022a. .

E. Guise et al. Dust reverberation mapping and light-curve modelling of Zw229-015. *Monthly Notices of the RAS*, 516(4):4898–4915, November 2022b. .

Alok C. Gupta et al. A peculiar multiwavelength flare in the blazar 3C 454.3. *Monthly Notices of the RAS*, 472(1):788–798, November 2017. .

Francesco Haardt and Laura Maraschi. X-Ray Spectra from Two-Phase Accretion Disks. *Astrophysical Journal*, 413:507, August 1993. .

Christopher Harrison. *Observational constraints on the influence of active galactic nuclei on the evolution of galaxies*. PhD thesis, Durham University, September 2014.

M. R. S. Hawkins. Gravitational microlensing, quasar variability and missing matter. *Nature*, 366(6452):242–245, November 1993. .

Kimitake Hayasaki, Shin Mineshige, and Hiroshi Sudou. Binary Black Hole Accretion Flows in Merged Galactic Nuclei. *Publications of the ASJ*, 59:427–441, April 2007. .

M. Hayashida et al. The Structure and Emission Model of the Relativistic Jet in the Quasar 3C 279 Inferred from Radio to High-energy γ-Ray Observations in 2008-2010. *Astrophysical Journal*, 754(2):114, August 2012. .

Stephen E. Healey et al. CRATES: An All-Sky Survey of Flat-Spectrum Radio Sources. *Astrophysical Journal, Supplement*, 171(1):61–71, July 2007. .

Timothy M. Heckman and Philip N. Best. The Coevolution of Galaxies and Supermassive Black Holes: Insights from Surveys of the Contemporary Universe. *Annual Review of Astron and Astrophys*, 52:589–660, August 2014. .

J. Heidt and S. J. Wagner. Statistics of optical intraday variability in a complete sample of radio-selected BL Lacertae objects. *Astronomy and Astrophysics*, 305:42, Jan 1996.

Luis Ho. Supermassive Black Holes in Galactic Nuclei: Observational Evidence and Astrophysical Consequences. In Sandip K. Chakrabarti, editor, *Observational Evidence for the Black Holes in the Universe*, volume 234 of *Astrophysics and Space Science Library*, page 157, January 1999. .

S. F. Hönig. VOILETTE Soton Reduction Pipeline. Private Communication, 2018.

S. F. Hönig. emcee.pro. Private Communication, 2020.

S. F. Hönig and M. Kishimoto. The dusty heart of nearby active galaxies. II. From clumpy torus models to physical properties of dust around AGN. *Astronomy and Astrophysics*, 523:A27, November 2010. .

S. F. Hönig and M. Kishimoto. Constraining properties of dusty environments by infrared variability. *Astronomy and Astrophysics*, 534:A121, Oct 2011. .

S. F. Hönig, T. Beckert, K. Ohnaka, and G. Weigelt. Radiative transfer modeling of three-dimensional clumpy AGN tori and its application to NGC 1068. *Astronomy and Astrophysics*, 452(2):459–471, June 2006. .

S. F. Hönig, M. Kishimoto, R. Antonucci, A. Marconi, M. A. Prieto, K. Tristram, and G. Weigelt. Parsec-scale Dust Emission from the Polar Region in the Type 2 Nucleus of NGC 424. *Astrophysical Journal*, 755(2):149, August 2012. .

S. F. Hönig, M. Kishimoto, K. R. W. Tristram, M. A. Prieto, P. Gandhi, D. Asmus, R. Antonucci, L. Burtscher, W. J. Duschl, and G. Weigelt. Dust in the Polar Region as a Major Contributor to the Infrared Emission of Active Galactic Nuclei. *Astrophysical Journal*, 771(2):87, July 2013. .

S. F. Hönig et al. Cosmology with AGN dust time lags-simulating the new VEILS survey. *Monthly Notices of the RAS*, 464(2):1693–1703, Jan 2017. .

Sebastian F. Hönig, Darach Watson, Makoto Kishimoto, and Jens Hjorth. A dust-parallax distance of 19 megaparsecs to the supermassive black hole in NGC 4151. *Nature*, 515(7528):528–530, November 2014. .

I. M. Hook, P. A. Shaver, C. A. Jackson, J. V. Wall, and K. I. Kellermann. The Parkes quarter-Jansky flat-spectrum sample. 2. New optical spectra and redshift measurements. *Astronomy and Astrophysics*, 399:469–487, Feb 2003. .

J. K. Hoormann et al. C IV black hole mass measurements with the Australian Dark Energy Survey (OzDES). *Monthly Notices of the RAS*, 487(3):3650–3663, August 2019. .

J. R. Houck et al. The Infrared Spectrograph (IRS) on the Spitzer Space Telescope. *Astrophysical Journal, Supplement*, 154(1):18–24, September 2004. .

Beth R. Hufnagel and Joel N. Bregman. Optical and Radio Variability in Blazars. *Astrophysical Journal*, 386:473, February 1992. .

Adam R. Ingram and Sara E. Motta. A review of quasi-periodic oscillations from black hole X-ray binaries: Observation and theory. *New Astronomy Review*, 85:101524, September 2019. .

W. Ishibashi and T. J. L. Courvoisier. X-ray variability time scales in active galactic nuclei. *Astronomy and Astrophysics*, 504(1):61–66, September 2009. .

Jedidah C. Isler et al. A Consolidated Framework of the Color Variability in Blazars: Long-term Optical/Near-infrared Observations of 3C 279. *Astrophysical Journal*, 844 (2):107, Aug 2017. .

Željko Ivezić et al. LSST: From Science Drivers to Reference Design and Anticipated Data Products. *Astrophysical Journal*, 873(2):111, March 2019. .

Jon M. Jenkins et al. Overview of the Kepler Science Processing Pipeline. *Astrophysical Journal, Letters*, 713(2):L87–L91, April 2010. .

Michael A. C. Johnson, Poshak Gandhi, Adriane P. Chapman, Luc Moreau, Philip A. Charles, William I. Clarkson, and Adam B. Hill. Prospecting for periods with LSST - low-mass X-ray binaries as a test case. *Monthly Notices of the RAS*, 484(1):19–30, March 2019. .

M. Kalamkar, P. Casella, P. Uttley, K. O'Brien, D. Russell, T. Maccarone, M. van der Klis, and F. Vincentelli. Detection of the first infra-red quasi-periodic oscillation in a black hole X-ray binary. *Monthly Notices of the RAS*, 460(3):3284–3291, August 2016. .

Vishal P. Kasliwal, Michael S. Vogeley, and Gordon T. Richards. Are the variability properties of the Kepler AGN light curves consistent with a damped random walk? *Monthly Notices of the RAS*, 451(4):4328–4345, August 2015. .

Shai Kaspi, Paul S. Smith, Hagai Netzer, Dan Maoz, Buell T. Jannuzi, and Uriel Giveon. Reverberation Measurements for 17 Quasars and the Size-Mass-Luminosity Relations in Active Galactic Nuclei. *Astrophysical Journal*, 533(2):631–649, April 2000. .

Guinevere Kauffmann, Timothy M. Heckman, and Philip N. Best. Radio jets in galaxies with actively accreting black holes: new insights from the SDSS. *Monthly Notices of the RAS*, 384(3):953–971, March 2008. .

Navpreet Kaur and Kiran S. Baliyan. CTA 102 in exceptionally high state during 2016-2017. *Astronomy and Astrophysics*, 617:A59, September 2018. .

Toshihiro Kawaguchi and Masao Mori. Orientation Effects on the Inner Region of Dusty Torus of Active Galactic Nuclei. *Astrophysical Journall*, 724(2):L183–L187, December 2010. .

Toshihiro Kawaguchi and Masao Mori. Near-infrared Reverberation by Dusty Clumpy Tori in Active Galactic Nuclei. *Astrophysical Journal*, 737(2):105, August 2011. .

K. I. Kellermann, R. Sramek, M. Schmidt, D. B. Shaffer, and R. Green. VLA Observations of Objects in the Palomar Bright Quasar Survey. *Astronomical Journal*, 98:1195, October 1989. .

Luke Zoltan Kelley, Laura Blecha, and Lars Hernquist. Massive black hole binary mergers in dynamical galactic environments. *Monthly Notices of the RAS*, 464(3): 3131–3157, January 2017. .

Brandon C. Kelly. Some Aspects of Measurement Error in Linear Regression of Astronomical Data. *Astrophysical Journal*, 665(2):1489–1506, Aug 2007. .

Brandon C. Kelly, Jill Bechtold, and Aneta Siemiginowska. Are the Variations in Quasar Optical Flux Driven by Thermal Fluctuations? *Astrophysical Journal*, 698(1): 895–910, June 2009. .

R. Kessler et al. The Difference Imaging Pipeline for the Transient Search in the Dark Energy Survey. *Astronomical Journal*, 150(6):172, December 2015. .

A. R. King, J. E. Pringle, and M. Livio. Accretion disc viscosity: how big is alpha? *Monthly Notices of RAS*, 376(4):1740–1746, April 2007. .

Anthea L. King et al. Simulations of the OzDES AGN reverberation mapping project. *Monthly Notices of the RAS*, 453(2):1701–1726, October 2015. .

J. G. Kirk, F. M. Rieger, and A. Mastichiadis. Particle acceleration and synchrotron emission in blazar jets. *Astronomy and Astrophysics*, 333:452–458, May 1998.

M. Kishimoto, S. F. Hönig, R. Antonucci, T. Kotani, R. Barvainis, K. R. W. Tristram, and G. Weigelt. Exploring the inner region of type 1 AGNs with the Keck interferometer. *Astronomy and Astrophysics*, 507(3):L57–L60, December 2009. .

Makoto Kishimoto et al. The characteristic blue spectra of accretion disks in quasars as uncovered in the infrared. *Nature*, 454(7203):492–494, July 2008. .

Makoto Kishimoto et al. Evidence for a Receding Dust Sublimation Region around a Supermassive Black Hole. *Astrophysical Journal, Letters*, 775(2):L36, October 2013. .

John Kormendy and Douglas Richstone. Inward Bound—The Search For Supermassive Black Holes In Galactic Nuclei. *Annual Review of Astron and Astrophys*, 33:581, January 1995. .

Shintaro Koshida et al. Reverberation Measurements of the Inner Radius of the Dust Torus in 17 Seyfert Galaxies. *Astrophysical Journal*, 788(2):159, June 2014. .

Andjelka B. Kovačević et al. On possible proxies of AGN light-curves cadence selection in future time domain surveys. *Monthly Notices of the RAS*, 505(4): 5012–5028, August 2021. .

Sz. Kozłowski. Empirical Conversions of Broad-Band Optical and Infrared Magnitudes to Monochromatic Continuum Luminosities for Active Galactic Nuclei. *Acta Astronomica*, 65(3):251–265, September 2015.

Szymon Kozłowski. Revisiting Stochastic Variability of AGNs with Structure Functions. *Astrophysical Journal*, 826(2):118, August 2016. .

Szymon Kozłowski et al. Quantifying Quasar Variability as Part of a General Approach to Classifying Continuously Varying Sources. *Astrophysical Journal*, 708 (2):927–945, January 2010. .

J. H. Krolik, Keith Horne, T. R. Kallman, M. A. Malkan, R. A. Edelson, and G. A. Kriss. Ultraviolet Variability of NGC 5548: Dynamics of the Continuum Production Region and Geometry of the Broad-Line Region. *Astrophysical Journal*, 371:541, April 1991. .

Julian H. Krolik and Mitchell C. Begelman. Molecular Tori in Seyfert Galaxies: Feeding the Monster and Hiding It. *Astrophysical Journal*, 329:702, June 1988a. .

Julian H. Krolik and Mitchell C. Begelman. Molecular Tori in Seyfert Galaxies: Feeding the Monster and Hiding It. *Astrophysical Journal*, 329:702, June 1988b. .

K. Kuijken et al. OmegaCAM: the 16k×16k CCD camera for the VLT survey telescope. *The Messenger*, 110:15–18, December 2002.

Pankaj Kushwaha, Alok C. Gupta, Ranjeev Misra, and K. P. Singh. Multiwavelength temporal variability of the blazar 3C 454.3 during 2014 activity phase. *Monthly Notices of the RAS*, 464(2):2046–2052, January 2017. .

Cedric Lacey and Shaun Cole. Merger rates in hierarchical models of galaxy formation. *Monthly Notices of the RAS*, 262(3):627–649, June 1993. .

Stephanie M. LaMassa, Sabrina Cales, Edward C. Moran, Adam D. Myers, Gordon T. Richards, Michael Eracleous, Timothy M. Heckman, Luigi Gallo, and C. Megan Urry. The Discovery of the First "Changing Look" Quasar: New Insights Into the Physics and Phenomenology of Active Galactic Nucleus. *Astrophysical Journal*, 800 (2):144, February 2015. .

A. Lawrence. Classification of active galaxies and the prospect of a unified phenomenology. *Publications of the ASP*, 99:309–334, May 1987. .

A. Lawrence and I. Papadakis. X-Ray Variability of Active Galactic Nuclei: A Universal Power Spectrum with Luminosity-dependent Amplitude. *Astrophysical Journal, Letters*, 414:L85, September 1993. .

James H. Leftley, Konrad R. W. Tristram, Sebastian F. Hönig, Makoto Kishimoto, Daniel Asmus, and Poshak Gandhi. New Evidence for the Dusty Wind Model: Polar Dust and a Hot Core in the Type-1 Seyfert ESO 323-G77. *Astrophysical Journal*, 862(1):17, July 2018. .

Josef Lense and Hans Thirring. Über den Einfluß der Eigenrotation der Zentralkörper auf die Bewegung der Planeten und Monde nach der Einsteinschen Gravitationstheorie. *Physikalische Zeitschrift*, 19:156, January 1918.

I. J. Lewis et al. The Anglo-Australian Observatory 2dF facility. *Monthly Notices of the RAS*, 333(2):279–299, June 2002. .

Guang-Xing Li, Ye-Fei Yuan, and Xinwu Cao. Emergent Spectra from Disks Surrounding Kerr Black Holes: Effect of Photon Trapping and Disk Self-shadowing. *Astrophysical Journal*, 715(1):623–635, May 2010. .

Xiao-Pan Li et al. Multiband optical-IR variability of the blazar PKS 0537-441. *Journal of Astrophysics and Astronomy*, 39(3):30, April 2018. .

E. P. T. Liang and K. A. Thompson. Models of unsaturated Compton disks around supermassive black holes. *Monthly Notices of the RAS*, 189:421–432, November 1979. .

C. Lidman et al. OzDES multi-object fibre spectroscopy for the Dark Energy Survey: results and second data release. *Monthly Notices of the RAS*, 496(1):19–35, July 2020. .

Tingting Liu et al. A Periodically Varying Luminous Quasar at z = 2 from the Pan-STARRS1 Medium Deep Survey: A Candidate Supermassive Black Hole Binary in the Gravitational Wave-driven Regime. *Astrophysical Journal, Letters*, 803(2):L16, April 2015. .

N. R. Lomb. Least-Squares Frequency Analysis of Unequally Spaced Data. *Astrophysics and Space Science*, 39(2):447–462, February 1976. .

Jennifer M. Lotz, Patrik Jonsson, T. J. Cox, Darren Croton, Joel R. Primack, Rachel S. Somerville, and Kyle Stewart. The Major and Minor Galaxy Merger Rates at z ¡ 1.5. *Astrophysical Journal*, 742(2):103, December 2011. .

LSST Science Collaboration et al. LSST Science Book, Version 2.0. *arXiv e-prints*, art. arXiv:0912.0201, December 2009.

Jianwei Lyu and George H. Rieke. The Dusty Heart of NGC 4151 Revealed by $\lambda \sim$ 1-40 μm Reverberation Mapping and Variability: A Challenge to Current Clumpy Torus Models. *Astrophysical Journal*, 912(2):126, May 2021. .

Jianwei Lyu, G. H. Rieke, and Yong Shi. Dust-deficient Palomar-Green Quasars and the Diversity of AGN Intrinsic IR Emission. *Astrophysical Journal*, 835(2):257, February 2017. .

Jianwei Lyu, George H. Rieke, and Paul S. Smith. Mid-IR Variability and Dust Reverberation Mapping of Low-z Quasars. I. Data, Methods, and Basic Results. *Astrophysical Journal*, 886(1):33, November 2019. .

Yu. E. Lyubarskii. Flicker noise in accretion discs. *Monthly Notices of the RAS*, 292(3): 679–685, December 1997. .

Andrew I. MacFadyen and Miloš Milosavljević. An Eccentric Circumbinary Accretion Disk and the Detection of Binary Massive Black Holes. *Astrophysical Journal*, 672(1): 83–93, January 2008. .

C. L. MacLeod et al. Modeling the Time Variability of SDSS Stripe 82 Quasars as a Damped Random Walk. *Astrophysical Journal*, 721(2):1014–1033, October 2010. .

Elizabeth K. Mahony, Elaine M. Sadler, Scott M. Croom, Ronald D. Ekers, Ilana J. Feain, and Tara Murphy. Is the Observed High-frequency Radio Luminosity Distribution of QSOs Bimodal? *Astrophysical Journal*, 754(1):12, July 2012. .

Amit Kumar Mandal, Suvendu Rakshit, C. S. Stalin, Dominika Wylezalek, Markus Kissler Patig, Ram Sagar, Blesson Mathew, S. Muneer, and Indrani Pal. Dust reverberation mapping of Z229-15. *Monthly Notices of the RAS*, 501(3): 3905–3915, March 2021. .

Amit Kumar Mandal et al. Determination of the size of the dust torus in H0507+164 through optical and infrared monitoring. *Monthly Notices of the RAS*, 475(4): 5330–5337, April 2018. .

V. Manske, Th. Henning, and A. B. Men'shchikov. Flared dust disks and the IR emission of AGN. *Astronomy and Astrophysics*, 331:52–60, March 1998.

Lisheng Mao and Xuemei Zhang. Long-term optical variability properties of blazars in the SDSS Stripe 82. *Astrophysics and Space Science*, 361(10):345, October 2016. .

D. Maoz, H. Netzer, T. Mazeh, S. Beck, E. Almoznino, E. Leibowitz, N. Brosch, H. Mendelson, and A. Laor. High-Rate Active Galaxy Monitoring at the Wise Observatory. III. The Broad-Line Region of NGC 4151. *Astrophysical Journal*, 367:493, February 1991. .

Dan Maoz, Rick Edelson, and Kirpal Nandra. A Possible 100 Day X-Ray-to-Optical Lag in the Variations of the Seyfert 1 Nucleus NGC 3516. *Astronomical Journal*, 119 (1):119–125, January 2000. .

Dan Maoz, Alex Markowitz, Rick Edelson, and Kirpal Nandra. X-Ray versus Optical Variations in the Seyfert 1 Nucleus NGC 3516: A Puzzling Disconnectedness. *Astronomical Journal*, 124(4):1988–1994, October 2002. .

A. P. Marscher and W. K. Gear. Models for high-frequency radio outbursts in extragalactic sources, with application to the early 1983 millimeter-to-infrared flare of 3C 273. *Astrophysical Journal*, 298:114–127, November 1985. .

Alan P. Marscher et al. The inner jet of an active galactic nucleus as revealed by a radio-to-γ-ray outburst. *Nature*, 452(7190):966–969, April 2008. .

Thomas A. Matthews and Allan R. Sandage. Optical Identification of 3C 48, 3C 196, and 3C 286 with Stellar Objects. *Astrophysical Journal*, 138:30, July 1963. .

I. McHardy. X-Ray Variability of AGN and Relationship to Galactic Black Hole Binary Systems. In Tomaso Belloni, editor, *Lecture Notes in Physics, Berlin Springer Verlag*, volume 794, page 203. Springer, 2010. .

I. M. McHardy, E. Koerding, C. Knigge, P. Uttley, and R. P. Fender. Active galactic nuclei as scaled-up Galactic black holes. *Nature*, 444(7120):730–732, December 2006. .

Ian McHardy. EXOSAT observations of variability in active galactic nuclei. *Mem. Societa Astronomica Italiana*, 59:239–260, January 1988.

Nankun Meng, Xiaoyuan Zhang, Jianghua Wu, Jun Ma, and Xu Zhou. Multi-color Optical Monitoring of 10 Blazars from 2005 to 2011. *Astrophysical Journal, Supplement*, 237(2):30, Aug 2018. .

Matthew Middleton and Chris Done. The X-ray binary analogy to the first AGN quasi-periodic oscillation. *Monthly Notices of the RAS*, 403(1):9–16, March 2010. .

Takeo Minezaki et al. Inner Size of a Dust Torus in the Seyfert 1 Galaxy NGC 4151. *Astrophysical Journal, Letters*, 600(1):L35–L38, January 2004. .

Takeo Minezaki et al. Reverberation Measurements of the Inner Radii of the Dust Tori in Quasars. *Astrophysical Journal*, 886(2):150, December 2019. .

E. Morganson et al. The Dark Energy Survey Image Processing Pipeline. *Publications of the ASP*, 130(989):074501, Jul 2018. .

A. Mücke and R. J. Protheroe. A proton synchrotron blazar model for flaring in Markarian 501. *Astroparticle Physics*, 15(1):121–136, March 2001. .

R. F. Mushotzky, R. Edelson, W. Baumgartner, and P. Gandhi. Kepler Observations of Rapid Optical Variability in Active Galactic Nuclei. *Astrophysical Journal, Letters*, 743 (1):L12, December 2011. .

Brant O. Nelson. A Correlated Optical-Infrared Outburst of Markarian 744: The Strongest Evidence Yet for Thermal Dust Reverberation. *Astrophysical Journal, Letters*, 465:L87, July 1996. .

K. I. Nishikawa, P. Hardee, G. Richardson, R. Preece, H. Sol, and G. J. Fishman. Particle Acceleration and Magnetic Field Generation in Electron-Positron Relativistic Shocks. *Astrophysical Journal*, 622(2):927–937, April 2005. .

Hirofumi Noda and Chris Done. Explaining changing-look AGN with state transition triggered by rapid mass accretion rate drop. *Monthly Notices of RAS*, 480(3): 3898–3906, November 2018. .

V. L. Oknyanskij and Keith Horne. Reverberation Radii of Dust Holes in Active Galactic Nuclei. In Bradley M. Peterson, Richard W. Pogge, and Ronald S. Polidan, editors, *Probing the Physics of Active Galactic Nuclei*, volume 224 of *Astronomical Society of the Pacific Conference Series*, page 149, January 2001.

Christopher A. Onken, Laura Ferrarese, David Merritt, Bradley M. Peterson, Richard W. Pogge, Marianne Vestergaard, and Amri Wandel. Supermassive Black Holes in Active Galactic Nuclei. II. Calibration of the Black Hole Mass-Velocity Dispersion Relationship for Active Galactic Nuclei. *Astrophysical Journal*, 615(2): 645–651, November 2004. .

D. E. Osterbrock. Spectrophotometry of Seyfert 1 galaxies. *Astrophysical Journal*, 215: 733–745, August 1977. .

D. E. Osterbrock. Seyfert galaxies with weak broad H alpha emission lines. *Astrophysical Journal*, 249:462–470, October 1981. .

Thornton Page. QSO's, the Brightest Things in the Universe (Quasi-Stellar Objects). *Leaflet of the Astronomical Society of the Pacific*, 9(421):161, January 1964.

N. Palanque-Delabrouille et al. Luminosity function from dedicated SDSS-III and MMT data of quasars in 0.7 ¡ z ¡ 4.0 selected with a new approach. *Astronomy and Astrophysics*, 551:A29, March 2013. .

Anna Pancoast, Brendon J. Brewer, and Tommaso Treu. Geometric and Dynamical Models of Reverberation Mapping Data. *Astrophysical Journal*, 730(2):139, April 2011. .

Anna Pancoast, Brendon J. Brewer, Tommaso Treu, Aaron J. Barth, Vardha N. Bennert, Gabriela Canalizo, Alexei V. Filippenko, Elinor L. Gates, Jenny E. Greene, Weidong Li, Matthew A. Malkan, David J. Sand, Daniel Stern, Jong-Hak Woo, Roberto J. Assef, Hyun-Jin Bae, Tabitha Buehler, S. Bradley Cenko, Kelsey I. Clubb, Michael C. Cooper, Aleksandar M. Diamond-Stanic, Kyle D. Hiner, Sebastian F. Hönig, Michael D. Joner, Michael T. Kandrashoff, C. David Laney, Mariana S. Lazarova, A. M. Nierenberg, Dawoo Park, Jeffrey M. Silverman, Donghoon Son, Alessandro Sonnenfeld, Shawn J. Thorman, Erik J. Tollerud, Jonelle L. Walsh, and Richard Walters. The Lick AGN Monitoring Project 2011: Dynamical Modeling of the Broad-line Region in Mrk 50. *Astrophysical Journal*, 754(1):49, July 2012. .

Anna Pancoast, Brendon J. Brewer, Tommaso Treu, Daeseong Park, Aaron J. Barth, Misty C. Bentz, and Jong-Hak Woo. Modelling reverberation mapping data - II. Dynamical modelling of the Lick AGN Monitoring Project 2008 data set. *Monthly Notices of the RAS*, 445(3):3073–3091, December 2014. .

Christina M. Peters, Gordon T. Richards, Adam D. Myers, Michael A. Strauss, Kasper B. Schmidt, Željko Ivezić, Nicholas P. Ross, Chelsea L. MacLeod, and Ryan

Riegel. Quasar Classification Using Color and Variability. *Astrophysical Journal*, 811 (2):95, October 2015. .

B. M. Peterson and K. Horne. Echo mapping of active galactic nuclei. *Astronomische Nachrichten*, 325(3):248–251, March 2004. .

Bradley M. Peterson. Reverberation Mapping of Active Galactic Nuclei. *Publications of the ASP*, 105:247, March 1993. .

Bradley M. Peterson. *An Introduction to Active Galactic Nuclei*. Cambridge University Press, 1997.

F. Pozo Nuñez et al. The broad-line region and dust torus size of the Seyfert 1 galaxy PGC 50427. *Astronomy and Astrophysics*, 576:A73, April 2015. .

M. Almudena Prieto et al. Unveiling the Central Parsec Region of an Active Galactic Nucleus: The Circinus Nucleus in the Near-Infrared with the Very Large Telescope. *Astrophysical Journal*, 614(1):135–141, October 2004. .

D. Proust. Zwicky 229-15. *International Astronomical Union Circulars*, 5134:2, November 1990.

Brian Punsly, Paola Marziani, Marco Berton, and Preeti Kharb. The Extreme Red Excess in Blazar Ultraviolet Broad Emission Lines. *Astrophysical Journal*, 903(1):44, November 2020. .

David Raban, Walter Jaffe, Huub Röttgering, Klaus Meisenheimer, and Konrad R. W. Tristram. Resolving the obscuring torus in NGC 1068 with the power of infrared interferometry: revealing the inner funnel of dust. *Monthly Notices of the RAS*, 394 (3):1325–1337, April 2009. .

S. I. Raimundo, M. Vestergaard, M. R. Goad, C. J. Grier, P. R. Williams, B. M. Peterson, and T. Treu. Modelling the AGN broad-line region using single-epoch spectra - II. Nearby AGNs. *Monthly Notices of the RAS*, 493(1):1227–1248, March 2020. .

C. M. Raiteri et al. A new activity phase of the blazar ¡ASTROBJ¿3C 454.3¡/ASTROBJ¿. Multifrequency observations by the WEBT and XMM-Newton in 2007-2008. *Astronomy and Astrophysics*, 491(3):755–766, December 2008. .

Michael Ramolla et al. Simultaneous Hα and dust reverberation mapping of 3C 120: Testing the bowl-shaped torus geometry. *Astronomy and Astrophysics*, 620:A137, December 2018. .

Bindu Rani et al. Short-term flux and colour variations in low-energy peaked blazars. *Monthly Notices of the RAS*, 404(4):1992–2017, June 2010. .

M. J. Rees, M. C. Begelman, R. D. Blandford, and E. S. Phinney. Ion-supported tori and the origin of radio jets. *Nature*, 295(5844):17–21, January 1982. .

Martin J. Rees. Black Hole Models for Active Galactic Nuclei. *Annual Review of Astron and Astrophys*, 22:471–506, January 1984. .

G. H. Rieke et al. The Multiband Imaging Photometer for Spitzer (MIPS). *Astrophysical Journal, Supplement*, 154(1):25–29, September 2004. .

Vicente Rodriguez-Gomez et al. The merger rate of galaxies in the Illustris simulation: a comparison with observations and semi-empirical models. *Monthly Notices of the RAS*, 449(1):49–64, May 2015. .

Nicholas P. Ross et al. The SDSS-III Baryon Oscillation Spectroscopic Survey: The Quasar Luminosity Function from Data Release Nine. *Astrophysical Journal*, 773(1): 14, August 2013. .

George B. Rybicki and Alan P. Lightman. *Radiative Processes in Astrophysics*. John Wiley & Sons, 1986.

P. Z. Safna, C. S. Stalin, Suvendu Rakshit, and Blesson Mathew. Long-term optical and infrared variability characteristics of Fermi blazars. *Monthly Notices of the RAS*, 498 (3):3578–3591, November 2020. .

Yu Sakata et al. Long-Term Optical Continuum Color Variability of Nearby Active Galactic Nuclei. *Astrophysical Journal*, 711(1):461–483, March 2010. .

D. B. Sanders, E. S. Phinney, G. Neugebauer, B. T. Soifer, and K. Matthews. Continuum Energy Distributions of Quasars: Shapes and Origins. *Astrophysical Journal*, 347:29, December 1989. .

A. Savage. Identification of southern radio sources. *Monthly Notices of the RAS*, 174: 259–265, February 1976. .

J. D. Scargle. Studies in astronomical time series analysis. II. Statistical aspects of spectral analysis of unevenly spaced data. *Astrophysical Journal*, 263:835–853, December 1982. .

J. Scharwächter, M. A. Dopita, J. Zuther, S. Fischer, S. Komossa, and A. Eckart. Extended Narrow-line Emission in the Bright Seyfert 1.5 Galaxy HE 2211-3903. *Astronomical Journal*, 142(2):43, August 2011. .

Edward F. Schlafly and Douglas P. Finkbeiner. Measuring Reddening with Sloan Digital Sky Survey Stellar Spectra and Recalibrating SFD. *Astrophysical Journal*, 737 (2):103, August 2011. .

Kasper B. Schmidt, Hans-Walter Rix, Joseph C. Shields, Matthias Knecht, David W. Hogg, Dan Maoz, and Jo Bovy. The Color Variability of Quasars. *Astrophysical Journal*, 744(2):147, January 2012. .

M. Schmidt and R. F. Green. Quasar evolution derived from the Palomar bright quasar survey and other complete quasar surveys. *Astrophysical Journal*, 269:352–374, June 1983. .

Carl K. Seyfert. Nuclear Emission in Spiral Nebulae. *Astrophysical Journal*, 97:28, January 1943. .

N. I. Shakura and R. A. Sunyaev. Reprint of 1973A&A....24..337S. Black holes in binary systems. Observational appearance. *Astronomy and Astrophysics*, 500:33–51, June 1973a.

N. I. Shakura and R. A. Sunyaev. Reprint of 1973A&A....24..337S. Black holes in binary systems. Observational appearance. *Astronomy and Astrophysics*, 500:33–51, June 1973b.

Francesco Shankar. AGN sample from Quasar Luminosity Function Codes. Private Communication, 2022.

Francesco Shankar, David H. Weinberg, and Jordi Miralda-Escudé. Self-Consistent Models of the AGN and Black Hole Populations: Duty Cycles, Accretion Rates, and the Mean Radiative Efficiency. *Astrophysical Journal*, 690(1):20–41, January 2009. .

Yue Shen and Luis C. Ho. The diversity of quasars unified by accretion and orientation. *Nature*, 513(7517):210–213, September 2014. .

Yue Shen et al. A Catalog of Quasar Properties from Sloan Digital Sky Survey Data Release 7. *Astrophysical Journal, Supplement*, 194(2):45, June 2011. .

Y. Shi, G. H. Rieke, D. C. Hines, V. Gorjian, M. W. Werner, K. Cleary, F. J. Low, P. S. Smith, and J. Bouwman. 9.7 μm Silicate Features in Active Galactic Nuclei: New Insights into Unification Models. *Astrophysical Journal*, 653(1):127–136, December 2006. .

Yong Shi, George H. Rieke, Paul Smith, Jane Rigby, Dean Hines, Jennifer Donley, Gary Schmidt, and Aleksandar M. Diamond-Stanic. Unobscured Type 2 Active Galactic Nuclei. *Astrophysical Journal*, 714(1):115–129, May 2010. .

A. Sillanpaa, S. Haarala, M. J. Valtonen, B. Sundelius, and G. G. Byrd. OJ 287: Binary Pair of Supermassive Black Holes. *Astrophysical Journal*, 325:628, February 1988. .

T. Simm, M. Salvato, R. Saglia, G. Ponti, G. Lanzuisi, B. Trakhtenbrot, K. Nandra, and R. Bender. Pan-STARRS1 variability of XMM-COSMOS AGN. II. Physical correlations and power spectrum analysis. *Astronomy and Astrophysics*, 585:A129, January 2016. .

J. H. Simonetti, J. M. Cordes, and D. S. Heeschen. Flicker of extragalactic radio sources at two frequencies. *Astrophysical Journal*, 296:46–59, September 1985. .

M. F. Skrutskie et al. The Two Micron All Sky Survey (2MASS). *Astronomical Journal*, 131(2):1163–1183, Feb 2006. .

E. P. Smith, T. M. Heckman, G. D. Bothun, W. Romanishin, and B. Balick. On the Nature of QSO Host Galaxies. *Astrophysical Journal*, 306:64, July 1986. .

Greg A. Smith et al. *AAOmega: a multipurpose fiber-fed spectrograph for the AAT*, volume 5492 of *Society of Photo-Optical Instrumentation Engineers (SPIE) Conference Series*, pages 410–420. International Society for Optics and Photonics, 2004. .

Harlan J. Smith and Dorrit Hoffleit. Light Variations in the Superluminous Radio Galaxy 3C273. *Nature*, 198(4881):650–651, May 1963. .

Krista Lynne Smith, Richard F. Mushotzky, Patricia T. Boyd, Matt Malkan, Steve B. Howell, and Dawn M. Gelino. The Kepler Light Curves of AGN: A Detailed Analysis. *Astrophysical Journal*, 857(2):141, April 2018a. .

Krista Lynne Smith, Richard F. Mushotzky, Patricia T. Boyd, and Robert V. Wagoner. Evidence for an Optical Low-frequency Quasi-periodic Oscillation in the Kepler Light Curve of an Active Galaxy. *Astrophysical Journal, Letters*, 860(1):L10, June 2018b. .

Maddalena Spada, Gabriele Ghisellini, Davide Lazzati, and Annalisa Celotti. Internal shocks in the jets of radio-loud quasars. *Monthly Notices of the RAS*, 325(4): 1559–1570, August 2001. .

Luigi Stella and Mario Vietri. Lense-Thirring Precession and Quasi-periodic Oscillations in Low-Mass X-Ray Binaries. *Astrophysical Journal, Letters*, 492(1): L59–L62, January 1998. .

Luigi Stella, Mario Vietri, and Sharon M. Morsink. Correlations in the Quasi-periodic Oscillation Frequencies of Low-Mass X-Ray Binaries and the Relativistic Precession Model. *Astrophysical Journal, Letters*, 524(1):L63–L66, October 1999. .

Peter B. Stetson. DAOPHOT: A Computer Program for Crowded-Field Stellar Photometry. *Publications of the ASP*, 99:191, March 1987. .

Masahiro Suganuma et al. Reverberation Measurements of the Inner Radius of the Dust Torus in Nearby Seyfert 1 Galaxies. *Astrophysical Journal*, 639(1):46–63, Mar 2006. .

Wei-Hsin Sun and Matthew A. Malkan. Fitting Improved Accretion Disk Models to the Multiwavelength Continua of Quasars and Active Galactic Nuclei. *Astrophysical Journal*, 346:68, November 1989. .

M. Swain et al. Interferometer Observations of Subparsec-Scale Infrared Emission in the Nucleus of NGC 4151. *Astrophysical Journal, Letters*, 596(2):L163–L166, October 2003. .

L. J. Tacconi, R. Genzel, M. Blietz, M. Cameron, A. I. Harris, and S. Madden. The Nature of the Dense Obscuring Material in the Nucleus of NGC 1068. *Astrophysical Journal, Letters*, 426:L77, May 1994. .

Clive Tadhunter and Zlatan Tsvetanov. Anisotropic ionizing radiation in NGC5252. *Nature*, 341(6241):422–424, October 1989. .

M. Tagger and R. Pellat. An accretion-ejection instability in magnetized disks. *Astronomy and Astrophysics*, 349:1003–1016, September 1999.

S. S. Tie et al. A Study of Quasar Selection in the Supernova Fields of the Dark Energy Survey. *Astronomical Journal*, 153(3):107, Mar 2017. .

J. Timmer and M. Koenig. On generating power law noise. *Astronomy and Astrophysics*, 300:707, August 1995.

K. R. W. Tristram et al. Resolving the complex structure of the dust torus in the active nucleus of the Circinus galaxy. *Astronomy and Astrophysics*, 474(3):837–850, November 2007. .

Marie-Helene Ulrich, Laura Maraschi, and C. Megan Urry. Variability of Active Galactic Nuclei. *Annual Review of Astron and Astrophys*, 35:445–502, January 1997. .

C. M. Urry and R. F. Mushotzky. PKS 2155-304 : relativistically beamed synchrotron radiation from a BL Lacertae object. *Astrophysical Journal*, 253:38–46, February 1982. .

C. Megan Urry and Paolo Padovani. Unified Schemes for Radio-Loud Active Galactic Nuclei. *Publications of the ASP*, 107:803, September 1995a. .

C. Megan Urry and Paolo Padovani. Unified Schemes for Radio-Loud Active Galactic Nuclei. *Publications of the ASP*, 107:803, Sep 1995b. .

P. Uttley, I. M. McHardy, and I. E. Papadakis. Measuring the broad-band power spectra of active galactic nuclei with RXTE. *Monthly Notices of the RAS*, 332(1): 231–250, May 2002. .

M. Valtonen, A. Sillanpää, S. Haarala, L. Valtaoja, E. Valtaoja, B. Sundelius, G. G. Byrd, H. Teräsranta, and S. Urpo. OJ:287 as a Binary System. In H. Richard Miller and Paul J. Wiita, editors, *Active Galactic Nuclei*, volume 307, page 68. Springer, 1988. .

M. van der Klis. Quantifying Rapid Variability in Accreting Compact Objects. In G. Jogesh Babu and Eric D. Feigelson, editors, *Statistical Challenges in Modern Astronomy II*, page 321, January 1997.

Daniel E. Vanden Berk et al. The Ensemble Photometric Variability of ~25,000 Quasars in the Sloan Digital Sky Survey. *Astrophysical Journal*, 601(2):692–714, February 2004. .

Jacob T. VanderPlas and Željko Ivezić. Periodograms for Multiband Astronomical Time Series. *Astrophysical Journal*, 812(1):18, October 2015. .

S. Vaughan and P. Uttley. Where are the X-ray quasi-periodic oscillations in active galaxies? *Monthly Notices of the RAS*, 362(1):235–244, September 2005. .

S. Vaughan, R. Edelson, R. S. Warwick, and P. Uttley. On characterizing the variability properties of X-ray light curves from active galaxies. *Monthly Notices of the RAS*, 345 (4):1271–1284, November 2003. .

S. Vaughan, P. Uttley, A. G. Markowitz, D. Huppenkothen, M. J. Middleton, W. N. Alston, J. D. Scargle, and W. M. Farr. False periodicities in quasar time-domain surveys. *Monthly Notices of the RAS*, 461(3):3145–3152, September 2016. .

Billy Vazquez et al. Spitzer Space Telescope Measurements of Dust Reverberation Lags in the Seyfert 1 Galaxy NGC 6418. *Astrophysical Journal*, 801(2):127, March 2015. .

M. Vestergaard. Determining Central Black Hole Masses in Distant Active Galaxies. *Astrophysical Journal*, 571(2):733–752, June 2002. .

Marianne Vestergaard and Bradley M. Peterson. Determining Central Black Hole Masses in Distant Active Galaxies and Quasars. II. Improved Optical and UV Scaling Relationships. *Astrophysical Journal*, 641(2):689–709, April 2006. .

M. Villata and C. M. Raiteri. Helical jets in blazars. I. The case of MKN 501. *Astronomy and Astrophysics*, 347:30–36, July 1999.

Marta Volonteri, Joseph Silk, and Guillaume Dubus. The Case for Supercritical Accretion onto Massive Black Holes at High Redshift. *Astrophysical Journal*, 804(2): 148, May 2015. .

S. J. Wagner, M. Camenzind, O. Dreissigacker, U. Borgeest, S. Britzen, W. Brinkmann, U. Hopp, K. J. Schramm, and J. von Linde. Simultaneous optical and gamma-ray flaring in PKS 0420-014. Implications for emission processes and rotating jet models. *Astronomy and Astrophysics*, 298:688, June 1995.

A. Wandel, B. M. Peterson, and M. A. Malkan. Central Masses and Broad-Line Region Sizes of Active Galactic Nuclei. I. Comparing the Photoionization and Reverberation Techniques. *Astrophysical Journal*, 526(2):579–591, December 1999. .

Jian-Min Wang, Pu Du, Yan-Rong Li, Luis C. Ho, Chen Hu, and Jin-Ming Bai. A New Approach to Constrain Black Hole Spins in Active Galaxies Using Optical Reverberation Mapping. *Astrophysical Journall*, 792(1):L13, September 2014. .

Wayne Webb and Matthew Malkan. Rapid Optical Variability in Active Galactic Nuclei and Quasars. *Astrophysical Journal*, 540(2):652–677, September 2000. .

G. Weigelt et al. VLTI/AMBER observations of the Seyfert nucleus of NGC 3783. *Astronomy and Astrophysics*, 541:L9, May 2012. .

W. F. Welsh. On the Reliability of Cross-Correlation Function Lag Determinations in Active Galactic Nuclei. *Publications of the ASP*, 111(765):1347–1366, November 1999. .

M. W. Werner et al. The Spitzer Space Telescope Mission. *Astrophysical Journal, Supplement*, 154(1):1–9, Sep 2004. .

Richard L. White et al. The FIRST Bright Quasar Survey. II. 60 Nights and 1200 Spectra Later. *Astrophysical Journal, Supplement*, 126(2):133–207, February 2000. .

D. R. Wilkins, E. M. Cackett, A. C. Fabian, and C. S. Reynolds. Towards modelling X-ray reverberation in AGN: piecing together the extended corona. *Monthly Notices of the RAS*, 458(1):200–225, May 2016. .

B. J. Wills and I. W. A. Browne. Relativistic Beaming and Quasar Emission Lines. *Astrophysical Journal*, 302:56, March 1986. .

Beverley J. Wills, D. Wills, Michel Breger, R. R. J. Antonucci, and Richard Barvainis. A Survey for High Optical Polarization in Quasars with Core-dominant Radio Structure: Is There a Beamed Optical Continuum? *Astrophysical Journal*, 398:454, October 1992. .

A. S. Wilson and E. J. M. Colbert. The Difference between Radio-loud and Radio-quiet Active Galaxies. *Astrophysical Journal*, 438:62, January 1995. .

H. Winkler. The extinction, flux distribution and luminosity of Seyfert 1 nuclei derived from UBV(RI)_C aperture photometry. *Monthly Notices of the RAS*, 292(2): 273–288, December 1997. .

Caitlin A. Witt, Maria Charisi, Stephen R. Taylor, and Sarah Burke-Spolaor. Quasars with Periodic Variability: Capabilities and Limitations of Bayesian Searches for Supermassive Black Hole Binaries in Time-Domain Surveys. *arXiv e-prints*, art. arXiv:2110.07465, October 2021.

Jong-Hak Woo and C. Megan Urry. Active Galactic Nucleus Black Hole Masses and Bolometric Luminosities. *Astrophysical Journal*, 579(2):530–544, November 2002. .

Jong-Hak Woo, Yosep Yoon, Songyoun Park, Daeseong Park, and Sang Chul Kim. The Black Hole Mass-Stellar Velocity Dispersion Relation of Narrow-line Seyfert 1 Galaxies. *Astrophysical Journal*, 801(1):38, March 2015. .

Jianghua Wu, Xu Zhou, Jun Ma, and Zhaoji Jiang. Optical variability and colour behaviour of 3C 345. *Monthly Notices of the RAS*, 418(3):1640–1648, December 2011. .

Yuzuru Yoshii, Yukiyasu Kobayashi, Takeo Minezaki, Shintaro Koshida, and Bruce A. Peterson. A New Method for Measuring Extragalactic Distances. *Astrophysical Journal, Letters*, 784(1):L11, March 2014. .

Bing-Kai Zhang, Sen Wang, Xiao-Yun Zhao, Ben-Zhong Dai, and Min Zha. Long-term optical and infrared variability of the BL Lac object PKS 0537 - 441. *Monthly Notices of the RAS*, 428(4):3630–3635, February 2013. .

Bing-Kai Zhang, Xiao-Shan Zhou, Xiao-Yun Zhao, and Ben-Zhong Dai. Long-term optical-infrared color variability of blazars. *Research in Astronomy and Astrophysics*, 15(11):1784, Nov 2015. .

Peng Zhang, Peng-fei Zhang, Jing-zhi Yan, Yi-zhong Fan, and Qing-zhong Liu. An X-Ray Periodicity of $\sim$1.8 hr in Narrow-line Seyfert 1 Galaxy Mrk 766. *Astrophysical Journal*, 849(1):9, November 2017. .

Peng-fei Zhang, Peng Zhang, Neng-hui Liao, Jing-zhi Yan, Yi-zhong Fan, and Qing-zhong Liu. Two Transient X-Ray Quasi-periodic Oscillations Separated by an Intermediate State in 1H 0707-495. *Astrophysical Journal*, 853(2):193, February 2018. .

Zhen-Ya Zheng, Nathaniel R. Butler, Yue Shen, Linhua Jiang, Jun-Xian Wang, Xian Chen, and Jorge Cuadra. SDSS J0159+0105: A Radio-Quiet Quasar with a Centi-Parsec Supermassive Black Hole Binary Candidate. *Astrophysical Journal*, 827 (1):56, August 2016. .

Xin-Lin Zhou, Weimin Yuan, Hai-Wu Pan, and Zhu Liu. Universal Scaling of the 3:2 Twin-peak Quasi-periodic Oscillation Frequencies With Black Hole Mass and Spin Revisited. *Astrophysical Journal, Letters*, 798(1):L5, January 2015. .

S. F. Zhu and Y. Q. Xue. Using Leaked Power to Measure Intrinsic AGN Power Spectra of Red-noise Time Series. *Astrophysical Journal*, 825(1):56, July 2016. .

Ying Zu, C. S. Kochanek, and Bradley M. Peterson. An Alternative Approach to Measuring Reverberation Lags in Active Galactic Nuclei. *Astrophysical Journal*, 735 (2):80, July 2011. .

Ying Zu, C. S. Kochanek, Szymon Kozłowski, and Andrzej Udalski. Is Quasar Optical Variability a Damped Random Walk? *Astrophysical Journal*, 765(2):106, March 2013. .